The Nature and Nurture of a Starburst Supermassive H I Galaxy: HIZOA J0836-43

Michelle E. Cluver

Department of Astronomy
University of Cape Town
South Africa

A dissertation submitted in fulfillment of the Degree of Doctor of Philosophy
UNIVERSITY OF CAPE TOWN

October 2008

Abstract

Hidden behind the Vela Supernova Remnant in the southern Milky Way, the nature of a remarkably massive and luminous galaxy is rapidly coming to light. Only a few years ago, HIZOA J0836-43 was discovered as part of a systematic H I survey of the southern Zone of Avoidance; the enormous H I ($M_{\rm HI} = 7.5 \times 10^{10}\,M_{\odot}$) and dynamical mass in its extended disk revealed it to be one of the most H I-massive galaxies ever found. Since these high-mass systems are rare in the local universe, it is fortuitous that the galaxy is only 148 Mpc away, a distance that allows detailed study of the internal stellar and gas composition. The galaxy, significantly, has unusual properties compared to other H I-massive systems.

Unlike other Malin 1-type gas-rich disks, HIZOA J0836-43 it is not a low surface brightness galaxy. In the near-infrared it has a prominent bulge, indicative of previous star formation, and properties typical of an S0 system. However, radio observations suggest a much later morphological type ($\sim$ Sc) and powerful 20 cm radio emission arising from the central region is evidence of recent star formation.

Due to the galaxy's location in the Zone of Avoidance ($l = 262.48°$, $b = -1.64°$), it is heavily obscured by foreground dust and not observable at optical wavelengths. The star crowding this close to the Galactic plane is also problematic and as a result very little is known about its environment. The only feasible means to probe the origin and nature of this unusual galaxy, given these mitigating factors, is by utilising longer wavelengths within the electromagnetic spectrum, in particular the near-, mid- and far-infrared regime.

This project discerns the nature of HIZOA J0836-43 by analysing spectroscopy and photometry from the *Spitzer Space Telescope*, with ancillary deep, near-infrared photometry using the IRSF in South Africa. The imaging of HIZOA J0836-43 was done with the IRAC and MIPS instruments on *Spitzer*, and the IRS instrument was used to obtain low resolution (IRS-SL) and high resolution spectra (IRS-SH; IRS-LH).

HIZOA J0836-43 is shown to be a luminous infrared starburst galaxy with a star formation rate of $\sim 21\,M_{\odot}\,{\rm yr}^{-1}$, arising from exceptionally strong molecular PAH emission ($L_{7.7\mu{\rm m}} = 1.50 \times 10^{9} L_{\odot}$) and far-infrared emission from cold dust. The galaxy exhibits a weakly rising mid-infrared continuum compared to other starforming galaxies and U/LIRGs (Ultra Luminous Infrared Galaxies). This relative lack of emission from small grains suggests atypical interstellar medium conditions compared to other starbursts. The starburst is concentrated in the central regions of the galaxy. We do not, however, detect significant [Ne V] or [O IV] in the nucleus, which implies an absent or very weak AGN (Active Galactic Nucleus).

The galaxy possesses a prominent bulge of evolved stars and a stellar mass of 4.4(±1.4) $\times 10^{10}\,M_\odot$. HIZOA J0836-43's specific star formation rate implies an early stage of stellar mass building. With its plentiful gas supply, a doubling of stellar mass would occur on a timescale of $\sim$2 Gyr.

The PAH emission of HIZOA J0836-43, compared to its stellar light distribution, suggests extended current star formation in the disk. The disk appears to be warped along the eastern side, possibly the result of a recent tidal interaction, which may have triggered the starburst that is observed today. Compared to local galaxies, HIZOA J0836-43 appears to be a "scaled-up" spiral undergoing inside-out formation, possibly resembling stellar disk building processes at intermediate redshifts.

A further aspect of this project is to explore the greater environment of the galaxy. This work includes a near-infrared survey of a 2.24 square degree area around HIZOA J0836-43. The immediate environment of HIZOA J0836-43 appears sparsely populated by galaxies. These conditions would be favourable for the galaxy to maintain its HI disk. On a larger scale, however, HIZOA J0836-43 appears to lie in a region noticeably underdense in massive or L^* galaxies. It appears plausible that the surrounding large scale structure has influenced the formation and survival of HIZOA J0836-43, allowing it to evolve into the unusual LIRG starburst we observe today with *Spitzer* and the IRSF.

Acknowledgements

First and foremost I would like to thank my two UCT supervisors, Prof. Renée Kraan-Korteweg and Dr Patrick Woudt, for their help and support during my PhD. Without their wisdom and guidance, this dissertation would not have been possible. Renée, thank you for giving me this fantastic opportunity, and expecially for your support over the last few months. I have really enjoyed working with you. Thank you, Patrick, for taking me on as your padawan and for all your input on this project. I have learnt a great deal and benefitted immensely from your keen eye!

A big thank you to my supervisor and IPAC mentor, Tom Jarrett, for making me feel so welcome in Pasadena and for introducing me to the wonders of the mid-infrared. I have learnt such a great deal under your guidance and I really appreciate that you always made time to discuss my work. Thank you for giving me access to your software, the 2MASS XSC and your photometric redshifts. Most importantly, thank you for teaching me that the quest is the quest!

Thank you to Phil Appleton for assisting with my Visiting Graduate Fellowship at IPAC, and also for determining the warm molecular hydrogen estimates in Secton 5.2.3. I really enjoyed our discussions about the massive galaxy and derived much benefit from your wisdom.

Thank you to Baerbel Koribalski for helpful input regarding HIZOA J0836-43 and its observations prior to this work.

I am very grateful to Danny Dale and the SINGS team for data access. Also to Justin Howell and Joe Mazzarella for allowing me to sneak a peak at the fantastic GOALS data set. Justin, thank you for always patiently replying to my volleys of emails.

Thank you to everyone at IPAC for making my visit so great. I had a fantastic time!

To all my friends in the Astronomy Department at UCT, I've really enjoyed working with you and benefitted by knowing each and every one of you. Thank you, especially, for your encouragement over the past few months. I wish you all the best for the future.

In particular I must single out two people. Thank you to Ewald Zietsman for discovering and sharing the "awesomeness" of Python. You are my Python Yoda and I am very grateful to you for sharing your knowledge so willingly. Thank you to Paul Kotze for being my on call IT and Python support, especially in these last few weeks when frustrations ran high. I appreciate you always answering your phone, even at strange hours of the night. Thank you for being such a great friend over these last few months. Your calming influence has meant a lot, as well as the company on weekends and the emergency chilli poppers.

Also, a big thank you to Pamela Wyatt and Kelle Cruz for being such awesome people. I couldn't ask for better friends!

On a personal note, I would like to thank my parents for making it possible for me to get to this point. I am so grateful for everything you have done for me and for always being in my corner. Thank you, Mom, for feeding me and doing my laundry and doing my worrying for me when I had no energy left. Thank you, Dad, for great chats about "stuff" and for introducing me to astronomy and especially Halley's Comet one very cold night in 1986.

Thank you to my sister, Penelope, for being my best friend in the world. I think you are the coolest person ever and I can never thank you enough for being my lifeline when things are rough. There were many times that your phonecall was the highlight of my day and you could make me laugh when no else could.

I would like to thank the NRF for financial support for the duration of this thesis, as well as IPAC/Caltech for financial support through a Visiting Graduate Fellowship.

This publication makes use of data products from the Two Micron All Sky Survey, which is a joint project of the University of Massachusetts and the Infrared Processing and Analysis Center/California Institute of Technology, funded by the National Aeronautics and Space Administration and the National Science Foundation.

Key results of this dissertation have been published as a letter to the Astrophysical Journal, of which I was first author (Cluver et al. 2008).

Contents

List of Figures

Chapter 1

Introduction

Massive galaxies are fundamentally interesting objects; their properties and characteristics have widespread implications for theories of galaxy formation and evolution. The existence of H I-massive disk galaxies is of particular interest to these models. They provide an essential test of theories of disk formation, but are rare in the local universe. Since they are predicted to form recently and be in an early stage of stellar building, they provide a unique laboratory to test theories of galaxy evolution.

HIZOA J0836-43 is one of the most massive H I galaxies ($M_{\mathrm{HI}} = 7.5 \times 10^{10}\, M_{\odot}$) ever found, with a dynamical mass of $1.4{\times}10^{12}\, M_{\odot}$. Despite having an H I mass comparable to Malin 1, it is unlike other H I-massive galaxies in that it is not low surface brightness. Its near-infrared properties appear typical for an S0/Sa system, possessing a prominent bulge and an extended disk. However, radio observations suggest recent active star formation. An understanding of the nature of HIZOA J0836-43 could be of great consequence to current theories in extragalactic astronomy and cosmology. This is, however, hampered by its location behind the southern Milky Way.

This thesis provides a detailed study of the near-, mid- and far-infrared properties of HIZOA J0836-43, probing the nature and current state of the galaxy. A deep near infrared survey of the galaxy's surroundings explores the environment that facilitated the formation of this H I-massive disk galaxy.

1.1 Discovery and First Observations of HIZOA J0836-43

HIZOA J0836-43 was only recently discovered, as it lies in the Vela region of what is termed the "Zone of Avoidance", the part of the sky that is obscured by the Milky Way. It was first noticed during a blind H I study, the H I Parkes Deep Zone of Avoidance (HIZOA) Survey, which was performed using the 64-m Parkes telescope (Kraan-Korteweg et al. 2005; Donley et al. 2005). It was independently identified by the H I Parkes All-Sky Survey, HIPASS (Meyer et al. 2004).

The HIZOA survey sought to probe hidden large-scale structure in the Zone of Avoidance (ZoA) and made observations between 1997 March and 2002 June using the 21-cm multibeam receiver (Staveley-Smith et al. 1996). The survey covered $196^\circ \leq l \leq 52^\circ$ and $|b| \leq 5^\circ$ between $-1200 < cz < 12,700$ $\mathrm{km\,s^{-1}}$ (Kraan-Korteweg et al. 2005; Henning et al. 2005; Donley et al. 2005). The survey was deeper and more sensitive than the southern sky HIPASS survey.

HIZOA J0836-43 is not only the most massive H I galaxy in the HIZOA survey, but also in the southern and northern-extension HIPASS catalogues (Meyer et al. 2004; Wong et al. 2006). Despite having shorter integration times compared to the HIZOA survey, the large area coverage of HIPASS made it more sensitive to the largest H I mass objects. The large H I mass of HIZOA J0836-43 makes it unique within this catalogue, illustrating the importance of its discovery.

The original detection showed a strong signal at $v_{hel} \approx 10,700$ $\mathrm{km\,s^{-1}}$ with a velocity width of ≈ 600 $\mathrm{km\,s^{-1}}$ (see Fig. 1.1), corresponding to $M_{\rm HI} \approx 7 \times 10^{10}\,M_\odot$. The galaxy is located at $l = 262.48^\circ$, $b = -1.64^\circ$ and has no optical counterpart due to the severity of the dust obscuration: the *IRAS*/DIRBE dust maps estimate extinction of $A_V = 7.5$ mag for the region at large (Schlegel et al. 1998).

Follow-up observations (H I line and 20 cm radio continuum) of HIZOA J0836-43 were obtained with the Australia Telescope Compact Array (ATCA) in 2003 February and November, confirming the original detection. Counterparts to the H I detection were looked for in the 2MASS (2 Micron All-Sky Survey) Extended Source Catalogue (Skrutskie et al. 2006), as the near-infrared is less effected by the extinction at this location (2.0, 1.3 and 0.8 magnitudes in J, H and K_s respectively; from Schlegel et al. 1998, using Cardelli et al. 1989). The ATCA observations identified 2MASX J08363600-4337556 as the 2MASS counterpart to the galaxy. In order to improve analysis of the near-infrared (NIR) properties, additional H and K_s data were acquired on the 4-m AAT (Anglo-Australian Telescope) in 2003 April.

The derived global H I and K_s band properties are shown in Table 1.1. The dynamical mass of $1.4{\times}10^{12}\,M_\odot$ is derived from the inclination-corrected ($i \sim 66^\circ$) rotational velocity and the H I radius (see Fig. 1.2). This enormous dynamical mass is comparable to that of the largest disk galaxies found in the local universe. The derived luminosity distance of D_L=148 Mpc is from its recessional velocity, $v_{hel} = 10,689\,\mathrm{km\,s^{-1}}$, using $H_0 = 75\,\mathrm{km\,s^{-1}Mpc^{-1}}$.

Unlike most other giant disk galaxies, however, HIZOA J0836-43 is not a low surface brightness galaxy. Central to its H I gas, the galaxy harbours a stellar disk with a mean K_s-band surface brightness $> 18.0\,\mathrm{mag\,arcsec^{-2}}$. The majority of NIR light arises from a prominent bulge of evolved stars, indicative of previous star building evolution. Intriguingly, the galaxy continues to actively form stars as traced by the centrally-concentrated 20 cm radio continuum emission (see Fig. 1.2), whose intensity implies a high star formation rate (SFR) of $\sim 35\,M_\odot\,\mathrm{yr^{-1}}$ (using the Bell et al. 2003 radio-to-FIR correlation).

The radio and NIR results imply a puzzling mix in Hubble Type morphology: H I observations show a gas-rich, rapidly rotating disk and high SFR indicative of an Sb or Sc type (Kennicutt 1992; Roberts & Haynes 1994), while the NIR light distribution and colours appear to be typical for S0/Sa galaxies (Jarrett 2000; Jarrett et al. 2003). Donley et al. (2006) showed that HIZOA J0836-43 lies on the NIR Tully-Fisher relation, at the extreme high-mass end, suggesting relatively normal mass-to-light properties.

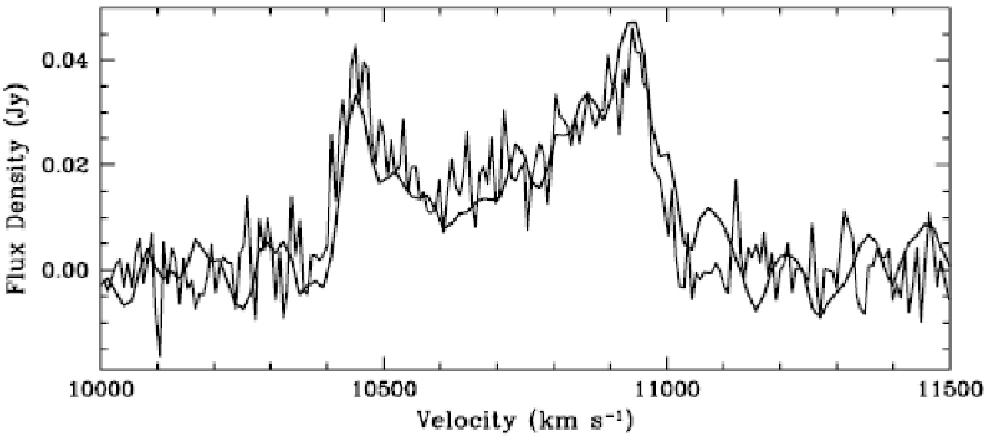

Figure 1.1: Global H I profile of HIZOA J0836-43, as obtained by the Parkes telescope (thick line) and ATCA 750D array (thin line). Image reproduced from Donley et al. (2006).

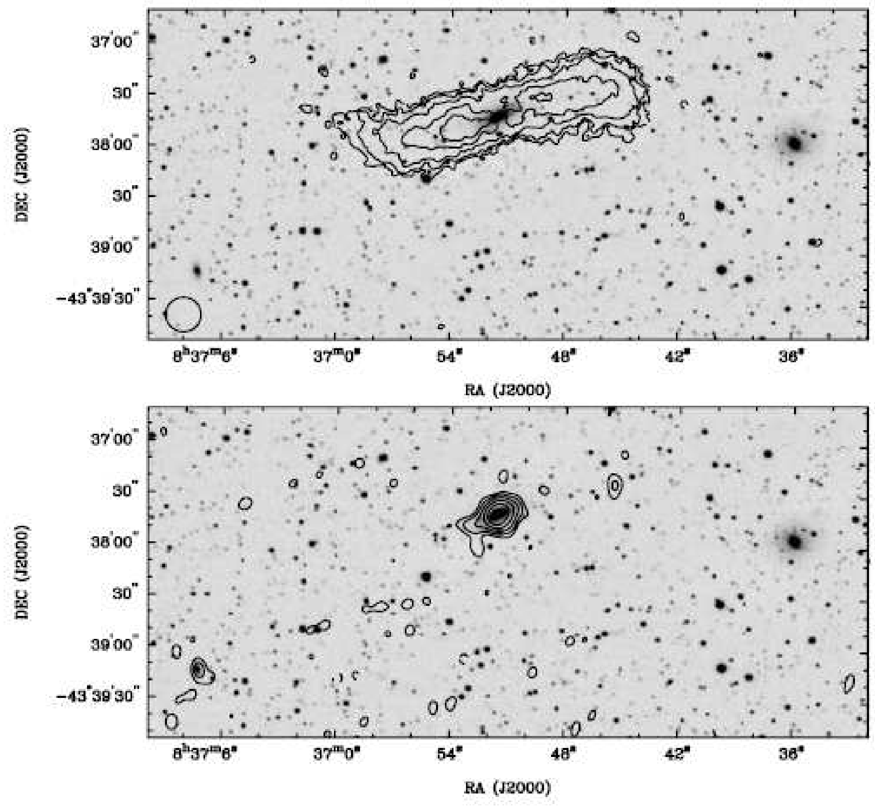

Figure 1.2: Top panel: H I distribution of HIZOA J0836-43 (contours) at a resolution of 20 arcsec overlaid on the AAT K_s-band image. Bottom panel: 20 cm radio continuum image of HIZOA J0836-43 (contours levels are -0.26, 0.26, 0.52, 1.04, 2.08 and 4.16 mJy beam^{-1}) overlaid on same K_s-band image. Two neighbouring galaxies are also visible in the image. Image reproduced from Donley et al. (2006).

Table 1.1: Derived Global H I and K_s properties (from Donley et al. 2006).

Property	Value
Centre Position, α, δ (J2000)	$08^h36^m52.5^s$, $-43^\circ37'51.1''$
Heliocentric velocity, v_{hel}	$10,689$ km s^{-1}
Luminosity Distance, D_L	148 Mpc
H I mass, $M_{\rm HI}$	$7.5\times10^{10}\,M_\odot$
HI radius at 1 $M_\odot$ pc^{-2}	66 kpc
Total Dynamical Mass, $M_{\rm dyn}$	$1.4\times10^{12}\,M_\odot$
w_{20}	610 km s^{-1}
w_{50}	566 km s^{-1}
Intrinsic rotational velocity, v_{rot}	304 km s^{-1}
Inclination angle, i	66°
Absolute magnitude, M_{Ks}	-25.03
Radius corresponding to $\mu_{Ks} = 20$ mag arcsec^{-2}	13.4 kpc
Bulge scale length in K_s	1.7 kpc
Disc scale length in K_s	4.7 kpc
Central Surface Brightness (Bulge) in K_s	14.81 mag arcsec^{-2}
Central Surface Brightness (Disc) in K_s	16.75 mag arcsec^{-2}

1.2 The Large Scale Structure Environment of HIZOA J0836-43

Due to the galaxy's location in the Zone of Avoidance (see Fig. 1.3) very little is known about its environment. This is further complicated by its position behind the Vela Supernova Remnant (see Fig. 1.4) in the Milky Way. Optical surveys are not able to penetrate the foreground extinction and stellar confusion becomes problematic so close to the Galactic Plane (GP). Very deep Parkes Multibeam observations (~ 2 hr integrations) were obtained to search for H I-rich neighbours to HIZOA J0836-43, but did not reveal any additional sources (R. Kraan-Korteweg, private communication). Strong continuum emission from the supernova remnant (SNR) in the area is, however, a negating factor. The NIR images did reveal two close, potential companions to HIZOA J0836-43 (see Fig. 1.2). These will be discussed in more detail in Chapter 6.

Using the 2MASS Extended Source Catalogue and compensating for lower completeness in the K_s band due to extinction, Donley et al. (2006) found that the on-sky distribution of sources in the area suggests an overdensity (by a factor of 5) compared to the mean density of 2MASS galaxies away from the GP. Inspecting the redshift slices of Jarrett (2004), it is possible to speculate about the large-scale structure environment of the galaxy. The galaxy is located at $z = 0.036$ and looking at the $0.03 < z < 0.04$ and $0.04 < z < 0.05$ redshift slices, there appears to be a filamentary structure that points toward the Shapley Concentration. The Shapley supercluster is located at $z \approx 0.048$ and is believed to be the co-dominant contributing factor, along with the "Great Attractor", to the large-scale flow of the Local Group due to distant overdensities (Kocevski & Ebeling 2006). The filament in the redshift slices appears to cross the GP at the position of HIZOA J0836-43 and could explain the projected overdensity of 2MASS extended sources in the region. The possible connection to the Shapley region is also deserving

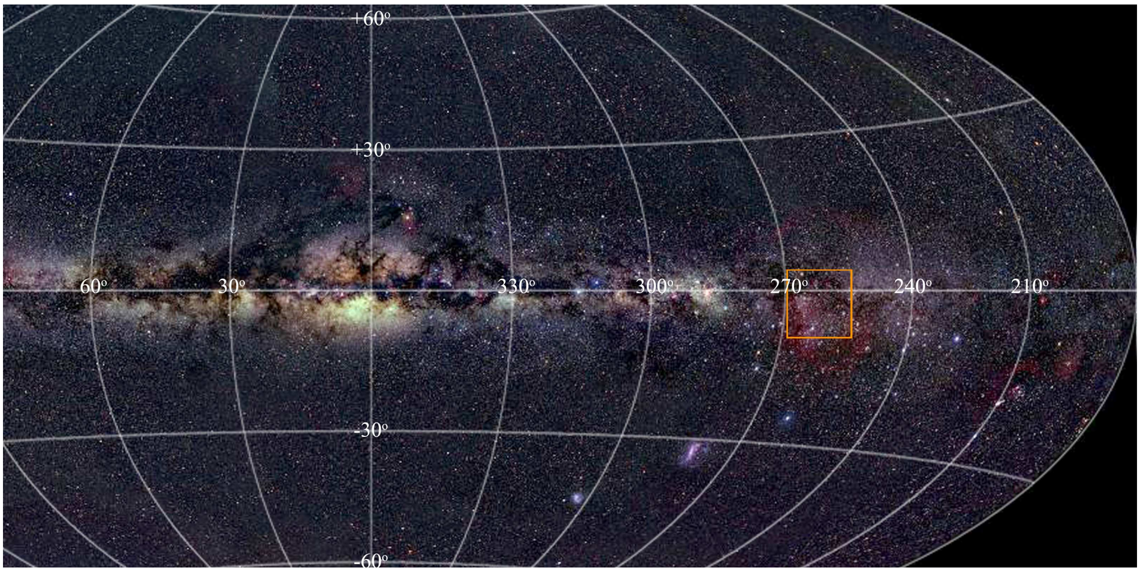

Figure 1.3: The Southern Milky Way as seen at visible wavelengths. The orange box shows the Vela Region where HIZOA J0836-43 is located. Credit: Axel Mellinger.

of further investigation.

Hudson et al. (2004) investigated the streaming motions of galaxy clusters in the SMAC (Streaming Motions of Abell Clusters) sample. This showed a bulk flow of $687 \pm 203\,\mathrm{km\,s^{-1}}$ towards $l = 260° \pm 13°$, $b = 0° \pm 11°$. The fact that the apex of this flow is relatively close to the position of HIZOA J0836-43 could indicate influence from large-scale structure in the region. However, recent work by Erdoğdu et al. (2006a) has used the 2MRS (2MASS Redshift Survey) to estimate the acceleration of the Local Group and finds the direction of the flux dipole to be $l = 251° \pm 12°$, $b = 37° \pm 10°$ and the Local Group velocity relative to the Cosmic Microwave Background to be in the direction of $l = 273° \pm 3°$, $b = 29° \pm 3°$. The discrepancy in the measured optical and infrared dipoles relative to the CMB dipole remains an outstanding problem and will only be resolved when the ZoA is fully mapped to a depth and completeness comparable to the current all-sky surveys (e.g., 2MASS).

1.3 Probing Structure in the Zone of Avoidance

Knowledge of the galaxy distribution in the neighbourhood of HIZOA J0836-43 may provide clues regarding how such massive systems form. Given the galaxy's relative proximity, it is feasible to explore its environment and map the large scale structure in which it is embedded.

Our view of the universe was revolutionised by the advancement of observational techniques and computing power in the last half of the 20th century. In particular, deeper surveys revealed galaxies and clusters to be distributed in a labyrinth of structure on an enormous scale (Fairall 1998 and references within). We see the universe as constructed of filaments and "walls", overdensities and voids, resembling a cosmic web as it takes shape.

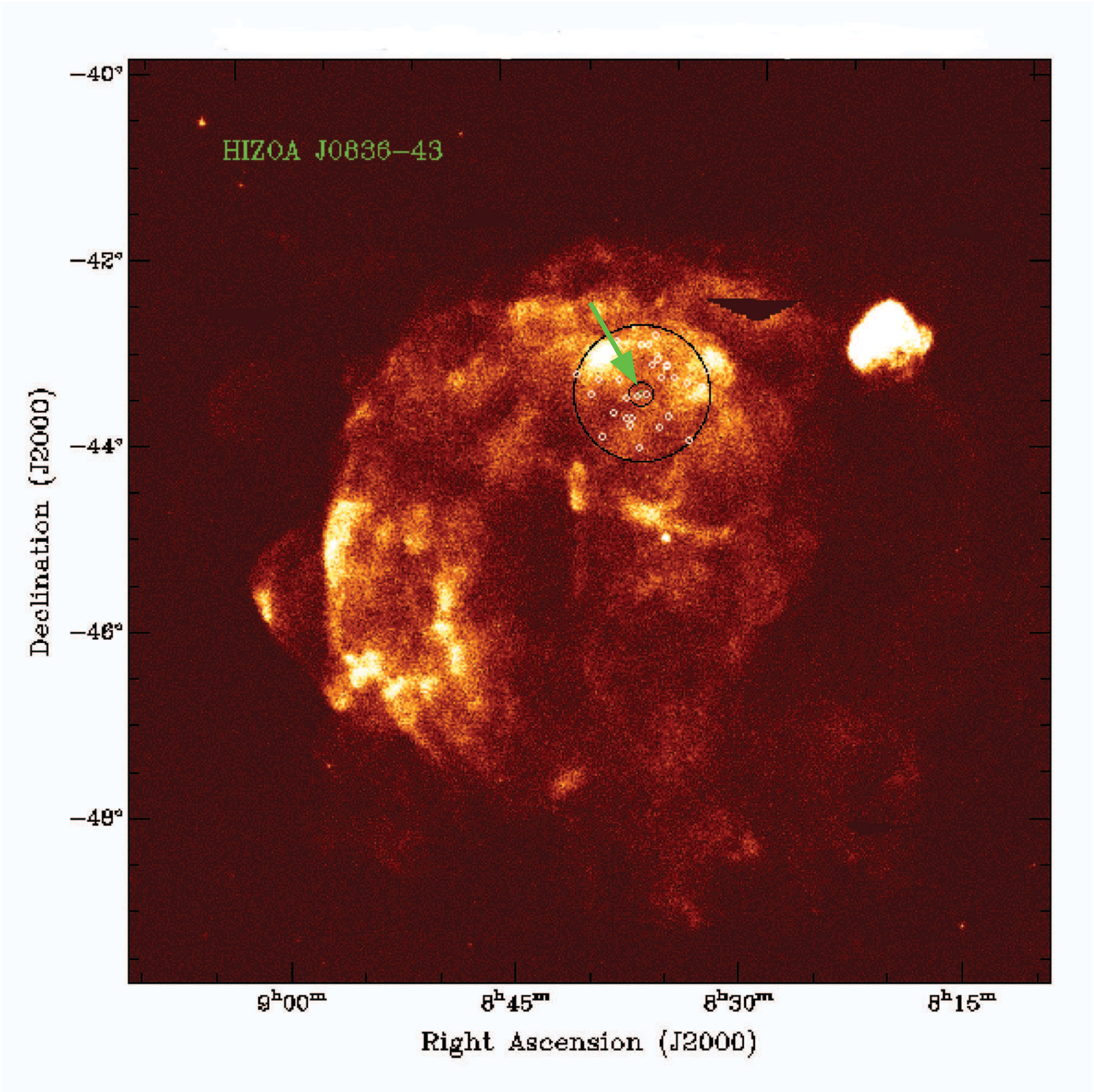

Figure 1.4: ROSAT All-Sky image of the Vela Supernova Remnant (and Puppis A). The small circles show the 2MASS extended sources within 45′ (large circle) of the galaxy. The inner circle shows the three possible 2MASS counterparts to the original detection, the correct one being at the centre of the circle, as shown by the arrow. Image courtesy of B. Koribalski.

Observational cosmology serves as the link between large-scale structure and cosmological models that predict stucture formation in the universe. The observed distribution of galaxies has implications for models of early structure formation and the subsequent formation and evolution of galaxies. Knowledge of the distribution and clustering of galaxies is also crucial for understanding the dynamics in the local universe. The peculiar motion of the Local Group and the velocity distribution of galaxies in the local universe is intimately connected to the baryon mass underlying the galaxy light. The observed dynamics, in conjunction with the mass

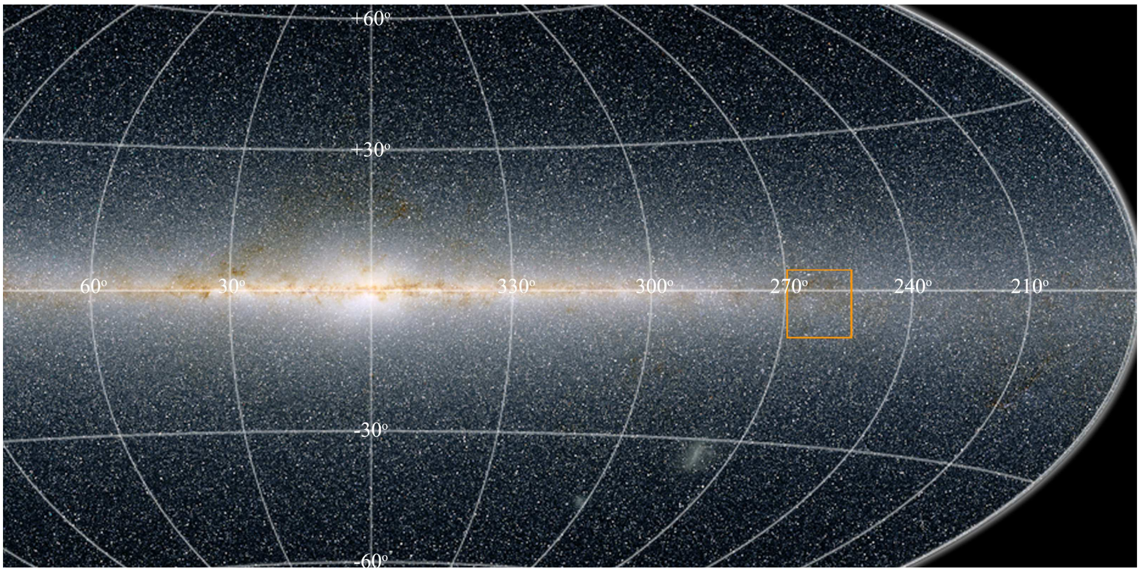

Figure 1.5: The Southern Milky Way as seen in the near-infrared window. The orange box shows the Vela Region where HIZOA J0836-43 is located. Image credit: T. Jarrett and the 2MASS team.

distribution of galaxies and clusters, constrains models of the properties and nature of dark matter and dark energy.

It is therefore essential to have a complete map of large-scale matter distribution. This is, however, complicated by the foreground stellar confusion and dust obscuration of the Milky Way galaxy which blocks ~20% of the entire optical sky; a substantial band that has traditionally been avoided in extragalactic studies. But the Zone of Avoidance cannot be left unexplored. Significant extragalactic structures are located behind it. Foremost amongst these is a mass concentration behind the southern Milky Way. The so-called "Great Attractor" is located at $l \sim 320°$, $b \sim 0°$ and $cz \sim 4000\,\mathrm{km\,s^{-1}}$ (Kolatt et al. 1995). A deep optical survey found Abell 3627 (the Norma Cluster), located at $l = 325°$, $b = -7°$ and $cz = 4848\,\mathrm{km\,s^{-1}}$, comparable to the Coma Cluster in mass and richness (Kraan-Korteweg et al. 1996). This is the likely density peak within the potential well of the Great Attractor (Woudt 1998).

Similarly, dedicated multiwavelength studies have for decades gradually been uncovering the hidden structures behind the ZoA in an effort to probe the local mass-density field (see Kraan-Korteweg 2005 and Kraan-Korteweg & Lahav 2000, for reviews). This in combination with improved all-sky surveys, notably 2MASS (see Fig. 1.5), provides an ever-increasingly complete picture of the observable universe (Jarrett 2004; Huchra et al. 2005; Erdoğdu et al. 2006b).

We aim to probe a relatively modest area of the the ZoA centred on $l = 262.48°$, $b = -1.64°$, the location of HIZOA J0836-43, by means of a deep NIR survey.

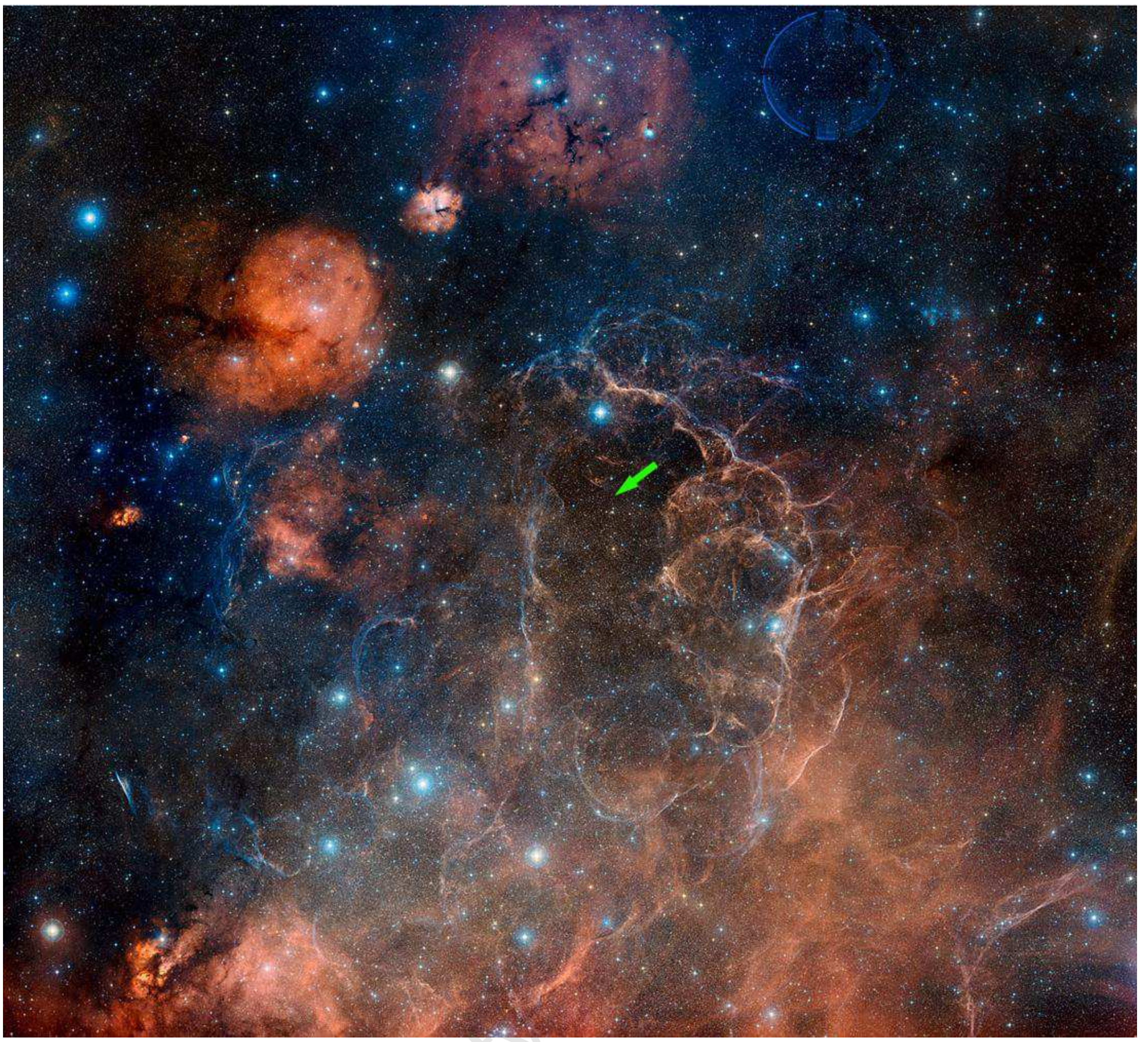

Figure 1.6: Optical image of the Vela Supernova Remnant showing the location of HIZOA J0836-43 (green arrow). Credit: Davide De Martin.

1.4 Unveiling HIZOA J0836-43 and its environment

At optical wavelengths, HIZOA J0836-43 is completely hidden by the Milky Way (see Fig. 1.6). At infrared wavelengths we can penetrate the foreground obscuration while simultaneously studying the star formation properties of the galaxy. Information gained at different infrared wavelengths will allow an understanding of the galaxy's composition and evolutionary state. It also enables effective probing of the galaxy's environment to determine the possible influence of neighbouring galaxies and large-scale structure.

Deep NIR observations of HIZOA J0836-43 (J, H and K_s) will probe the evolved stellar population and provide information about previous star formation. The NIR has been used effectively as a direct measure of the total stellar mass, which is for the most part independent of galaxy colors or Hubble Type. In this study we will be using the K_s integrated flux to estimate the stellar mass of HIZOA J0836-43, which in combination with the current star formation rate and the available reservoir of gas, provides clues as to the star building history and future of the galaxy.

Mid-infrared (MIR), $3 < \lambda < 50$ μm, emission arises from a variety of sources. Apart from continuum emission from starlight, there is emission from the ionised interstellar medium, transiently heated dust grains, PAHs (Polycyclic Aromatic hydrocarbons), thermal radiation from dust grains and non-thermal (synchrotron) radiation. Hence, infrared observations enable the study of the composition and physical processes that drive the evolution of the interstellar medium (ISM), including stellar feedback mechanisms.

MIR emission arises from dust "reprocessing" of starlight: dust absorbs ultraviolet radiation from massive stars and is heated, then re-radiates this energy as thermal emission at mid-infrared wavelengths. At wavelengths $\lambda < 5$ μm the "old" stellar light is sampled, as well as continuum emission from hot ($T \gtrsim 300$ K) dust. The $\lambda > 6$ μm emission is sensitive to warm ($T \gtrsim 100$ K) dust and emission from PAHs found between $6 - 17\,\mu$m. PAHs produce broad emission bands in the MIR and are linked to ongoing or recent star formation (Léger & Puget 1984; Allamandola et al. 1985). However, PAH molecules are destroyed by intense radiation such as found in H II regions and close to AGN (Genzel et al. 1998) and therefore provide a sensitive diagnostic for determining the dominant processes contributing to observed MIR emission.

The far-infrared (FIR), $\lambda > 50$ μm, emission arises from cold ($T \sim 10 - 50$ K) dust as blackbody radiation, and as IRAS first showed, is ubiquitous throughout the Milky Way and galaxies alike. The cold dust component of the ISM is by far the most important mechanism for absorbing starlight. It is therefore an effective measure of the current star formation in dust-rich systems, as the ultraviolet and blue radiation from massive stars is absorbed by the interstellar grains and re-radiated as thermal continuum (Cram et al. 1998). We will show that HIZOA J0836-43 emits the bulk of its bolometric luminosity in the FIR, the primary reason that it belongs to the class of Luminous Infrared Galaxies or LIRGS (discussed in Section 1.6).

Both ISO and *Spitzer* have shown that mid-infrared spectroscopy is essential for decoding the internal physics that drives galaxy evolution. This probes ionised gas (that produce fine-structure lines), molecular gas (eg. warm molecular hydrogen) and dust grains in the interstellar medium. Warm (small graphite) dust grains produce the mid-infrared continuum longwards of $10\,\mu$m, while large dust grains (silicates) give rise to absorption features (Chiar & Tielens 2006). Large molecules produce emission and absorption features, in particular the bending and stretching modes of PAHs (Puget & Léger 1989). Using the mid-infrared diagnostics available, we can determine the likelihood of an AGN being present and the composition of the interstellar medium. This will provide crucial insight into the morphology and nature of the galaxy (Chapter 5).

Near- and mid-infrared observations of the region around HIZOA J0836-43 will probe its immediate environment and reveal any interactions with neighbouring galaxies, as well as potential members of a cluster or group. An extended near-infrared survey of the greater environment of HIZOA J0836-43 will assist in determining the density of its environment and its connection to the large-scale structure of the region (Chapter 6).

1.5 H I-massive Disk Galaxies in the Local Universe

Massive galaxies play a key role in understanding the fundamental cosmology of our universe, from galaxy formation to their subsequent evolution. Advances in multi-wavelength observations and numerical simulations (Springel et al. 2005) have created compelling support for a cold dark matter (CDM) dominated universe where structure forms hierarchically (Press & Schechter 1974; White & Rees 1978). Thus, the galaxies we see today are products of the coalescence and subsequent evolution of low mass systems which have formed earlier (Kauffmann et al. 1993; Bertschinger 1998; Cole et al. 2000).

The ΛCDM-predicted, as well as observed luminosity functions show an exponential decline in the volume density of very massive galaxies (eg. Blanton et al. 2003), a fundamental result consistent with the timescales required for such massive systems to virialise (Lynden-Bell 1967). Massive early type galaxies are a direct consequence of hierarchical structure growth, although models tend to overpredict the population between $z = 1$ and $z = 0$ (Renzini 2007). As such, questions regarding their formation and nature remain (Conselice et al. 2007). In the more general case, models of formation and evolution of galaxy disks continue to mature (Stringer & Benson 2007) as observations provide new insights and constraints (Bell 2008). Present day disk galaxies, especially low surface brightness (LSB) galaxies, are predicted to form as recently as $z \leq 1$ (Mo et al. 1998). Massive, gas-rich disk galaxies in the local universe are both rare in number and young in star building evolution (Mao et al. 1998). Because of their relatively pristine phase in evolution, they provide an ideal laboratory to test models of merging, star formation and disk stability through detailed observations.

Giant low surface brightness galaxies are defined as having disks with a low central surface brightness, $\mu_B(0) \geq 23.0$ mag arcsec^{-2} (Bothun et al. 1997). They exhibit a wide range of properties, but the majority are late-type disks with large gas mass fractions (Schombert et al. 1992). They have low star formation rates, $\leq 0.1\ M_\odot\,\mathrm{yr}^{-1}$ (van den Hoek et al. 2000), but with modest bursts (eg. Vallenari et al. 2005) and low metallicities (McGaugh 1994). They appear rich in neutral hydrogen (O'Neil et al. 2004), deficient in H II (de Naray et al. 2004) and very few exhibit molecular emission (Das et al. 2006). Their characteristics imply that they are underevolved and that their evolution differs from high surface brightness disks (McGaugh 1994).

An extreme example is the giant low surface brightness (LSB) galaxy Malin 1, discovered serendipitously by Bothun et al. (1987). Its size is unprecedented, with an H I radius of $\sim$ 110 kpc and $M_{\mathrm{HI}} = 6.8 \times 10^{10}\ M_\odot$ (Pickering et al. 1997). Yet the galaxy has a low star formation rate (Impey & Bothun 1989) and is undergoing only quiescent evolution.

Donley et al. (2006) compare the properties of four massive H I galaxies, HIZOA J0836-43, UGC 1752, Malin 1 and UGC 4288. Other than comparably large H I mass, they have large gas disks and high rotational velocities in common. HIZOA J0836-43 is the closest at a distance of D_L = 148 kpc, compared to Malin 1 at approximately twice this distance. In H I mass, Malin

1 and HIZOA J0836-43 are similar ($M_{\rm HI} \approx 6.8 \times 10^{10}\,M_\odot$ and $7.5 \times 10^{10}\,M_\odot$ respectively), but Malin 1 has a larger H I diameter (∼220 kpc vs ∼130 kpc). It is interesting to note that these H I-massive galaxies all exhibit prominent bulges, indicative of previous star formation.

Despite the similarities that exist between these H I-rich disks, HIZOAJ0836-43 appears fundamentally different. It is not an LSB galaxy and instead has a visibly extended stellar disk and a high star formation rate from newly forming, massive stars. The galaxy, therefore, shows intriguingly contradictory properties. A near-infrared analysis indicates an early-type morphology (S0-Sa), whereas H I observations show a rapidly rotating, gas-rich galaxy with a star formation rate ($\sim 35\,M_\odot\,{\rm yr}^{-1}$) suggestive of a late-type spiral (Sb-Sc). The far-reaching implications of studying one of the most H I-massive systems known, potentially undergoing a starburst, has motivated a broader, in-depth study of HIZOA J0836-43 and its environment.

1.6 Luminous Infrared Galaxies in the Local Universe

The high star formation rate of HIZOA J0836-43, as calculated from its radio continuum flux (Donley et al. 2006), suggests that the galaxy will likely be very luminous in the mid- and far-infrared. Indeed it will be shown that it is infrared bright, emitting the bulk of its light at long wavelengths. Luminous Infrared Galaxies (LIRGS) are galaxies with a total infrared luminosity ($8 - 1000\,\mu$m) of $> 10^{11} L_\odot$. Their high luminosities are believed to be the result of emission from dust heated by starbursts and active galactic nuclei (Sanders & Mirabel 1996).

LIRGS in the local universe are relatively rare and generally associated with galaxy mergers and dynamically strong interactions, as evidenced by their disturbed morphologies (see eg. Farrah et al. 2001; Ishida 2004). Additionally, local LIRGS appear to uniformly contain bars (Wang et al. 2006) and exhibit centrally concentrated star formation (Sanders & Mirabel 1996). As we show in this work, HIZOA J0836-43 is unusual for a local LIRG in that it does not exhibit dynamical disruption, nor is the presence of a bar discerned from the imaging, and in addition its star formation is extended beyond the nuclear region.

1.7 In this thesis

The intriguingly contradictory properties of HIZOA J0836-43 and its dissimilarity compared to other H I-massive disks compels intensive study of this galaxy and its environment. The only feasible means to probe the origin and nature of HIZOA J0836-43, given its location in the Zone of Avoidance and its active phase in star building, is by utilising the infrared regime.

To this end my thesis embodies a dual approach. The first phase comprises a mid- and far-infrared study of the galaxy using the *Spitzer Space Telescope*. The aim is to uncover the nature of this unusual galaxy using the unique capabilities of high resolution spatial imaging and spectroscopy from the telescope. We use these observations, in combination with deep NIR imaging, to study the stellar, PAH and dust emission of the galaxy. This enables us to probe the past and current star formation and the overall stellar evolution of the galaxy. MIR spectral diagnostics of fine-structure and molecular emission lines enable us to probe the composition and conditions of the interstellar medium. We also explore which mechanisms of MIR emission dominate in HIZOA J0836-43, their impact on the system as a whole and their evolutionary implications.

The second phase of this project entails a near-infrared (J, H and K_s) survey of a 2.2 square degree area surrounding the HIZOA J0836-43, using the Infrared Survey Facility (IRSF) in Sutherland, South Africa. As the near-infrared is relatively unaffected by obscuring dust, this enables exploration of the greater environment of the galaxy. The aim is to find clues regarding the formation and evolution of HIZOA J0836-43 by looking at the distribution of galaxies in this region. It is plausible that the large-scale structure and velocity fields in the neighbourhood of the galaxy influenced its formation.

In Chapter 2, I describe the observations and data reduction procedures used for the *Spitzer* and IRSF data obtained of the galaxy and its surroundings.

Chapter 3, 4 and 5 focus on the results and analysis of the data obtained for HIZOA J0836-43. We discuss the implications of the galaxy's properties and relevance to current theories of galaxy formation and evolution.

Chapter 6 reports results of the survey of the environment of HIZOA J0836-43, including the distribution of the galaxies and their photometric redshifts. This chapter also discusses this distribution and its connection to the large-scale structure around HIZOA J0836-43.

The main results and conclusions from this research are presented in Chapter 7. The results from this dissertation provide new insights for understanding the formation and evolution of HIZOA J0836-43.

I outline planned future observations relating to HIZOA J0836-43 and its environment in Chapter 8.

Throughout this dissertation we adopt a cosmology with a matter density parameter $\Omega_m = 0.3$, a cosmological constant $\Omega_\Lambda = 0.7$ and a Hubble constant of $H_0 = 75\ \mathrm{km\,s^{-1}\,Mpc^{-1}}$.

Chapter 2

Observations and Data Reductions

In this chapter we discuss the observations and reductions of the data obtained from the *Spitzer Space Telescope* and the InfraRed Survey Facility (IRSF) telescope situated at Sutherland, South Africa. Ancillary data products are from the Parkes Radio Telescope and the Australia Telescope Compact Array (ATCA), both facilities of the ATNF (Australia Telescope National Facility).

2.1 Observations

2.1.1 The *Spitzer Space Telescope*

The *Spitzer Space Telescope* is a 0.85-m infrared telescope with three cryogenically-cooled instruments onboard. It was launched on 2003 August 25 into an Earth-trailing, heliocentric orbit. Its primary cryogen-cooled mission is to last until early 2009, beyond which it will continue operating in a "warm" capacity ($\sim 15\,$K) reduced to its $3.6\,\mu$m and $4.5\,\mu$m imaging capabilities.

The *Spitzer* observations presented here are derived from the *Spitzer* GO-3 programme 30914 (*Spitzer* Study of the Hidden Galaxy HIZOAJ0836-43), whose Principal Investigator is R.C. Kraan-Korteweg. A total of 12.1 hours of *Spitzer* observing time was allocated to this programme. Of this, 3.4 hours were devoted to IRAC (Infrared Array Camera) observations, 3.0 hours on the MIPS (Multiband Imaging Photometer for Spitzer) instrument and $\sim$ 6 hours of spectroscopy with the IRS (InfraRed Spectrograph).

IRAC Observations

IRAC is an infrared camera consisting of four detector arrays which perform broadband photometry at 3.6, 4.5, 5.8 and $8.0\,\mu$m, respectively, with a full width at half maximum (FWHM) beam of $\sim 2''$ for all four channels (see Fazio et al. 2004 for instrument details). The bandwidths of the four channels are $0.75\,\mu$m, $1.01\,\mu$m, $1.42\,\mu$m and $2.93\,\mu$m corresponding to central wavelengths of $\lambda = 3.53\,\mu$m, $\lambda = 4.46\,\mu$m, $\lambda = 5.67\,\mu$m and $\lambda = 7.70\,\mu$m respectively. The 3.6 and $4.5\,\mu$m detectors are InSb arrays and the 5.8 and $8.0\,\mu$m are Si:As detectors. Each detector has a field of view of $5.2' \times 5.2'$ and a pixel scale of $1.2''$. IRAC observations were carried out on 2007 May

6 by means of two AORs (Astronomical Observation Requests) mapping two adjacent regions with a ~10% overlap. A total area of $\sim 23' \times 28'$ was imaged. Observations were done in High Dynamic Range (HDR) Mode and mapped two 9×5 grid maps with steps of $154'' \times 154''$ (as shown in Fig. 2.1) with integrations of $5 \times 4 \times 12 = 240\,\mathrm{s}$ (i.e. 5 small random dithers with $4 \times \frac{1}{2}$ image overlaps for redundancy), each frame integrating for 12 s.

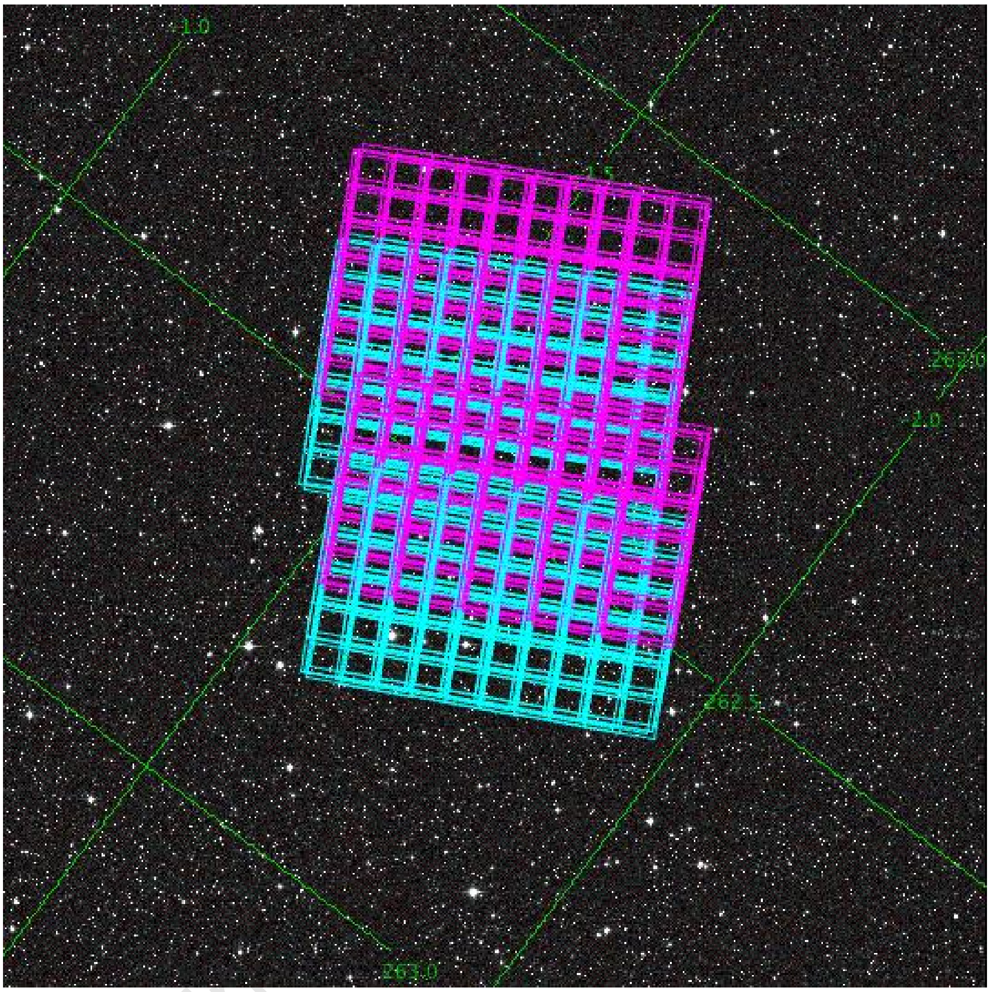

Figure 2.1: IRAC AOR showing the $3.6\,\mu$m and $5.8\,\mu$m coverage in blue and the $4.5\,\mu$m and $8.0\,\mu$m coverage in magenta. The background image is a 2MASS K_s band image centred on $l = 262.5°$ and $b = -1.64°$. The green grid shows spacings of 0.5° in Galactic coordinates. The image has a field of view (FoV) of $\sim 2.2° \times 2.2°$.

MIPS Observations

MIPS observations were taken on 2007 April 12. The MIPS instrument performs imaging at 24, 70 and $160\,\mu$m simultaneously using three separate detector arrays with angular resolutions of $\sim 6''$, $\sim 18''$ and $\sim 40''$, respectively (instrument details are given in Rieke et al. 2004). The

24 μm detector consists of a Si:As array and the 70 and 160 μm detectors are Ge:Ga arrays. The bandwidths of the arrays are ~ 5, 19 and 35 μm for the 24, 70 and 160 μm detectors respectively, with central wavelengths of $\lambda = 23.7\,\mu$m, $\lambda = 71\,\mu$m and $\lambda = 156\,\mu$m. The 24 μm band has a field of view of $5.4' \times 5.4'$ and a pixel scale of $2.55''$. The 70 and 160 μm bands have $5.2' \times 2.6'$ and $5.3' \times 2.1'$ fields of view, respectively. The 70 μm band pixel size is $9.98''$ and the 160 μm detector has a $16.0'' \times 18.0''$ pixel size. Observations were done in $\frac{1}{2}$ degree medium scan mode with $80''$ cross-scan steps ($\frac{1}{4}$ array), totalling 21 scans $\times \frac{1}{2}$ degree (see Fig. 2.2). The total area imaged was $\sim 30' \times 38'$. An integration time of 42 s was used for the 24 μm and 70 μm observations. The 160 μm integration time was 4.2 s. The 160 μm observation is necessarily short to avoid saturation of the array due to the sky background in this wavelength regime. The extended emission in the Milky Way can saturate the array in < 10 s.

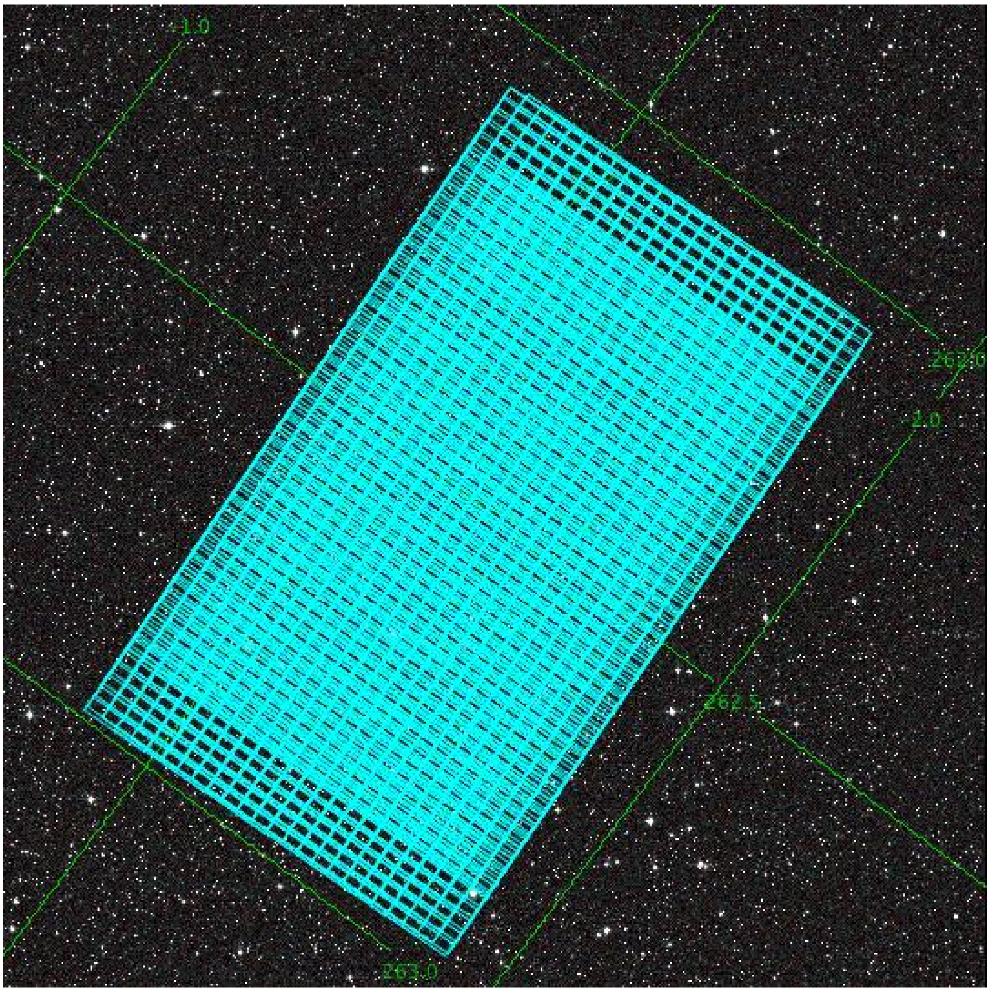

Figure 2.2: MIPS AOR showing the 24 μm coverage (which is also the 70 μm and 160 μm coverage). The background image is the same as shown in Fig. 2.1, with a FoV of $\sim 2.2° \times 2.2°$.

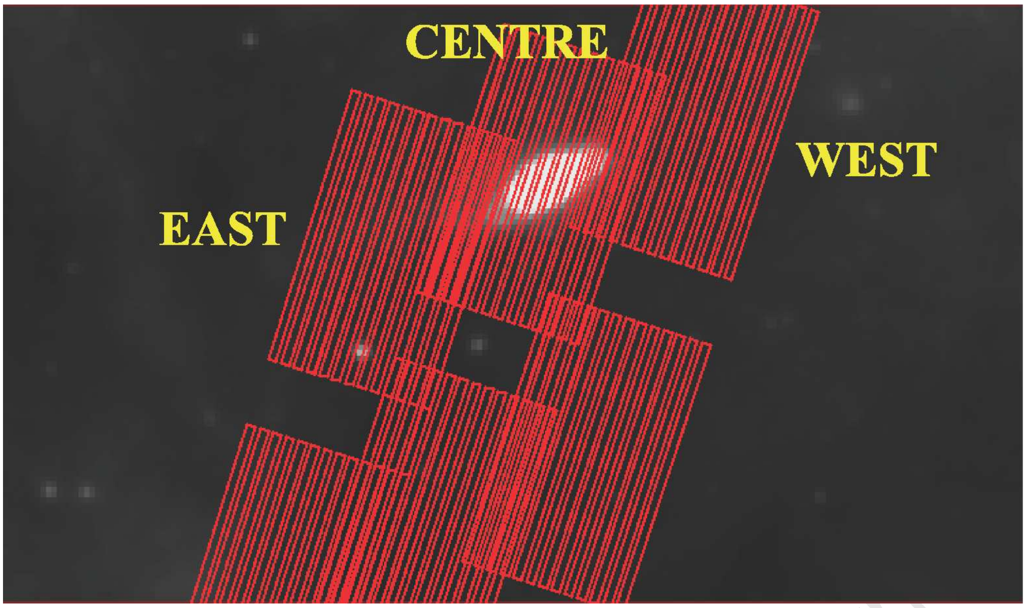

Figure 2.3: SL observations of the massive galaxy shown on the IRAC-8 μm image. The upper maps are (from left to right) East, Centre and West maps. The lower maps correspond to the background observations done by means of a $26''$ step parallel to the slit. The FoV of the image is $\sim 2.4' \times 1.5'$. North is up, east is to the left.

IRS Observations

Spectroscopy of HIZOA J0836-43 was obtained on 2007 May 2 and 3 using the IRS instrument, see Houck et al. (2004) for instrument specifications. Observations were done in low-resolution "mapping mode" (short-low; SL) covering $5-14\,\mu$m as well as high-resolution "staring mode" covering $10-20\,\mu$m (short-high; SH) and $19-38\,\mu$m (long-high; LH). The modules have pixel sizes of $1.8''$, $2.3''$ and $4.5''$ for SL, SH and LH, respectively. SL mode was used to map the entire disk, whereas SH and LH observations were of the nucleus only. The short wavelength detectors (SL and SH) are Si:As arrays and the LH detector is a Si:Sb array.

The SL mode has a low spectral resolution, $R\,(=\lambda/\Delta\lambda) \sim 64-128$. This set of observations consists of three separate mappings: Centre, East and West of the galaxy nucleus. Each consists of 3×60 s integrations with 13×3 perpendicular (to the slit) steps (see Fig. 2.3). Each map covers $0.4' \times 0.7'$ corresponding to a $\frac{1}{3}$ of the disk. The adjacent maps fully cover the disk with $\sim$10% overlap. In this way the entire disk is mapped. Outlier regions for background subtraction were observed using the same mapping scheme, but with a $26''$ step parallel to the slit. Given the large area covered by the spectral maps and the galaxy's location in the Milky Way, sky observations are crucial for accurate flux determination of the extracted spectrum.

High resolution ($R \sim 650$) SH (see Fig. 2.4) and LH (see Fig. 2.5) data consist of 4×30 s and 4×14 s on source "stares" respectively, with $\frac{1}{3}$ slit offset between orders. A region $\sim 1'$ south of the galaxy without confusion from foreground Galactic emission was observed for background subtraction. Sky removal is not only crucial for accurate flux calibration, but also helps alleviate the effects of rogue pixels in the array. When the sky observation is subtracted at the BCD (Basic Calibrated Data) level, the majority of the hot or anomalous pixels are brought into range.

2.1.2 The Infrared Survey Facility (IRSF)

The IRSF is a 1.4-m telescope situated at the South African Astronomical Observatory in Sutherland, South Africa. The telescope is a F/10 altazimuth Cassegrain design and has a $7.7' \times 7.7'$ field of view making it a good survey telescope. NIR observations were performed using the SIRIUS (Simultaneous InfraRed Imager for Unbiased Survey) camera (Nagayama et al. 2003) mounted on the IRSF.

SIRIUS consists of three 1024×1024 HgCdTe (HAWAII) arrays with a J, H and K_s broadband filter respectively. This allows for the simultaneous acquisition of photometry in all three bands with a pixel scale of $0.45''$. The bands are centered on $\lambda = 1.25$ μm (J Band), $\lambda = 1.65$ μm (H Band) and $\lambda = 2.15$ μm (K_s Band) with bandwidths of 0.17 μm, 0.30 μm and 0.32 μm respectively. Table 2.1 shows a comparison between 2MASS and the IRSF/SIRIUS observations. The improved resolution in combination with longer exposure times makes it the ideal instrument with which to probe the ZoA.

Table 2.1: Comparison of 2MASS and SIRIUS.

	2MASS	SIRIUS
wavelength (μm)	1.25 1.65 2.16	1.25 1.63 2.14
bands	J H K_s	J H K_s
pixels	256	1024
pixel scale	$2''$	$0.45''$
field of view	$8.5'$	$7.8'$
limiting magnitudes	16.5 15.8 15.0	18.9 18.3 17.3 [a]
integration times	total 7.8 s	total 600 s
telescope	1.3 m	1.4 m

[a] Kandori et al. (2005)

The bandpasses of the 2MASS filters differ slightly from the SIRIUS bands. Kato et al. (2007) derived transformations between the IRSF/SIRIUS and 2MASS systems. This was done using the 2MASS Point Source Catalogue and IRSF data of their Magellanic Cloud survey, as well as other sources. Assuming a linear relation between the IRSF/SIRIUS and 2MASS magnitudes and the 2MASS colours, they determine the following conversion equations:

$$J_{\mathrm{IRSF}} = J_{\mathrm{2MASS}} - (0.043 \pm 0.002)(J - H)_{\mathrm{2MASS}} + (0.018 \pm 0.000)$$

$$H_{\mathrm{IRSF}} = H_{\mathrm{2MASS}} - (0.015 \pm 0.002)(J - H)_{\mathrm{2MASS}} + (0.024 \pm 0.000)$$

$$K_{s\,\mathrm{IRSF}} = K_{s\,\mathrm{2MASS}} - (0.010 \pm 0.001)(J - K_s)_{\mathrm{2MASS}} + (0.014 \pm 0.001)$$

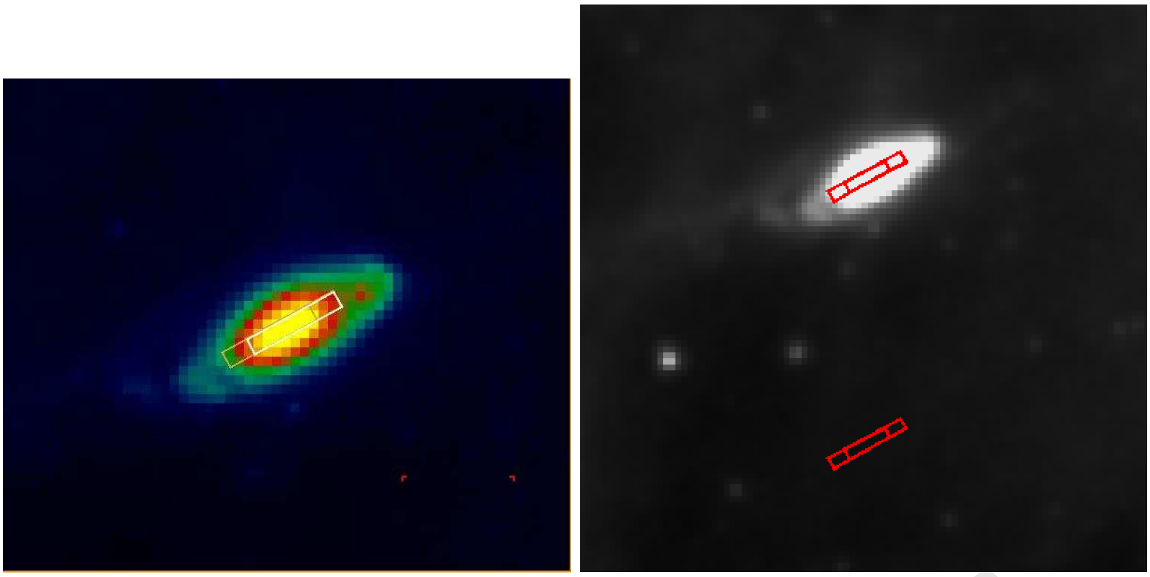

(a) (b)

Figure 2.4: (a) The SH observation of the galaxy showing both orders (the second order is offset by $\frac{1}{3}$ of the slit. The FoV of the image is $\sim$ 1′× 1′. (b) The "on" source slit positions and "off" source observations (south of the galaxy) used for background subtraction. The FoV of the image is $\sim$ 2′× 2′. Background image is IRAC-8 μm for both. North is up, east is to the left.

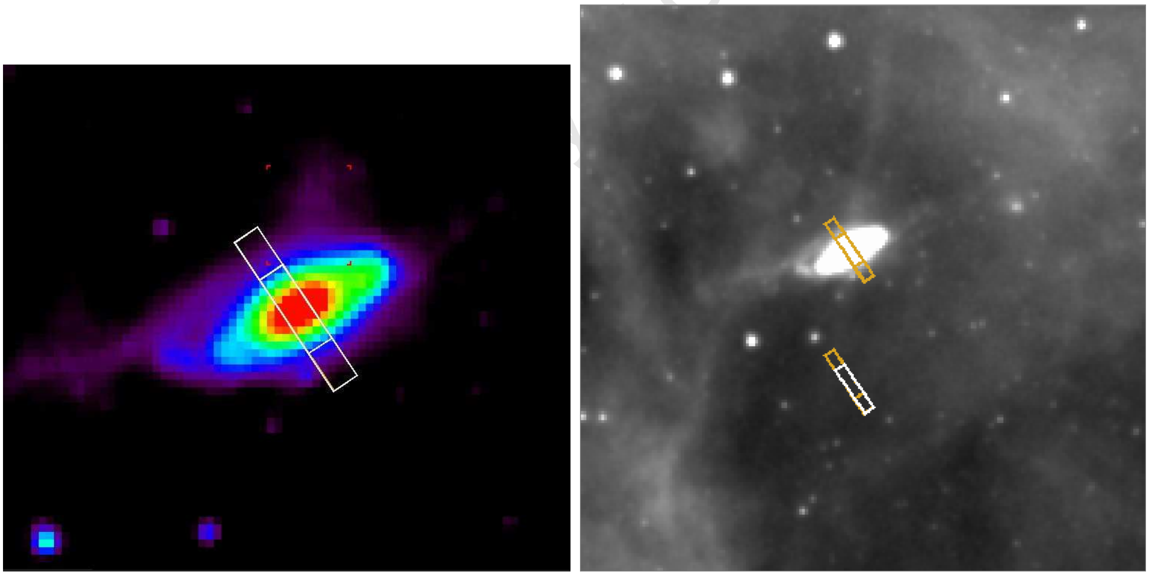

(a) (b)

Figure 2.5: (a) The LH observation of the galaxy showing both orders (the second order is offset by $\frac{1}{3}$ of the slit. The FoV of the image is $\sim$1′× 1′. (b) The "on" source slit positions and "off" source observations (south of the galaxy) used for background subtraction. The FoV of the image is $\sim$ 4′× 4′. Background image is IRAC-8 μm for both. North is up, east is to the left.

These relations hold for $0 \lesssim J - H \lesssim 4.5$ and $0 \lesssim H - K_s \lesssim 2.7$.

IRSF Observations

Imaging of the massive galaxy was done on 2006 April 11. Survey data of the environment of HIZOA J0836-43 were obtained over 20 nights in 2006 March and April. Observations consisted of a 13×13 grid of fields centred on HIZOA J0836-43 (field $+0+0$). Fields are numbered to indicate their distance from HIZOA J0836-43 (see Fig. 2.6). If the first number is positive, the field is located East of the galaxy, and vice versa. If the second number is positive, the field is located North of the galaxy, and vice versa.

Two fields ($+3+1; -5-3$) were reobserved on 2007 April 5 due to poor image quality and a further three ($+3-1, +4-1$ and $+5-1$) reobserved on 2008 March 19 because of a telescope pointing error in the initial observations. Details of the observations (date of observation, central pointing, seeing and magnitude zeropoints) are shown in Table A.1 in the Appendix section. An area of $\sim 1.6^\circ \times 1.6^\circ$ was imaged, covering a total area of 2.24 square degrees. Observations consisted of twenty-five dithered 24 s exposures giving a total exposure time of 600 s. For the 169 fields, the mean seeing was $1.3'' \pm 0.2''$ in the K_s band. The dithering technique is used to generate a sky image, as well as minimise the effect of bad pixels in the array.

2.2 Data Reduction

2.2.1 The *Spitzer Space Telescope*

IRAC and MIPS Instruments

Primary data reductions were done by the *Spitzer* Science Center (SSC) pipeline version S16.1.0. which delivers Basic Calibrated Data (BCD) which are flat-fielded and dark subtracted. The pipeline also flux calibrates the BCDs according to a system of celestial standards which are measured at regular intervals. Astrometric calibration is also done by the pipeline and has an accuracy of $\sim 0.3''$ for the IRAC bands ($\sim \frac{1}{4}$ pixel size).

The resulting IRAC BCDs were cleaned using artifact correction codes written by Sean Carey (available as SSC contributed software). This code corrected muxbleed (a saturation artifact), column pulldown/pullup and electronic banding. The SSC-developed MOPEX[1] tool was used to perform background matching, pointing refinement, distortion corrections, apply cosmic ray rejection and mosaic the individual BCDs to produce a final science image. MIPS BCDs were similarly combined using MOPEX and the MIPS 24 μm mosaic corrected for the first frame effect. IRAC spatial resolution is $\sim 2''$ in all bands and MIPS achieves $6''$, $18''$ and $40''$ at 24 μm, 70 μm and 160 μm respectively.

---

[1] See http://ssc.spitzer.caltech.edu/postbcd/mopex.html

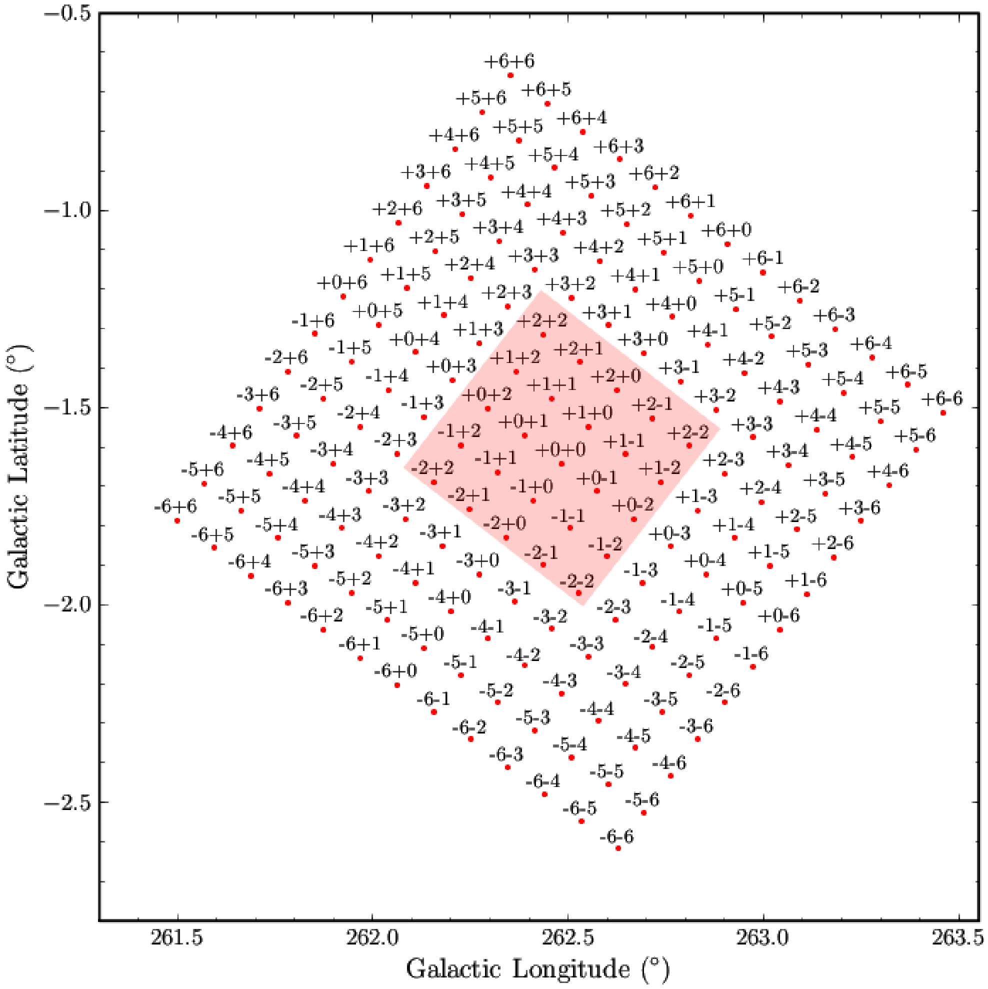

Figure 2.6: Grid showing fields observed as part of the HIZOA J0836-43 survey. The grid is centred on the HIZOA J0836-43 and the area covered is 2.24 square degrees (∼ 1.6°× 1.6°). The fields that overlap with the Spitzer footprint are shown in the pink shaded region (from $-2-2$ to $+2+2$).

IRS Instrument

For the IRS data, BCDs were produced by the *Spitzer* Science Center (SSC) IRS pipeline version S16.1.0. The spectral reductions done by the pipeline include wavelength and flux calibration, ramp fitting, dark subtraction and droop and linearity corrections. The wavelength calibration is done using observations of standard stars, some bright extragalactic regions, and in the case of SH, Titan. The wavelength calibration is accurate within $\approx \frac{1}{5}$ of a resolution element (2 pixels). BCDs of the sky background (or outrigger) observations for the SL Centre and West maps were used for background removal by means of the SSC tool, CUBISM[2] (Smith et al. 2007). Contaminating emission in the East outrigger observation resulted in a combination of East, West and Centre outriggers being used for the East map background removal. This was done by smoothing the East background observations and subtracting them from the original frames to create an image of the East array's behaviour (with the background removed). The Centre and West outriggers were smoothed and combined to produce a background map. This was added to the East array map to make a suitable background for CUBISM. Outlier rejection was done using the CUBISM algorithm, as well as by visual inspection.

SH and LH data were reduced by subtracting median-combined background images (from the "off" position observations) and carefully cleaning individual BCDs of bad pixels and cosmic ray contamination. CUBISM was used to combine the BCDs into a spectral cube and further outliers found by visually inspecting the cube.

2.2.2 The Infrared Survey Facility (IRSF)

The data was processed using the SIRIUS pipeline[1] which makes use of IRAF[2] scripts to perform the standard procedures of infrared image reduction.

For each exposure time, 10 dark frames (i.e. the cold shutter is closed) are taken and these are then averaged and combined. The dark current correction is then applied by subtracting this combined frame from the image frame. A flat field correction is then applied.

The flat field correction is done by choosing pairs of frames with suitable counts that are not saturated and in the linear regime (i.e. counts less than 6000 in J and H and less than 4500 in K_s) and a level difference of about 2000 counts. Difference images are created by subtracting the fainter frame from the brighter frame for each pair. The image is normalised using the median value across the frame and all the normalised frames are in turn median-combined. The raw frames are divided by this resultant frame.

The pipeline generates sky fields which will be subtracted from the object frames once the dark current and flat field corrections have been applied. The sky fields are generated from the same set of dithered exposures that are combined to form an object frame. This 'self-sky' technique is accomplished by median combining the frames. In this way the contributions from objects in the frame are eliminated and only the contribution from the sky background is left.

This "sky" image (a superflat) is subtracted from each dithered exposure. The individual frames are aligned and median-combined to generate a final "deep" image, free from bad pixels and with the sky background variation removed. Due to the dithering process, the final images are generally slightly larger than the 1024 × 1024 pixels of the arrays.

Using IRAF, the final images were astrometrically-calibrated using the 2MASS PSC (Skrutskie et al. 2006), simultaneously solving for plate scale and rotation. No distortion corrections were

---

[2] See http://ssc.spitzer.caltech.edu/archanaly/contributed/cubism/index.html

[1] see http://optik2.mtk.nao.ac.jp/%7Eyas /pipeline/manual/pipeline020510-e.html

[2] IRAF is distributed by the National Optical Astronomy Observatory, which is operated by the Association of Universities for Research in Astronomy, Inc., under cooperative agreement with the National Science Foundation

applied. The 2MASS astrometric accuracy is $\sim 0.08''$ and the typical RMS (root mean square) for the astrometric calibration is $\sim 0.2''$ (approximately half the pixel scale).

The photometric calibration zero points were determined using 2MASS PSC fluxes as the flux calibration scale. This is achieved using circular apertures to capture the total flux of the point sources and comparing the 2MASS and instrumental fluxes. Since we use an aperture large enough to capture the total flux of the point sources, we do not require a seeing correction. Sources that were bright enough to be saturated were eliminated from the fit, as well as sources fainter than a signal-to-noise (S/N) of 10, corresponding to 15.3, 15.0 and 14.5 mag in J, H and K_s respectively. The distribution of magnitude zeropoints in the J, H and K_s bands are shown in Fig. 2.7. The mean values are 20.80 ± 0.05 mag, 20.95 ± 0.06 mag and 20.17 ± 0.05 mag for J, H and K_s, respectively. The uncertainty due to the 2MASS absolute calibration is $2-3\%$, while the typical Poisson uncertainty is $\sim 5-6\%$. The conversion between 2MASS and IRSF/SIRIUS, given in Section 2.1.2, corresponds to a $\sim 0.01-0.03$ mag difference in the two photometric systems respectively. Given the calibration and typical measurement uncertainties combined with the large uncertainty in extinction at the location of this survey ($\sim 10\%$), we do not incorporate this colour transformation.

2.3 *Spitzer* and IRSF Photometry of HIZOA J0836-43

Galaxy photometry was performed using a matched elliptical aperture for the IRAC and MIPS $24\,\mu$m bands in order to capture the total light of the galaxy with minimal confusion from foreground emission. The aperture was determined using the IRAC-$3.6\,\mu$m image, the optimal window to determine the shape and size of the galaxy after factoring in sensitivity, angular resolution and extinction mitigation. A symmetric isophotal fit of the light distribution down to the 1σ level was performed. This determined an elliptical aperture with a semi-major axis radius (a) of $39.35''$, axis ratio (b/a) of 0.42 ± 0.02 and a position angle of $110 \pm 10°$ (east from north). Foreground contaminating stars were masked and replaced by the isophotal value of the source. Stars were masked to well beyond the radius of the background annulus. The local background was determined from the median pixel value distribution within an annulus, well beyond the extent of the galaxy, once sources and outliers were trimmed. Accurate background subtraction in combination with the isophotal fit of the light distribution negates the effect of sky variations. This procedure is illustrated in Figs. 2.8 and 2.9.

We calculate the disk inclination from the position angle using the formula from Dale et al. (2007):

$$\cos^2 i = \frac{(b/a)^2 - (b/a)^2_{\text{int}}}{1 - (b/a)^2_{\text{int}}}$$

where $(b/a)^2_{\text{int}} \simeq 0.2$ for Sbc and earlier morphological types (Dale et al. 1997). This gives an inclination of $i = 67.9° \pm 1.5°$ (in the IRAC $3.6\,\mu$m band), in good agreement with the value of $\sim 66°$ obtained by Donley et al. (2006).

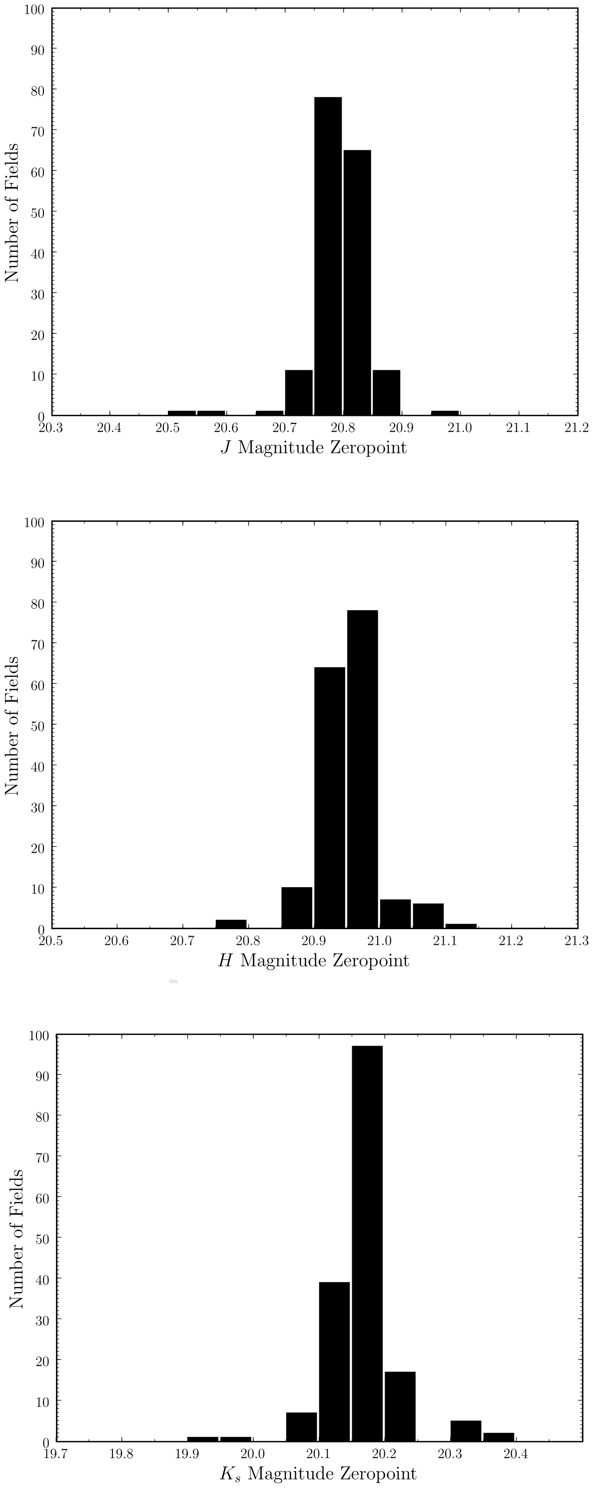

Figure 2.7: Distribution of magnitude zeropoints for the J, H and K_s bands

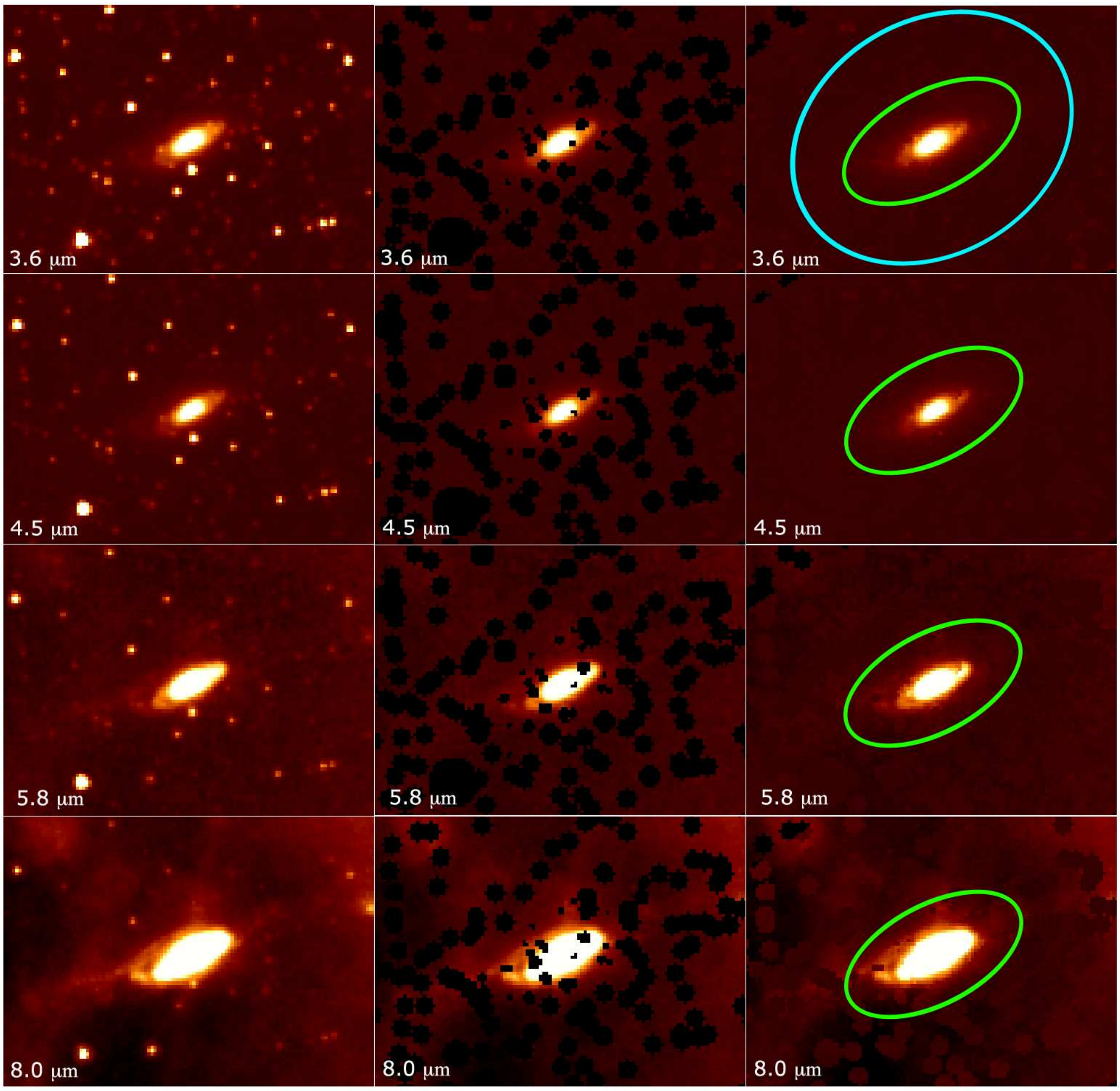

Figure 2.8: Left Panel: Raw postage stamps (FoV of $\sim 95'' \times 95''$) of HIZOA J0836-43 in the four IRAC bands ($3.6\,\mu$m, $4.5\,\mu$m, $5.8\,\mu$m and $8.0\,\mu$m). Middle Panel: The images after stars have been masked. Right Panel: Elliptical aperture (green) and width of background annulus (cyan) overlaid on the images, after pixels have been replaced.

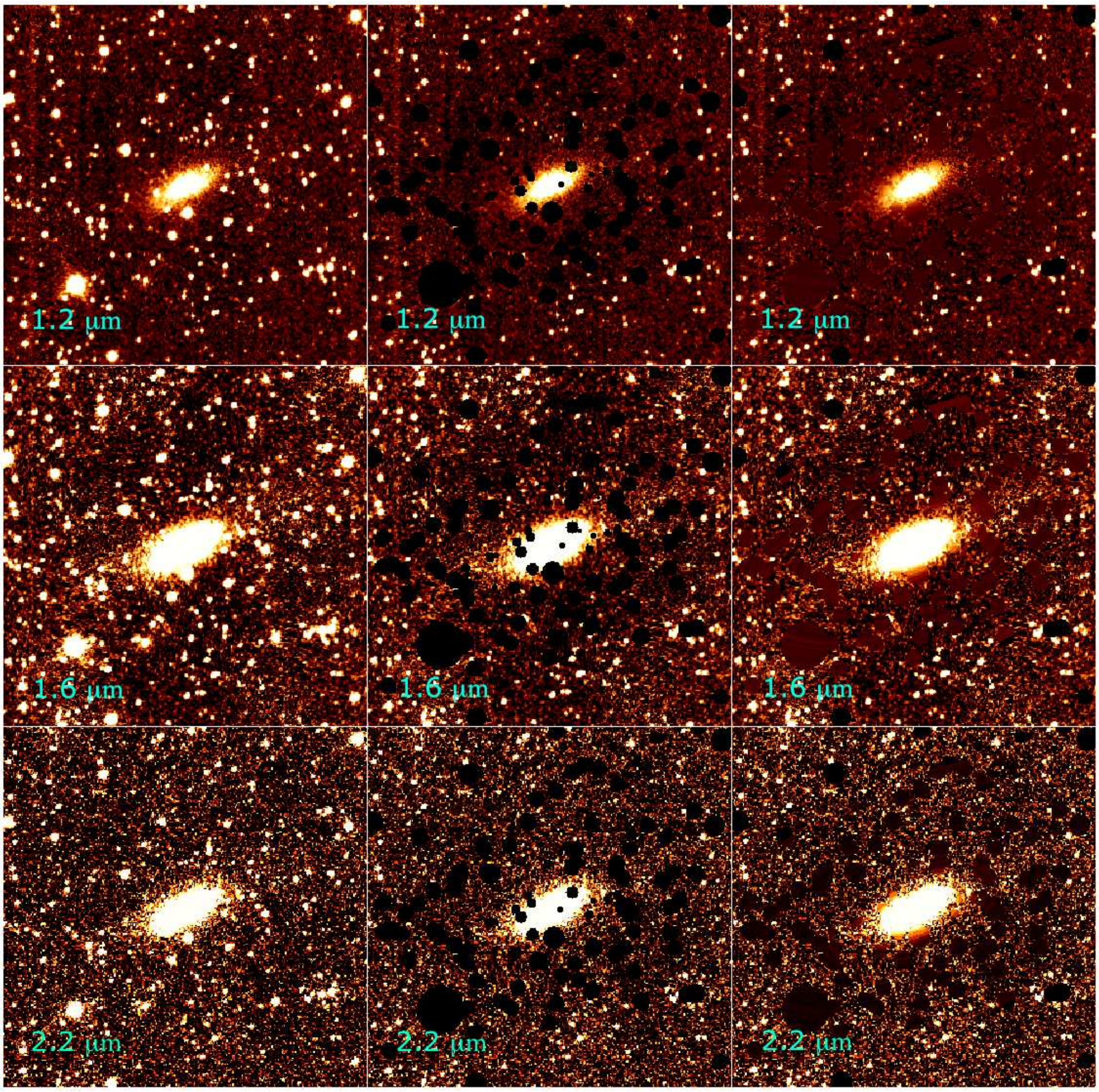

Figure 2.9: Left Panel: Raw postage stamps (FoV of $\sim 95'' \times 95''$) of HIZOA J0836-43 in the near-infrared ($1.2\,\mu$m, $1.6\,\mu$m and $2.2\,\mu$m). Middle Panel: The images after stars have been masked. Right Panel: Images after pixels have been replaced.

Extended source aperture corrections, as prescribed by the SSC[1], were applied to the IRAC bands as for an effective circular aperture with radius 25.50″. Flux scaling values are as follows: 0.940, 0.974, 0.871 and 0.814 for 3.6, 4.5, 5.8, 8.0 μm respectively. The aperture correction[2] for the MIPS-24 μm flux was 1.107.

For the MIPS 70 and 160 μm data, photometry was extracted using a circular aperture with radius 39.4″. This was deemed large enough to capture the total flux of the unresolved galaxy, but small enough to avoid contamination from other sources. Images were corrected for a dark pattern gradient near the source and fluxes scaled according to documented aperture correction factors (1.240 and 1.705 for MIPS 70 and 160 μm respectively)[2].

NIR photometry was extracted using the same elliptical aperture and method as used for the IRAC and MIPS-24 bands (as shown in Figs. 2.8 and 2.9). These photometric procedures were carried out using IRAF tasks in combination with Fortran code, written by T. Jarrett.

2.4 Spectroscopy of HIZOA J0836-43

The SSC post-BCD software, CUBISM (Smith et al. 2007), was used to extract a spectrum of the entire galaxy (37″ aperture), as well as smaller extractions (9.25″ aperture) of the Nucleus, East and West disk. The SL1 (1^{st} order) and SL2 (2^{nd} order) apertures were matched and SL2 scaled to match SL1 (scale factor of 1.475).

The LH extraction was performed using CUBISM with an aperture size matching the SL extraction. To match the SH and LH apertures, LH was scaled by a factor of 1.48. The LH spectrum was scaled down by 55% to match the SH continuum flux at 19.3 μm, a consequence of the differing slit sizes.

2.5 Survey of Surrounding Area: Galaxies and Candidates

The IRSF J, H and K_s bands for the 169 fields were combined to make RGB composite colour images. These were searched by eye for reddish, relative to the Milky Way stars, extended (discernible from the typical FWHM of point sources $\sim 1.2''$) objects. 529 galaxy candidates were found, with 16 matches to sources in the 2MASS XSC (Extended Source Catalogue). Postage stamps were made for each candidate and viewed before performing photometry.

2.5.1 Photometry of Galaxies and Candidates in *Spitzer* Footprint

A total number of 65 galaxies and galaxy candidates are found in the *Spitzer* footprint. Of these, 61 have IRAC and NIR observations, and several have MIPS 24 μm detections. Photometry was done using the same method as for HIZOA J0836-43 (refer to Section 2.3). The other four are contaminated by stars in the IRAC bands, due to the large pixel size, and have NIR photometry only.

---

[1] See http://ssc.spitzer.caltech.edu/irac/calib/extcal/index.html

[2] See http://ssc.spitzer.caltech.edu/mips/apercorr/

2.5.2 Photometry of Galaxies and Candidates in Greater IRSF Area

There are 464 galaxies and candidates in the area outside the *Spitzer* footprint that have J, H and K_s imaging. Photometry was performed after masking stars close to the galaxy and then choosing an optimal elliptical aperture (with an appropriate axis ratio and radius) for each source. This ensures that the total flux of the galaxy is captured (down to $\sim 1\sigma$ level). The background was determined from an annulus around the aperture (ensuring that the median pixel value is an accurate reflection of the background value) and subtracted from the flux in the aperture. This was achieved by means of Fortran scripts running contiguous IRAF procedures. This procedure is illustrated in Fig. 2.10.

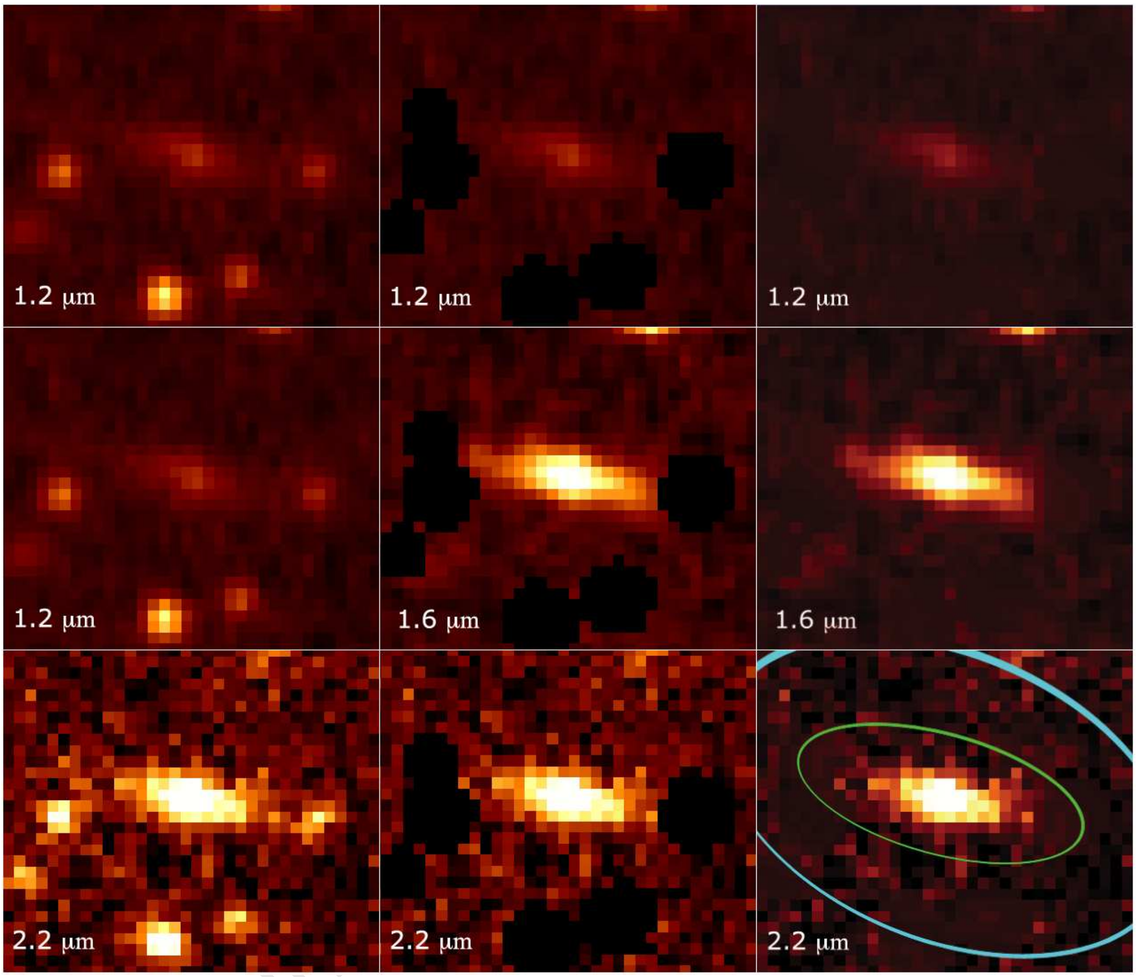

Figure 2.10: Left Panel: Raw postage stamps (FoV of $\sim 20'' \times 20''$) of a galaxy shown in J, H and K_s ($1.2\,\mu$m, $1.6\,\mu$m and $2.2\,\mu$m respectively). Middle Panel: Images with stars masked. Right Panel: Elliptical aperture (green) and annulus (cyan) on the images after masked pixels have been replaced.

Chapter 3

HIZOA J0836-43: NIR and MIR Photometry

In this Section we present the NIR and MIR photometry of HIZOA J0836-43. We make use of the data acquired from the *Spitzer Space Telescope* and the IRSF.

3.1 HIZOA J0836-43: Photometric Measurements

The photometry of HIZOA J0836-43 was performed as described in Section 2.3. The isophotal parameters were determined using the IRAC 3.6 μm image and the same elliptical aperture ($a = 39.35''$, $b/a = 0.42$, $\phi = -70°$) was used in all bands. The measured flux densities, aperture-corrected flux densities and their measured uncertainties are shown in Table 3.1. The measurement uncertainty includes a Poisson term from the source and the background brightness, and an uncertainty due to the background determination, typically between 1 to 4%. We note that we resolve the extended emission of HIZOA J0836-43 at 24 μm, but not its nucleus. This is illustrated in Appendix Section A.2. The galaxy is not resolved at 70 μm and 160 μm. We determine the integrated flux within a circular aperture of radius $a = 39.35''$ for these wavelengths. The estimated absolute calibration error, $\sim 5\%$ for the NIR and IRAC, $\sim 10 - 20\%$ for MIPS, is not reported in the formal errors, but is in fact the dominant uncertainty in the reported absolute flux of the source.

3.2 Surface Brightness Profiles

Surface brightness profiles of the NIR and MIR bands allow us to probe the relative distribution of emission. HIZOA J0836-43 has a prominent bulge in the NIR, but using the IRAC bands, we can probe the emission from stellar light, traced predominantly by the 3.6 μm and 4.5 μm bands, compared to dust emission, traced predominantly by the 5.8 μm and 8.0 μm bands. We determine the effective surface brightness and total flux in each band as follows.

The effective surface brightness corresponds to the mean surface brightness within an ellip-

Table 3.1: Measured flux densities.

Band	λ (μm)	F_ν [a] (mJy)	F_ν [b] (mJy)
J	1.25	8.54 ±0.11	8.54 ±0.11
H	1.63	18.41 ±0.23	18.41 ±0.23
K_s	2.14	24.24 ±0.30	24.24 ±0.30
IRAC-1	3.53	23.55 ±0.36	22.13 ±0.34
IRAC-2	4.46	17.51 ±0.27	17.05 ±0.26
IRAC-3	5.67	40.74 ±0.75	35.48 ±0.65
IRAC-4	7.70	140.05 ±2.86	114.07 ±2.33
MIPS-24	24	114.28 ±2.42	126.52 ±2.68
MIPS-70	70	1847.8 ±116.2	2291.3 ±144.1
MIPS-160	160	1807.7 ±198.8	3082.1 ±339.2

Aperture parameters for NIR, IRAC and MIPS-1:
$a = 39.35'', b/a = 0.42, \phi = -70°$;
MIPS-2 and MIPS-3 (aperture flux) have $a = 39.35'', b/a = 1$

[a] Flux density - no aperture corrections applied; the formal measurement errors are reported.

[b] IRAC and MIPS measurements have been aperture corrected as follows: 0.940, 0.974, 0.871, 0.814, 1.107, 1.240, 1.705 for 3.6, 4.5, 5.8, 8.0, 24, 70, 160 μm respectively.

tical area which contains the "half-light" of the total flux of the galaxy. The total flux of the galaxy was determined by integrating the light of the galaxy to the $a = 39.35''$ isophotal radius, and then fitting a Sérsic (1968) modified exponential function to the outer radial surface brightness distribution and integrating to a radius corresponding to three times the disk scale length modulated by the Sérsic index: $3 \times \alpha^{1/\beta}$, in the 4.5 μm band, or a radius of $70''$.

This defines the "total" flux of the galaxy. The half-light radius is then determined by integrating the flux of the galaxy in radial steps until half of the total flux is included. This defines the half-light radius, $r_{\rm eff}$, and the mean flux enclosed corresponds to the effective surface brightness of the galaxy. The surface brightness profiles and Sérsic fits for the near-infrared bands are shown in Fig. 3.1 and profiles for the four IRAC bands are shown in Fig. 3.2.

In Table 3.2 we list the surface brightness measurements obtained of HIZOAJ0836-43. The surface brightness profiles shown in Figs. 3.1 and 3.2, as well as Sérsic fit parameters, show that in the $2 - 4\,\mu$m range a strong bulge component dominates the light, as first reported by Donley et al. (2006). However, as we probe the longer wavelengths of the IRAC bands, and sample more of the interstellar medium, the profiles become nearly "disk" exponential. Similarly, at the shortest wavelength, the J band light falls off exponentially. These bands are tracking the younger stellar population and ISM distribution that comprises the disk. We note that the IRAC 8.0 μm profile also shows a relatively bright nucleus, indicative of a nuclear starburst.

We can compare our H and K_s photometric measurements to those obtained by Donley et al. (2006) using the AAT. They find $m_{\rm tot}(H) = 11.73 \pm 0.01$ mag and $m_{\rm tot}(K_s) = 10.82 \pm 0.01$ mag. The H band measurements agree well, but the K_s IRSF magnitude is marginally fainter (~ 0.18

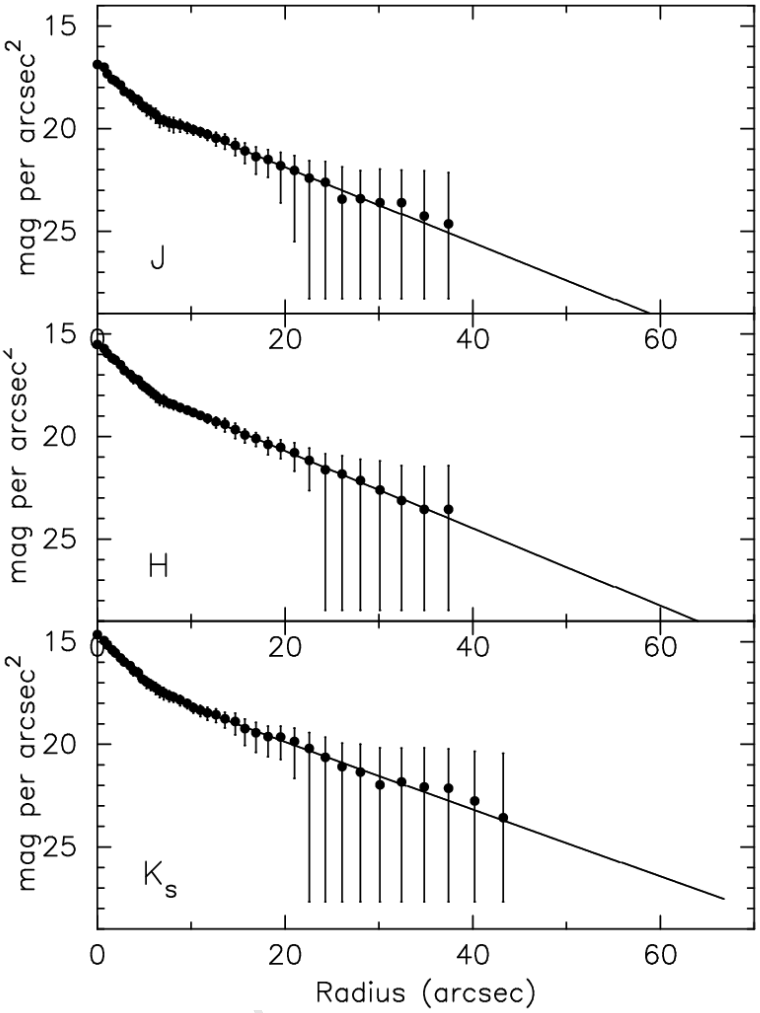

Figure 3.1: Surface brightness profiles of HIZOA J0836-43 for the three NIR passbands.

mag). This difference is likely due to our careful removal of foreground stellar contamination. Our effective surface brightness for H and K_s is ≈ 0.45 mag arcsec^{-2} brighter than the Donley et al. (2006), who obtain 17.77 mag arcsec^{-2} and 17.02 mag arcsec^{-2}, respectively.

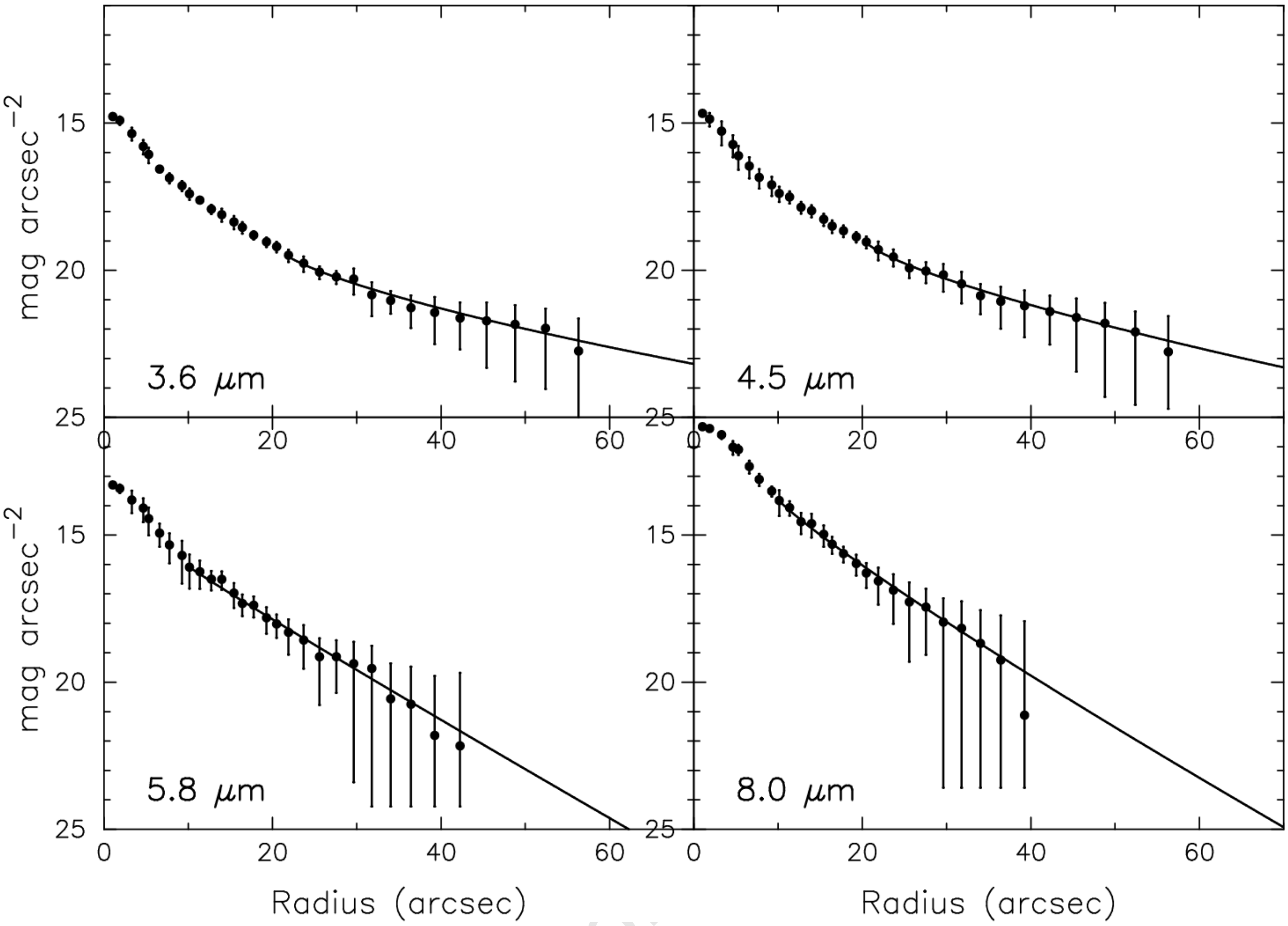

Figure 3.2: Surface brightness profiles of HIZOA J0836-43 for the four IRAC passbands.

Table 3.2: Total flux and surface brightness of HIZOAJ0836-43.

Band	λ (μm)	F_ν [a] (mJy)	Total Magnitude [b] (mag)	$r_{\rm eff}$ (arcsec)	Sérsic Index (β)	Surface Brightness ($r_{\rm eff}$) [c] (mag arcsec^{-2})
J	1.25	9.66 ±0.24	13.05 ±0.03	8.49	1.01	18.74
H	1.63	19.88 ±0.48	11.78 ±0.03	7.88	1.05	17.32
K_s	2.14	25.57 ±0.58	11.00 ±0.03	8.00	1.13	16.57
IRAC-1	3.53	25.30 ±0.76	10.12 ±0.03	8.56	1.45	15.94
IRAC-2	4.46	18.57 ±0.71	9.97 ±0.04	7.80	1.35	15.59
IRAC-3	5.67	42.52 ±1.45	7.09 ±0.04	6.83	1.03	13.92
IRAC-4	7.70	144.77 ±5.45	7.16 ±0.04	6.90	1.11	11.97

[a] Total Flux Density - no reddening corrections applied

[b] No reddening corrections applied; calibration error included

[c] No reddening corrections applied

Table 3.3: Adopted extinction laws (Cardelli et al. 1998 convolved with the filter bandpasses).

Band	λ (μm)	A_λ (A_V)
I	0.82	0.570
J	1.25	0.272
H	1.63	0.177
K_s	2.14	0.114
IRAC-1	3.53	0.052
IRAC-2	4.46	0.036
IRAC-3	5.67	0.036
IRAC-4	7.70	0.036
MIPS-24	24	0.000

3.3 Compensating for extinction

The effect of dust reddening at the location of HIZOA J0836-43 (l = 262.48°, $b = -1.64°$) is severe. Correcting for this selective extinction must be done carefully because analysis and interpretation of the Spectral Energy Distribution (SED) depends on accurate photometry. The Schlegel et al. (1998) DIRBE/IRAS maps give an extinction of $A_V = 7.5$ mag at the location of HIZOA J0836-43. Although these maps are a good measure of the Galactic extinction in general, they are less accurate at high dust column densities – effectively uncalibrated at low Galactic latitudes ($|b| < 5°$), they have been shown to overestimate the extinction near the Galactic Plane (eg. Dutra et al. 2002). The FIR maps are also course in angular resolution, unable to track the patchy ISM that characterizes the Vela region (see also Kraan-Korteweg & Lahav 2000).

In order to obtain a better estimate of the Galactic extinction, we exploit the morphology-independent NIR colours of galaxies (Jarrett 2000). We can utilise the NIR sensitivity to the relatively well-modeled old stellar population and compare HIZOA J0836-43's SED (after correcting for its redshift) to templates for Population II-dominated galaxies (GRASIL code; Silva et al. 1998). By varying the extinction we can obtain a best-fit of the NIR component of HIZOA J0836-43's SED to the models. The resultant extinction will be a combination of the foreground extinction and the value intrinsic to the inclined galaxy.

We adopt for our wavelength-dependent extinction relation the Cardelli et al. (1989) extinction law[1] convolved with the IRSF and IRAC bandpass filters, with $A_V/A_K = 8.8$. The form of these relations are listed in Table 3.3. We use the J, H and K_s photometry, as well as the DENIS I band measurement (Donley et al. 2006) to constrain the extinction. The GRASIL templates are normalised to the galaxy K_s-band value.

Fig. 3.3 shows how varying the extinction affects the SED compared to the template spec-

---

[1] The adopted relations are consistent $\sim 10 - 20\%$ with (Indebetouw et al. 2005) and (Flaherty et al. 2007) derived for IRAC

trum. The blue points represent the GRASIL "old" model template, for a 13 Gyr old galaxy, integrated for the J, H and K_s filter passbands. The short-wavelength I and J bands are the most sensitive to changes in extinction.

The best-fit SED corresponds to a total extinction of $A_V = 7.3 \pm 0.2$ mag, where the uncertainty corresponds to the range in A_V that is constrained by the uncertainty in the NIR photometry.

Since we are fitting the SED to a model template, this extinction incorporates both internal and foreground extinction. We can calculate the contribution of each by using the measured axis ratio ($b/a = 0.42$) to estimate the internal extinction. We adopt the relation from Masters et al. (2003), $\Delta m\gamma = 0.26 \log(a/b)$. The γ_K value corresponding to the K_s band is 0.26, which gives $\Delta m_K = 0.098$, corresponding to $\Delta m_V \sim 0.9$ (using the Cardelli Law). This implies a foreground extinction of $A_V = 6.4$ mag. This value is $\sim 20\%$ lower than *IRAS*/DIRBE value ($A_V = 7.5$ mag) from NED[2], consistent with previous findings that the FIR maps tend to over-estimate the extinction when the column density is high.

3.4 HIZOA J0836-43: Extinction-corrected Photometry

With the extinction well constrained by the SED and redshifted model fits, we can compute the extinction-corrected photometry of the galaxy. In Table 3.4 we list the flux densities and spectral luminosities corrected for the total extinction, $A_V = 7.3$ mag. The MIPS bands are essentially unaffected by foreground dust extinction due to their longer wavelength. The extinction-corrected surface brightness measurements are shown in Table 3.5.

We next check the adopted extinction correction to see if it is consistent with what is expected for the near-infrared colours of an average galaxy at a redshift of $z \sim 0.04$. HIZOA J0836-43, using the integrated magnitudes from Table 3.4, has an extinction-corrected $(J - K_s)^0$ colour of 0.92 mag and a $(H - K_s)^0$ colour of 0.30 mag. Similarly the total magnitudes (from Table 3.5) give a $(J - K_s)^0$ colour of 0.89 mag and a $(H - K_s)^0$ colour of 0.32 mag. This is consistent with what is expected for typical early-type disk galaxies, at this redshift, from the empirical work using 2MASS photometry (Jarrett 2004) namely, $J - K_s = 0.96$ and $H - K_s = 0.32$ (Tom Jarrett - private communication).

---

[2] The NASA/IPAC Extragalactic Database (NED) is operated by the Jet Propulsion Laboratory, California Institute of Technology, under contract with the National Aeronautics and Space Administration

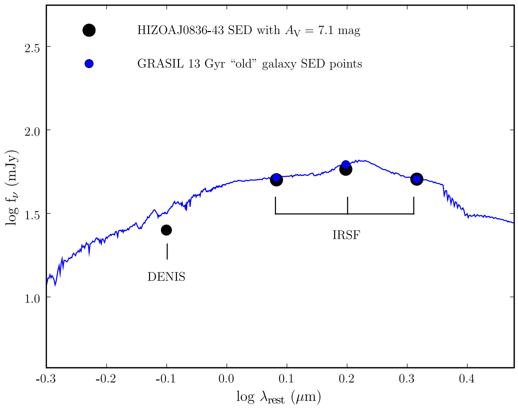

(a) A_V=7.1 mag

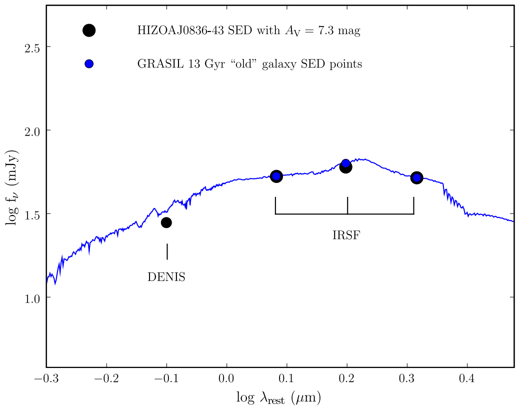

(b) A_V=7.3 mag

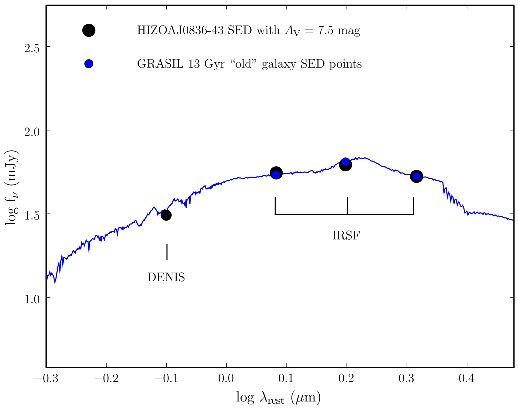

(c) A_V=7.5 mag

Figure 3.3: The HIZOA J0836-43 SED is shifted by varying the extinction to find the best match with the GRASIL "old" galaxy template. The blue points represent the GRASIL "old" model SED corresponding to the J, H and K_s passbands. The DENIS I band was not used in the fit.

Table 3.4: Extinction-corrected flux densities and spectral luminosities

Band	λ (μm)	A_λ (mag)	F_ν [a] (mJy)	Integrated Magnitude [b] (mag)	νL_ν [b,c] ($10^9 L_\odot$)
I [d]	0.82	4.16	28.12 ±2.81	12.42 ±0.10	69.2 ±6.4
J	1.25	1.99	53.18 ±0.69	11.19 ±0.05	85.6 ±3.9
H	1.63	1.29	60.53 ±0.76	10.57 ±0.05	73.1 ±3.4
K_s	2.14	0.83	52.17 ±0.65	10.27 ±0.05	49.0 ±2.3
IRAC-1	3.6	0.38	31.40 ±0.47	9.88 ±0.05	17.6 ±0.8
IRAC-2	4.5	0.26	21.72 ±0.33	9.79 ±0.05	9.7 ±0.5
IRAC-3	5.8	0.26	45.20 ±0.83	8.51 ±0.06	15.7 ±0.9
IRAC-4	8.0	0.26	145.31 ±2.96	6.61 ±0.06	36.7 ±2.0
MIPS-24	24		126.52 ±2.68	4.38 ±0.10	10.6 ±0.9
MIPS-70	70		2291.3 ±143.8	-1.17 ±0.20	65.9 ±12.1
MIPS-160	160		3082.1 ±339.2	-3.21 ±0.20	38.7 ±7.1
Total IR [e]	3 - 1100				119.5 ±22.01

[a] Flux density - aperture and extinction corrected (A_V = 7.3 mag)

[b] Calibration error included: 5% for NIR & IRAC, 10% for MIPS-24 μm, 20% for MIPS-70 μm and MIPS-160 μm

[c] Assuming D_L=148 Mpc (Donley et al. 2006)

[d] As in Donley et al. (2006)

[e] Calculated from Dale and Helou (2002) relation

Uncertainties due to extinction are not included. They are 4%, 3% and 2% for J, H and K_s respectively and 1% for the IRAC bands

Table 3.5: Extinction-corrected total flux and surface brightness

Band	λ (μm)	A_λ (mag)	F_ν [a] (mJy)	Total Magnitude [b] (mag)	$r_{\rm eff}$ (arcsec)	Surface Brightness ($r_{\rm eff}$) [b] (mag arcsec^{-2})
J	1.25	1.99	60.15 ±1.51	11.06 ±0.03	8.49	16.75
H	1.63	1.29	65.35 ±1.59	10.49 ±0.03	7.88	16.03
K_s	2.14	0.83	57.18 ±1.30	10.17 ±0.03	8.00	15.74
IRAC-1	3.53	0.38	35.73 ±1.07	9.74 ±0.03	8.94	15.56
IRAC-2	4.46	0.26	23.57 ±0.89	9.71 ±0.04	8.14	15.33
IRAC-3	5.67	0.26	54.21 ±1.85	8.32 ±0.04	7.34	13.70
IRAC-4	7.70	0.26	198.78 ±7.48	6.27 ±0.04	7.34	11.71

[a] Total Flux Density - corrected for extinction (A_V = 7.3 mag)

[b] Extinction corrected

3.5 HIZOA J0836-43: Spectral Energy Distribution

The extinction-corrected global photometry of the galaxy is shown in Table 3.4. We now construct an SED for HIZOA J0836-43 using our near-, mid- and far-infrared measurements. The resulting SED is shown in Fig. 3.4 and includes the I band DENIS measurement from Donley et al. (2006). GRASIL templates for Sc-type, S0-type and the "old" (13 Gyr) elliptical galaxy are shown for comparison. We also include the spectrum of M82 (Sturm et al. 2000), a prototypical starburst galaxy in the local universe.

In the range of $0.8 - 25\,\mu$m, the galaxy most closely matches a dusty Sc-type galaxy, i.e. possessing strong PAH emission and rising MIR continuum. As mentioned previously, in the NIR the galaxy's stellar distribution (dominated by its bulge) resembles a lenticular (S0) or Sa spiral. However, in the MIR we are sampling the interstellar medium of the galaxy.

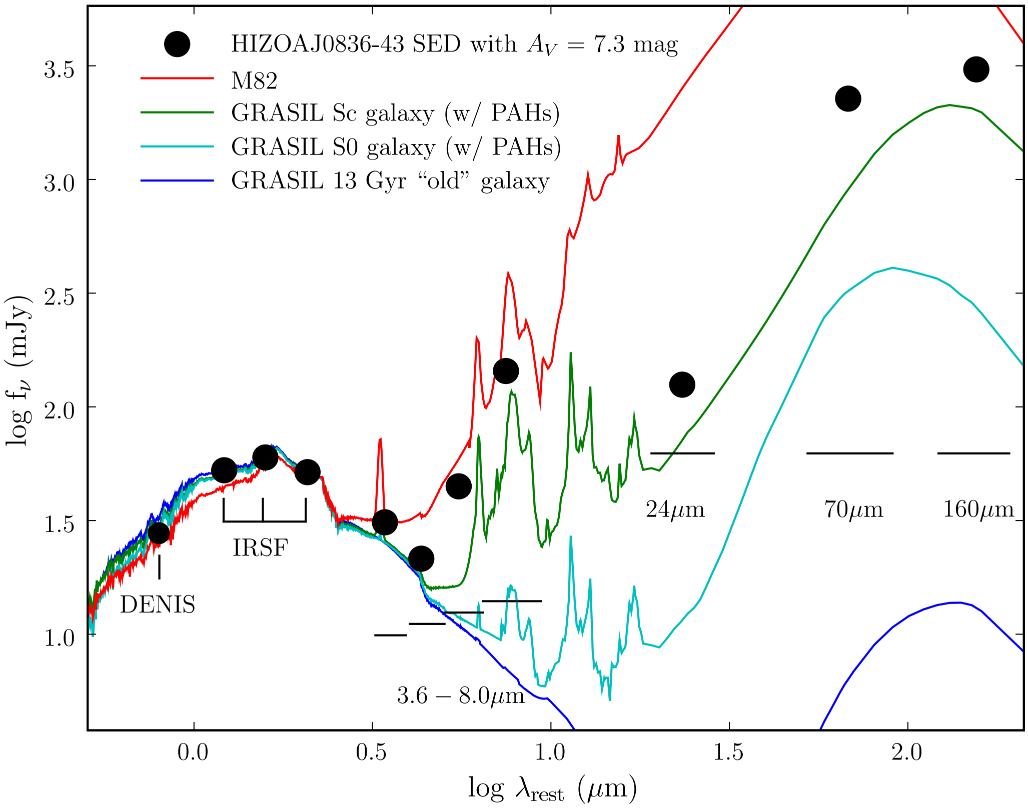

Figure 3.4: HIZOAJ0836-43 global SED with I band data from DENIS (Donley 2006), J, H, K_s data from the IRSF and mid-infrared values from IRAC and MIPS. Also shown are the GRASIL model templates and M82 spectrum for comparison. The templates are normalised to the galaxy K_s band value.The galaxy SED wavelengths are shifted to rest (using $v_{hel} = 10,689$ km s^{-1}) and an extinction correction of $A_V = 7.3$ mag has been applied.

We note that most of the infrared energy, however, arises from the far-infrared, longwards of 60 μm. Relative to the 24 μm global measurement, the far-infrared measurements indicate a significant cold component of dust.

The total infrared luminosity, $L_{\rm TIR}$ of the galaxy can be calculated using the relation of Dale & Helou (2002):

$$L_{\rm TIR} = 1.559 L_{24} + 0.7686 L_{70} + 1.347 L_{160},$$

where $L_{24} = \nu L_\nu(24\,\mu\rm m)$, $L_{70} = \nu L_\nu(70\,\mu\rm m)$ and $L_{160} = \nu L_\nu(160\,\mu\rm m)$. As shown in Table 3.4, the galaxy has an infrared luminosity $> 10^{11} L_\odot$. HIZOA J0836-43 is therefore classified as a Luminous Infrared Galaxy or LIRG. Since LIRGs are usually associated with intense star formation, we shall investigate its star formation properties in Section 3.9.

3.6 Blackbody fit

The SED of HIZOA J0836-43, shown in Fig. 3.4, indicates that most of the infrared energy arises from the far-infrared, longwards of 60 μm. Relative to the 24 μm global measurement, the far-infrared measurements indicate a significant cold component of dust. Dust grains heated by starlight produce emission that can be approximated by means of a modified blackbody spectrum (Boulanger et al. 1998), with an emissivity index $\beta = 1.5$, as shown below:

$$B_\lambda(T) = \lambda^{-\beta} \frac{2hc^2\lambda^{-5}}{e^{hc/k\lambda T} - 1} \text{ with } \beta = 1.5$$

We can estimate the temperature of the warm and cold dust by fitting a two-temperature blackbody curve to HIZOA J0836-43's dust SED. We subtract the stellar components from the IRAC wavelengths (using the 3.6 μm measurement scaled to each IRAC band) to leave only the emission from dust. We then fit the modified blackbody curve to the IRAC and MIPS 24 μm flux densities. As shown in Fig. 3.5, we estimate the temperature of the warm dust component to be $\sim$ 230 K. Fitting the function to the 70 μm and 160 μm SED values estimates a cold dust temperature of $\sim$ 30 K. We note that this is a crude estimate of the ISM dust temperature given that there is a range in temperature and dust grain sizes.

3.7 Cross-convolution of images

In order to perform detailed band-to-band comparisons between the NIR, IRAC and MIPS imaging, it is first necessary to cross-convolve the images to remove the band-dependent PSF (which is substantially different for these instruments). For each pair of images being compared to produce a flux ratio or colour, one image is first convolved with the Point Spread Function (PSF) of the other image and vice versa. For example, if we want to compare an IRAC-1 image with an IRAC-2 image, we first convolve the IRAC-1 image with the IRAC-2 PSF and then convolve IRAC-1 with IRAC-2's PSF, and so this cross-convolution technique forces each image

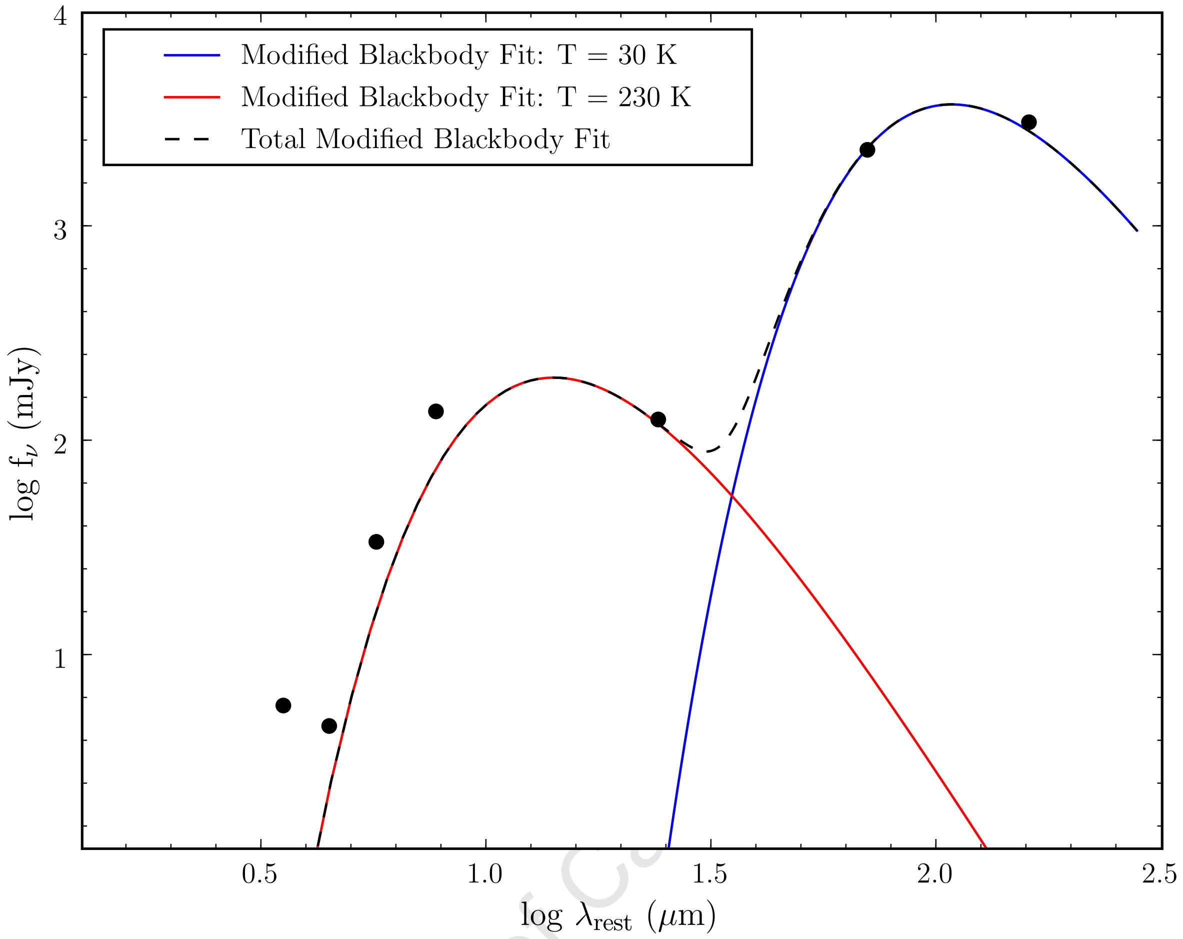

Figure 3.5: The best-fit modified blackbody curve for the cold and warm dust components is shown. The black points show the SED of HIZOA J0836-43 with stellar light removed (using the GRASIL "old" galaxy template) and therefore only show the contribution from dust.

to have the same PSF response. This technique therefore allows detailed comparison, but has the disadvantage of degrading the angular resolution, smearing the extended emission close to the bright nucleus of the galaxy where the PSF dominates.

3.8 Radial-dependent Colours

We can determine the radial-dependent colours across the disk of HIZOA J0836-43, shown in Figs. 3.6 and 3.7, using cross-convolved images. These measurements are obtained by integrating small circular apertures along a vector, starting at the nucleus centre and extending along the "Eastern" (blue) and "Western" (green) major axis of the galaxy, $\sim 40''$ in radius and with a position angle of 110° (east from north). These measurements allow us to determine the colour at that position along the axis. The size of the aperture is varied from the centre (radius $= 1''$) to the outer disk (radius = 4″) in order to optimise the S/N (Signal to Noise) in the aperture. The mean surface brightness (in mag arcsec^{-2}) is calculated for each aperture and extinction corrected ($A_V = 7.3$ mag). The extinction-corrected surface brightness is differenced and converted to a magnitude to give the traditional colour metric. Uncertainties in the measurements, as shown in Figs. 3.6 and 3.7, follow from the error propagation of each aperture measurement.

Figure 3.6 shows that the East and West disks of HIZOA J0836-43 are asymmetric in their colour distribution; the West major axis appears redder on average in $J - K_s$. This could be due to the East side having a more diffuse, extended structure compared to the West, as will be discussed in Section 5.1.1. The profiles indicates a red structure at the outer part of the disk. IRAC-1 vs. K_s profile shows a region towards the edge of the West disk that is bluer (i.e. more luminous in K_s compared to IRAC-1). Since they both trace evolved stars, but IRAC-1 also contains emission from hot dust, this could indicate that this region has a paucity of hot dust compared to the rest of the disk.

Figure 3.7 also shows the MIR asymmetry between the East and West disks. The upper

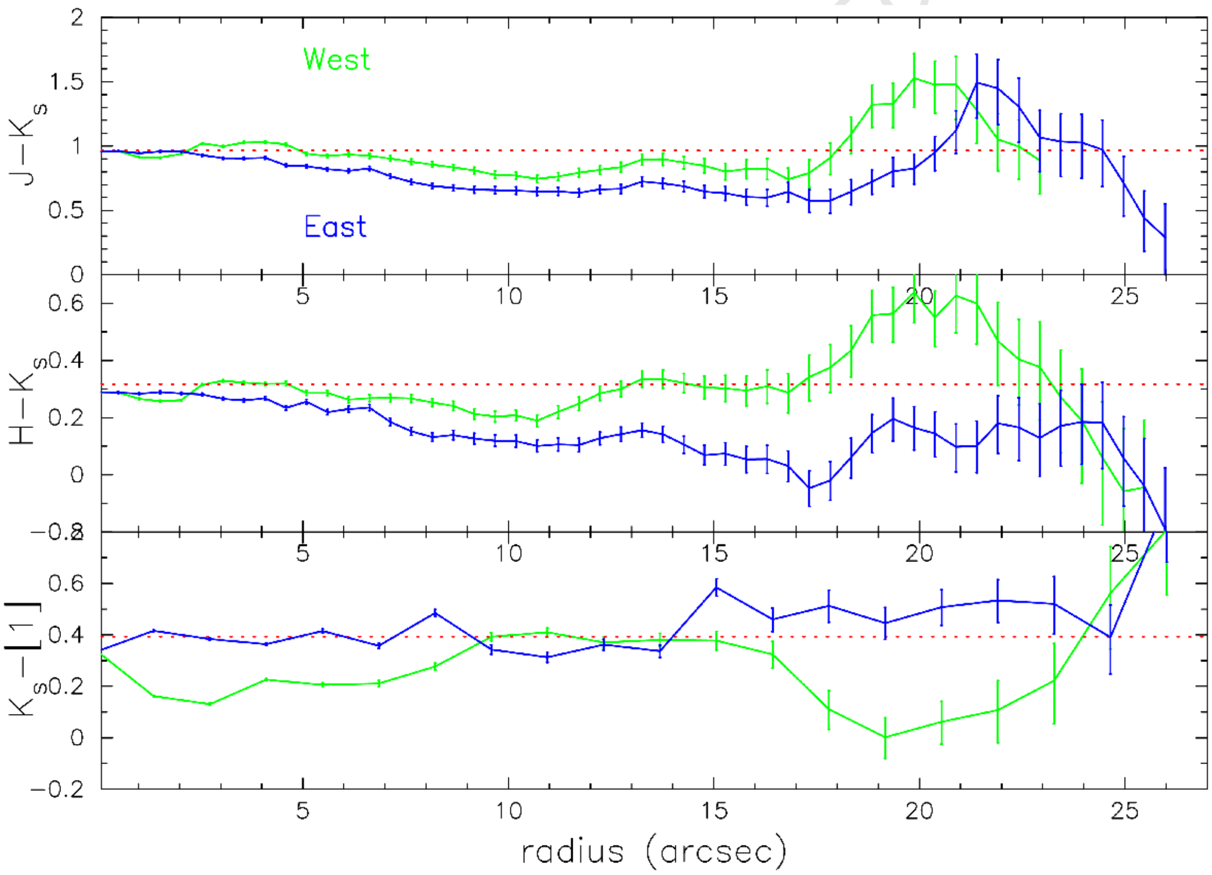

Figure 3.6: Radial colours (in magnitudes) of HIZOA J0836-43 using J, H, K_s and IRAC-1 passbands. The red dotted lines indicate the expected value for an early-type spiral at a redshift $z = 0.036$.

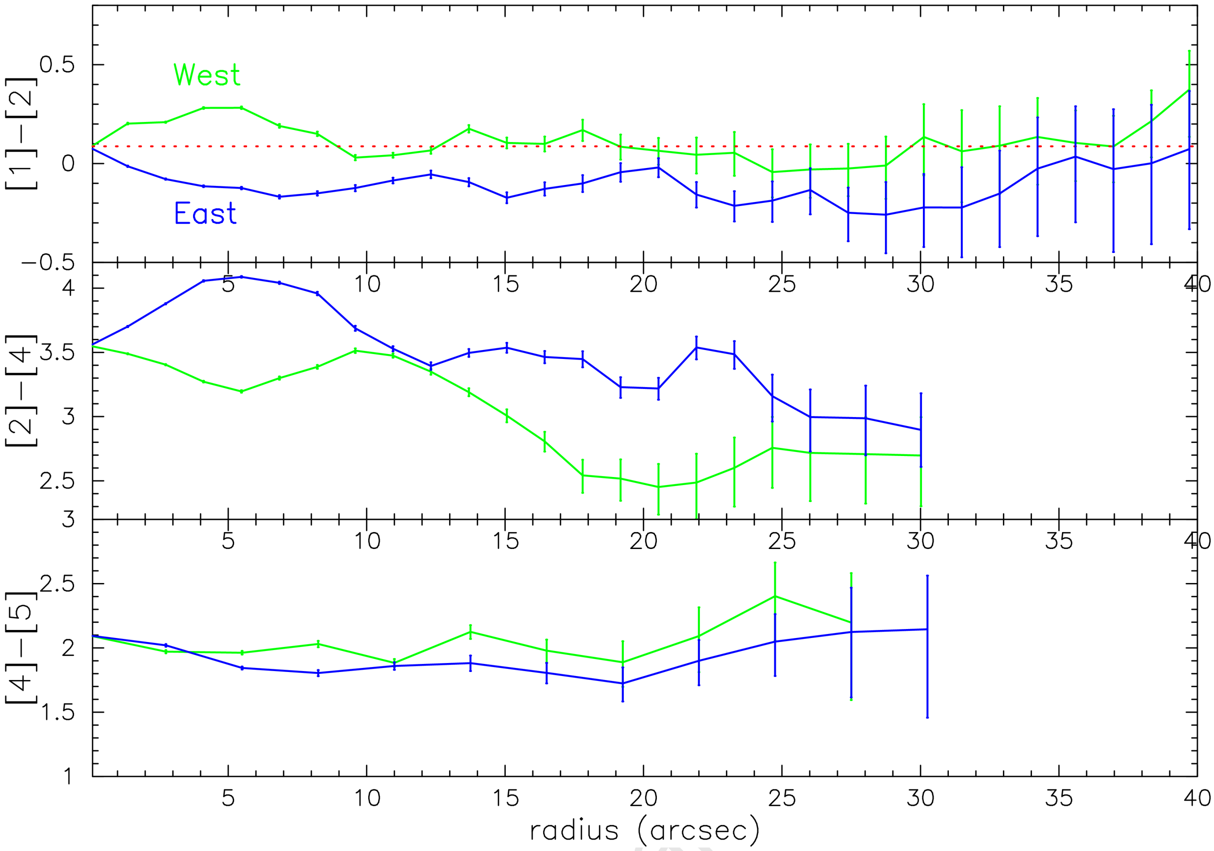

Figure 3.7: Radial colours (in magnitudes) of HIZOA J0836-43 using the IRAC passbands ([1],[2],[3] and [4] refering to 3.6, 4.5, 5.8, 8.0 μm respectively) and MIPS 24 μm (labeled as [5]).

panel shows that East is slightly bluer compared to the West, indicating more emission from stars (IRAC-1) compared to emission from stars and hot dust (IRAC-2). The middle panel compares emission from IRAC-2 (old stars and hot dust) with IRAC-4 which is dominated by PAH emission. The East disk appears redder, indicating stronger PAH emission compared to the West disk. The emission also appears to extend across the disk, as opposed to the West disk where the emission appears more concentrated in the central region. The lower panel shows the close correlation between PAH emission (IRAC-4, 8 μm) and warm dust emission (MIPS-24 μm) across the disk, both originating in star forming regions. The poorer spatial resolution of the MIPS 24 μm band ($\sim$ 4 kpc beam) does not allow us to trace localised regions of star formation.

3.9 Star Formation Relations

Infrared photometry of HIZOA J0836-43 has indicated that the galaxy is a LIRG (Section 3.4), suggesting active star formation on a large scale. In this section we investigate several star formation relations used to determine the star formation rate (SFR) of HIZOA J0836-43, in particular those that pertain to the MIR and FIR.

The infrared provides a powerful measure of star formation as the ultraviolet photons from massive star formation are absorbed by dust and reprocessed in proportion to the radiation field. Unlike direct measurements of the ultraviolet stellar continuum, it is unaffected by dust attenuation (Kennicutt 1998b). Since MIR emission can arise from a number of sources that do not trace star formation, it is a complex indicator. In particular, radiation from the evolved stellar population can result in a significant contribution of dust reradiating at MIR wavelengths. The MIR has, however, been shown to be an effective tracer of star formation (Helou et al. 2004; Calzetti et al. 2005).

Donley et al. (2006) used the relation of Bell et al. (2003) to calculate the SFR from their 20 cm radio flux. This relation is calibrated by comparing Hα attenuation-corrected star formation rates and TIR/FUV (Total IR/Far-UV) determined rates (using the Kennicutt 1998a starburst model). The linear radio-IR correlation then allows a direct determination from the 1.4 GHz measurement.

Condon (1992) derived a FIR-based star formation indicator on the basis of thermal reradiation of dust grains acting as a tracer of star formation. This is based on *IRAS* data and hence calibrated for 60 μm fluxes. This is included as a rough indicator of star formation since we use the similar bandpass MIPS 70 μm value.

In starburst galaxies there exists an improved relation between SFR and IR luminosity compared to normal disk galaxies, where stars of all ages contribute significantly to dust heating. The relation of Kennicutt (1998a) is based on the starburst synthesis models of Leitherer & Heckman (1995). They derive a L_{FIR}-SFR conversion using IRAS fluxes for 61 galaxies on the assumption of $10 - 100$ Myr continuous bursts, solar abundances, a Salpeter IMF and the assumption that the dust reradiates all of the bolometric luminosity.

Work by Schmitt et al. (2006) investigating star formation rates of nearby galaxies, using a range of indicators, has led to a new calibration for the non-thermal part of the radio SFR estimator. This is based on a comparison between 1.4 GHz measurements and a new estimator of the bolometric luminosity of star-forming regions.

A sample of 91 galaxies from the *Spitzer* First Look Survey was used by Wu et al. (2005) to investigate the global correlation between 1.4 GHz and Hα luminosities with 8 μm (with the stellar component removed) and 24 μm luminosities, respectively. The 8 μm luminosity covers the strongest PAH band (7.7 μm), while the 24 μm band measures the continuum emission from VSGs (Very Small Grains) without contamination from PAHs. The sample covered a wide range of metallicities, as well as star formation rates. They find a strong correlation with both MIR bands, but find a shallower slope with 8 μm luminosity. Wu et al. (2005) conclude that it may not be a linear measure of intense starburst activity, since PAH emission can be strong in moderate UV radiation fields (and therefore not trace massive star formation, but rather the less massive B-star formation), but is less intense in hard radiation fields because PAHs are easily destroyed.

Alonso-Herrero et al. (2006) used a sample of 30 local LIRGS to calibrate SFR and 24 μm emission, utilising the linear empirical relationship between hydrogen recombination luminosity (through extinction corrected Paα) and 24 μm luminosity. This empirical calibration of SFR to monochromatic 24 μm luminosity is therefore applicable to luminous, dusty galaxies.

Calzetti et al. (2007) extended the work of Alonso-Herrero et al. (2006) using 33 galaxies from the SINGS (*Spitzer* Infrared Nearby Galaxy Survey) sample and reports two SFR calibrations based on the correlation between 24 μm emission and extinction-corrected Paα line emission. They determine one relation from a fit through the high-metallicity data points where the correlation is strongest. This combined with a SFR - Hα luminosity relation derived from a 100 Myr constant star formation model, allows a direct measure of star formation rate from the 24 μm luminosity. This relation is, however, limited to metal-rich objects and will underestimate SFRs by a factor of between 2 and 4 as metallicity decreases (Calzetti et al. 2007).

A second calibration from Calzetti et al. (2007) uses the same SFR - Hα luminosity relation, but uses a combination of 24 μm and Hα luminosities to derive the calibration. By incorporating emission from both obscured and unobscured star formation regions, it enables a more representative global star formation relation.

Calzetti et al. (2007) also investigated the feasibility of using 8 μm emission as a SFR calibrator, but deemed it unsuitable as it showed strong dependence on metallicity and environment.

We show in Table 3.6 the different star formation rates we obtain for HIZOA J0836-43 using the calibrated relations discussed above.

Table 3.6: Star Formation Rates.

Calibration Method	Reference	Wavelength Required	SFR ($M_\odot$ yr^{-1})
1.4 GHz	Bell (2003)	20 cm	34.7 [a]
$L_{60\mu m}$	Condon (1992)	70 μm	11.8
L_{FIR}	Kennicutt (1998a)	24 μm 70 μm 160 μm	20.5
Radio - $L_{24\mu m}$	Wu et al. (2005)	24 μm	15.9
Radio - $L_{8\mu m}$	Wu et al. (2005)	8 μm	26.4
Hα - $L_{24\mu m}$	Wu et al. (2005)	24 μm	16.5
Hα - $L_{8\mu m}$	Wu et al. (2005)	8 μm	23.4
$L_{24\mu m}$	Alonso-Herrero et al. (2006)	24 μm	8.3
1.4 GHz	Schmitt et al. (2006)	20 cm	39.0
$L_{24\mu m}$	Calzetti et al. (2007) (*) [b]	24 μm	5.1
$L_{(H_\alpha)}$ - $L_{24\mu m}$	Calzetti et al. (2007) (**) [c]	24 μm	21.0

[a] As calculated in Donley et al. (2006)

[b] This relation is derived from a best-fit through high metallicity data points. Using the SFR density relation (with $S_{24\mu m} = 3.94 \times 10^{40} \mathrm{erg\,s^{-1}\,kpc^{-2}}$ and $A = 1051.5$ kpc^2) gives a SFR of 13.0 $M_\odot$ yr^{-1}

[c] This relation is derived for a 100 Myr constant star formation model with solar metallicity.

The differing bandpasses and calibrations used in the relations result in a range of star formation rates. Use of a single wavelength (eg. 24 μm) appears too dependent on the calibration method used. Also, the 8 μm luminosity as a trace of star formation must be used with caution as it appears strongly influenced by environment (Calzetti et al. 2007).

The FIR wavelengths of 70 μm and 160 μm trace (cold) dust in thermal equilibrium. This is a direct trace of star formation. The relation of Kennicutt (1998a) incorporates information from the 24 μm, 70 μm and 160 μm wavelengths. This SFR is close to the average value of the other relations, $\sim 20.2\ M_{\odot}\ \mathrm{yr}^{-1}$, and likely the most reliable given its wavelength coverage. We therefore adopt the value from the relation of Kennicutt (1998a), $20.5\ M_{\odot}\ \mathrm{yr}^{-1}$ for the analysis to follow.

Chapter 4

HIZOA J0836-43: MIR Spectroscopy

In this chapter we present the spectra from the infrared observations of HIZOA J0836-43. The disk and nucleus of the galaxy was observed in the low-resolution mode of the IRS-SL instrument onboard *Spitzer*. In addition, the two high-resolution modules (SH and LH) were used to observe the nucleus of the galaxy. The wavelength coverage of the SL module is $5 - 14\,\mu$m and the SH and LH have complementary wavelength coverage of $10 - 20\,\mu$m and $19 - 38\,\mu$m respectively.

We present the low-resolution and high-resolution spectra of HIZOA J0836-43, as well as the emission line measurements obtained. Spectral features were measured using the ISO Spectral Analysis Package (ISAP)[1] and the 'CUbe Builder for IRS Spectra Maps' (CUBISM) package developed by the Spitzer-SINGS project (Smith et al. 2007).

4.1 Measurement of Emission Lines

Emission-line fluxes and equivalent widths are measured from continuum-subtracted (a) Gaussian fits to the PAH features, and (b) flux histograms of atomic and molecular line species. First, second and third-order polynomial fits to the continuum were used. The measurements for a large extraction of the entire disk ($37''$ aperture) and a smaller extraction of just the nucleus ($9.25''$ aperture) are listed in Sections 4.3.1 and 4.3.2 respectively.

4.2 Measurement of PAH features

The *Infrared Space Observatory* (*ISO*) enabled detailed study of PAH emission features, many of which were previously unknown (Sturm et al. 2000). Similarly, *Spitzer* has revealed that PAH emission is complex, with both strong and weak contributions to the broad-band features (Smith et al. 2007; Draine & Li 2007). The combined emission produces a "PAH family" consisting of broad, strong emission features with weaker features giving rise to a "continuum" feature. This is particularly noticeable between 5.5 and $9\,\mu$m and between 11 and $14\,\mu$m. Measurements

---

[1] The ISO Spectral Analysis Package (ISAP) is a joint development by the LWS and SWS Instrument Teams and Data Centers. Contributing institutes are CESR, IAS, IPAC, MPE, RAL and SRON.

of these PAH features can therefore be done in several ways, giving rise to different results for the same data. We have chosen to use two techniques currently employed in the literature and present both here. This enables direct comparison with other PAH feature studies, depending on the technique used.

As pioneered by analysis of ISO spectra, the first method requires fitting a cubic spline to the continuum at certain pivot points (the "Spline" Method) and subtracting this from the spectrum. The strongest PAH features are left and these are then measured as listed in Section 4.3.

The second method simultaneously fits several PAH features (the "Multifit" Method) that comprise a "PAH family"; these results are shown in Section 4.4. These methods are compared in Smith et al. (2007) and Section 5.2.4.

The equivalent widths for all PAH features are derived by dividing the integrated PAH flux above the adopted continuum by the continuum flux density at the centre of the feature.

4.3 Results: Emission lines and PAH Spline Measurements

In this section, PAH features are measured by means of a spline continuum as described by Peeters et al. (2002) and Spoon et al. (2007). The flux above this continuum is measured for the following PAH emission bands: 6.2 μm, 7.7 μm, 8.6 μm, 11.4 μm, 12.7 μm, 16.4 μm, 17.0 μm and 17.4 μm.

The PAH features between 5.5 and 14 μm are measured using a spline continuum through the following pivot points: 6.0, 6.8, 7.1, 8.2, 9.3, 10.0, 11.7, 12.2 and 13.0 μm as illustrated in Fig. 4.1. This method has been used in conjunction with *Spitzer* IRS data in, for example, Brandl et al. (2006) and Armus et al. (2007).

4.3.1 Entire disk - $37''$ aperture

In Fig. 4.2 we show the SL spectrum for the entire disk ($37''$ aperture). Emission features and PAH bands are labeled and their measurements are given in Table 4.1. Column 1 and 2 list the emission feature and its rest wavelength, respectively. The measured full-width at half maximum (FWHM) for the line is given in column 3. Column 4 gives the equivalent width of the line (calculated by dividing the integrated flux above the continuum, by the continuum flux density at the centre of the feature). Column 5 is the flux of the line and the following three columns represent the signal to noise ratio (S/N) calculated using three different metrics. The first corresponds to the line flux relative to the line fit residuals, the second to the peak height above the continuum relative to the root mean square (RMS) of the baseline and the third corresponds to the line flux relative to the baseline continuum RMS.

The spectrum is dominated by strong PAH emission, but rotational emission lines from (warm) molecular hydrogen are also present. Fine structure lines of [Ne II] and [Ar II] are clearly detected. Due to the [Ne II] 12.81 μm line being close to the 12.7 μm PAH feature, these were Gaussian-fitted simultaneously, to deblend the individual fluxes.

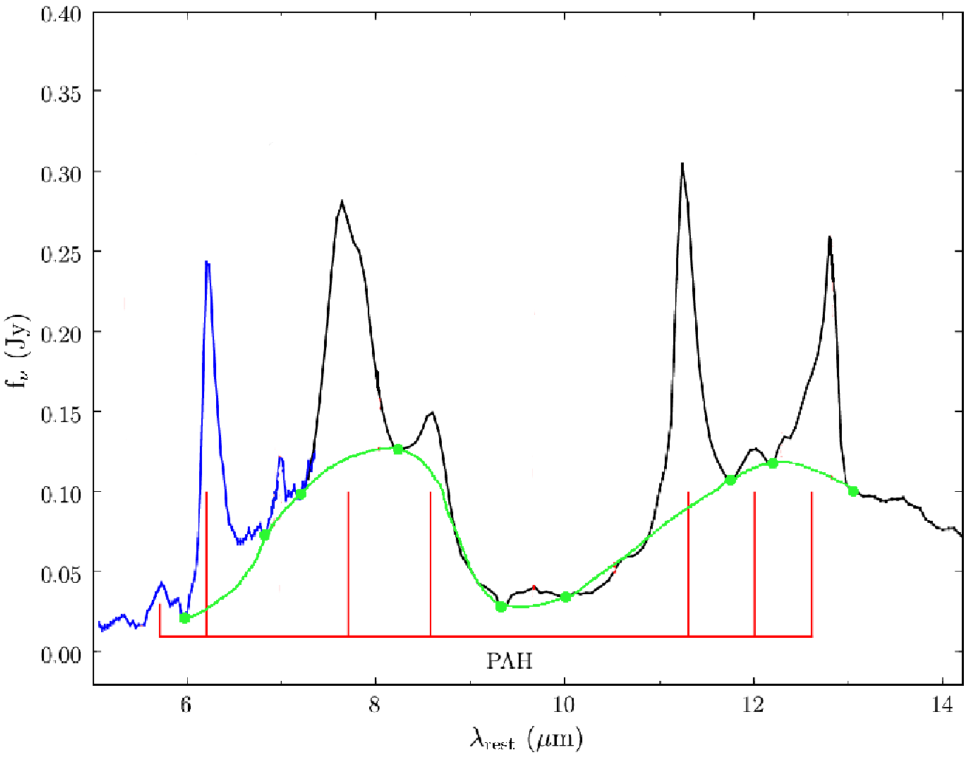

Figure 4.1: IRS SL Spectrum of the entire disk of HIZOA J0836-43 (37″ aperture) showing the pivot points and spline continuum in green. The PAH flux of the bands shown is measured above this continuum.

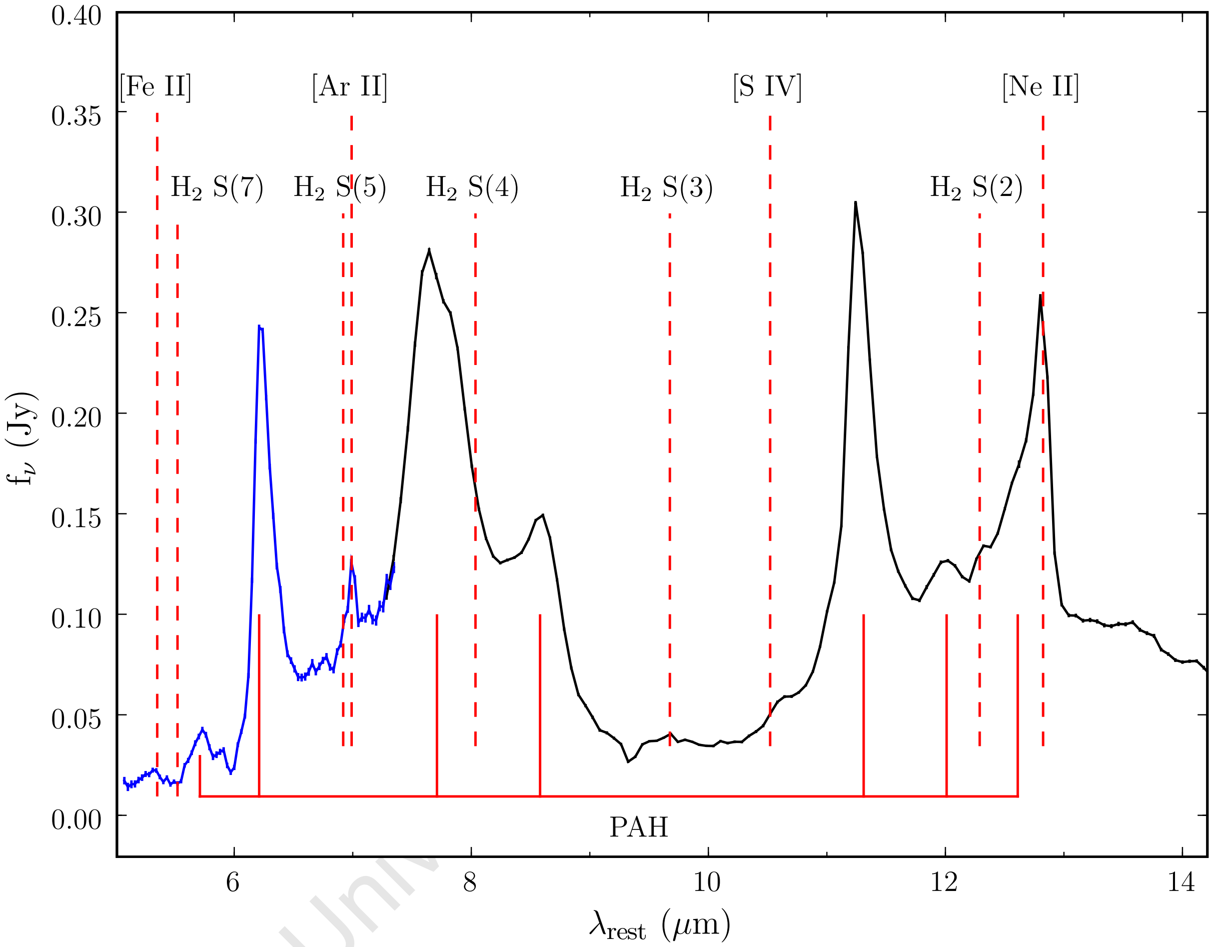

Figure 4.2: IRS SL Spectrum - HIZOA J0836-43 - 37″ aperture. The black line denotes the IRS-SL1 module and the blue line denotes the IRS-SL2 module.

Table 4.1: Emission line measurements - 37″ Aperture (SL).

Line	λ_{rest} μm	Line FWHM $10^{-3}\mu$m	Equivalent Width μm	Flux 10^{-17} W m^{-2}	S/N [a]	S/N [b]	S/N [c]
PAH	6.23	186.1	− 0.996	295.09	13.3	40.1	42.7
[Ar II] [d]	6.98	88.2	− 0.043	21.17	7.4	12.6	13.5
PAH	7.67	456.3	− 0.744	423.16	20.5	42.1	44.8
PAH	8.61	277.4	− 0.106	59.87	59.7	44.1	47.0
PAH	11.26	275.7	− 0.735	141.16	15.4	59.9	63.8
H_2 $S(2)$	12.28	200.0	− 0.157	4.54	0.3	4.7	5.0
PAH	12.60	250.0	− 0.361	33.10	1.4	27.2	29.0
[Ne II]	12.81	155.0	− 0.281	40.47	3.3	53.7	57.1

[a] Signal-to-noise ratio corresponding to the line flux relative to the line fit residuals.

[b] Signal-to-noise ratio corresponding to the peak height above the continuum relative to the baseline RMS.

[c] Signal-to-noise ratio corresponding to the line flux relative to the baseline RMS.

[d] [Ar II] is blended with H_2 $S(2)$.

4.3.2 Nucleus - 9.25″ aperture

The SL spectrum for the galaxy nucleus is shown in Fig. 4.3 and the corresponding high-resolution spectrum is shown in Fig. 4.4. At high resolution, we see that the high excitation AGN-tracers [Ne V] and [O IV] lines are very weak or absent, whereas the the fine-structure lines of [Ne II], [Ne III], [S III] and [Si II] are clearly detected. The integrated flux measurements, see Table 4.2, are dominated by the very strong PAH emission coming from the nuclear region. Less prominent, we also detect the rotational lines of warm molecular hydrogen, namely $S(1)$, $S(2)$ and $S(3)$. Fig. 4.5 shows the line profiles of individual prominent emission lines in the SH and LH spectra.

Beyond 14 μm, the only significant PAH feature is at 17 μm and is much weaker than its short-wavelength counterparts. This PAH family was measured by fitting a first-order baseline

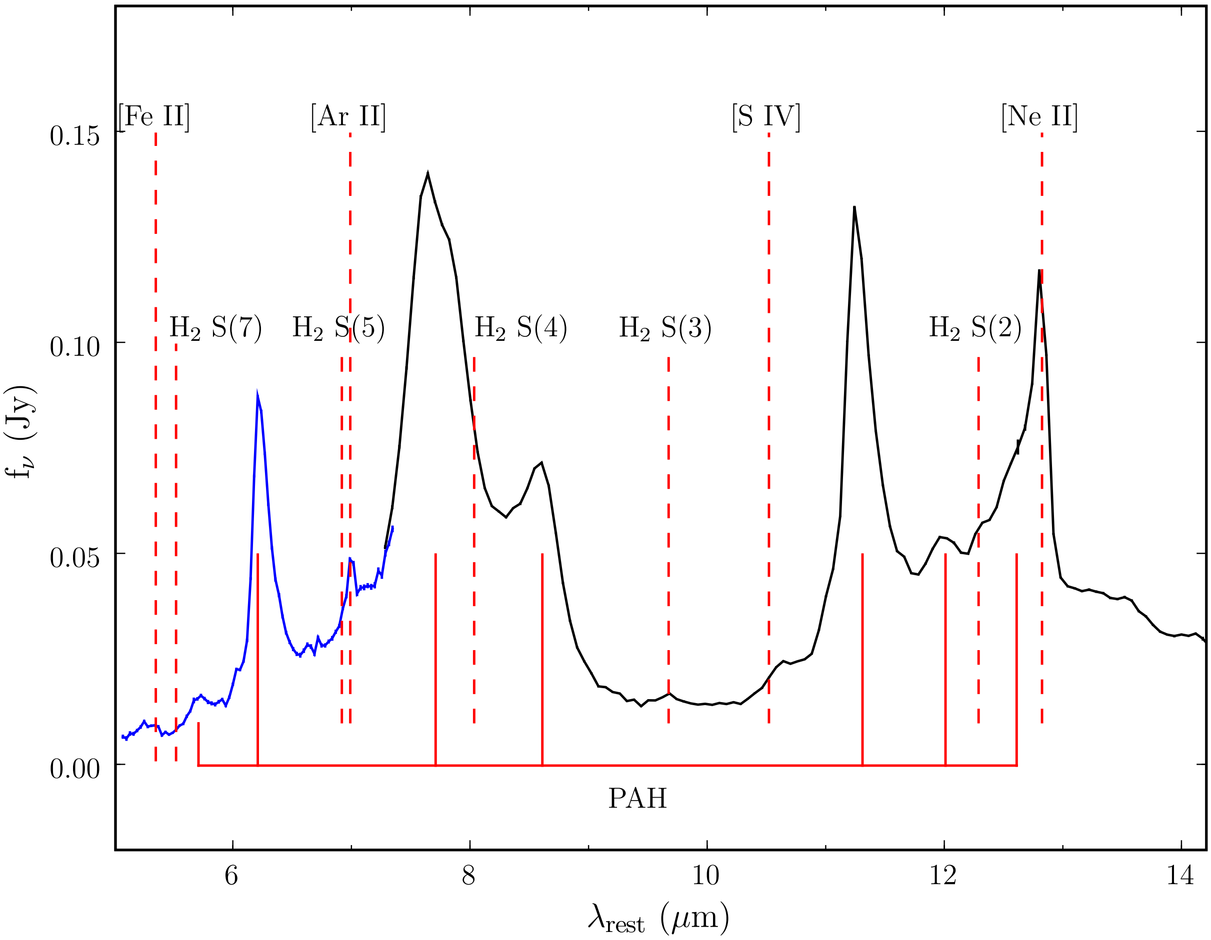

Figure 4.3: IRS SL spectrum - nucleus with 9.25″ aperture. The black line denotes the IRS-SL1 module and the blue line denotes the IRS-SL2 module.

Table 4.2: Emission line measurements - nucleus (SL+SH+LH).

Line	λ_{rest} μm	Line FWHM $10^{-3}\mu$m	Equivalent Width μm	Flux 10^{-17} W m^{-2}	S/R [a]	S/R [b]	S/R [c]
PAH	6.23	186.6	− 0.722	97.58	14.7	42.9	45.6
[Ar II] [d]	6.99	88.4	− 0.039	7.55	8.5	11.4	12.1
PAH	7.67	454.2	− 0.819	219.21	23.9	43.3	46.1
PAH	8.59	322.4	− 0.227	44.00	22.0	27.2	29.0
H_2 $S(3)$	9.66	32.7	− 0.037	1.31	7.0	8.4	9.0
[Si IV]	10.51			< 0.02			
PAH	11.27	238.3	− 0.851	59.33	9.7	54.0	57.5
H_2 $S(2)$	12.28	24.6	− 0.009	0.92	7.8	11.8	12.5
PAH	12.60	374.7	− 0.419	20.43	1.1	14.0	14.9
[Ne II]	12.81	32.8	− 0.208	13.02	10.2	101.5	108.1
[Ne V] [e]	14.32						
				< 0.22			
[Cl II] [e]	14.37						
[Ne III]	15.56	41.1	− 0.051	1.40	12.7	15.6	16.6
PAH	16.44	230.0	− 0.052	4.17	1.6	8.3	8.9
H_2 $S(1)$	17.04	41.0	− 0.186	1.57	1.8	17.5	18.7
PAH	17.04	1100.0	− 1.573	21.79	2.4	9.1	9.7
PAH	17.37	200.0	− 0.057	1.20	0.3	2.8	2.9
[S III]	18.71	52.4	− 0.165	3.18	12.7	27.6	29.4
[Ne V]	24.32			< 0.16			
[O IV] [e]	25.89						
	25.94	41.8		0.71	9.4		
[Fe II] [e]	25.99						
H_2 $S(0)$	28.22	98.0	− 0.042	0.61	6.7	4.2	4.5
[S III]	33.47	98.3	− 0.156	4.52	13.1	15.1	16.1
[Si II]	34.81	92.3	− 0.247	8.84	13.6	17.2	18.3

[a] Signal-to-noise ratio corresponding to the line flux relative to the line fit residuals.

[b] Signal-to-noise ratio corresponding to the peak height above the continuum relative to the baseline RMS.

[c] Signal-to-noise ratio corresponding to the line flux relative to the baseline RMS.

[d] [Ar II] is blended with H_2 $S(2)$.

[e] Blended emission lines

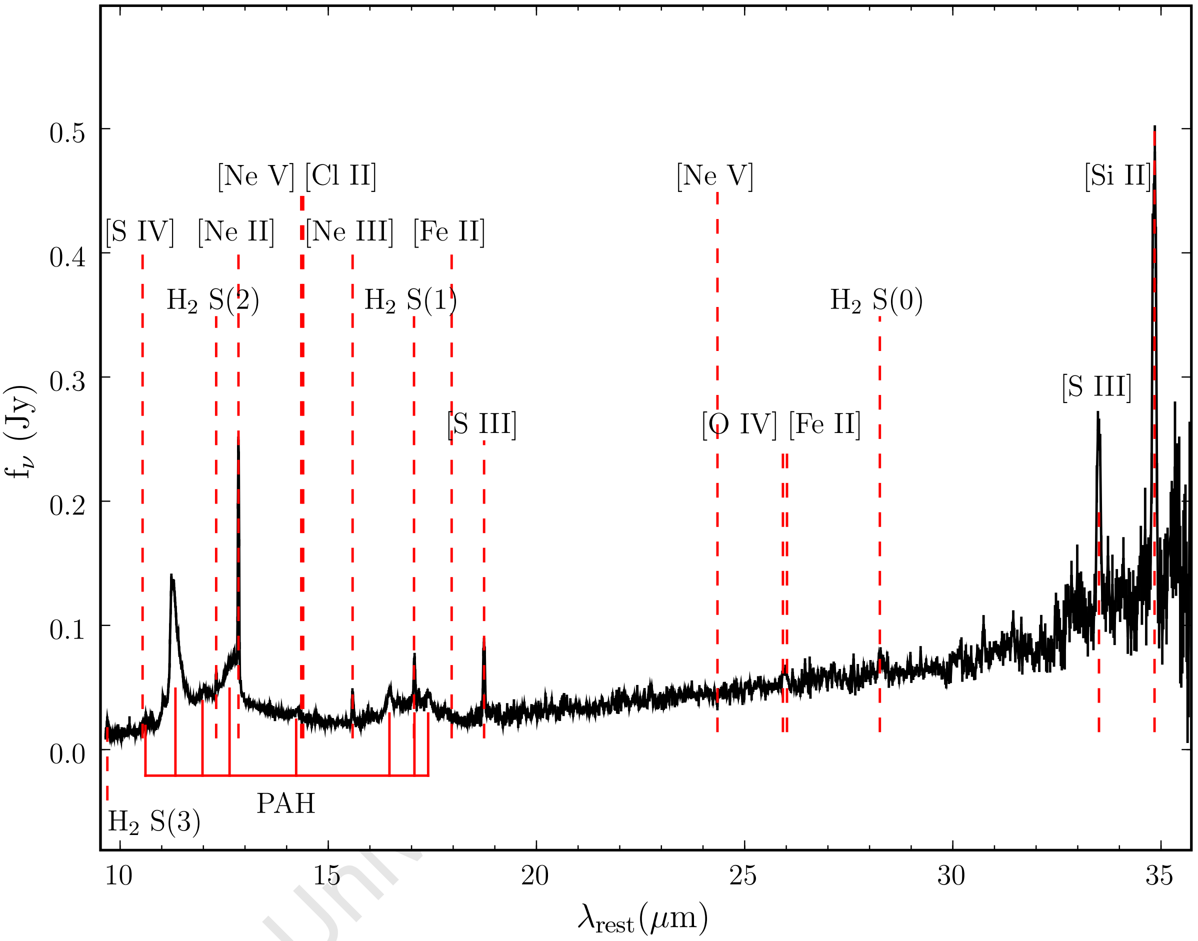

Figure 4.4: IRS SH and LH spectrum - nucleus with 9.25″ aperture.

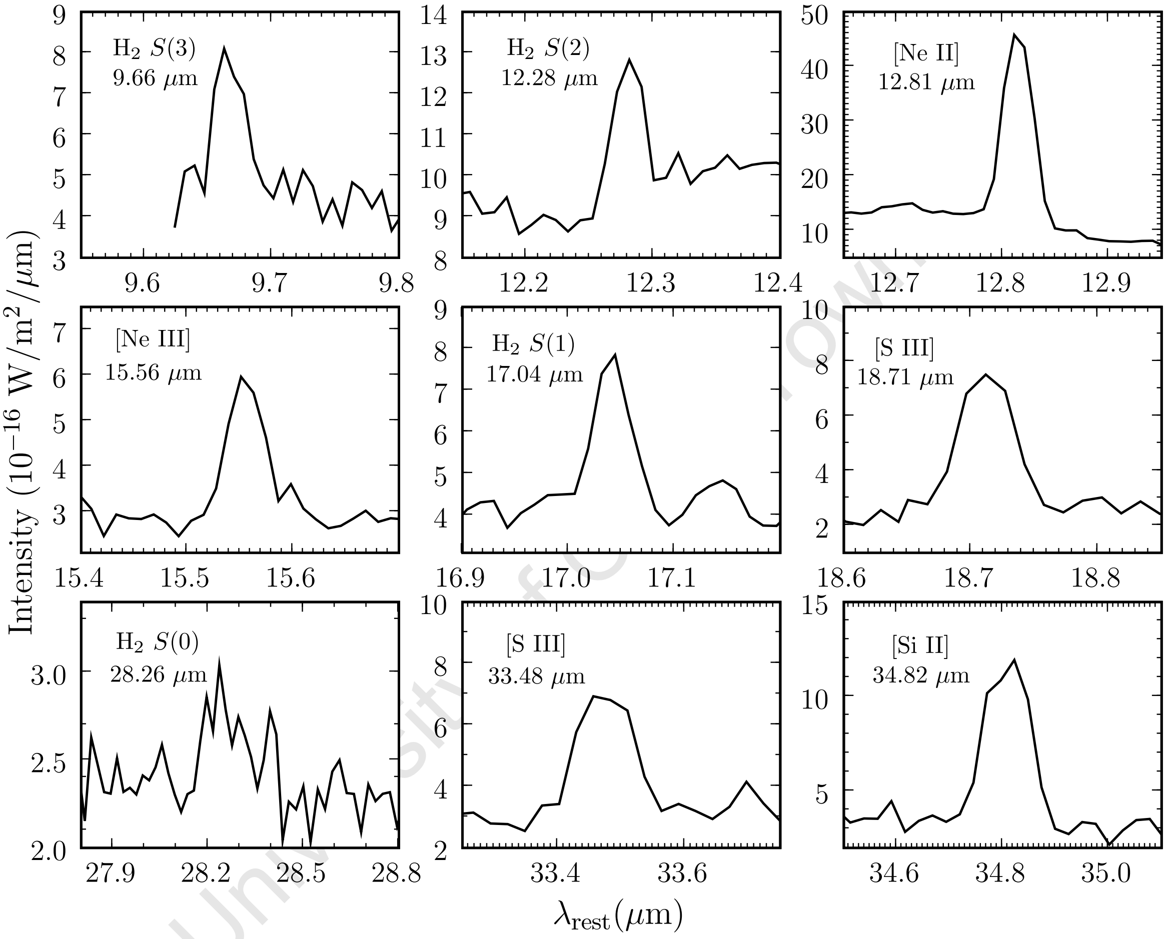

Figure 4.5: Emission lines from the SH and LH spectra of the nucleus (9.25″ aperture) showing their intensities.

4.4 Results: PAH Multifit Measurements

In this section we measure the PAH emission bands using the "Multifit" technique described in Section 4.2. We use the positions and FWHM of the PAH features prescribed by Smith et al. (2007). These PAH complexes are simultaneously fit with first and second-order baseline fits for the continuum. This method incorporates the contribution of the PAH features to the continuum, instead of subtracting it as done in section 4.3. This is illustrated in Fig. 4.6, where the PAH complex is decomposed into individual PAH bands and a second-order baseline is used (as opposed to the spline baseline used in Section 4.3).

Non-PAH emission lines that are part of the PAH complexes are remeasured as part of the multifit.

4.4.1 Entire disk - 37″ aperture

Table 4.3: Emission line measurements - 37″ aperture (SL) - using the PAH Multifit.

Line	λ_{rest} μm	Line FWHM 10^{-3}μm	Equivalent Width μm	Flux 10^{-17} W m^{-2}	S/R [a]	S/R [b]	S/R [c]
PAH	5.70	200.0	− 0.368	37.35	2.5	15.8	16.8
PAH	6.23	175.2	− 2.344	275.07	5.8	132.5	141.1
PAH	6.69	944.6	−10.269	360.82	0.8	32.2	34.3
[Ar II]	6.98	82.5	− 0.037	20.30	6.1	10.9	11.6
PAH	7.42	622.8	− 9.529	226.16	0.6	30.6	32.6
PAH	7.62	346.3	− 6.142	210.79	1.1	51.4	54.7
PAH	7.85	541.6	− 7.931	401.70	1.7	62.6	66.7
PAH	8.33	420.0	− 5.632	111.98	0.4	22.5	24.0
PAH	8.61	340.0	− 2.674	139.53	1.2	34.6	36.9
PAH	10.58	300.0	− 0.654	11.84	0.3	9.4	10.0
PAH	11.23	167.8	− 1.468	59.98	1.3	85.0	90.5
PAH	11.33	556.3	− 2.372	165.82	2.8	70.8	75.4
PAH	11.95	300.0	−1.056	36.25	0.7	28.7	30.6
H_2 $S(2)$	12.28	306.8	− 1.138	32.63	0.7	25.3	26.9
PAH	12.60	300.0	− 0.982	55.64	1.6	44.1	46.9
[Ne II]	12.81	161.4	− 0.606	46.16	2.2	68.0	72.4

[a] Signal-to-noise ratio corresponding to the line flux relative to the line fit residuals.

[b] Signal-to-noise ratio corresponding to the peak height above the continuum relative to the baseline RMS.

[c] Signal-to-noise ratio corresponding to the line flux relative to the baseline RMS.

[d] [Ar II] is blended with H_2 $S(2)$.

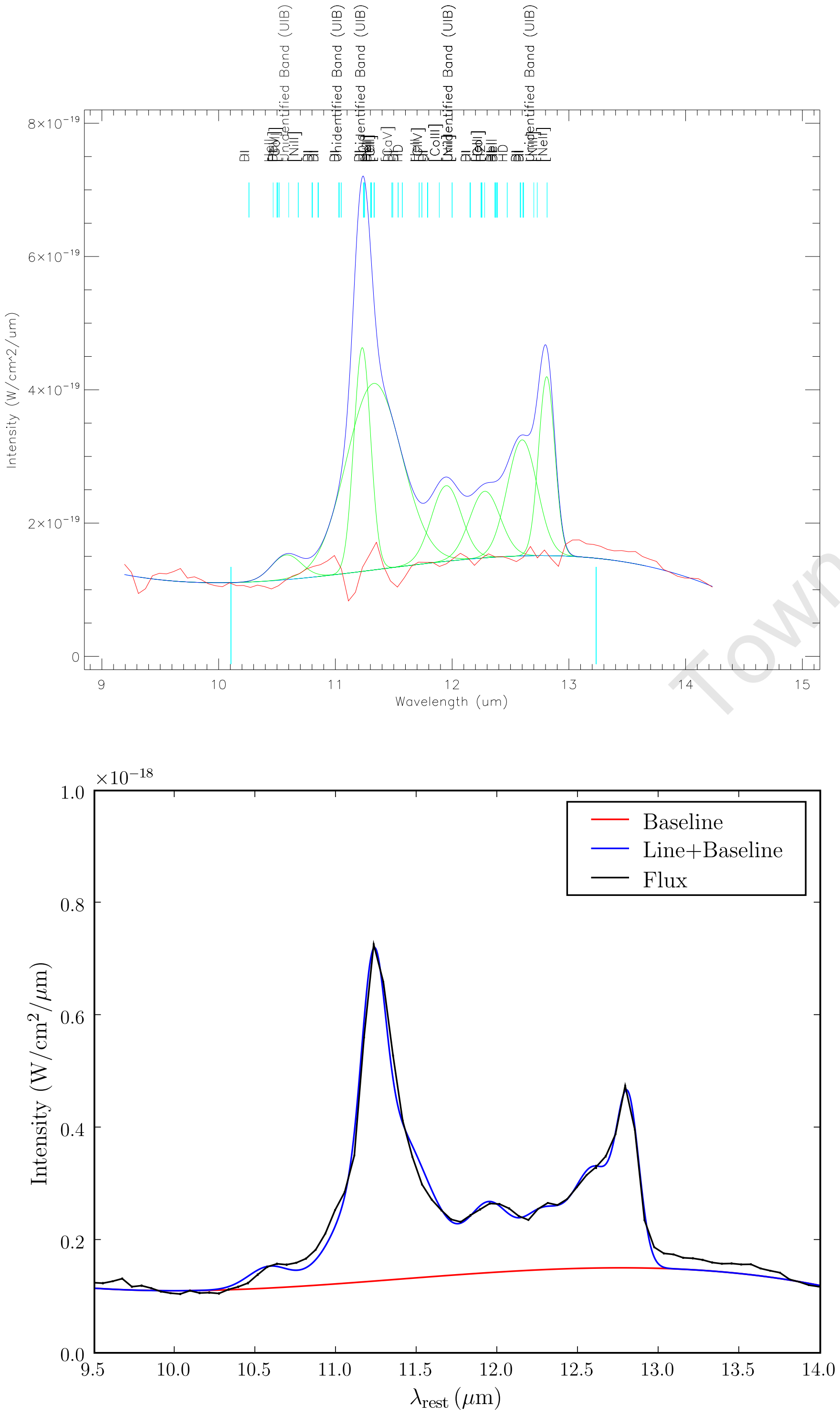

Figure 4.6: Top panel: ISAP output for the PAH multifit of the 12 μm complex. The individual profiles are shown, with the residual from the fit in red. Bottom panel: Plot of the continuum baseline in red and resulting fit to the flux in blue.

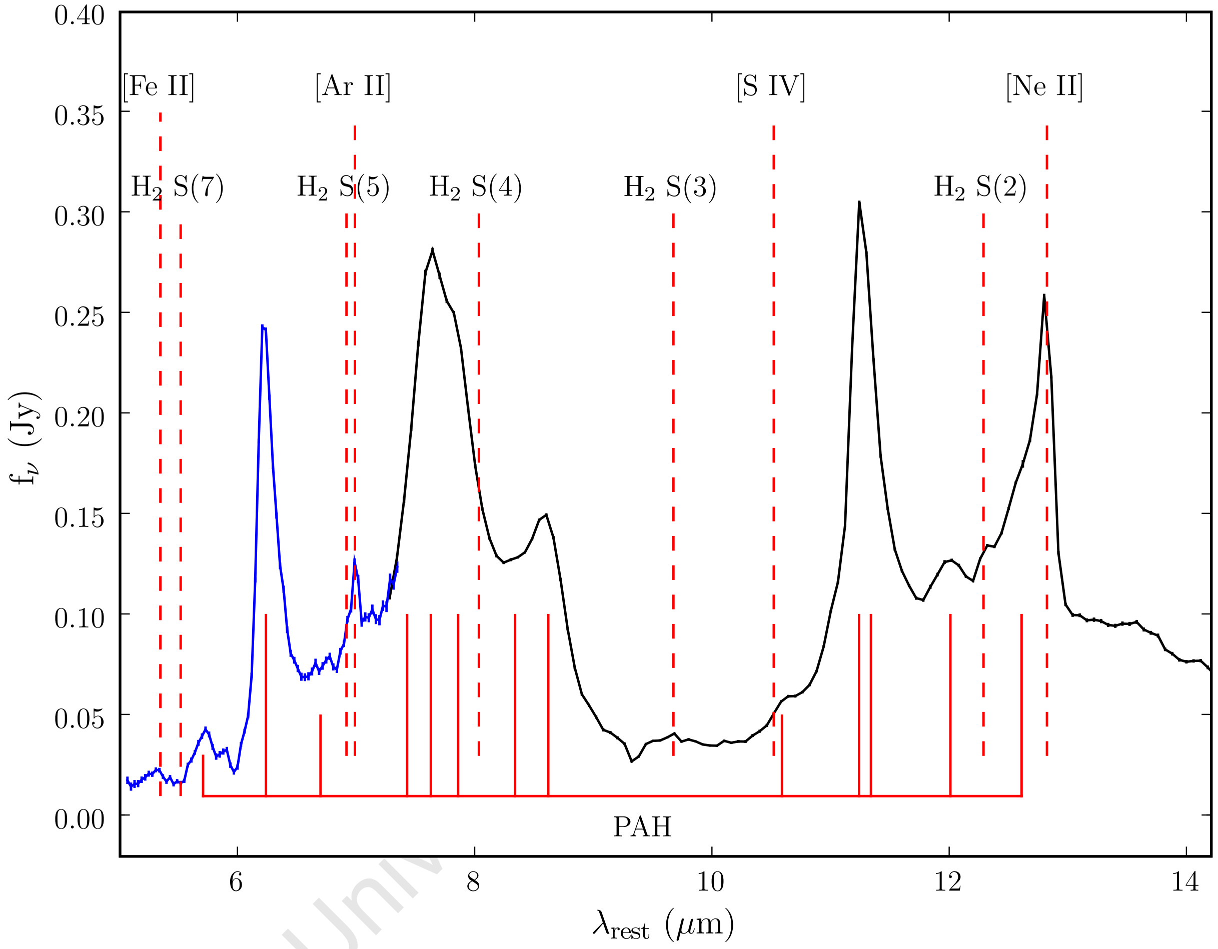

Figure 4.7: IRS SL spectrum - HIZOAJ0836-43 - 37″ aperture, showing the lines that are simultaneously fit.

4.4.2 Nucleus - 9.25″ aperture

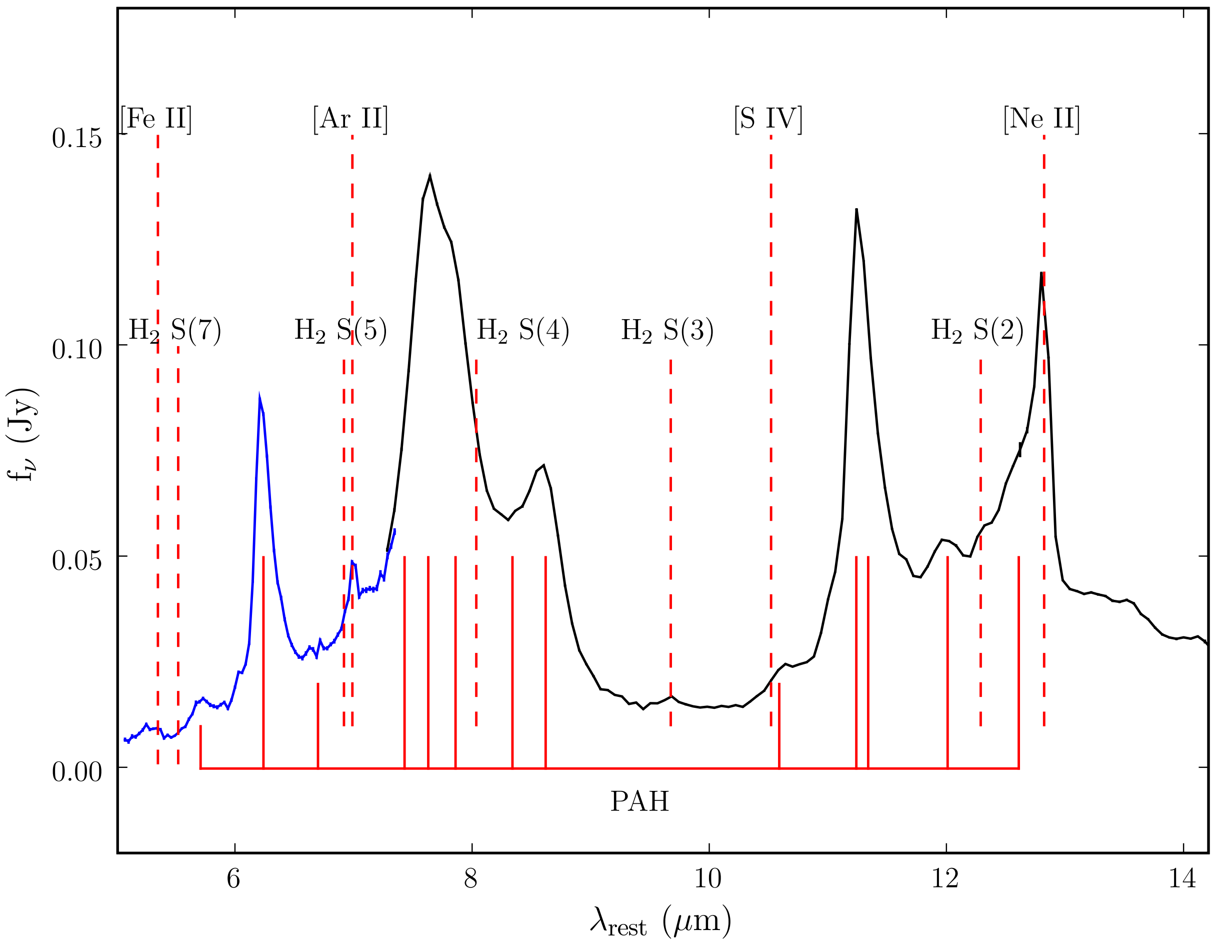

Figure 4.8: IRS SL spectrum - HIZOAJ0836-43 - nucleus with 9.25″ aperture.

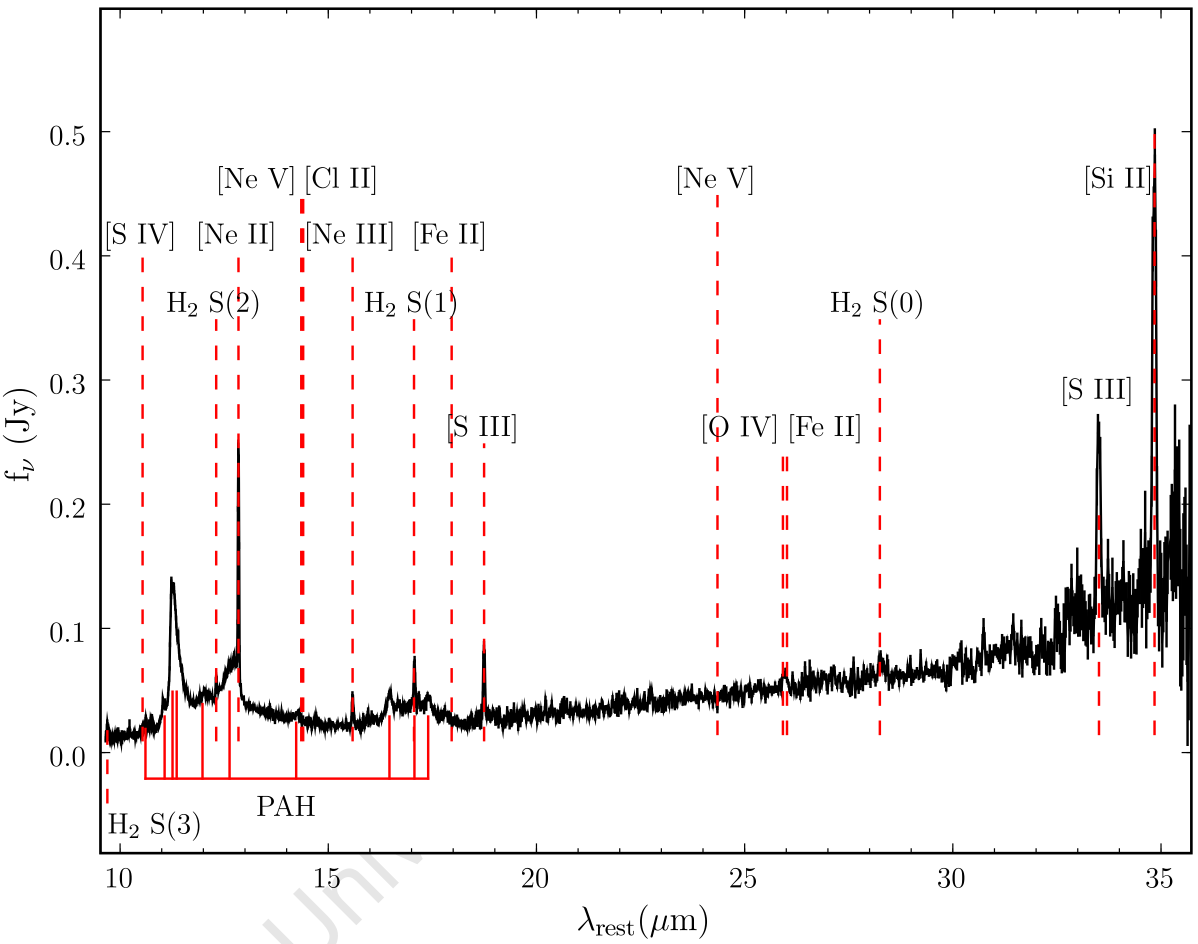

Figure 4.9: IRS SH and LH spectrum - nucleus with 9.25″ aperture.

Table 4.4: Emission Line Measurements - Nucleus (SL+SH+LH) - using the PAH Multifit.

Line	λ_{rest} μm	Line FWHM $10^{-3}\mu$m	Equivalent Width μm	Flux 10^{-17} W m^{-2}	S/R [a]	S/R [b]	S/R [c]
PAH	5.70	200.0	− 0.405	15.04	1.6	7.1	7.5
PAH	6.22	206.4	− 2.156	112.58	6.2	51.2	54.5
PAH	6.69	700.0	− 9.758	82.67	0.5	11.1	11.8
PAH	7.42	900.0	− 12.583	145.58	0.7	15.2	16.2
PAH	7.62	416.7	− 8.474	177.95	2.0	40.1	42.7
PAH	7.85	446.6	− 9.265	88.19	0.7	18.5	19.7
PAH	8.33	813.4	− 10.161	151.01	0.8	17.4	18.6
PAH	8.61	281.8	− 2.837	30.95	0.7	10.3	11.0
PAH	11.04	127.0	− 0.919	4.272	0.3	7.5	8.0
PAH	11.23	118.2	− 1.371	20.79	1.6	39.3	41.8
PAH	11.33	334.9	− 1.998	54.43	3.2	36.3	38.6
PAH	11.95	540.0	− 3.288	27.84	0.5	11.5	12.3
H_2 $S(2)$	12.28	24.6	− 0.906	0.90	0.7	8.2	8.8
PAH	12.6	500.0	− 1.783	44.45	1.8	19.9	21.1
[Ne II]	12.81	32.9	− 0.384	13.07	6.3	88.8	94.6

[a] Signal-to-noise ratio corresponding to the line flux relative to the line fit residuals.

[b] Signal-to-noise ratio corresponding to the peak height above the continuum relative to the baseline RMS.

[c] Signal-to-noise ratio corresponding to the line flux relative to the baseline RMS.

4.5 Continuum Flux Density

The flux density of the continuum was measured at wavelengths applicable to diagnostics dependent on the MIR continuum flux (see Section 5.2.1). They are chosen as regions relatively free of emission features; shown in Table 4.5.

Table 4.5: Continuum fluxes.

λ_{rest} μm	Flux Density Jy	Flux Density 10^{-17} W m$^{-2}\mu$m^{-1}
5.5	0.017 ±0.001	167.2 ±6.2
6.0	0.022 ±0.003	188.2 ±24.5
15.0	0.022 ±0.002	29.8 ±2.9
30.0	0.068 ±0.004	22.6 ±1.3

4.6 Spectra of the East and West Disk

The SL spectrum for the East and West disk extractions (9.25$''$ aperture) are shown in Fig. 4.10. As can be seen the flux density of the East disk is lower compared to the West disk. This asymmetry could be attributed to diffuse, extended emission on the East side (seen as the warped tail-like structure in Fig. 5.1 and 5.2).

4.7 Combined Spectrum with HIZOA J0836-43's SED

We show in Fig. 4.11 HIZOA J0836-43's SED, as described in Section 3.5, with the combined SL, SH and LH spectrum (5 - 36 μm) for the galaxy's nucleus (9.25$''$ extraction). The spectrum is normalised to the 24 μm value of the SED. The features seen in both are consistent.

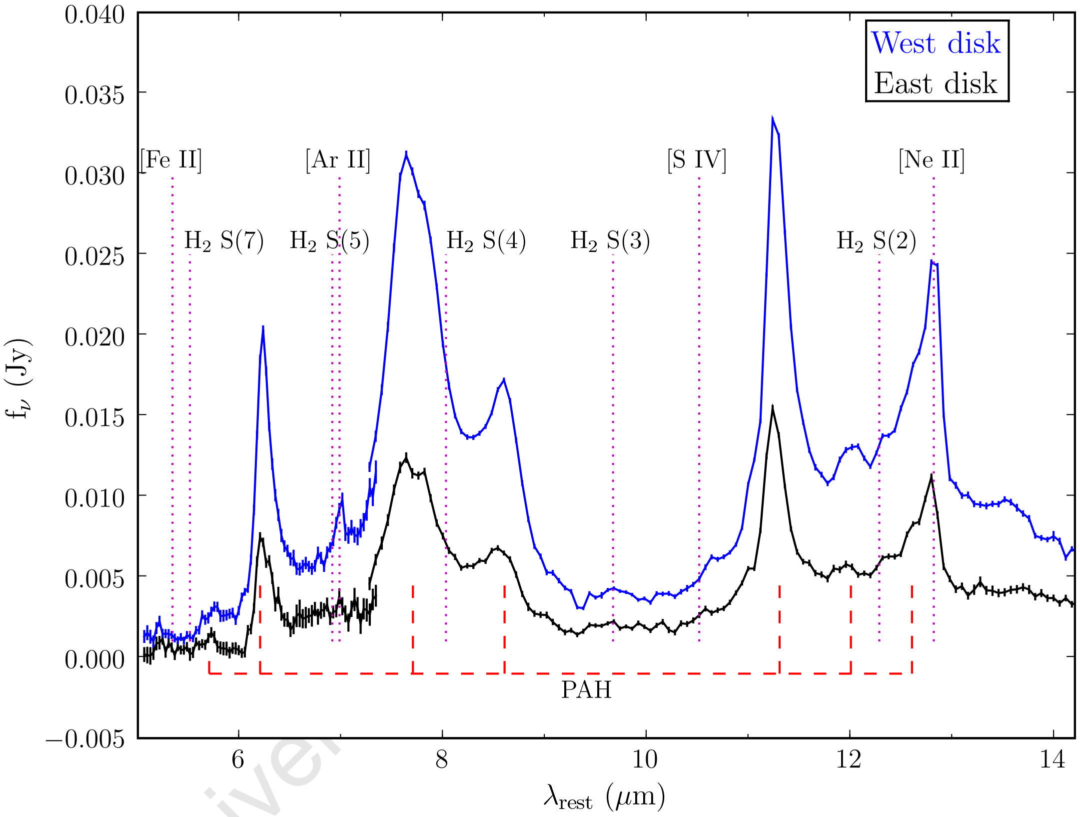

Figure 4.10: IRS SL spectrum - comparison between the East (black) and West (blue) disk (9.25″ aperture).

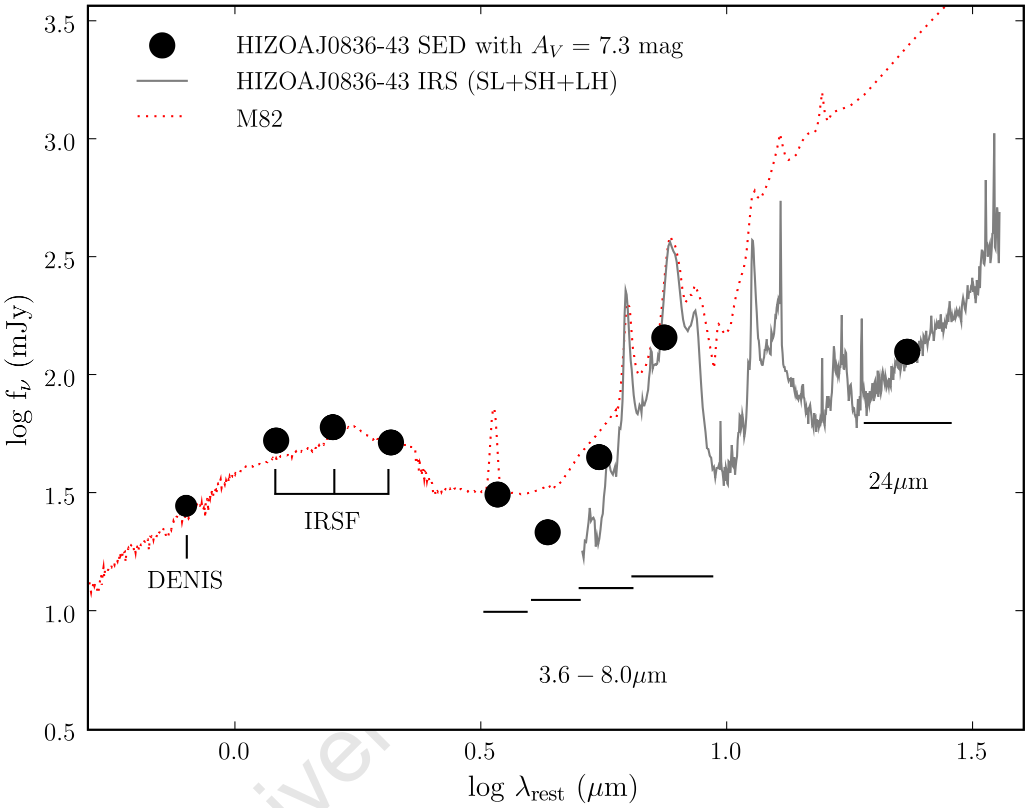

Figure 4.11: HIZOAJ0836-43 SED with combined IRS spectrum (SL+SH+LH). The spectrum of M82, a starburst galaxy, is also shown for comparison.

Chapter 5

HIZOA J0836-43: Photometric and Spectroscopic Analysis

5.1 Photometric Analysis

5.1.1 An Infrared Overview of HIZOA J0836-43

In the infrared we can effectively penetrate the foreground dust of the Milky Way to reveal HIZOA J0836-43. The imaging of the galaxy at infrared wavelengths can be used to construct a quantitative view, i.e. a SED of the distribution and strength of the galaxy's emission. We also gain insight by combining imaging at different wavelengths to probe differing sources of emission. In this Section we consider the infrared and mid-infrared components that give rise to this intriguing LIRG.

Figure 5.1 shows the contributions from the range of wavelengths sampled. The near-infrared, J, H and K_s ($1-2.2\,\mu$m), is sensitive to old, evolved stars which dominate the total stellar population mass. The prominent bulge of HIZOA J0836-43 is most apparent at these wavelengths. IRAC-1 ($3.6\,\mu$m) also samples the old stellar light, with a small PAH and hot dust contribution. IRAC-2 ($4.5\,\mu$m) is sensitive to the tail-end of the Rayleigh-Jeans light distribution from the evolved, luminous stellar component. IRAC-3 ($5.6\,\mu$m) includes hot dust and contributions from PAHs are also present. IRAC-4 ($8\,\mu$m) is predominantly sensitive to emission from PAH molecules, while the MIPS-24$\,\mu$m image samples the warm dust continuum. Apart from the strong bulge component, we see that the contribution from PAHs is exceptionally strong and there is a significant amount of cold dust. Dust emission in the MIR and FIR represents reprocessed starlight where ultraviolet photons are absorbed by dust which reradiates in proportion to the strength of the radiation field. The strong PAH and dust emission seen in the images is indicative of copious star formation in HIZOA J0836-43.

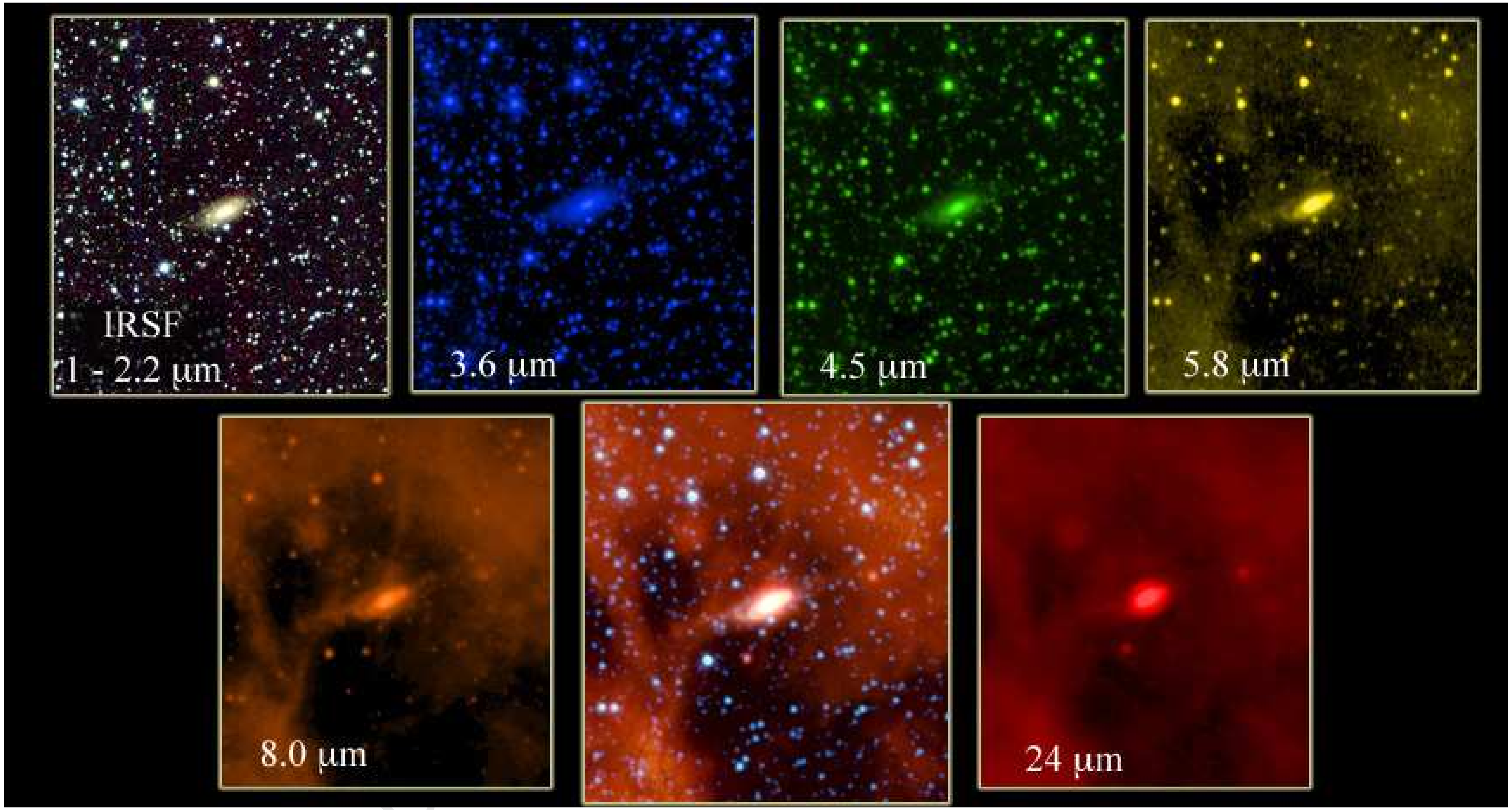

Figure 5.1: Images of HIZOA J0836-43 showing a composite J, H and K_s stamp and individual stamps for the IRAC and MIPS-24 band, as well as an image combining all wavelengths (bottom, center). At $\lambda > 8\,\mu$m, note the strong emission from the Milky Way's interstellar medium that is foreground to the galaxy.

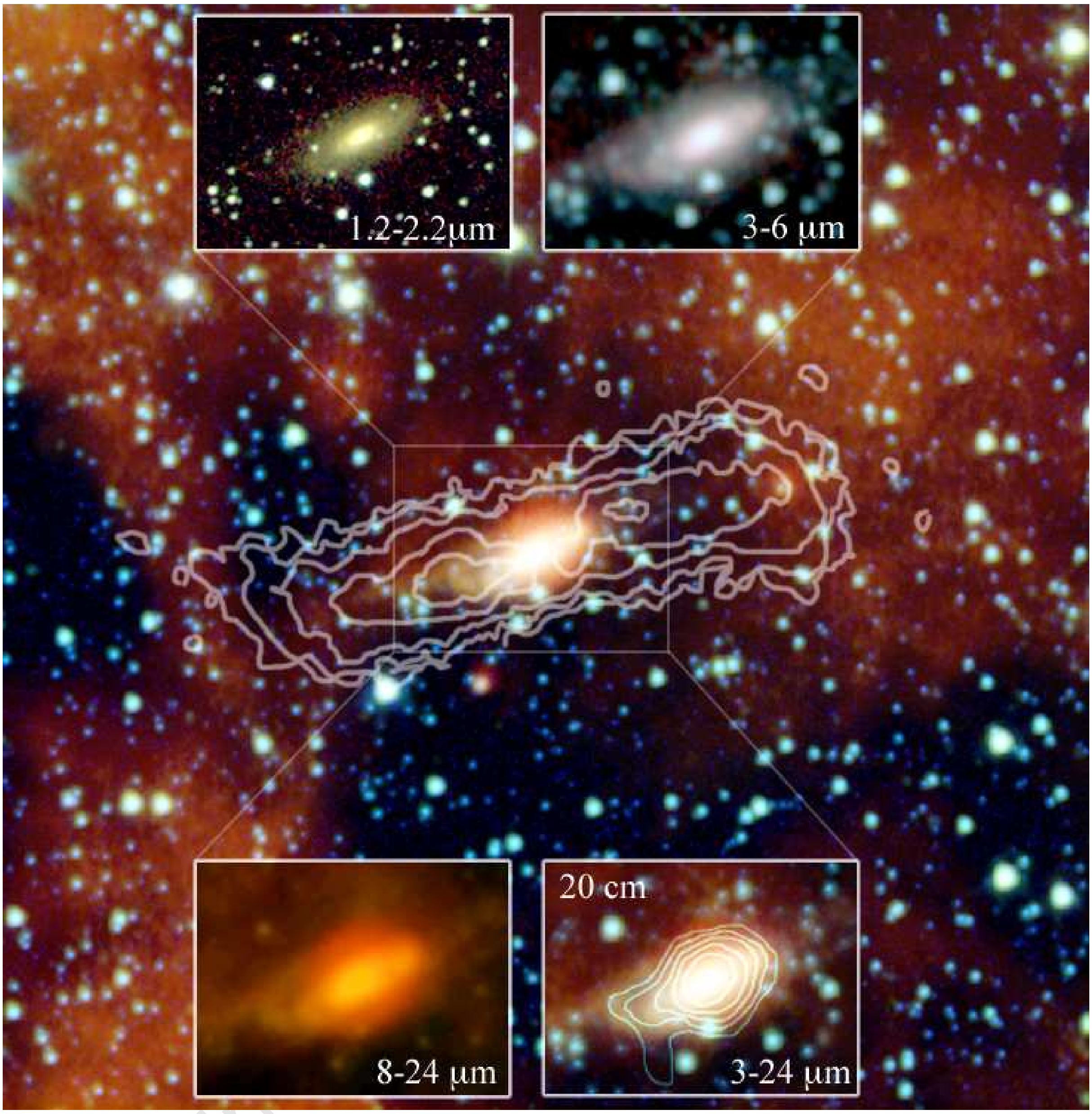

Figure 5.2: Composite $1-24\,\mu$m image of HIZOA J0836-43 ($\sim 4'$ FoV or $\sim$ 170 kpc) with H I contours overlaid (from Donley et al. 2006; insets show zoomed versions of the inner $1'$ region; 20 cm radio contours overlay the combined $3-24\,\mu$m inset (bottom right).

Figure 5.2 shows a composite $1-24\,\mu$m image of the galaxy and its local $\sim 4'$ (170 kpc) environment. H I contours from Donley et al. (2006) demonstrate the enormous size of the disk, extending $\sim 3'$ or $\sim$ 130 kpc in diameter. The galaxy appears as an inclined extended disk galaxy with a significant bulge population whose light distributions indicates an early Hubble Type of $\sim$ S0/Sa, but whose bolometric luminosity largely arises from infrared radiation.

The $1-5\,\mu$m window traces the old stellar population (top panel in Fig. 5.2), while the

MIR ($\lambda > 5\mu$m) is sensitive to the interstellar medium, notably the warm dust continuum and emission from PAH molecules. PAHs produce broad emission bands in the MIR and are linked to ongoing or recent star formation (Allamandola et al. 1985). The emission likely arises from photodissociation regions (PDRs) which form adjacent to H II regions produced by star formation (Hollenbach & Tielens 1997). The $8 - 24\,\mu$m composite shows strong emission from PAH molecules and warm dust. The 20 cm radio continuum is correlated with the $8 - 24\,\mu$m emission, indicating a common star-formation origin. While the bulk of the infrared emission is concentrated in the central nuclear region, it is clearly extended and exhibits spiral-arm asymmetries.

5.1.2 Stellar Mass of HIZOA J0836-43

The near-infrared imaging of HIZOA J0836-43, as well as its surface brightness profiles (Donley et al. 2006), suggests that the galaxy has a evolved stellar population within a prominent bulge and an extended disk of stars both evolved and newly forming. Knowledge of the amount of stellar mass within the galaxy is essential for determining its composition and evolution and also provides a diagnostic to probe star formation.

To calculate the stellar mass of HIZOA J0836-43, we adopt the mass-to-light relation of Bell et al. (2003) appropriate for relatively massive galaxies. The M/L_K distribution has a mean value of 0.90 $M_\odot/L_\odot$ with a 1σ range of 0.68 to 1.12. This range incorporates various star formation histories of massive galaxies. But note that HIZOA J0836-43 is actively forming stars and is not typical of other massive galaxies. A "hybrid" solution is required, which will lead to a larger uncertainty in our estimate. We adopt the mean value for the M/L_K distribution of $< M/L_K > = 0.90\ M_\odot/L_\odot$. This gives a stellar mass of $M_{\rm stellar} = 4.4 \pm 1.4 \times 10^{10}\,M_\odot$.

This value is just less than the median mass ($M_{\rm stellar} = 4.6 \pm 1.4 \times 10^{10}\,M_\odot$) found for 10^5 local universe galaxies in the Sloan Digital Sky Survey (Kauffmann et al. 2003). They find that most of the stellar mass in the local universe resides in galaxies with stellar masses between $2.5 - 10 \times 10^{10}\,M_\odot$.

However, the stellar mass of HIZOA J0836-43 is at the low end compared to the sample of 159 local LIRGS from Wang et al. (2006) who find a range of $3 \times 10^{10} - 5 \times 10^{11}\,M_\odot$, which suggests that HIZOA J0836-43 is still actively building its stellar population.

5.1.3 Mass of Cold Molecular Hydrogen in HIZOA J0836-43

The composition of a galaxy is intimately connected to its formation and past and future evolution. In this regard, the distribution and mass of gas and dust in a galaxy enables the study of the physical processes taking place. We already have detailed knowledge of the atomic gas and stellar mass in HIZOA J0836-43 and seek to extend this inventory to other metrics, the most important being the molecular hydrogen distribution and mass. The molecular gas gives a direct measure of the amount of fuel that is available for star formation and is therefore a crucial component of the star formation process. Unfortunately this region of the sky has yet to be surveyed with mm-wavelength telescopes sensitive to molecular CO, a useful tracer of the underlying molecular hydrogen. In the absence of CO observations, we can obtain only a rough measure from our infrared measurements and, accordingly, will use this cautiously as a probe of the gas content of the galaxy.

We estimate the mass of molecular hydrogen using the method of Gao & Solomon (2004). They find a tight correlation between the far-infrared and mm-wave molecular emission for gas-rich galaxies. Starting with the FIR-HCN (far-infrared - hydrogen cyanide) luminosity relation, as follows:

$$\log L_{\mathrm{IR}} = 1.00 \log \mathrm{L}'_{\mathrm{HCN}} + 2.9, \tag{1}$$

where L_{IR} represents the far-infrared luminosity and $\mathrm{L}'_{\mathrm{HCN}}$ is the line luminosity of the HCN molecule in units of $\mathrm{K\,km\,s^{-1}\,pc^{2}}$. Using a Two-Parameter Correlation fit, they determine the following relation between L'_{HCN} and L'_{CO}, both in units of $\mathrm{K\,km\,s^{-1}\,pc^{2}}$:

$$\log L'_{\mathrm{HCN}} = 1.26 \log L'_{\mathrm{CO}} - 3.73 \tag{2}$$

Combining the above two equations yields the relation:

$$\log L_{\mathrm{IR}} = 1.26 \log L'_{\mathrm{CO}} - 0.83 \tag{3}$$

Substituting the FIR luminosity determined in Section 3.5, $L_{\mathrm{FIR}} = 1.2 \times 10^{11} L_{\odot}$, we predict a CO luminosity of $L'_{\mathrm{CO}} = 2.82 \times 10^{9}\,\mathrm{K\,km\,s^{-1}\,pc^{2}}$.

Using the relation $M(\mathrm{H_2}) = \alpha L'_{\mathrm{CO}}$ (Solomon & Van den Bout 2005) and the approximate value found for the Milky Way value, $\alpha = 4.6\,M_{\odot}(\mathrm{K\,km\,s^{-1}\,pc^{2}})^{-1}$ (Solomon & Barrett 1991), provides the following estimate for the mass of molecular hydrogen:

$$M(\mathrm{H_2}) \approx 1.3 \times 10^{10}\,\mathrm{M_{\odot}} \tag{4}$$

corresponding to $\sim \frac{1}{6}$ the amount of neutral hydrogen in HIZOA J0836-43. This value of $M(\mathrm{H_2})$ is typical for LIRGs as shown by Gao & Solomon (2004) who find an average value of $2.2 \times 10^{10} M_{\odot}$ for the 22 LIRGs in their study. Hinz & Rieke (2006) find an average of $1.6 \times 10^{10} M_{\odot}$ for 10 LIRGS in their study, ranging from $3.3 \times 10^{9} M_{\odot}$ to $3.0 \times 10^{10} M_{\odot}$.

Given the nature of this estimate, its close tie to the far-infrared emission, we consider this number to be mostly illustrative of the tremendous atomic and molecular mass that is fueling this system.

5.1.4 Star Formation Efficiency

The efficiency of star formation in a galaxy tells us how the galaxy is evolving and potentially how much star formation has and will take place. Since the current star formation is traced by the total infrared luminosity, we can consider star formation efficiency by relating it to the amount of gas available to be converted into stars. We know the mass of H I gas in HIZOA

J0836-43 quite accurately, but star formation is more closely related to $M(\mathrm{H}_2)$ for which we only have a rough estimate. The reliability of the following calculation of star formation efficiency is therefore less reliable than if it had been derived from a more direct measure of the gas (e.g., CO observations).

We can use the estimate of the mass of molecular hydrogen determined in Section 5.1.3 to calculate the ratio of molecular to neutral hydrogen as follows:

$$M(\mathrm{H}_2)/M(\mathrm{HI}) \approx \frac{1.3\times10^{10}M_\odot}{7.5\times10^{10}\,M_\odot} \approx 0.17 \qquad (5)$$

This ratio is typical for late-type galaxies, as shown by Boselli et al. (2002) who find an average value of 0.14. HIZOA J0836-43 appears to be similar to a late-type galaxy in terms of its gas fraction.

The Star Formation Efficiency (SFE) is defined as the ratio of total IR luminosity to gas mass. Using the H I mass for HIZOA J0836-43 we obtain a SFE of

$$L_{\mathrm{TIR}}/M(\mathrm{HI}) = \frac{1.19\times10^{11}\,L_\odot}{7.5\times10^{10}\,M_\odot} = 1.6\pm0.3\frac{L_\odot}{M_\odot} \qquad (6)$$

The mass of molecular hydrogen determined in Section 5.1.3 is based on the galaxy's L_{TIR}. Since these quantities are not independent, we consider the SFE of HIZOA J0836-43, in terms of $M(\mathrm{H}_2)$, with caution.

$$L_{\mathrm{TIR}}/M(\mathrm{H}_2) \approx \frac{1.19\times10^{11}\,L_\odot}{1.3\times10^{10}\,M_\odot} \approx 9.2\frac{L_\odot}{M_\odot} \qquad (7)$$

HIZOA J0836-43's star formation appears less efficient at star formation when considering its H I mass compared to $M(\mathrm{H}_2)$. Its H I-disk is enormous and we would only expect a fraction of it to reach the density required to form H_2.

If there exists a large amount of molecular hydrogen in relation to the amount of star formation, it could cause the interstellar medium to behave differently compared to "normal" star forming galaxies, especially in terms of lowering the radiation field density outside of the star forming regions. In section 5.5.1, we consider this scenario in light of the exceptionally low MIR continuum relative to the exceptionally bright PAH emission features.

5.1.5 q Ratios

We now consider the q ratios of the galaxy to probe the nature and efficiency of the physical processes that are heating the interstellar medium. The q ratio is the quantitative measure of the FIR to radio flux ratio, which is correlated to the efficiency of a galaxy to produce infrared emission relative to the radio continuum that traces synchrotron emission associated with massive star formation (Helou et al 1985).

The q ratios are defined as the flux density in the infrared divided by the flux density of the radio continuum, i.e.

$$q_{\mathrm{IR}} = \log(S_{\mathrm{IR}}/S_{20\mathrm{cm}})$$

Bell et al. (2003) defines $q_{\rm TIR}$ as the ratio of total $8 - 1000\,\mu$m infrared luminosity to the radio power and Appleton et al. (2004) define q_{24} and q_{70} as the ratio of $24\,\mu$m flux density and $70\,\mu$m flux density respectively to the radio flux density. These ratios for HIZOA J0836-43 are shown in Table 5.1.

Table 5.1: q ratios for HIZOA J0836-43.

q ratio	Reference	Value
$q_{\rm TIR}$	Bell (2003)	2.3 ±0.5
q_{24}	Appleton et al. (2004)	0.72 ±0.07
q_{70}	Appleton et al. (2004)	1.98 ±0.40

In a sample of 162 galaxies which do not appear to harbour active galactic nuclei, Bell (2003) find a median $q_{\rm TIR}$ value of 2.64 ± 0.02. Compared to the galaxies in the Bell (2003) survey, HIZOA J0836-43 appears to be on the lower end of the relation, but within the scatter. This is also true compared to the sample of Bressan et al. (2002) who find a range of $q_{\rm FIR}$ between 2.10 and 3.11 for a sample of 26 compact ULIRGs, where $S_{\rm FIR} = 1.26 \times 10^{14}\,(2.58\,S_{60\mu{\rm m}} + S_{100\mu{\rm m}}{\rm W\,m^{-2}})$,

Starburst galaxies generally have a relatively high $q_{\rm FIR}$ with an average of ~ 2.75, whereas pure AGN have $q_{\rm FIR} < 2$ (Baan & Klöckner 2006). However, it is possible for intense nuclear starbursts to mimic the presence of an AGN (Baan & Klöckner 2006).

Appleton et al. (2004) investigated the mid-IR/radio correlation using 179 sources between $z \sim 0.1$ and $z \sim 1$ from the *Spitzer* First Look Survey. The correlation was observed for both wavelengths, but the dispersion was far greater for the q_{24} ratio. They attributed this to the wide range of SED shape within the population. They find a mean value of 0.94 ± 0.23 for q_{24} and 2.15 ± 0.16 for q_{70}.

A comparison with the q_{24} and q_{70} ratios from the *Spitzer* Infrared Nearby Galaxy Sample (SINGS) will be done in the next Section.

5.1.6 Photometric Comparison to SINGS Galaxies

HIZOA J0836-43 appears to be unusual in the context of it being a LIRG and having a H I-massive disk. To determine how its infrared properties are similar or different to other galaxies, it is useful to compare it to a sample of local galaxies. In this Section we compare the photometric properties of HIZOA J0836-43 to the *Spitzer* Legacy Study, SINGS, to delineate its characteristics.

The *Spitzer* Infrared Nearby Galaxy Survey is an infrared imaging and spectroscopic survey of 75 nearby ($d < 30\,$Mpc) galaxies aimed at characterizing infrared emission over a broad range of morphological types and environments (Kennicutt et al. 2003). Utilising *Spitzer's* imaging and low-resolution spectroscopy in combination with multiwavelength ancillary data, SINGS will

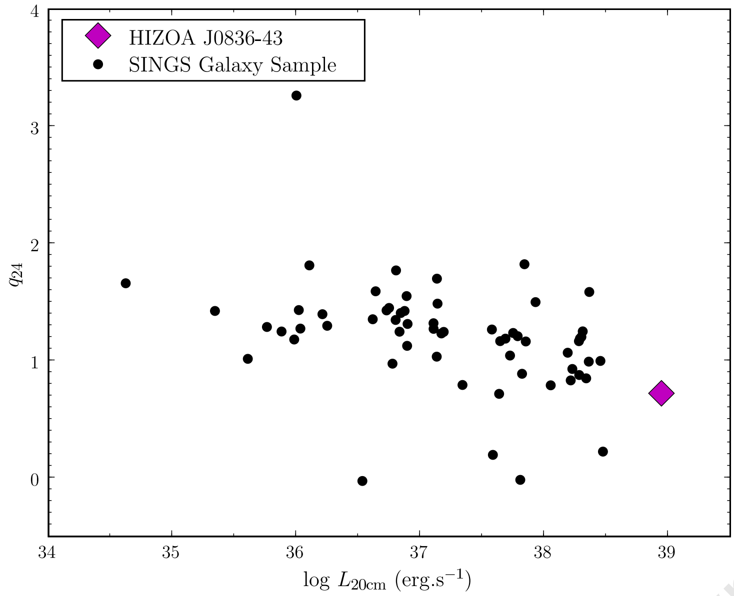

Figure 5.3: The HIZOA J0836-43 q_{24} ratio versus 20 cm luminosity compared to SINGS.

probe the physics of the star-forming interstellar medium and galaxy evolution. This archive of data provides a valuable and unique comparison sample for other *Spitzer* galaxy projects. The SINGS measurements are provided by courtesy of D. Dale (2008).

SINGS covers a diverse range of "normal" local galaxies. Approximately a dozen galaxies were chosen in the galaxy types E-S0, Sa-Sab, Sb-Sbc, Sc-Scd, Sd-Sm, Im-I0 and with a wide range in infrared luminosity ($< 10^7 - 3 \times 10^{11} L_\odot$) and infrared/optical ratio ($L_{\mathrm{IR}}/L_{\mathrm{v}} < 0.02 - 42$). SINGS can be considered a representative cross section of galaxies found in the Local Supercluster. Although it does not include galaxies with absolute extreme properties, it provides a useful comparative tool. We compare the photometric, star formation and radio properties of HIZOA J0836-43 to 74 of the SINGS galaxies. The only galaxy in the sample not represented is NGC 3034 (M82), the observations of this galaxy suffered from severe saturation effects, due to the bright core, which prevented reliable flux densities from being extracted from the *Spitzer* data (Dale et al. 2007).

q Ratios

In the first SINGS comparison, we look at the q ratios (described in Section 5.1.5) of the SINGS sample.

In Fig. 5.3 we plot q_{24} against the 20 cm luminosity for HIZOA J0836-43. The 61 SINGS galaxies with 20 cm luminosities have an average q_{24} value of 1.21 ± 0.49, or ~ 16 times more $24\,\mu$m flux compared to 20 cm flux. HIZOA J0836-43 has one of the lowest q ratios, $q_{24} = 0.72 \pm 0.07$, by comparison, indicating only ≈ 5 times more $24\,\mu$m flux compared to 20 cm flux, and thus a paucity of MIR emission compared to the radio continuum.

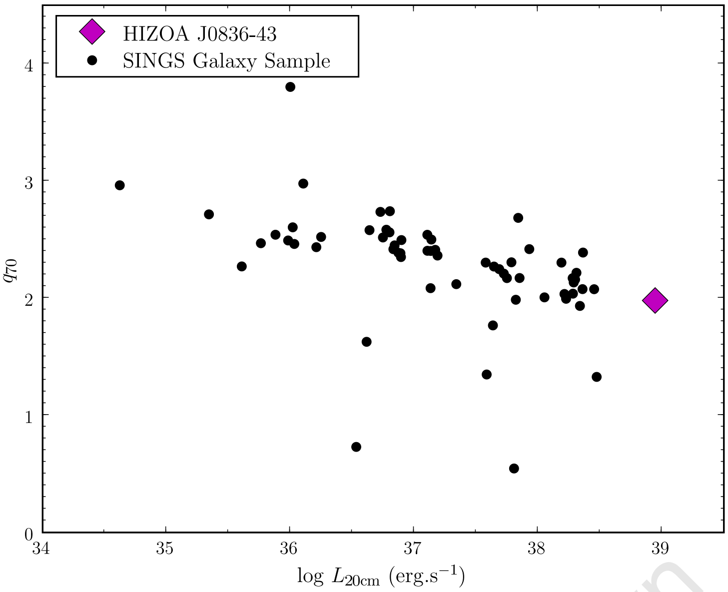

Figure 5.4: The HIZOA J0836-43 q_{70} ratio versus 20 cm luminosity compared to SINGS.

In Fig. 5.4 we plot q_{70} versus 20 cm luminosity which shows a similar result to that seen for q_{24}. The 61 SINGS galaxies have an average q_{70} of 2.27 ± 0.47, corresponding to a flux ratio of $F(70\mu\mathrm{m})/F(20\mathrm{cm}) \sim 190$. HIZOA J0836-43 has a q_{70} ratio of 1.98 ± 0.40, indicative of ~ 95 times more 70 μm flux compared to its radio continuum emission.

For both q ratios, HIZOA J0836-43 is below average for the sample, but within the linear trend seen for SINGS galaxies. We attribute this to an exceptionally strong radio continuum flux density compared to 24 μm and 70 μm, and to the paucity of 24 μm emission relative to the FIR.

We see that HIZOA J0836-43 has relatively low q_{TIR} (see Section 5.1.5), q_{70} and to a lesser extent q_{24} ratios. In the absence of evidence of an AGN, this implies strong non-thermal emission from supernovae as a result of recent, active star formation. Since the galaxy is a LIRG and producing copious amounts of MIR emission, the geometry of heating sources plays a key role. The strong radio emission is centrally concentrated and likely coming from an intense nuclear starburst. The intensity of radiation would be very high and not conducive to dust emission due to grains being destroyed by hard radiation. However, the majority of MIR/FIR radiation could be coming from a larger area with less strong ultraviolet radiation, perhaps circumnuclear. This would require large amounts of molecular gas to shield the outer areas from the intense nuclear starburst and produce strong dust emission through the formation of PDRs.

In Fig. 5.5 we show $L_{24\mu\mathrm{m}}/L_{70\mu\mathrm{m}}$ versus $L_{20\mathrm{cm}}$. The $L_{24\mu\mathrm{m}}/L_{70\mu\mathrm{m}}$ is low, compared to other star forming galaxies. HIZOA J0836-43 has the greatest 20-cm luminosity ($L_{20\mathrm{cm}} = 8.81 \times 10^{38}\mathrm{erg\,s^{-1}}$) due to its high star formation rate (Bell et al. 2003). Given the large 20 cm luminosity, HIZOA J0836-43 is seen to be deficient in 24 μm emission, roughly a factor of ~ 2

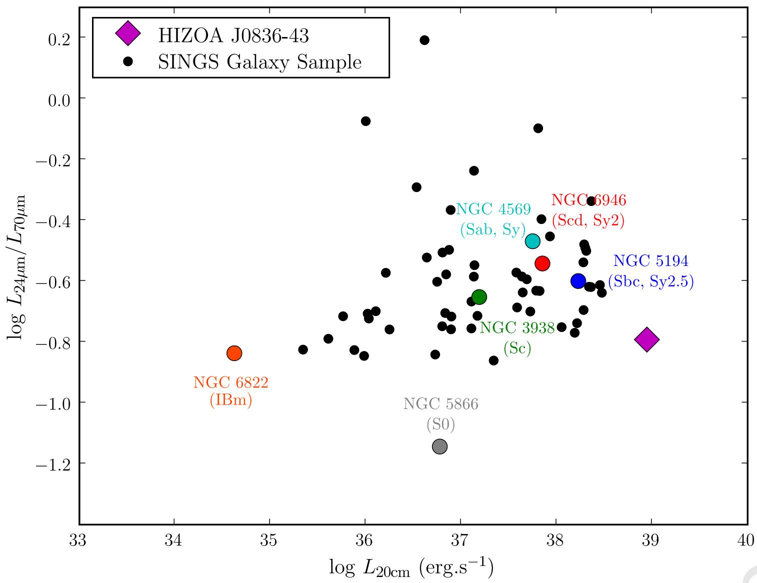

Figure 5.5: Ratio of 24 μm over 70 μm luminosity versus 20 cm luminosity for HIZOA J0836-43 and SINGS galaxies.

compared to the trend seen in this diagram.

Star Formation Rate Comparison

HIZOA J0836-43 has a high star formation rate ($\sim 20.5\,M_\odot\,\mathrm{yr}^{-1}$) which is typical of most local LIRGs (see Section 1.6). We show in Fig. 5.6 the star formation rates of the SINGS galaxies and HIZOA J0836-43 to emphasise this extreme property in comparison to relatively “normal” galaxies in the local universe. The highest star formation rate in SINGS is that of NGC 4254, an Sc galaxy with a SFR of $\sim 11\,M_\odot\,\mathrm{yr}^{-1}$ (calculated from Hα emission; Kennicutt et al. 2003).

Luminosity relations

In this section we compare the luminosities and luminosity ratios of HIZOA J0836-43, to the galaxies in SINGS. Table 5.2 summarises the galaxy's luminosities in different wavelength bands (from Section 3.4), as well as key ratios that probe the galaxy's emission. By comparing HIZOA J0836-43 to SINGS galaxies, we can probe the behaviour of the galaxy at different wavelength bands.

In Fig. 5.7 we compare the $L_{8\mu m}/L_{24\mu m}$ luminosity ratio to the 3.6 μm luminosity which traces mostly stellar light. It is evident that HIZOA J0836-43 is very luminous at 3.6 μm compared to the SINGS galaxies, and therefore has a higher stellar mass: HIZOA J0836-43 has $L_{3.6\mu m} = 6.85 \times 10^{43}\,\mathrm{erg\,s^{-1}}$, just less than the largest $L_{3.6\mu m}$ in SINGS, NGC 4594 with $L_{3.6\mu m} = 7.39 \times 10^{43}\,\mathrm{erg\,s^{-1}}$. HIZOA J0836-43 has a high $L_{8\mu m}/L_{24\mu m}$ ratio compared to other star forming galaxies. The average $L_{8\mu m}/L_{24\mu m}$ ratio for 27 Sb/Sc galaxies in SINGS is 2.33

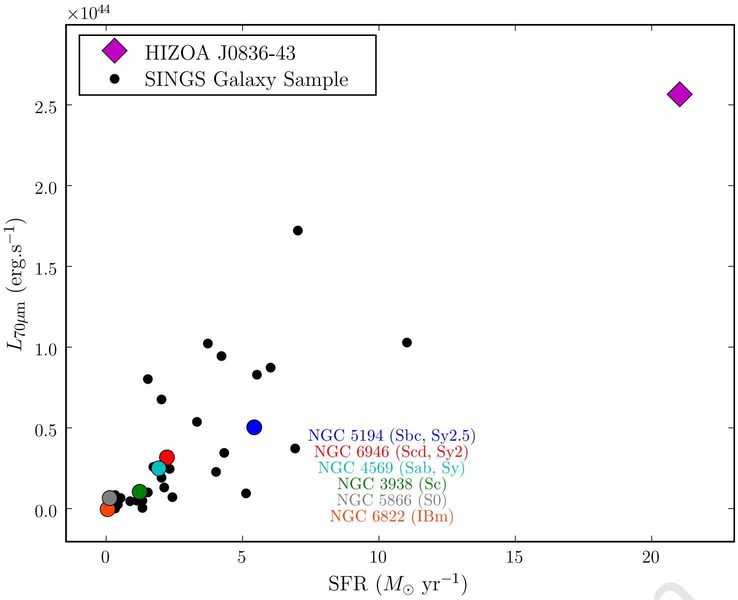

Figure 5.6: 70 μm luminosity versus SFR for HIZOA J0836-43 and SINGS galaxies.

Table 5.2: Luminosity Ratios of HIZOA J0836-43

Waveband	Luminosity
$L_{3.6\mu\mathrm{m}}$	17.6 ±0.8 × $10^9 L_\odot$
$L_{4.5\mu\mathrm{m}}$	9.7 ±0.5 × $10^9 L_\odot$
$L_{5.8\mu\mathrm{m}}$	15.7 ±0.9 × $10^9 L_\odot$
$L_{8\mu\mathrm{m}}$	36.7 ±2.0 × $10^9 L_\odot$
$L_{24\mu\mathrm{m}}$	10.6 ±0.9 × $10^9 L_\odot$
$L_{70\mu\mathrm{m}}$	65.9 ±12.1 × $10^9 L_\odot$
$L_{160\mu\mathrm{m}}$	38.7 ±7.1 × $10^9 L_\odot$
$L_{4.5\mu\mathrm{m}}/L_{8\mu\mathrm{m}}$	0.27 ±0.02
$L_{8\mu\mathrm{m}}/L_{24\mu\mathrm{m}}$	3.45 ±0.34
$L_{24\mu\mathrm{m}}/L_{70\mu\mathrm{m}}$	0.16 ±0.03
$L_{70\mu\mathrm{m}}/L_{160\mu\mathrm{m}}$	1.70 ±0.26

(or log $L_{8\mu\mathrm{m}}/L_{24\mu\mathrm{m}}$= 0.37), compared to HIZOA J0836-43's value of 3.4. Galaxies with similar ratios are either S0/Sa galaxies (eg. NGC 1266, NGC 1291, NGC 1316) or Sb/Sc galaxies with low star formation ($< 1.5\ M_\odot\,\mathrm{yr}^{-1}$) such as NGC 2841, NGC 4450 and NGC 3184.

As is evident in Fig. 5.8, HIZOA J0836-43 has stronger PAH emission (as traced by $L_{8\mu\mathrm{m}}$) than any of the SINGS galaxies. The largest $L_{8\mu\mathrm{m}}$ value observed in SINGS is from NGC 4254,

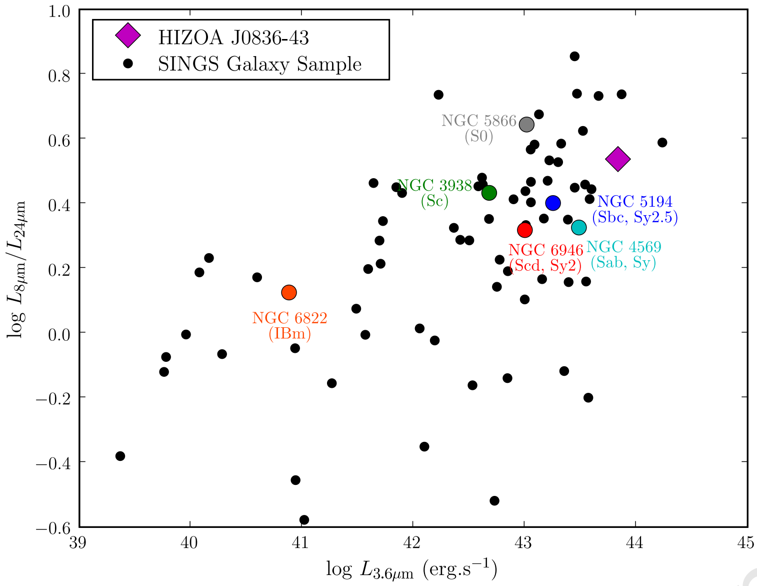

Figure 5.7: Ratio of 8 μm over 24 μm luminosity versus 3.6 μm luminosity for HIZOA J0836-43 and SINGS galaxies. Several well-known galaxy types are also shown for comparison.

an Sc galaxy with a SFR of 11.0 $M_\odot\,\mathrm{yr}^{-1}$. It has $L_{8\mu m} = 7.09 \times 10^{43}\,\mathrm{erg\,s^{-1}}$ compared to HIZOA J0836-43 which has $L_{8\mu m} = 1.43 \times 10^{44} L_\odot$.

We know that the spectra indicate very strong PAH emission, but relatively weak mid-infrared continuum emission. We conclude that compared to the 8 μm luminosity, the galaxy's $L_{24\mu m}$ is relatively low. This suggests low emission from small grains, which is believed to be the source of this emission (Draine et al. 2007). As will be presented below, this paucity of 24 μm continuum emission extends to the entire MIR window, a very intriguing anomaly exhibited by HIZOA J0836-43.

Figure 5.9 shows that HIZOA J0836-43 has a fairly average value of $L_{4.5\mu m}/L_{8\mu m} = 0.27$ compared to other star forming galaxies. The average value for 27 Sb/Sc galaxies in SINGS is $L_{4.5\mu m}/L_{8\mu m} = 0.48$, while 9 S0/Sa galaxies have a higher average of 1.8. This can be explained by relatively weak PAH emission compared to radiation from the stellar population, since the early-type galaxies (S0/Sa) will have relatively little star formation activity and therefore weak PAH signatures. Given that HIZOA J0836-43 is very luminous at 8 μm compared to the other SINGS galaxies (Fig. 5.8), $L_{4.5\mu m}$ must be similarly strong to give an overall ratio of 0.48. We can therefore conclude that HIZOA J0836-43 is both massive in stars but also undergoing strong star formation activity.

We now consider the transition from the mid-infared to the far-infrared, mixing the warm dust component, $T \sim 200$ K, with the colder, more massive dust component at $T \sim 30$ K. Figure 5.10 shows that HIZOA J0836-43 has a high 24 μm luminosity ($L_{24\mu m} = 4.15 \times 10^{43} L_\odot$), but low 24 to 70 μm luminosity. The only galaxy in SINGS with 24 μm emission greater than this is NGC 7552 ($L_{24\mu m} = 7.95 \times 10^{43} L_\odot$) which is an Sc, starburst galaxy with a SFR of 7.0

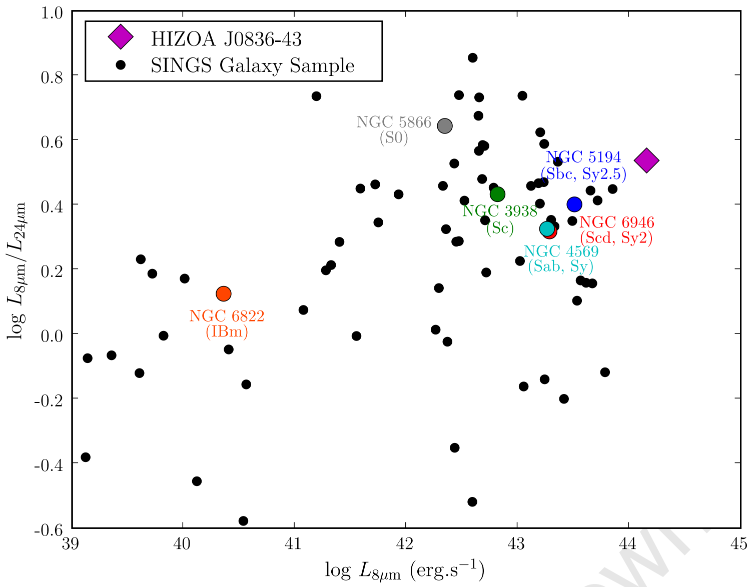

Figure 5.8: Ratio of 8 μm over 24 μm luminosity versus 8 μm luminosity for HIZOA J0836-43 and SINGS galaxies.

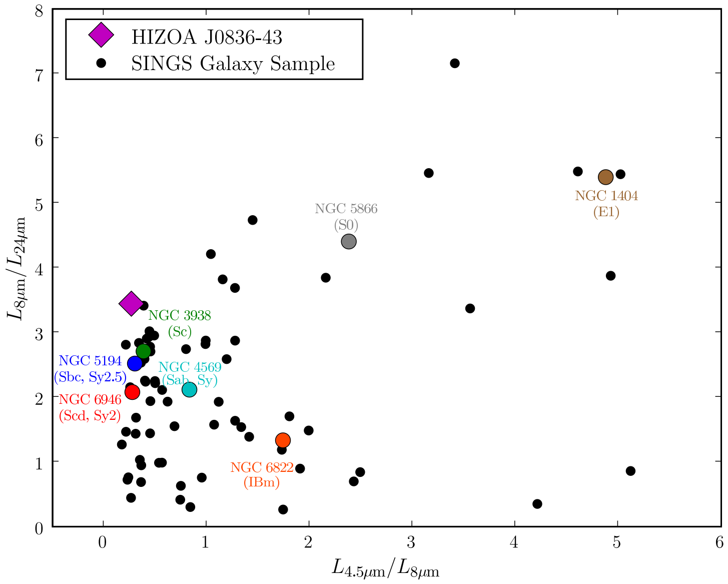

Figure 5.9: Ratio of 8 μm over 24 μm luminosity versus 4.5 μm over 8 μm luminosity for HIZOA J0836-43 and SINGS galaxies.

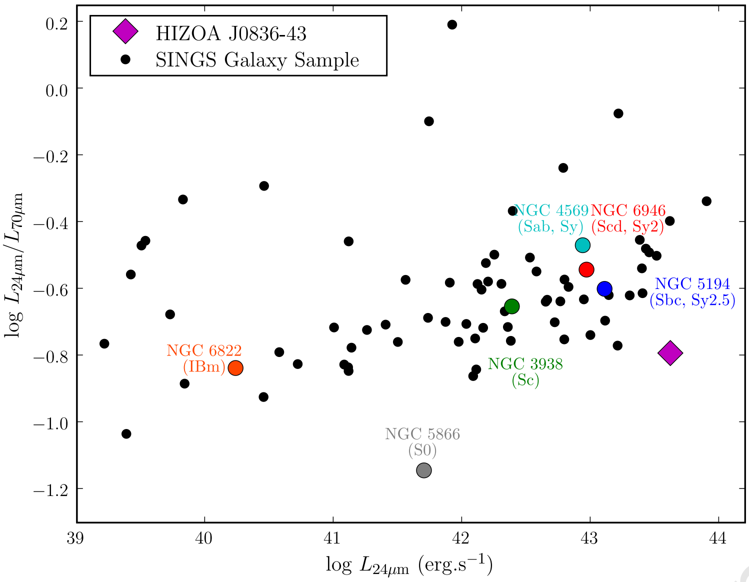

Figure 5.10: Ratio of 24 μm over 70 μm luminosity versus 24 μm luminosity for HIZOA J0836-43 and SINGS galaxies.

$M_\odot$ yr^{-1}. HIZOA J0836-43 appears to have a low log(L$_{24\mu m}$/L$_{70\mu m}$) ratio with a value of -0.79 ($L_{24\mu m}/L_{70\mu m} = 0.16$). The average for Sb/Sc galaxies in SINGS is -0.62 ($L_{24\mu m}/L_{70\mu m} = 0.24$). This implies very large 70 μm luminosity relative to the 24 μm luminosity, or conversely low $L_{24\mu m}$ compared to $L_{70\mu m}$. Based on the trend seen in the SINGS measurements, we would expect at least a factor of $\sim$2 more 24 μm emission given the 70 μm emission strength.

Figure 5.11 shows a similar plot, but with $L_{70\mu m}$ on the abscissa. We see that HIZOA J0836-43 has a larger $L_{70\mu m}$ value compared to all other galaxies in SINGS. HIZOA J0836-43 has $L_{70\mu m} = 2.57 \times 10^{44}$ erg s^{-1} with NGC 7552 being the most luminous galaxy in SINGS ($L_{70\mu m} = 1.73 \times 10^{44}$ erg s^{-1}). This result shows that HIZOA J0836-43 has both a large cold dust component and a radiation field sufficient to heat the dust, i.e. typical of active star formation.

The $L_{24\mu m}/L_{70\mu m}$ ratio for HIZOA J0836-43 appears low given the large amount of star formation in this galaxy (as discussed above). We show in Fig. 5.11 the median value for LIRGS in the GOALS (Great Observatory All-Sky LIRG Survey) sample (Justin Howell - private communication). GOALS consists of 180 LIRGs and 23 ULIRGS and incorporates the full range of nuclear spectral types and interaction stages (major mergers, minor mergers and isolated galaxies). This makes the combination of both SINGS and GOALS an ideal comparative sample for HIZOA J0836-43.

HIZOA J0836-43 has a value of -0.79 for log$L_{24\mu m}/L_{70\mu m}$ ($L_{24\mu m}/L_{70\mu m} = 0.16$) which makes it low even when compared to the GOALS mean of -0.63 ($L_{24\mu m}/L_{70\mu m} = 0.23$), which is very similar to the average found for the SINGS Sb/Sc galaxies above. HIZOA J0836-43 has the 20th lowest $L_{24\mu m}/L_{70\mu m}$ ratio compared to the GOALS sample, bearing in mind that GOALS includes S0/Sa galaxies undergoing bursts of star formation due to a major dynamical

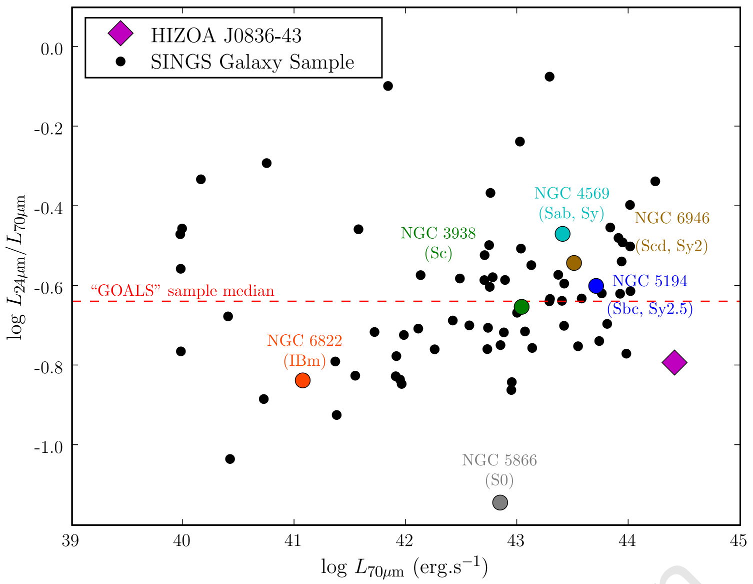

Figure 5.11: Ratio of 24 μm over 70 μm luminosity versus 70 μm luminosity for HIZOA J0836-43 and SINGS galaxies. The median 24 μm over 70 μm luminosity for the GOALS sample is also shown.

interaction. We conclude that HIZOA J0836-43 has below average 24 μm luminosity compared to the 70 μm luminosity, substantiated by Fig. 5.8 which compares 24 μm luminosity to its 8 μm luminosity.

In Fig. 5.12 we display the 70 μm luminosity versus 70 μm over 160 μm luminosity for the SINGS sample. HIZOA J0836-43 has a $L_{70\mu m}/L_{160\mu m}$ value of 1.70. The average for the sample is 1.16. There are 9 galaxies in SINGS with higher $L_{70\mu m}/L_{160\mu m}$ ratio compared to HIZOA J0836-43, but they are of morphological type E, S0, Sa or Irr.

HIZOA J0836-43 has a $f_\nu(70\mu m)/f_\nu(160\mu m)$ ratio of 0.74. Compared to SINGS this is the largest ratio for a disk galaxy, but we note that that NGC 7227 has a similar value, namely $f_\nu(70\mu m)/f_\nu(160\mu m) = 0.72$ (Dale et al. 2007). The larger $70\mu m$ emission relative to the $160\mu m$ emission implies a dominant cold dust component. In comparison to other disk galaxies in SINGS, HIZOA J0836-43 has greater emission from cold dust which could be the result of copious star formation in combination with large amounts of molecular gas. This scenario is discussed more fully in Section 5.5.1.

Luminosity and Radio Property Comparisons

In this sub-section we consider the relationships between the mid-infrared luminosities and radio properties of the galaxies in SINGS and HIZOA J0836-43. Figure 5.13 compares the $L_{70\mu m}$ to H I mass for the SINGS galaxies and HIZOA J0836-43. The upper limit for $L_{70\mu m}$ for Malin 1 from Rahman et al. (2007) is also shown. $L_{70\mu m}$ and $M_{\rm HI}$ show a correlation which we can attribute to both quantities being related to star formation. A least squares fit through the points (excluding upper limits for H I mass) gives the following relation:

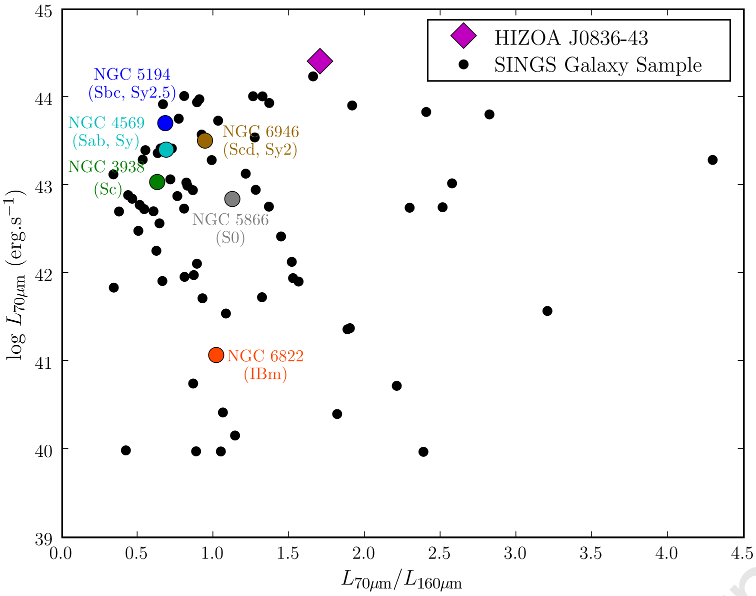

Figure 5.12: Ratio of 70 μm luminosity versus 70 μm over 160 μm luminosity for HIZOA J0836-43 and SINGS galaxies.

$$\log\left[\frac{L_{70\mu\text{m}}}{\text{erg}\,\text{s}^{-1}}\right] = 32.1 + \log\left[\frac{M_{\text{HI}}}{M_{\odot}}\right] 1.1 \qquad (8)$$

The standard error of the fit is 0.66. We see that HIZOA J0836-43 lies on this relation, but at the extreme high-mass end. It is clearly very different compared to Malin 1 (Pickering et al. 1997) which is relatively inactive despite having a similarly large reservoir of H I gas. HIZOA J0836-43 appears to be a “scaled-up” star forming galaxy compared to the SINGS sample, suggesting relatively “normal” evolution despite lying at the extreme high end (i.e., early evolutionary stage) of the relation. This was also mentioned by Donley et al. (2006) who determined the position of HIZOA J0836-43 on the NIR Tully-Fisher relation.

If we compare star formation rate and H I mass directly (see Fig. 5.14), we find the same trend. A least squares fit through the points (excluding upper limits for H I mass) gives the following relation:

$$\log\left[\frac{\text{SFR}}{M_{\odot}\,\text{yr}^{-1}}\right] = -10.7 + \log\left[\frac{M_{\text{HI}}}{M_{\odot}}\right] 1.1 \qquad (9)$$

The standard error of the fit is 0.57. The star formation rates for the SINGS galaxies are calculated from their Hα emission (Kennicutt et al. 2003). The star formation rate of Malin 1 is from Rahman et al. (2007). This direct comparison again shows the relative quiescence of Malin 1, especially in view of its H I mass.

Comparing 8 μm luminosity to H I mass as seen in Fig. 5.15 shows a similar trend to that seen in the 70 μm comparison (Fig. 5.13). This arises because $L_{8\mu\text{m}}$ is sensitive to PAH emission

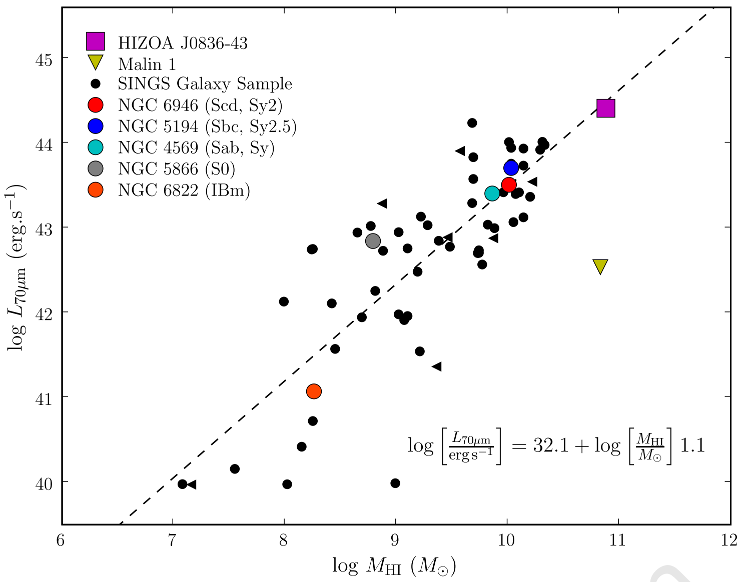

Figure 5.13: 70 μm luminosity versus H I mass for HIZOA J0836-43 and SINGS galaxies. SINGS galaxies which only have an upper limit for $M_{\rm HI}$ are shown as black triangles. The upper limit of $L_{70\mu m}$ for Malin 1 is included.

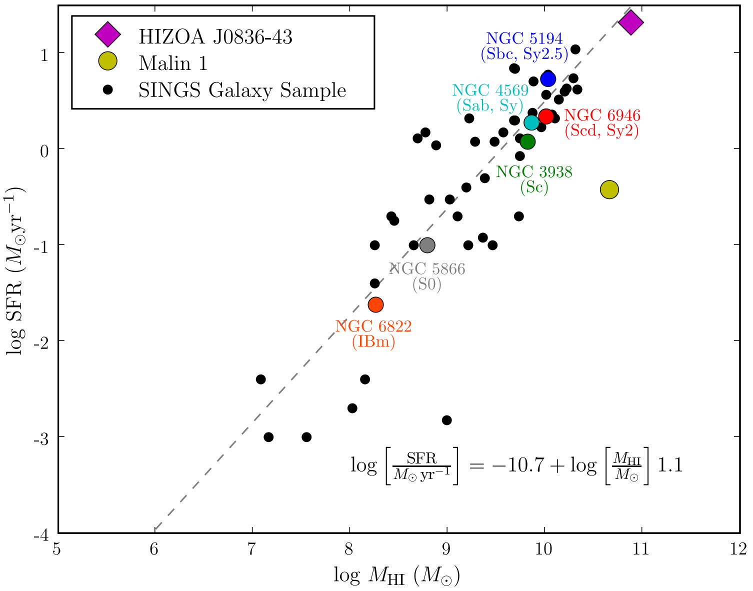

Figure 5.14: SFR versus H I mass for HIZOA J0836-43 and SINGS galaxies.

which we associate with star forming regions and is found to be a crude measure of star formation (see Section 3.9). HIZOA J0836-43 lies at the extreme point, being both very luminous in $L_{8\mu m}$ and very massive in H I content.

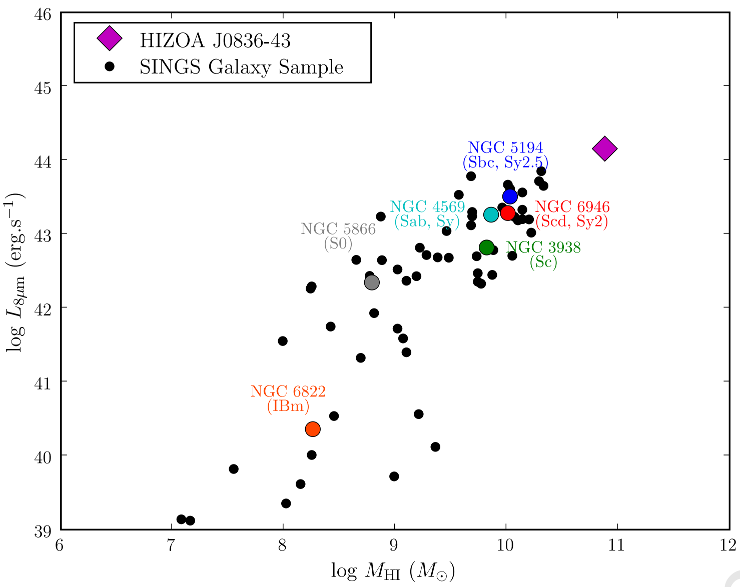

Figure 5.15: 8 μm luminosity versus H I mass for HIZOA J0836-43 and SINGS galaxies.

5.1.7 Application of Dust Models to HIZOA J0836-43

Understanding the mechanism of dust formation and heating and the physical properties of interstellar dust grains is essential for understanding galaxy structure and evolution. The SINGS galaxy sample of nearby galaxies has provided an invaluable resource for testing and developing physical dust models. In this section we utilise the models of Draine & Li (2007) and Dale & Helou (2002) to estimate the dust mass, PAH abundance and heating intensity of the interstellar medium in HIZOA J0836-43. We again compare HIZOA J0836-43 to the SINGS sample in an effort to find galaxies with similar characteristics which may provide insight into the mechanism of the star formation activity in HIZOA J0836-43.

The Draine and Li Dust Models

The dust grains in any given galaxy will be illuminated through a range of heating intensities based on the geometry of heating sources. Most dust in the interstellar medium will be subjected to the diffuse radiation field resulting from the contribution of many stars. Dust in PDRs close to luminous O and B stars in PDRs will, however, be exposed to more intense starlight heating. Draine & Li (2007) use a parametric form to describe the fraction of dust mass exposed to a distribution of starlight intensities (U) consisting of a delta function and a power-law distribution for $U_{\rm min} < U < U_{\rm max}$:

$$\frac{dM_{\rm dust}}{dU} = (1-\gamma)\,M_{\rm dust}\,\delta(U-U_{\rm min}) + \gamma\,M_{\rm dust}\frac{(\alpha-1)}{U_{\rm min}^{1-\alpha}-U_{\rm max}^{1-\alpha}}U^{-\alpha}, \alpha \neq 1, \qquad (10)$$

where $dM_{\rm dust}$ is the mass of dust heated by starlight intensities in the interval $[U, U+dU]$, $M_{\rm dust}$ is the total mass of dust, $(1-\gamma)$ is the fraction of the dust mass exposed to starlight intensity $U_{\rm min}$ and α is a power-law index.

Draine et al. (2007) find that the galaxies in SINGS have SEDs that can be suitably fit by $\alpha = 2$ and $U_{\rm max} = 10^6$. By adopting these values, dust emission can be described by the parameters $M_{\rm dust}$, $U_{\rm min}$, α and the PAH abundance parameter $q_{\rm PAH}$ (the percentage of total dust grain mass contributed by PAH particles containing $< 10^3$ C atoms); i.e. the shape of the dust emission spectrum is described by $U_{\rm min}$, α and $q_{\rm PAH}$. Different models correspond to different PAH abundances since the PAHs represent the small end of the carbonaceous grain distribution (small grains are thought to be clusters of PAH molecules). Changing the PAH abundance varies the grain size distribution, but the overall extinction remains constant.

The *Spitzer* MIPS and IRAC photometry can be used to estimate these free parameters. Following Draine & Li (2007), we define three ratios of observables:

$$P_{7.9} \equiv \frac{\langle \nu F_\nu^{\rm ns} \rangle_{7.9}}{\langle \nu F_\nu \rangle_{71} + \langle \nu F_\nu \rangle_{160}}, \qquad (11)$$

$$P_{24} \equiv \frac{\langle \nu F_\nu^{\rm ns} \rangle_{24}}{\langle \nu F_\nu \rangle_{71} + \langle \nu F_\nu \rangle_{160}}, \qquad (12)$$

$$R_{71} \equiv \frac{\langle \nu F_\nu \rangle_{71}}{\langle \nu F_\nu \rangle_{160}}, \qquad (13)$$

where $\langle F_\nu^{\rm ns} \rangle_{7.9}$ and $\langle F_\nu^{\rm ns} \rangle_{24}$ represent the flux densities of the IRAC-8 μm and MIPS-24 μm bands respectively from which the stellar contribution has been removed (as prescribed by Helou et al. 2004). $\langle F_\nu^{\rm ns} \rangle_{71}$ and $\langle F_\nu^{\rm ns} \rangle_{160}$ represent the flux densities of the MIPS-70 μm and MIPS-160 μm bands respectively. We obtain $P_{7.9} = 0.33, P_{24} = 0.10, R_{71} = 1.70$ for HIZOA J0836-43.

The model grids of Draine & Li (2007), find these ratios correspond to $q_{\rm PAH} \approx 4.6\%$. This result lies near the largest percentage modelled (Draine et al. 2007), namely $\gamma \approx 0.005$ and $U_{\rm min} \approx 8$. A galaxy with a value similar to $U_{\rm min}$ (~ 8) is NGC 7552, a spiral galaxy that contains a circumnuclear starburst, with molecular H_2 of mass $\sim 10^9 M_\odot$ within the ring (Schinnerer et al. 1997).

The values determined above can be used to estimate the parameter ψ from the models, where ψ relates the dust mass to the observed fluxes for a particular dust model (as denoted by $q_{\rm PAH}$). We find $\psi = 0.0535\,{\rm g}\,({\rm erg\,s^{-1}})^{-1}$.

By determining the mean starlight intensity scale factor

$$\langle U \rangle = (1-\gamma)\, U_{\rm min} + \frac{\gamma\, U_{\rm min} \ln(U_{\rm max}/U_{\rm min})}{1 - U_{\rm min}/U_{\rm max}} = 8.43, \qquad (14)$$

we can calculate the dust mass

$$M_{\rm dust} = \frac{\psi}{\langle U \rangle}(\langle \nu F_\nu^{\rm ns} \rangle_{24} + \langle \nu F_\nu^{\rm ns} \rangle_{71} + \langle \nu F_\nu^{\rm ns} \rangle_{160}) D^2 = 2.27 \times 10^{41}\,{\rm g} = 1.14 \times 10^8\, M_\odot \qquad (15)$$

The value of $\langle U \rangle = 8.43$ implies a large amount of dust heating from stellar radiation; galaxies in SINGS show $0.7 \leq \langle U \rangle \leq 29.5$ with a median value of 2.41. The dust mass of HIZOA J0836-43 is at the high end compared to the SINGS sample which ranges from $10^4 - 4 \times 10^8 M_\odot$ with a mean of $1.05 \times 10^7 M_\odot$.

The value of $q_{\rm PAH}$ calculated above is consistent with metal-rich (solar) grains since the fraction of dust in the form of PAHs correlates with metallicity. This value is at the high end compared to the SINGS average of 3.4% (Draine et al. 2007), although approximately half (30/61 galaxies) have $q_{\rm PAH} > 3.25\%$.

From the values of $U_{\rm min}$, $U_{\rm max}$ and γ, we can calculate $f_{\rm PDR}$ which is defined as the fraction of total dust luminosity radiated by dust grains in regions of high-intensity, $U > 10^2$. This emission is expected to arise mostly in star-forming regions where dust is located close to luminous stars.

$$f_{\rm PDR} = \frac{\gamma \ln(U_{\rm max}/10^2)}{(1-\gamma)(1-U_{\rm min}/U_{\rm max}) + \gamma \ln(U_{\rm min}/U_{\rm max})} \qquad (16)$$

Substituting the values determined above gives $f_{\rm PDR} \approx 0.044$ corresponding to $\sim 4\%$. Although this indicates significant star formation, it is on the low side compared to the average of $\sim 8\%$ for SINGS galaxies (Draine et al. 2007) where the values range between 0 and 50%. This implies that a smaller fraction of the total dust is being heated in regions with high intensity radiation ($U > 10^2$) compared to the average SINGS galaxy. This would be consistent with large PDRs heated by less intense starlight dominating the emission.

A galaxy with a similar $f_{\rm PDR}$ and $q_{\rm PAH}$ value (5.6% and 4.2% respectively) is NGC 7331. It also has a similar dust mass, $1.12 \times 10^8 M_\odot$, compared to HIZOA J0836-43, with only NGC 4631 having a larger dust mass in the SINGS sample. NGC 7331 has a central dust ring which has vigorous star formation, approximately one third of the total rate, namely $\sim 5.5\, M_\odot {\rm yr}^{-1}$ (Thilker et al. 2007). This galaxy has a massive H I disk with $M_{\rm HI} \sim 1.2 \times 10^{10} M_\odot$ (Braun et al. 2003) with a molecular hydrogen content of $M_{\rm H_2} = 4.7 \times 10^9 M_\odot$ confined to a molecular ring (Young & Scoville 1982). This geometry could be similar to that of HIZOA J0836-43.

The Dale-Helou Dust Models

We next consider the dust models of Dale & Helou (2002) (in future cited as DH02). They developed a semi-empirical model to describe dust emission from galaxies for a wide range of interstellar environments and heating intensities. A power-law distribution of dust mass over heating intensity is used, ranging from 0.3 to 10^5 times the local interstellar radiation field. In this formalism, $\alpha_{\rm SED}$ parametrizes the distribution of dust mass as a function of local heating intensity U given by

$$dM_{\rm dust}(U) \propto U^{-\alpha_{\rm SED}}\, dU, \;\; 0.3 \leq U \leq 10^5, \qquad (17)$$

where $M(U)$ is the dust mass heated by U.

In general smaller values of $\alpha_{\rm SED}$ imply more heating from stronger interstellar radiation and correspond to later Hubble types and larger infrared-to-ultraviolet ratios. These models were used in Dale et al. (2005) and Dale et al. (2007) to model the dust emission for SINGS galaxies. They found values of $\alpha_{\rm SED}$ ranging from ~ 1 for active galaxies to ~ 2.6 at the quiescent end.

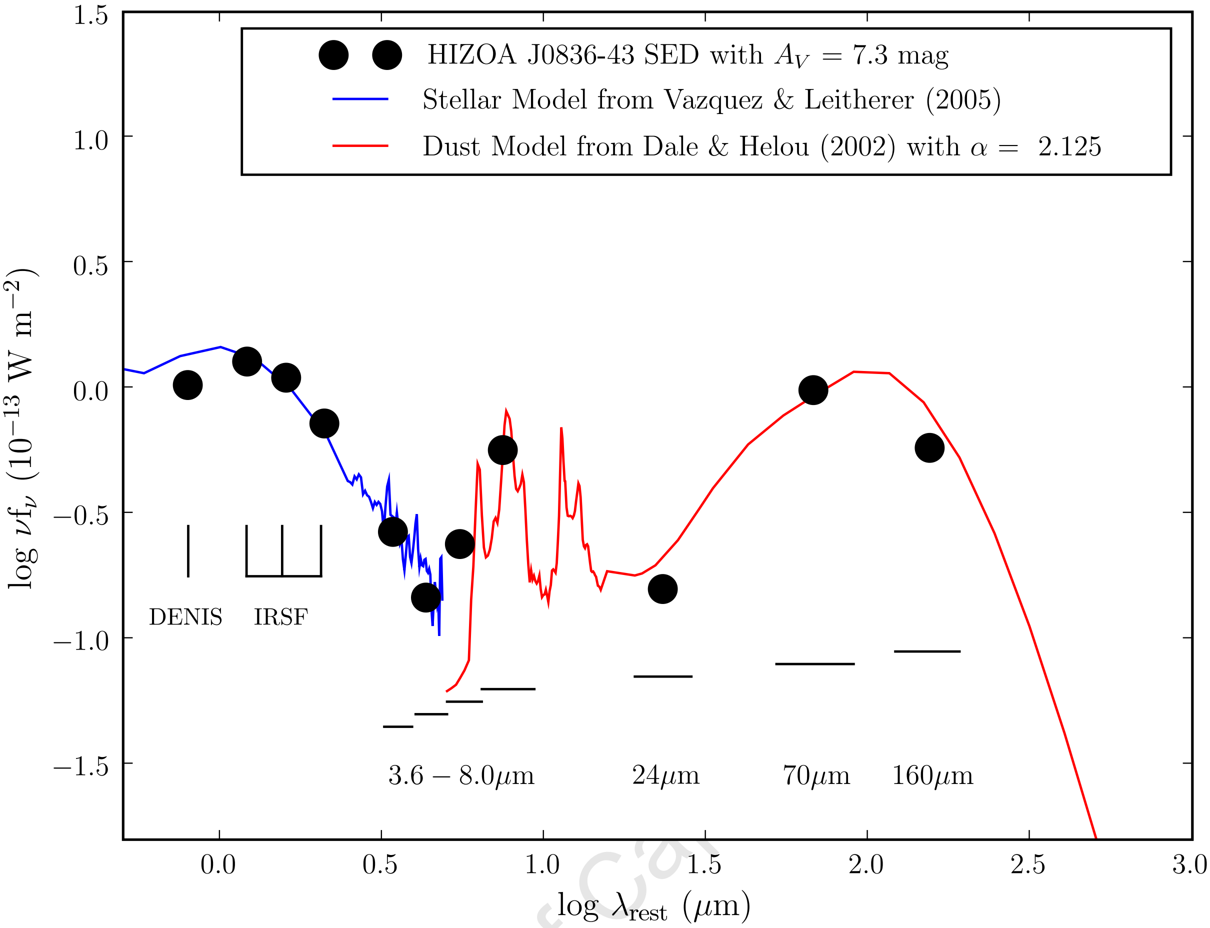

Figure 5.16: HIZOAJ0836-43 SED with $\alpha_{\rm SED} = 2.125$ from the dust emission models of Dale & Helou (2002). The stellar curve is a 1 Gyr continuous star formation, solar metallicity curve from Vázquez & Leitherer (2005).

We apply these models[1] to HIZOA J0836-43 by scaling them to the galaxy for $\lambda > 5\mu$m and varying $\alpha_{\rm SED}$ to find a best fit. Figure 5.16 shows the resulting spectrum. We also show the 1 Gyr continuous star formation, solar metallicity curve from Vázquez & Leitherer (2005) (normalised to K_s) which models the stellar component of HIZOA J0836-43. The MIR dust emission is best modelled by $\alpha_{\rm SED} = 2.125$.

For comparison we show in Fig. 5.17 and Fig. 5.18 how the dust emission spectrum changes for different values of $\alpha_{\rm SED}$. Figure 5.17 shows a large range of $\alpha_{\rm SED}$. The photometry constrains the heating parameter to $2.0 < \alpha_{\rm SED} < 2.3$, which we show in Fig. 5.18.

Dale et al. (2007) have applied the DH02 models to the ultraviolet-to-radio continuum SEDs for the 75 galaxies in SINGS. By comparison to this sample, we find that HIZOA J0836-43 has a lower $\alpha_{\rm SED}$ value (2.125) than the average for Sb/Sc galaxies (2.8). Galaxies with similar $\alpha_{\rm SED}$ values are NGC 1097 (an Sb galaxy with $\alpha_{\rm SED} = 2.15$) and NGC 6946 (an Sd galaxy with $\alpha_{\rm SED}$

---

[1] Available at http://faraday.uwyo.edu/ ddale/research/seds/seds.html

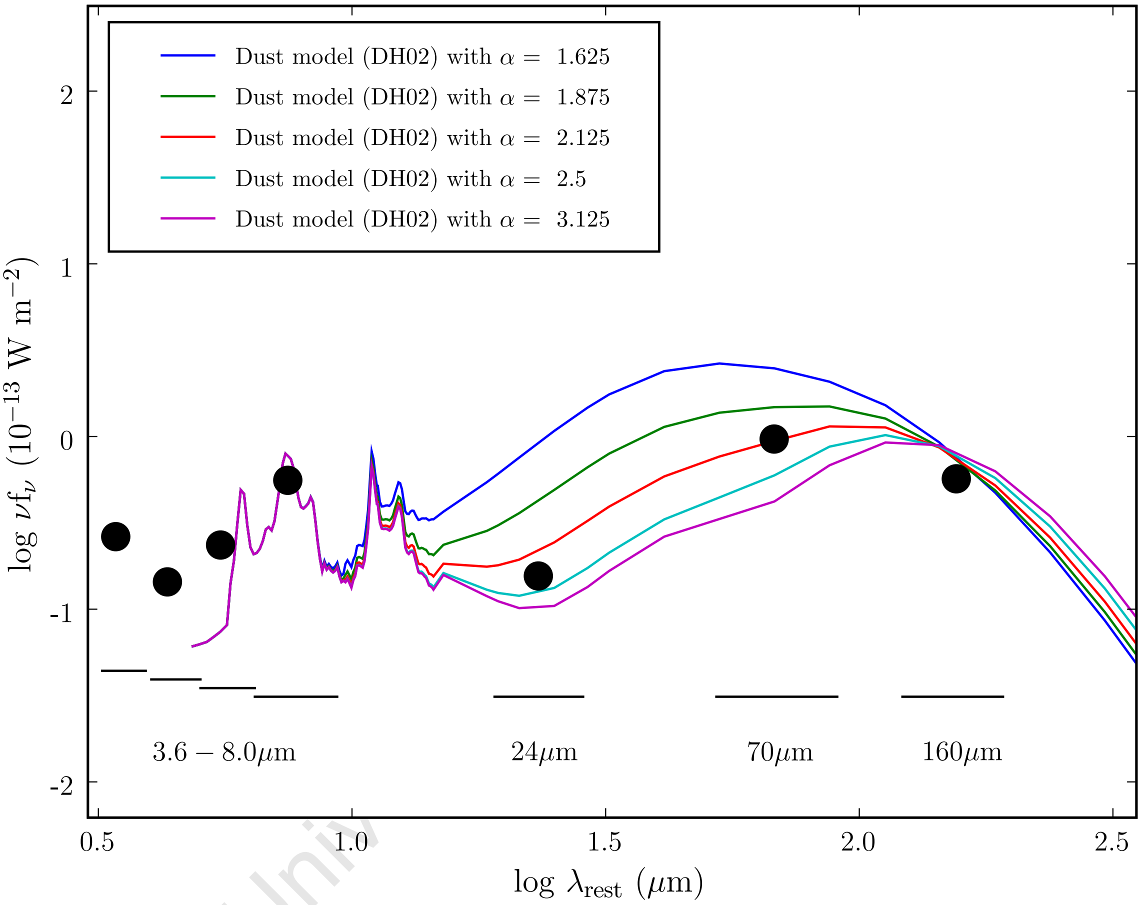

Figure 5.17: HIZOAJ0836-43 SED ($\lambda > 5\,\mu$m) with the DH02 model infrared SEDs overplotted for a broad range in $\alpha_{\rm SED}$.

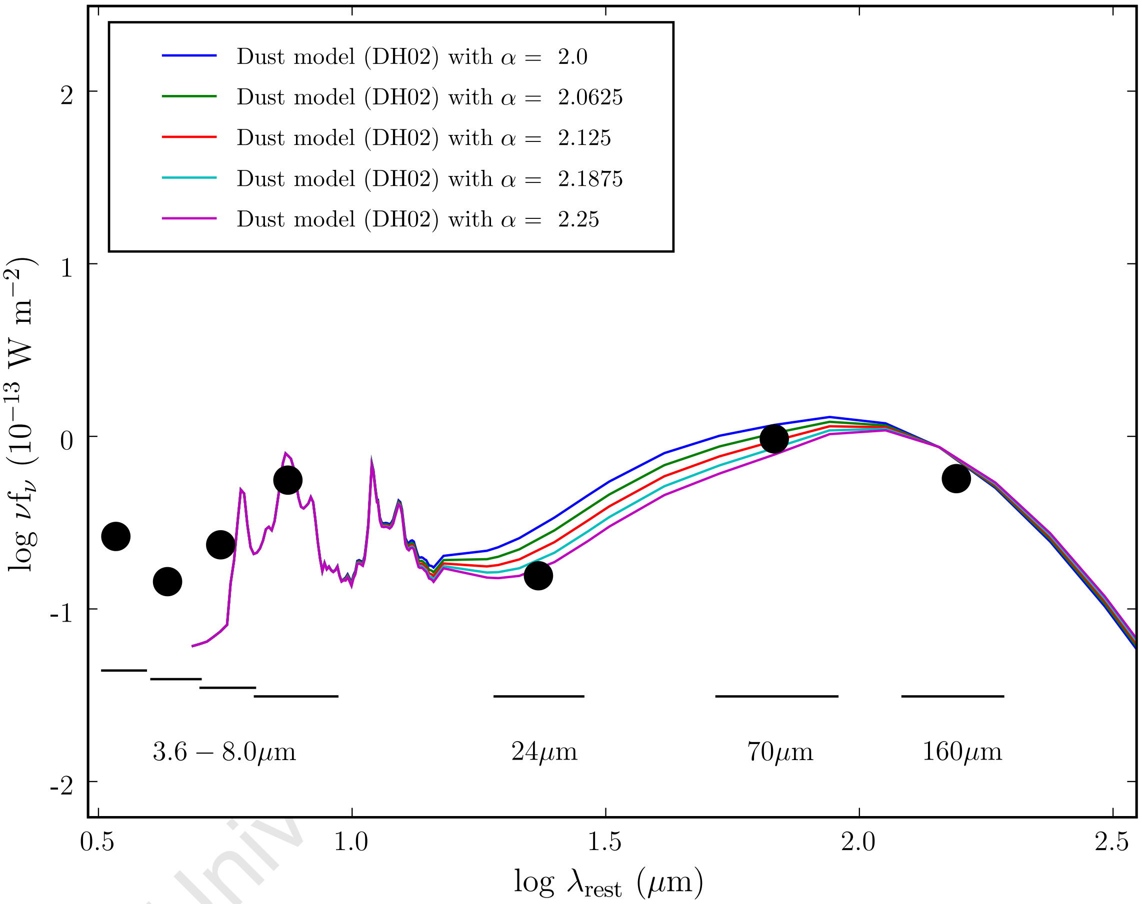

Figure 5.18: HIZOAJ0836-43 SED ($\lambda > 5\,\mu$m) with the DH02 model infrared SEDs overplotted for α_{SED} values close to HIZOA J0836-43's value of $\alpha_{SED} = 2.125$.

= 2.15). We note that NGC 7227 has the lowest α_{SED} value (1.75) for Sb/Sc galaxies in SINGS which is consistent with its starburst activity.

5.1.8 Summary

The broadband photometry of HIZOA J0836-43 has allowed us to determine several properties of the galaxy and analyse how they compare to other galaxies. We summarise some key results from this Section in Table 5.3.

Table 5.3: Summary of Photometric and Derived Properties of HIZOA J0836-43.

Property	Value
M_{stellar}	$4.4 \pm 1.4 \times 10^{10}\,M_\odot$
M_{dust}	$\approx 1.1 \times 10^{8} M_\odot$
$M(\mathrm{H}_2)$	$\approx 1.3 \times 10^{10} M_\odot$
L_{TIR}	$1.20 \pm 0.22 \times 10^{11} L_\odot$
$L_{\mathrm{TIR}}/M(\mathrm{H\,I})$	$1.6 \pm 0.3\,L_\odot/M_\odot$
q_{TIR}	2.3 ± 0.5
q_{24}	0.72 ± 0.07
q_{70}	1.98 ± 0.40
$L_{4.5\mu\mathrm{m}}/L_{8\mu\mathrm{m}}$	0.27 ± 0.02
$L_{8\mu\mathrm{m}}/L_{24\mu\mathrm{m}}$	3.45 ± 0.34
$L_{24\mu\mathrm{m}}/L_{70\mu\mathrm{m}}$	0.16 ± 0.03
$L_{70\mu\mathrm{m}}/L_{160\mu\mathrm{m}}$	1.70 ± 0.26
q_{PAH}	$\approx 4.6\%$
f_{PDR}	$\approx 4.4\%$
α_{SED}	≈ 2.125

The galaxy appears to have a typical stellar mass, but contains a large quantity of molecular hydrogen and dust. Its luminosity ratios indicate strong $L_{8\mu\mathrm{m}}$ and $L_{70\mu\mathrm{m}}$ emission, whereas the $L_{24\mu\mathrm{m}}$ and $L_{160\mu\mathrm{m}}$ emission is low by comparison. The relatively poor 24 μm, but strong 70 μm emission suggests that dust grains that normally radiate in the 24 μm wavelength band are radiating at longer wavelengths (i.e. are colder) causing the high 70 μm luminosity. This means that the cold dust component is dominating the emission.

Since we have active star formation, this scenario requires large amounts of molecular gas around H II regions generated by star formation to absorb the most intense radiation and produce copious dust and PAH emission. This is consistent with the findings from dust models that indicate large amounts of relatively low intensity dust heating ($f_{\mathrm{PDR}} \approx 4.4\%$) producing large amounts of dust and emission from PAH molecules ($q_{\mathrm{PAH}} \approx 4.6\%$) and seen as luminous 8 μm emission.

The galaxy, however, appears to be very active ($\alpha_{\rm SED} \approx 2.125$). Its relatively low $q_{\rm TIR}$, q_{70} and q_{24} ratios indicate vigorous star formation. HIZOA J0836-43's ability to produce a large amount of dust and subsequently enough thermal emission to make it a LIRG, suggests an important interplay between the geometry of gas and heating sources. We speculate that the strong radio emission is likely coming from an intense nuclear starburst and that the majority of MIR/FIR radiation is coming from a larger area around the starburst, possibly circumnuclear. This would require large amounts of molecular gas to (a) shield this region from the hard radiation from the intense nuclear starburst and (b) produce strong dust emission through the formation of PDRs.

5.2 Spectroscopic Analysis

Mid-infrared spectra of star forming galaxies provide a plethora of diagnostics for determining interstellar medium conditions through fine-structure lines, molecular hydrogen emission lines, broad PAH emission features and MIR continuum. Key relationships between detected elements provide information about star formation, AGN activity, hardness of interstellar radiation fields and molecular composition.

The nuclear spectrum of HIZOA J0836-43 has emission from PAH molecules, warm molecular hydrogen and fine structure lines of neon, sulphur, silicon and argon (see Fig. 5.19 from Section 4.3.2). In this section we use the flux and equivalent width measurements determined in Section 4.3.2 as diagnostics for probing the interstellar medium conditions of HIZOA J0836-43.

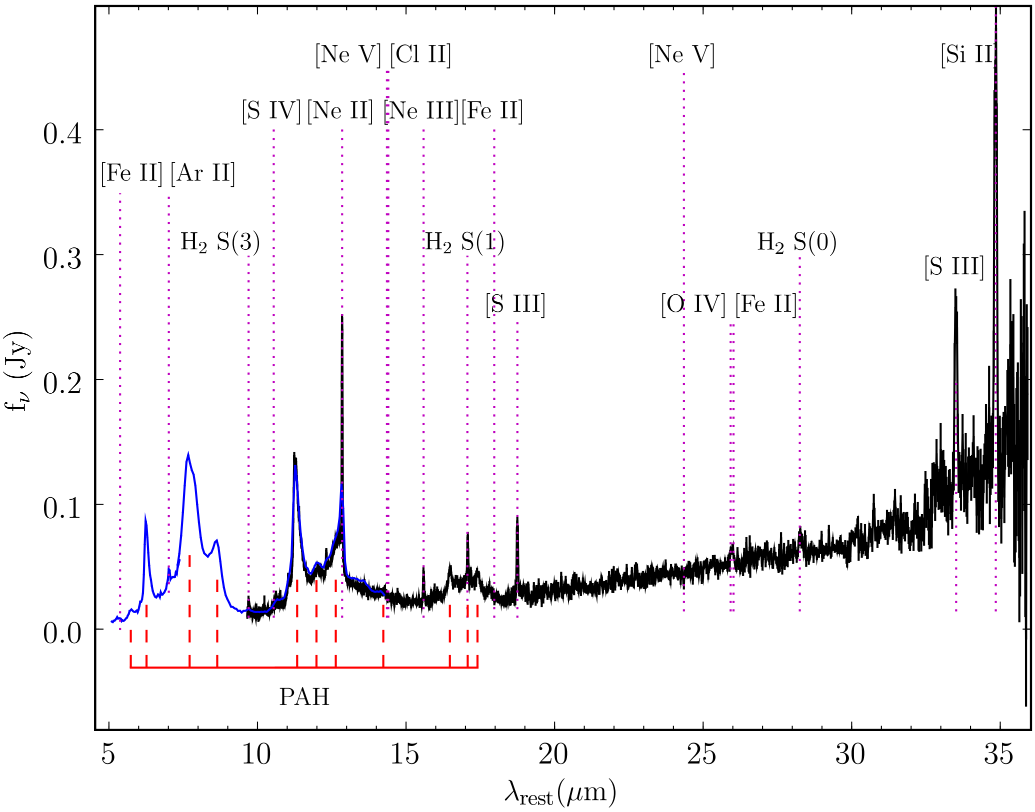

Figure 5.19: Combined low and high resolution (SL, SH, LH) spectrum of HIZOA J0836-43 showing prominent emission features, both detected and non-detected.

5.2.1 Continuum Diagnostics

The mid-infrared continuum is generated by emission from dust with varying grain sizes and temperatures. The relative strength of the overall continuum and parts thereof provides insight into the heating mechanisms, as well as their relative contributions. This is investigated further in this section.

Table 5.4 summarises the continuum measurements from Section 4.5 and their spectral luminosities.

Table 5.4: Continuum Fluxes.

λ_{rest} μm	Flux Density Jy	Flux Density 10^{-17} W m$^{-2}\mu$m^{-1}	νL_ν ($10^9 L_\odot$)
5.5	0.017 ±0.001	167.2 ±6.2	6.35 ±0.24
6.0	0.022 ±0.003	188.2 ±24.5	7.53 ±0.98
15.0	0.022 ±0.002	29.8 ±2.9	3.01 ±0.29
30.0	0.068 ±0.004	22.6 ±1.3	4.65 ±0.27

The 6 μm and 15 μm continuum values are approximately the same, suggesting a quiescent galaxy (Dale et al. 2000). Fig. 5.20 shows the combined spectrum of HIZOA J0836-43 and the scaled spectrum of NGC 6240, a starburst ULIRG with strong PAH emission. HIZOA J0836-43 does not show a sharply rising dust continuum one might expect from a luminous infrared galaxy with a high star formation rate. Instead, it appears that the galaxy is dominated by cold dust which results in the spectrum having only a weak contribution from MIR continuum emission. The paucity of warm dust, evident from the weakly rising continuum seen in its spectrum, is consistent with its low $L_{24\mu\mathrm{m}}/L_{70\mu\mathrm{m}}$ colour compared to normal and star-forming systems in the SINGS (see Section 5.1.6).

Brandl et al. (2006) showed that the flux densities at 15 μm and 30 μm could be used to estimate the total infrared luminosity of starbursts using the following equation:

$$L_{\mathrm{IR}}^{\mathrm{est}} = D^2(4.27F_{15\mu\mathrm{m}} + 11F_{30\mu\mathrm{m}}), \qquad (18)$$

where D is the distance in kiloparcses and $F_{15\mu m}$ and $F_{30\mu m}$ are the IRS flux densities in Janskys. Substituting the values from Table 5.4 gives $L_{\mathrm{IR}}^{\mathrm{est}} \approx 1.8 \times 10^{10} L_\odot$. This is $\sim$ 6 times smaller than the value determined from the broadband photometry in Section 3.5, namely $1.2 \times 10^{11} L_\odot$. Therefore, using the continuum values of HIZOA J0836-43 underestimates the total infrared emission from the galaxy.

Very Small Grains (VSGs) are believed to radiate in the 15–60 μm wavelength region, i.e. between emission from PAHs and radiation from classical interstellar grains (Puget & Léger 1989). Ongoing studies explore the possibility that the VSGs are PAH "clusters" and that isolated PAH molecules are actually produced by the destruction of these small carbonaceous

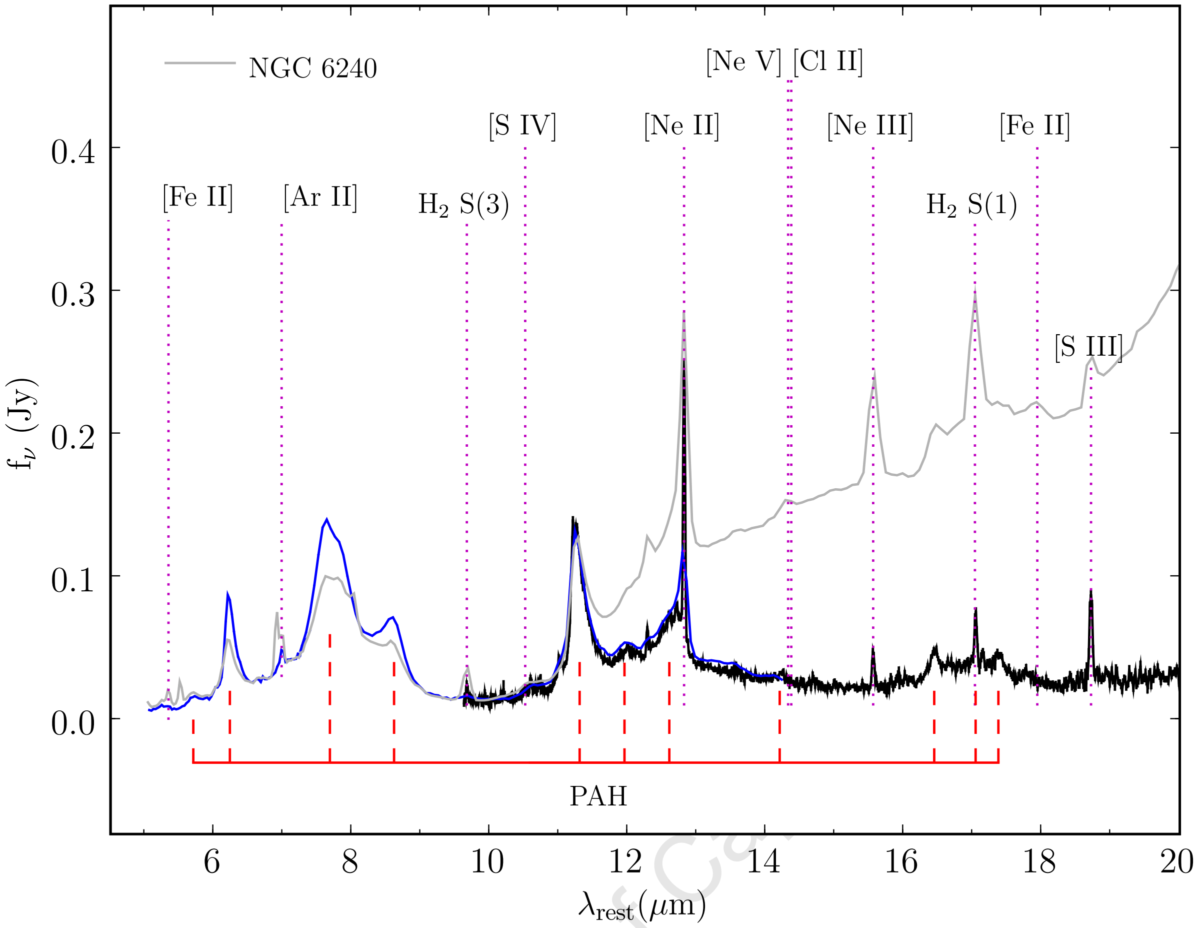

Figure 5.20: Spectrum (SL, SH, LH) of HIZOA J0836-43 and scaled spectrum of NGC 6240, the starburst ULIRG, for comparison.

grains (Boulanger et al. 1998; Rapacioli et al. 2006). The spectrum of HIZOA J0836-43 shows a distinct lack of emission from these VSGs. We discuss possible scenarios for this in Section 5.5.

5.2.2 Ionic Emission Line Diagnostics

In the following analysis we use the relative strengths of the emission lines to probe the heating mechanisms, metallicity, electron density and star formation activity in the central region of HIZOA J0836-43.

In the high-resolution spectra of HIZOA J0836-43 we detect the fine-structure lines of [Ne II] 12.81 μm, [Ne III] 15.56 μm, [S III] 18.71 μm, [S III] 33.38 μm, [Si III] 34.82 μm, and [Ar II] 6.99 μm. For ease of reference we list the measurements of these lines, from Section 4.3.2, and their ionisation potentials in Table 5.5.

With the exception of the [Si II] 34.82 μm line, these are all nebular lines from ionised hydrogen gas regions. The [Si II] line, however, can be produced in ionised regions as well as warm atomic

Table 5.5: Emission Line Measurements - Nucleus (SL+SH+LH)

Line	λ_{rest} μm	Line FWHM $10^{-3}\mu$m	Equivalent Width μm	Flux [a] 10^{-17} W m^{-2}	Luminosity [a] ($10^7 L_\odot$)	$E_{\rm ion}$ [b] eV
[Ar II] [c]	6.99	88.40	− 0.039	7.55 ±0.62	5.12 ±0.11	27.6
[Ne II]	12.81	32.80	− 0.208	13.02 ±0.12	8.92 ±0.08	21.6
[Ne III]	15.56	41.09	− 0.051	1.40 ±0.08	0.96 ±0.06	41.0
[S III]	18.71	52.40	− 0.165	3.18 ±0.11	2.12 ±0.07	23.3
[S III]	33.47	98.30	− 0.156	4.52 ±0.28	3.09 ±0.20	23.3
[Si II]	34.81	92.34	− 0.247	8.84 ±0.48	6.05 ±0.33	8.2

[a] Error calculated from the line flux relative to the baseline RMS

[b] Ionisation Potential

[c] [Ar II] is blended with H_2 $S(2)$

gas such as found in photodissociation regions.

Mid-infrared spectroscopy plays a key role in determining the dominant heating source powering the strong infrared emission of (U)LIRGs. Determining the relative contributions of Active Galactic Nuclei (AGN) and starbursts, manifested as H II regions and PDRs, to the overall luminosity allows us to probe the heating mechanisms and geometry of the system (Laurent et al. 2000).

The simplest diagnostic for determining the presence of an AGN is the detection of high-ionization lines [Ne V] and [O IV] (Sturm et al. 2000). The 14.3 μm and 24.3 μm lines of [Ne V] imply AGN heating due to the high ionisation potention of [Ne^{3+}], namely 97.1 eV. This excitation cannot be produced by radiation from O stars and as a result "pure" starburst galaxies do not produce [Ne V] emission (Genzel et al. 1998).

By comparison, [O IV] has been detected in starbursts (Lutz et al. 1998; Smith et al. 2004) as [O^{2+}] only has an ionisation potential of 54.9 eV and can be produced by shocks and Wolf-Rayet stars (Smith et al. 2004). Moreover, it is blended with another shock-tracer, [Fe II], at 25.9 μm which may produce a combined detectable signal. Nevertheless, strong [O IV] emission requires an AGN to provide sufficient high-energy photons. Galaxies with AGNs therefore have [O IV] emission, but its detection requires further diagnostics to determine the source.

We do not detect significant [Ne V], and the [O IV] + [Fe II] blend is very weak, $< 2\sigma$. Both null results implies an absent or very weak AGN.

[Ne III]/[Ne II]: Radiation Field Strength

The ratios of the fine structure line fluxes between different ionic species of the same element (eg. Ne^{2+}/Ne^{1+}) provides a measure of the excitation and thus an indication of the hardness of the radiation field. For a fixed number of ionising photons per hydrogen atom, this ratio is approximately proportional to the number of photons with sufficient energy to ionise the specie, relative to the number of Lyman continuum photons. For example, a higher value of [Ne III] 15.56/[Ne II] 12.81 with an ionization potential of 41 eV/21.6 eV, indicates a harder radiation field.

We find a value of 0.11(±0.01) for [Ne III] 15.56 μm/[Ne II] 12.81 μm. Typical values for starbursting systems are shown by Brandl et al. (2006), who find a range of $\sim 0.06 - 3.2$ and Verma et al. (2003) with values between $\sim 0.03 - 15$.

While the [Ne III] 15.56 μm/[Ne II] 12.81 μm ratio is typical for disk galaxies, it is at the low end compared to other starbursts and star-forming regions in SINGS (Dale et al. 2008). This implies greater weight in the lower ionization line [Ne II] compared to the higher ionization line [Ne III] 15.56 μm. The [Ne II] 12.81 μm emission acts as an indication of the surface density of H II regions given its much lower ionisation potential compared to [Ne III] 15.56 μm. The low [Ne III] 15.56 μm/[Ne II] 12.81 μm ratio indicates a relatively soft radiation field resulting in H II emission and potentially large amounts of emission from PDRs.

[Ne III]/[Ne II]: Metallicity

There exists a correlation between the neon ratio and metallicity for star-forming regions as shown by Dale et al. (2008) for star-forming nuclear and extranuclear targets in SINGS:

$$\log[\text{NeIII}]\,15.56\mu\text{m}/[\text{NeII}]\,12.81\mu\text{m} = -2.05[\pm0.13](12 + \log(\text{O/H})) + 17.9[\pm1.2] \tag{19}$$

We use this to estimate the metallicity by substituting [Ne III] 15.56 μm/[Ne II] 12.81 μm = 0.11. This corresponds to a (12 + log(O/H)) value of ∼ 9.2. The galaxy is therefore a super-solar metallicity system (12 + log(O/H)) $\geq$ 9.0 for the Kobulnicky & Kewley 2004 strong-line calibration), with solar oxygen abundance being (12 + log(O/H)) ∼ 8.7 (Allende Prieto et al. 2001). This oxygen abundance corresponds to a metal mass fraction of $Z \sim 0.046$ (compared to $Z_\odot \sim 0.015$). HIZOA J0836-43 therefore has an apparent metallicity of $Z \sim 3Z_\odot$. Since we are using an indirect empirical relation to estimate the metallicity, this metric only acts as an indication of the softness of the radiation field. It is possible that the radiation field is quenched by the geometry of heating sources, gas and dust and not the result of very high metallicity. We cannot distinguish between these two scenarios without a direct measurement of the oxygen abundance. Unfortunately, the high optical extinction at the location of HIZOA J0836-43 makes this an impossible measurement.

[Ne III]/[Ne II]: Star Formation Rate

Ho & Keto (2007) show that the sum of [Ne II] and [Ne III] luminosities are tightly correlated with total infrared luminosity, which in turn is correlated to star formation rate. This relation was modified by Desai et al. (2007) who obtain

$$\text{SFR}(M_\odot\,\text{yr}^{-1}) = 2.69 \times 10^{-41} \frac{L_N(\text{erg}\,\text{s}^{-1})}{f_{ion}(f_{\text{Ne}^+} + 1.67 f_{\text{Ne}^{++}})} \tag{20}$$

where L_N is the combined luminosity of the two neon lines, f_{ion} is the fraction of photons contributing to the ionising the gas and f_{Ne^+} and $f_{\mathrm{Ne}^{++}}$ are the fractional abundances of [Ne II] and [Ne III] respectively. Using $f_{ion} = 0.6$, $f_{\mathrm{Ne}^+} = 0.75$ and $f_{\mathrm{Ne}^{++}} = 0.1$ (Ho & Keto 2007) and $L_N = 3.95 \times 10^{41}\,\mathrm{erg\,s^{-1}}$, yields a SFR of $\sim 21 M_\odot\,\mathrm{yr}^{-1}$. This line-emission derived-SFR agrees surprising well with the SFR obtained using dust continuum $\mathrm{L_{FIR}}$, namely $20.5\,M_\odot\,\mathrm{yr}^{-1}$ (see Section3.9).

[S III]/[S III]: Electron Density

The electron density can be estimated using two lines with transitions that have the same principal and angular momentum quantum numbers, but with different numbers of electrons in the orbital or suborbital, for example, the ${}^3p_2 - {}^3p_1$ and ${}^3p_1 - {}^3p_0$ transition of [S III] at 18.71 μm and 33.48 μm respectively. At $T \sim 10,000$K (typical of ionised regions; Verma et al. 2003), this line ratio is insensitive to temperature and therefore provides a diagnostic of the density of the ionised gas. By solving the relevant rate equation, the electron density can be determined.

Using the fluxes listed in Table 5.5, we find [S III] 18.71 μm/[S III] 33.48 μm $= 0.70 \pm 0.05$. We then make use of the density dependence relations of Alexander et al. (1999), shown in Fig. 5.21, to determine an electon density of $n_e \sim 100 - 200\,\mathrm{cm}^{-3}$, assuming $T \sim 10,000$ K . If we determine the electron density using the more precise relation used for SINGS (Dale et al. 2008), we find $n_e \sim 300\,\mathrm{cm}^{-3}$.

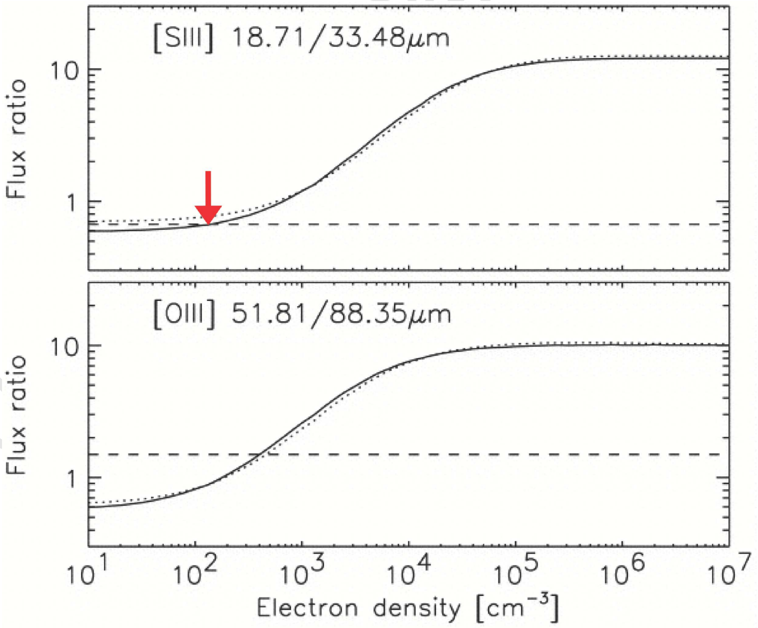

Figure 5.21: Density-sensitive ratios of fine-structure transitions from the ground-state triplets [S III], and [O III]. Solid lines show an electron temperature of 10,000 K; dotted lines show 20,000 K. The location of HIZOA J0836-43 is shown by a red arrow. (From Alexander et al. 1999)

Dale et al. (2006) investigated spectral diagnostics of nuclear and extranuclear regions in the SINGS sample. For the 50 galaxies with nuclear measurements, they find an average line ratio of [S III] 18.71 μm/[S III] 33.48 μm = 0.82 with a 1σ dispersion of 0.27. This corresponds to an average electron density of $n_e \sim 400\,\mathrm{cm}^{-3}$. Further study of this sample showed that the median value for star-forming nuclear regions was $300\,\mathrm{cm}^{-3}$ (Dale et al. 2008). Similarly, the average electron density found by Verma et al. (2003) for 11 starburst galaxies is $n_e \sim 300\,\mathrm{cm}^{-3}$. However, Armus et al. (2007) find an average value of [S III] 18.71 μm/[S III] 33.48 μm= 0.51 for the ULIRGS in the IRAS Bright Galaxy Sample (BGS) which corresponds to a slightly lower electron density of $100-200\,\mathrm{cm}^{-3}$. We can conclude that HIZOA J0836-43 has a typical electron density compared to other starbursting and normal disk systems.

[Si II] 34.82 μm/[S III] 33.48 μm: Galaxy Classification Diagnostic

Dense PDRs and X-ray dominated regions, powered by AGN, show strong [Si II] 34.82 μm emission due to the significant cooling effect of this line (Hollenbach & Tielens 1999), while the [S III] 33.48 μm line acts as a strong tracer of H II regions (Dale et al. 2006). Using this in combination with [Ne III] 15.56 μm/[Ne II] 12.81 μm as an excitation indicator, Dale et al. (2006) obtains a galaxy classification diagnostic shown in Fig. 5.22.

The Roman numerals indicate the classification of the region based on the sources as follows: Region I consists of 69% Seyferts and 31% LINERs. Region II consists of 55% Seyferts, 32% LINERs and 14% H II nuclei, Region III consists of 0% Seyferts, 4% LINERs, 51% H II nuclei and 45% Extranuclear H II regions and Region IV consists of 100% Extranuclear H II regions.

With a [S III] 33.48 μm/ [Si II] 34.82 μm value of 0.51 ± 0.04, these line tracers indicate that HIZOA J0836-43 falls on the border between star-forming (Region III) and AGN dominated galaxies (Region II).

Compared to the AGN and star-forming regions in Dale et al. (2008), we also find the [Si II] 34.82 μm/[S III] 33.48 μm ratio of 1.96 ± 0.16 to be high compared to starforming regions in SINGS (with an average of ~ 1.2), but low for the AGN galaxies (with an average of ~ 2.9). If there were a contribution from an undetected weak AGN, it could result in HIZOA J0836-43 not appearing as a "pure" star-forming nucleus. On the other hand, a more likely scenario is that this galaxy has large amounts of dense PDRs producing powerful [Si II] emission which dominates the [S III] coming from H II regions. This would cause a high [Si II] 34.82 μm/[S III] 33.48 μm ratio as seen in HIZOA J0836-43. Dale et al. (2008) show that dust grain destruction, such as caused by an AGN or shocks, will increase the amount of [Si II] 34.82 μm and [Fe II] 25.99 μm in the interstellar medium. These species are therefore enhanced in active galaxies. In HIZOA J0836-43 we do not detect significant [Fe II] 25.99 μm which indicates that [Si II] 34.82 μm enhancement is coming from elsewhere. We also know that the radiation field is not hard enough to encourage such a mechanism. Since [Si II] 34.82 μm traces strong PDR emission, we conclude that the elevated [Si II] 34.82 μm/[S III] 33.48 μm ratio is the result of strong PDR emission compared to emission from H II regions.

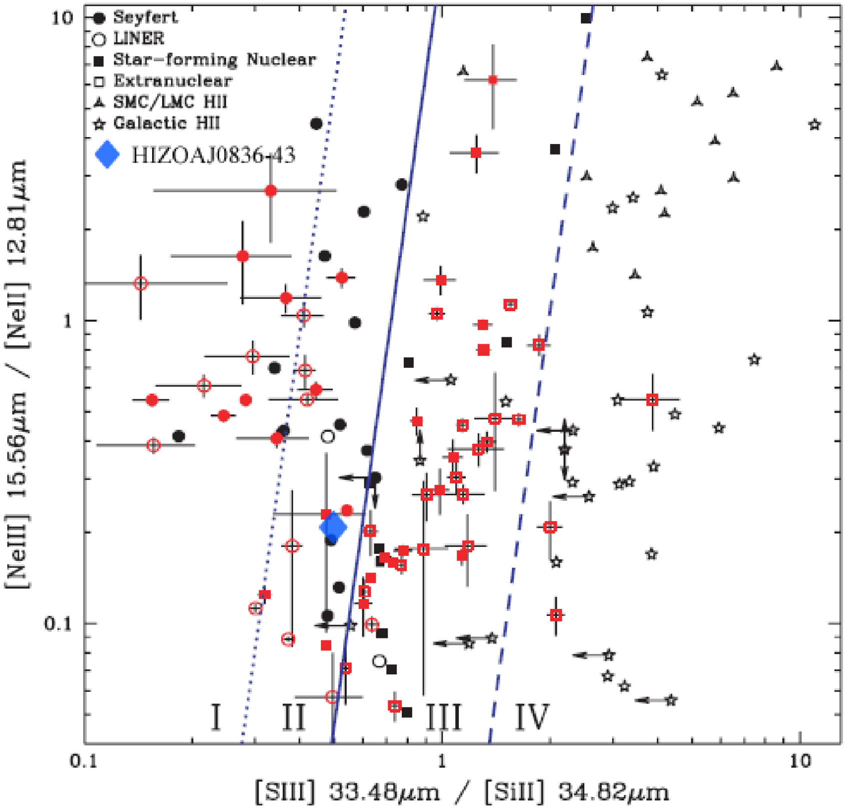

Figure 5.22: Neon, sulphur and silicon diagnostic diagram using line ratios at different ionisations. The lines and Roman numerals delineate regions distinguished by Seyfert galaxies, LINERs and star forming H II regions. (Adapted from Dale et al. 2006)

5.2.3 Warm Molecular Hydrogen Emission

Molecular hydrogen is the most prolific molecule in the universe and dominates the content of the dense gas in galaxies. Molecular clouds form stars and also act as a coolant to enable star formation to take place. Molecular hydrogen may also facilitate accretion of material onto an AGN in its capacity as a coolant. The mid-infrared allows us to directly probe the warm ($T \gtrsim 100$ K) molecular hydrogen component of galaxies; we do this here for HIZOA J0836-43.

In the high-resolution spectrum of HIZOA J0836-43 (see Fig 5.19) we detect the rotational lines of warm molecular hydrogen ($S(0)$, $S(1)$, $S(2)$ and $S(3)$ transitions). These likely arise in PDRs neighbouring H II regions, but other possible heating mechanisms are from shock heating, X-ray heating and cosmic ray heating (Rigopoulou et al. 2002). These emission lines of pure rotational hydrogen act as a powerful probe of the interstellar medium as they constrain the energy injection that excites the H_2. They can be be used to estimate the temperature and mass of (warm) molecular hydrogen as shown, for example, by Rigopoulou et al. (2002) and Higdon et al. (2006). The measured properties of these lines for HIZOA J0836-43 are summarised in Table 5.6.

Table 5.6: H_2 emission line measurements (nucleus).

Line	λ_{rest} μm	Line FWHM $10^{-3}\mu$m	Equivalent Width μm	Flux [a] 10^{-17} W m^{-2}
H_2 $S(3)$	9.66	32.66	– 0.037	1.31 (±0.15)
H_2 $S(2)$ [b]	12.28	24.63	– 0.009	0.92 (±0.07)
H_2 $S(1)$	17.04	41.00	– 0.186	1.57 (±0.08)
H_2 $S(0)$	28.22	98.00	– 0.042	0.61 (±0.14)

[a] Error calculated from the line flux relative to the baseline RMS
[b] H_2 $S(2)$ is blended with [Ar II]

These H_2 emission lines can be used to estimate the temperature and mass of (warm) molecular hydrogen by means of an excitation diagram constructed from the Boltzmann equation:

$$N_i/N = [g(i)/Z(T_{\rm ex})]\, e^{-T_i/T_{\rm ex}} \qquad (21)$$

where $g(i)$ is the statistical weight of state i, $Z(T_{\rm ex})$ is the partition function, T_i is the energy level of a given state and $T_{\rm ex}$ is the excitation temperature. N is the total column density and N_i is the column density of a given state i. N_i is determined directly from the measured flux as follows

$$N_i = 4\pi \times {\rm flux}(i)/[\Omega A(i) h\nu(i)] \qquad (22)$$

where $A(i)$ is the Einstein A-coefficient, $\nu(i)$ is the frequency of the state i, h is Planck's constant and Ω is the solid angle of the beam. Table 5.7 lists the properties of the rotational states of H_2 including $\Delta E/k$. Since these lines are ground state transitions, the energy of the upper state is equal to the energy of the transition, $\Delta E/k$.

The excitation diagram is constructed by plotting the column density divided by the statistical weight in the upper level of the transition versus the energy level. Data points lying on a straight line indicate that the H_2 is characterised by a single temperature, the excitation temperature $T_{\rm ex}$ being the inverse of the slope of the line.

The mass of warm H_2 can be determined from the line luminosity and the the excitation temperature. The total mass is given by $\frac{4}{3}M_o$ where M_o is the mass of gas in the ortho state: $M_o = m_{\rm H_2} N_T$, where $m_{\rm H_2}$ is the molecular mass of H_2 and N_T is the total number of molecules. Hence the mass is determined from equation (21) above.

We plot the excitation diagram for our measurements in Fig. 5.23. A single temperature fit can be performed through $S(3)$ - $S(1)$. However, we do not have enough data points for a cold component fit through $S(0)$. The results of a least squares fit through these points are listed in Table 5.8 (Phil Appleton – private communication).

Table 5.7: Rotational States of H_2

Line	Rotational state (J)	A (s^{-1})	Statistical Weight (g)	$\Delta E/k$ [a] (K)
$H_2(0-0)$ $S(3)$	5	9.84×10^{-9}	33	2504
$H_2(0-0)$ $S(2)$	4	2.76×10^{-9}	9	1682
$H_2(0-0)$ $S(1)$	3	4.76×10^{-10}	21	1015
$H_2(0-0)$ $S(0)$	2	2.94×10^{-11}	5	510

[a] $\Delta E/k$ is the energy of the transition

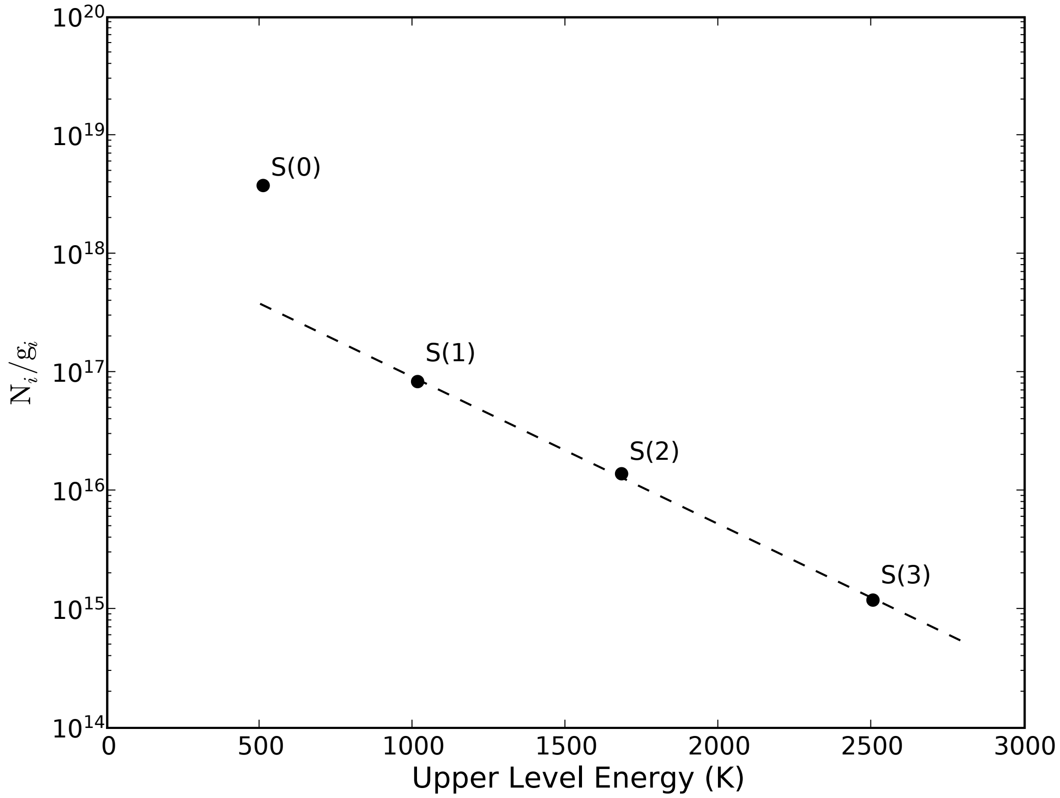

Figure 5.23: Molecular hydrogen excitation diagram. The solid line shows a fit to the S(1), S(2) and S(3) measurements, consistent with a single temperature component at $T_{\text{ex}} = 333$ K.

HIZOA J0836-43 has approximately 1.25×10^7 $M_\odot$ of warm molecular hydrogen at an average temperature of 333 K. Higdon et al. (2006) investigated the warm molecular hydrogen content of 77 ULIRGs and determined an average temperature of $T_{\text{ex}} = 336 \pm 15$ K, corresponding to $\sim 2 \times 10^8 M_\odot$ of warm H_2. The range of mass, however, is between 10^7 and $10^9 M_\odot$. HIZOA J0836-43 therefore has a relatively low mass of warm molecular hydrogen considering the large amount of star formation taking place. In a study of molecular hydrogen in 12 starburst galaxies,

Table 5.8: Determined Properties from Warm H_2 Excitation Diagram

Property	Determined Value
$T_{\rm ex}$	≈ 333 K
OPR [a]	≈ 3
$N(H_2)$	1.78×10^{19} cm^{-2}
$M(H_2)$	$\approx 1.25 \times 10^{7}\ M_\odot$

[a] Ortho-to-Para Ratio

Rigopoulou et al. (2002) find masses ranging from $3 \times 10^6 M_\odot - 1 \times 10^9 M_\odot$. Despite HIZOA J0836-43 appearing to have a relatively "typical" amount of warm H_2, this is only 0.02% of the total H I gas. If we assume that the warm gas constitutes at most 10% of the total molecular gas content for starbursts (Rigopoulou et al. 2002), this only implies $\sim 10^8\ M_\odot$ of molecular hydrogen in the nucleus. This is a factor of $\sim$ 100 less than the estimate derived from $L_{\rm IR}$ in Section 5.1.3. The most likely scenario is that there is a paucity of warm H_2, most likely related to the corresponding paucity of warm MIR continuum.

5.2.4 PAH Diagnostics

We now consider the PAH emission seen in the IRS observations of HIZOA J0836-43. Since the galaxy appeared far more luminous at $8.0\,\mu$m compared to the SINGS galaxies (see Section 5.1.6), we expect relatively strong emission from PAH molecules. This is further evidenced by the broad distinct emission features at 6.2, 7.7, 8.6, 11.3, 12.7 and $17\,\mu$m seen in the nuclear spectrum of HIZOA J0836-43 (see Section 4.3.2).

The so-called Unidentified Infrared Bands (UIBs) are mid-infrared emission bands discovered by Gillett et al. (1973) and subsequently linked to vibrational transitions of C-C and C-H bonds. Léger & Puget (1984) identified PAH molecules as the carriers of these Aromatic Infrared Bands (AIBs). Copious PAH emission is found in the Milky Way (Puget & Léger 1989; Boulanger et al. 1998). In other galaxies the PAH emission is linked to large-scale star formation (Genzel et al. 1998; Laurent et al. 2000). This emission likely arises from UV-excited PAH molecules in the diffuse interstellar medium and within photodissociation regions (PDRs). These are usually associated with H II regions, where ultraviolet radiation from O and B-type stars excite the surrounding hydrogen gas and produce H II emission. Less energetic photons from this radiation field are able to dissociate H_2 to form H I at the interface with the molecular hydrogen cloud. This neutral atomic hydrogen, as well as the regions of the molecular cloud where the radiation field penetrates, is the photodissociation region (Tielens & Hollenbach 1985), as shown in Fig. 5.24.

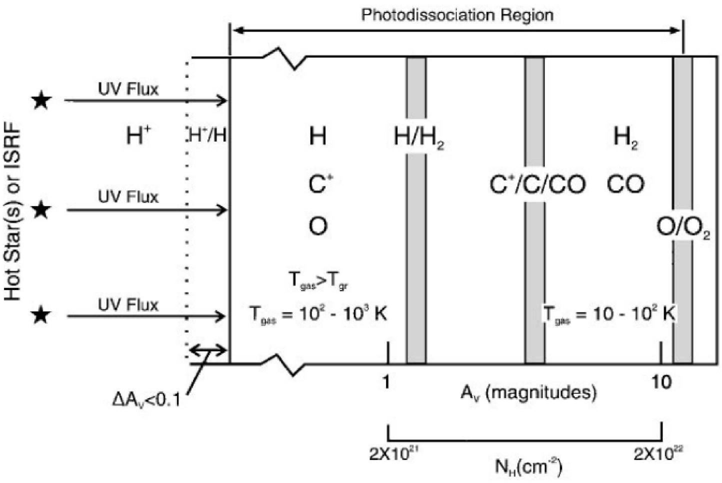

Figure 5.24: A schematic diagram of a photodissociation region from Hollenbach & Tielens (1997). The PDR is illuminated from the left and extends from the predominantly atomic surface region to the point where O_2 is not appreciably photodissociated ($A_V \simeq 10$ mag). Hence, the PDR includes gas whose hydrogen is mainly H_2 and whose carbon is mostly CO. Large columns of warm O, C, C^+ and CO and vibrationally excited H_2 are produced in the PDR.

PAHs are believed to form in this region because the less energetic UV photons dissociate CO in addition to H_2 and are energetic enough to cause the photoionisation of carbon (Hollenbach & Tielens 1997). PDRs are encountered in a wide range of astrophysical environments, including close to cooler A and F stars and associated with molecular clouds exposed to the average interstellar radiation field (Peeters et al. 2004). Since PAH molecules are destroyed by intense radiation such as found in H II regions and close to AGN (Genzel et al. 1998), they provide a diagnostic for determining the dominant processes contributing to observed MIR emission.

In our Milky Way, PDRs are also found in reflection nebulae such as NGC 7023 and NGC 2023. Reflection nebulae are gas and dust clouds which are close to hot young stars. On the surfaces of these clouds PDRs form due to the interaction of the star with its molecular environment. NGC 7023 is illuminated by HD 200775, a Herbig B3Ve star, which is located in the cavity of the molecular cloud (Fuente et al. 2000). A dense PDR has formed on the walls of the cavity and due to the proximity and geometry of the reflection nebula, it serves as an ideal laboratory to study the physical and chemical processes taking place in the PDR.

Quantifying PAH Emission in HIZOA J0836-43

We now investigate the strength of the PAH emission in HIZOA J0836-43. In the analysis that follows, equivalent widths are treated as positive, as per the current convention in the literature. The spectrum of HIZOA J0836-43 with the location of the PAH emission features are shown in

Table 5.9: PAH emission line equivalent widths and luminosities (measurements made using a spline continuum).

PAH λ_{rest} (μm)	Equivalent Width (EQW) ($-\mu$m)	Flux [a] 10^{-17} W m^{-2}	Luminosity [a] ($10^7 L_\odot$)
6.23	0.722	97.58 ±2.14	66.9 ±1.5
7.67	0.819	219.21 ±4.76	150.0 ±3.3
8.59	0.227	44.00 ±1.52	30.2 ±1.0
11.27	0.851	59.33 ±1.03	40.7 ±0.7
12.60	0.419	20.43 ±1.37	14.0 ±0.9
16.44	0.052	4.17 ±0.47	2.9 ±0.3
17.04	1.573	21.79 ±2.25	14.9 ±1.5
17.37	0.057	1.20 ±0.41	0.8 ±0.3

[a] Error calculated from the line flux relative to the baseline RMS

Fig. 5.20; measurements and luminosities of these lines are summarised in Table 5.9. The scaled spectrum of NGC6240, a starburst galaxy, is also shown in Fig. 5.20 for comparison. This shows the exceptionally strong PAH emission of HIZOA J0836-43 compared to NGC 6240: equivalent width measurements (EQW) of 0.72 compared to 0.52 μm (Armus et al. 2006) for the 6.23 μm PAH.

Brandl et al. (2006) investigated the properties of 22 starburst nuclei and found that an average value of 0.53 μm for both the 6.2 μm and 7.7 μm PAH EQWs. They find that the 7.7 μm PAH EQW remains constant over an order of magnitude of [Ne III] 15.56 μm/[Ne II] 12.81 μm (which indicates the hardness of the radiation field). We show in Fig. 5.25, taken from Brandl et al. (2006), that HIZOA J0836-43 has a 7.7 μm EQW of 0.82 μm, much greater than what is found for other starbursts.

In the same study, Brandl et al. (2006) find no significant variation in the 7.7 μm/11.3 μm PAH ratio over an order of magnitude of [Ne III] 15.56 μm/[Ne II] 12.81 μm. We show in Fig. 5.26 the location of HIZOA J0836-43 in comparison to the 7.7 μm/11.3 μm PAH ratio of starburst galaxies. HIZOA J0836-43 has a PAH flux ratio of 3.69 ± 0.11, which is typically a factor of ~ 2 greater than what is found for the starbursts.

For the 8.6 μm and 11.3 μm PAH feature, they find a range of EQWs from $0.003 - 0.192$ μm and $0.180 - 0.931$ μm respectively. HIZOA J0836-43 has corresponding EQWs of 0.227 μm and 0.851 μm by comparison. This corresponds to the largest 8.6 μm value and only less than NGC 7252 for the 11.3 μm PAH feature.

The 17 μm PAH feature clearly shows the difference between HIZOA J0836-43 and other starbursts. The largest value is an EQW of 0.792 μm for NGC 7252, while in strong contrast, HIZOA J0836-43 has an EQW of 1.573 μm, almost twice as large as that found for NGC 7252. We attribute these large equivalent widths to a combination of power in the PAH emission lines and the absence of a sharply rising dust continuum typical of starburst systems (see Fig. 5.20).

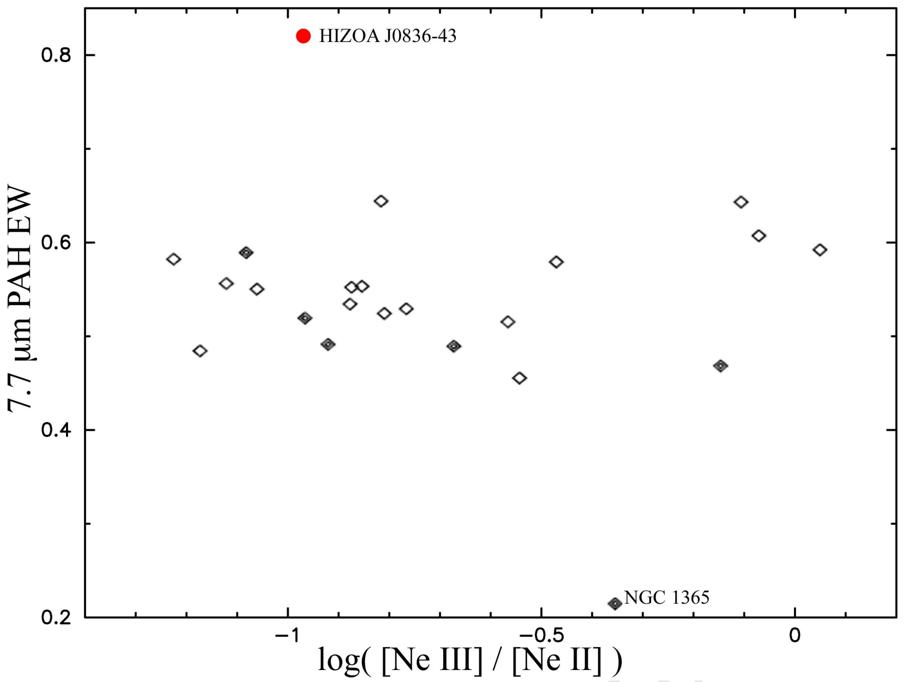

Figure 5.25: Comparison of 7.7 μm PAH EQW of starbursts, modified from Brandl et al. (2006). Filled diamonds correspond to starbursts with a weak AGN component. HIZOA J0836-43 has a 7.7 μm PAH EQW of 0.82 μm, 60% greater than the average value.

PAH Emission as a Measure of Infrared Luminosity

PAH emission is closely related to the total infrared luminosity of a starbursting system. Since PAHs originate in star forming regions and the total infrared luminosity of a system is measure of star formation, they share a common origin. This relationship was investigated by Brandl et al. (2006) who showed that the 6.2 μm PAH flux can be used to estimate the total infrared luminosity ($L_{\rm IR}^{\rm PAH}$) within a factor of 2. Using their equation,

$$\log(L_{\rm IR}^{\rm PAH}) = 1.13\log\,(F_{6.2\mu{\rm mPAH}}D^2), \qquad (23)$$

where $F_{6.2\mu{\rm mPAH}}$ is the 6.2 μm PAH flux in units of 10^{-19} W cm^{-2}, D is the distance in kiloparsecs and $L_{\rm IR}^{\rm PAH}$ is in units of solar luminosity, we find $L_{\rm IR}^{\rm PAH} \approx 4.7 \times 10^{11} L_\odot$. Interestingly, this is ~ 4 times the total luminosity determined from the photometry in Section 3.5 ($1.2 \times 10^{11} L_\odot$). This further illustrates the abnormally strong PAH emission in relation to the total infrared emission of the galaxy, most notably the weak emission from a warm dust continuum. Strong PAH emission such as this could well result in a large total infrared luminosity if emission from the continuum was similarly strong. HIZOA J0836-43 appears atypical, as it has powerful PAH emission, but lacks similarly strong continuum emission, thus giving rise to the observed large discrepancies in the star-formation metrics as compared to other starburst systems.

Now consider a comparison with the most luminous infrared galaxies. Desai et al. (2007)

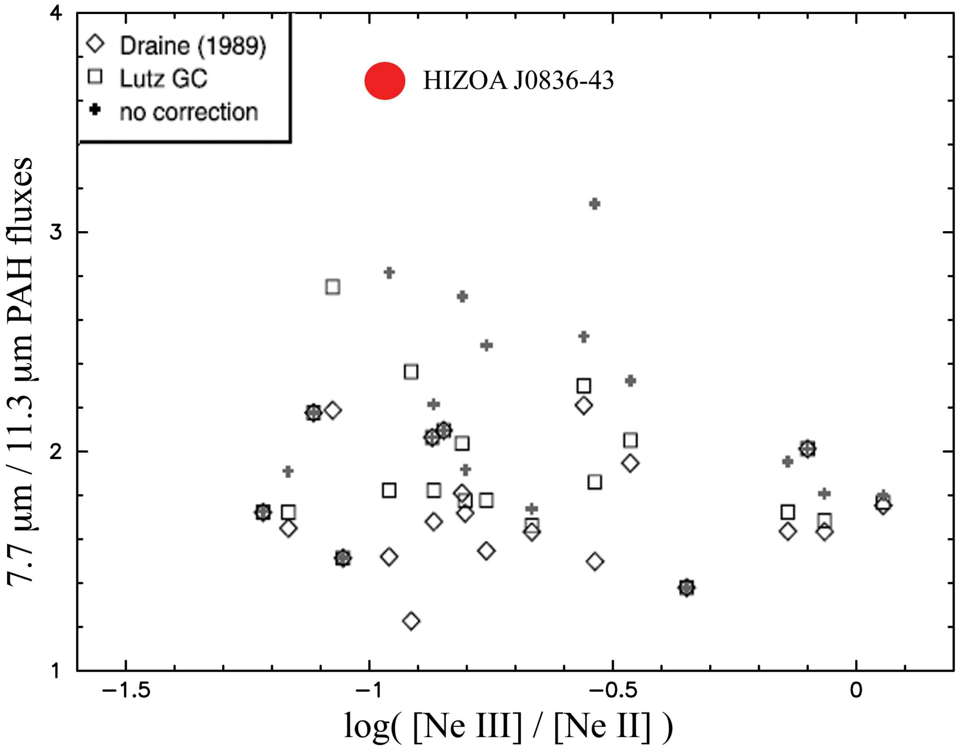

Figure 5.26: Comparison of 7.7 μm/11.3 μm PAH ratio for starburst galaxies (adapted from Brandl et al. 2006). The diamonds and squares employ different extinction corrections, while the crosses have no correction applied. The position of HIZOA J0836-43 is denoted by the red circle. It is significantly higher than the typical starburst values.

investigated PAH emission in 107 ULIRGS. They find 6.2 μm EQWs ranging between 0.006 – 0.864 μm. For the 11.3 μm feature they find a range of 0.006 – 1.169 μm. The highest average values for the 6.2 μm and 11.3 μm EQW were found for the 15 ULIRGS classified as H II-like galaxies, which had an average value of $0.27 \pm 0.18\,\mu$m and $0.41 \pm 0.20\,\mu$m respectively.

In this sample, 66 ULIRGS were classified as “cold” from their IRAS flux densities (i.e. $f_\nu(25\,\mu m)/f_\nu(60\,\mu m) < 0.2$) and they showed the largest PAH EQWs. The average for the 6.2 μm EQW and 11.3 μm EQW is 0.27 ± 0.18 and 0.52 ± 0.24 respectively. They conclude that the H II-like galaxies and cold ULIRGS have a median 6.2 μm PAH EQW value which is ~ 50% of lower luminosity starbursts. Similarly, the median 11.3 μm PAH EQW value for cold ULIRGs is ~ 80% of the starburst median. Possible reasons for this could be PAH destruction due to the presence of an AGN and larger quantities of hot dust in ULIRGs diluting PAH emission from star formation (Desai et al. 2007).

Brandl et al. (2006) find that low-luminosity starbursts show a correlation between $L(6.2\mu m)$ PAH and $\nu L_\nu(5.5\mu m)$ given by:

$$\log[L(6.2\mu m)\mathrm{PAH}] = -0.49 + 0.96\log[\nu L_\nu(5.5\mu m)]. \qquad (24)$$

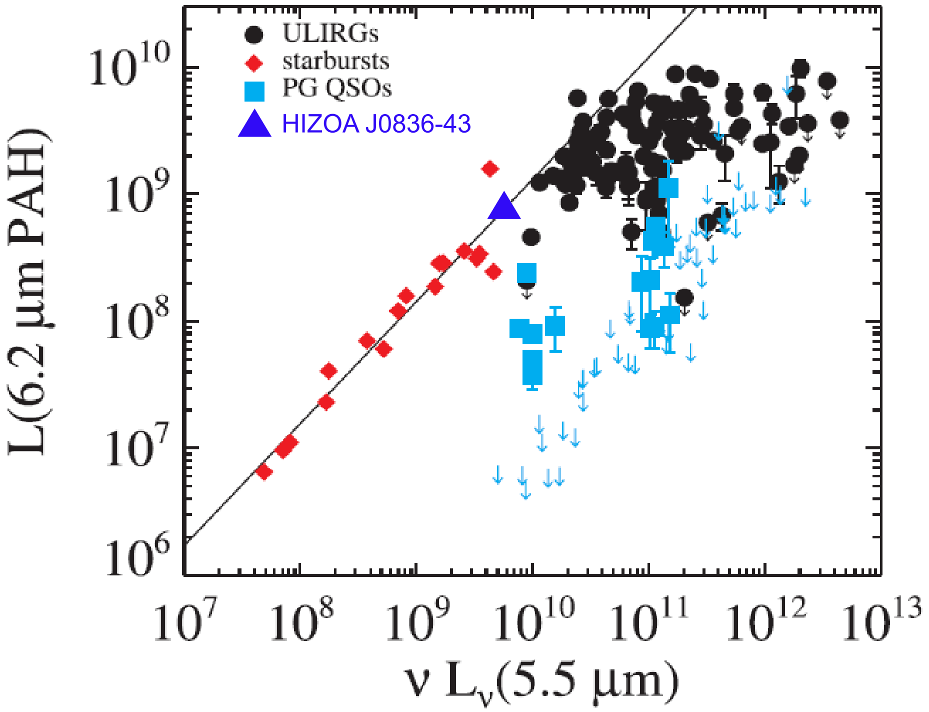

Figure 5.27: Luminosity of 6.2 μm feature as a function of 5.5 μm luminosity. Brandl et al. (2006) starbursts are shown as red diamonds with the solid black line a fit to these points. HIZOA J0836-43 is shown as the blue triangle. It lies on the starburst relation. Adapted from Desai et al. (2007).

Fig. 5.27 shows the plot from Desai et al. (2007) and includes starbursts from Brandl et al. (2006). The position of HIZOA J0836-43 is also shown. As can be seen, HIZOA J0836-43 lies on the relation for starbursts (shown as the black line), but at the high-luminosity end. The ULIRGs and QSOs (Quasi-stellar Objects), however, do not lie on the extrapolation of this relation to higher luminosities.

PAH Emission as a Measure of Star Formation

The strongest PAH features (6.2 μm and 11.3 μm) can be used to estimate the star formation rate, since the mechanism of their production is closely linked to star formation. Desai et al. (2007) derive the following relation:

$$\mathrm{SFR}(M_\odot\,\mathrm{yr}^{-1}) = 1.18 \times 10^{-41} L_P(\mathrm{erg\,s}^{-1}), \qquad (25)$$

with L_P corresponding to the sum of the 6.2 μm and 11.3 μm PAH luminosities. Based on our value, $L_P = 4.12 \times 10^{42}$, we obtain a SFR of $\sim 49\,M_\odot\,\mathrm{yr}^{-1}$. This is approximately twice the

SFR calculated using L_{FIR} ($20.5\,M_{\odot}\,\mathrm{yr}^{-1}$) in Section 3.9, confirming the overluminosity of PAH emission in comparison to the total IR emission of the galaxy.

PAH Emission: Total Luminosity

Let us consider the total PAH luminosity compared to the total infrared luminosity of the galaxy. Summing over the luminosities of the PAH emission features (see Table 5.9) leads to a total PAH luminosity of $L_{\mathrm{PAH}} = 3.2 \times 10^9 L_{\odot}$. Given that the galaxy has a total infrared luminosity $L_{\mathrm{TIR}} = 1.2 \times 10^{11} L_{\odot}$, the PAH emission constitutes $\sim 2.7\%$ of the total infrared emission. The 10 ULIRGs studied by Armus et al. (2007) have percentages ranging from $0.4-2.1\%$ by comparison. We note that their comparison source NGC 7714 has the highest percentage, namely 4.4%. Like HIZOA 0836-43, this galaxy is a starburst with no hot dust emission.

Other studies of PAH strengths and luminosities have been made using the PAH decomposition method described in Section 4.4. We summarise in Table 5.10 the PAH equivalent widths and luminosities obtained using the PAH decomposition method. We use these measurements to compare to studies done by for eg., Smith et al. (2007).

We calculate the total PAH luminosity by summing the individual luminosities for each feature and find a total PAH luminosity of $L_{\mathrm{PAH}} = 6.5 \pm 1.4 \times 10^9 L_{\odot}$. This is approximately twice the luminosity obtained above using the spline continuum measurements. This corresponds to a $L_{\mathrm{PAH}}/L_{\mathrm{TIR}}$ ratio of 0.06 or 6%.

Table 5.10: PAH emission line equivalent widths and luminosities (measurements made using the PAH multifit decomposition).

PAH λ_{rest} μm	Equivalent Width μm	Flux [a] 10^{-17} W m^{-2}	Luminosity [a] ($10^7 L_{\odot}$)
5.70	− 0.405	15.04 ±2.00	10.3 ±1.3
6.22	− 2.156	112.58 ±2.07	77.2 ±1.4
6.69	− 9.758	82.67 ±7.01	56.6 ±4.8
7.42	− 12.583	145.58 ±8.99	99.8 ±6.2
7.62	− 8.474	177.95 ±4.17	121.9 ±2.9
7.85	− 9.265	88.19 ±4.48	60.4 ±3.1
8.33	− 10.161	151.01 ±8.12	103.5 ±5.6
8.61	− 2.837	30.95 ±2.81	21.2 ±1.9
11.04	− 0.919	4.27 ±0.53	2.9 ±0.4
11.23	− 1.371	20.79 ±0.50	14.2 ±0.3
11.33	− 1.998	54.43 ±1.41	37.2 ±1.0
11.95	− 3.288	27.84 ±2.26	19.1 ±1.6
12.60	− 1.783	44.45 ±2.11	30.5 ±0.9

[a] Error calculated from the line flux relative to the baseline RMS

We compare this result to the study of Smith et al. (2007) who used the PAH decomposition method to investigate PAH emission in 59 starforming galaxies in SINGS. They find that the majority of H II galaxies and AGN have $L_{\mathrm{PAH}}/L_{\mathrm{TIR}}$ close to 0.1, with lower and upper limits of ~ 0.02 and 0.11. HIZOA J0836-43's ratio of 0.06 is on the low side compared to the majority of their galaxies.

When we consider $L_{\mathrm{PAH}}/\nu L_\nu(24\mu m)$, we obtain

$$L_{\mathrm{PAH}}/\nu L_\nu(24\mu m) = \frac{6.5 \times 10^9 L_\odot}{1.1 \times 10^9 L_\odot} = 5.9 \pm 0.2 \qquad (26)$$

This corresponds to ~ 6 times more power coming from PAH features compared to warm dust emission.

We show in Table 5.11 the luminosities for the strongest PAH complexes (6.2, 7.7 and 11.3 μm) and the luminosities obtained using the spline continuum. The $L(\mathrm{decomp})/L(\mathrm{spline})$ ratios are similar to what has been found for star forming galaxies (Smith et al. 2007), but below the average values (1.70, 3.53 and 1.86 for the 6.2, 7.7 and 11.3 μm features respectively). This is consistent with HIZOA J0836-43 not having a strong warm dust continuum, which results in a less dramatic difference between the two decomposition methods.

Table 5.11: PAH feature luminosities and Multifit method versus Spline ratio.

PAH Feature	$L(\mathrm{decomp})$ $(10^8 L_\odot)$	$L(\mathrm{decomp})/L(\mathrm{spline})$
6.2 μm	7.72 ±0.62	1.15
7.7 μm complex	28.21 ±2.26	1.88
11.3 μm complex	5.14 ±0.19	1.26

Using the PAH luminosities listed in Table 5.11, we can calculate $L_{\mathrm{PAH}}/\nu L_\nu(24\mu m)$ ratios of those corresponding features. We list these in Table 5.12, as well as values from the study of Brandl et al. (2006).

Table 5.12: Ratios of PAH luminosity to 24 μm luminosity

Ratio	$L_{\mathrm{PAH}}/\nu L_\nu(24\mu m)$	$L_{\mathrm{PAH}}/\nu L_\nu(24\mu m)^a$
$L_{6.2\mu\mathrm{m}}/\nu L_\nu(24\mu m)$	0.70 ±0.08	~ 0.1
$L_{7.7\mu\mathrm{m}}/\nu L_\nu(24\mu m)$	2.56 ±0.30	~ 0.4
$L_{11.3\mu\mathrm{m}}/\nu L_\nu(24\mu m)$	0.47 ±0.04	~ 0.1

[a] Brandl et al. (2006)

We find that $L_{7.7\mu\mathrm{m}}/\nu L_\nu(24\mu m)$ for HIZOA J0836-43 is ~ 2.5 times larger than the highest ratio (~ 1.0) found by Brandl et al. (2006). This is a consequence of the low 24 μm luminosity compared to the strong PAH emission.

5.2.5 Summary

Spectroscopy of HIZOA J0836-43 has revealed various properties of HIZOA J0836-43. We summarise some key ratios and quantities determined in this Section in Table 5.13.

Table 5.13: Summary of spectroscopic properties of HIZOA J0836-43

Derived Property	Value
[Ne III] 15.56 μm/[Ne II] 12.81 μm	0.11 ±0.01
[S III] 18.71 μm/[S III] 33.48 μm	0.70 ±0.05
[Si II] 34.82 μm/[S III] 33.48 μm	1.96 ±0.16
12 + log(O/H) [a]	~ 9.2
SFR [a]	$\sim 21\,M_\odot\,\mathrm{yr}^{-1}$
n_e [b]	$\sim 300\,\mathrm{cm}^{-3}$
T_{ex} (warm H_2)	≈ 333.1 K
$M(H_2)$ (warm)	$\approx 1.25 \times 10^7\ M_\odot$
6.2 μm PAH EQW	− 0.72 μm
7.7 μm PAH EQW	− 0.82 μm
F(7.7μm PAH)/F(11.3μm PAH)	3.69 ±0.10
$L_{\mathrm{IR}}^{\mathrm{PAH}}$ [c]	$\approx 4.7 \times 10^{11} L_\odot$
SFR [d]	$\sim 49\,M_\odot\,\mathrm{yr}^{-1}$
L_{PAH}	$6.5 \pm 1.4 \times 10^9 L_\odot$
$L_{\mathrm{IR}}^{\mathrm{est}}$ [e]	$\approx 1.8 \times 10^{10} L_\odot$

[a] Estimated from [Ne III]15.56 μm/[Ne II]12.81 μmratio

[b] Estimated from [S III]18.71 μm/[S III]33.48 μm ratio

[c] Estimated from 6.2 μm PAH Flux

[d] Estimated from 6.2 μm and 11.3 μm PAH luminosities

[e] Estimated from 15 μm and 30 μm flux densities

The galaxy appears to have a relatively soft radiation field compared to other starbursts ([Ne III] 15.56 μm/[Ne II] 12.81 μm ratio), suggesting large amounts of PDR emission compared to emission from H II regions. The [Si II] 34.82 μm/[S III] 33.48 μm ratio appears elevated compared to other starbursts which is consistent with a scenario of PDR-dominated emission.

However, the amount of warm molecular hydrogen in HIZOA J0836-43 is low compared to other starbursts and ULIRGs, and also in relation to its H I content. The paucity of warm H_2 is likely connected to the lack of strong continuum dust emission in HIZOA J0836-43.

We have shown that the galaxy possesses exceptionally strong PAH emission compared to other star-forming galaxies. This is consistent with a relatively mild radiation field, as PAHs are easily destroyed. Coupled to this, we expect large amounts of PDR-associated emission, as this is where PAHs form.

5.3 HIZOA J0836-43 as an H I-massive Galaxy

In Section 1.5 we described the importance of the formation and evolution of gas-rich disk galaxies for theories of cosmology. The origin of HIZOA J0836-43 could be connected to the formation of H I-massive galaxies in general and provide clues regarding their evolutionary history. In this Section we highlight key aspects of these giant disks and provide a comparison of HIZOA J0836-43 and Malin 1.

After the discovery of Malin 1 (Bothun et al. 1987), subsequent surveys and catalogue searches revealed other giant LSB galaxies (eg. Impey & Bothun 1989; Sprayberry et al. 1995; Schinnerer et al. 1997), but they remain extremely rare in the local universe. Their properties are intriguing in that their disks are faint, but their H I mass, size and luminosities are high compared to other disk galaxies (Matthews et al. 2001). The colours of giant LSBs are similar to normal, high surface brightness galaxies and redder than smaller LSBs (Sprayberry et al. 1995). These massive disks also differ from other LSBs in that they usually have a significant bulge (Knezek 1993), which often harbours an AGN (Schombert 1998).

This has given rise to speculation that the evolution of giant LSBs is distinctly different compared to other, less massive LSB and dwarf galaxies. Hoffman et al. (1992) propose a scenario where the LSB giants form in low density regions from rare 3σ density fluctuations. They predict that these galaxies would have gas-rich disks that are relatively unevolved and inactive. An alternative scenario proposed by Knezek (1993) suggests that these galaxies have formed dissipatively from massive dark matter halos that are relatively metal-poor. The evolutionary history of giant LSB galaxies, as well as their observed properties remain enigmatic (O'Neil & Schinnerer 2004; Villegas et al. 2008).

Malin 1 in particular continues to be studied in detail. Analysis of *HST* imaging of Malin 1 by Barth (2007) revealed that it could contain a normal stellar disk only recognisable in high resolution data (Malin 1 lies at a redshift of 0.083). Barth (2007) showed that Malin 1 resembles an early-type (S0/a) barred spiral, embedded in an extended gas-rich outer disk that is optically faint. Re-analysis of the H I data by Sancisi & Fraternali (2007) supports this hypothesis. Barth (2007) speculates that other giant LSB galaxies may have normal surface brightness disks that have gone undetected due to inadequate spatial resolution (many lie at distances comparable to Malin 1 and beyond). Indeed, most giant LSB galaxies have prominent bulges (Knezek 1993) that could hinder the detection of a disk.

The presence of an evolved disk in Malin 1 could be explained by relatively normal evolution that ceased before more of the H I-rich disk could be converted into stars. Alternatively, the H I gas could have been acquired during recent accretions or mergers. Like nearly all giant LSB galaxies, Malin 1 is in a relatively quiescent state (Rahman et al. 2007), providing few clues as to its future evolution.

The infrared flux densities of Malin 1 and HIZOA J0836-43 are shown in Table 5.14. The inactivity of Malin 1 is evident by the weak emission in the IRAC and MIPS-24 μm bands. The galaxy is not detected by MIPS-70 μm and MIPS-160 μm. The bulge light of Malin 1 (J,

Table 5.14: Infrared flux densities of HIZOA J0836-43 and Malin 1.

Band	λ (μm)	HIZOA J0836-43 F_ν [a] (mJy)	Malin 1 F_ν [a] (mJy)
J	1.25	53.18 [1]	3.93 [2]
H	1.63	60.53 [1]	3.41 [2]
K_s	2.14	52.17 [1]	2.00 [2]
IRAC-1	3.6	31.40 [1]	1.61 [3]
IRAC-2	4.5	21.72 [1]	1.10 [3]
IRAC-3	5.8	45.20 [1]	0.73 [3]
IRAC-4	8.0	145.31 [1]	0.74 [3]
MIPS-24	24	126.52 [1]	0.57 [3]
MIPS-70	70	2291.3 [1]	—[b]
MIPS-160	160	3082.1 [1]	— [b]

[a] Flux densities are aperture and reddening corrected

[1] Reference: This work

[2] 2MASS

[3] Reference: Rahman et al. (2007)

[b] Undetected

H, K_s bands) clearly dominates its infrared emission, compared to HIZOA J0836-43 where the mid-infrared and far-infrared dominates the emission.

Table 5.15 shows the physical properties of Malin 1 and HIZOA J0836-43. The galaxies are similarly massive in terms of H I-content and dynamical properties, but HIZOA J0836-43 is ~ 40 times more luminous in the infrared. When comparing star formation rates using the 24 μm law from Alonso-Herrero et al. (2006), HIZOA J0836-43 still has a SFR ~ 20 times greater than Malin 1, despite its 24 μm luminosity underestimating its SFR.

We have shown above how similar the H I-massive Malin 1 and HIZOA J0836-43 are. Yet in the infrared they are distinctly different, a direct result of active star formation in HIZOA J0836-43. As the only example in the local universe of a massive gas-rich spiral undergoing a starburst, the galaxy provides a unique laboratory for further study and modeling of the physics of H I-massive galaxies.

Table 5.15: Physical properties of HIZOAJ0836-43 and Malin 1.

Property	HIZOAJ0836-43	Malin 1
v_{hel} ($\mathrm{km\,s^{-1}}$)	$10,689$ [1]	$24,750$ [2]
D_L(Mpc)	148 [1]	366 [2]
log ($M_{HI}/M_\odot$)	10.88 [1]	10.83 [3]
HI radius (kpc)	66 [1]	130 [4]
w_{20} (km s^{-1})	610 [1]	455 [3]
log ($L_{TIR}/L_\odot$)	11.07 [5]	9.49 [6**]
SFR ($M_\odot$ yr^{-1})	21.5 [5]	0.38 [6***]

[1] Reference: Donley et al. (2006)
[2] NASA Extragalactic Database (NED)
[3] Reference: Pickering et al. (1997)
[4] Reference: Impey & Bothun (1989)
[5] This work
[6] Reference: Rahman et al. (2007)
** estimated using Calzetti et al. (2005)
*** estimated using Alonso-Herrero et al. (2006)

5.4 HIZOA J0836-43 as a local LIRG

We now consider the properties of HIZOA J0836-43 compared to other LIRG systems. Of fundamental consideration is the mechanism or combination of events that has caused the observed starburst. Figure 5.2 showed that the mid-infrared emission is clearly extended and exhibits asymmetry, or a warp, along the eastern side along the major axis. This extended morphology, also evident in the radio continuum and H I distribution (Donley et al. 2006), is reminiscent of a tidal tail, possibly due to a minor disturbance from a passing galaxy. Studies of (U)LIRGS have shown that high star formation can be induced by major mergers, minor mergers, bar instabilities or interactions with neighbours as highlighted below.

LIRGS are galaxies with a total IR luminosity ($8 - 1000\,\mu$m) of $> 10^{11} L_\odot$, and for ULIRGS $> 10^{12} L_\odot$. Their high luminosities are believed to be the result of emission from dust heated by starbursts and active galactic nuclei (Sanders & Mirabel 1996), provoking intense interest in their formation and subsequent evolution.

LIRGS in the local universe are relatively rare and generally associated with galaxy mergers and strong interactions, as evidenced by their disturbed morphologies (see eg. Farrah et al. 2001; Ishida 2004). They appear more common at higher redshifts with $\sim 70\%$ of the infrared background at $z = 1$ being produced by LIRGS (Le Floc'h et al. 2005). However, $\sim 50\%$ of intermediate redshift LIRGS have disks that show little evidence of a recent merger (Bell et al. 2005; Melbourne et al. 2005; Wang et al. 2006). These LIRGs could be triggered by weak interactions with neighbours, minor mergers and internal bar instabilities, achieving heightened star formation as a result of higher gas fractions compared to local disks (Melbourne et al. 2005).

In general, local LIRGS appear to contain bars (Wang et al. 2006) and exhibit centrally concentrated star formation (Sanders & Mirabel 1996). Melbourne et al. (2008) have shown that at intermediate redshifts $\sim 10\%$ of LIRGS contain bars and only one third show signs of an interaction, major or minor. This suggests that these LIRG disks have star formation rates that are "normal" for that epoch, i.e. they are less dependent on major interactions to achieve heightened star formation because they are more gas-rich compared to local disks. Having a plentiful reservoir of gas is one of the requirements for active star formation.

We noted in Section 5.1.6 that HIZOA J0836-43 exhibits a cold $L_{24\mu\mathrm{m}}/L_{70\mu\mathrm{m}}$ colour compared to the LIRGs in GOALS. We now consider the spectrum of HIZOA J0836-43 compared to that of NGC 5734 (shown in Fig. 5.28), the LIRG in GOALS with the weakest dust continuum and otherwise closely matching in properties. NGC 5734 is an S0 galaxy undergoing a burst of star formation due to a major interaction with another galaxy (NGC 5743). HIZOA J0836-43 displays a colder dust continuum compared to even this galaxy – HIZOA J0836-43 has the weakest MIR continuum compared to any other local LIRG studied to date.

It is intriguing that NGC 5734, which has a continuum that is only slightly less cold than HIZOA J0836-43, is an S0 galaxy. We saw in Section 5.1.6 that HIZOA J0836-43 has several properties that are more typical of an S0/Sa galaxy than a disk galaxy ($L_{8\mu\mathrm{m}}/L_{24\mu\mathrm{m}}$, $L_{24\mu\mathrm{m}}/L_{70\mu\mathrm{m}}$, $L_{70\mu\mathrm{m}}/L_{160\mu\mathrm{m}}$. In Fig. 5.29 we illustrate the near-infrared and mid-infrared composites of both

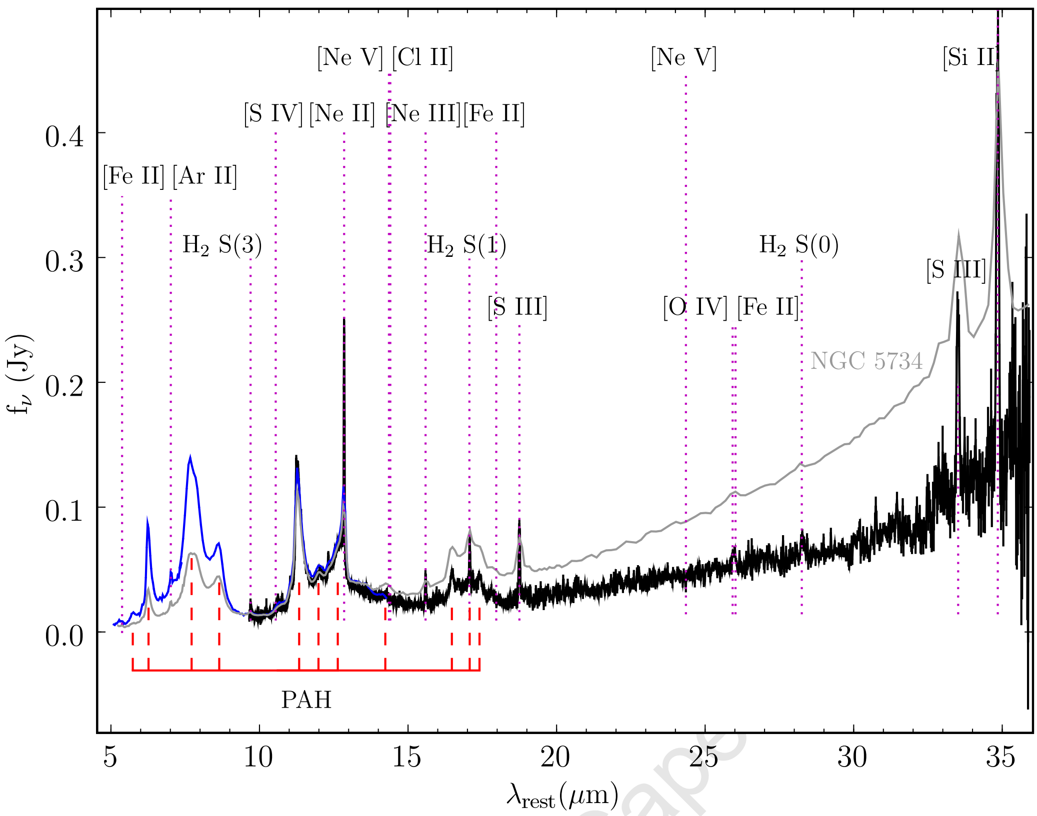

Figure 5.28: Spectrum of HIZOA J0836-43 compared to the low-resolution spectrum of NGC 5734, the LIRG in GOALS with the coldest MIR continuum.

galaxies for comparison. NGC 5734 appears bulge-dominated in the near-infrared, but has extended mid-infrared emission, similar to HIZOA J0836-43. The galaxies have very similar total infrared luminosities ($L_{\rm TIR} = 1.20 \times 10^{11} L_\odot$ for HIZOA J0836-43 and $L_{\rm TIR} = 1.15 \times 10^{11} L_\odot$ for NGC 5734 – J. Howell; private comminication).

Many nearby early-type galaxies have significant H I gas ($\sim 5 \times 10^9 M_\odot$) often in large-scale rotating discs and rings (Oosterloo et al. 2007). PAH emission has also been found in elliptical galaxies such as NGC 4697 (Bregman et al. 2006) and NGC 3265 (Kaneda et al. 2005).

Let us consider the growth progress of HIZOA J0836-43 compared to other LIRGS. This can be deduced from the stellar population and current star formation rate. First we calculate the specific star formation rate defined as the SFR per Gyr per unit stellar mass. From the SFR determined in Section 3.9 and the stellar mass calculated in Section 5.1.2, we find a specific SFR (SSFR) of

$$\mathrm{SSFR} = \frac{20.5 \times 10^9\, M_\odot\, \mathrm{Gyr}^{-1}}{4.4 \times 10^{10}\, M_\odot} = 0.47\, \mathrm{Gyr}^{-1}. \qquad (27)$$

This corresponds to a doubling of stellar mass occuring on a timescale of $\sim$ 2 Gyr, assuming

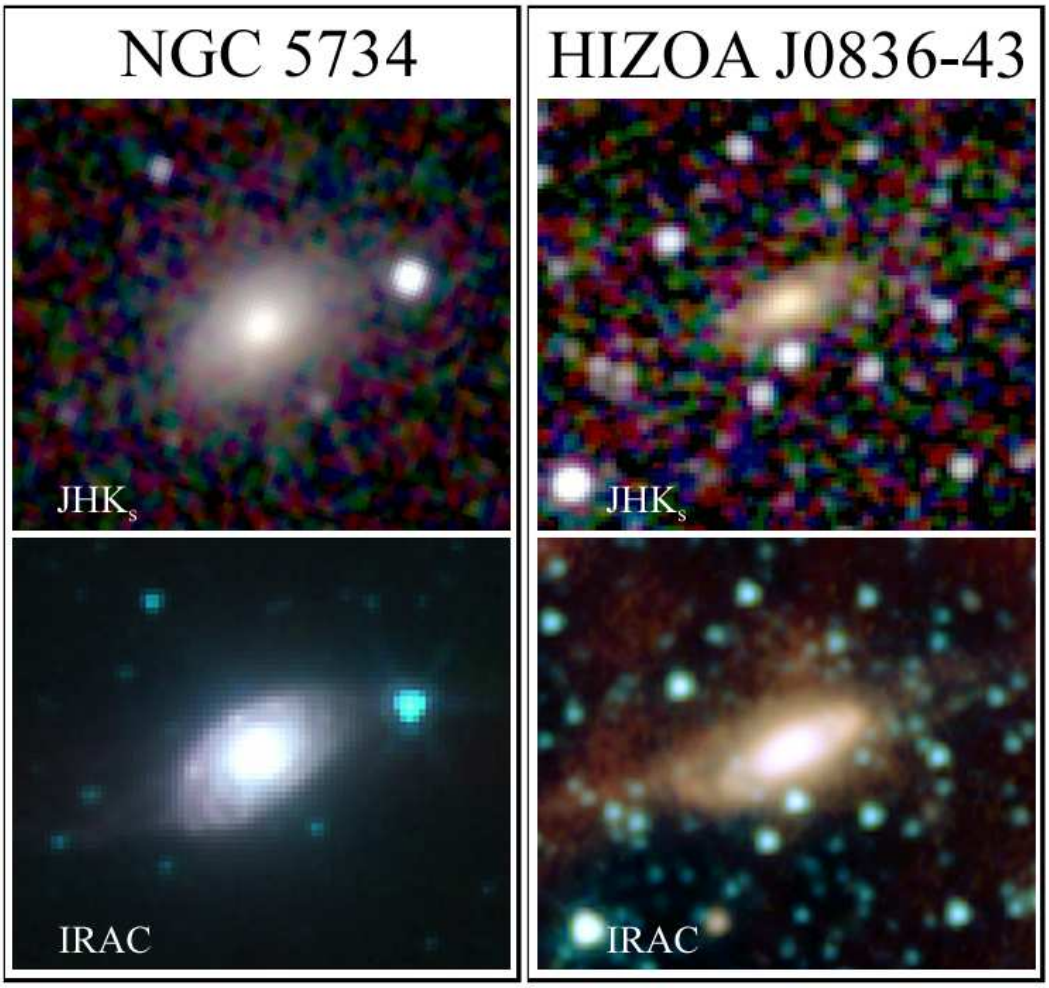

Figure 5.29: Comparison between HIZOA J0836-43 and NGC 5734 using a J, H, K_s composite image (from 2MASS) and a composite using the four IRAC bands (from *Spitzer*). The images show an area of $\sim 2' \times 2'$. NGC 5734 lies at a distance of 60.2 Mpc compared to HIZOA J0836-43's distance of 148 Mpc.

a sustained level of enhanced star formation.

Similarly, the cold gas fraction can be used to estimate the progress of stellar building. This is possible with the stellar mass and cold molecular hydrogen determined in Sections 5.1.2 and 5.1.3, respectively:

$$f_{\rm cold} = M({\rm H_2})/[M({\rm H_2}) + M_*] = \frac{1.3 \times 10^{10}\, M_\odot}{1.3 \times 10^{10}\, M_\odot + 4.4 \times 10^{10}\, M_\odot} \approx 0.228. \qquad (28)$$

This corresponds to ∼23% of cold gas.

In Fig. 5.30 we put this value in context to the sample of 159 local LIRGS from Wang et al. (2006). HIZOA J0836-43 has a SSFR of 0.47 Gyr^{-1}, which is high compared to the other LIRGs with an average of ~ 0.2 Gyr^{-1}. HIZOA J0836-43 also has a slightly smaller stellar mass in comparison to the majority of LIRGs in the Wang et al. (2006) sample. The location of HIZOA J0836-43 in the SSFR - Stellar Mass plane implies active stellar building as facilitated by its plentiful supply of gas. As it builds stellar mass it will move along the line of constant star formation, trading its gas reservoir for stellar matter. Compared to the other LIRGs it appears relatively early in the building of stellar mass, implying abundant future mass growth. We speculate that HIZOA J0836-43's current level of active star formation comes after a relatively long period of inactivity in which the galaxy would have appeared as an S0 type of galaxy (much as Malin 1 appears today).

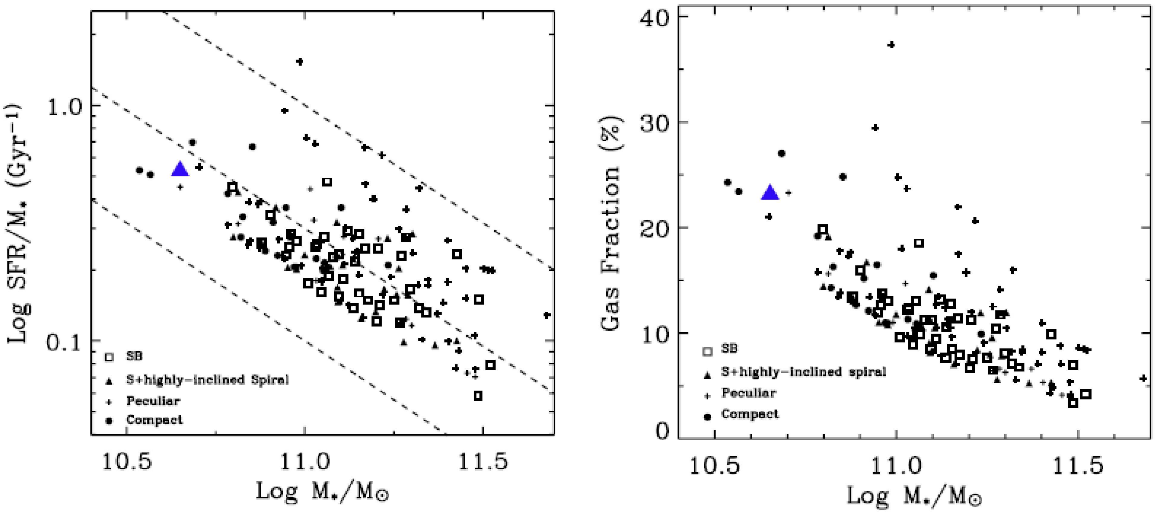

Figure 5.30: Left: Specific star formation rate vs. stellar mass for different morphological types of LIRGS (adapted from Wang et al. 2006). The three dashed lines (from bottom to top) denote a SFR of 10, 30 and 100 $M_\odot\,\mathrm{yr}^{-1}$. Right: Cold molecular mass fraction vs. stellar mass. HIZOA J0836-43 is shown as a blue triangle in both diagrams.

5.5 Global Analysis

5.5.1 Mid-Infrared Properties

As mentioned in Section 5.2.3, HIZOA J0836-43 appears to have a meagre amount of warm molecular hydrogen, $1.25 \times 10^7 M_\odot$ in its nuclear region. Combined with the exceptionally strong PAH and notably weak MIR continuum, this points to distinctly unusual properties compared to the overall starburst galaxy population. Rigopoulou et al. (2002) discuss an apparent relationship between the luminosities of the 7.7 μm PAH and H$_2$ $S(1)$ emission lines, since both types of emission are thought to originate in molecular clouds with star formation. We find $L_{7.7\mu\mathrm{m}} = 5.8 \times 10^{35}\,\mathrm{W}$ and $L_{\mathrm{H_2S(1)}} = 3.3 \times 10^{32}\,\mathrm{W}$. For the starbursts in the sample of Rigopoulou et al. (2002), $L_{7.7\mu\mathrm{m}}$ would imply a $L_{\mathrm{H_2S(1)}}$ value of $\sim 10^{36}\,\mathrm{W}$ which is a factor of ~ 3000 greater than the measured value.

The low amount of warm molecular hydrogen is unusual in the context of a starburst and suggests atypical interstellar medium conditions or heating mechanisms. In order to gain further insight, we plan to obtain CO observations to gauge the amount of cold molecular hydrogen directly.

We have shown in Section 5.2.4 that the PAH emission of HIZOA J0836-43 is strong, especially compared to the 24 μm luminosity. The study by Desai et al. (2007) finds that local ULIRGs with the highest 24 μm luminosities have the lowest 6.2 μm PAH EQWs. This suggests that an excess of hot dust causes a decreased PAH EQW, as opposed to destruction of PAHs due to hard radiation fields. A fit to the correlation seen in their sample is given by:

$$\log(6.2\mu\mathrm{m\,PAH\,EQW}[\mu\mathrm{m}]) = 7.71 - 0.723 \log\left(\nu \mathrm{L}_\nu(24\mu\mathrm{m})[\mathrm{L}_\odot]\right) \qquad (29)$$

We see a similar effect in HIZOA J0836-43, but with a low 24 μm luminosity and a large 6.2 μm PAH EQW. If we substitute the EQW found for the 6.2 μm PAH feature (0.722 μm as listed in Table 5.9), the correlation predicts $\nu L_\nu(24\mu m) = 7.23 \times 10^{10} L_\odot$. This is ~ 66 times larger than the observed value of $1.1 \times 10^9 L_\odot$. HIZOA J0836-43, therefore, does not fall on this correlation. This confirms our result from Section 5.2.4. We can conclude that the physics that results in the large 6.2 μm EQW and low 24 μm luminosity is distinct from the mechanisms that produce small 6.2 μm EQW and high 24 μm luminosities in ULIRGS.

HIZOA J0836-43 appears to have strong PAH emission, but weak continuum emission. This is quantified in Section 5.2.4 where the PAH luminosity overpredicts the total infrared luminosity of the galaxy by a factor of ~ 4. Conversely, we see in Section 5.2.1 that the continuum fluxes underestimate L_{TIR} for HIZOA J0836-43 by a factor of ~ 6.

The PAH strengths and continuum fluxes can be used to determine the dominant mechanisms producing MIR emission and their relative contributions. Armus et al. (2007) modified the diagnostic of Laurent et al. (2000) to determine the relative contributions of MIR emission sources in ULIRGS with AGN and starburst galaxies for comparison. By using the 15 to 5.5 μm continuum flux ratio (to separate starbursts and AGN) versus the 6.2 μm equivalent width to the 5.5 μm continuum (to determine quiescent star formation contribution), one can discern

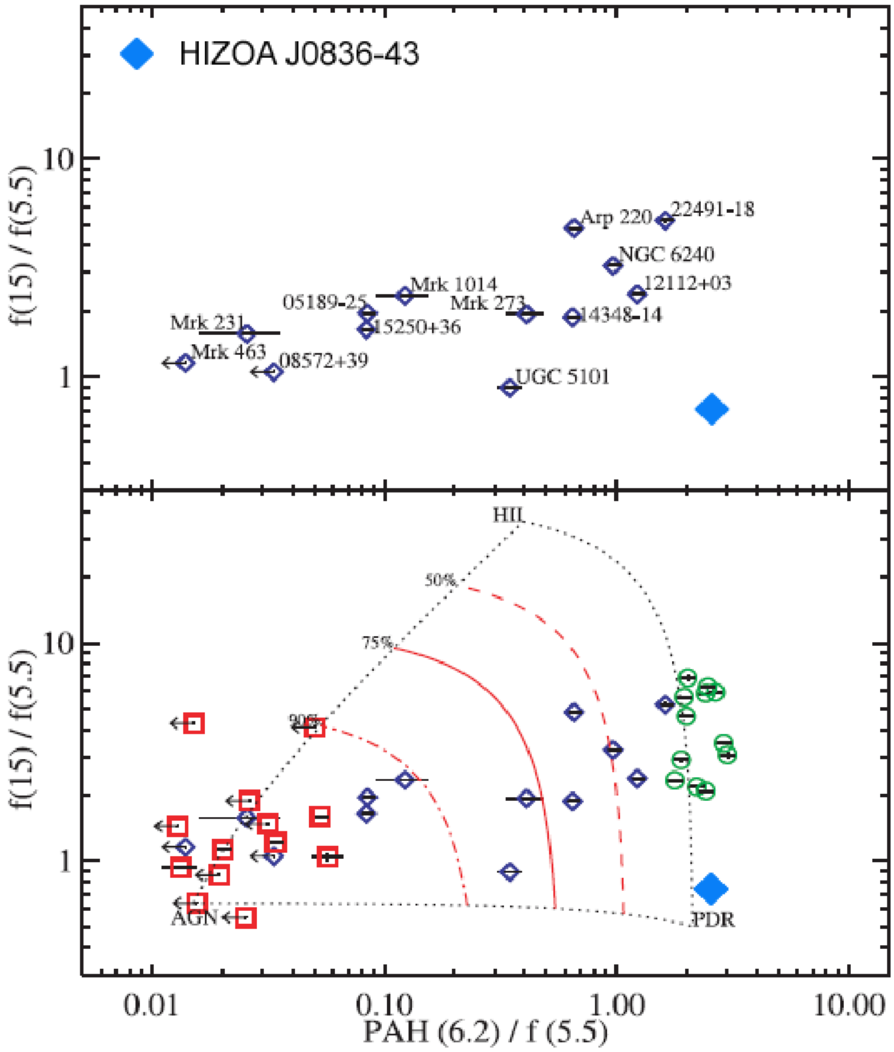

Figure 5.31: MIR diagnostic diagram from Armus et al. (2007) modified to include HIZOA J0836-43. ULIRGS from their study are shown as blue diamonds. AGN and starburst comparison galaxies are shown as red squares and green circles respectively. The three vertices represent prototypical AGN, H II and PDR emission respectively. The dashed lines show the fractional AGN contribution to the MIR emission.

between AGN, H II and PDR dominated emission.

Figure 5.31 shows the diagram from Armus et al. (2007). We see that the galaxy's MIR emission must be strongly dominated by emission arising from PDRs to the extent that emission from Active Galactic Nuclei (AGN) and H II regions is insignificant. We note that the PDR emission corresponds to the location of the reflection nebula NGC 7023 (Peeters et al. 2004).

In Fig. 5.32 we consider a similar diagnostic diagram from Peeters et al. (2004). We see that the strength of the PAH emission in HIZOA J0836-43, both in luminosity and relative strength of the bands compared to the continuum, is amongst the largest observed in any star-forming

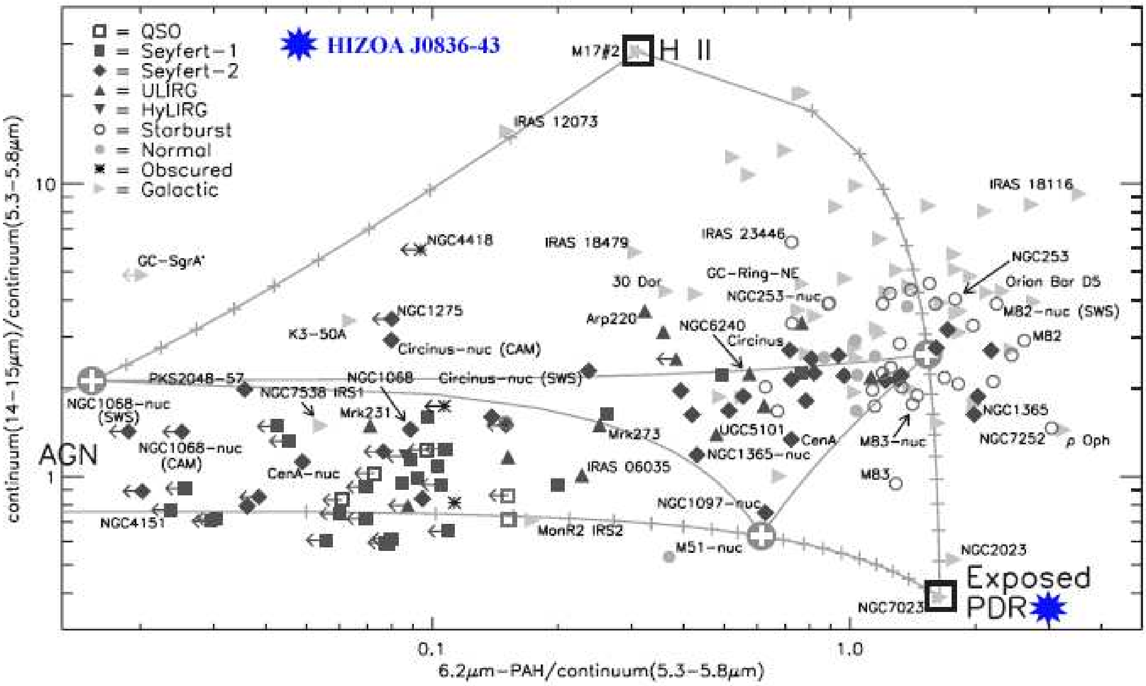

Figure 5.32: MIR diagnostic diagram modified from Peeters et al. (2004) showing the locations of different MIR emission systems. We show the location of HIZOA J0836-43 as a blue star.

galaxy, implying unusually strong PDR emission. It appears similar to NGC 7023 and NGC 2023 (both reflection nebulae within the Milky Way), but with stronger 6.2 μm PAH emission. Both are considered prototypical of PDR emission, arising from B stars producing a small region of ionised gas and illuminating a shell of molecular gas (Wyrowski et al. 2000; Fuente et al. 2000).

The location of HIZOA J0836-43 in these diagrams is unlike that of any extragalactic object, and poses a real challenge to explain its origin.

HIZOA J0836-43 appears to have dust emission characteristics similar to that of NGC 7023, a reflection nebula. To explore this similarity further, we plot in Fig. 5.33 the low resolution (SL/LL) spectrum of NGC 7023 scaled to match HIZOA J0836-43.

As we would expect, the composition of the two regions is quite different with HIZOA J0836-43 showing strong emission from ionic species. However, the PAH emission of NGC 7023 is remarkably similar to that of HIZOA J0836-43, further confirming our hypothesis of PDR dominated emission. The most noticeable difference between these two systems is that for $\lambda > 20\,\mu$m, NGC 7023 has a steeply rising continuum indicating far more warm dust emission compared to HIZOA J0836-43. This arises from the H II region within the reflection nebula. It is apparent that the PAH emission from HIZOA J0836-43 closely resembles that of a reflection nebula such as NGC 7023. However, the dust grain composition and environment in HIZOA J0836-43 is clearly different, seen most notably in the weak dust continuum of the galaxy.

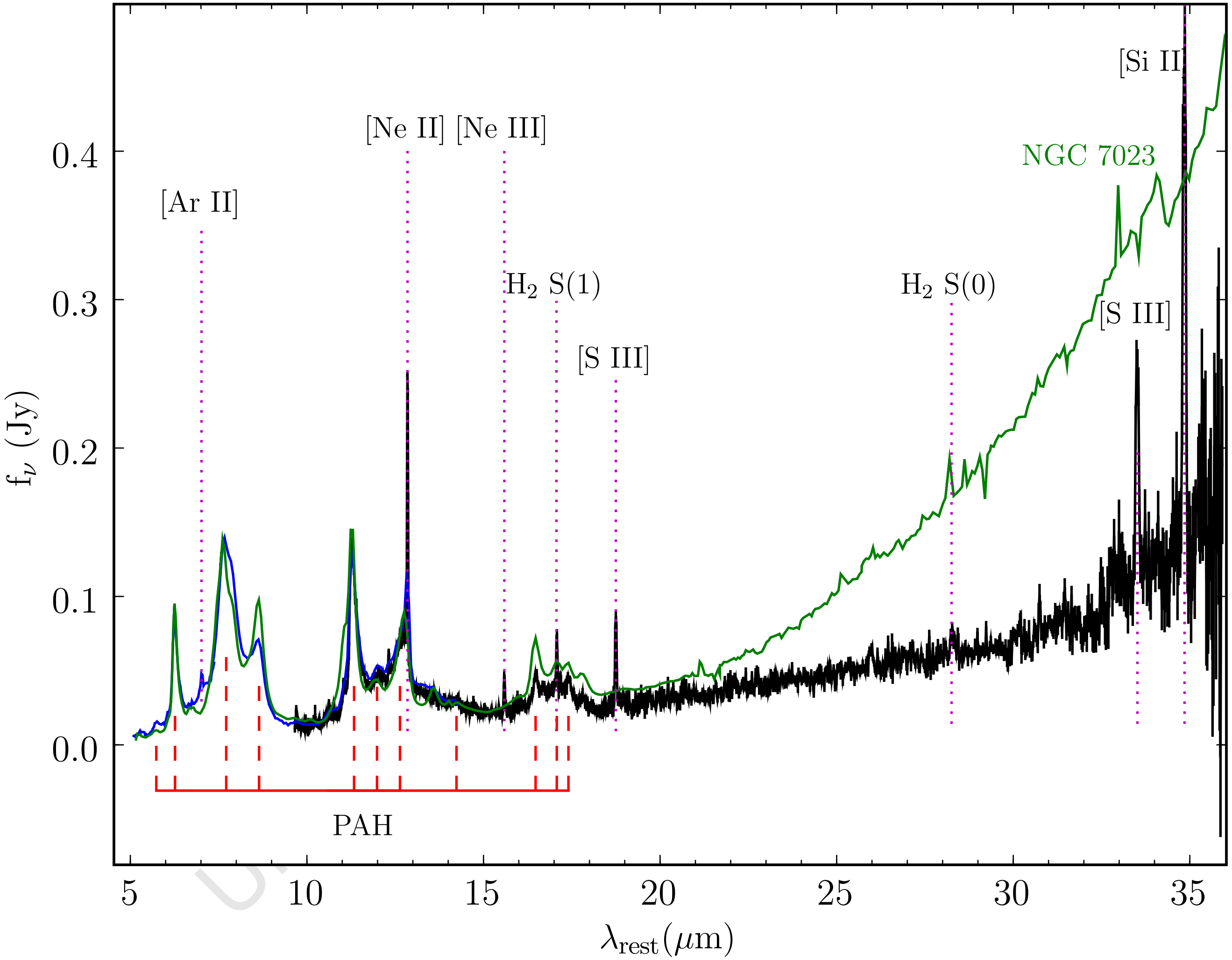

Figure 5.33: The spectrum of HIZOA J0836-43 in comparison to NGC 7023 (green) for $\lambda < 30\,\mu$m. The low resolution *Spitzer* spectrum of NGC 7023 has been scaled to match HIZOA J0836-43 at $10\,\mu$m.

The broadband photometry of HIZOA J0836-43, with an excess of 8 μm and 70 μm emission relative to 24 μm and 160 μm, is consistent with the strong PAH emission bands and weakly rising continuum seen in the galaxy's spectrum. The spectroscopy and photometry independently indicate this characteristic of HIZOA J0836-43.

5.5.2 PDR emission in HIZOA J0836-43

HIZOA J0836-43's PDR-dominated emission manifested as strong PAH emission coupled with a weak MIR continuum, makes it unusual in the local universe. These properties may arise from (1) a paucity of very small grains (VSGs) and/or (2) a soft UV radiation field. Powered by massive star formation, transiently heated VSGs are thought to be the source of MIR radiation. A weaker radiation field would give rise to cooler VSGs (Draine & Li 2007), which would re-radiate at longer FIR wavelengths along with the large grain, cool ($T \sim 20$ K) component. Both mechanisms would be consistent with an evolutionary phase in which the activity is confined to heavily gas/dust-obscured star forming regions, thus shielding the hard UV radiation from the rest of the disk, which in turn would yet to have experienced significant grain processing. The geometry of star formation and distribution of hot dust, cold dust and gas would play a crucial role in such a system. In particular, UV radiation from lower mass (B and A) stars in combination with a cold gas reservoir would be conducive to prolific PDR emission due to lower intensity heating of molecular clouds. What is surprising is that this scenario is not seen in any other active star forming galaxy, but seems to be unique to HIZOA J0836-43, perhaps due to its rare, gigantic atomic hydrogen reservoir.

5.5.3 Inside-out Disk Growth

The images of HIZOA J0836-43 shown in Section 5.1.1 hinted at large amounts of star formation with its emission originating from hot dust and PAH's. We noted an asymmetry in the mid-infrared disk, also suggested by the H I- and 20 cm contours shown in Fig. 5.2. The strength of the PAH emission has been quantitatively discussed in Section 5.2.4. We now consider the distribution of this emission as an observational trace of regions of star formation.

In Fig. 5.34 we show a composite of spectral maps for the 6.6 μm (blue), 7.7 μm (green) and 11.3 μm (red) PAH emission bands (tracing active star formation), overlaid with [Ne II] 12.8 μm contours (tracing H II emission). This clearly demonstrates the exponential distribution of PAH emission from the nucleus outwards, and the spiral arm warp on the East side of the major axis. Quantitatively the plot shows the surface brightness profile of the 11.3 μm PAH map and IRAC 4.5 μm band (tracing stellar light). We see that the PAH emission is slightly more extended compared to the bulge-dominated stellar light.

The growth progress of HIZOA J0836-43 was discussed in Section 5.4. We saw that HIZOA J0836-43 has a high specific SFR (~ 0.5 Gyr^{-1}) compared to local LIRGS in the sample of Wang et al. (2006) which have a median value of ~ 0.2 Gyr^{-1}. The galaxy is actively forming stars, but its location implies a relatively early stage of stellar building. We now compare this SSFR

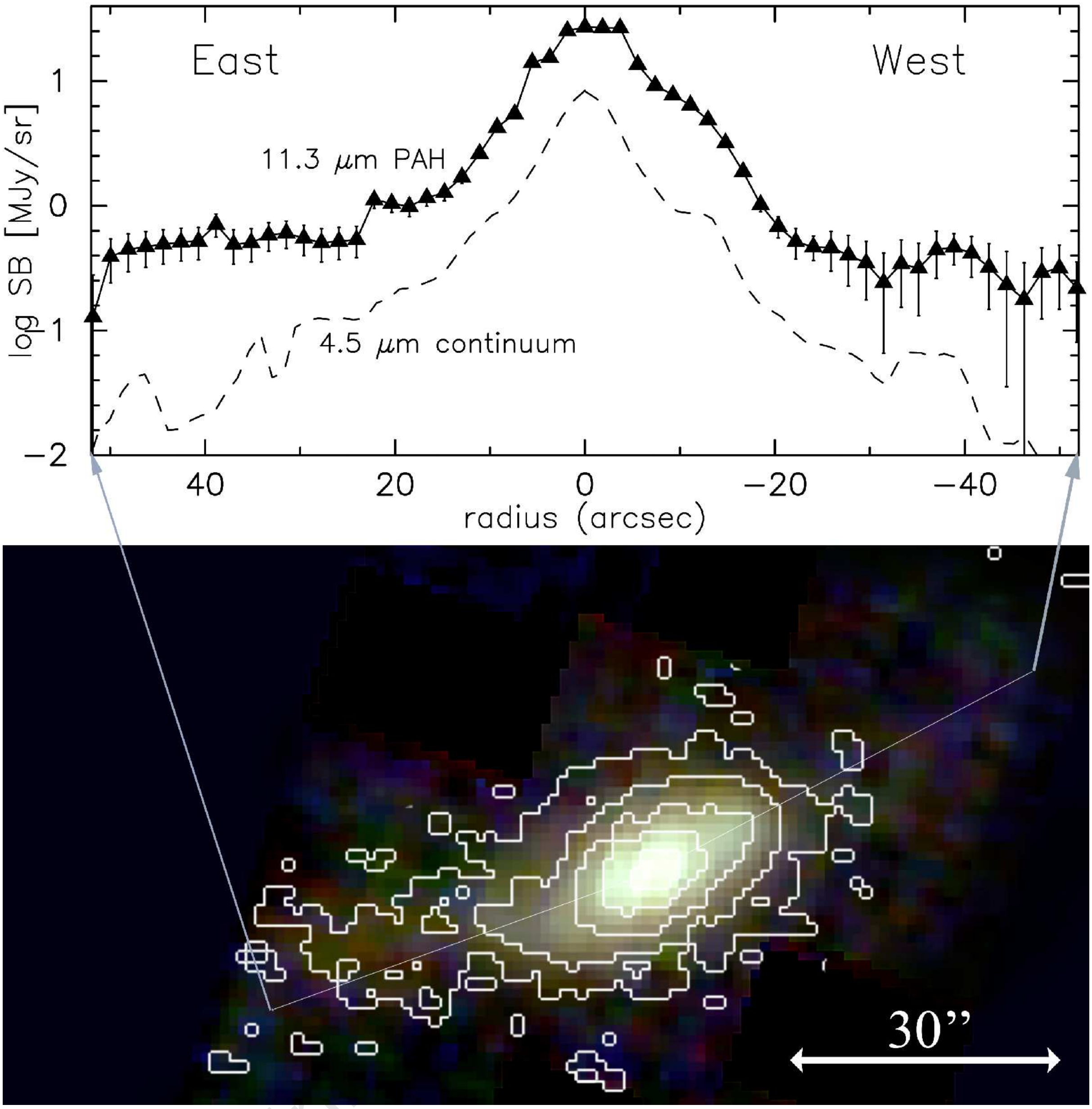

Figure 5.34: Composite of spectral maps for the 6.6 μm (blue), 7.7 μm (green) and 11.3 μm (red) PAH emission bands, overlaid with [Ne II] 12.8μm contours; the plot shows the 11.3 μm PAH and IRAC 4.5μm surface brightness across the East-West major axis, demonstrating the East warp and disk extended PAH emission relative to the bulge-dominated stellar light. From Cluver et al. (2008).

to star-forming galaxies at different redshifts.

In Fig. 5.35 we see SSFR for $z \sim 0.7$ (from a sample of $\sim$ 1500 galaxies) and local galaxies plotted vs. stellar mass from Bell et al. (2005). They find that more than half of the intensely star-forming galaxies are spirals, with less than $\sim$ 30% being strongly interacting. They conclude

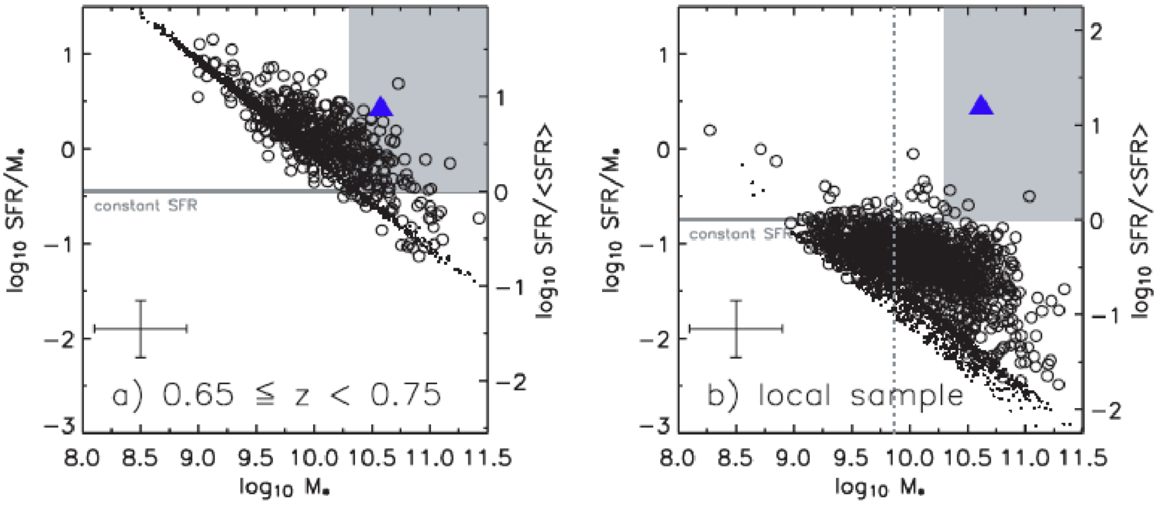

Figure 5.35: Specific star fomation rates for $z \sim 0.7$ (left panel) and local galaxies (right panel) vs. stellar mass modified from Bell et al. (2005). The gray box shows intermediate- and high-mass galaxies with ongoing bursts of significant star formation. HIZOA J0836-43 is shown as a blue triangle.

that the rapid demise of intermediate and high-mass star-forming galaxies between $z \sim 0.7$ and the present day is not directly caused by a decline in major merging events, but due to physical processes such as gas consumption and weak tidal interactions with small satellite galaxies.

The specific star formation rate of HIZOA J0836-43 in combination with its stellar mass is more consistent with star-forming galaxies at $z \sim 0.7$ (Fig. 5.35), where gas fractions of disks were likely higher compared to local galaxies (Bell et al. 2005; Pérez-González et al. 2005). This agrees with Fig. 5.13, which shows that the MIR luminosity is strongly correlated with H I content. Even with its extreme H I mass, HIZOA J0836-43 appears consistent with being a "scaled-up" disk galaxy (as suggested by Donley et al. 2006), unlike Malin 1 which is explicitly quiescent by comparison. Despite lying at the extreme high end (i.e., early evolutionary stage) of the relation, this suggests relatively "normal" evolution in HIZOA J0836-43.

HIZOA J0836-43 is a gas-rich spiral galaxy exhibiting a warp in its disk (Fig. 5.2), likely the result of a disturbance in its recent past ($\ll 1$ Gyr). Such an event could cause the observed starburst as gas from the extended H I disk loses angular moment and flows into the central region of the galaxy, possibly facilitated by a large-scale dynamical bar. That is to say, the starburst is powered by gas consumption, as opposed to a major merger event. Gas-rich galaxies, like HIZOA J0836-43, were likely more common in the distant universe and there is evidence that gas consumption and not merger interactions were driving stellar mass growth in the distant universe (Daddi et al. 2008). Recent work has suggested that many LIRGs seen at intermediate redshifts ($z \sim 0.8$) achieve heightened star formation as a result of the high gas fractions of their disks and were less dependent on major interactions, compared to local LIRGs, to induce starburst activity (Melbourne et al. 2008; Marcillac et al. 2006).

Observational evidence suggests that disk galaxies evolve along the stellar mass-radius relation and have built stellar mass intensely since $z = 1$, on average by means of inside-out growth (Barden et al. 2005; Trujillo et al. 2006). Comparing the extended regions of active star formation with the more centrally concentrated stellar bulge distribution (see Fig 5.34 radial profile) suggests that HIZOA J0836-43 is undergoing vigorous disk building, an instance of inside-out growth.

This combined with its PDR-dominated emission manifested as strong PAH emission coupled with a weak MIR continuum, makes it enigmatic in the local universe. Observing a galaxy at such a key point in its evolution could have far reaching implications for theories of galaxy formation and evolution.

Chapter 6

The Infrared Survey Around HIZOAJ0836-43

The mechanisms of galaxy formation remain poorly understood (Cole et al. 2000), particularly in relation to massive H I disks in a hierarchical structure formalism (Hoffman et al. 1992; Knezek 1993). Owing to its relatively close proximity, HIZOA provides a unique opportunity to study both its local environment in detail, and its place in the larger cosmic web. The direct aim of the work presented in this chapter is to obtain a census of galaxies in the neighbourhood of HIZOA J0836-43 and to compare this local distribution with the larger region as provided by the 2MASS Extended Source Catalogue (Skrutskie et al. 2006). The distribution of galaxies on a small and large scale may provide clues regarding the formation and survival of this galaxy. The galaxy being part of a group of galaxies could have facilitated the accretion of gas through merging; a lower density environment would be preferable to keep the reservoir of gas undisturbed.

This study is, however, complicated by foreground dust obscuration and stellar crowding. The near-infrared is less affected by extinction and is a powerful means of probing the Zone of Avoidance (Kraan-Korteweg & Lahav 2000; Jarrett et al. 2000), provided the stellar density is not extreme (Kraan-Korteweg & Jarrett 2005). Since the near-infrared is sensitive to early-type galaxies, it tracks groups and clusters and thus regions of mass.

In this Section we present the results of the *Spitzer* and IRSF surveys of the region around HIZOA J0836-43 (Section 2) and compare its distribution with the 2MASS XSC (Extended Source Catalogue). This study will enable candidates to be chosen for follow-up spectroscopy in an effort to explore the environment of HIZOA J0836-43 more rigorously.

6.1 Locating Galaxies in the Zone of Avoidance

In the Zone of Avoidance (ZoA), automated galaxy identification algorithms are hampered by star crowding and extinction. Blended stars often appear as extended sources and extincted galaxies are increasingly missed due to reduced surface brightness. Searching images by eye remains the most effective way to find galaxy candidates.

The J, H and K_s bands of the 169 fields imaged (see Section 2 for details) were combined to form three-colour (J=blue, H=green, K_s=red) composite images[1]. These were searched by eye for yellow/reddish extended sources discernable from the typical FWHM of point sources ($\sim 1.3''$ in K_s). This method has been used effectively in the near-infrared ZoA by, for example, Nagayama et al. (2004) and Nagayama et al. (2006). A total of 529 galaxies and candidates were found in the entire 2.24 deg^2 area surveyed. Of these 21 were later deemed to be stars (blended and isolated false candidates) and were removed from the catalogue, leaving 508 galaxies and candidates. In this same area, the 2MASS XSC has 44 sources. We find that 28 are unreliable detections (discussed in Section 6.6.4).

6.2 The IRSF Survey around HIZOA J0836-43

In order to ensure the reliability and repeatability of the photometric and astrometric measurements of the 508 galaxy candidates in this survey, we use the NIR measurements to determine the photometric quality of sources. Galaxy candidates with J, H and K_s measurement errors of > 0.33 mag (S/N < 3) in each band are deemed photometrically unreliable for analysis purposes and rejected; these sources and measurements are listed in the Rejected Sources Section in Appendix B.3. We have rejected 104 sources based on this, approximately 20% of the sample.

The on-sky distribution of the remaining 404 galaxies, comprising the Infrared Catalogue (see Section 6.5 below), is shown in Fig. 6.1, centred on $l = 262.48°$ and $b = -1.64°$, the location of HIZOA J0836-43. We show extinction contours in A_V and NED and 2MASS XSC detections. Due to the extinction levels in this area, the distribution and number of galaxies in this region was poorly sampled. As shown in Fig. 6.1, this survey has created a more complete map of the area.

We show the distribution of J, H and K_s magnitudes in Fig. 6.2. These magnitudes have not been corrected for foreground extinction. In Fig. 6.3 we plot the NIR mean surface brightness of the sample (no extinction correction applied). The mean values are 21.40 ± 0.60 mag arcsec^2 in the J band, 20.03 ± 0.59 mag arcsec^2 in the H band and 19.12 ± 0.62 mag arcsec^2 in the K_s band. The surface brightness distribution shows a large number of faint sources and very few high surface brightness objects.

The galaxy catalogue is summarized in Section 6.5, with the catalogue itself in Appendix B. Here we list the photometric parameters (position, radius, position angle etc.), measured fluxes, extinction-corrected magnitudes and photometric redshifts of the sources. Detailed characterization and analysis of the photometric and spatial distribution properties are presented in the sections to follow.

---

[1] These can be viewed at http://www.ast.uct.ac.za/∼michelle/HIZOAgridnone.html

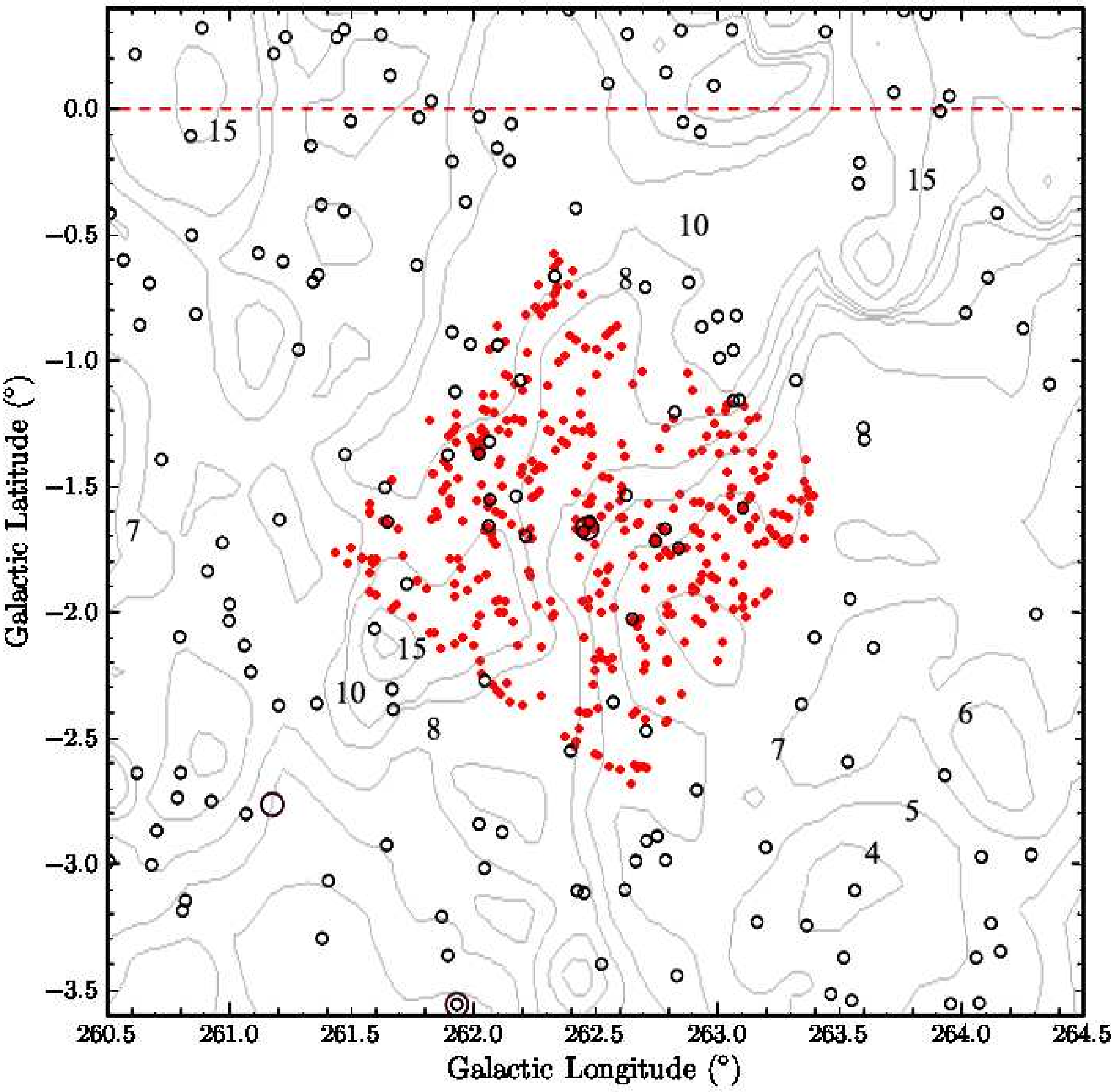

Figure 6.1: On-sky distribution of sources from this survey shown in relation to the Galactic Plane (red dashed line), HIZOA J0836-43 is at the centre. Large black circles are NED sources and small black circles are from the 2MASS XSC. Extinction contours (from Schlegel et al. 1998) are shown in grey (contours are in units of $A_{\rm V}$ mag as follows: 4, 5, 6, 7, 8, 10, 12.5, 15).

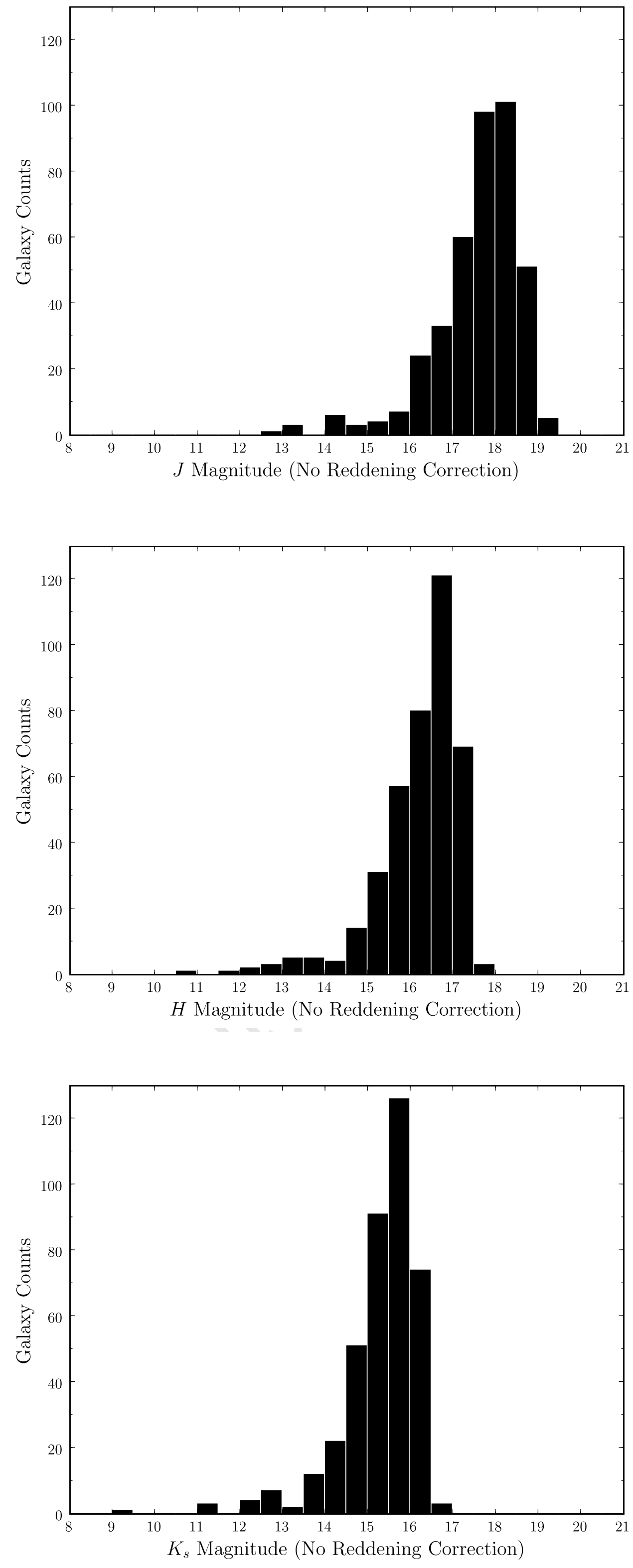

Figure 6.2: Magnitude bins for the J, H and K_s bands showing raw magnitudes without reddening corrections.

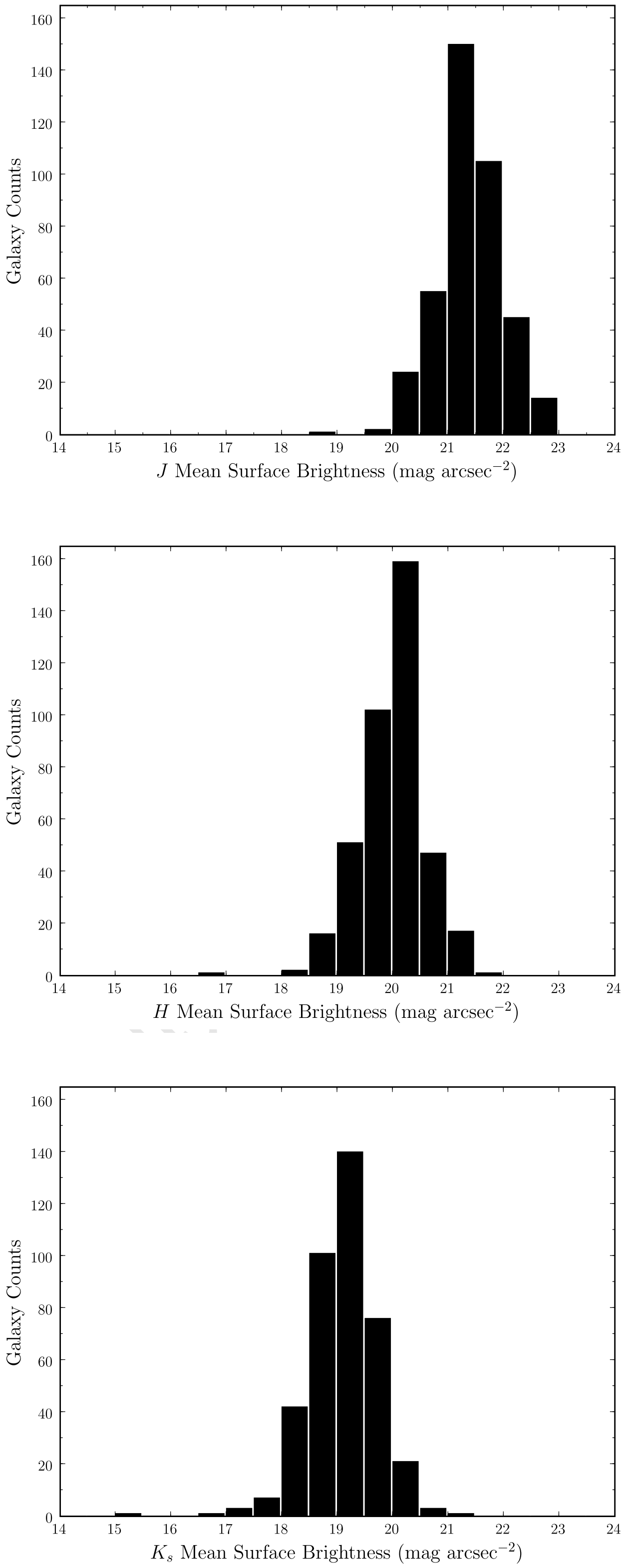

Figure 6.3: Mean Surface Brightness bins for the J, H and K_s bands. No reddening correction has been applied.

6.3 The Spitzer Survey of the HIZOA J0836-43 Region

The *Spitzer Space Telescope* IRAC camera was used to image an area of $\sim 23' \times 28'$ around HIZOA J0836-43 (forming a sub-region of the $1.6° \times 1.6°$ IRSF survey area). In addition, a similar overlapping region was observed using the MIPS detector. In Fig. 6.4 we show a combined 5-colour image of the *Spitzer* footprint made using all four IRAC bands and the MIPS-24 μm image.

As discussed in Section 2, galaxy candidates in this *Spitzer* survey region were identified on JHK_s composite images obtained from the IRSF. Excluding HIZOA J0836-43, a total of 64 near-infrared candidates were located in the *Spitzer* footprint. All sources were found to have corresponding detections in the IRAC bands. Inspection of the MIR images did not reveal any additional candidates.

Photometry of candidates in this region was performed using a matched elliptical aperture for the NIR, IRAC and MIPS 24 μm bands. This aperture was determined using the IRAC-3.6 μm band, but in the instances where no IRAC-3.6 μm counterpart was available (due to offsets between the arrays), the IRAC-4.5 μm band was used.

Due to the larger beam of the IRAC bands, compared to the near-infrared, galaxy candidates in close proximity to neighbouring stars could have contaminating flux from the star. Four such candidates only have J,H and K_s measurements and will be included in the larger IRSF survey described in Section 2.5.2; their designations are 08354713-4328169, 08370946-4319383, 08364646-4319369 and 08372709-4343023 (in Table B.6).

Photometric parameters for the 56 remaining sources are given in Table B.1 with MIR fluxes and magnitudes given in Table B.2 and J, H and K_s measurements in Table B.3.

6.3.1 Neighbours of HIZOA J0836-43

The immediate environment of HIZOA J0836-43 clearly reveals two galaxies (seen in Fig. 6.5), already identified by Donley et al. (2006) as 2MASX J08363600-4337556 (west of HIZOA J0836-43) and 2MASX J08370723-4339137 (south-east). Using the NIR effective surface brightnesses, they found 2MASX J08363600-4337556 to have an early-type morphology corresponding to an E/S0/Sa and 2MASX J08370723-4339137 to be a spiral galaxy between Sab and Sc type. This galaxy was also detected in radio continuum observations by Donley et al. (2006).

The two galaxies are identified as 08363597-4337554 ($l = 262.45°$, $b = -1.68°$) and 08370727-4339136 ($l = 262.53°$, $b = -1.62°$) in our catalogue (see Table B.1), corresponding to 2MASX J08363600-4337556 and 2MASX J08370723-4339137 respectively. We shall refer to 2MASX J08363600-4337556 as Companion A and 2MASX J08370723-4339137 as Companion B. Figure 6.6 displays NIR and MIR close-ups of the two neighbouring galaxies.

The flux measurements for Companion A are listed in Table 6.1. The Schlegel et al. (1998) extinction for this galaxy is $A_{\rm V} = 6.3$ mag. We do not have a redshift for this galaxy, but we can use the template spectra of Section 3.5 to refine the extinction of the galaxy using a crude redshift. Using $cz = 10,000\,\mathrm{km\,s^{-1}}$ gives a reasonable fit to the template spectra. Varying the

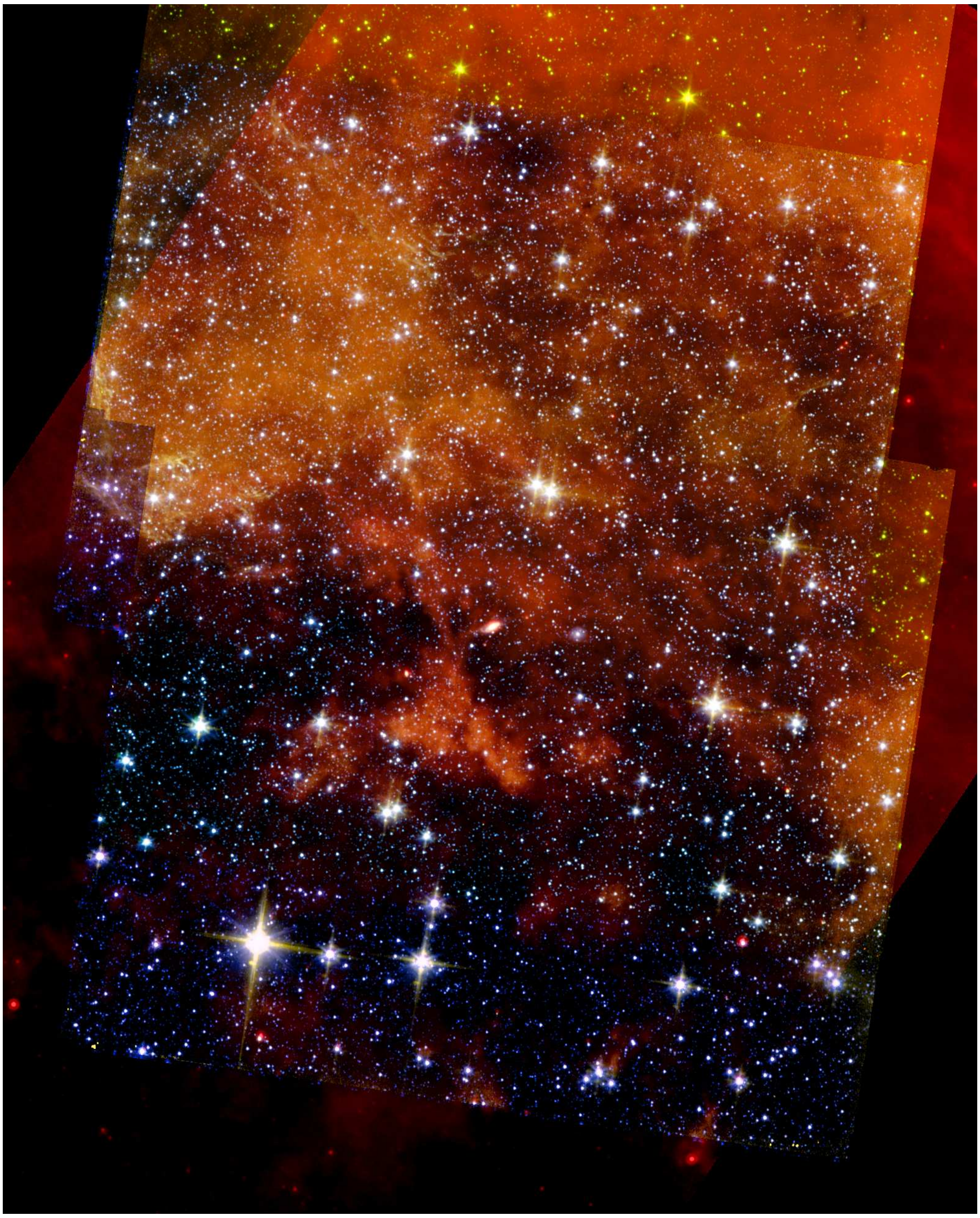

Figure 6.4: A five colour composite of the *Spitzer* Footprint centred on HIZOA J0836-43, made using all four IRAC bands and the MIPS-24 μm image. The area shown is $\sim 25' \times 30'$, with north up and east to the left.

extinction, we find a good fit for $A_{\rm V} \sim 6.0$ mag between the galaxy SED and the GRASIL templates, as shown in Fig. 6.7. The advantage of using the SED to determine the extinction is that we mitigate the effect of Galactic and internal extinction. The extinction-corrected flux densities and magnitudes are also listed in Table 6.1.

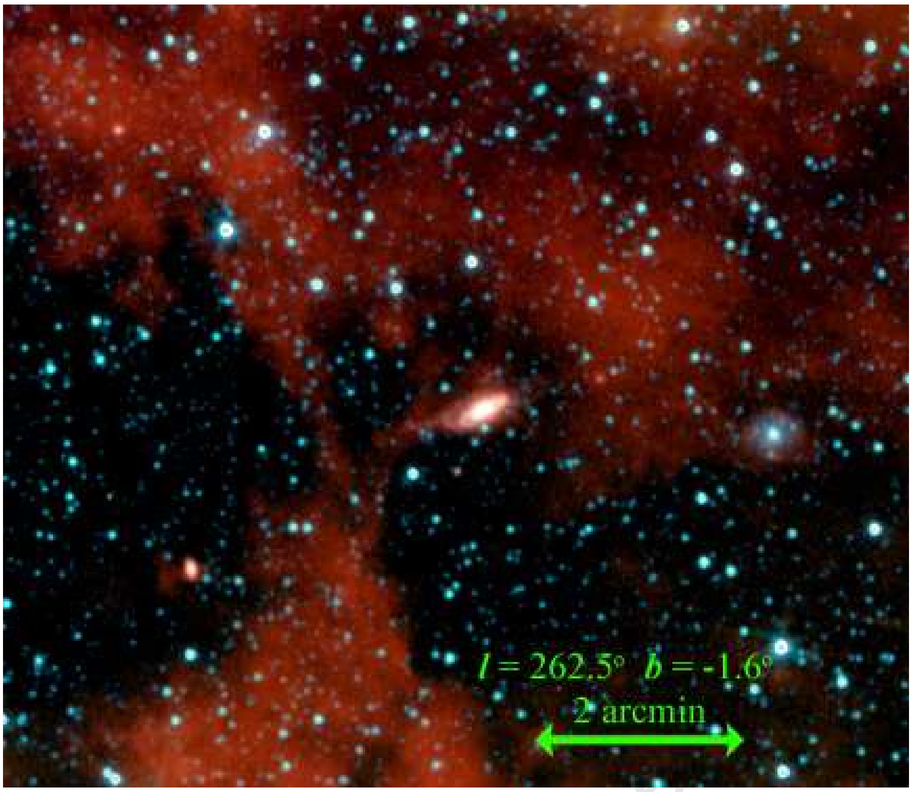

Figure 6.5: Composite IRAC image using all four bands (with the 3.6 μm stellar emission subtracted from each band – see Section 3.6). The image shows Companion A ($\sim 3'$ west of HIZOA J0836-43) and Companion B ($\sim 3'$ south-east of HIZOA J0836-43). North is up, east to the left.

From Fig. 6.7 we see that the SED of Companion A matches the GRASIL template for an S0 galaxy consistent with its appearance in the near-infrared. However, the galaxy shows the signature emission of PAHs, suggestive of star formation.

The flux densities of the late-type galaxy, Companion B, are given in Table 6.2 and its Schlegel et al. (1998) extinction is $A_{\rm V} = 7.3$ mag. We attempt to refine the extinction as we did for Companion A above. Using a crude redshift of $cz = 10,000\,{\rm km\,s^{-1}}$ we find a reasonable fit to the template spectra for an extinction of $A_{\rm V} \sim 6.0$ mag as shown in Fig. 6.8. This extinction corresponds to a combination of foreground and internal extinction. The galaxy SED corresponds to an Sc galaxy with PAHs, indicative of current star formation.

We note that since we do not have redshifts for these sources, there is an error associated with the extinction determined (~ 0.4 mag in $A_{\rm V}$). However, the Schlegel et al. (1998) extinction maps only have a resolution of $\sim 6'$. In Fig. 6.5 we can see the distribution of dust in the region around the companions varies a great deal. The poor spatial resolution of Schlegel et al. (1998) would not reflect these small-scale variations. Since we have accurate photometry of these bright sources, we believe the SED determined values to be more reliable, even with the uncertainty associated with the fit. It also incorporates internal extinction. We therefore adopt

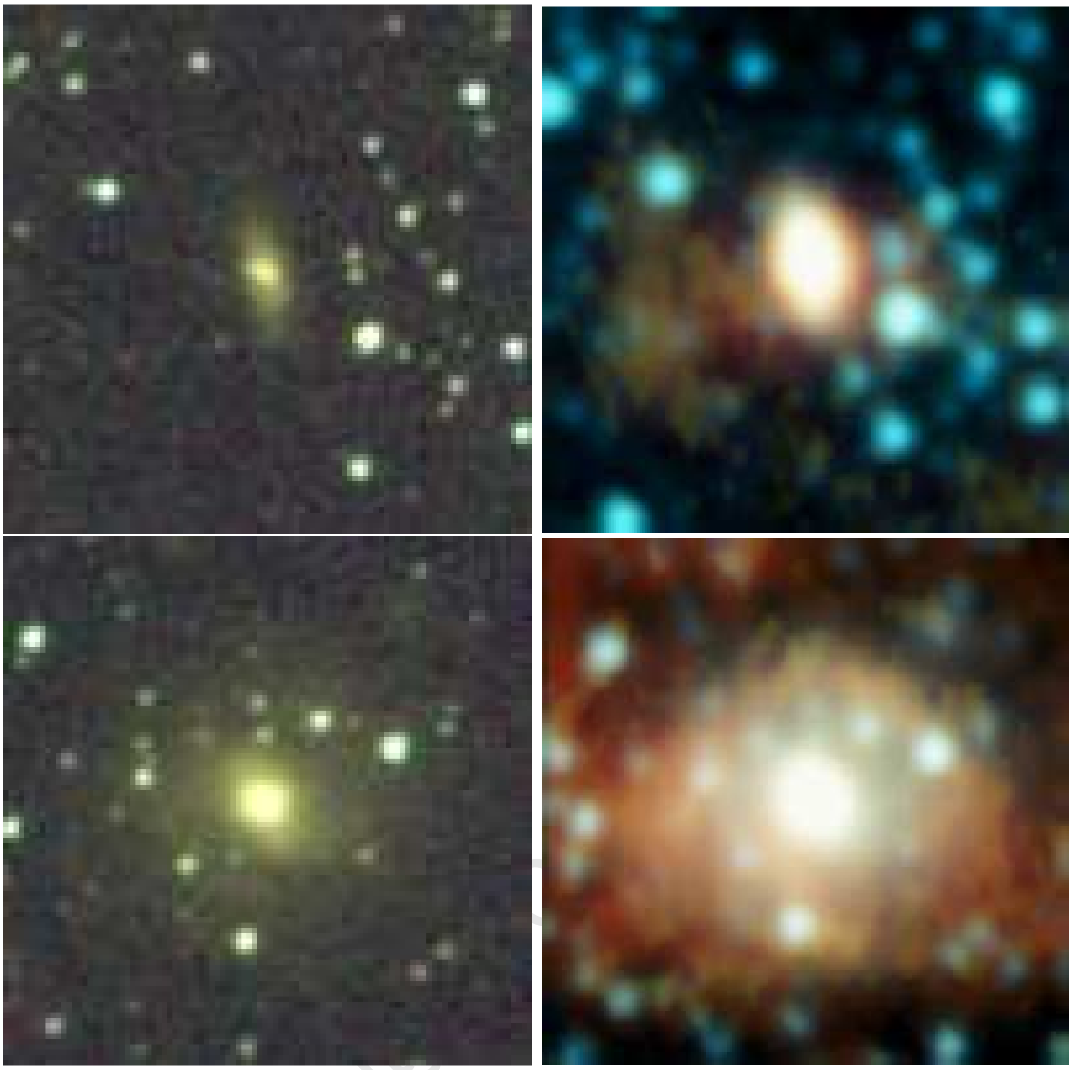

Figure 6.6: Near-infrared (JHK_s) and mid-infrared (IRAC+MIPS with the stellar contribution removed) close-up images of Companion A (top) and Companion B (bottom). The images are $45'' \times 45''$. We note the poorer resolution in the MIR (IRAC pixel size is $1.2''$) compared to the NIR (IRSF pixel size is $0.45''$).

an extinction of $A_{\rm V} = 6.0$ mag for Companion A and B, corresponding to 95% and 82% of the Schlegel et al. (1998) value, respectively. We note that in Section 6.8.1 we find photometric redshifts of $z = 0.033$ and $z = 0.039$ for Companion A and B, respectively, which are not too disimilar to the $z = 0.03$ redshift used for fitting the SED.

Preliminary photometric results of these two neighbours suggests that they are relatively close to HIZOA J0836-43, which implies that they are considerably smaller in size compared to the galaxy. At the distance of HIZOA J0836-43, they would lie $\sim$ 140 kpc from HIZOA J0836-43, or roughly 3 times the distance of the Large Magellanic Cloud to the Milky Way. Hence, we cannot rule out possible past interactions of HIZOA J0836-43 with either satellite galaxy.

Table 6.1: Flux densities of 2MASX J08363600-4337556 (Companion A).

Band	Flux Density [a] (mJy)	Flux Density [b] (mJy)	Magnitude [c] (mag)	Magnitude [d] (mag)
J	7.74 ±0.13		13.29 ±0.05	11.65 ±0.05
H	15.25 ±0.31		12.07 ±0.05	11.01 ±0.05
K_s	17.53 ±0.38		11.45 ±0.06	10.77 ±0.06
IRAC-1	14.61 ±0.37	13.81 ±0.35	10.77 ±0.06	10.46 ±0.06
IRAC-2	9.72 ±0.25	9.52 ±0.24	10.69 ±0.06	10.47 ±0.06
IRAC-3	8.78 ±0.27	7.76 ±0.24	10.43 ±0.06	10.21 ±0.06
IRAC-4	10.47 ±0.46	8.64 ±0.38	9.68 ±0.07	9.46 ±0.07
MIPS-24	8.75 ±0.44	9.81 ±0.49	7.16 ±0.11	7.16 ±0.11

Aperture parameters for NIR, IRAC and MIPS-1: $a = 23.59'', b/a = 0.88, \phi = 83.6°$

[a] Flux Density - no aperture correction

[b] Flux Density - aperture-corrected

[c] Integrated Magnitude - no reddening corrections applied

[d] Integrated Magnitude - corrected for extinction ($A_{\rm V}$ = 6.0 mag)

Table 6.2: Flux densities of 2MASX J08370723-4339137 (Companion B).

Band	Flux Density [a] (mJy)	Flux Density [b] (mJy)	Magnitude [c] (mag)	Magnitude [d] (mag)
J	1.16 ±0.04		15.34 ±0.06	13.71 ±0.06
H	2.29 ±0.06		14.12 ±0.06	13.06 ±0.06
K_s	2.62 ±0.10		13.51 ±0.07	12.83 ±0.07
IRAC-1	2.35 ±0.06	2.32 ±0.06	12.71 ±0.06	12.39 ±0.06
IRAC-2	1.71 ±0.04	1.76 ±0.05	12.52 ±0.06	12.31 ±0.06
IRAC-3	4.17 ±0.13	4.00 ±0.13	11.15 ±0.06	10.93 ± 0.06
IRAC-4	13.86 ±0.49	12.49 ±0.44	9.28 ±0.06	9.06 ±0.06
MIPS-24	16.62 ±0.48	21.91 ±0.64	6.29 ±0.10	6.29 ±0.10

Aperture parameters for NIR, IRAC and MIPS-1: $a = 11.93'', b/a = 0.70, \phi = 10.0°$

[a] Flux Density - no aperture correction

[b] Flux Density - aperture-corrected

[c] Integrated Magnitude - no reddening corrections applied

[d] Integrated Magnitude - corrected for extinction ($A_{\rm V}$ = 6.0 mag)

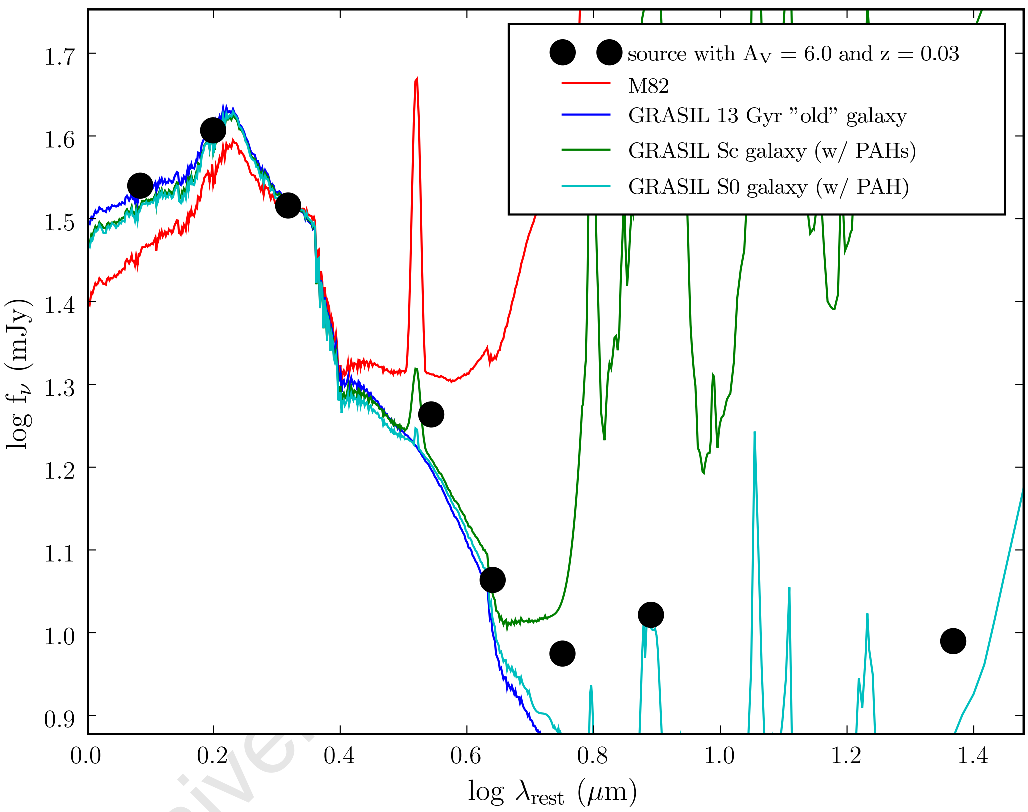

Figure 6.7: SED of 2MASX J08363600-4337556 (Companion A).

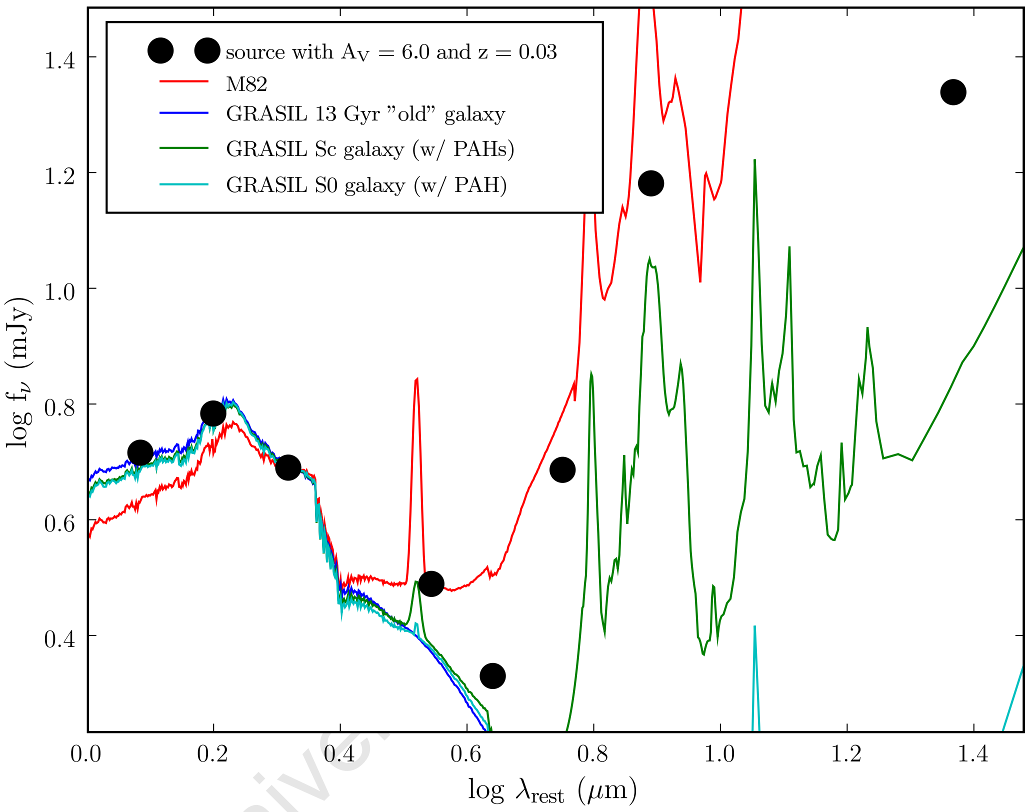

Figure 6.8: SED of 2MASX J08370723-4339137 (Companion B).

6.4 Extinction in the Zone of Avoidance

Based on the NIR+MIR SED of HIZOA J0836-43, we are able to accurately deduce the amount of foreground extinction toward the galaxy. For its two companions we have used the same method to estimate the extinction. However, in the absence of reliable redshifts for SED fitting for the rest of sources detected in the IRSF and *Spitzer* surveys, we resort to using extinction based on the dust column density as measured by DIRBE/IRAS.

The effect of Galactic reddening in the region of $l = 262.5°$ and $b = -1.6°$ is an important consideration. The Schlegel et al. (1998) maps indicate that the extinction ranges from $A_{\rm V} \sim$ 4.4 mag to 12.3 mag. We adopt the extinction laws of Cardelli et al. (1989) as outlined in Section 3.5. This range corresponds to $\sim$ 0.4 to 1.2 mag in the K_s band.

However, the Schlegel et al. (1998) extinction maps determined from DIRBE/IRAS are uncalibrated at low Galactic latitudes ($|b| < 5°$) and are believed to overestimate the extinction in high extinction areas (Dutra et al. 2002). Several studies at high extinctions have attempted to obtain a quantitative measure of this overestimation.

Using NIR counterparts of galaxies with H I detections in the southern ZoA, Schröder et al. (2005) find that the DIRBE extinction maps overestimate the true extinction by $17 \pm 3\%$. Using the colour excess of giant stars around in the region of PKS 1343-601, Nagayama et al. (2004) find an extinction of $A_V = 0.67\ A_V^{\rm Schlegel\,98}$. In the same region, Schröder et al. (2007) use the NIR colours of nearby galaxies to determine an extinction value of $A_V = 0.87 \pm 0.04 A_{\rm V}^{\rm Schlegel\,98}$. Tagg (2008) surveyed seven regions in the vicinity of the Great Attractor, covering a total area of $\sim$ 2.5 deg^2. Estimating the extinction from the NIR colours of galaxies gave a value of $A_V = 0.75 \pm 0.12 A_{\rm V}^{\rm Schlegel98}$.

In Section 3.5, we used the known redshift and SED of HIZOA J0836-43 to determine its extinction. We find a foreground extinction of $A_V = 6.4$ mag compared to the Schlegel et al. (1998) value of 7.6 mag, corresponding to 84%. Using this in combination with the results from other studies, we adopt an extinction correction of 80% of the Schlegel et al. (1998) value; $A_V = 0.8 A_{\rm V}^{\rm Schlegel\,98}$ throughout this Chapter.

We now consider the implications of this extinction correction for our NIR measurements. We first plot $J - H$ vs K_s for galaxies with $J - H$ error < 0.33 mag (i.e. 3 σ and higher). The error in colour is calculated from the flux errors before converting to a magnitude.

The 2MASS XSC finds that the typical $J - H$ colour for galaxies ($8 < K_s < 14$ mag), between $z = 0$ and $z = 0.2$, is $0.65 < J - H < 0.72$ (Jarrett et al. 2003). In Fig. 6.9 we show candidates corrected using the Schlegel et al. (1998) value correction (top panel) and using an 80% correction (bottom panel). For the 100% correction we find a mean value of 0.60 ± 0.17 and for the 80% correction, a mean of 0.73 ± 0.16 (bearing in mind we include galaxies beyond $K_s = 14$ mag). Using the unchanged Schlegel et al. (1998) value causes galaxies to appear too blue (i.e. $J - H < 0.65$ for $K_s < 14$ mag) a result of the extinction being overestimated. The 80% correction, however, shows a distribution more consistent with what we expect from our sample (mostly faint, distant galaxies).

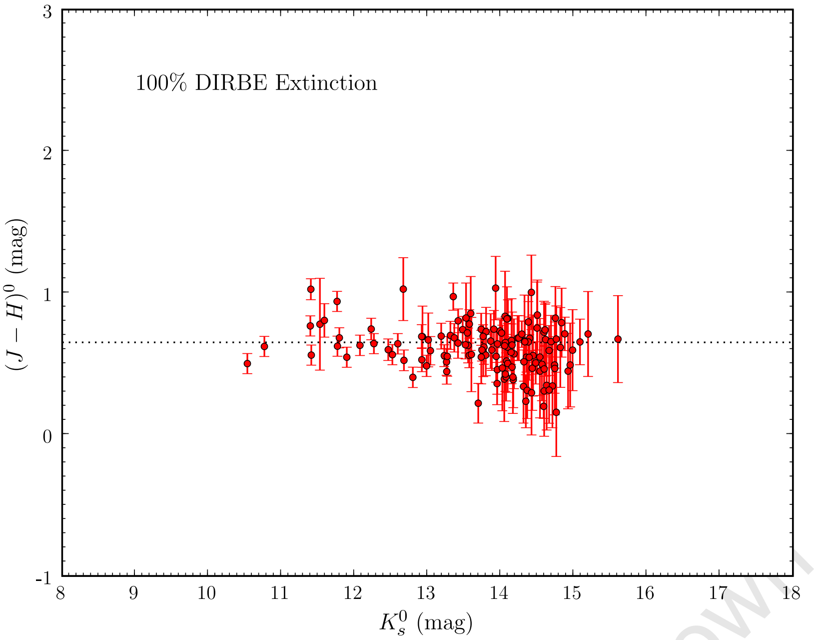

(a) 100% Schlegel et al. (1998) extinction

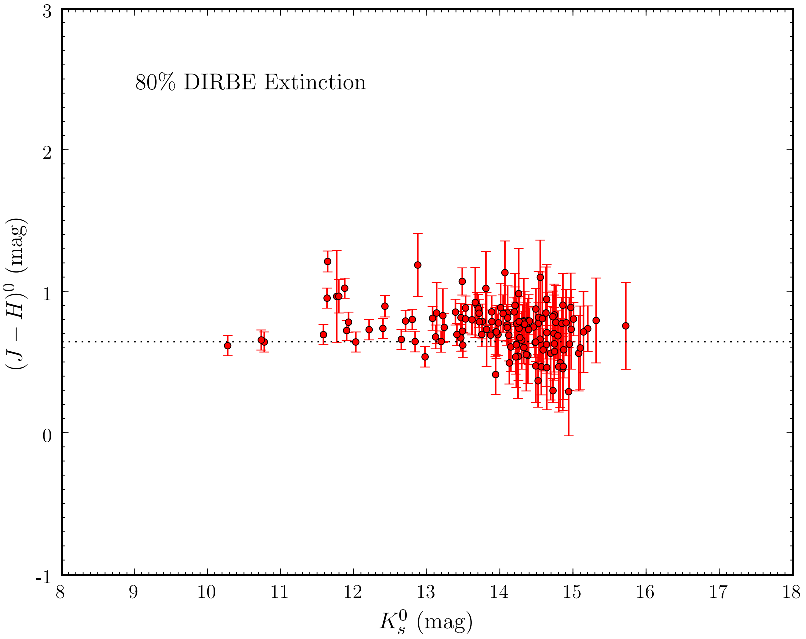

(b) 80% Schlegel et al. (1998) extinction

Figure 6.9: $(J-H)$ vs K_s distribution for galaxies with $(J-H)$ error < 0.33 mag using two extinction corrections. The dotted line shows $J-H=0.65$, the typical colour for a galaxy at $z=0$ (Jarrett et al. 2003) The k-correction is expected to be minimal for this colour and flux range of the IRSF sample.

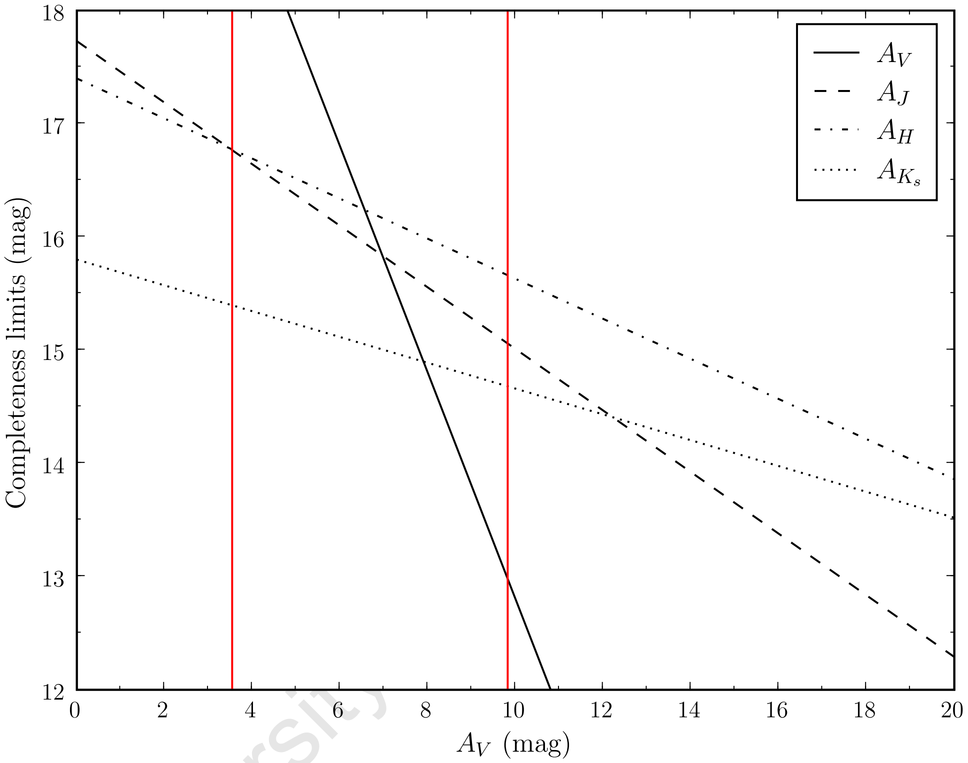

Figure 6.10: The effect of extinction on the magnitudes of galaxies. We show the effect of increasing A_V on completeness limits determined for the IRSF. The limits for an integration time of 600 s are 17.7 mag in J and 17.4 mag in H (Kotze 2007), and 15.8 in K_s (Skelton 2007). The V band is plotted for comparison (with a completeness limit of 22 mag). The range of extinction in the region covered in the survey is shown between the red lines.

In Fig. 6.10 we show the effect of increased extinction on the completeness limits of an IRSF NIR survey for an integration time of 600 s. The completeness limits are 17.7 mag in J and 17.4 mag in H (scaled from Kotze 2007) and 15.8 in K_s (Skelton 2007).

If we consider a galaxy at the redshift of HIZOA J0836-43 ($z \sim 0.04$) and use the 2MASS relation between $J - K_s$ and redshift for faint galaxies ($13.5 < K_s < 14$ mag), we expect a $J - K_s$ colour of ~ 0.75. We similarly expect galaxies at $z = 0$ to have a $J - K_s$ colour of ~ 0.6 (Jarrett et al. 2003).

At a high value of A_V such as 10 mag, we can only detect galaxies brighter than 14.7 mag in K_s. At this extinction, the corresponding detection limit is $J = 15.1$ mag, so we won't detect the galaxy in the J band. For nearby galaxies this will happen from $A_V \sim 9$ mag, where a galaxy with a J magnitude of 15.4 will have a K_s magnitude of 14.8. For galaxies at the redshift of HIZOA J0836-43, we stop detecting them in J at $A_V \sim 7.7$ mag. As a result, H and in particular K_s, which is less affected by extinction, become the best bands for finding galaxies. This will have the effect of making the galaxies appear redder in the colour composites compared to those in areas of less extinction. In Fig. 6.11 we shown the central pointings of the fields covering this region (discussed in Section 2.1.2). The naming convention is used to convey the distance from the central field (+0+0), the location of HIZOA J0836-43. The central pointings of adjacent fields are offset by $7'$.

We show the A_V value for the central pointing of each field in diagram Fig. 6.12. The fields containing the greatest extinction, $A_V \sim 9.8$ mag ($A_{Ks} \sim 1.1$ mag) , were $-6+4$, $-6+3$, $-6+2$ and $-5+3$. We were able to find several galaxies at this extinction (3, 2, 4 and 2 galaxies in the fields $-6+4$, $-6+3$, $-6+2$ and $-5+3$, respectively). Several fields did not contain any candidates, namely +4+5, +6+2, +4+2, +6+1, +5+1, +4+1, +5+0, −2+6, −2+0, −5+6, −2−6 and $-4-2$.

The on-sky distribution of sources found in this survey are shown in Fig. 6.1. Comparing to the map of A_V shown in Fig. 6.12, we do not see an obvious effect due to extinction. Even in regions of relatively high extinction, we are still able to detect and extract galaxies, although the completeness at the faint end is altered.

There is one notable exception to the detection uniformity of the survey. The Field $-3+2$ appeares very reddened compared to the fields around it – it appears to be heavily affected by extinction as can be seen in Fig. 6.13. The extinction here is given to be only $A_V \sim 8$ mag, but is clearly higher than the DIRBE value. At the $\sim 6'$ resolution of the Schlegel et al. (1998) DIRBE/IRAS maps this variation was not detected. Due to the severe reddening here, no sources were found in this field.

6.5 Infrared Galaxy Catalogue

The infrared galaxy catalogue is comprised of sources extracted from the 2.24 sq. degree NIR IRSF survey and the smaller 0.18 sq. degree Spitzer survey, both centered on the HIZOA J0836-43 galaxy. The catalogue is split into two separate tables: NIR and NIR+MIR measurements.

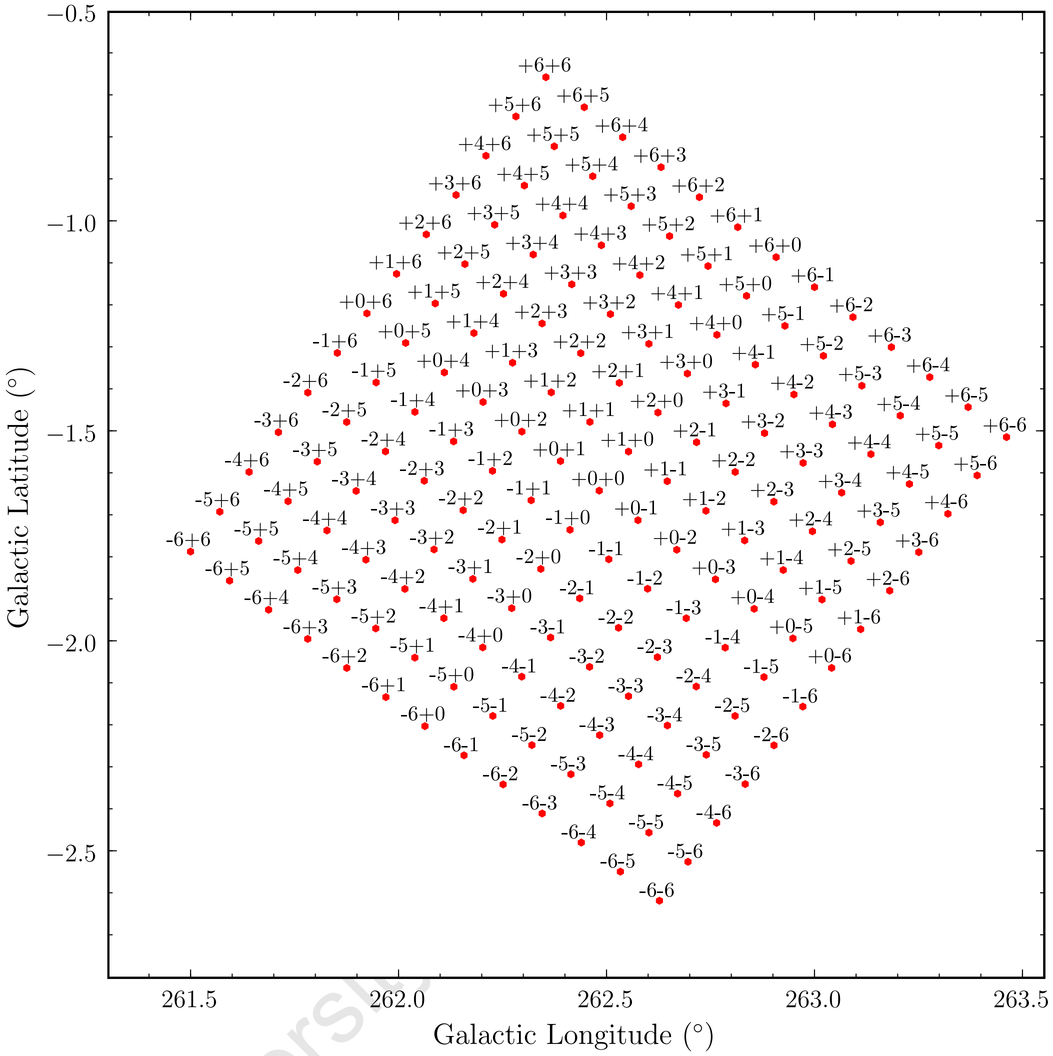

Figure 6.11: Diagram showing the central pointing for each field in Galactic coordinates.

In addition to these tables, there are associated “reject” tables consisting of low S/N sources; the catalogue is summarized below. In the analysis to follow, we focus on the larger area NIR catalogue results. The aim is to determine how this area is connected to the large scale structure in Vela and surrounding constellation regions.

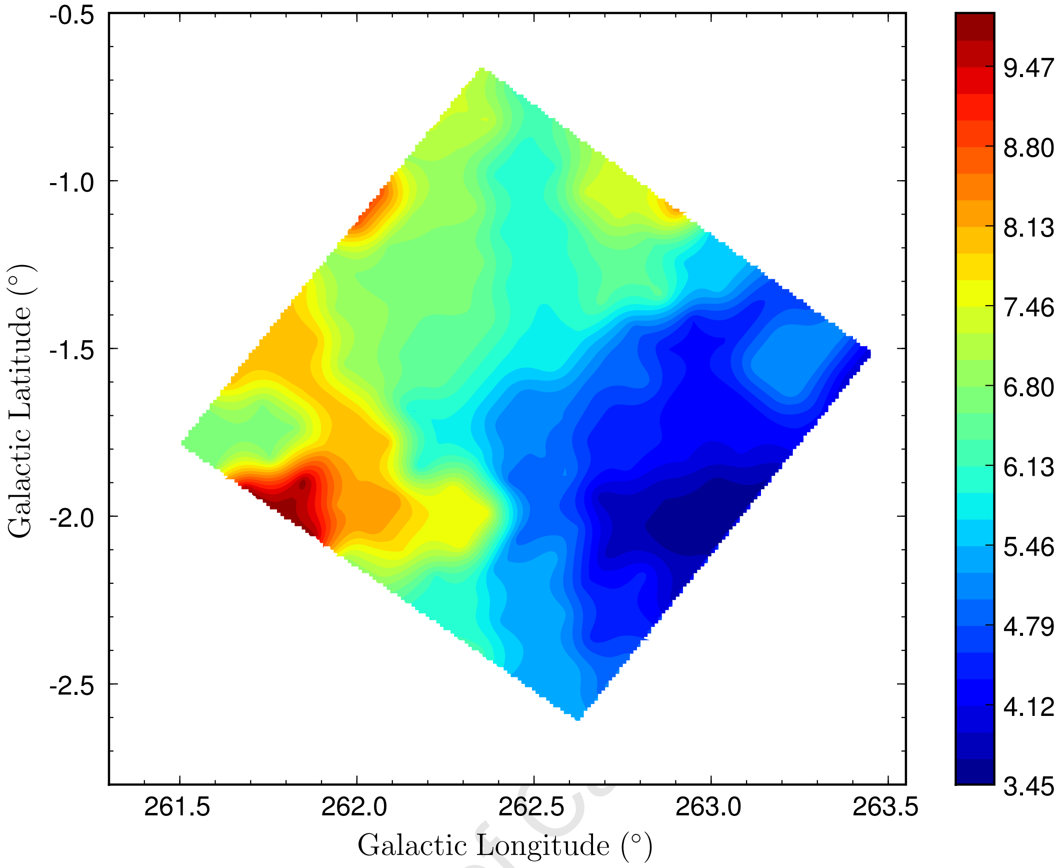

Figure 6.12: Diagram showing A_V for the survey region. Areas with the lowest extinction in A_V are shown in blue, highest extinction in A_V are shown in red (as indicated by the legend on the right).

Table 6.3: Infrared Galaxy Catalogue and Reject Tables

Description	Table Name	No. Sources	Comment
Spitzer + IRSF Catalogue	Table B.2; Table B.3	56	NIR and MIR measurements combined
IRSF NIR Catalogue	Table B.6	348	S/N > 3 for at least one band
Spitzer + IRSF Reject List	Table B.8; Table B.9	5	low S/N sources
IRSF Reject List	Table B.11	99	low S/N sources

6.6 Characterisation of the Near-Infrared Catalogue

We have 404 sources in the combined IRSF NIR catalogue. Their NIR postage stamps are shown in Appendix C. In this Section we investigate the characteristics of this sample by considering

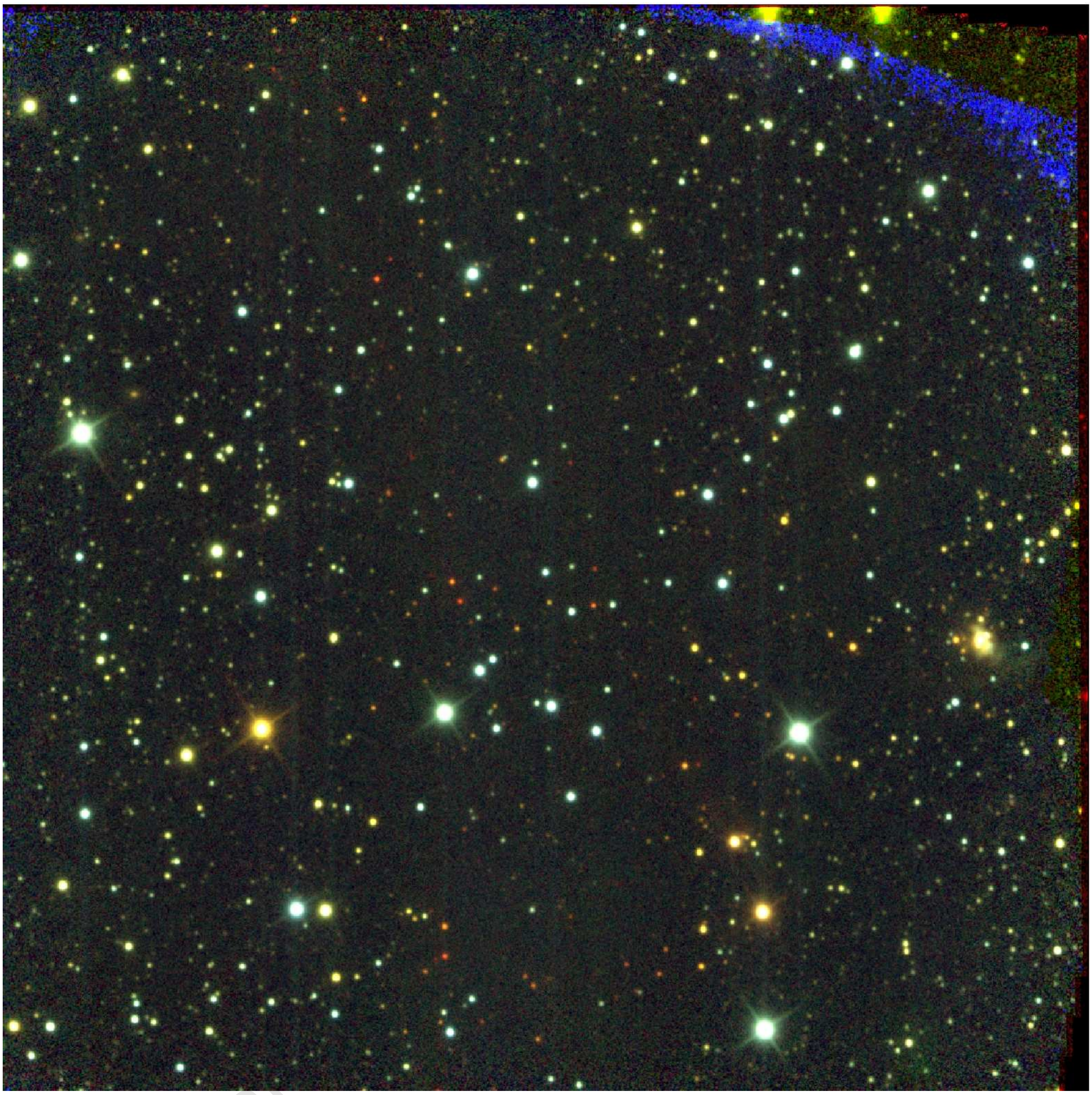

Figure 6.13: Colour composite image of HIZOA Field −3+2 showing the heavy dust obscuration at $l = 262.1°$and $b = -1.8°$. The size of the image is $\sim 8' \times 8'$. North is up and east is left.

its distribution in magnitude, near-infrared colour and how it compares to the 2MASS XSC.

6.6.1 Near-Infrared Magnitude Distribution

We have divided the catalogue into bins of 0.5 magnitude as shown in Fig. 6.14. We show the uncorrected and extinction-corrected magnitudes for comparison.

We note that the brightest source in our catalogue is 08343306-4324351. It is displayed in Fig. 6.15 and appears unusual compared to the other galaxies. The objects colours appear

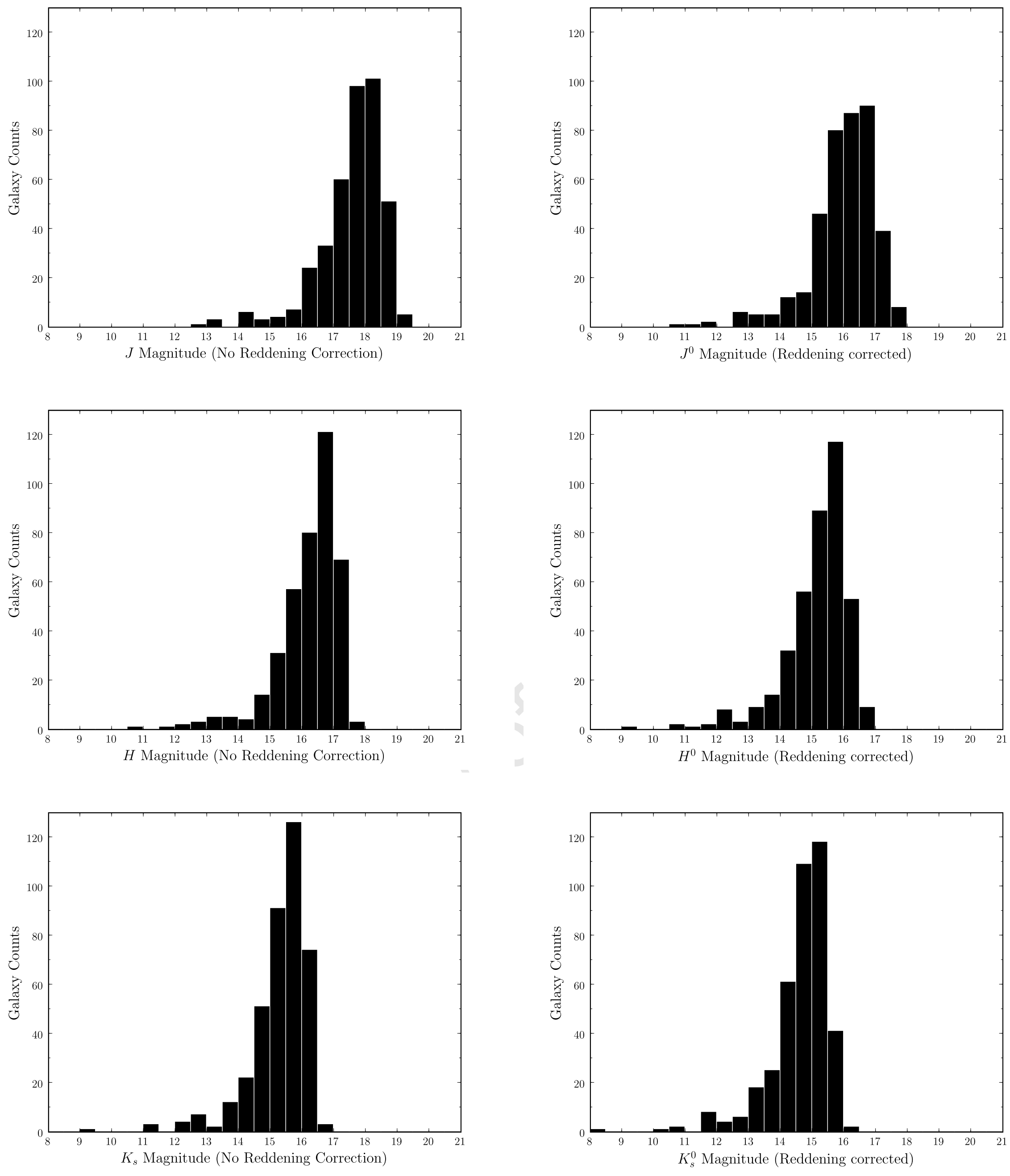

Figure 6.14: Magnitude bins for the J, H and K_s bands showing uncorrected magnitude on the left and extinction-corrected magnitudes on the right.

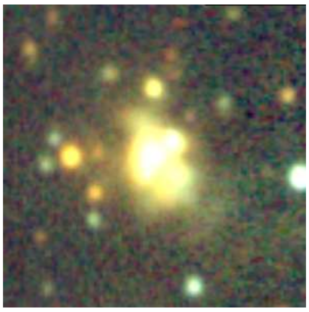

Figure 6.15: Near-infrared image of 08343306-4324351 which is the brightest source in the NIR catalogue. Its appearance is unusual compared to other sources in the survey, and is likely a foreground Milky Way object. The image size is $45'' \times 45''$.

too red to be extragalactic ($(J - K_s)^0 = 2.16$ mag and $(J - H)^0 = 1.15$ mag) and its surface brightness too high. This is likely an HII region from the foreground Milky Way. Since it is presumably Galactic, we remove this source from the analysis that follows.

6.6.2 Near-Infrared Mean Integrated Surface Brightness

The mean surface brightness of the sample provides distance-independent indication of the light (and therefore mass) distribution within the sample. We show in Fig. 6.16 the extinction-corrected mean integrated surface brightness for the sample.

The mean values obtained are 19.79 ± 0.66 mag arcsec^2 in the J band, 18.99 ± 0.65 mag arcsec^2 in the H band and 18.45 ± 0.66 mag arcsec^2 in the K_s band. The 2MASS K_s mean surface brightness in a $5''$ radius for the faintest galaxies $13 < K_s < 14$ mag is ~ 18.5 mag arcsec^2 (Jarrett 2000). For the faintest galaxies in 2MASS, this sized aperture would capture all the flux, so we can compare it to our results. Our distribution appears typical for near-infrared surveys of field galaxies or regions of the sky that do not include galaxy clusters (Jarrett et al. 2004).

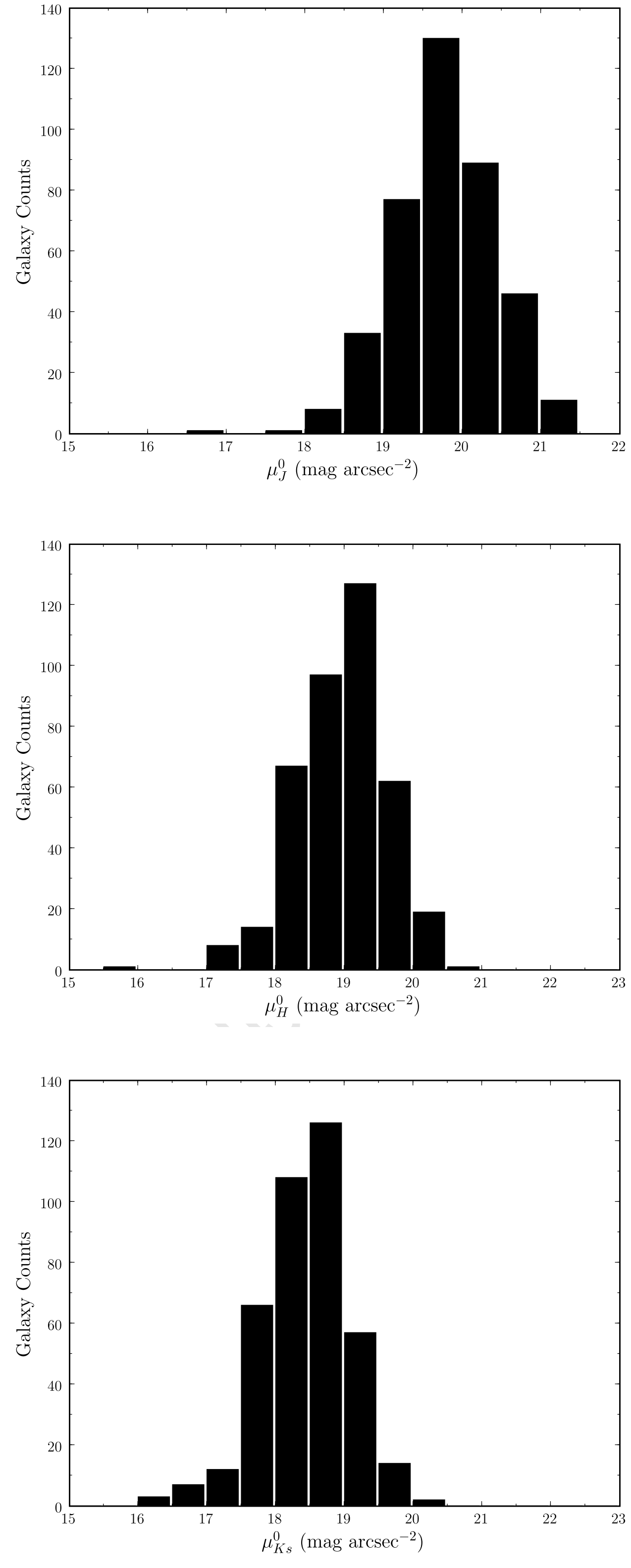

Figure 6.16: Mean integrated surface brightness (extinction-corrected) distribution for the 404 sources.

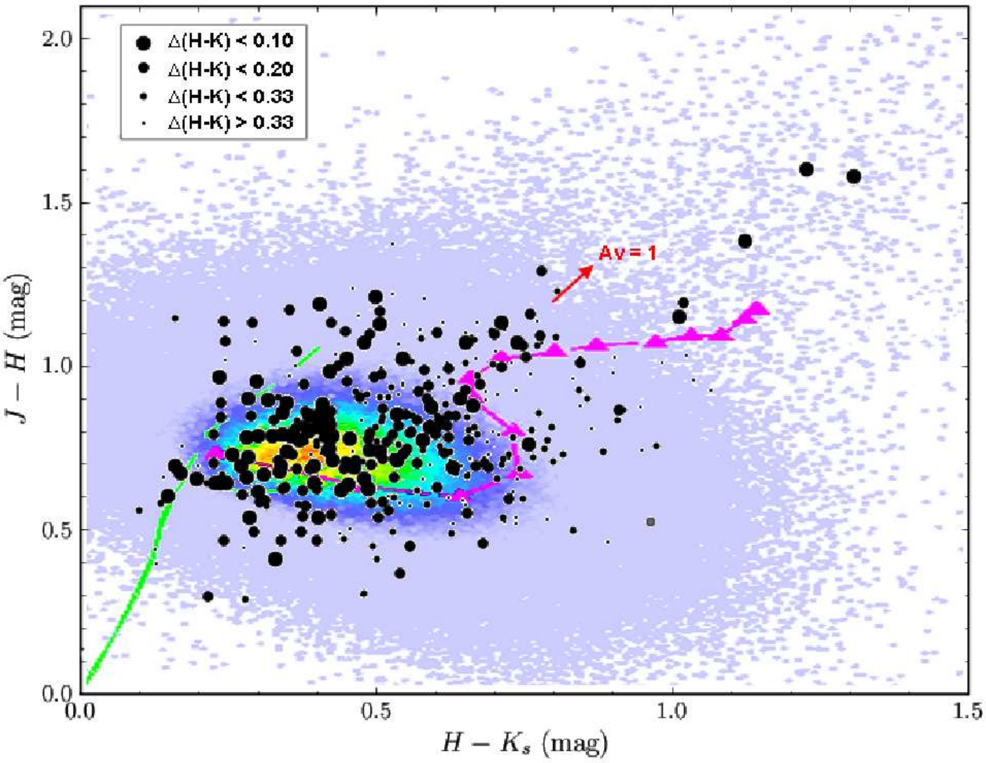

Figure 6.17: $J - H$ vs $H - K_s$ colour diagram superimposed on the 2MASS XSC 'Hess plot' constructed from the relatively clean, high Galactic latitude region of the sky. The IRSF survey points are shown in black and are extinction-corrected. For comparison, the stellar main-sequence and evolved (giant) tracks are shown in green and the magenta triangles correspond to the expected cosmic-reddening 'k-correction' for an Sab type galaxy with no evolution cosmology. The first triangle represents $z = 0$ and each further triangle is an increment of 0.1. These are adapted from the models of Bruzual & Charlot (1993) and McLeod & Rieke (1995). Thanks to T. Jarrett for use of the 2MASS XSC Hess plot.

6.6.3 Extinction-corrected Near-Infrared Colours

In this Section we consider the extinction-corrected NIR colours of the galaxy catalogue, and for comparison purposes, only the higher S/N measurements. Fig. 6.17 displays the $J - H$ vs $H - K_s$ colour plot of sources and the 2MASS Hess diagram.

The Hess diagram plots the density of sources in colour-colour space (Hess 1924). We demark the points according to their $H - K_s$ error as shown. We find statistically good agreement with 2MASS all-sky results. From the 2MASS XSC we expect a galaxy to have a $(J - H)^0$ colour of ~ 0.6 mag and a $(H - K_s)^0$ colour of 0.25 mag for local (low redshift) galaxies (Jarrett 2004). At higher redshift, $0 < z < 0.3$, the $H - K_s$ colours become redder while the $J - H$ colours remain roughly constant, following a track that pushes the distribution to the right side of the colour-colour diagram (see the magenta track in the diagram). The selective extinction track, note the

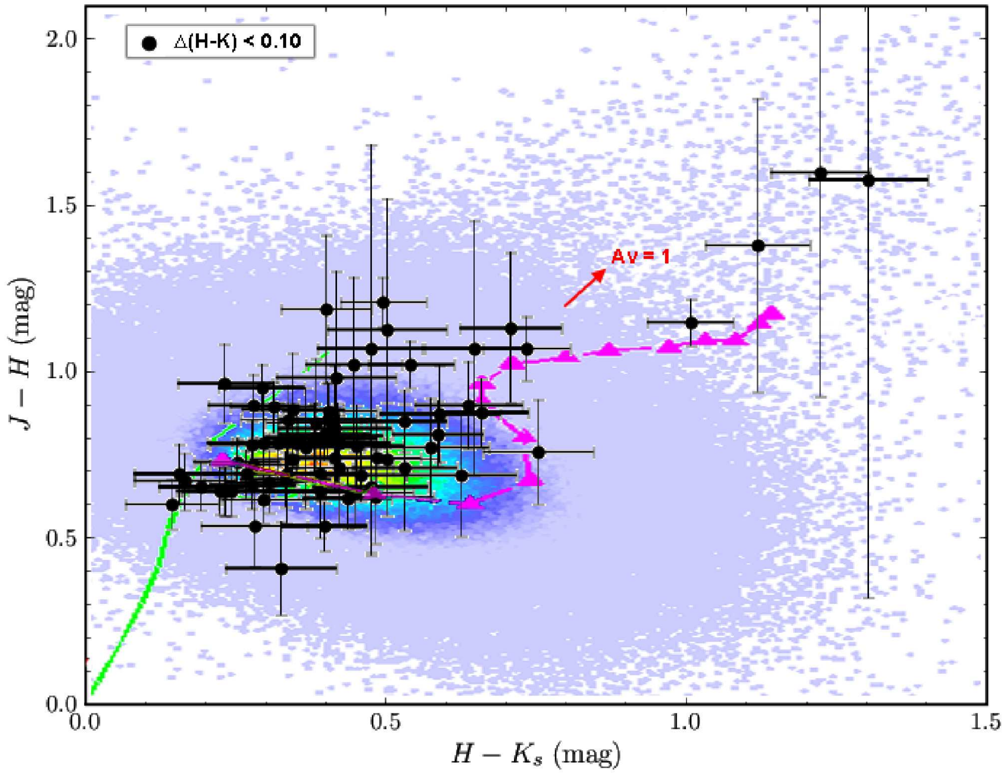

Figure 6.18: $J - H$ vs $H - K_s$ colour diagram superimposed on the 2MASS XSC Hess plot, as before, but for sources with $\Delta(H - K_s) < 0.1$ mag. One-sigma uncertainty error bars are also shown.

red arrow in the diagram, follows a more diagonal trend. If the extinction correction applied to the NIR measurements is correct, then the overall trend in the distribution is consistent with our sample containing mostly faint, distant galaxies.

In Fig. 6.18 we show the $J - H$ vs $H - K_s$ colour diagram for the most reliable photometric points, $S/N > 10$. Similarly, the trend is consistent with cosmic reddening. The reddest points may also contain AGN contribution to the total NIR light, which is typically much redder than that of normal galaxies. Finally, we show the $(J - K_s)^0$ vs K_s^0 plot for sources with $\Delta(J - K_s)^0 < 0.33$ mag. From Jarrett et al. (2003) we expect $J - K_s \sim 0.7$ mag for disk galaxies at zero redshift, $J - K_s \sim 1.0$ mag for early types. The expected colour at a given redshift for a $K_s = 14$ mag galaxy is indicated on the right side axis of the plot, showing that galaxies are redder at higher redshift.

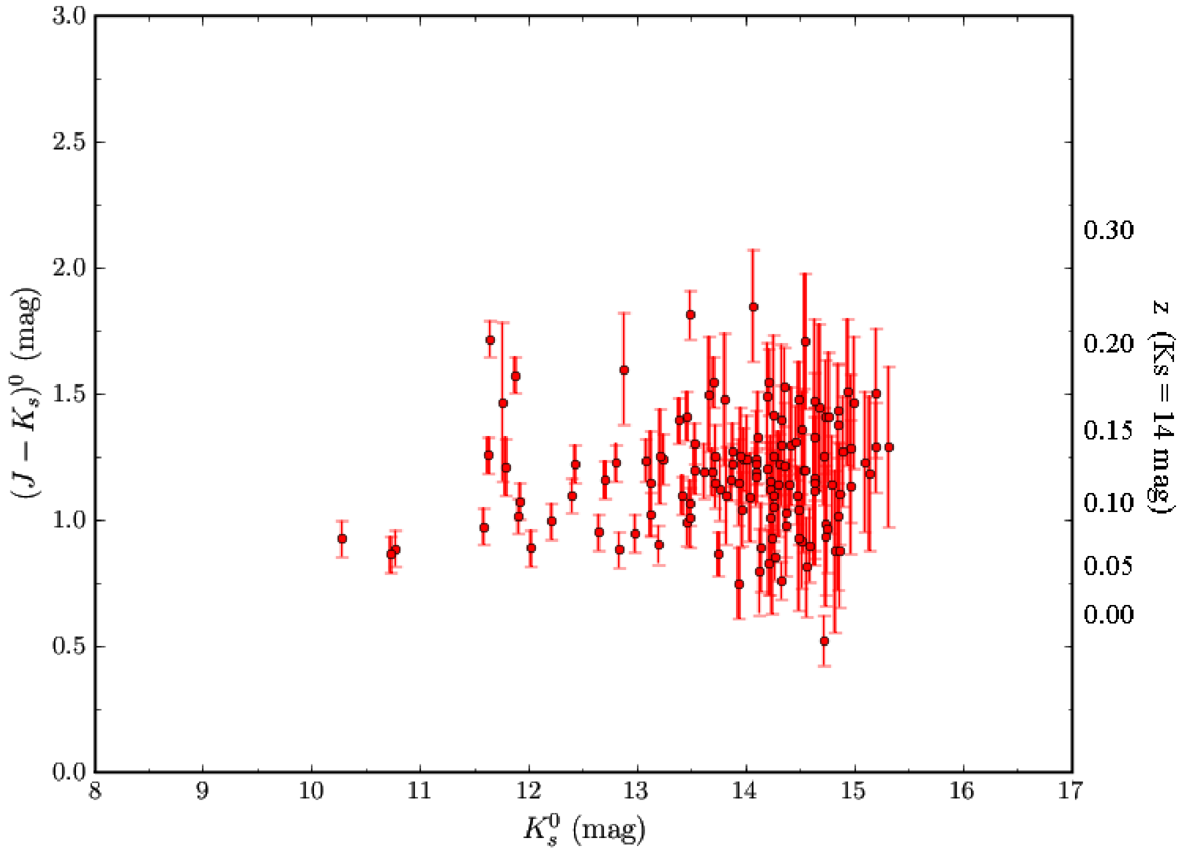

Figure 6.19: $(J-K_s)^0$ vs K_s^0 with $\Delta(J-K_s)^0 < 0.33$ mag. The effect of cosmic reddening is shown on the right axis for a $K_s = 14$ mag galaxy. A 'k-corrected' version will be presented in Fig. 6.29.

6.6.4 Comparison with 2MASS XSC

Here we compare our survey of the region around HIZOA J0836-43 with the 2MASS XSC survey of the same area. There are 44 sources in the 2MASS XSC in the region covered by the IRSF survey, of which 16 are confirmed galaxies ($\sim 36\%$) by our deeper and higher spatial resolution IRSF survey. For the remaining 28 2MASS XSC galaxies, which were not identified as galaxy candidates in the IRSF survey, visual inspection of the IRSF images revealed most of them to be blended stars that mimic galaxy profiles at lower (2MASS) spatial resolution. Indeed, a number of these sources were already identified by 2MASS as being probable Galactic sources. We show in the Appendix D.1 the 2MASS postage stamps of the rejected galaxies alongside the IRSF stamps.

We summarise the IRSF and 2MASS photometry of the 16 matched sources in Table 6.4. Photometry is not extinction-corrected. Source 08325794-4322119 was rejected from the IRSF catalogue due to large measurement errors (it does not appear well-resolved), but is included here for completeness.

Sources with very discrepant magnitudes were visually examined and are shown in Fig. 6.20. It was revealed that all of them were star+galaxy blends, rendering systematically brighter (i.e., contaminated) fluxes for the 2MASS measurements. These sources are marked with an asterisk in Table 6.4.

After removing contaminated sources from the list in Table 6.4, and restricting to only those sources with clean 3-band J, H and K_s extractions, the comparison results are shown in Fig. 6.21, where the isophotal photometry from the IRSF survey is compared to the 2MASS K_s^{20} isophotal photometry. K_s^{20} is the integrated magnitude down to the $K_s = 20$ mag arcsec^2 isophote. J^{20} and H^{20} correspond to the magnitude determined by integrating to the radius defined by the K_s^{20} isophote.

We find the following offsets for the IRSF$-$2MASS photometry: $\Delta J = -0.07 \pm 0.11$ mag, $\Delta H = -0.03 \pm 0.12$ mag and $\Delta K_s = 0.02 \pm 0.07$ mag. The K_s offset is consistent with what is found by Skelton (2007) for their Norma cluster comparison. They find $\Delta K_s = 0.007 \pm 0.016$ mag for 69 sources. The brighter 2MASS magnitudes are likely the result of small stars on or near the galaxy that have been blended into the photometry, which is consistent with the larger J-band offset (since the J-band is the most sensitive 2MASS channel). We would therefore expect our carefully star-subtracted images to give fainter magnitudes on average. The offset is within the 1σ errors and we therefore find relatively good agreement with 2MASS, particularly in the $2\,\mu$m window, despite limited star subtraction in the 2MASS photometry. We also expect an offset given the differences in isophotal limits between the two surveys.

Table 6.4: Comparison between IRSF and 2MASS photometry in the survey region

IRSF ID	J mag ^{a}	H mag ^{a}	K_s mag ^{a}	ΔJ mag ^{c}	ΔH mag ^{c}	ΔK_s mag ^{c}
2MASS ID	J mag ^{b}	H mag ^{b}	K_s mag ^{b}			
IRSF 08363597-4337554	13.29 ±0.05	12.07 ±0.05	11.45 ±0.06	-0.15	-0.01	0.00
2MASX J08363600-4337556	13.43 ±0.10	12.08 ±0.08	11.45 ±0.08			
IRSF 08365156-4337410	13.18 ±0.05	11.86 ±0.05	11.10 ±0.06	-0.07	0.05	-0.08
2MASX J08365157-4337407	13.25 ±0.08	11.81 ±0.06	11.18 ±0.06			
IRSF 08370727-4339136	15.34 ±0.06	14.12 ±0.06	13.51 ±0.07	...	...	-0.20
2MASX J08370723-4339137	...	...	13.71 ±0.14			
IRSF 08325331-4251430	15.43 ±0.06	13.90 ±0.05	13.17 ±0.05	...	...	0.00
2MASX J08325332-4251439	...	...	13.17 ±0.15			
IRSF 08340728-4257538	18.34 ±0.79	16.40 ±0.12	15.20 ±0.08	4.11	3.10	2.81
2MASX J08340700-4257545 ∗	14.23 ±0.17	13.30 ±0.16	12.39 ±0.14			
IRSF 08341220-4330200	16.11 ±0.06	14.53 ±0.05	13.64 ±0.05	...	0.26	0.03
2MASX J08341240-4330246	...	14.27 ±0.13	13.61 ±0.12			
IRSF 08352270-4319378	15.42 ±0.31	13.68 ±0.10	12.68 ±0.07	...	0.17	0.12
2MASX J08352270-4319378	...	13.51 ±0.11	12.56 ±0.10			
IRSF 08352483-4318232	15.08 ±0.05	13.36 ±0.05	12.55 ±0.05	-0.05	-0.05	0.04
2MASX J08352481-4318238	15.13 ±0.24	13.41 ±0.12	12.50 ±0.11			
IRSF 08354348-4359584	14.45 ±0.05	13.07 ±0.05	12.29 ±0.05	-0.17	-0.03	-0.09
2MASX J08354348-4359578	14.62 ±0.15	13.10 ±0.09	12.38 ±0.09			
IRSF 08355302-4314552	14.88 ±0.10	13.25 ±0.06	12.58 ±0.05	0.17	0.11	0.05
2MASX J08355302-4314554	14.71 ±0.14	13.14 ±0.09	12.53 ±0.10			
IRSF 08363189-4306118	13.43 ±0.05	12.13 ±0.05	11.50 ±0.05	0.54	0.49	0.43
2MASX J08363186-4306116 ∗	12.89 ±0.10	11.64 ±0.09	11.07 ±0.10			
IRSF 08372490-4353237	14.11 ±0.05	12.96 ±0.05	12.40 ±0.05	0.01	-0.12	0.02
2MASX J08372492-4353234	14.10 ±0.09	13.09 ±0.08	12.38 ±0.08			
IRSF 08373629-4358532	14.20 ±0.05	12.99 ±0.05	12.42 ±0.05	0.61	0.43	0.61
2MASX J08373630-4358524 ∗	13.59 ±0.11	12.56 ±0.10	11.81 ±0.10			
IRSF 08374566-4353314	14.40 ±0.05	13.25 ±0.05	12.71 ±0.05	-0.11	0.10	0.13
2MASX J08374565-4353314	14.51 ±0.15	13.14 ±0.10	12.58 ±0.11			
IRSF 08391189-4405384	14.08 ±0.05	13.03 ±0.05	12.51 ±0.05	-0.16	-0.27	0.09
2MASX J08391193-4405383	14.24 ±0.15	13.29 ±0.13	12.42 ±0.12			
IRSF 08325794-4322119	17.94 ± 7.63	16.44 ± 3.31	15.38 ± 1.99			
2MASX J08325794-4322129	...	...	13.86 ± 0.15			

[a] IRSF Isophotal Magnitude

[b] 2MASS K_s^{20} Isophotal Magnitude

[c] Δ mag = IRSF− 2MASS

∗ 2MASS photometry contaminated by stars

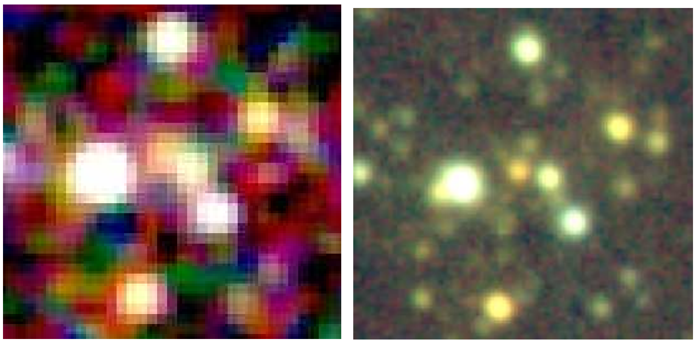

(a) 2MASX J08340700-4257545 (b) 08340728-4257538

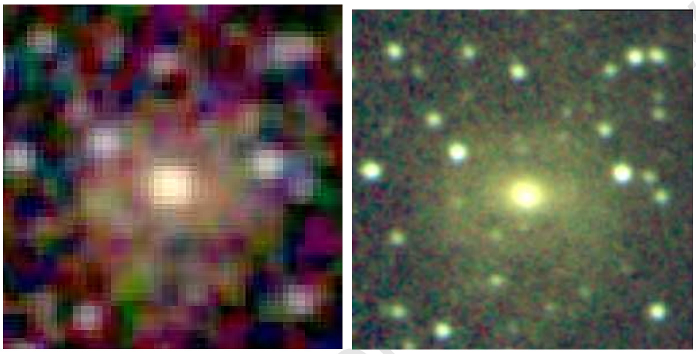

(c) 2MASX J08363186-4306116 (d) 08363189-4306118

(e) 2MASX J08373630-4358524 (f) 08373629-4358532

Figure 6.20: 2MASX sources with contaminated photometry showing the 2MASS and IRSF stamps for comparison.

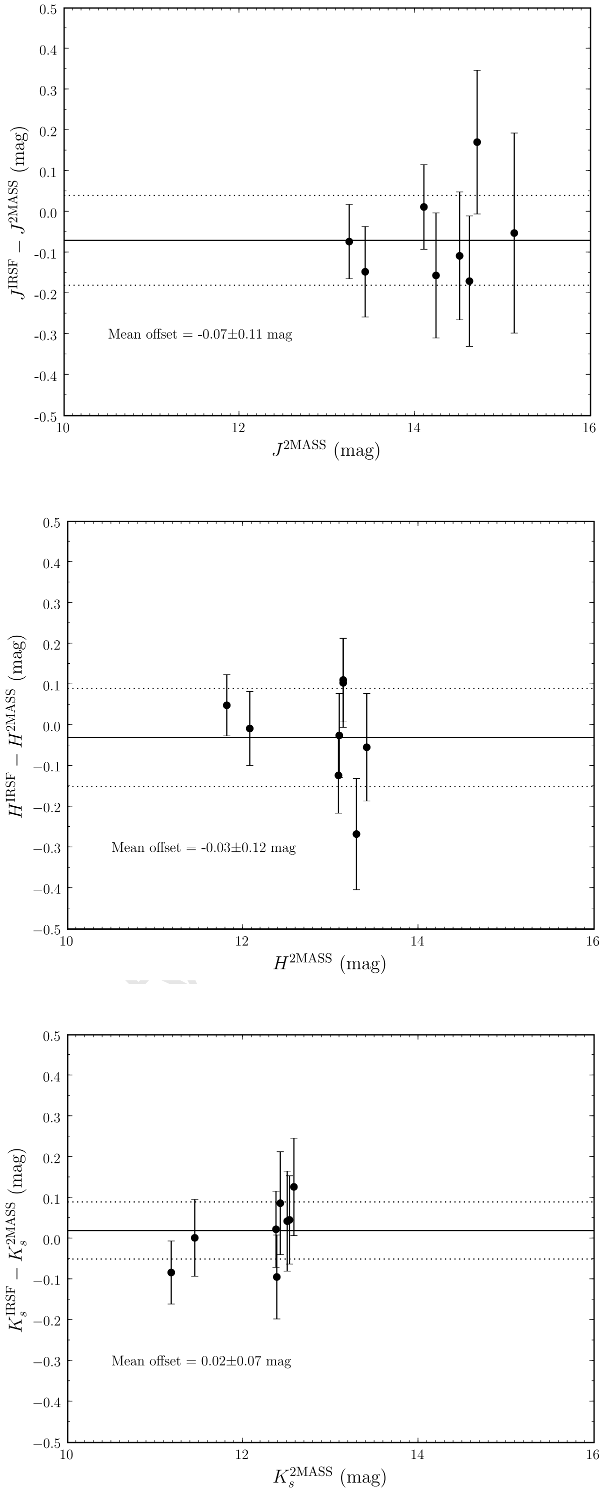

Figure 6.21: Comparison between 2MASS and IRSF isophotal magnitudes for the J, H and K_s bands. The dotted lines represent the mean $\pm 1\sigma$.

6.7 Galaxy Counts

In this section we show the number counts obtained for the 404 sources in this 2.24 sq. degree survey, including the differential and cumulative distributions.

Figure 6.22 shows the galaxy counts per square degree per magnitude bin interval for the J, H and K_s bands, respectively.

Focusing on the K_s-band results, Fig. 6.23 shows the IRSF survey galaxy counts compared to field galaxy values from Glazebrook et al. (1994) and Huang et al. (1997), and the 2MASS XSC results for ~ 24000 sq. degrees of sky, $|b| > 25°$ (Cutri et al. 2000) . Striking from this figure is that the number counts toward the heavily-extincted Vela region of the sky agree remarkably well with the field values where the extinction is negligible, demonstrating the effectiveness of the IRSF to penetrate and map galaxies to a high level of completeness in the ZoA. The IRSF counts follow both Glazebrook et al. (1994) and Huang et al. (1997) to the 13.0 mag bin. Compared to the Glazebrook et al. (1994) result, the IRSF survey matches it closely at the faint end and is complete down to $K_s \approx 14.8 - 15.0$ mag, or roughly a full magnitude deeper than 2MASS at high Galactic latitude. The deviation from the Huang et al. (1997) counts are likely the result of poorer spatial resolution ($\sim 2.0''$ pixel) compared to the IRSF ($0.45''$ per pixel) and Glazebrook et al. (1994) counts ($1.2''$ per pixel). The counts suggest that the Vela region is not harbouring any hidden galaxy clusters or significant over-densities.

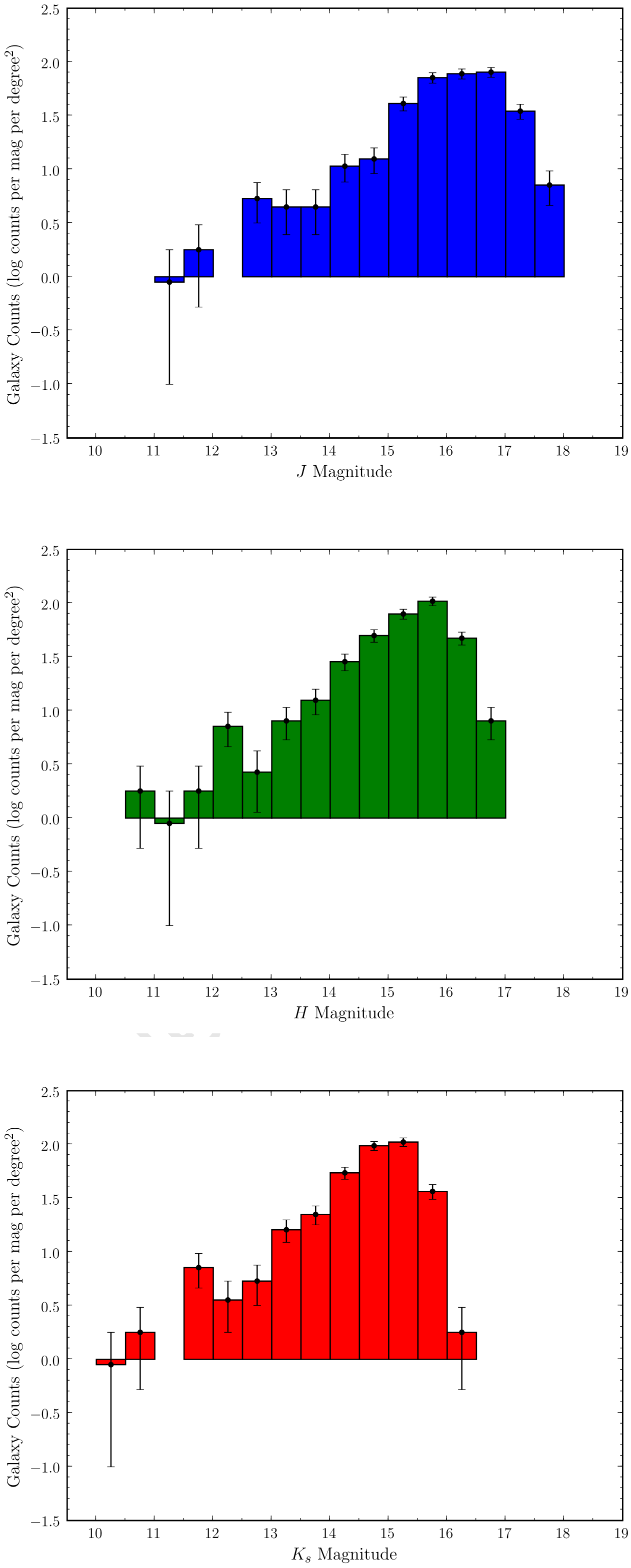

Figure 6.22: Distribution of differential galaxy counts for the J, H and K_s bands per square degree per magnitude interval. We show the Poisson errors ($\sqrt{N}$) for the counts.

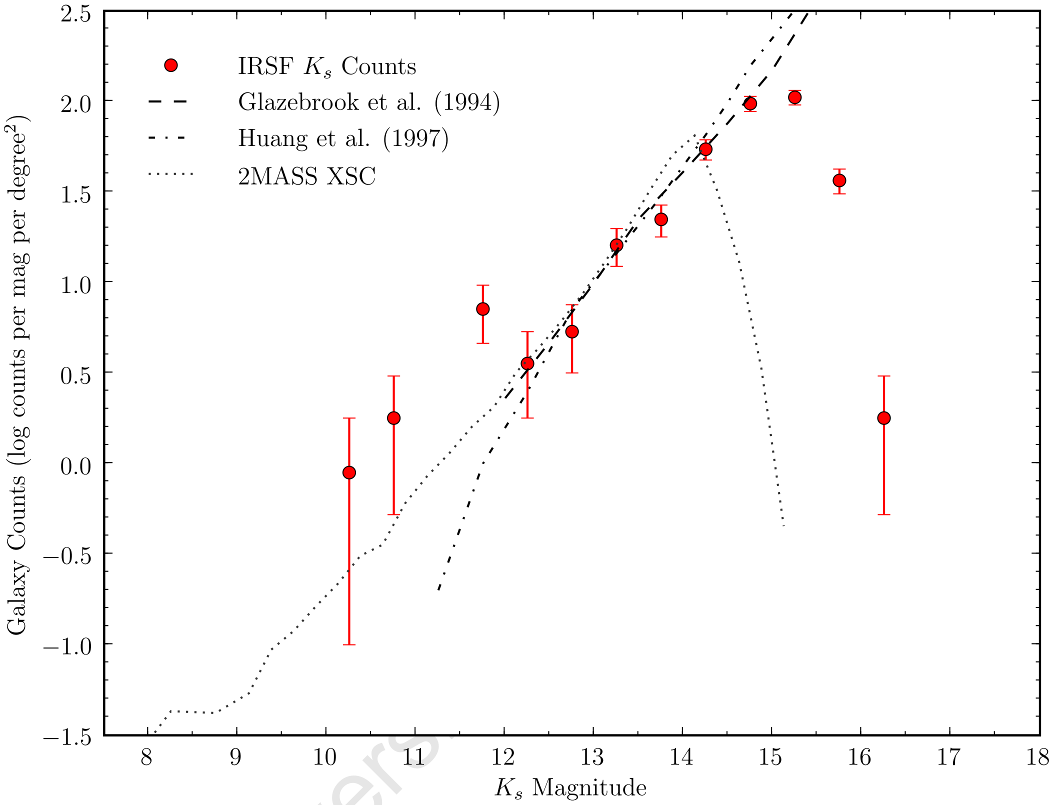

Figure 6.23: Differential K_s galaxy counts per square degree per mag interval compared to Huang et al. (1997), Glazebrook et al. (1994) and the 2MASS XSC ($|b| > 25°$). The Glazebrook et al. (1994) counts are a composite of the no-evolution model from their paper for $K_s < 13$ mag and their counts for $K_s < 17$ mag, with Cowie et al. (1990) counts for $K_s > 17$ mag.

A further demonstration of the IRSF depth compared to 2MASS is shown with a K_s cumulative number count diagram, Fig. 6.24, where the 2MASS counts now represent the density of galaxies found in the Vela region ($260 < l < 265°$; $-4 < b < 1°$).

As compared to the IRSF survey, 2MASS is missing faint sources, incomplete by a factor of 2-3 compared to the deeper and higher spatial resolution IRSF observations. This is illustrated in Fig. 6.1 where we can compare the number of sources found by 2MASS and the IRSF. The cumulative galaxy counts per square degree for each band are shown in Fig. 6.25.

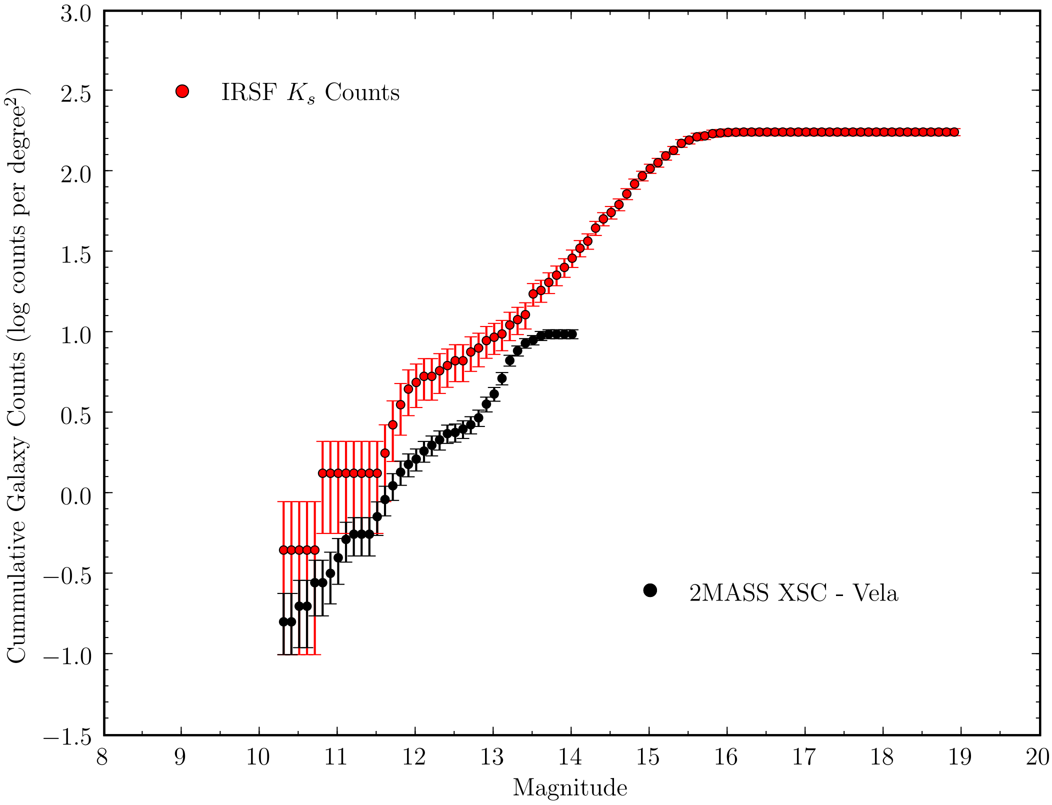

Figure 6.24: Cumulative galaxy counts for the K_s band compared to the 2MASS XSC for the Vela region ($260 < l < 265°$; $-4 < b < 1°$).

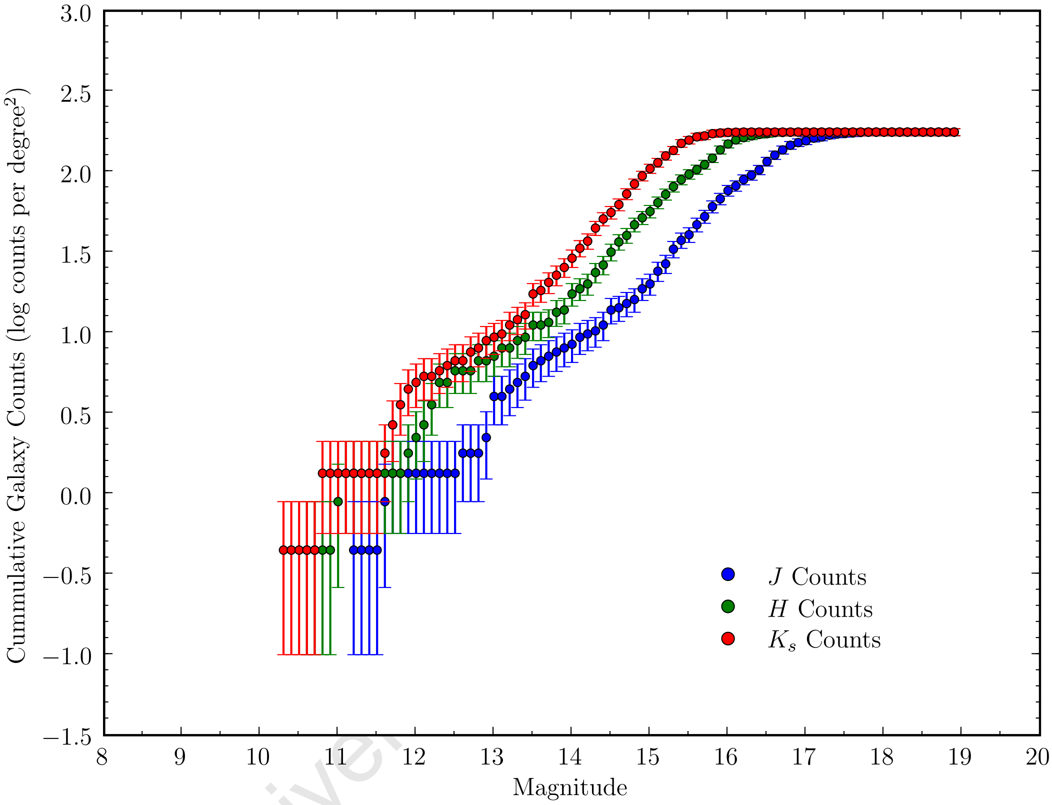

Figure 6.25: Cumulative galaxy counts per square degree for the J band (blue), H band (green) and K_s band (red). Poisson errors ($\sqrt{N}$) for the counts are shown.

6.8 Completeness limits from Cumulative Galaxy Counts

As presented in the previous section, the source counts become incomplete relative to field number densities at $K_s \sim 14.8 - 15.0$ mag. In this section we measure the departure in the cumulative number count trends. In Fig. 6.26 we plot the cummulative galaxy counts for the J, H and K_s bands. We fit a linear regression to the slope of the counts to see where they begin to deviate. We use the following ranges of magnitude for the fit: $14.8 - 16$ mag for J, $13.7 - 16.1$ mag for H and $13.3 - 15.4$ mag for K_s. We find slopes of 0.497, 0.487 and 0.529 respectively.

The counts begin to deviate from this fit at 16.4 mag in the J band, 15.8 mag in H and 15.4 mag in K_s. Considering the differential and cumulative distributions, the NIR survey appears to be complete down to $K_s \sim 15.0$ mag.

6.8.1 Photometric Redshifts

The on-sky distribution of sources was shown in Fig. 6.1. However, this does not give us an indication of how the mass is distributed in a volume delineated by the on-sky area. This requires knowledge of the relative distances of the sources in this survey. There are no spectroscopic redshifts for any sources in this region except for HIZOA J0836-43 itself, but we can use broad-band photometric redshifts, in combination with its projected location, to roughly construct the 3-dimensional source distribution. These spatial coordinates enable comparison of the HIZOA J0836-43 region with the larger structures that comprise the cosmic web, which may provide vital clues as to the origin and evolution of the massive galaxy. The photometric redshift catalogue will also serve as a pilot survey catalogue for future spectroscopic follow-up observations of sources suspected to be part of the HIZOA J0836-43 volume.

We utilise the photometric redshift (photo-z) code of Jarrett (2004) to estimate the luminosity distances to the galaxies in our sample. The accuracy of this technique is relatively crude, $\sim 20 - 30\%$, limited by the minimal information that the NIR window provides regarding cosmic reddening (e.g., see Fig. 6.17). It does nonetheless provide a qualitative map of the 3-D spatial distribution of galaxies.

The photo-z extraction procedure is based on two fundamental assumptions: (1) that galaxies have approximately the same luminosity in the K_s band, and (2) that their near-infrared colours are affected by cosmic reddening (the 'k-correction'). This technique was also deployed by Kochanek et al. (2003). The photometric redshifts are determined by optimally combining the extinction-corrected integrated K_s^0 flux, the $(J - K_s)^0$ and $(H - K_s)^0$ colours and the angular size of the galaxy. Angular size is, however, only a good discriminant of distance for well-resolved sources with isophotal radius of $> 25''$ and is also affected by extinction.

Studies of the K_s band luminosity function by Cole et al. (2001), Kochanek et al. (2001) and Bell et al. (2003) have shown independently that $M^*_{Ks} = -24.0$ mag. The most important metric is the galaxy colour grouped in families of integrated flux: there is a linear correlation between the slope of the colour vs redshift relation and the integrated flux (e.g., fainter galaxies tend to

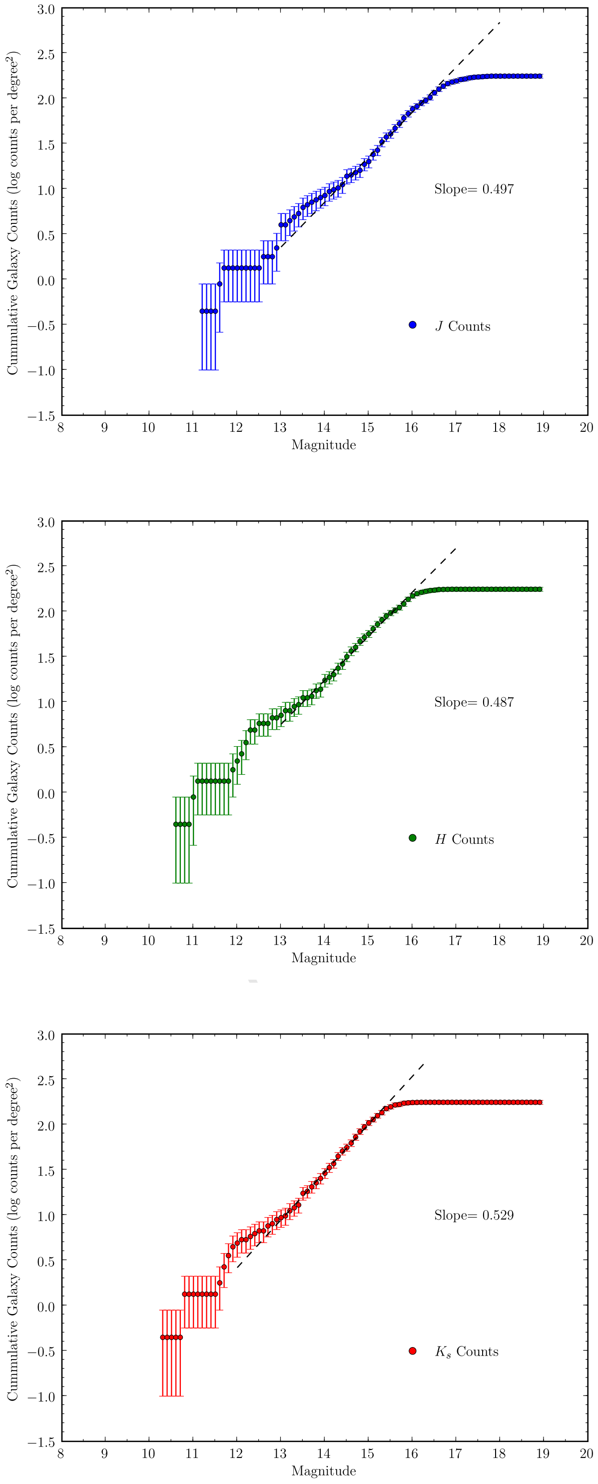

Figure 6.26: Cummulative Galaxy Counts for the J, H and K_s bands. We fit a linear regression to the slope of each as shown.

have a steep colour versus redshift relation), which appears to be extensible to fainter sources than the 2MASS XSC limits. The photo-z method and performance using 2MASS measurements are presented at: http://spider.ipac.caltech.edu/staff/jarrett/XSCz/photoz.html.

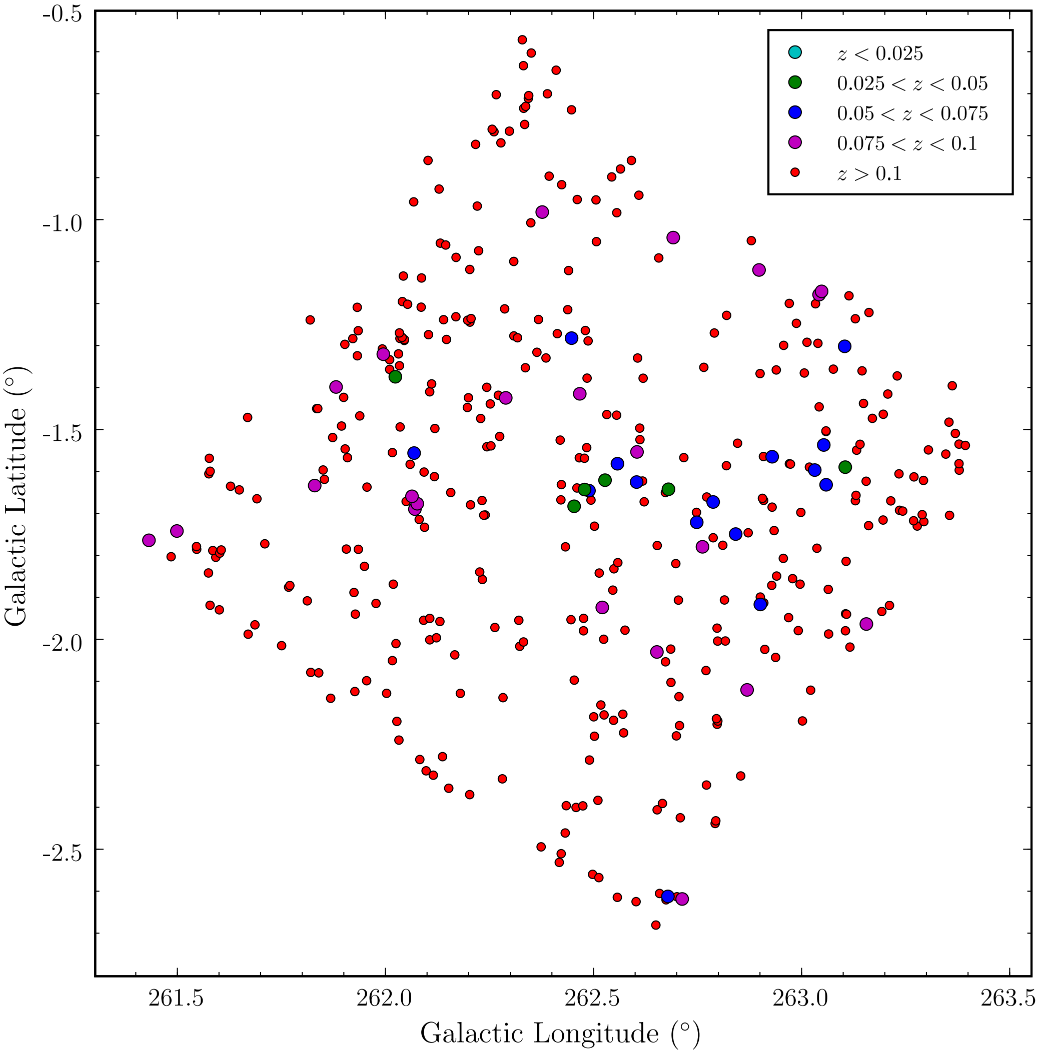

Figure 6.27: Distribution of sources with colour-coded photometric redshifts. There are no sources with a photometric redshift of $z < 0.025$ (cyan). Green sources have a photometric redshift of $0.025 < z < 0.05$, blue for $0.05 < z < 0.075$, purple for $0.075 < z < 0.1$ and red for all sources with $z > 0.1$.

The resulting photometric redshift distribution is plotted for individual sources, Fig. 6.27, and with individual redshift slices shown in Fig. 6.28 for comparison. The slices are in redshift increments of 0.025 due to the large uncertainty in the distance estimates, with distances especially uncertain for the fainter (higher redshift) sources. The individual photometric redshifts for sources are listed in Column 11 of Tables B.3 and B.6.

The photometric redshift obtained for HIZOA J0836-43 is 0.034, which closely matches its known spectroscopic redshift (0.036). This is consistent with the massive galaxy having NIR properties that are common to typical 2MASS galaxies used to calibrate the photo-z extraction algorithm, notably the high luminosity and early-type spiral galaxy colours. For the two neighbouring galaxies, we find redshifts of 0.0325 (Companion A) and 0.0389 (Companion B). This agrees reasonably well with the result from our SED fitting: the "satellite" galaxies are at a similar, and possibly the same, redshift to HIZOA J0836-43.

We note the small number of galaxies in the redshift range of $0.025 < z < 0.05$ where HIZOA J0836-43 is found. The two neighbouring galaxies and another source (08391189-4405384 or 2MASX J08391193-4405383) slightly further away are the only significant sources. It is therefore unlikely that HIZOA J0836-43 is found in a high-density environment such as a cluster. Considering the massive H I disk of the galaxy, a high-density environment would likely have resulted in the gas being stripped due to galaxy interactions, reducing the likelihood of a large gas disk persisting over Gyrs of time; hence, a relatively sparse population around HIZOA J0836-43 is not unexpected.

The redshift slice $0.05 < z < 0.075$ suggests a conglomeration of galaxies in the direction of HIZOA J0836-43, but more distant. This is likely related to the projected overdensity noticed by Donley et al. (2006) when considering the 2MASS XSC sources around HIZOA J0836-43. In the next Section we shall investigate a possible connection to the large scale structure around HIZOA J0836-43.

In order to check the self-consistency of the results, we plot in Fig. 6.29 the extinction-corrected $(J - K_s)^0$ colours vs K_s^0 magnitude after applying a k-correction determined from the photometric redshifts of the sources. Comparing to the colour vs. magnitude diagram presented earlier in Fig. 6.19, we see that the colours are now consistent with zero redshift colours of normal galaxies. We find a mean of $(J - K_s)^0 = 0.94 \pm 0.18$ mag.

The majority of sources appear to be of early-type. This is a consequence of the NIR being sensitive to the "old" stellar population, as found in bulges of spirals and early-type galaxies. The lower surface brightness of disks in the NIR creates a selection effect, further worsened by extinction in the ZoA.

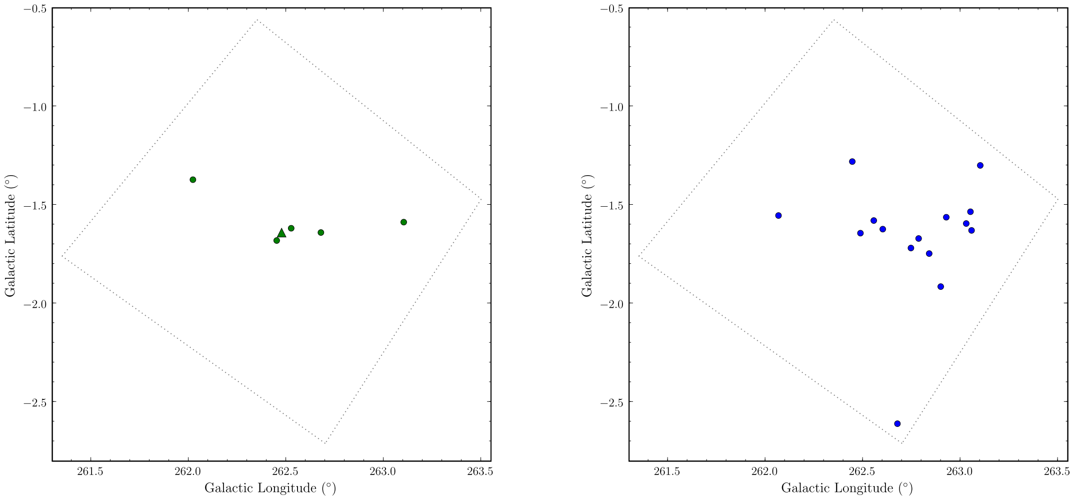

(a) $0.025 < z < 0.05$ (b) $0.05 < z < 0.075$

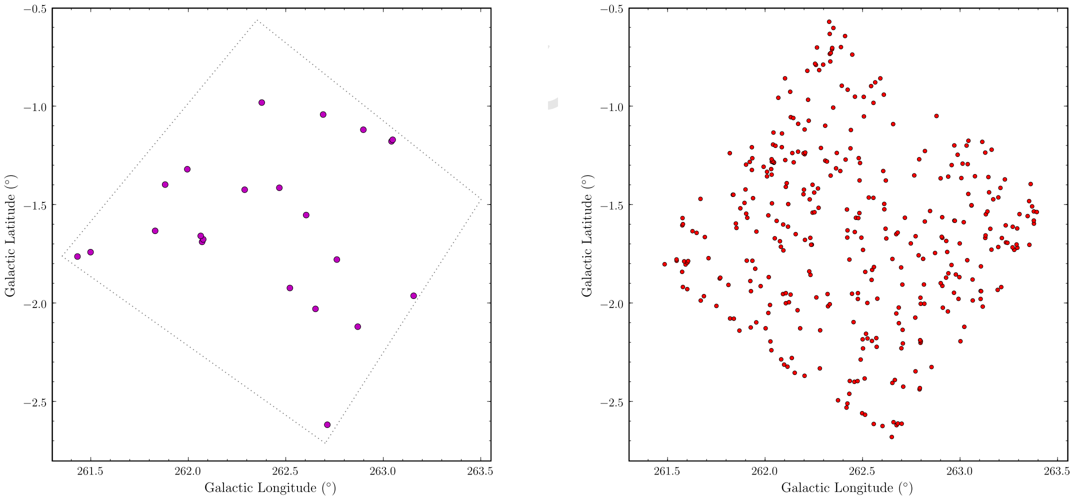

(c) $0.075 < z < 0.1$ (d) $z > 0.1$

Figure 6.28: Distribution of sources within each photometric redshift slice. HIZOA J0836-43 is shown as a green triangle in the $0.025 < z < 0.05$ slice. The dotted outline shows the area covered by the survey.

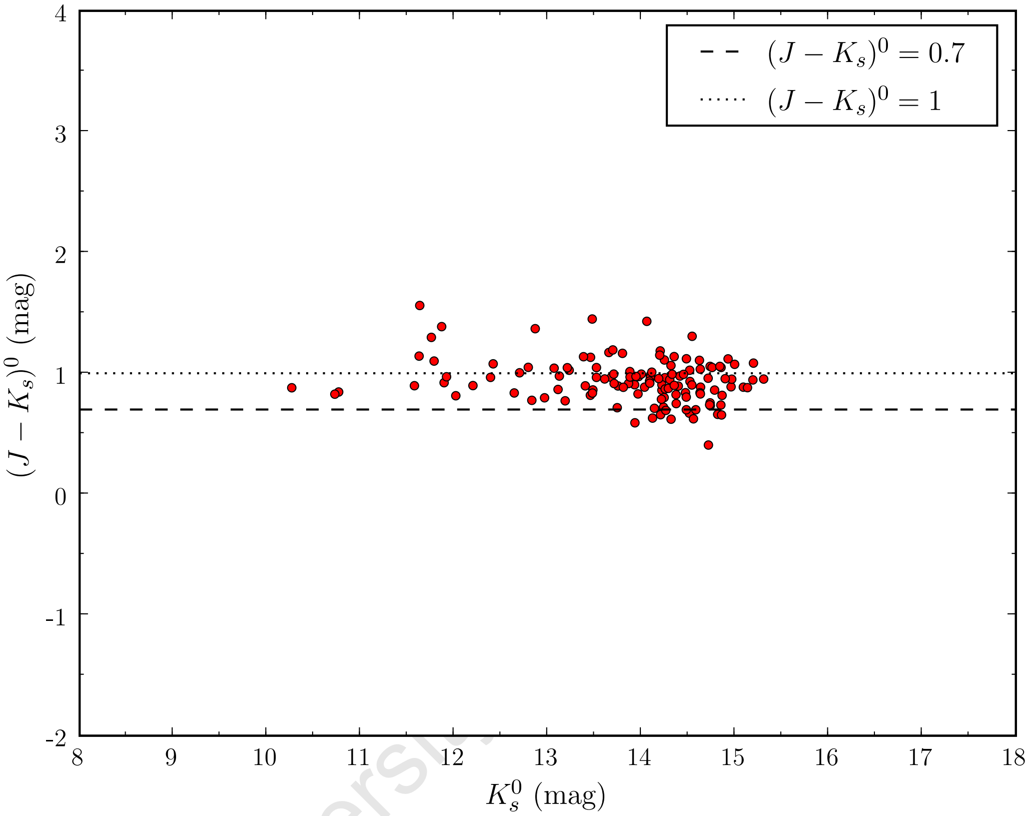

Figure 6.29: The $(J-K_s)^0$ colours for sources with $\Delta(J-K_s) < 0.33$ mag, after applying a k-correction using the photometric redshifts determined by the Jarrett (2004) code. The plot also shows the expected colour at zero redshift for S0/Sa and Sb galaxies ($J-K_s \sim 1.0$ mag) and late-type spirals ($J-K_s \sim 0.7$ mag) from Jarrett et al. (2003). See Fig. 6.19 for colours that have not been corrected for cosmic reddening.

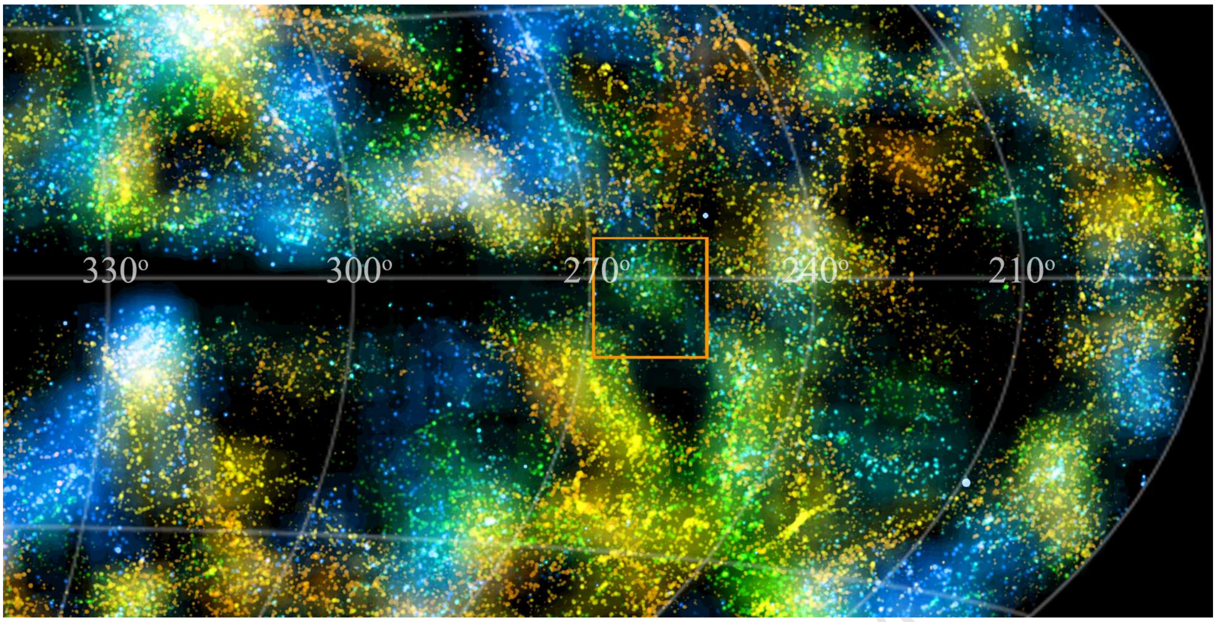

Figure 6.30: The smoothed distribution of XSCz galaxies centred on the Vela region, where HIZOA J0836-43 is located. The orange box corresponds to 15° × 15°. Note the fuzzy 'green' structure in Vela, which correspond to $0.03 < z < 0.04$, the redshift location of HIZOA J0836-43. The massive galaxy and its satellites are located near the edge of the fuzzy structure and the void. The "yellow" contribution corresponds to $0.04 < z < 0.05$ and the "cyan" shows $0.02 < z < 0.03$ galaxies. Image credit: T. Jarrett and the 2MASS team.

6.9 Large Scale Structure around HIZOA J0836-43

In this final section we consider the large-scale structure around HIZOA J0836-43. We utilise the 2MASS XSCz (XSC redshift catalogue) from Jarrett (2004)[1]. This catalogue combines photometric redshifts with available spectroscopic redshifts from, for example, the Sloan Digital Sky Survey (Strauss et al. 2002), 6dFGS (Jones et al. 2004) and Zcat (Huchra et al. 1983). It allows us to probe the large scale distribution of galaxies around HIZOA J0836-53 in an effort to explore the mass distribution that may have influenced its formation.

The XSCz catalogue contains approximately 1 million galaxies and is complete down to $z = 0.09$ ($K_s < 14$ mag), but also extends to greater redshifts, $z \sim 0.2$, for luminous galaxies.

To enhance the large scale structures, a highly surface-smoothed[2] version of the XSCz distribution for $0.01 < z < 0.06$, centred on the Vela region, is shown in Fig. 6.30. The Vela region, where HIZOA J0836-43 is located, is outlined by a $15° \times 15°$ orange box. The redshift is encoded by the following colours: $0.01 < z < 0.02$ = blue, $0.02 < z < 0.03$ = cyan, $0.03 < z < 0.04$ = green, $0.04 < z < 0.05$ = yellow and $0.05 < z < 0.06$ = orange.

---

[1] http://spider.ipac.caltech.edu/staff/jarrett/lss/

[2] Surface smoothing is a technique in which the edges of a structure are preserved after a blurring filter is convolved with the structure, which is particularly useful for filamentary structures

We see in Fig. 6.30 a large (tens of Mpc in size) forked structure just below the Vela region, which appears particularly prominent in the $0.03 < z < 0.05$ redshift range. The Vela region itself shows a concentration of galaxies which appears to cross the Galactic plane diagonally. This apparent overdensity appears to be dominated by the $0.03 < z < 0.04$ (green) redshift range. The massive galaxy and its satellites are located near the edge of this dense structure.

By considering only the $0.03 < z < 0.04$ redshift slice (shown in Fig. 6.31) we can better analyse the structure at this redshift. We see the diffuse concentration of galaxies in Vela, prominent in this redshift slice. The symbols used to plot the galaxies reflect their absolute K_s magnitude, with more luminous (smaller M_{Ks}) sources appearing brighter in the plots.

The brightest point in Fig. 6.31 corresponds to the location of HIZOA J0836-43 and the two neighbouring galaxies (Companion A and Companion B). This indicates that the structure seen here is formed by the association of many lower luminosity galaxies, with no other massive galaxies in the vicinity. Aside from HIZOA J0836-43, the galaxies are spread over mostly lower luminosities.

The location of HIZOA J0836-43 in relation to the low-luminosity structure is striking. It lies close to the edge of the feature, adjacent to an underdense 'void' region. As noted in the previous section, this would be consistent with HIZOA J0836-43 requiring a relatively gentle environment to avoid loss of its H I disk through tidal interactions and ram-pressure stripping, as is common in a typical cluster environment (Schröder et al. 2001). The Vela structure is in stark contrast to the filamentary structures seen in the Columba 'forked' structure, south of the Vela region, which contains many dense clusters and high luminosity galaxies (Fig. 6.31).

We now investigate the distribution of the 2MASS XSCz galaxies and the IRSF galaxies, by means of their derived photometric redshifts. In Fig. 6.32 we show the redshift slice for a region at constant Galactic longitude centered on Vela and $|b| < 20°$. The redshift wedge diagram shows sources extending to 1000 Mpc, which is well beyond the limits of 2MASS (black points), but within the capability of the IRSF survey (blue points). The grey-scale corresponds to the luminosity of the source; intrinsically brighter sources will stand out in this diagram. We notice several luminous, distant sources (likely early-type galaxies) in the IRSF survey, which is a selection effect seen in all NIR surveys. HIZOA J0836-43 appears to inhabit the transitional area between the void-like region and the conglomeration of relatively low luminosity galaxies that have clustered in the Vela vicinity.

For a closer view of the HIZOA J0836-43 region, we show in Fig. 6.33 the same area of the sky, but sampling to a smaller distance of 400 Mpc. The red arrow denotes the location of the massive galaxy. In this diagram we can see that the galaxies within 10 Mpc of HIZOA J0836-43 form an association of relatively low luminosity and therefore low mass galaxies. HIZOA J0836-43 is by far the most luminous galaxy in the Vela region. The other major structure highlighted by this wedge diagram is the Columba supercluster 'fork' structure at ~ 160 Mpc, $b \sim -20°$ to $-10°$. Considering both Fig. 6.31 and Fig. 6.33, there is no evidence that this structure extends across the ZoA, connecting to the Vela region. The bubble or 'fork' structure does not appear to terminate in Vela.

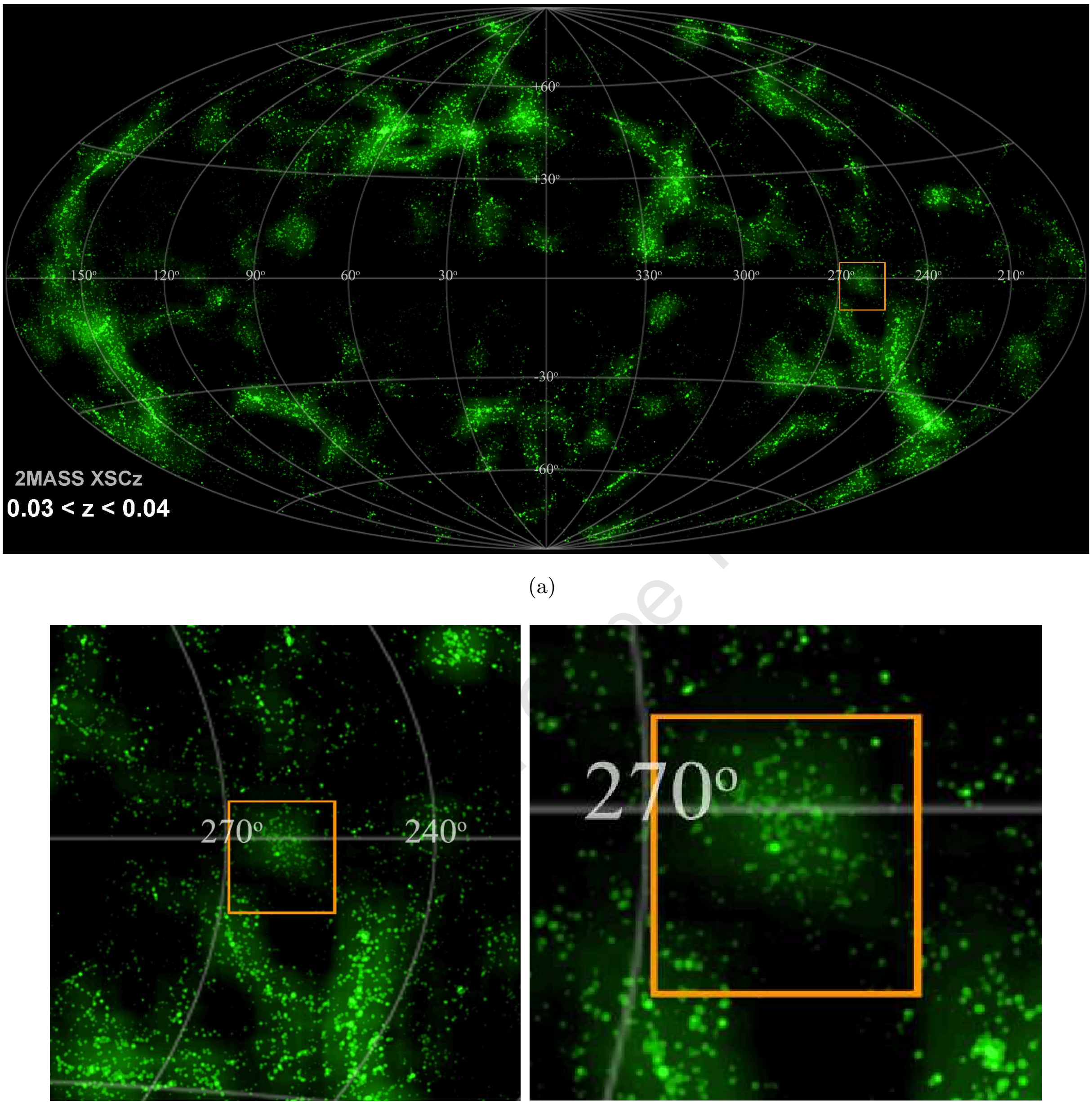

(a)

(b)

(c)

Figure 6.31: Smoothed distribution for redshift layer $0.03 < z < 0.04$ galaxies; the Vela region around HIZOA J0836-43 is outlined by the orange box (15°×15°). An overdensity is visible within the region. To the south of Vela is the large Columba supercluster ‘fork’ structure that dominates this redshift layer. Image credit: T. Jarrett and the 2MASS team.

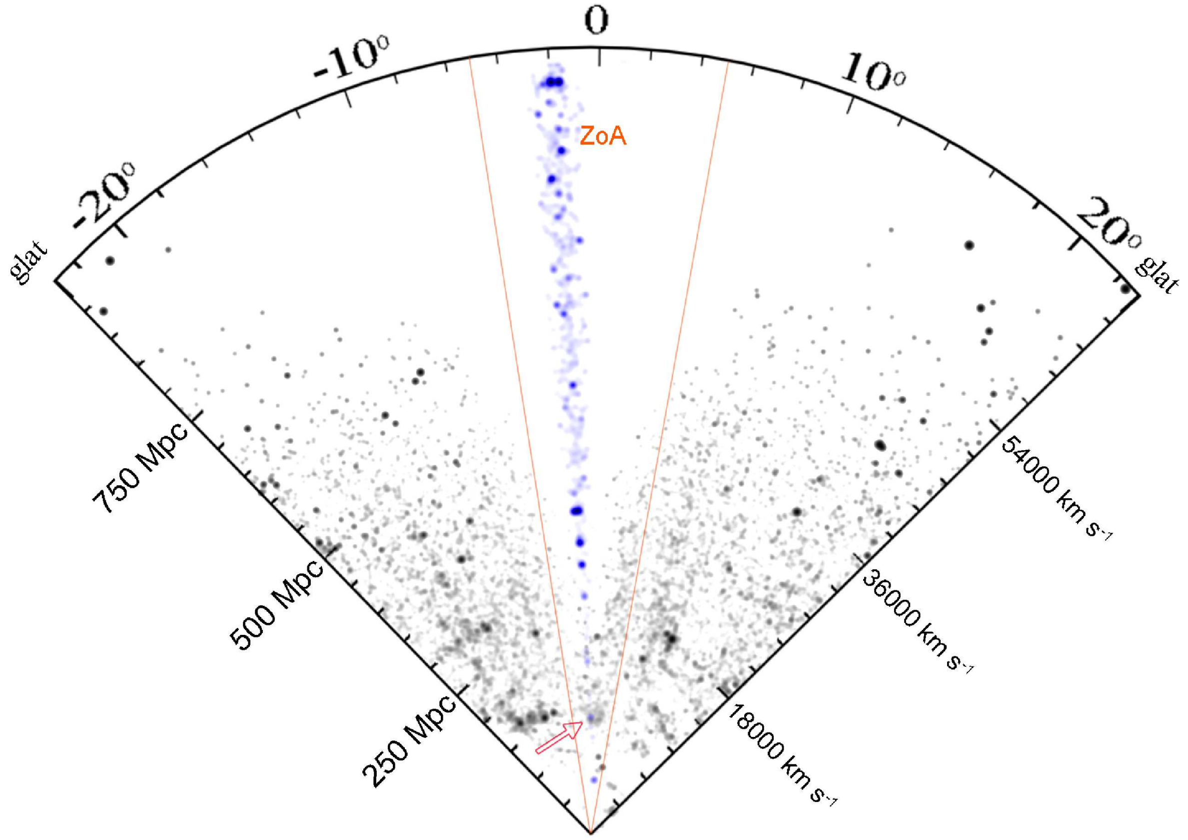

Figure 6.32: Deep photometric redshift slice of the region within $|\Delta l| = 5^\circ$ of HIZOA J0836-43, extending to $D < 1000$ Mpc. The IRSF survey galaxies are shown in blue and the 2MASS extended sources are shown in black. the position of HIZOA J0836-43 is indicated by the red arrow. The Zone of Avoidance ($|b| < 5^\circ$), where 2MASS is most incomplete, is shown between the red lines.

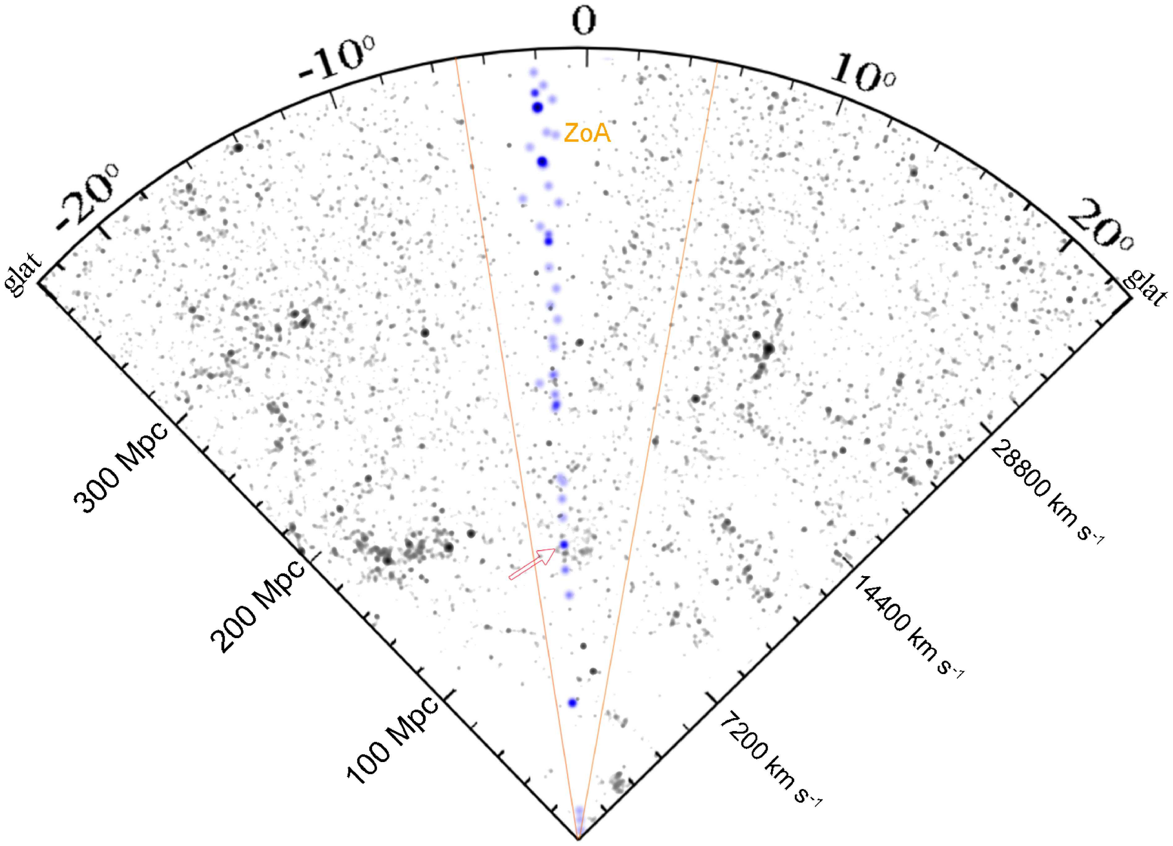

Figure 6.33: Shallow photometric redshift slice of the Vela region ($D < 400$ Mpc) within $|\Delta l| = 5°$ of HIZOA J0836-43. The IRSF survey galaxies are shown in blue and the 2MASS extended sources are shown in black. The position of HIZOA J0836-43 is indicated by the red arrow. The area between the red lines demarcates the Zone of Avoidance ($|b| < 5°$), where 2MASS is most incomplete.

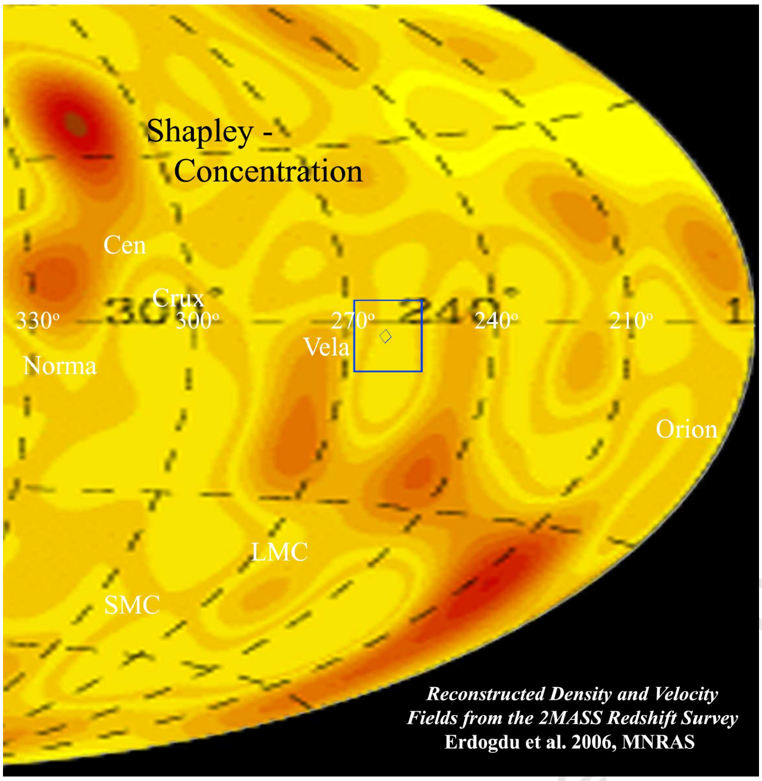

Figure 6.34: 2MRS reconstructed density field for $v_{hel} = 10,000$ km s^{-1} from Erdoğdu et al. (2006b). The Vela region is denoted with a blue box, and the location of HIZOA J0836-43 is marked with a diamond. Low density regions appear yellow with the higher density regions in red.

Preliminary spectroscopic work of Kraan-Korteweg et al. (private communication) in the Zone of Avoidance is consistent with a fairly underdense region for $0.02 < z < 0.03$ at $l \sim 260°$. At $0.03 < z < 0.04$ they find a low concentration of galaxies spread across the $l \sim 240°$and $l \sim 270°$ region, consistent with the low-mass structure seen in the XSCz.

An alternative way to view the higher luminosity distribution of sources in the local universe comes from a density and velocity field reconstruction using the $K_s < 11.5$ mag Two Micron Redshift Survey (2MRS); Erdoğdu et al. (2006b).

We show in Fig. 6.34 the reconstructed density field for $v_{hel} \sim 10,000$ km s^{-1}. The forked supercluster structure in Columba appears prominently in this diagram. Interestingly, we see an underdense void-like area surrounding the IRSF survey region that extends down between the fork-like filaments. Further deep NIR observations in the Vela region of the Galactic plane are necessary to determine a complete picture of the structure, in particular, to definitively determine whether the left branch of the fork extends to the location of HIZOA J0836-43.

The formation of HIZOA J0836-43 so close to an area that appears relatively underdense is intriguing. The Vela region appears to have only low luminosity systems, distinctly different from galaxy clusters, filamentary structures and low density (field) regions. This is most clearly

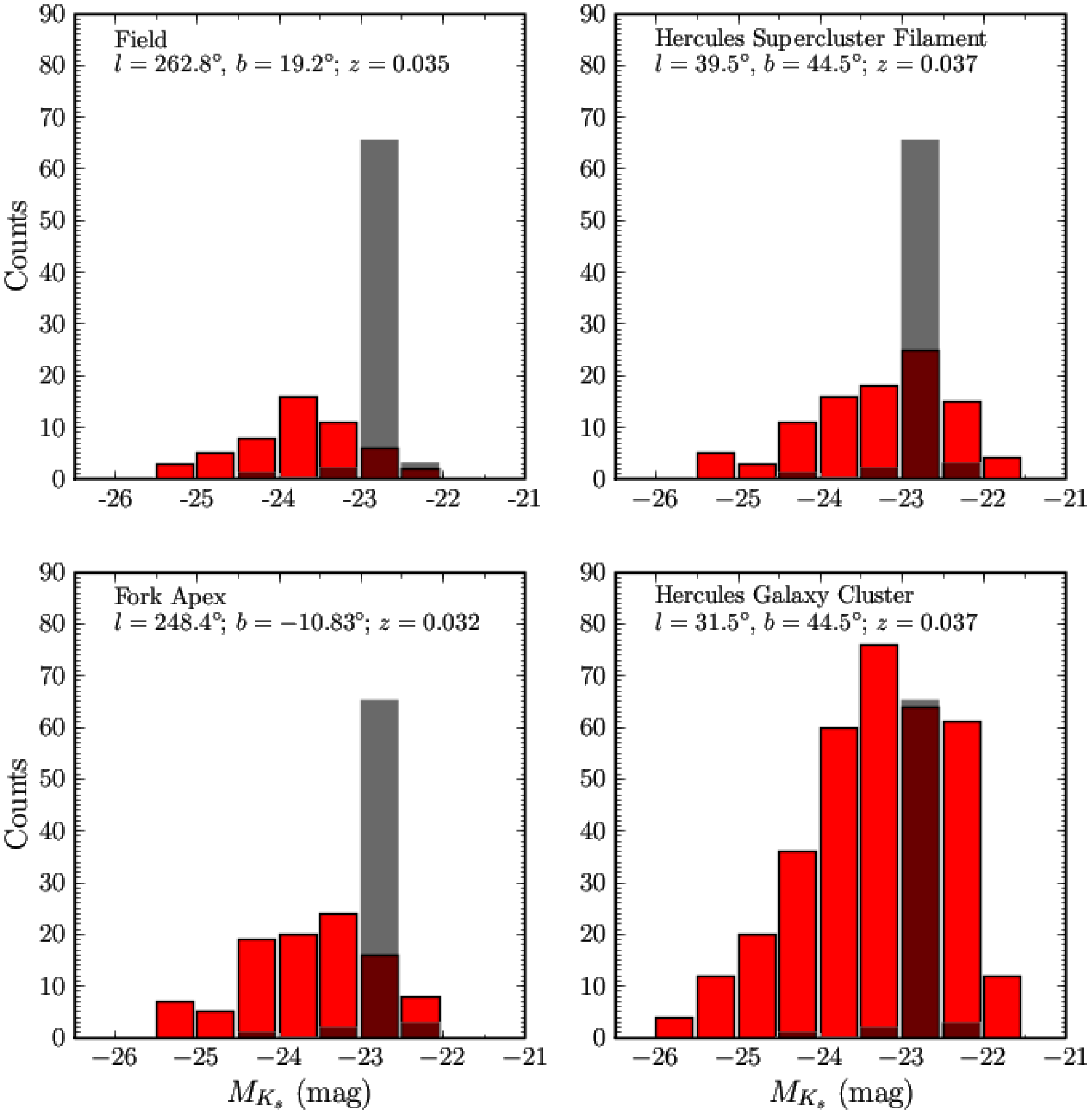

Figure 6.35: The K_s-band luminosity distribution of galaxies within 10 Mpc of HIZOA J0836-43 (dark grey histogram). HIZOA J0836-43 is the most luminous object in the distribution. For comparison, four regions of the sky are selected (shown in red), including galaxies with 10 Mpc of the Columba "Fork" supercluster, Hercules Galaxy Cluster, Hercules filamentary structure, and a field galaxy.

demonstrated in Fig. 6.35, which compares the K_s luminosity distribution of galaxies within 10 Mpc of HIZOA J0836-43 with that of galaxies within (a) 10 Mpc of a random field galaxy, (b) 10 Mpc of a filament in the Hercules supercluster, (c) 10 Mpc of the Columba "fork" supercluster, and (d) 10 Mpc of the Hercules Galaxy Cluster. It is clear that the Vela region is missing M^* systems, populated with mostly low-luminosity ($\sim$ 1 to 2 mag fainter than M^*) systems, similar in total number (73 vs. 97) to the Hercules filament, but considerably lower in total mass.

In hierarchical structure formation, luminous galaxies in lower density environments form later compared to luminous galaxies in dense environments (Kauffmann 1996). Also, in underdense regions like voids, there would be more gas and dust present for active star formation, likely triggered by close companions (Grogin & Geller 2000).

Λ CDM cosmology predicts a population of low surface brightness and dwarf irregular galaxies to be present in voids (Peebles 2001), but this is not seen observationally. The galaxies in voids appear to be very blue, late-type galaxies with higher star formation rates linked to their less dense environments (Grogin & Geller 2000). Szomoru et al. (1996) studied the H I content of *IRAS* selected galaxies in the Boötes void and found them to be late-type, gas rich systems, but found no Malin 1-type disks. This is consistent with the findings of Bothun et al. (1993) who find that the environment of Malin 1-type galaxies is not underdense on a large scale. A sample of $\sim$ 1000 void galaxies studied by Rojas et al. (2005) showed a higher specific star formation rate compared to galaxies residing in higher density regions, indicating a younger stage of star building evolution. There are therefore some similarities between HIZOA J0836-43 and galaxies residing in large scale, low density environments.

It is therefore plausible that H I-massive disk of HIZOA J0836-43 owes its existence to both its proximity to a large scale 'void' and to the relatively rare low-mass environment that it formed and evolved within. If indeed HIZOA J0836-43 has been "nutured" by this environment, it would have great impact on current theories regarding galaxy formation. HIZOA J0836-43 provides a challenging case for Λ-CDM cosmology and models of structure formation.

Chapter 7

Conclusion

In this final Section, we summarize the main results and conclusions of this dissertation. The aim of this work was to probe the past evolution and current state of the H I-massive galaxy, HIZOA J0836-43, as well as perform a census of its greater environment. Deep near-infrared photometry, in combination with mid-infrared photometry and spectroscopy from the *Spitzer Space Telescope*, enabled us to fully probe the stellar population and interstellar medium of HIZOA J0836-43. A near-infrared survey around HIZOA J0836-43 uncovered the distribution of galaxies in its neighbourhood.

We have determined that HIZOA J0836-43 is unique amongst known H I-massive galaxies. The galaxy is undergoing a vigorous LIRG starburst central to its H I disk, with a SFR of 20.5 $M_\odot$ yr^{-1}. Given the galaxy's stellar mass, $M_{\rm stellar} = 4.4 \pm 1.4 \times 10^{10}\,M_\odot$, its specific star formation rate indicates that the galaxy is in a phase of active stellar building, fueled by its huge reservoir of gas.

HIZOA J0836-43 has exceptionally strong PAH emission as seen in its 8 μm photometry, as well as the prominent emission bands in its spectra ($L_{7.7\mu{\rm m}} = 1.50 \times 10^9 L_\odot$). This PAH emission is produced within photodissociation regions associated with the active star formation taking place in the galaxy. Compared to other starburst systems, the PAH emission in HIZOA J0836-43 appears to be particularly intense. The 6.2 and 7.7 μm PAH features have equivalent widths of 0.72 μm and 0.82, μm, which are ~20% and 50% respectively, larger than the average value of 0.53 μm found for starbursts. However, most of the bolometric energy is dominated by dust emission longwards of 60 μm. The mid-infared emission from HIZOA J0836-43 appears to come predominantly from cold dust.

In strong contrast to the luminous emission from PAHs and cold dust in the galaxy, its 24 μm emission is low compared to other starforming and starburst systems. The 24 μm photometry and dust continuum seen in its high resolution spectra show independently the paucity of emission from warm dust. The lack of emission from Very Small Grains (VSGs), believed to be the source of the mid-infrared continuum, suggests that the interstellar medium conditions are atypical for a starburst or LIRG system. This could be due to a lack of small grains, or alternatively a weak or dust-cloaked radiation field causing the VSGs to emit at longer wavelengths.

The relative strengths of PAH and continuum emission are an indicator of the contributions from different sources of mid-infrared emission. Such strong PAH emission coupled with a weak MIR continuum is indicative of PDR dominated emission. In this regard, the galaxy has emission characteristics similar to PDRs observed in reflection nebulae, and unlike any other extragalactic system in its extreme PDR-emission properties.

HIZOA J0836-43 has a prominent bulge of evolved stars, as seen in its J, H, K_s, IRAC-1 and IRAC-2 photometry, indicating past centralised star formation. However, the 8 μm photometry and combined PAH emission spectral maps (6.6 μm, 7.7 μm and 11.3 μm) show that the PAH emission, and therefore star formation, is extended with respect to the stellar population (as traced by the 4.5 μm photometry). This suggests that we are observing a galaxy in the process of building its stellar disk, an instance of inside-out disk growth thought to be ubiquitous at higher redshifts, but rare in the local universe.

HIZOA J0836-43 possesses at least two satellite galaxies, as inferred from the small angular separations ($\sim$ 140 kpc) and their similar photometric redshifts (z $\sim$ 0.035). Both galaxies have a much smaller stellar mass compare to HIZOA J0836-43, and one of them has infrared emission properties that suggest active star formation.

The immediate environment of the galaxy appears conducive to the survival of an H I-massive disk, as the galaxy has relatively few neighbours and appears to exist in an underdense region. On a larger scale, we note that the galaxy appears to reside in a “transition” region between a void-like structure and a concentration of low mass galaxies. HIZOA J0836-43 lies on the edge of this concentration, which is noticably lacking in massive and L^* galaxies. The abundance of gas and dust in such a region would likely have been crucial to the galaxy’s formation and subsequent evolution.

HIZOA J0836-43 appears enigmatic in the local universe. Its large H I content and central starburst causes it to resemble a “scaled-up” galaxy in the process of actively building a disk. Its specific star formation rate in combination with its stellar mass appears more typical of $z \sim 0.7$ systems, where gas fractions were likely higher on average. The formation of HIZOA J0836-43 and its evolution to a PDR-dominated, H I-massive LIRG makes it enigmatic in the local universe. It poses a challenge for models of hierarchical structure formation, and its properties will likely have widespread implications for theories of gas-rich disk galaxy formation and evolution.

Chapter 8

Future Work on HIZOA J0836-43

As a final Section to this dissertation, but also as a continuing study of the mechanisms at work within and around HIZOA J0836-43, we outline planned future observations and analysis.

We plan to submit a proposal to the Australia Telescope Compact Array (ATCA) for further H I observations of HIZOA J0836-43. Using an optimised baseline configuration will provide better spectral resolution of substructure in the H I disk. This will allow us to study the apparent warp in the disk and look for clues regarding the extent of past interactions with satellites and neighbouring galaxies. We aim to determine if the galaxy is currently accreting gas or has a cohesive H I-disk in place.

Molecular CO observations of the galaxy will provide an indication of the molecular hydrogen content of the galaxy. Currently we have only the MIR warm H_2 and FIR dust emission to deduce the molecular gas that is fueling the starburst. The geometry and distribution of this gas will help resolve key issues regarding the mechanisms that produce the combination of intense star formation, copious PDR emission and weakly rising mid-infrared continuum seen in HIZOA J0836-43.

In an effort to probe the state of the cold interstellar gas that is traced by FIR emission lines, we will propose to use the Herschel Space Observatory and its Photodetector Array Camera and Spectrometer (PACS) instrument. For example, by mapping the HIZOA J0836-43 nucleus using the powerful molecular cloud tracer, neutral hydrogen at $63\,\mu$m, we may discern the geometry and chemical state (e.g., metallicity) of the starburst.

We wish to obtain an accurate picture of the 3-D distribution of galaxies in the neighbourhood of HIZOA J0836-43. The NIR photometric redshifts have an intrinsic uncertainty, $\sim 20-30\%$, that smears out the spatial structures. To this end we require spectroscopic redshifts of galaxies close to HIZOA J0836-43, as well as galaxies in its greater environment, in order to accurately probe the large scale structure in this region. Spectroscopic redshifts will also allow us to determine the extinction more accurately by means of SED-fitting. We plan to use the South African Large Telescope (SALT) to acquire the radial velocity measurements. Alternatively, we propose to use the AAOmega, the spectrograph mounted on the Anglo-Australian Telescope. This instrument can perform multi-object spectroscopy of 392 objects, using fibres with a $2''$

angular size. Its 2° field of view is ideal for our survey requirements.

South Africa currently has a bid to host the SKA (Square Kilometer Array). As part of this endeavour, South Africa is building a prototype radio telescope array, MeerKat. By 2012 it will have 80 dishes in place with a spatial resolution of $10''$ resolution and an instantaneous field of view of 0.73 deg^2. Due to the unfortunate location of HIZOA J0836-43, radio observations have been contaminated by the continuum emission from the Milky Way and the Vela Supernova Remnant. Since Meerkat is an interferometer with a beam that will resolve the galaxy, this will greatly mitigate this problem. MeerKat will enable unprecedented depth and clarity of HIZOA J0836-43 and its environment.

Appendix A

Observations

A.1 IRSF Survey Observations

Details of the IRSF survey observations (date observed, central pointing, seeing and magnitude zeropoints) of the HIZOA J0836-43 region are shown in Table A.1 (see Fig. 2.6 for the layout of fields in Right Ascension and Declination).

Table A.1: IRSF Observations

Image	**Date Observed**	**Right Ascension (J2000)**	**Declination (J2000)**	**Seeing** (J; H; K_s)	**Zeropoint** [a] (J; H; K_s) **(mag)**		
HIZOA−6+0	2006-04-08	$08^{h}33^{m}00.4^{s}$	-43°37′51.2″	1.4″; 1.5″; 1.3″	20.81	20.95	20.17
HIZOA−6+1	2006-04-08	$08^{h}33^{m}00.4^{s}$	-43°30′51.2″	1.6″; 1.5″; 1.4″	20.81	20.96	20.18
HIZOA−6−1	2006-04-08	$08^{h}33^{m}00.4^{s}$	-43°44′51.6″	1.4″; 1.4″; 1.3″	20.82	20.95	20.18
HIZOA−6+2	2006-04-08	$08^{h}33^{m}00.4^{s}$	-43°23′51.0″	1.7″; 1.6″; 1.4″	20.79	20.94	20.17
HIZOA−6−2	2006-04-08	$08^{h}33^{m}00.4^{s}$	-43°51′51.6″	1.6″; 1.6″; 1.4″	20.82	20.96	20.18
HIZOA−6+3	2006-04-08	$08^{h}33^{m}00.4^{s}$	-43°16′51.0″	1.6″; 1.5″; 1.3″	20.82	20.94	20.18
HIZOA−6−3	2006-04-08	$08^{h}33^{m}00.4^{s}$	-43°58′51.2″	1.5″; 1.5″; 1.4″	20.82	20.97	20.19
HIZOA−6+4	2006-04-08	$08^{h}33^{m}00.4^{s}$	-43°09′50.7″	1.6″; 1.5″; 1.4″	20.80	20.95	20.19
HIZOA−6−4	2006-04-08	$08^{h}33^{m}00.4^{s}$	-44°05′51.4″	1.4″; 1.5″; 1.3″	20.81	20.94	20.18
HIZOA−6−5	2006-04-07	$08^{h}33^{m}00.4^{s}$	-44°12′51.5″	1.9″; 1.8″; 1.6″	20.78	20.93	20.16
HIZOA−6+5	2006-04-08	$08^{h}33^{m}00.4^{s}$	-43°02′51.1″	1.6″; 1.5″; 1.4″	20.82	20.95	20.19
HIZOA−6−6	2006-04-07	$08^{h}33^{m}00.4^{s}$	-44°19′51.3″	1.8″; 1.8″; 1.6″	20.76	20.92	20.14
HIZOA−6+6	2006-04-08	$08^{h}33^{m}00.4^{s}$	-42°55′51.1″	1.9″; 1.7″; 1.5″	20.81	20.94	20.16
HIZOA−5+0	2006-03-18	$08^{h}33^{m}39.1^{s}$	-43°37′51.2″	1.8″; 1.6″; 1.5″	20.76	20.92	20.12
HIZOA−5+1	2006-04-03	$08^{h}33^{m}39.1^{s}$	-43°30′51.5″	1.3″; 1.3″; 1.1″	20.71	20.88	20.07
HIZOA−5−1	2006-04-10	$08^{h}33^{m}39.1^{s}$	-43°44′51.1″	1.5″; 1.5″; 1.2″	20.78	20.93	20.16
HIZOA−5+2	2006-03-21	$08^{h}33^{m}39.1^{s}$	-43°23′51.1″	1.7″; 1.6″; 1.5″	20.81	20.95	20.17
HIZOA−5−2	2006-03-21	$08^{h}33^{m}39.1^{s}$	-43°51′51.1″	1.8″; 1.8″; 1.6″	20.83	20.97	20.17
HIZOA−5+3	2006-03-22	$08^{h}33^{m}39.1^{s}$	-43°16′51.3″	1.4″; 1.4″; 1.2″	20.82	20.95	20.14

Table A.1: IRSF Observations

Image	**Date Observed**	**Right Ascension (J2000)**	**Declination (J2000)**	**Seeing** (J; H; K_s)	**Zeropoint** ^{a} (J; H; K_s) **(mag)**
HIZOA−5−3	2007-04-05	$08^h33^m39.1^s$	-43°58′51.1″	1.4″; 1.3″; 1.1″	20.85 20.96 20.19
HIZOA−5+4	2006-03-26	$08^h33^m39.1^s$	-43°09′51.0″	1.5″; 1.5″; 1.3″	20.79 20.95 20.15
HIZOA−5−4	2006-03-26	$08^h33^m39.1^s$	-44°05′51.2″	1.5″; 1.5″; 1.3″	20.81 20.96 20.16
HIZOA−5+5	2006-03-28	$08^h33^m39.0^s$	-43°02′51.0″	1.6″; 1.6″; 1.5″	20.76 20.92 20.13
HIZOA−5−5	2006-03-30	$08^h33^m39.1^s$	-44°12′51.0″	1.1″; 1.1″; 0.9″	20.84 20.98 20.20
HIZOA−5−6	2006-04-04	$08^h33^m39.1^s$	-44°19′51.4″	1.4″; 1.3″; 1.2″	20.73 20.88 20.11
HIZOA−5+6	2006-04-06	$08^h33^m39.1^s$	-42°55′51.4″	1.7″; 1.9″; 1.7″	20.74 20.89 20.10
HIZOA−4+0	2006-03-18	$08^h34^m17.8^s$	-43°37′51.0″	1.7″; 1.6″; 1.4″	20.77 20.92 20.14
HIZOA−4+1	2006-04-03	$08^h34^m17.8^s$	-43°30′51.7″	1.3″; 1.3″; 1.2″	20.71 20.85 20.05
HIZOA−4−1	2006-04-10	$08^h34^m17.8^s$	-43°44′50.8″	1.4″; 1.3″; 1.2″	20.78 20.93 20.16
HIZOA−4+2	2006-03-21	$08^h34^m17.8^s$	-43°23′51.3″	1.6″; 1.6″; 1.4″	20.81 20.93 20.16
HIZOA−4−2	2006-03-21	$08^h34^m17.8^s$	-43°51′50.8″	1.9″; 1.8″; 1.6″	20.86 20.97 20.18
HIZOA−4+3	2006-03-22	$08^h34^m17.8^s$	-43°16′51.2″	1.3″; 1.3″; 1.1″	20.81 20.94 20.17
HIZOA−4−3	2006-03-23	$08^h34^m17.8^s$	-43°58′51.4″	1.3″; 1.3″; 1.1″	20.87 21.00 20.21
HIZOA−4+4	2006-03-25	$08^h34^m17.8^s$	-43°09′51.4″	1.3″; 1.1″; 1.0″	20.80 20.93 20.15
HIZOA−4−4	2006-03-26	$08^h34^m17.8^s$	-44°05′50.9″	1.5″; 1.4″; 1.3″	20.85 20.98 20.17
HIZOA−4+5	2006-03-28	$08^h34^m17.8^s$	-43°02′51.9″	1.6″; 1.6″; 1.4″	20.79 20.91 20.14
HIZOA−4−5	2006-03-30	$08^h34^m17.8^s$	-44°12′51.0″	1.2″; 1.2″; 1.0″	20.84 20.97 20.18
HIZOA−4−6	2006-04-04	$08^h34^m17.8^s$	-44°19′51.6″	1.4″; 1.3″; 1.2″	20.75 20.90 20.10
HIZOA−4+6	2006-04-06	$08^h34^m17.8^s$	-42°55′51.6″	1.7″; 1.7″; 1.5″	20.76 20.90 20.12
HIZOA−3+0	2006-04-11	$08^h34^m56.4^s$	-43°37′51.1″	1.2″; 1.2″; 1.0″	20.78 20.92 20.14
HIZOA−3+1	2006-04-03	$08^h34^m56.4^s$	-43°30′51.4″	1.3″; 1.3″; 1.2″	20.72 20.85 20.05
HIZOA−3−1	2006-04-10	$08^h34^m56.4^s$	-43°44′50.9″	1.4″; 1.3″; 1.1″	20.77 20.93 20.14
HIZOA−3+2	2006-03-21	$08^h34^m56.5^s$	-43°23′51.5″	1.7″; 1.6″; 1.5″	20.78 20.93 20.16
HIZOA−3−2	2006-04-11	$08^h34^m56.4^s$	-43°51′51.5″	1.2″; 1.3″; 1.1″	20.84 20.98 20.18
HIZOA−3+3	2006-03-22	$08^h34^m56.4^s$	-43°16′51.3″	1.3″; 1.3″; 1.1″	20.79 20.95 20.16
HIZOA−3−3	2006-03-23	$08^h34^m56.4^s$	-43°58′51.7″	1.3″; 1.2″; 1.1″	20.83 20.97 20.19
HIZOA−3+4	2006-03-25	$08^h34^m56.4^s$	-43°09′51.4″	1.2″; 1.2″; 1.0″	20.78 20.95 20.17
HIZOA−3−4	2006-03-26	$08^h34^m56.4^s$	-44°05′51.3″	1.5″; 1.5″; 1.3″	20.83 20.97 20.15
HIZOA−3+5	2006-03-28	$08^h34^m56.4^s$	-43°02′51.6″	1.4″; 1.4″; 1.3″	20.78 20.94 20.16
HIZOA−3−5	2006-03-30	$08^h34^m56.4^s$	-44°12′51.0″	1.3″; 1.2″; 1.1″	20.85 20.98 20.20
HIZOA−3−6	2006-04-04	$08^h34^m56.4^s$	-44°19′51.3″	1.5″; 1.4″; 1.3″	20.75 20.91 20.12
HIZOA−3+6	2006-04-06	$08^h34^m56.4^s$	-42°55′51.3″	1.7″; 1.6″; 1.4″	20.76 20.91 20.13
HIZOA−2+0	2006-04-11	$08^h35^m35.1^s$	-43°37′50.9″	1.2″; 1.2″; 0.9″	20.77 21.03 20.16
HIZOA−2+1	2006-04-03	$08^h35^m35.1^s$	-43°30′50.9″	1.4″; 1.4″; 1.3″	20.65 20.94 20.14
HIZOA−2−1	2006-04-10	$08^h35^m35.1^s$	-43°44′51.3″	1.4″; 1.3″; 1.2″	20.75 20.98 20.19
HIZOA−2+2	2006-03-21	$08^h35^m35.1^s$	-43°23′51.5″	1.7″; 1.6″; 1.5″	20.78 20.96 20.18
HIZOA−2−2	2006-04-11	$08^h35^m35.1^s$	-43°51′51.4″	1.2″; 1.3″; 1.1″	20.81 21.05 20.30
HIZOA−2+3	2006-03-22	$08^h35^m35.1^s$	-43°16′50.9″	1.2″; 1.2″; 1.1″	20.79 20.95 20.15

Table A.1: IRSF Observations

Image	**Date Observed**	**Right Ascension (J2000)**	**Declination (J2000)**	**Seeing** (J; H; K_s)	**Zeropoint** [a] (J; H; K_s) **(mag)**		
HIZOA−2−3	2006-03-23	$08^{h}35^{m}35.1^{s}$	-43°58′51.4″	1.2″; 1.2″; 1.1″	20.87	20.97	20.21
HIZOA−2+4	2006-03-25	$08^{h}35^{m}35.1^{s}$	-43°09′51.4″	1.2″; 1.2″; 1.1″	20.78	20.95	20.14
HIZOA−2−4	2006-03-26	$08^{h}35^{m}35.1^{s}$	-44°05′51.2″	1.6″; 1.5″; 1.3″	20.85	20.95	20.17
HIZOA−2+5	2006-03-28	$08^{h}35^{m}35.1^{s}$	-43°02′51.5″	1.3″; 1.3″; 1.2″	20.79	20.95	20.15
HIZOA−2−5	2006-03-30	$08^{h}35^{m}35.1^{s}$	-44°12′51.2″	1.3″; 1.2″; 1.0″	20.87	20.98	20.21
HIZOA−2−6	2006-04-04	$08^{h}35^{m}35.1^{s}$	-44°19′51.7″	1.5″; 1.5″; 1.3″	20.75	20.91	20.11
HIZOA−2+6	2006-04-06	$08^{h}35^{m}35.1^{s}$	-42°55′51.2″	2.0″; 2.0″; 1.6″	20.76	20.93	20.13
HIZOA−1+0	2006-04-11	$08^{h}36^{m}13.8^{s}$	-43°37′51.1″	1.2″; 1.1″; 0.9″	20.76	21.00	20.20
HIZOA−1+1	2006-04-03	$08^{h}36^{m}13.8^{s}$	-43°30′51.1″	1.5″; 1.6″; 1.4″	20.74	20.92	20.11
HIZOA−1−1	2006-04-10	$08^{h}36^{m}13.8^{s}$	-43°44′51.1″	1.4″; 1.3″; 1.1″	20.77	20.96	20.20
HIZOA−1+2	2006-03-21	$08^{h}36^{m}13.8^{s}$	-43°23′51.5″	1.7″; 1.6″; 1.5″	20.77	21.02	20.19
HIZOA−1−2	2006-04-11	$08^{h}36^{m}13.8^{s}$	-43°51′51.5″	1.2″; 1.2″; 1.0″	20.85	21.05	20.32
HIZOA−1+3	2006-03-22	$08^{h}36^{m}13.8^{s}$	-43°16′51.0″	1.3″; 1.3″; 1.1″	20.79	20.96	20.16
HIZOA−1−3	2006-03-26	$08^{h}36^{m}13.8^{s}$	-43°58′51.4″	1.6″; 1.5″; 1.4″	20.87	20.98	20.20
HIZOA−1+4	2006-03-25	$08^{h}36^{m}13.8^{s}$	-43°09′51.3″	1.3″; 1.3″; 1.1″	20.77	20.94	20.17
HIZOA−1−4	2006-03-26	$08^{h}36^{m}13.8^{s}$	-44°05′51.2″	1.7″; 1.6″; 1.4″	20.84	20.97	20.17
HIZOA−1+5	2006-03-28	$08^{h}36^{m}13.8^{s}$	-43°02′51.6″	1.3″; 1.3″; 1.2″	20.77	20.93	20.15
HIZOA−1−5	2006-03-30	$08^{h}36^{m}13.8^{s}$	-44°12′51.0″	1.4″; 1.3″; 1.1″	20.84	20.97	20.20
HIZOA−1−6	2006-04-04	$08^{h}36^{m}13.8^{s}$	-44°19′51.5″	1.6″; 1.5″; 1.4″	20.74	20.89	20.12
HIZOA−1+6	2006-04-06	$08^{h}36^{m}13.8^{s}$	-42°55′51.2″	1.9″; 2.1″; 1.7″	20.75	20.89	20.11
HIZOA+0+0	2006-04-11	$08^{h}36^{m}52.5^{s}$	-43°37′51.1″	1.1″; 1.1″; 1.0″	20.72	20.94	20.17
HIZOA+0+1	2006-04-03	$08^{h}36^{m}52.5^{s}$	-43°30′50.8″	1.4″; 1.5″; 1.4″	20.51	20.77	19.95
HIZOA+0−1	2006-04-10	$08^{h}36^{m}52.5^{s}$	-43°44′51.3″	1.4″; 1.3″; 1.1″	20.77	20.99	20.17
HIZOA+0+2	2006-03-21	$08^{h}36^{m}52.5^{s}$	-43°23′51.6″	1.8″; 1.7″; 1.5″	20.76	20.89	20.17
HIZOA+0−2	2006-04-11	$08^{h}36^{m}52.5^{s}$	-43°51′51.4″	1.1″; 1.1″; 1.0″	20.95	21.09	20.36
HIZOA+0+3	2006-03-22	$08^{h}36^{m}52.5^{s}$	-43°16′51.1″	1.3″; 1.3″; 1.1″	20.79	20.96	20.18
HIZOA+0−3	2006-03-26	$08^{h}36^{m}52.5^{s}$	-43°58′51.4″	1.7″; 1.7″; 1.5″	20.84	20.97	20.20
HIZOA+0+4	2006-03-25	$08^{h}36^{m}52.5^{s}$	-43°09′51.1″	1.4″; 1.4″; 1.2″	20.78	20.96	20.17
HIZOA+0−4	2006-03-26	$08^{h}36^{m}52.5^{s}$	-44°05′51.2″	1.6″; 1.5″; 1.4″	20.82	20.95	20.16
HIZOA+0+5	2006-03-28	$08^{h}36^{m}52.5^{s}$	-43°02′51.5″	1.4″; 1.4″; 1.2″	20.78	20.94	20.15
HIZOA+0−5	2006-03-30	$08^{h}36^{m}52.5^{s}$	-44°12′51.0″	1.3″; 1.2″; 1.1″	20.84	20.97	20.19
HIZOA+0−6	2006-04-04	$08^{h}36^{m}52.5^{s}$	-44°19′50.9″	1.5″; 1.5″; 1.3″	20.75	20.89	20.10
HIZOA+0+6	2006-04-06	$08^{h}36^{m}52.5^{s}$	-42°55′51.2″	1.7″; 1.7″; 1.5″	20.78	20.93	20.15
HIZOA+1+0	2006-04-11	$08^{h}37^{m}31.2^{s}$	-43°37′51.0″	1.2″; 1.1″; 0.9″	20.76	21.02	20.18
HIZOA+1+1	2006-04-03	$08^{h}37^{m}31.2^{s}$	-43°30′50.9″	1.4″; 1.5″; 1.3″	20.75	20.40	20.11
HIZOA+1−1	2006-04-10	$08^{h}37^{m}31.2^{s}$	-43°44′51.2″	1.4″; 1.2″; 1.1″	20.83	21.01	20.22
HIZOA+1+2	2006-03-21	$08^{h}37^{m}31.2^{s}$	-43°23′51.5″	1.6″; 1.6″; 1.4″	20.84	21.05	20.31
HIZOA+1−2	2006-03-21	$08^{h}37^{m}31.2^{s}$	-43°51′51.2″	1.9″; 1.7″; 1.5″	20.85	21.09	20.33
HIZOA+1+3	2006-03-22	$08^{h}37^{m}31.2^{s}$	-43°16′51.0″	1.4″; 1.3″; 1.2″	20.80	20.94	20.16

Table A.1: IRSF Observations

Image	**Date Observed**	**Right Ascension (J2000)**	**Declination (J2000)**	**Seeing** (J; H; K_s)	**Zeropoint** [a] (J; H; K_s) **(mag)**		
HIZOA+1−3	2006-03-26	$08^h37^m31.2^s$	-43°58′51.8″	1.4″; 1.3″; 1.2″	20.82	20.97	20.19
HIZOA+1+4	2006-03-25	$08^h37^m31.2^s$	-43°09′50.9″	1.4″; 1.4″; 1.2″	20.77	20.93	20.14
HIZOA+1−4	2006-03-26	$08^h37^m31.2^s$	-44°05′51.1″	1.6″; 1.5″; 1.3″	20.80	20.97	20.16
HIZOA+1+5	2006-03-28	$08^h37^m31.2^s$	-43°02′51.1″	1.5″; 1.4″; 1.3″	20.58	20.75	19.93
HIZOA+1−5	2006-03-30	$08^h37^m31.3^s$	-44°12′51.2″	1.4″; 1.3″; 1.1″	20.82	20.97	20.19
HIZOA+1−6	2006-04-04	$08^h37^m31.2^s$	-44°19′51.2″	1.5″; 1.5″; 1.3″	20.75	20.92	20.14
HIZOA+1+6	2006-04-06	$08^h37^m31.2^s$	-42°55′51.1″	1.7″; 1.7″; 1.5″	20.76	20.94	20.15
HIZOA+2+0	2006-03-18	$08^h38^m09.9^s$	-43°37′50.8″	1.7″; 1.5″; 1.4″	20.78	20.96	20.13
HIZOA+2+1	2006-04-03	$08^h38^m09.9^s$	-43°30′51.3″	1.5″; 1.4″; 1.3″	20.76	21.01	20.20
HIZOA+2−1	2006-04-10	$08^h38^m09.9^s$	-43°44′51.3″	1.3″; 1.2″; 1.1″	20.77	20.90	20.09
HIZOA+2+2	2006-03-21	$08^h38^m09.9^s$	-43°23′51.2″	1.9″; 1.8″; 1.6″	20.83	21.06	20.30
HIZOA+2−2	2006-03-21	$08^h38^m09.9^s$	-43°51′51.3″	1.8″; 1.7″; 1.5″	20.84	21.10	20.36
HIZOA+2+3	2006-03-22	$08^h38^m09.9^s$	-43°16′51.0″	1.4″; 1.3″; 1.2″	20.78	20.94	20.16
HIZOA+2−3	2006-03-26	$08^h38^m09.9^s$	-43°58′51.5″	1.5″; 1.4″; 1.3″	20.83	20.95	20.20
HIZOA+2+4	2006-03-25	$08^h38^m09.9^s$	-43°09′51.0″	1.5″; 1.5″; 1.3″	20.78	20.95	20.16
HIZOA+2−4	2006-03-26	$08^h38^m09.9^s$	-44°05′51.0″	1.6″; 1.5″; 1.3″	20.82	20.96	20.17
HIZOA+2+5	2006-03-28	$08^h38^m09.9^s$	-43°02′51.1″	1.5″; 1.5″; 1.3″	20.74	20.91	20.12
HIZOA+2−5	2006-03-30	$08^h38^m09.9^s$	-44°12′51.3″	1.4″; 1.3″; 1.1″	20.83	20.96	20.19
HIZOA+2−6	2006-04-04	$08^h38^m09.9^s$	-44°19′51.2″	1.4″; 1.4″; 1.2″	20.74	20.91	20.16
HIZOA+2+6	2006-04-06	$08^h38^m09.9^s$	-42°55′51.1″	1.7″; 1.6″; 1.4″	20.78	20.93	20.15
HIZOA+3+0	2006-03-18	$08^h38^m48.6^s$	-43°37′50.9″	1.7″; 1.5″; 1.3″	20.82	20.95	20.14
HIZOA+3+1	2007-04-05	$08^h38^m48.6^s$	-43°30′51.3″	1.3″; 1.3″; 1.1″	20.76	20.92	20.13
HIZOA+3−1	2008-03-19	$08^h38^m48.6^s$	-43°44′51.8″	1.6″; 1.5″; 1.3″	20.83	20.95	20.14
HIZOA+3+2	2006-03-21	$08^h38^m48.6^s$	-43°23′51.9″	1.7″; 1.8″; 1.6″	20.78	20.93	20.16
HIZOA+3−2	2006-03-21	$08^h38^m48.6^s$	-43°51′51.4″	1.8″; 1.7″; 1.5″	20.82	20.96	20.16
HIZOA+3+3	2006-03-22	$08^h38^m48.6^s$	-43°16′51.2″	1.5″; 1.4″; 1.3″	20.79	20.95	20.17
HIZOA+3−3	2006-03-26	$08^h38^m48.6^s$	-43°58′51.5″	1.5″; 1.4″; 1.2″	20.81	20.98	20.16
HIZOA+3+4	2006-03-25	$08^h38^m48.6^s$	-43°09′51.3″	1.4″; 1.5″; 1.3″	20.80	20.96	20.17
HIZOA+3−4	2006-03-26	$08^h38^m48.6^s$	-44°05′51.2″	1.8″; 1.6″; 1.5″	20.81	20.98	20.16
HIZOA+3+5	2006-03-28	$08^h38^m48.6^s$	-43°02′51.2″	1.7″; 1.6″; 1.5″	20.75	20.93	20.13
HIZOA+3−5	2006-03-30	$08^h38^m48.7^s$	-44°12′51.2″	1.4″; 1.3″; 1.1″	20.80	20.96	20.17
HIZOA+3−6	2006-04-04	$08^h38^m48.6^s$	-44°19′51.0″	1.5″; 1.4″; 1.2″	20.77	20.94	20.14
HIZOA+3+6	2006-04-06	$08^h38^m48.6^s$	-42°55′50.8″	1.5″; 1.5″; 1.3″	20.79	20.96	20.16
HIZOA+4+0	2006-03-18	$08^h39^m27.2^s$	-43°37′51.1″	1.6″; 1.5″; 1.3″	20.78	20.94	20.15
HIZOA+4+1	2006-04-03	$08^h39^m27.2^s$	-43°30′51.2″	1.5″; 1.5″; 1.3″	20.77	20.90	20.09
HIZOA+4−1	2008-03-19	$08^h39^m27.2^s$	-43°44′51.0″	1.5″; 1.4″; 1.3″	20.78	20.93	20.14
HIZOA+4+2	2006-03-21	$08^h39^m27.2^s$	-43°23′50.9″	1.7″; 1.7″; 1.5″	20.79	20.97	20.15
HIZOA+4−2	2006-03-21	$08^h39^m27.2^s$	-43°51′51.5″	1.6″; 1.5″; 1.3″	20.83	20.97	20.18
HIZOA+4+3	2006-03-22	$08^h39^m27.2^s$	-43°16′51.0″	1.4″; 1.3″; 1.1″	20.77	20.94	20.15

Table A.1: IRSF Observations

Image	**Date Observed**	**Right Ascension (J2000)**	**Declination (J2000)**	**Seeing** (J; H; K_s)	**Zeropoint** [a] (J; H; K_s) (mag)		
HIZOA+4−3	2006-03-26	$08^{h}39^{m}27.2^{s}$	-43°58′51.6″	1.6″; 1.5″; 1.3″	20.83	20.98	20.19
HIZOA+4+4	2006-03-25	$08^{h}39^{m}27.2^{s}$	-43°09′51.3″	1.5″; 1.5″; 1.4″	20.77	20.93	20.15
HIZOA+4−4	2006-03-26	$08^{h}39^{m}27.2^{s}$	-44°05′51.3″	1.7″; 1.6″; 1.4″	20.80	20.95	20.18
HIZOA+4+5	2006-03-28	$08^{h}39^{m}27.2^{s}$	-43°02′50.9″	1.6″; 1.5″; 1.4″	20.75	20.92	20.14
HIZOA+4−5	2006-03-30	$08^{h}39^{m}27.2^{s}$	-44°12′51.5″	1.4″; 1.3″; 1.1″	20.81	20.96	20.22
HIZOA+4−6	2006-04-04	$08^{h}39^{m}27.2^{s}$	-44°19′51.0″	1.4″; 1.5″; 1.3″	20.76	20.94	20.14
HIZOA+4+6	2006-04-06	$08^{h}39^{m}27.2^{s}$	-42°55′51.2″	1.5″; 1.5″; 1.3″	20.80	20.97	20.17
HIZOA+5+0	2006-03-18	$08^{h}40^{m}06.0^{s}$	-43°37′50.9″	1.9″; 1.8″; 1.5″	20.75	20.90	20.12
HIZOA+5+1	2006-04-03	$08^{h}40^{m}05.9^{s}$	-43°30′51.3″	1.5″; 1.5″; 1.3″	20.74	20.91	20.07
HIZOA+5−1	2008-03-19	$08^{h}40^{m}05.9^{s}$	-43°44′50.9″	1.6″; 1.6″; 1.4″	20.77	20.89	20.09
HIZOA+5+2	2006-03-21	$08^{h}40^{m}05.9^{s}$	-43°23′51.0″	1.7″; 1.6″; 1.5″	20.78	20.95	20.16
HIZOA+5−2	2006-03-21	$08^{h}40^{m}05.9^{s}$	-43°51′51.4″	1.7″; 1.5″; 1.4″	20.81	20.93	20.17
HIZOA+5+3	2006-03-22	$08^{h}40^{m}05.9^{s}$	-43°16′51.2″	1.5″; 1.4″; 1.2″	20.79	20.96	20.16
HIZOA+5−3	2006-03-26	$08^{h}40^{m}05.9^{s}$	-43°58′51.4″	1.6″; 1.5″; 1.3″	20.83	20.98	20.20
HIZOA+5+4	2006-03-25	$08^{h}40^{m}05.9^{s}$	-43°09′50.8″	1.5″; 1.5″; 1.4″	20.76	20.96	20.14
HIZOA+5−4	2006-03-26	$08^{h}40^{m}05.9^{s}$	-44°05′51.2″	1.7″; 1.6″; 1.4″	20.82	20.98	20.20
HIZOA+5+5	2006-03-28	$08^{h}40^{m}05.9^{s}$	-43°02′51.0″	1.6″; 1.5″; 1.4″	20.76	20.94	20.13
HIZOA+5−5	2006-03-30	$08^{h}40^{m}05.9^{s}$	-44°12′51.4″	1.4″; 1.2″; 1.1″	20.83	20.97	20.22
HIZOA+5−6	2006-04-04	$08^{h}40^{m}05.9^{s}$	-44°19′51.0″	1.5″; 1.4″; 1.3″	20.76	20.91	20.15
HIZOA+5+6	2006-04-06	$08^{h}40^{m}05.9^{s}$	-42°55′51.1″	1.5″; 1.5″; 1.3″	20.76	20.94	20.14
HIZOA+6+0	2006-04-09	$08^{h}40^{m}44.6^{s}$	-43°37′51.1″	1.6″; 1.5″; 1.3″	20.82	20.96	20.18
HIZOA+6+1	2006-04-09	$08^{h}40^{m}44.6^{s}$	-43°30′51.0″	1.7″; 1.6″; 1.5″	20.82	20.95	20.18
HIZOA+6−1	2006-04-09	$08^{h}40^{m}44.6^{s}$	-43°44′51.1″	1.5″; 1.5″; 1.3″	20.83	20.95	20.18
HIZOA+6+2	2006-04-09	$08^{h}40^{m}44.6^{s}$	-43°23′50.9″	1.7″; 1.5″; 1.4″	20.82	20.94	20.16
HIZOA+6−2	2006-04-09	$08^{h}40^{m}44.6^{s}$	-43°51′51.2″	1.5″; 1.4″; 1.3″	20.82	20.95	20.18
HIZOA+6+3	2006-04-09	$08^{h}40^{m}44.6^{s}$	-43°16′51.3″	1.6″; 1.5″; 1.4″	20.79	20.94	20.15
HIZOA+6−3	2006-04-09	$08^{h}40^{m}44.6^{s}$	-43°58′51.5″	1.5″; 1.5″; 1.4″	20.81	20.95	20.18
HIZOA+6+4	2006-04-09	$08^{h}40^{m}44.6^{s}$	-43°09′51.1″	1.7″; 1.6″; 1.5″	20.80	20.92	20.15
HIZOA+6−4	2006-04-09	$08^{h}40^{m}44.6^{s}$	-44°05′51.7″	1.4″; 1.4″; 1.3″	20.80	20.96	20.17
HIZOA+6+5	2006-04-09	$08^{h}40^{m}44.6^{s}$	-43°02′51.2″	1.7″; 1.6″; 1.4″	20.80	20.92	20.15
HIZOA+6−5	2006-04-09	$08^{h}40^{m}44.6^{s}$	-44°12′51.5″	1.5″; 1.5″; 1.4″	20.80	20.96	20.17
HIZOA+6+6	2006-04-09	$08^{h}40^{m}44.6^{s}$	-42°55′51.0″	1.8″; 1.7″; 1.5″	20.78	20.93	20.15
HIZOA+6−6	2006-04-09	$08^{h}40^{m}44.6^{s}$	-44°19′51.5″	1.8″; 1.8″; 1.6″	20.79	20.93	20.15

A.2 Resolving HIZOA J0836-43 at 24 μm

The MIPS instrument has diffraction limited-limited imaging as a result of the MIPS pixels scales and the telescope's Point Spread Function (PSF). The profiles of the MIPS 24 μm Point Response Functions (PRF) is shown in Fig. A.1 with the profile of the Massive Galaxy at this wavelengths shown for comparison. Simplistically, we can think of a PSF as an image of a point source (i.e. before sampling from the detector), whereas a PRF is a list of responses of the mosaic pixels to a point source (i.e. relative pixel values output from the array). This incorporates intra-pixel sensitivity variations. The MIPS PRF profile plotted in Fig. A.1 is from the SSC APEX calibration files [1] and is resampled.

As can be seen the galaxy's emission is extended compared to the MIPS-24 μm PRF. So, although we do not resolve the nucleus, we do resolve the galaxy enough to see extended emission. The galaxy is not resolved at 70 μm and 160 μm.

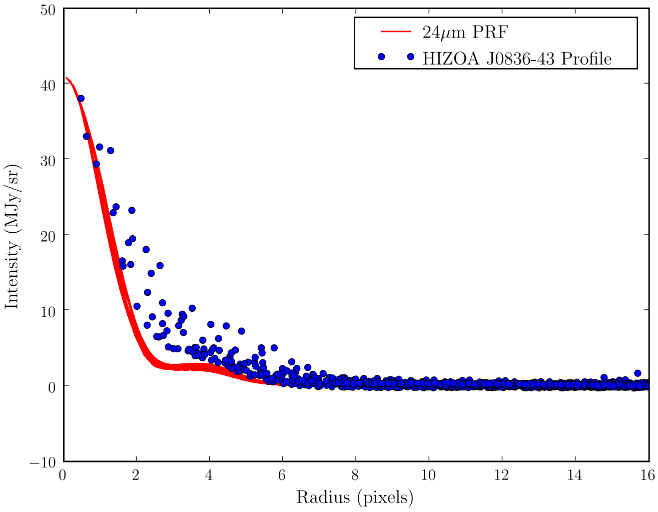

Figure A.1: MIPS PRF Profile for the 24 μm band (black) with measurements of the HIZOA J0836-43 profile shown in blue

---

[1] http://ssc.spitzer.caltech.edu/mips/dh/index.html

Appendix B

Spitzer Survey

This Appendix contains the catalogues described in Chapter 6. This consists of sources observed by *Spitzer* and the IRSF (MIR and NIR measurements) as listed in Section B.1 and sources with IRSF (NIR) measurements only listed in Section B.2.

B.1 Spitzer + IRSF Catalogue

B.1.1 Photometric Parameters

Table B.1 lists the photometric parameters for sources in the *Spitzer* footprint as follows:

Column 1: Reference ID
Column 2: Source IRSF ID
Column 3: Right Ascension
Column 4: Declination
Column 5: Galactic Longitude (deg)
Column 6: Galactic Latitute (deg)
Column 7: A_V (mag)
Column 8: Isophotal Radius, a (arcsec)
Column 9: Axis ratio, b/a
Column 10: Position Angle (deg) – measured east of north

In this Table, HIZOA J0836-43 is source 31, Companion A is source 24 and Companion B is source 34.

Table B.1: Spitzer + IRSF Catalogue - Photometric Parameters.

ID	Source ID.	R.A. (J2000)	Dec. (J2000)	l (deg)	b (deg)	A_V (mag)	a (arcsec)	b/a	P.A. (deg)
1	08353645-4319330	$08^{h}\,35^{m}\,36.5^{s}$	$-43^\circ19'33.0''$	262.10	-1.64	8.1	4.84	1.00	0.0
2	08354552-4349514	$08^{h}\,35^{m}\,45.5^{s}$	$-43^\circ49'51.4''$	262.52	-1.92	4.8	5.16	1.00	0.0
3	08354566-4322322	$08^{h}\,35^{m}\,45.7^{s}$	$-43^\circ22'32.2''$	262.15	-1.65	5.8	5.91	1.00	0.0
4	08354584-4317422	$08^{h}\,35^{m}\,45.8^{s}$	$-43^\circ17'42.2''$	262.09	-1.60	6.9	7.55	1.00	0.0
5	08354707-4326455	$08^{h}\,35^{m}\,47.1^{s}$	$-43^\circ26'45.6''$	262.21	-1.69	5.8	3.66	1.00	0.0
6	08354735-4325524	$08^{h}\,35^{m}\,47.4^{s}$	$-43^\circ25'52.5''$	262.20	-1.68	5.8	5.25	1.00	0.0
7	08354788-4319169	$08^{h}\,35^{m}\,47.9^{s}$	$-43^\circ19'17.0''$	262.12	-1.61	6.9	3.73	1.00	0.0
8	08354796-4328263	$08^{h}\,35^{m}\,48.0^{s}$	$-43^\circ28'26.3''$	262.24	-1.70	5.8	5.32	1.00	0.0
9	08354984-4322381	$08^{h}\,35^{m}\,49.8^{s}$	$-43^\circ22'38.1''$	262.16	-1.64	5.8	4.55	1.00	0.0
10	08355554-4326494	$08^{h}\,35^{m}\,55.5^{s}$	$-43^\circ26'49.5''$	262.23	-1.67	5.8	4.20	1.00	0.0
11	08360154-4349352	$08^{h}\,36^{m}\,01.5^{s}$	$-43^\circ49'35.3''$	262.54	-1.88	4.8	5.41	1.00	0.0
12	08360585-4346333	$08^{h}\,36^{m}\,05.9^{s}$	$-43^\circ46'33.4''$	262.51	-1.84	5.0	6.39	1.00	0.0
13	08360622-4340246	$08^{h}\,36^{m}\,06.2^{s}$	$-43^\circ40'24.6''$	262.43	-1.78	5.0	4.79	1.00	0.0
14	08360764-4340367	$08^{h}\,36^{m}\,07.6^{s}$	$-43^\circ40'36.8''$	262.44	-1.78	5.0	3.66	1.00	0.0
15	08361558-4347530	$08^{h}\,36^{m}\,15.6^{s}$	$-43^\circ47'53.0''$	262.55	-1.83	5.0	4.51	1.00	0.0
16	08361792-4352366	$08^{h}\,36^{m}\,17.9^{s}$	$-43^\circ52'36.7''$	262.61	-1.87	5.0	3.66	1.00	0.0
17	08362115-4317323	$08^{h}\,36^{m}\,21.2^{s}$	$-43^\circ17'32.3''$	262.15	-1.51	6.5	3.66	1.00	0.0
18	08362134-4347480	$08^{h}\,36^{m}\,21.4^{s}$	$-43^\circ47'48.0''$	262.56	-1.81	5.0	3.71	1.00	0.0
19	08363168-4322455	$08^{h}\,36^{m}\,31.7^{s}$	$-43^\circ22'45.6''$	262.24	-1.54	6.5	3.85	1.00	0.0
20	08363203-4333505	$08^{h}\,36^{m}\,32.0^{s}$	$-43^\circ33'50.6''$	262.39	-1.65	5.0	3.67	1.00	0.0
21	08363315-4341585	$08^{h}\,36^{m}\,33.2^{s}$	$-43^\circ41'58.6''$	262.50	-1.73	5.0	5.76	1.00	0.0
22	08363367-4335509	$08^{h}\,36^{m}\,33.7^{s}$	$-43^\circ35'50.9''$	262.42	-1.67	5.0	3.81	1.00	0.0
23	08363416-4323089	$08^{h}\,36^{m}\,34.2^{s}$	$-43^\circ23'08.9''$	262.25	-1.54	6.5	4.24	1.00	0.0
24	08363597-4337554	$08^{h}\,36^{m}\,36.0^{s}$	$-43^\circ37'55.4''$	262.45	-1.68	6.0	23.59	0.88	83.6
25	08364352-4334353	$08^{h}\,36^{m}\,43.5^{s}$	$-43^\circ34'35.3''$	262.42	-1.63	5.0	5.15	1.00	0.0
26	08364427-4323207	$08^{h}\,36^{m}\,44.3^{s}$	$-43^\circ23'20.7''$	262.27	-1.51	6.5	7.85	1.00	0.0
27	08364670-4350329	$08^{h}\,36^{m}\,46.7^{s}$	$-43^\circ50'33.0''$	262.64	-1.78	4.4	3.66	1.00	0.0
28	08364797-4339197	$08^{h}\,36^{m}\,48.0^{s}$	$-43^\circ39'19.8''$	262.49	-1.67	5.0	5.17	1.00	0.0
29	08364885-4336399	$08^{h}\,36^{m}\,48.9^{s}$	$-43^\circ36'40.0''$	262.46	-1.64	5.0	5.02	1.00	0.0
30	08365114-4350515	$08^{h}\,36^{m}\,51.1^{s}$	$-43^\circ50'51.5''$	262.65	-1.77	4.4	6.26	0.59	-51.0
31	08365156-4337410	$08^{h}\,36^{m}\,51.6^{s}$	$-43^\circ37'41.0''$	262.48	-1.64	7.3	39.35	0.42	-70.0
32	08365296-4338169	$08^{h}\,36^{m}\,53.0^{s}$	$-43^\circ38'16.9''$	262.49	-1.64	5.0	5.46	1.00	0.0
33	08370018-4319277	$08^{h}\,37^{m}\,00.2^{s}$	$-43^\circ19'27.7''$	262.25	-1.44	6.5	3.73	1.00	0.0
34	08370727-4339136	$08^{h}\,37^{m}\,07.3^{s}$	$-43^\circ39'13.6''$	262.53	-1.62	6.0	11.93	0.70	10.0
35	08370902-4334203	$08^{h}\,37^{m}\,09.0^{s}$	$-43^\circ34'20.4''$	262.46	-1.56	5.9	4.18	1.00	0.0
36	08371095-4330370	$08^{h}\,37^{m}\,11.0^{s}$	$-43^\circ30'37.1''$	262.42	-1.52	5.9	6.54	1.00	0.0
37	08371117-4334581	$08^{h}\,37^{m}\,11.2^{s}$	$-43^\circ34'58.1''$	262.48	-1.57	5.9	5.79	1.00	0.0
38	08371136-4320430	$08^{h}\,37^{m}\,11.4^{s}$	$-43^\circ20'43.1''$	262.29	-1.42	6.5	6.87	1.00	0.0
39	08371248-4345354	$08^{h}\,37^{m}\,12.5^{s}$	$-43^\circ45'35.5''$	262.62	-1.67	5.0	3.66	1.00	0.0
40	08371284-4326311	$08^{h}\,37^{m}\,12.8^{s}$	$-43^\circ26'31.2''$	262.37	-1.48	6.5	4.14	1.00	0.0
41	08372130-4343012	$08^{h}\,37^{m}\,21.3^{s}$	$-43^\circ43'01.3''$	262.60	-1.62	5.9	12.75	0.80	-17.0
42	08372360-4339139	$08^{h}\,37^{m}\,23.6^{s}$	$-43^\circ39'13.9''$	262.55	-1.58	5.9	5.97	1.00	0.0
43	08372480-4343369	$08^{h}\,37^{m}\,24.8^{s}$	$-43^\circ43'36.9''$	262.62	-1.62	5.9	3.66	1.00	0.0
44	08372853-4347138	$08^{h}\,37^{m}\,28.5^{s}$	$-43^\circ47'13.9''$	262.67	-1.65	4.4	5.20	1.00	0.0
45	08373104-4352304	$08^{h}\,37^{m}\,31.0^{s}$	$-43^\circ52'30.5''$	262.74	-1.69	4.4	3.66	1.00	0.0
46	08373210-4347178	$08^{h}\,37^{m}\,32.1^{s}$	$-43^\circ47'17.8''$	262.68	-1.64	4.4	3.66	1.00	0.0
47	08374047-4340275	$08^{h}\,37^{m}\,40.5^{s}$	$-43^\circ40'27.6''$	262.60	-1.55	5.9	8.56	1.00	0.0

ID	Source ID.	R.A. (J2000)	Dec. (J2000)	l (deg)	b (deg)	A_V (mag)	a (arcsec)	b/a	P.A. (deg)
48	08374943-4328517	$08^{h}\ 37^{m}\ 49.4^{s}$	$-43°28'51.8''$	262.46	-1.41	5.9	5.69	1.00	0.0
49	08374942-4333454	$08^{h}\ 37^{m}\ 49.4^{s}$	$-43°33'45.5''$	262.53	-1.46	5.9	4.12	1.00	0.0
50	08374962-4339440	$08^{h}\ 37^{m}\ 49.6^{s}$	$-43°39'44.0''$	262.61	-1.52	5.9	4.39	1.00	0.0
51	08375375-4334564	$08^{h}\ 37^{m}\ 53.8^{s}$	$-43°34'56.4''$	262.55	-1.46	5.9	5.31	1.00	0.0
52	08375484-4320213	$08^{h}\ 37^{m}\ 54.9^{s}$	$-43°20'21.3''$	262.36	-1.31	6.7	6.29	1.00	0.0
53	08375565-4321530	$08^{h}\ 37^{m}\ 55.7^{s}$	$-43°21'53.1''$	262.38	-1.33	6.0	4.32	1.00	0.0
54	08375675-4338428	$08^{h}\ 37^{m}\ 56.8^{s}$	$-43°38'42.8''$	262.61	-1.49	5.9	4.22	1.00	0.0
55	08375948-4346194	$08^{h}\ 37^{m}\ 59.5^{s}$	$-43°46'19.4''$	262.71	-1.56	4.9	3.69	1.00	0.0
56	08380277-4328206	$08^{h}\ 38^{m}\ 02.8^{s}$	$-43°28'20.7''$	262.48	-1.38	5.9	4.34	1.00	0.0

B.1.2 MIR Photometry

Table B.2 gives the MIR measurements and corrected fluxes and magnitudes for sources in the *Spitzer* footprint as follows:

Column 1: Reference ID

Column 2: Source IRSF ID

Column 3, **Column 7**, **Column 11**, **Column 15**: Flux density (mJy) for the four IRAC bands - raw measurements and their errors

Column 4, **Column 8**, **Column 12**, **Column 16**: Flux density (mJy) for the four IRAC bands - aperture-corrected measurements and their errors

Column 5, **Column 9**, **Column 13**, **Column 17**: Integrated Magnitude (mag) – no reddening correction applied; 5% calibration error included

Column 6, **Column 10**, **Column 14**, **Column 18**: Integrated Magnitude (mag) – reddening-corrected; 5% calibration error included

Sources with no measurements (...) are due to differing coverage by the IRAC bands, as discussed in Chapter 2.

Table B.2: MIR Photometry.

		3.6 μm				4.5 μm				5.8 μm				8.0 μm			
ID	Source ID.	f_ν (mJy)	f_ν (mJy)	Mag. (mag)	Mag. (mag)	f_ν (mJy)	f_ν (mJy)	Mag. (mag)	Mag. (mag)	f_ν (mJy)	f_ν (mJy)	Mag. (mag)	Mag. (mag)	f_ν (mJy)	f_ν (mJy)	Mag. (mag)	Mag. (mag)
1	08353645-4319330	...	...	...	...	0.303	0.33	14.33	14.04	...	...	...	...	0.903	1.05	11.97	11.68
		...	...	...	...	±0.012	±0.01	±0.07	±0.07	...	...	...	...	±0.052	±0.06	±0.08	±0.08
2	08354552-4349514	0.479	0.52	14.33	14.08	...	...	...	...	0.535	0.6	13.20	13.03	...	...	...	...
		±0.016	±0.02	±0.06	±0.06	...	...	...	...	±0.028	±0.03	±0.08	±0.08	...	...	...	...
3	08354566-4322322	0.778	0.83	13.82	13.52	0.539	0.58	13.74	13.53	1.021	1.12	12.53	12.31	2.104	2.35	11.09	10.88
		±0.022	±0.02	±0.06	±0.06	±0.015	±0.02	±0.06	±0.06	±0.053	±0.06	±0.08	±0.08	±0.075	±0.08	±0.06	±0.06
4	08354584-4317422	...	...	...	...	0.820	0.87	13.29	13.04	...	...	...	...	0.787	0.74	12.35	12.10
		...	...	...	...	±0.026	±0.03	±0.06	±0.06	...	...	...	...	±0.067	±0.06	±0.11	±0.11
5	08354707-4326455	0.217	0.25	15.15	14.84	0.153	0.17	15.04	14.82	0.202	0.24	14.20	13.99	1.013	1.25	11.78	11.57
		±0.011	±0.01	±0.07	±0.07	±0.009	±0.01	±0.08	±0.08	±0.016	±0.02	±0.10	±0.10	±0.038	±0.05	±0.06	±0.06
6	08354735-4325524	0.611	0.66	14.07	13.77	0.412	0.45	14.01	13.80	0.204	0.23	14.25	14.04	0.169	0.19	13.80	13.60
		±0.018	±0.02	±0.06	±0.06	±0.012	±0.01	±0.06	±0.06	±0.020	±0.02	±0.12	±0.12	±0.021	±0.02	±0.15	±0.15
7	08354788-4319169	...	...	...	...	0.174	0.2	14.90	14.65	...	...	...	...	0.335	0.41	12.98	12.73
		...	...	...	...	±0.007	±0.01	±0.07	±0.07	...	...	...	...	±0.019	±0.02	±0.08	±0.08
8	08354796-4328263	0.439	0.47	14.43	14.13	0.404	0.44	14.03	13.82	0.412	0.46	13.49	13.28	3.287	3.74	10.59	10.38
		±0.013	±0.01	±0.06	±0.06	±0.013	±0.01	±0.06	±0.06	±0.027	±0.03	±0.09	±0.09	±0.116	±0.13	±0.06	±0.06
9	08354984-4322381	0.312	0.34	14.78	14.48	0.292	0.32	14.37	14.15	0.214	0.25	14.17	13.96	1.621	1.9	11.32	11.11
		±0.014	±0.01	±0.07	±0.07	±0.010	±0.01	±0.06	±0.06	±0.019	±0.02	±0.11	±0.11	±0.058	±0.07	±0.06	±0.06
10	08355554-4326494	0.573	0.64	14.11	13.81	0.460	0.51	13.86	13.65	0.325	0.38	13.71	13.50	1.251	1.5	11.58	11.37
		±0.029	±0.03	±0.07	±0.07	±0.018	±0.02	±0.07	±0.07	±0.023	±0.03	±0.09	±0.09	±0.046	±0.05	±0.06	±0.06
11	08360154-4349352	0.542	0.58	14.21	13.95	...	...	...	...	0.252	0.28	14.03	13.85	...	...	...	...
		±0.017	±0.02	±0.06	±0.06	...	...	...	...	±0.018	±0.02	±0.09	±0.09	...	...	...	...
12	08360585-4346333	1.104	1.17	13.45	13.19	0.940	0.99	13.14	12.96	0.635	0.69	13.05	12.87	0.422	0.46	12.85	12.67
		±0.033	±0.03	±0.06	±0.06	±0.026	±0.03	±0.06	±0.06	±0.036	±0.04	±0.08	±0.08	±0.041	±0.04	±0.12	±0.12
13	08360622-4340246	0.671	0.73	13.96	13.70	0.947	1.04	13.10	12.91	1.431	1.63	12.12	11.94	2.466	2.87	10.88	10.69
		±0.020	±0.02	±0.06	±0.06	±0.025	±0.03	±0.06	±0.06	±0.056	±0.06	±0.07	±0.07	±0.087	±0.10	±0.06	±0.06
14	08360764-4340367	0.210	0.24	15.18	14.92	0.169	0.19	14.93	14.75	0.179	0.21	14.33	14.15	0.953	1.17	11.84	11.66
		±0.021	±0.02	±0.12	±0.12	±0.015	±0.02	±0.11	±0.11	±0.022	±0.03	±0.14	±0.14	±0.043	±0.05	±0.07	±0.07
15	08361558-4347530	0.269	0.30	14.94	14.68	...	...	...	...	0.139	0.16	14.64	14.46	...	...	...	...
		±0.011	±0.01	±0.07	±0.07	...	...	...	...	±0.013	±0.02	±0.12	±0.12	...	...	...	...

Table B.2 continued...

		3.6 μm				4.5 μm				5.8 μm				8.0 μm			
		f_ν	f_ν	Mag.	Mag.	f_ν	f_ν	Mag.	Mag.	f_ν	f_ν	Mag.	Mag.	f_ν	f_ν	Mag.	Mag.
ID	Source ID.	(mJy)	(mJy)	(mag)	(mag)	(mJy)	(mJy)	(mag)	(mag)	(mJy)	(mJy)	(mag)	(mag)	(mJy)	(mJy)	(mag)	(mag)
16	08361792-4352366	0.159	0.18	15.48	15.22	...	...	...	...	0.077	0.09	15.24	15.06	...	...	...	...
		±0.007	±0.01	±0.07	±0.07	...	...	...	...	±0.014	±0.02	±0.20	±0.20	...	...	...	...
17	08362115-4317323	...	...	...	...	0.144	0.16	15.10	14.87	...	...	...	...	0.075	0.09	14.60	14.37
		...	...	...	...	±0.010	±0.01	±0.09	±0.09	...	...	...	...	±0.015	±0.02	±0.22	±0.22
18	08362134-4347480	0.216	0.24	15.15	14.89	...	...	...	...	0.105	0.13	14.91	14.73	...	...	...	...
		±0.011	±0.01	±0.07	±0.07	...	...	...	...	±0.010	±0.01	±0.12	±0.12	...	...	...	...
19	08363168-4322455	0.321	0.36	14.73	14.39	0.270	0.3	14.43	14.19	0.211	0.25	14.16	13.93	0.102	0.12	14.28	14.05
		±0.016	±0.02	±0.07	±0.07	±0.017	±0.02	±0.08	±0.08	±0.041	±0.05	±0.22	±0.22	±0.027	±0.03	±0.29	±0.29
20	08363203-4333505	0.211	0.24	15.18	14.92	0.224	0.26	14.62	14.44	0.167	0.2	14.40	14.22	0.730	0.9	12.13	11.95
		±0.008	±0.01	±0.07	±0.07	±0.007	±0.01	±0.06	±0.06	±0.016	±0.02	±0.12	±0.12	±0.035	±0.04	±0.07	±0.07
21	08363315-4341585	0.849	0.91	13.73	13.46	0.638	0.68	13.55	13.37	0.445	0.49	13.42	13.24	0.533	0.6	12.58	12.40
		±0.028	±0.03	±0.06	±0.06	±0.020	±0.02	±0.06	±0.06	±0.024	±0.03	±0.08	±0.08	±0.036	±0.04	±0.09	±0.09
22	08363367-4335509	0.154	0.17	15.52	15.26	0.121	0.14	15.30	15.12	0.091	0.11	15.07	14.89	0.064	0.08	14.79	14.61
		±0.008	±0.01	±0.07	±0.07	±0.006	±0.01	±0.07	±0.07	±0.012	±0.01	±0.15	±0.15	±0.017	±0.02	±0.29	±0.29
23	08363416-4323089	0.321	0.36	14.74	14.40	0.239	0.27	14.57	14.34	0.036	0.04	16.10	15.86	...	...	...	...
		±0.013	±0.01	±0.07	±0.07	±0.010	±0.01	±0.07	±0.07	±0.023	±0.03	±0.710	±0.71	...	...	...	...
24	08363597-4337554	14.605	13.81	10.77	10.46	9.720	9.52	10.69	10.47	8.781	7.76	10.43	10.21	10.469	8.64	9.68	9.46
		±0.366	±0.35	±0.06	±0.06	±0.245	±0.24	±0.06	±0.06	±0.269	±0.24	±0.06	±0.06	±0.455	±0.38	±0.07	±0.07
25	08364352-4334353	0.348	0.38	14.68	14.42	0.271	0.29	14.46	14.28	0.137	0.15	14.68	14.50	0.274	0.31	13.28	13.10
		±0.013	±0.01	±0.06	±0.06	±0.010	±0.01	±0.07	±0.07	±0.017	±0.02	±0.14	±0.14	±0.031	±0.03	±0.13	±0.13
26	08364427-4323207	0.628	0.63	14.12	13.78	0.468	0.49	13.90	13.67	0.339	0.33	13.85	13.61	0.969	0.9	12.13	11.90
		±0.025	±0.02	±0.07	±0.07	±0.018	±0.02	±0.06	±0.06	±0.032	±0.03	±0.11	±0.11	±0.053	±0.05	±0.08	±0.08
27	08364670-4350329	0.122	0.14	15.77	15.54	...	...	...	...	0.090	0.11	15.07	14.92	...	...	...	...
		±0.008	±0.01	±0.09	±0.09	...	...	...	...	±0.013	±0.02	±0.17	±0.17	...	...	...	...
28	08364797-4339197	0.320	0.35	14.77	14.51	0.258	0.28	14.52	14.34	0.127	0.14	14.76	14.58	0.135	0.15	14.05	13.87
		±0.010	±0.01	±0.06	±0.06	±0.008	±0.01	±0.06	±0.06	±0.017	±0.02	±0.15	±0.15	±0.014	±0.02	±0.12	±0.12
29	08364885-4336399	0.163	0.18	15.50	15.24	0.121	0.13	15.34	15.15	0.089	0.1	15.14	14.96	0.086	0.1	14.53	14.35
		±0.006	±0.01	±0.06	±0.06	±0.005	±0.00	±0.07	±0.07	±0.020	±0.02	±0.25	±0.25	±0.038	±0.04	±0.48	±0.48
30	08365114-4350515	0.399	0.44	14.52	14.29	...	...	...	...	0.358	0.41	13.63	13.47	...	...	...	...
		±0.013	±0.01	±0.06	±0.06	...	...	...	...	±0.019	±0.02	±0.08	±0.08	...	...	...	...
31	08365156-4337410	23.552	22.13	10.26	9.88	17.508	17.05	10.06	9.79	40.737	35.48	8.78	8.51	140.048	114.07	6.88	6.61
		±0.591	±0.56	±0.06	±0.06	±0.439	±0.43	±0.06	±0.06	±1.193	±1.04	±0.06	±0.06	±4.794	±3.91	±0.06	±0.06
32	08365296-4338169	0.374	0.40	14.61	14.35	0.264	0.28	14.50	14.32	0.367	0.41	13.62	13.44	0.924	1.05	11.97	11.79
		±0.013	±0.01	±0.06	±0.06	±0.009	±0.01	±0.06	±0.06	±0.020	±0.02	±0.08	±0.08	±0.048	±0.05	±0.08	±0.08

Table B.2 continued...

		3.6 μm				4.5 μm				5.8 μm				8.0 μm			
ID	Source ID.	f_ν (mJy)	f_ν (mJy)	Mag. (mag)	Mag. (mag)	f_ν (mJy)	f_ν (mJy)	Mag. (mag)	Mag. (mag)	f_ν (mJy)	f_ν (mJy)	Mag. (mag)	Mag. (mag)	f_ν (mJy)	f_ν (mJy)	Mag. (mag)	Mag. (mag)
33	08370018-4319277	...	...	...	...	0.367	0.42	14.09	13.85	...	...	...	...	0.278	0.34	13.19	12.95
		...	...	...	...	±0.017	±0.02	±0.07	±0.07	...	...	...	...	±0.019	±0.02	±0.09	±0.09
34	08370727-4339136	2.350	2.32	12.71	12.39	1.706	1.76	12.52	12.31	4.172	4.0	11.15	10.93	13.857	12.49	9.28	9.06
		±0.060	±0.06	±0.06	±0.06	±0.044	±0.05	±0.06	±0.06	±0.133	±0.13	±0.06	±0.06	±0.487	±0.44	±0.06	±0.06
35	08370902-4334203	0.297	0.33	14.82	14.52	0.274	0.31	14.42	14.21	0.183	0.21	14.33	14.12	0.227	0.27	13.43	13.22
		±0.015	±0.02	±0.07	±0.07	±0.011	±0.01	±0.07	±0.07	±0.015	±0.02	±0.10	±0.10	±0.023	±0.03	±0.12	±0.12
36	08371095-4330370	0.654	0.69	14.03	13.72	0.499	0.53	13.83	13.62	0.301	0.33	13.87	13.66	0.640	0.7	12.40	12.19
		±0.020	±0.02	±0.06	±0.06	±0.015	±0.02	±0.06	±0.06	±0.028	±0.03	±0.11	±0.11	±0.046	±0.05	±0.09	±0.09
37	08371117-4334581	0.609	0.65	14.09	13.78	0.451	0.48	13.93	13.71	0.677	0.75	12.97	12.76	3.891	4.35	10.42	10.21
		±0.018	±0.02	±0.06	±0.06	±0.013	±0.01	±0.06	±0.06	±0.033	±0.04	±0.07	±0.07	±0.153	±0.17	±0.07	±0.07
38	08371136-4320430	0.685	0.72	13.98	13.64	0.516	0.54	13.80	13.57	0.258	0.28	14.04	13.81	0.340	0.37	13.10	12.87
		±0.022	±0.02	±0.06	±0.06	±0.017	±0.02	±0.06	±0.06	±0.030	±0.03	±0.13	±0.13	±0.036	±0.04	±0.13	±0.13
39	08371248-4345354	0.196	0.22	15.26	14.99	0.170	0.19	14.92	14.74	0.083	0.1	15.16	14.98	0.144	0.18	13.90	13.71
		±0.012	±0.01	±0.08	±0.08	±0.010	±0.01	±0.08	±0.08	±0.012	±0.01	±0.16	±0.16	±0.019	±0.02	±0.15	±0.15
40	08371284-4326311	0.267	0.30	14.94	14.60	0.225	0.25	14.63	14.40	0.100	0.12	14.98	14.75	0.107	0.13	14.25	14.01
		±0.010	±0.01	±0.06	±0.06	±0.008	±0.01	±0.06	±0.06	±0.014	±0.02	±0.16	±0.16	±0.032	±0.04	±0.33	±0.33
41	08372130-4343012	5.606	5.49	11.77	11.47	3.661	3.73	11.71	11.49	3.159	2.98	11.46	11.25	4.077	3.62	10.62	10.41
		±0.144	±0.14	±0.06	±0.06	±0.095	±0.10	±0.06	±0.06	±0.105	±0.10	±0.06	±0.06	±0.185	±0.16	±0.07	±0.07
42	08372360-4339139	0.389	0.41	14.58	14.27	0.271	0.29	14.48	14.27	0.189	0.21	14.36	14.15	0.361	0.4	13.01	12.80
		±0.016	±0.02	±0.07	±0.07	±0.011	±0.01	±0.07	±0.07	±0.018	±0.02	±0.11	±0.11	±0.029	±0.03	±0.10	±0.10
43	08372480-4343369	0.173	0.20	15.39	15.09	0.105	0.12	15.44	15.23	0.080	0.1	15.20	14.99	0.069	0.09	14.69	14.48
		±0.011	±0.01	±0.09	±0.09	±0.010	±0.01	±0.11	±0.11	±0.013	±0.02	±0.19	±0.19	±0.026	±0.03	±0.41	±0.41
44	08372853-4347138	0.492	0.53	14.31	14.07	...	...	...	...	0.296	0.33	13.85	13.69	...	...	...	...
		±0.015	±0.02	±0.06	±0.06	...	...	...	...	±0.015	±0.02	±0.07	±0.07	...	...	...	...
45	08373104-4352304	0.233	0.26	15.07	14.84	...	...	...	...	1.397	1.67	12.10	11.94	...	...	...	...
		±0.022	±0.02	±0.11	±0.11	...	...	...	...	±0.488	±0.58	±0.38	±0.38	...	...	...	...
46	08373210-4347178	0.317	0.36	14.73	14.50	...	...	...	...	0.255	0.3	13.95	13.79	...	...	...	...
		±0.044	±0.05	±0.16	±0.16	...	...	...	...	±0.072	±0.08	±0.31	±0.31	...	...	...	...
47	08374047-4340275	1.390	1.39	13.26	12.96	1.028	1.07	13.06	12.85	0.628	0.61	13.19	12.97	0.313	0.29	13.37	13.16
		±0.040	±0.04	±0.06	±0.06	±0.031	±0.03	±0.06	±0.06	±0.031	±0.03	±0.07	±0.07	±0.036	±0.03	±0.14	±0.14
48	08374943-4328517	0.611	0.65	14.08	13.78	0.405	0.43	14.04	13.83	0.243	0.27	14.08	13.87	0.567	0.64	12.51	12.30
		±0.022	±0.02	±0.06	±0.06	±0.016	±0.02	±0.07	±0.07	±0.026	±0.03	±0.13	±0.13	±0.037	±0.04	±0.09	±0.09
49	08374942-4333454	0.394	0.44	14.52	14.21	0.399	0.45	14.01	13.80	0.312	0.36	13.75	13.54	0.594	0.71	12.38	12.17
		±0.015	±0.02	±0.07	±0.07	±0.017	±0.02	±0.07	±0.07	±0.025	±0.03	±0.10	±0.10	±0.039	±0.05	±0.09	±0.09

Table B.2 continued...

		3.6 μm				4.5 μm				5.8 μm				8.0 μm			
ID	Source ID.	f_ν (mJy)	f_ν (mJy)	Mag. (mag)	Mag. (mag)	f_ν (mJy)	f_ν (mJy)	Mag. (mag)	Mag. (mag)	f_ν (mJy)	f_ν (mJy)	Mag. (mag)	Mag. (mag)	f_ν (mJy)	f_ν (mJy)	Mag. (mag)	Mag. (mag)
50	08374962-4339440	0.319	0.35	14.75	14.45	0.253	0.28	14.52	14.30	0.134	0.15	14.68	14.46	0.168	0.2	13.77	13.56
		±0.010	±0.01	±0.06	±0.06	±0.009	±0.01	±0.06	±0.06	±0.016	±0.02	±0.14	±0.14	±0.026	±0.03	±0.17	±0.17
51	08375375-4334564	0.484	0.52	14.33	14.02	0.424	0.46	13.98	13.77	0.332	0.37	13.73	13.51	1.505	1.71	11.43	11.22
		±0.019	±0.02	±0.07	±0.07	±0.019	±0.02	±0.07	±0.07	±0.052	±0.06	±0.18	±0.18	±0.089	±0.10	±0.08	±0.08
52	08375484-4320213	0.676	0.72	13.98	13.64	0.520	0.55	13.78	13.54	0.286	0.31	13.92	13.68	1.920	2.12	11.21	10.96
		±0.022	±0.02	±0.06	±0.06	±0.018	±0.02	±0.06	±0.06	±0.049	±0.05	±0.19	±0.19	±0.079	±0.09	±0.07	±0.07
53	08375565-4321530	0.340	0.38	14.68	14.37	0.291	0.32	14.36	14.14	0.172	0.2	14.40	14.19	0.218	0.26	13.48	13.27
		±0.015	±0.02	±0.07	±0.07	±0.013	±0.01	±0.07	±0.07	±0.029	±0.03	±0.19	±0.19	±0.050	±0.06	±0.25	±0.25
54	08375675-4338428	0.304	0.34	14.80	14.49	0.221	0.25	14.66	14.45	0.120	0.14	14.79	14.58	0.056	0.07	14.96	14.74
		±0.012	±0.01	±0.07	±0.07	±0.010	±0.01	±0.07	±0.07	±0.016	±0.02	±0.16	±0.16	±0.021	±0.03	±0.41	±0.41
55	08375948-4346194	0.314	0.35	14.75	14.49	...	...	...	...	0.151	0.18	14.52	14.34	...	...	...	...
		±0.014	±0.02	±0.07	±0.07	...	...	...	...	±0.022	±0.03	±0.17	±0.17	...	...	...	...
56	08380277-4328206	0.472	0.52	14.33	14.02	0.487	0.54	13.80	13.59	0.338	0.39	13.67	13.46	2.050	2.43	11.05	10.84
		±0.016	±0.02	±0.06	±0.06	±0.044	±0.05	±0.11	±0.11	±0.032	±0.04	±0.12	±0.12	±1.435	±1.70	±0.76	±0.76

B.1.3 NIR Photometry

Table B.3 gives the NIR measurements and corrected fluxes and magnitudes for sources in the *Spitzer* footprint as follows:
Column 1: Reference ID
Column 2: Source IRSF ID
Column 3, **Column 6**, **Column 9**: Flux density (mJy) for the J, H, K_s - raw measurements
Column 4, **Column 7**, **Column 10**: Integrated Magnitude (mag) no reddening correction applied; 5% calibration error included
Column 5, **Column 8**, **Column 11**: Integrated Magnitude (mag) - reddening-corrected; 5% calibration error included. The extinction-corrected magnitudes have an error of ∼10% which is not accounted for.
Column 12: Photometric redshift

Table B.3: NIR Photometry.

			J			H			K_s		
ID	Source ID.	f_ν (mJy)	Mag. (mag)	Mag. (mag)	f_ν (mJy)	Mag. (mag)	Mag. (mag)	f_ν (mJy)	Mag. (mag)	Mag. (mag)	Photo-z
1	08353645-4319330	0.047 ±0.059	18.83 ±1.36	16.63 ±1.36	0.275 ±0.071	16.43 ±0.28	15.00 ±0.28	0.455 ±0.137	15.41 ±0.33	14.49 ±0.33	0.2553
2	08354552-4349514	0.330 ±0.021	16.71 ±0.09	15.40 ±0.09	0.673 ±0.024	15.46 ±0.06	14.60 ±0.06	0.717 ±0.050	14.92 ±0.09	14.37 ±0.09	0.0941
3	08354566-4322322	0.344 ±0.025	16.66 ±0.09	15.08 ±0.09	0.714 ±0.030	15.39 ±0.07	14.36 ±0.07	0.969 ±0.050	14.59 ±0.08	13.93 ±0.08	0.1222
4	08354584-4317422	0.317 ±0.009	16.75 ±0.06	14.87 ±0.06	0.859 ±0.021	15.19 ±0.06	13.96 ±0.06	1.088 ±0.038	14.47 ±0.06	13.68 ±0.06	0.1127
5	08354707-4326455	0.058 ±0.036	18.60 ±0.68	17.01 ±0.68	0.217 ±0.044	16.68 ±0.22	15.65 ±0.22	0.265 ±0.071	16.00 ±0.30	15.34 ±0.30	0.2067
6	08354735-4325524	0.367 ±0.024	16.59 ±0.09	15.01 ±0.09	0.748 ±0.028	15.34 ±0.06	14.31 ±0.06	0.938 ±0.047	14.63 ±0.07	13.96 ±0.07	0.1044
7	08354788-4319169	0.044 ±0.005	18.90 ±0.14	17.01 ±0.14	0.119 ±0.006	17.34 ±0.07	16.11 ±0.07	0.218 ±0.019	16.21 ±0.11	15.42 ±0.11	0.2516
8	08354796-4328263	0.149 ±0.018	17.57 ±0.14	15.98 ±0.14	0.296 ±0.024	16.35 ±0.10	15.31 ±0.10	0.495 ±0.069	15.32 ±0.16	14.66 ±0.16	0.1847
9	08354984-4322381	0.077 ±0.052	18.29 ±0.73	16.70 ±0.73	0.191 ±0.053	16.82 ±0.30	15.79 ±0.30	0.336 ±0.081	15.74 ±0.27	15.08 ±0.27	0.2377
10	08355554-4326494	0.191 ±0.015	17.30 ±0.10	15.71 ±0.10	0.426 ±0.018	15.95 ±0.07	14.92 ±0.07	0.678 ±0.033	14.98 ±0.07	14.32 ±0.07	0.1758
11	08360154-4349352	0.347 ±0.019	16.66 ±0.08	15.34 ±0.08	0.609 ±0.025	15.56 ±0.07	14.71 ±0.07	0.824 ±0.049	14.77 ±0.08	14.22 ±0.08	0.1269
12	08360585-4346333	0.511 ±0.025	16.23 ±0.07	14.87 ±0.07	1.083 ±0.038	14.94 ±0.06	14.05 ±0.06	1.630 ±0.065	14.03 ±0.07	13.46 ±0.07	0.1562
13	08360622-4340246	0.166 ±0.016	17.46 ±0.11	16.09 ±0.11	0.364 ±0.021	16.12 ±0.08	15.23 ±0.08	0.528 ±0.040	15.25 ±0.10	14.68 ±0.10	0.1776
14	08360764-4340367	0.032 ±0.031	19.24 ±1.04	17.88 ±1.04	0.091 ±0.039	17.63 ±0.46	16.74 ±0.46	0.264 ±0.074	16.01 ±0.31	15.43 ±0.31	0.2903
15	08361558-4347530	0.129 ±0.014	17.73 ±0.13	16.36 ±0.13	0.240 ±0.015	16.57 ±0.08	15.69 ±0.08	0.376 ±0.037	15.62 ±0.12	15.05 ±0.12	0.1877
16	08361792-4352366	0.105 ±0.034	17.95 ±0.35	16.59 ±0.35	0.184 ±0.044	16.86 ±0.27	15.97 ±0.27	0.274 ±0.091	15.96 ±0.36	15.39 ±0.36	0.1776
17	08362115-4317323	0.035 ±0.014	19.15 ±0.44	17.38 ±0.44	0.167 ±0.016	16.97 ±0.12	15.82 ±0.12	0.222 ±0.051	16.19 ±0.25	15.45 ±0.25	0.2511
18	08362134-4347480	0.122 ±0.011	17.79 ±0.11	16.42 ±0.11	0.211 ±0.013	16.71 ±0.08	15.83 ±0.08	0.366 ±0.030	15.65 ±0.10	15.08 ±0.10	0.2045
19	08363168-4322455	0.132 ±0.009	17.70 ±0.09	15.94 ±0.09	0.309 ±0.013	16.30 ±0.07	15.15 ±0.07	0.430 ±0.026	15.48 ±0.08	14.73 ±0.08	0.1518
20	08363203-4333505	0.082 ±0.023	18.22 ±0.31	16.86 ±0.31	0.138 ±0.027	17.18 ±0.22	16.29 ±0.22	0.233 ±0.076	16.14 ±0.36	15.57 ±0.36	0.2099
21	08363315-4341585	0.395 ±0.019	16.52 ±0.07	15.15 ±0.07	0.870 ±0.029	15.18 ±0.06	14.29 ±0.06	1.107 ±0.050	14.45 ±0.07	13.88 ±0.07	0.1260
22	08363367-4335509	0.068 ±0.008	18.43 ±0.14	17.06 ±0.14	0.167 ±0.011	16.97 ±0.08	16.08 ±0.08	0.234 ±0.025	16.14 ±0.13	15.56 ±0.13	0.2104
23	08363416-4323089	0.062 ±0.012	18.52 ±0.22	16.76 ±0.22	0.183 ±0.017	16.87 ±0.11	15.72 ±0.11	0.259 ±0.030	16.03 ±0.13	15.29 ±0.13	0.2002
24	08363597-4337554	7.735 ±0.130	13.29 ±0.05	11.65 ±0.05	15.249 ±0.313	12.07 ±0.05	11.01 ±0.05	17.527 ±0.384	11.45 ±0.06	10.77 ±0.06	0.0325
25	08364352-4334353	0.222 ±0.021	17.14 ±0.11	15.77 ±0.11	0.373 ±0.023	16.10 ±0.08	15.21 ±0.08	0.527 ±0.056	15.26 ±0.12	14.68 ±0.12	0.1405
26	08364427-4323207	0.269 ±0.028	16.93 ±0.12	15.16 ±0.12	0.505 ±0.036	15.77 ±0.09	14.62 ±0.09	0.681 ±0.067	14.98 ±0.12	14.24 ±0.12	0.1070
27	08364670-4350329	0.104 ±0.032	17.96 ±0.34	16.76 ±0.34	0.169 ±0.045	16.96 ±0.29	16.17 ±0.29	0.194 ±0.088	16.34 ±0.49	15.84 ±0.49	0.1221
28	08364797-4339197	0.109 ±0.016	17.91 ±0.17	16.55 ±0.17	0.240 ±0.019	16.57 ±0.10	15.69 ±0.10	0.427 ±0.050	15.48 ±0.14	14.91 ±0.14	0.2341
29	08364885-4336399	0.103 ±0.017	17.97 ±0.19	16.61 ±0.19	0.196 ±0.017	16.80 ±0.10	15.91 ±0.10	0.206 ±0.044	16.27 ±0.24	15.70 ±0.24	0.1054
30	08365114-4350515	0.189 ±0.016	17.32 ±0.10	16.11 ±0.10	0.382 ±0.021	16.07 ±0.08	15.29 ±0.08	0.570 ±0.043	15.17 ±0.10	14.66 ±0.10	0.1842

Table B.3 continued...

		J			H			K_s			
ID	Source ID.	f_ν (mJy)	Mag. (mag)	Mag. (mag)	f_ν (mJy)	Mag. (mag)	Mag. (mag)	f_ν (mJy)	Mag. (mag)	Mag. (mag)	Photo-z
31	08365156-4337410	8.541 ±0.156	13.18 ±0.05	11.19 ±0.05	18.414 ±0.384	11.86 ±0.05	10.57 ±0.05	24.242 ±0.532	11.10 ±0.06	10.27 ±0.06	0.0356
32	08365296-4338169	0.229 ±0.018	17.11 ±0.10	15.74 ±0.10	0.385 ±0.022	16.06 ±0.08	15.17 ±0.08	0.370 ±0.049	15.64 ±0.15	15.07 ±0.15	0.0563
33	08370018-4319277	0.141 ±0.016	17.63 ±0.13	15.86 ±0.13	0.322 ±0.022	16.26 ±0.09	15.11 ±0.09	0.443 ±0.037	15.44 ±0.10	14.70 ±0.10	0.1454
34	08370727-4339136	1.161 ±0.039	15.34 ±0.06	13.71 ±0.06	2.294 ±0.057	14.12 ±0.06	13.06 ±0.06	2.620 ±0.101	13.51 ±0.07	12.83 ±0.07	0.0389
35	08370902-4334203	0.106 ±0.017	17.94 ±0.19	16.35 ±0.19	0.185 ±0.020	16.86 ±0.13	15.82 ±0.13	0.411 ±0.059	15.53 ±0.16	14.86 ±0.16	0.2428
36	08371095-4330370	0.209 ±0.021	17.21 ±0.12	15.61 ±0.12	0.567 ±0.026	15.64 ±0.07	14.60 ±0.07	0.778 ±0.083	14.83 ±0.13	14.16 ±0.13	0.1595
37	08371117-4334581	0.171 ±0.016	17.42 ±0.11	15.83 ±0.11	0.520 ±0.019	15.74 ±0.06	14.70 ±0.06	0.760 ±0.045	14.86 ±0.08	14.19 ±0.08	0.1866
38	08371136-4320430	0.304 ±0.020	16.80 ±0.09	15.03 ±0.09	0.606 ±0.027	15.57 ±0.07	14.42 ±0.07	0.744 ±0.049	14.88 ±0.09	14.14 ±0.09	0.0909
39	08371248-4345354	0.091 ±0.010	18.11 ±0.13	16.74 ±0.13	0.191 ±0.013	16.82 ±0.09	15.93 ±0.09	0.245 ±0.026	16.09 ±0.13	15.51 ±0.13	0.1658
40	08371284-4326311	0.082 ±0.011	18.22 ±0.16	16.45 ±0.16	0.192 ±0.014	16.82 ±0.09	15.67 ±0.09	0.358 ±0.030	15.68 ±0.10	14.93 ±0.10	0.2280
41	08372130-4343012	3.493 ±0.064	14.15 ±0.05	12.55 ±0.05	7.141 ±0.153	12.89 ±0.06	11.85 ±0.06	8.425 ±0.197	12.25 ±0.06	11.58 ±0.06	0.0526
42	08372360-4339139	0.229 ±0.020	17.11 ±0.11	15.51 ±0.11	0.323 ±0.021	16.25 ±0.09	15.21 ±0.09	0.384 ±0.053	15.60 ±0.16	14.93 ±0.16	0.0692
43	08372480-4343369	0.130 ±0.011	17.72 ±0.10	16.12 ±0.10	0.238 ±0.013	16.58 ±0.08	15.54 ±0.08	0.292 ±0.029	15.90 ±0.12	15.23 ±0.12	0.1145
44	08372853-4347138	0.217 ±0.015	17.16 ±0.09	15.96 ±0.09	0.492 ±0.020	15.80 ±0.07	15.01 ±0.07	0.589 ±0.038	15.13 ±0.09	14.63 ±0.09	0.1455
45	08373104-4352304	0.117 ±0.008	17.84 ±0.09	16.63 ±0.09	0.197 ±0.009	16.79 ±0.07	16.00 ±0.07	0.281 ±0.024	15.94 ±0.11	15.43 ±0.11	0.1737
46	08373210-4347178	0.421 ±0.010	16.45 ±0.06	15.24 ±0.06	0.527 ±0.016	15.72 ±0.06	14.94 ±0.06	0.544 ±0.028	15.22 ±0.07	14.72 ±0.07	0.0438
47	08374047-4340275	0.996 ±0.026	15.51 ±0.06	13.91 ±0.06	1.763 ±0.046	14.41 ±0.06	13.37 ±0.06	2.342 ±0.082	13.64 ±0.06	12.97 ±0.06	0.0815
48	08374943-4328517	0.396 ±0.027	16.51 ±0.09	14.91 ±0.09	0.673 ±0.031	15.46 ±0.07	14.42 ±0.07	0.810 ±0.088	14.79 ±0.13	14.12 ±0.13	0.0789
49	08374942-4333454	0.067 ±0.015	18.44 ±0.25	16.84 ±0.25	0.185 ±0.016	16.86 ±0.11	15.82 ±0.11	0.314 ±0.054	15.82 ±0.19	15.15 ±0.19	0.2441
50	08374962-4339440	0.247 ±0.013	17.02 ±0.08	15.43 ±0.08	0.374 ±0.018	16.09 ±0.07	15.05 ±0.07	0.564 ±0.041	15.18 ±0.09	14.51 ±0.09	0.1249
51	08375375-4334564	0.279 ±0.016	16.89 ±0.08	15.29 ±0.08	0.495 ±0.022	15.79 ±0.07	14.75 ±0.07	0.723 ±0.053	14.91 ±0.09	14.24 ±0.09	0.1288
52	08375484-4320213	0.244 ±0.024	17.04 ±0.12	15.22 ±0.12	0.501 ±0.027	15.78 ±0.08	14.59 ±0.08	0.682 ±0.048	14.97 ±0.09	14.21 ±0.09	0.1156
53	08375565-4321530	0.093 ±0.012	18.09 ±0.15	16.45 ±0.15	0.257 ±0.016	16.50 ±0.08	15.44 ±0.08	0.432 ±0.032	15.47 ±0.10	14.79 ±0.10	0.2264
54	08375675-4338428	0.189 ±0.012	17.32 ±0.08	15.72 ±0.08	0.364 ±0.015	16.12 ±0.07	15.08 ±0.07	0.460 ±0.040	15.40 ±0.11	14.73 ±0.11	0.1171
55	08375948-4346194	0.244 ±0.011	17.04 ±0.07	15.70 ±0.07	0.411 ±0.017	15.99 ±0.07	15.12 ±0.07	0.507 ±0.034	15.30 ±0.09	14.74 ±0.09	0.1122
56	08380277-4328206	0.252 ±0.020	17.00 ±0.10	15.41 ±0.10	0.420 ±0.027	15.97 ±0.09	14.93 ±0.09	0.581 ±0.077	15.15 ±0.15	14.48 ±0.15	0.1154

B.1.4 MIPS 24 μm Photometry

Sources in the *Spitzer Footprint* with MIPS 24 μm detections are listed in Table B.4.
Column 1: Reference ID
Column 2: Source IRSF ID
Column 3: Flux density (mJy) for the 24 μm band - raw measurements
Column 4: Flux density (mJy) for the 24 μm band - aperture-corrected
Column 5: Integrated Magnitude (mag) - 10% calibration error included

Table B.4: Sources with MIPS 24 μm Detections.

ID	Source ID	Flux Density [a] (mJy)	Flux Density [b] (mJy)	Integrated Magnitude [c] (mag)
11	08360154-4349352	0.088 ±0.141	0.16 ±0.26	11.60 ±1.74
12	08360585-4346333	0.621 ±0.141	1.05 ±0.24	9.59 ±0.27
24	08363597-4337554	8.754 ±0.440	9.81 ±0.49	7.16 ±0.11
30	08365114-4350515	1.461 ±0.143	2.73 ±0.27	8.55 ±0.15
31	08365156-4337410	114.283 ±1.892	126.52 ±2.09	4.38 ±0.10
34	08370727-4339136	16.615 ±0.484	21.91 ±0.64	6.29 ±0.10
36	08371095-4330370	0.361 ±0.282	0.61 ±0.48	10.18 ±0.85
37	08371117-4334581	1.817 ±0.566	3.06 ±0.95	8.42 ±0.35
41	08372130-4343012	1.952 ±0.144	2.39 ±0.18	8.69 ±0.13
51	08375375-4334564	0.570 ±0.141	1.06 ±0.26	9.57 ±0.29

B.2 IRSF NIR Catalogue

B.2.1 Photometric Parameters

Table B.5 lists the photometric parameters for sources in the IRSF NIR catalogue as follows:
Column 1: Reference ID
Column 2: Source IRSF ID
Column 3: Right Ascension
Column 4: Declination
Column 5: Galactic Longitude (deg)
Column 6: Galactic Latitute (deg)
Column 7: A_V (mag)
Column 8: Number of duplicates (from overlapping fields)
Column 9: Radius, a (arcsec)
Column 10: Axis ratio (b/a)
Column 11: Position Angle (deg) – measured east of north
Duplicate photometry was combined using an inverse-variance weighted mean.

Table B.5: IRSF Catalogue - Photometric Parameters

ID	Source ID.	R.A. (J2000)	Dec. (J2000)	l (deg)	b (deg)	A_V (mag)	Dup.	a (arcsec)	b/a	P.A. (deg)
57	08323738-4347314	$08^h\ 32^m\ 37.4^s$	$-43^\circ47'31.4''$	262.15	-2.35	6.1	1	2.94	1.00	0.00
58	08323780-4343251	$08^h\ 32^m\ 37.8^s$	$-43^\circ43'25.1''$	262.10	-2.31	6.9	1	3.10	1.00	0.00
59	08323841-4344374	$08^h\ 32^m\ 38.4^s$	$-43^\circ44'37.5''$	262.11	-2.32	6.9	1	4.16	1.00	0.00
60	08323888-4326120	$08^h\ 32^m\ 38.9^s$	$-43^\circ26'12.0''$	261.87	-2.14	6.7	1	5.15	1.00	0.00
61	08324065-4311114	$08^h\ 32^m\ 40.7^s$	$-43^\circ11'11.5''$	261.67	-1.99	9.8	1	4.56	1.00	0.00
62	08324104-4304193	$08^h\ 32^m\ 41.0^s$	$-43^\circ04'19.4''$	261.58	-1.92	6.5	1	3.39	1.00	0.00
63	08324201-4341439	$08^h\ 32^m\ 42.0^s$	$-43^\circ41'43.9''$	262.08	-2.28	6.9	1	2.36	1.00	0.00
64	08324241-4406375	$08^h\ 32^m\ 42.4^s$	$-44^\circ06'37.6''$	262.42	-2.53	5.4	1	2.65	1.00	0.00
65	08324251-4305471	$08^h\ 32^m\ 42.5^s$	$-43^\circ05'47.1''$	261.60	-1.93	6.5	2	3.10	0.95	0.00
66	08324325-4350295	$08^h\ 32^m\ 43.3^s$	$-43^\circ50'29.5''$	262.20	-2.37	6.1	1	4.76	0.60	-70.00
67	08324375-4403122	$08^h\ 32^m\ 43.8^s$	$-44^\circ03'12.3''$	262.37	-2.49	6.3	1	2.65	1.00	0.00
68	08324450-4337397	$08^h\ 32^m\ 44.5^s$	$-43^\circ37'39.7''$	262.03	-2.24	6.9	1	3.36	0.90	-40.00
69	08324590-4321417	$08^h\ 32^m\ 45.9^s$	$-43^\circ21'41.8''$	261.82	-2.08	9.8	1	3.44	1.00	0.00
70	08324765-4416192	$08^h\ 32^m\ 47.7^s$	$-44^\circ16'19.2''$	262.55	-2.61	5.4	2	4.42	1.00	0.00
71	08324820-4423085	$08^h\ 32^m\ 48.2^s$	$-44^\circ23'08.6''$	262.65	-2.68	4.8	1	2.36	1.00	0.00
72	08324889-4406068	$08^h\ 32^m\ 48.9^s$	$-44^\circ06'06.8''$	262.42	-2.51	5.4	1	2.37	1.00	0.00
73	08324912-4316026	$08^h\ 32^m\ 49.1^s$	$-43^\circ16'02.6''$	261.75	-2.01	9.8	1	3.24	0.80	0.00
74	08324937-4322396	$08^h\ 32^m\ 49.4^s$	$-43^\circ22'39.6''$	261.84	-2.08	9.8	1	2.80	1.00	0.00
75	08324974-4311110	$08^h\ 32^m\ 49.7^s$	$-43^\circ11'11.1''$	261.68	-1.96	9.8	2	3.12	0.75	5.00
76	08325061-4411304	$08^h\ 32^m\ 50.6^s$	$-44^\circ11'30.4''$	262.50	-2.56	5.4	1	6.01	0.50	-20.00
77	08325151-4412305	$08^h\ 32^m\ 51.5^s$	$-44^\circ12'30.6''$	262.51	-2.57	5.4	1	3.56	0.80	-40.00
78	08325331-4251430	$08^h\ 32^m\ 53.3^s$	$-42^\circ51'43.1''$	261.43	-1.76	6.6	1	13.59	0.50	-50.00
79	08325337-4255412	$08^h\ 32^m\ 53.4^s$	$-42^\circ55'41.3''$	261.48	-1.80	6.6	1	2.21	1.00	0.00
80	08325381-4418517	$08^h\ 32^m\ 53.8^s$	$-44^\circ18'51.7''$	262.60	-2.62	5.4	1	3.77	0.90	50.00
81	08325454-4328259	$08^h\ 32^m\ 54.5^s$	$-43^\circ28'26.0''$	261.92	-2.12	8.3	1	6.14	0.40	-30.00
82	08325459-4344074	$08^h\ 32^m\ 54.6^s$	$-43^\circ44'07.4''$	262.13	-2.28	6.1	1	3.23	0.50	-45.00
83	08325543-4335501	$08^h\ 32^m\ 55.4^s$	$-43^\circ35'50.1''$	262.20	-2.19	6.9	1	2.72	0.90	-88.00
84	08330064-4301238	$08^h\ 33^m\ 00.6^s$	$-43^\circ01'23.8''$	261.57	-1.84	6.6	1	3.83	1.00	0.00
85	08330409-4404493	$08^h\ 33^m\ 04.1^s$	$-44^\circ04'49.4''$	262.43	-2.46	5.4	1	3.39	1.00	0.00
86	08330697-4328526	$08^h\ 33^m\ 07.0^s$	$-43^\circ28'52.6''$	261.95	-2.10	8.3	1	2.80	1.00	0.00
87	08330839-4332159	$08^h\ 33^m\ 08.4^s$	$-43^\circ32'16.0''$	262.00	-2.13	6.9	1	3.24	1.00	0.00
88	08330882-4352564	$08^h\ 33^m\ 08.8^s$	$-43^\circ52'56.5''$	262.28	-2.33	6.1	1	3.40	1.00	0.00
89	08330932-4422108	$08^h\ 33^m\ 09.3^s$	$-44^\circ22'10.8''$	262.67	-2.62	4.9	1	3.96	0.80	-45.00
90	08331000-4258011	$08^h\ 33^m\ 10.0^s$	$-42^\circ58'01.1''$	261.54	-1.78	6.6	1	2.80	1.00	0.00
91	08331030-4420535	$08^h\ 33^m\ 10.3^s$	$-44^\circ20'53.6''$	262.66	-2.60	4.9	1	3.24	1.00	0.00
92	08331163-4257458	$08^h\ 33^m\ 11.6^s$	$-42^\circ57'45.8''$	261.54	-1.78	6.6	1	2.94	1.00	0.00
93	08331221-4254102	$08^h\ 33^m\ 12.2^s$	$-42^\circ54'10.3''$	261.50	-1.74	6.6	1	11.14	0.50	-45.00
94	08331241-4422065	$08^h\ 33^m\ 12.4^s$	$-44^\circ22'06.6''$	262.68	-2.61	4.9	1	3.55	0.70	-85.00
95	08331295-4422124	$08^h\ 33^m\ 13.0^s$	$-44^\circ22'12.5''$	262.68	-2.61	4.9	1	4.89	0.60	75.00
96	08331391-4300547	$08^h\ 33^m\ 13.9^s$	$-43^\circ00'54.8''$	261.59	-1.80	6.6	1	2.71	0.70	-45.00
97	08331652-4423113	$08^h\ 33^m\ 16.5^s$	$-44^\circ23'11.3''$	262.07	-2.61	4.9	1	2.50	1.00	0.00
98	08331675-4259594	$08^h\ 33^m\ 16.7^s$	$-42^\circ59'59.4''$	261.58	-1.79	6.6	2	3.39	1.00	0.00
99	08331759-4423585	$08^h\ 33^m\ 17.6^s$	$-44^\circ23'58.6''$	262.71	-2.62	4.9	1	3.45	0.80	40.00
100	08331840-4301009	$08^h\ 33^m\ 18.4^s$	$-43^\circ01'00.9''$	261.60	-1.79	6.6	1	2.06	1.00	0.00
101	08332108-4300552	$08^h\ 33^m\ 21.1^s$	$-43^\circ00'55.2''$	261.60	-1.78	6.6	2	3.45	0.93	0.00
102	08332207-4402372	$08^h\ 33^m\ 22.1^s$	$-44^\circ02'37.2''$	262.43	-2.39	5.4	1	2.84	0.60	-17.00

ID	Source ID.	R.A. (J2000)	Dec. (J2000)	l (deg)	b (deg)	A_V (mag)	Dup.	a (arcsec)	b/a	P.A. (deg)
103	08332560-4403545	$08^{h}\ 33^{m}\ 25.6^{s}$	-44°03′54.5″	262.46	-2.40	5.4	1	3.50	0.80	-30.00
104	08332934-4311535	$08^{h}\ 33^{m}\ 29.3^{s}$	-43°11′53.5″	261.76	-1.87	6.8	1	2.28	0.90	-88.00
105	08332949-4315127	$08^{h}\ 33^{m}\ 29.5^{s}$	-43°15′12.7″	261.81	-1.91	9.8	1	2.12	1.00	0.00
106	08332986-4404336	$08^{h}\ 33^{m}\ 29.9^{s}$	-44°04′33.6″	262.47	-2.39	5.4	1	2.25	0.90	-11.00
107	08333095-4311535	$08^{h}\ 33^{m}\ 31.0^{s}$	-43°11′53.6″	261.77	-1.87	6.8	1	2.14	1.00	0.00
108	08333187-4330093	$08^{h}\ 33^{m}\ 31.9^{s}$	-43°30′09.3″	262.01	-2.05	8.3	1	2.13	1.00	0.00
109	08334058-4405503	$08^{h}\ 33^{m}\ 40.6^{s}$	-44°05′50.4″	262.51	-2.38	5.4	1	2.06	0.70	-2.00
110	08334327-4340484	$08^{h}\ 33^{m}\ 43.3^{s}$	-43°40′48.5″	262.18	-2.13	6.1	2	4.35	0.40	21.00
111	08334375-4321546	$08^{h}\ 33^{m}\ 43.8^{s}$	-43°21′54.7″	261.93	-1.94	8.3	1	1.83	0.80	-50.00
112	08334433-4329071	$08^{h}\ 33^{m}\ 44.3^{s}$	-43°29′07.2″	262.02	-2.01	8.3	1	1.45	1.00	0.00
113	08334542-4305265	$08^{h}\ 33^{m}\ 45.4^{s}$	-43°05′26.5″	261.71	-1.77	6.8	1	2.21	0.70	-90.00
114	08335677-4319546	$08^{h}\ 33^{m}\ 56.8^{s}$	-43°19′54.7″	261.92	-1.89	8.3	1	4.78	0.60	37.00
115	08340029-4323232	$08^{h}\ 34^{m}\ 00.3^{s}$	-43°23′23.3″	261.97	-1.91	8.3	1	4.30	0.80	52.00
116	08340083-4346065	$08^{h}\ 34^{m}\ 00.8^{s}$	-43°46′06.5″	262.28	-2.14	6.1	1	1.41	1.00	0.00
117	08340231-4401256	$08^{h}\ 34^{m}\ 02.3^{s}$	-44°01′25.7″	262.49	-2.29	5.4	1	1.88	1.00	0.00
118	08340272-4332425	$08^{h}\ 34^{m}\ 02.7^{s}$	-43°32′42.5″	262.10	-2.00	8.3	1	3.44	0.40	47.00
119	08340285-4413297	$08^{h}\ 34^{m}\ 02.9^{s}$	-44°13′29.7″	262.65	-2.40	4.9	1	2.89	1.00	0.00
120	08340306-4253001	$08^{h}\ 34^{m}\ 03.1^{s}$	-42°53′00.1″	261.57	-1.60	6.7	1	3.00	1.00	0.00
121	08340506-4336530	$08^{h}\ 34^{m}\ 05.1^{s}$	-43°36′53.1″	262.16	-2.03	7.7	1	2.77	1.00	0.00
122	08340525-4252559	$08^{h}\ 34^{m}\ 05.3^{s}$	-42°52′56.0″	261.58	-1.60	6.7	1	2.08	1.00	0.00
123	08340546-4256344	$08^{h}\ 34^{m}\ 05.5^{s}$	-42°56′34.5″	261.63	-1.63	6.8	1	3.01	0.70	-68.00
124	08340718-4333183	$08^{h}\ 34^{m}\ 07.2^{s}$	-43°33′18.3″	262.12	-1.99	8.3	1	2.27	1.00	0.00
125	08340728-4257538	$08^{h}\ 34^{m}\ 07.3^{s}$	-42°57′53.9″	261.65	-1.64	6.8	1	1.39	1.00	0.00
126	08340887-4416511	$08^{h}\ 34^{m}\ 08.9^{s}$	-44°16′51.1″	262.71	-2.42	4.9	1	1.87	1.00	0.00
127	08340945-4413341	$08^{h}\ 34^{m}\ 09.5^{s}$	-44°13′34.2″	262.66	-2.39	4.9	1	1.47	1.00	0.00
128	08341000-4300414	$08^{h}\ 34^{m}\ 10.0^{s}$	-43°00′41.5″	261.69	-1.66	6.8	1	1.84	0.70	-88.00
129	08341220-4330200	$08^{h}\ 34^{m}\ 12.2^{s}$	-43°30′20.1″	262.09	-1.95	8.3	1	4.27	0.75	88.00
130	08341298-4251439	$08^{h}\ 34^{m}\ 13.0^{s}$	-42°51′43.9″	261.57	-1.57	6.7	1	2.16	1.00	0.00
131	08341630-4330529	$08^{h}\ 34^{m}\ 16.3^{s}$	-43°30′53.0″	262.10	-1.95	8.3	1	1.40	1.00	0.00
132	08341822-4318533	$08^{h}\ 34^{m}\ 18.2^{s}$	-43°18′53.3″	261.95	-1.82	8.1	1	2.60	0.80	45.00
133	08341914-4332191	$08^{h}\ 34^{m}\ 19.1^{s}$	-43°32′19.2″	262.13	-1.95	7.7	1	2.54	1.00	0.00
134	08341986-4359582	$08^{h}\ 34^{m}\ 19.9^{s}$	-43°59′58.3″	262.50	-2.23	5.4	1	1.91	1.00	0.00
135	08342055-4315195	$08^{h}\ 34^{m}\ 20.6^{s}$	-43°15′19.5″	261.90	-1.78	8.1	1	1.91	0.90	67.00
136	08342060-4323449	$08^{h}\ 34^{m}\ 20.6^{s}$	-43°23′44.9″	262.02	-1.87	8.1	1	3.13	0.80	29.00
137	08342193-4421221	$08^{h}\ 34^{m}\ 21.9^{s}$	-44°21′22.1″	262.79	-2.44	4.9	1	1.94	1.00	0.00
138	08342398-4421130	$08^{h}\ 34^{m}\ 24.0^{s}$	-44°21′13.0″	262.79	-2.43	4.9	1	1.59	1.00	0.00
139	08342607-4316438	$08^{h}\ 34^{m}\ 26.1^{s}$	-43°16′43.8″	261.93	-1.78	8.1	1	1.71	1.00	0.00
140	08343190-4358137	$08^{h}\ 34^{m}\ 31.9^{s}$	-43°58′13.8″	262.50	-2.18	5.4	1	2.44	1.00	0.00
141	08343306-4324351	$08^{h}\ 34^{m}\ 33.1^{s}$	-43°24′35.2″	262.05	-1.84	8.1	2	10.51	0.77	29.00
142	08343599-4403034	$08^{h}\ 34^{m}\ 36.0^{s}$	-44°03′03.5″	262.57	-2.22	5.4	2	2.20	1.00	0.00
143	08343806-4359159	$08^{h}\ 34^{m}\ 38.1^{s}$	-43°59′16.0″	262.52	-2.18	5.4	2	2.88	0.50	53.00
144	08343918-4400493	$08^{h}\ 34^{m}\ 39.2^{s}$	-44°00′49.3″	262.55	-2.19	5.4	1	4.73	0.70	-37.00
145	08344140-4343398	$08^{h}\ 34^{m}\ 41.4^{s}$	-43°43′39.9″	262.32	-2.01	7.7	1	2.36	1.00	0.00
146	08344150-4339111	$08^{h}\ 34^{m}\ 41.5^{s}$	-43°39′11.1″	262.26	-1.97	7.7	1	2.00	1.00	0.00
147	08344240-4417049	$08^{h}\ 34^{m}\ 42.4^{s}$	-44°17′05.0″	262.77	-2.34	4.4	1	6.80	0.30	38.90
148	08344286-4358028	$08^{h}\ 34^{m}\ 42.9^{s}$	-43°58′02.8″	262.52	-2.15	5.4	1	2.00	0.90	84.00
149	08344552-4306144	$08^{h}\ 34^{m}\ 45.5^{s}$	-43°06′14.4″	261.83	-1.63	6.8	2	5.39	0.88	-33.00
150	08344596-4343437	$08^{h}\ 34^{m}\ 46.0^{s}$	-43°43′43.7″	262.33	-2.00	7.7	1	2.19	1.00	0.00
151	08344595-4352511	$08^{h}\ 34^{m}\ 46.0^{s}$	-43°52′51.2″	262.45	-2.09	4.8	1	3.31	0.50	21.00
152	08344751-4401224	$08^{h}\ 34^{m}\ 47.5^{s}$	-44°01′22.4″	262.57	-2.18	5.4	2	3.32	1.00	0.00
153	08345401-4306499	$08^{h}\ 34^{m}\ 54.0^{s}$	-43°06′49.9″	261.85	-1.62	8.1	1	2.02	0.80	-10.50

ID	Source ID.	R.A. (J2000)	Dec. (J2000)	l (deg)	b (deg)	A_V (mag)	Dup.	a (arcsec)	b/a	P.A. (deg)
154	08345655-4252401	$08^{h}\ 34^{m}\ 56.6^{s}$	-42°52′40.1″	261.67	-1.47	8.1	1	2.12	0.90	-70.00
155	08345744-4341199	$08^{h}\ 34^{m}\ 57.4^{s}$	-43°41′19.9″	262.32	-1.95	7.7	2	1.89	1.00	0.00
156	08345927-4305527	$08^{h}\ 34^{m}\ 59.3^{s}$	-43°05′52.7″	261.85	-1.59	8.1	2	1.72	1.00	0.00
157	08345938-4409244	$08^{h}\ 34^{m}\ 59.4^{s}$	-44°09′24.4″	262.70	-2.23	4.4	1	1.97	1.00	0.00
158	08350472-4420156	$08^{h}\ 35^{m}\ 04.7^{s}$	-44°20′15.7″	262.85	-2.32	4.4	1	2.49	1.00	0.00
159	08350590-4333378	$08^{h}\ 35^{m}\ 05.9^{s}$	-43°33′37.9″	262.23	-1.85	5.8	1	2.89	0.90	52.00
160	08350744-4408534	$08^{h}\ 35^{m}\ 07.4^{s}$	-44°08′53.5″	262.70	-2.20	4.4	2	4.61	0.75	-53.00
161	08350928-4312245	$08^{h}\ 35^{m}\ 09.3^{s}$	-43°12′24.5″	261.95	-1.63	8.1	1	1.84	1.00	0.00
162	08350935-4332412	$08^{h}\ 35^{m}\ 09.4^{s}$	-43°32′41.3″	262.22	-1.84	5.8	2	3.86	0.90	0.00
163	08351133-4322293	$08^{h}\ 35^{m}\ 11.3^{s}$	-43°22′29.4″	262.09	-1.73	8.1	2	2.97	1.00	0.00
164	08351371-4321122	$08^{h}\ 35^{m}\ 13.7^{s}$	-43°21′12.2″	262.08	-1.71	8.1	2	3.45	0.70	80.00
165	08351819-4319491	$08^{h}\ 35^{m}\ 18.2^{s}$	-43°19′49.2″	262.07	-1.69	8.1	1	5.96	0.90	-13.00
166	08351851-4307381	$08^{h}\ 35^{m}\ 18.5^{s}$	-43°07′38.1″	261.91	-1.56	6.9	1	4.71	0.40	-61.00
167	08351883-4318094	$08^{h}\ 35^{m}\ 18.8^{s}$	-43°18′09.5″	262.05	-1.67	8.1	1	5.93	0.50	-25.00
168	08352012-4319580	$08^{h}\ 35^{m}\ 20.1^{s}$	-43°19′58.0″	262.07	-1.68	8.1	1	2.36	1.00	0.00
169	08352171-4349417	$08^{h}\ 35^{m}\ 21.7^{s}$	-43°49′41.7″	262.47	-1.98	4.8	1	1.29	1.00	0.00
170	08352270-4319378	$08^{h}\ 35^{m}\ 22.7^{s}$	-43°19′37.9″	262.07	-1.67	8.1	2	10.38	0.75	-48.00
171	08352278-4347181	$08^{h}\ 35^{m}\ 22.8^{s}$	-43°47′18.1″	262.44	-1.95	4.8	2	3.03	1.00	0.00
172	08352288-4306371	$08^{h}\ 35^{m}\ 22.9^{s}$	-43°06′37.1″	261.90	-1.54	6.9	2	3.25	0.95	0.00
173	08352414-4304121	$08^{h}\ 35^{m}\ 24.1^{s}$	-43°04′12.2″	261.87	-1.52	8.1	1	1.99	1.00	0.00
174	08352483-4318232	$08^{h}\ 35^{m}\ 24.8^{s}$	-43°18′23.3″	262.06	-1.66	8.1	1	11.32	0.80	-36.00
175	08352562-4406211	$08^{h}\ 35^{m}\ 25.6^{s}$	-44°06′21.1″	262.70	-2.13	4.4	1	2.51	1.00	0.00
176	08352601-4352450	$08^{h}\ 35^{m}\ 26.0^{s}$	-43°52′45.0″	262.52	-2.00	4.8	1	1.56	1.00	0.00
177	08352639-4413073	$08^{h}\ 35^{m}\ 26.4^{s}$	-44°13′07.3″	262.79	-2.20	4.4	1	1.33	1.00	0.00
178	08352880-4412551	$08^{h}\ 35^{m}\ 28.8^{s}$	-44°12′55.2″	262.80	-2.19	4.4	1	1.55	1.00	0.00
179	08352964-4348385	$08^{h}\ 35^{m}\ 29.6^{s}$	-43°48′38.6″	262.47	-1.95	4.8	1	2.08	0.80	45.00
180	08352964-4412335	$08^{h}\ 35^{m}\ 29.6^{s}$	-44°12′33.5″	262.79	-2.19	4.4	1	2.60	0.90	43.00
181	08353086-4404125	$08^{h}\ 35^{m}\ 30.9^{s}$	-44°04′12.5″	262.68	-2.10	3.7	1	8.86	0.20	-5.00
182	08353468-4259528	$08^{h}\ 35^{m}\ 34.7^{s}$	-42°59′52.8″	261.83	-1.45	8.1	1	2.58	1.00	0.00
183	08353523-4259598	$08^{h}\ 35^{m}\ 35.2^{s}$	-42°59′59.8″	261.83	-1.45	8.1	1	3.35	0.50	40.00
184	08353553-4304142	$08^{h}\ 35^{m}\ 35.5^{s}$	-43°04′14.3″	261.89	-1.49	6.9	1	4.15	1.00	0.00
185	08354136-4401486	$08^{h}\ 35^{m}\ 41.4^{s}$	-44°01′48.6″	262.67	-2.05	3.7	1	1.82	1.00	0.00
186	08354200-4354258	$08^{h}\ 35^{m}\ 42.0^{s}$	-43°54′25.8″	262.57	-1.98	4.8	2	1.79	1.00	0.00
187	08354300-4312228	$08^{h}\ 35^{m}\ 43.0^{s}$	-43°12′22.8″	262.01	-1.55	6.9	2	9.05	0.50	24.00
188	08354348-4359584	$08^{h}\ 35^{m}\ 43.5^{s}$	-43°59′58.5″	262.65	-2.03	3.7	1	14.76	0.40	-42.00
189	08354407-4315260	$08^{h}\ 35^{m}\ 44.1^{s}$	-43°15′26.0″	262.06	-1.58	6.9	1	4.87	0.70	-86.00
190	08354713-4328169	$08^{h}\ 35^{m}\ 47.1^{s}$	-43°28′17.0″	262.23	-1.70	5.8	1	2.66	1.00	0.00
191	08355052-4305281	$08^{h}\ 35^{m}\ 50.5^{s}$	-43°05′28.2″	261.94	-1.47	6.9	3	4.66	0.90	48.00
192	08355195-4401194	$08^{h}\ 35^{m}\ 52.0^{s}$	-44°01′19.5″	262.68	-2.02	3.7	1	1.55	1.00	0.00
193	08355302-4314552	$08^{h}\ 35^{m}\ 53.0^{s}$	-43°14′55.3″	262.07	-1.55	6.9	2	13.45	0.55	51.00
194	08355447-4302014	$08^{h}\ 35^{m}\ 54.5^{s}$	-43°02′01.4″	261.90	-1.42	6.9	1	3.61	1.00	0.00
195	08355529-4407135	$08^{h}\ 35^{m}\ 55.3^{s}$	-44°07′13.5″	262.77	-2.07	3.7	2	2.84	0.90	44.00
196	08355735-4300151	$08^{h}\ 35^{m}\ 57.4^{s}$	-43°00′15.2″	261.88	-1.40	6.9	1	4.57	0.70	-33.00
197	08360276-4311041	$08^{h}\ 36^{m}\ 02.8^{s}$	-43°11′04.1″	262.03	-1.49	6.9	1	3.65	1.00	0.00
198	08360280-4413373	$08^{h}\ 36^{m}\ 02.8^{s}$	-44°13′37.4″	262.87	-2.12	3.7	1	5.74	0.30	-36.00
199	08360975-4422398	$08^{h}\ 36^{m}\ 09.8^{s}$	-44°22′39.8″	263.00	-2.19	3.7	1	3.10	1.00	0.00
200	08361832-4315123	$08^{h}\ 36^{m}\ 18.3^{s}$	-43°15′12.3″	262.12	-1.50	6.9	1	3.49	0.90	25.00
201	08361967-4406022	$08^{h}\ 36^{m}\ 19.7^{s}$	-44°06′02.2″	262.80	-2.00	3.7	1	3.17	1.00	0.00
202	08362343-4406549	$08^{h}\ 36^{m}\ 23.4^{s}$	-44°06′54.9″	262.81	-2.00	3.7	1	6.06	0.30	62.00
203	08362678-4358000	$08^{h}\ 36^{m}\ 26.8^{s}$	-43°58′00.0″	262.70	-1.90	3.7	1	5.11	0.70	-42.00
204	08362694-4251306	$08^{h}\ 36^{m}\ 26.9^{s}$	-42°51′30.6″	261.82	-1.24	7.7	1	3.95	1.00	0.00

ID	Source ID.	R.A. (J2000)	Dec. (J2000)	l (deg)	b (deg)	A_V (mag)	Dup.	a (arcsec)	b/a	P.A. (deg)
205	08362695-4300014	$08^{h}\ 36^{m}\ 27.0^{s}$	-43°00′01.4″	261.93	-1.32	6.8	1	2.83	1.00	0.00
206	08362761-4404515	$08^{h}\ 36^{m}\ 27.6^{s}$	-44°04′51.5″	262.79	-1.97	3.7	1	2.64	1.00	0.00
207	08362815-4257360	$08^{h}\ 36^{m}\ 28.2^{s}$	-42°57′36.1″	261.90	-1.29	6.8	1	3.50	0.80	49.00
208	08363189-4306118	$08^{h}\ 36^{m}\ 31.9^{s}$	-43°06′11.9″	262.02	-1.37	6.8	4	14.24	0.95	50.00
209	08363338-4420579	$08^{h}\ 36^{m}\ 33.4^{s}$	-44°20′57.9″	263.02	-2.12	3.5	1	2.94	1.00	0.00
210	08363380-4304547	$08^{h}\ 36^{m}\ 33.8^{s}$	-43°04′54.7″	262.01	-1.35	6.8	1	2.06	1.00	0.00
211	08363551-4258013	$08^{h}\ 36^{m}\ 35.5^{s}$	-42°58′01.3″	261.92	-1.28	6.8	1	7.27	0.50	-30.00
212	08363719-4412107	$08^{h}\ 36^{m}\ 37.2^{s}$	-44°12′10.7″	262.91	-2.02	3.5	1	2.67	1.00	0.00
213	08363727-4414067	$08^{h}\ 36^{m}\ 37.3^{s}$	-44°14′06.7″	262.94	-2.04	3.5	1	5.30	0.50	0.00
214	08363885-4311269	$08^{h}\ 36^{m}\ 38.9^{s}$	-43°11′27.0″	262.10	-1.41	6.9	1	3.66	0.70	50.00
215	08363984-4304047	$08^{h}\ 36^{m}\ 39.8^{s}$	-43°04′04.8″	262.01	-1.33	6.8	1	2.80	1.00	0.00
216	08364027-4302524	$08^{h}\ 36^{m}\ 40.3^{s}$	-43°02′52.5″	261.99	-1.32	6.8	1	2.36	1.00	0.00
217	08364075-4305437	$08^{h}\ 36^{m}\ 40.8^{s}$	-43°05′43.7″	262.03	-1.35	6.8	1	2.36	1.00	0.00
218	08364298-4257578	$08^{h}\ 36^{m}\ 43.0^{s}$	-42°57′57.8″	261.93	-1.26	6.8	1	4.28	1.00	0.00
219	08364308-4302186	$08^{h}\ 36^{m}\ 43.1^{s}$	-43°02′18.6″	261.99	-1.31	6.8	1	2.70	1.00	0.00
220	08364471-4310595	$08^{h}\ 36^{m}\ 44.7^{s}$	-43°10′59.6″	262.11	-1.39	6.9	1	2.70	0.80	60.00
221	08364645-4319369	$08^{h}\ 36^{m}\ 46.5^{s}$	-43°19′37.0″	262.23	-1.47	6.5	1	2.84	1.00	0.00
222	08364700-4317079	$08^{h}\ 36^{m}\ 47.0^{s}$	-43°17′08.0″	262.19	-1.45	6.5	1	3.19	1.00	0.00
223	08364769-4304357	$08^{h}\ 36^{m}\ 47.7^{s}$	-43°04′35.7″	262.03	-1.32	6.8	1	4.29	0.70	60.00
224	08364864-4354333	$08^{h}\ 36^{m}\ 48.6^{s}$	-43°54′33.3″	262.70	-1.82	4.4	1	1.94	1.00	0.00
225	08364908-4403170	$08^{h}\ 36^{m}\ 49.1^{s}$	-44°03′17.0″	262.81	-1.90	3.7	1	4.42	0.90	-20.00
226	08365359-4316249	$08^{h}\ 36^{m}\ 53.6^{s}$	-43°16′25.0″	262.20	-1.42	6.5	1	2.14	1.00	0.00
227	08365711-4255502	$08^{h}\ 36^{m}\ 57.1^{s}$	-42°55′50.2″	261.93	-1.21	6.8	1	3.11	1.00	0.00
228	08365802-4303255	$08^{h}\ 36^{m}\ 58.0^{s}$	-43°03′25.6″	262.03	-1.28	6.8	1	3.43	0.80	30.90
229	08365881-4304055	$08^{h}\ 36^{m}\ 58.8^{s}$	-43°04′05.6″	262.04	-1.29	6.8	1	1.85	1.00	0.00
230	08365946-4304027	$08^{h}\ 36^{m}\ 59.5^{s}$	-43°04′02.8″	262.04	-1.28	6.8	1	2.43	1.00	0.00
231	08365969-4303347	$08^{h}\ 36^{m}\ 59.7^{s}$	-43°03′34.8″	262.04	-1.28	6.8	1	3.12	0.90	-5.00
232	08370122-4302534	$08^{h}\ 37^{m}\ 01.2^{s}$	-43°02′53.4″	262.03	-1.27	6.8	1	2.31	0.90	10.00
233	08370360-4407476	$08^{h}\ 37^{m}\ 03.6^{s}$	-44°07′47.6″	262.90	-1.91	3.5	1	4.65	0.90	-10.00
234	08370535-4414245	$08^{h}\ 37^{m}\ 05.4^{s}$	-44°14′24.5″	262.99	-1.98	3.5	1	4.89	1.00	0.00
235	08370629-4408034	$08^{h}\ 37^{m}\ 06.3^{s}$	-44°08′03.4″	262.91	-1.91	3.5	1	3.41	0.90	-8.00
236	08370827-4407091	$08^{h}\ 37^{m}\ 08.3^{s}$	-44°07′09.2″	262.90	-1.90	3.5	1	3.09	1.00	0.00
237	08370889-4317373	$08^{h}\ 37^{m}\ 08.9^{s}$	-43°17′37.3″	262.24	-1.40	6.5	2	3.41	0.80	50.00
238	08370893-4412105	$08^{h}\ 37^{m}\ 08.9^{s}$	-44°12′10.6″	262.97	-1.95	3.5	1	1.91	1.00	0.00
239	08370946-4319383	$08^{h}\ 37^{m}\ 09.5^{s}$	-43°19′38.4″	262.27	-1.42	6.5	1	2.68	1.00	0.00
240	08371218-4356104	$08^{h}\ 37^{m}\ 12.2^{s}$	-43°56′10.4″	262.76	-1.78	4.4	2	5.10	1.00	0.00
241	08371400-4306231	$08^{h}\ 37^{m}\ 14.0^{s}$	-43°06′23.1″	262.10	-1.27	6.8	2	3.80	0.80	5.00
242	08371794-4418112	$08^{h}\ 37^{m}\ 17.9^{s}$	-44°18′11.2″	263.06	-1.98	3.5	1	2.95	1.00	0.00
243	08371958-4308521	$08^{h}\ 37^{m}\ 19.6^{s}$	-43°08′52.2″	262.14	-1.28	6.7	1	2.94	1.00	0.00
244	08371998-4421461	$08^{h}\ 37^{m}\ 20.0^{s}$	-44°21′46.1″	263.11	-2.02	3.5	1	4.07	0.90	-45.00
245	08372126-4407275	$08^{h}\ 37^{m}\ 21.3^{s}$	-44°07′27.6″	262.93	-1.87	4.2	1	5.22	0.90	-20.00
246	08372217-4300317	$08^{h}\ 37^{m}\ 22.2^{s}$	-43°00′31.8″	262.04	-1.19	6.8	1	2.07	1.00	0.00
247	08372295-4358225	$08^{h}\ 37^{m}\ 23.0^{s}$	-43°58′22.5″	262.81	-1.77	4.4	1	2.06	0.90	0.00
248	08372299-4301216	$08^{h}\ 37^{m}\ 23.0^{s}$	-43°01′21.6″	262.05	-1.20	6.8	1	2.95	1.00	0.00
249	08372306-4356371	$08^{h}\ 37^{m}\ 23.1^{s}$	-43°56′37.1″	262.79	-1.76	4.4	1	4.18	1.00	0.00
250	08372490-4353237	$08^{h}\ 37^{m}\ 24.9^{s}$	-43°53′23.7″	262.75	-1.72	4.4	1	13.63	0.40	65.00
251	08372764-4303101	$08^{h}\ 37^{m}\ 27.6^{s}$	-43°03′10.2″	262.08	-1.21	6.8	1	2.57	0.80	-10.00
252	08372818-4419504	$08^{h}\ 37^{m}\ 28.2^{s}$	-44°19′50.5″	263.10	-1.98	3.5	1	6.77	0.40	-45.00
253	08372953-4407128	$08^{h}\ 37^{m}\ 29.5^{s}$	-44°07′12.9″	262.94	-1.85	4.2	1	4.43	1.00	0.00
254	08373052-4306496	$08^{h}\ 37^{m}\ 30.5^{s}$	-43°06′49.6″	262.14	-1.24	6.7	1	9.58	0.30	45.00
255	08373205-4347180	$08^{h}\ 37^{m}\ 32.1^{s}$	-43°47′18.0″	262.68	-1.64	4.4	2	3.53	1.00	0.00

ID	Source ID.	R.A. (J2000)	Dec. (J2000)	l (deg)	b (deg)	A_V (mag)	Dup.	a (arcsec)	b/a	P.A. (deg)
256	08373564-4409162	$08^{h}\ 37^{m}\ 35.6^{s}$	-44°09′16.2″	262.98	-1.85	4.2	2	3.39	0.95	90.00
257	08373576-4410365	$08^{h}\ 37^{m}\ 35.8^{s}$	-44°10′36.6″	262.99	-1.87	4.2	1	3.39	0.90	0.00
258	08373629-4358532	$08^{h}\ 37^{m}\ 36.3^{s}$	-43°58′53.2″	262.84	-1.75	4.4	1	12.78	0.40	10.00
259	08373824-4307588	$08^{h}\ 37^{m}\ 38.2^{s}$	-43°07′58.9″	262.17	-1.23	6.7	1	2.06	1.00	0.00
260	08373853-4258258	$08^{h}\ 37^{m}\ 38.5^{s}$	-42°58′25.9″	262.04	-1.13	6.8	2	3.91	1.00	0.00
261	08373905-4418235	$08^{h}\ 37^{m}\ 39.1^{s}$	-44°18′23.6″	263.10	-1.94	3.5	1	3.09	1.00	0.00
262	08373922-4418322	$08^{h}\ 37^{m}\ 39.2^{s}$	-44°18′32.2″	263.11	-1.94	3.5	1	5.27	0.80	-55.00
263	08373963-4320219	$08^{h}\ 37^{m}\ 39.6^{s}$	-43°20′22.0″	262.33	-1.35	6.7	1	2.95	1.00	0.00
264	08374159-4310033	$08^{h}\ 37^{m}\ 41.6^{s}$	-43°10′03.4″	262.20	-1.24	6.7	1	2.21	1.00	0.00
265	08374170-4309379	$08^{h}\ 37^{m}\ 41.7^{s}$	-43°09′38.0″	262.20	-1.24	6.7	1	3.99	0.80	5.00
266	08374267-4421396	$08^{h}\ 37^{m}\ 42.7^{s}$	-44°21′39.6″	263.15	-1.96	3.6	1	3.64	0.90	45.00
267	08374317-4400126	$08^{h}\ 37^{m}\ 43.2^{s}$	-44°00′12.7″	262.87	-1.74	4.4	1	2.98	1.00	0.00
268	08374400-4406271	$08^{h}\ 37^{m}\ 44.0^{s}$	-44°06′27.2″	262.95	-1.80	4.2	1	3.56	0.90	45.00
269	08374435-4309529	$08^{h}\ 37^{m}\ 44.4^{s}$	-43°09′53.0″	262.20	-1.23	6.7	1	2.50	1.00	0.00
270	08374566-4353314	$08^{h}\ 37^{m}\ 45.7^{s}$	-43°53′31.5″	262.78	-1.67	4.4	2	8.64	1.00	0.00
271	08374570-4352214	$08^{h}\ 37^{m}\ 45.7^{s}$	-43°52′21.5″	262.77	-1.66	4.4	1	2.19	1.00	0.00
272	08374598-4300410	$08^{h}\ 37^{m}\ 46.0^{s}$	-43°00′41.1″	262.08	-1.14	6.8	1	3.39	1.00	0.00
273	08374616-4414176	$08^{h}\ 37^{m}\ 46.2^{s}$	-44°14′17.6″	263.06	-1.88	3.5	2	5.56	0.85	50.00
274	08375404-4316176	$08^{h}\ 37^{m}\ 54.0^{s}$	-43°16′17.7″	262.31	-1.27	6.7	1	3.73	1.00	0.00
275	08375462-4316522	$08^{h}\ 37^{m}\ 54.6^{s}$	-43°16′52.3″	262.31	-1.28	6.7	1	4.74	0.70	35.00
276	08375713-4402597	$08^{h}\ 37^{m}\ 57.1^{s}$	-44°02′59.8″	262.93	-1.74	4.2	1	2.80	1.00	0.00
277	08375821-4422211	$08^{h}\ 37^{m}\ 58.2^{s}$	-44°22′21.1″	263.19	-1.93	3.6	1	2.86	1.00	0.00
278	08380578-4422423	$08^{h}\ 38^{m}\ 05.8^{s}$	-44°22′42.3″	263.21	-1.92	3.6	1	3.09	0.70	90.00
279	08380650-4312537	$08^{h}\ 38^{m}\ 06.5^{s}$	-43°12′53.8″	262.28	-1.21	6.7	2	3.32	1.00	0.00
280	08380676-4409258	$08^{h}\ 38^{m}\ 06.8^{s}$	-44°09′25.9″	263.03	-1.78	4.2	2	2.88	1.00	0.00
281	08381099-4400442	$08^{h}\ 38^{m}\ 11.0^{s}$	-44°00′44.2″	262.93	-1.68	4.2	1	3.56	1.00	0.00
282	08381115-4359107	$08^{h}\ 38^{m}\ 11.2^{s}$	-43°59′10.8″	262.91	-1.67	4.2	1	4.38	0.80	20.00
283	08381187-4358518	$08^{h}\ 38^{m}\ 11.9^{s}$	-43°58′51.9″	262.90	-1.66	4.2	1	4.27	1.00	0.00
284	08381266-4413546	$08^{h}\ 38^{m}\ 12.7^{s}$	-44°13′54.7″	263.10	-1.81	4.2	1	2.50	1.00	0.00
285	08381436-4305290	$08^{h}\ 38^{m}\ 14.4^{s}$	-43°05′29.0″	262.20	-1.12	7.0	2	5.69	0.90	45.00
286	08381500-4351542	$08^{h}\ 38^{m}\ 15.0^{s}$	-43°51′54.3″	262.82	-1.58	4.9	1	3.54	1.00	0.00
287	08381530-4302517	$08^{h}\ 38^{m}\ 15.3^{s}$	-43°02′51.7″	262.17	-1.09	7.0	1	2.80	1.00	0.00
288	08381610-4317416	$08^{h}\ 38^{m}\ 16.1^{s}$	-43°17′41.6″	262.37	-1.24	6.7	1	3.72	0.80	55.00
289	08381629-4321046	$08^{h}\ 38^{m}\ 16.3^{s}$	-43°21′04.6″	262.41	-1.27	6.0	1	3.24	1.00	0.00
290	08381663-4259494	$08^{h}\ 38^{m}\ 16.6^{s}$	-42°59′49.5″	262.13	-1.05	7.0	1	4.42	1.00	0.00
291	08381804-4300361	$08^{h}\ 38^{m}\ 18.0^{s}$	-43°00′36.1″	262.14	-1.06	7.0	1	2.95	1.00	0.00
292	08382036-4323061	$08^{h}\ 38^{m}\ 20.4^{s}$	-43°23′06.2″	262.44	-1.28	6.0	1	7.59	0.50	70.00
293	08382163-4404292	$08^{h}\ 38^{m}\ 21.6^{s}$	-44°04′29.2″	263.00	-1.70	4.2	1	3.27	1.00	0.00
294	08382657-4325142	$08^{h}\ 38^{m}\ 26.6^{s}$	-43°25′14.3″	262.48	-1.29	6.0	2	4.33	0.80	-40.00
295	08382954-4253118	$08^{h}\ 38^{m}\ 29.5^{s}$	-42°53′11.8″	262.07	-0.96	8.8	1	2.51	1.00	0.00
296	08382972-4334467	$08^{h}\ 38^{m}\ 29.7^{s}$	-43°34′46.7″	262.62	-1.38	5.9	2	3.24	0.70	-50.00
297	08383023-4304524	$08^{h}\ 38^{m}\ 30.2^{s}$	-43°04′52.5″	262.22	-1.07	7.0	2	3.62	1.00	0.00
298	08383175-4324012	$08^{h}\ 38^{m}\ 31.8^{s}$	-43°24′01.3″	262.48	-1.26	6.0	1	2.81	1.00	0.00
299	08383456-4351141	$08^{h}\ 38^{m}\ 34.6^{s}$	-43°51′14.1″	262.84	-1.53	4.9	1	3.24	1.00	0.00
300	08383629-4320115	$08^{h}\ 38^{m}\ 36.3^{s}$	-43°20′11.6″	262.44	-1.21	6.0	1	3.41	1.00	0.00
301	08383876-4355210	$08^{h}\ 38^{m}\ 38.8^{s}$	-43°55′21.0″	262.91	-1.56	4.3	1	2.80	1.00	0.00
302	08383974-4332236	$08^{h}\ 38^{m}\ 39.7^{s}$	-43°32′23.6″	262.60	-1.33	6.0	1	3.84	1.00	0.00
303	08384043-4309495	$08^{h}\ 38^{m}\ 40.4^{s}$	-43°09′49.6″	262.31	-1.10	7.0	1	6.18	0.60	90.00
304	08384288-4356222	$08^{h}\ 38^{m}\ 42.9^{s}$	-43°56′22.2″	262.93	-1.56	4.3	1	2.51	1.00	0.00
305	08384628-4413235	$08^{h}\ 38^{m}\ 46.3^{s}$	-44°13′23.6″	263.16	-1.73	4.2	1	3.68	1.00	0.00
306	08384680-4358573	$08^{h}\ 38^{m}\ 46.8^{s}$	-43°58′57.3″	262.97	-1.58	4.3	1	4.05	0.60	-70.00

ID	Source ID.	R.A. (J2000)	Dec. (J2000)	l (deg)	b (deg)	A_V (mag)	Dup.	a (arcsec)	b/a	P.A. (deg)
307	08384711-4359061	$08^{h}\ 38^{m}\ 47.1^{s}$	-43°59′06.1″	262.97	-1.58	4.3	1	2.21	1.00	0.00
308	08384963-4254595	$08^{h}\ 38^{m}\ 49.6^{s}$	-42°54′59.6″	262.13	-0.92	7.0	1	3.54	1.00	0.00
309	08385142-4404589	$08^{h}\ 38^{m}\ 51.4^{s}$	-44°04′58.9″	263.06	-1.63	4.2	1	5.15	1.00	0.00
310	08385443-4401322	$08^{h}\ 38^{m}\ 54.4^{s}$	-44°01′32.3″	263.02	-1.59	4.3	1	4.73	0.50	90.00
311	08385517-4402243	$08^{h}\ 38^{m}\ 55.2^{s}$	-44°02′24.4″	263.03	-1.59	4.3	2	6.51	0.95	0.00
312	08385562-4409430	$08^{h}\ 38^{m}\ 55.6^{s}$	-44°09′43.0″	263.13	-1.67	4.2	1	2.21	1.00	0.00
313	08385692-4414339	$08^{h}\ 38^{m}\ 56.9^{s}$	-44°14′34.0″	263.19	-1.71	4.2	1	5.54	0.50	85.00
314	08385734-4300503	$08^{h}\ 38^{m}\ 57.3^{s}$	-43°00′50.4″	262.22	-0.97	7.0	1	2.08	1.00	0.00
315	08385931-4409192	$08^{h}\ 38^{m}\ 59.3^{s}$	-44°09′19.3″	263.13	-1.65	4.2	1	3.39	1.00	0.00
316	08390113-4316536	$08^{h}\ 39^{m}\ 01.1^{s}$	-43°16′53.7″	262.44	-1.12	6.0	1	3.25	1.00	0.00
317	08390206-4251143	$08^{h}\ 39^{m}\ 02.1^{s}$	-42°51′14.3″	262.10	-0.86	8.5	1	4.95	0.60	-50.00
318	08390594-4340469	$08^{h}\ 39^{m}\ 05.9^{s}$	-43°40′47.0″	262.76	-1.35	6.4	1	3.00	1.00	0.00
319	08390983-4418597	$08^{h}\ 39^{m}\ 09.8^{s}$	-44°18′59.8″	263.28	-1.73	4.2	2	2.43	1.00	0.00
320	08391113-4415360	$08^{h}\ 39^{m}\ 11.1^{s}$	-44°15′36.1″	263.23	-1.69	4.2	3	2.84	0.97	0.00
321	08391139-4418073	$08^{h}\ 39^{m}\ 11.4^{s}$	-44°18′07.3″	263.27	-1.71	4.2	1	2.65	1.00	0.00
322	08391189-4405384	$08^{h}\ 39^{m}\ 11.9^{s}$	-44°05′38.4″	263.10	-1.59	4.3	1	10.04	0.80	-80.00
323	08391218-4416021	$08^{h}\ 39^{m}\ 12.2^{s}$	-44°16′02.1″	263.24	-1.69	4.2	2	2.43	1.00	0.00
324	08391267-4308253	$08^{h}\ 39^{m}\ 12.7^{s}$	-43°08′25.4″	262.35	-1.01	7.0	1	2.83	0.80	40.00
325	08391282-4413470	$08^{h}\ 39^{m}\ 12.8^{s}$	-44°13′47.1″	263.21	-1.67	4.2	1	3.09	1.00	0.00
326	08391319-4409154	$08^{h}\ 39^{m}\ 13.2^{s}$	-44°09′15.5″	263.15	-1.62	5.2	2	3.40	0.95	0.00
327	08391541-4401153	$08^{h}\ 39^{m}\ 15.4^{s}$	-44°01′15.3″	263.05	-1.53	4.3	1	15.94	0.50	60.00
328	08391584-4419224	$08^{h}\ 39^{m}\ 15.8^{s}$	-44°19′22.4″	263.29	-1.72	4.2	1	3.24	1.00	0.00
329	08391947-4418343	$08^{h}\ 39^{m}\ 19.5^{s}$	-44°18′34.4″	263.29	-1.70	4.2	1	2.80	1.00	0.00
330	08392484-4308476	$08^{h}\ 39^{m}\ 24.8^{s}$	-43°08′47.7″	262.37	-0.98	7.0	1	6.33	0.80	90.00
331	08392501-4400205	$08^{h}\ 39^{m}\ 25.0^{s}$	-44°00′20.5″	263.06	-1.50	4.3	1	4.42	1.00	0.00
332	08392536-4400171	$08^{h}\ 39^{m}\ 25.4^{s}$	-44°00′17.2″	263.06	-1.50	4.3	1	6.49	0.70	-50.00
333	08392817-4405279	$08^{h}\ 39^{m}\ 28.2^{s}$	-44°05′28.0″	263.13	-1.55	5.2	1	2.83	1.00	0.00
334	08392934-4347456	$08^{h}\ 39^{m}\ 29.3^{s}$	-43°47′45.7″	262.90	-1.36	5.6	1	2.65	1.00	0.00
335	08393245-4421456	$08^{h}\ 39^{m}\ 32.5^{s}$	-44°21′45.6″	263.35	-1.70	4.2	1	2.67	1.00	0.00
336	08393256-4317336	$08^{h}\ 39^{m}\ 32.6^{s}$	-43°17′33.6″	262.50	-1.05	6.0	1	2.95	1.00	0.00
337	08393257-4339000	$08^{h}\ 39^{m}\ 32.6^{s}$	-43°38′60.0″	262.79	-1.27	6.4	1	3.24	1.00	0.00
338	08393355-4405207	$08^{h}\ 39^{m}\ 33.6^{s}$	-44°05′20.7″	263.14	-1.53	5.2	1	2.83	1.00	0.00
339	08393394-4412221	$08^{h}\ 39^{m}\ 33.9^{s}$	-44°12′22.2″	263.23	-1.60	5.2	1	2.43	1.00	0.00
340	08393480-4255169	$08^{h}\ 39^{m}\ 34.8^{s}$	-42°55′16.9″	262.21	-0.82	7.3	1	3.24	1.00	0.00
341	08393718-4357246	$08^{h}\ 39^{m}\ 37.2^{s}$	-43°57′24.7″	263.04	-1.44	4.3	1	3.18	1.00	0.00
342	08393937-4414206	$08^{h}\ 39^{m}\ 39.4^{s}$	-44°14′20.6″	263.27	-1.61	5.2	1	2.67	1.00	0.00
343	08393950-4349176	$08^{h}\ 39^{m}\ 39.5^{s}$	-43°49′17.7″	262.94	-1.36	5.6	1	2.67	1.00	0.00
344	08394178-4415444	$08^{h}\ 39^{m}\ 41.8^{s}$	-44°15′44.4″	263.29	-1.62	5.2	2	2.66	1.00	0.00
345	08394788-4258024	$08^{h}\ 39^{m}\ 47.9^{s}$	-42°58′02.4″	262.27	-0.81	7.3	2	2.44	1.00	0.00
346	08394951-4311421	$08^{h}\ 39^{m}\ 49.5^{s}$	-43°11′42.1″	262.46	-0.95	6.0	1	7.41	0.40	-20.00
347	08394958-4338518	$08^{h}\ 39^{m}\ 49.6^{s}$	-43°38′51.9″	262.82	-1.23	6.4	1	2.36	1.00	0.00
348	08395046-4306273	$08^{h}\ 39^{m}\ 50.5^{s}$	-43°06′27.4″	262.39	-0.89	6.0	1	3.03	0.70	-50.00
349	08395122-4308378	$08^{h}\ 39^{m}\ 51.2^{s}$	-43°08′37.9″	262.42	-0.91	6.0	1	2.80	1.00	0.00
350	08395126-4352460	$08^{h}\ 39^{m}\ 51.3^{s}$	-43°52′46.0″	263.00	-1.36	5.6	1	2.80	1.00	0.00
351	08395145-4256169	$08^{h}\ 39^{m}\ 51.5^{s}$	-42°56′16.9″	262.26	-0.79	7.3	1	2.05	1.00	0.00
352	08395210-4255515	$08^{h}\ 39^{m}\ 52.1^{s}$	-42°55′51.5″	262.25	-0.78	7.3	1	2.80	1.00	0.00
353	08395253-4326065	$08^{h}\ 39^{m}\ 52.5^{s}$	-43°26′06.5″	262.65	-1.09	7.3	1	2.95	1.00	0.00
354	08395597-4404297	$08^{h}\ 39^{m}\ 56.0^{s}$	-44°04′29.7″	263.17	-1.47	5.2	1	2.83	1.00	0.00
355	08395832-4313525	$08^{h}\ 39^{m}\ 58.3^{s}$	-43°13′52.6″	262.50	-0.95	6.0	1	5.63	0.60	-20.00
356	08395854-4347595	$08^{h}\ 39^{m}\ 58.5^{s}$	-43°47′59.6″	262.95	-1.30	5.6	1	2.37	1.00	0.00
357	08395921-4257596	$08^{h}\ 39^{m}\ 59.2^{s}$	-42°57′59.7″	262.30	-0.79	7.3	2	3.99	1.00	0.00

ID	Source ID.	R.A. (J2000)	Dec. (J2000)	l (deg)	b (deg)	A_V (mag)	Dup.	a (arcsec)	b/a	P.A. (deg)
358	08400040-4317220	08$^{\rm h}$ 40$^{\rm m}$ 00.4$^{\rm s}$	-43°17′22.1″	262.55	-0.98	6.0	1	3.69	0.50	-25.00
359	08400101-4402106	08$^{\rm h}$ 40$^{\rm m}$ 01.0$^{\rm s}$	-44°02′10.6″	263.15	-1.44	5.2	2	10.22	0.40	-70.00
360	08400351-4413386	08$^{\rm h}$ 40$^{\rm m}$ 03.5$^{\rm s}$	-44°13′38.6″	263.30	-1.55	5.2	1	2.36	1.00	0.00
361	08400387-4405227	08$^{\rm h}$ 40$^{\rm m}$ 03.9$^{\rm s}$	-44°05′22.7″	263.19	-1.46	5.2	1	2.52	1.00	0.00
362	08400585-4418557	08$^{\rm h}$ 40$^{\rm m}$ 05.9$^{\rm s}$	-44°18′55.8″	263.38	-1.59	3.8	1	5.53	0.30	-30.00
363	08400785-4355445	08$^{\rm h}$ 40$^{\rm m}$ 07.9$^{\rm s}$	-43°55′44.5″	263.07	-1.35	5.6	1	3.09	1.00	0.00
364	08400940-4415596	08$^{\rm h}$ 40$^{\rm m}$ 09.4$^{\rm s}$	-44°15′59.7″	263.34	-1.56	5.2	2	3.32	1.00	0.00
365	08400984-4418202	08$^{\rm h}$ 40$^{\rm m}$ 09.8$^{\rm s}$	-44°18′20.2″	263.38	-1.58	3.8	1	1.77	1.00	0.00
366	08401071-4259087	08$^{\rm h}$ 40$^{\rm m}$ 10.7$^{\rm s}$	-42°59′08.7″	262.33	-0.77	7.3	2	3.24	1.00	0.00
367	08401186-4350234	08$^{\rm h}$ 40$^{\rm m}$ 11.9$^{\rm s}$	-43°50′23.5″	263.01	-1.29	5.6	1	3.09	1.00	0.00
368	08401225-4325590	08$^{\rm h}$ 40$^{\rm m}$ 12.3$^{\rm s}$	-43°25′59.0″	262.69	-1.04	7.3	1	2.79	1.00	0.00
369	08401545-4253182	08$^{\rm h}$ 40$^{\rm m}$ 15.5$^{\rm s}$	-42°53′18.2″	262.26	-0.70	7.3	1	2.23	1.00	0.00
370	08401654-4351436	08$^{\rm h}$ 40$^{\rm m}$ 16.5$^{\rm s}$	-43°51′43.6″	263.04	-1.29	5.6	1	1.77	1.00	0.00
371	08401857-4347314	08$^{\rm h}$ 40$^{\rm m}$ 18.6$^{\rm s}$	-43°47′31.5″	262.98	-1.24	5.6	1	2.57	1.00	0.00
372	08401884-4404078	08$^{\rm h}$ 40$^{\rm m}$ 18.8$^{\rm s}$	-44°04′07.9″	263.20	-1.41	5.2	1	2.36	1.00	0.00
373	08402021-4313400	08$^{\rm h}$ 40$^{\rm m}$ 20.2$^{\rm s}$	-43°13′40.0″	262.54	-0.90	6.0	1	2.71	0.80	-10.00
374	08402024-4257373	08$^{\rm h}$ 40$^{\rm m}$ 20.2$^{\rm s}$	-42°57′37.4″	262.33	-0.73	7.3	1	2.36	1.00	0.00
375	08402083-4359102	08$^{\rm h}$ 40$^{\rm m}$ 20.8$^{\rm s}$	-43°59′10.2″	263.14	-1.36	4.7	2	2.95	1.00	0.00
376	08402198-4318217	08$^{\rm h}$ 40$^{\rm m}$ 22.0$^{\rm s}$	-43°18′21.7″	262.61	-0.94	6.0	1	2.95	1.00	0.00
377	08402221-4416380	08$^{\rm h}$ 40$^{\rm m}$ 22.2$^{\rm s}$	-44°16′38.0″	263.38	-1.53	3.8	2	3.30	1.00	0.00
378	08402241-4257408	08$^{\rm h}$ 40$^{\rm m}$ 22.4$^{\rm s}$	-42°57′40.9″	262.33	-0.73	7.3	2	4.20	1.00	0.00
379	08402450-4417281	08$^{\rm h}$ 40$^{\rm m}$ 24.5$^{\rm s}$	-44°17′28.1″	263.39	-1.54	3.8	1	6.21	0.50	20.00
380	08402714-4415167	08$^{\rm h}$ 40$^{\rm m}$ 27.1$^{\rm s}$	-44°15′16.8″	263.37	-1.51	5.2	1	2.65	1.00	0.00
381	08402758-4344585	08$^{\rm h}$ 40$^{\rm m}$ 27.6$^{\rm s}$	-43°44′58.6″	262.97	-1.20	5.6	1	2.83	1.00	0.00
382	08402774-4355026	08$^{\rm h}$ 40$^{\rm m}$ 27.7$^{\rm s}$	-43°55′02.7″	263.10	-1.30	5.6	2	4.03	1.00	0.00
383	08402862-4257172	08$^{\rm h}$ 40$^{\rm m}$ 28.6$^{\rm s}$	-42°57′17.2″	262.34	-0.71	7.3	1	4.13	1.00	0.00
384	08402937-4313583	08$^{\rm h}$ 40$^{\rm m}$ 29.4$^{\rm s}$	-43°13′58.4″	262.56	-0.88	6.0	1	2.80	1.00	0.00
385	08403050-4257055	08$^{\rm h}$ 40$^{\rm m}$ 30.5$^{\rm s}$	-42°57′05.5″	262.34	-0.70	7.3	1	3.84	1.00	0.00
386	08403114-4413340	08$^{\rm h}$ 40$^{\rm m}$ 31.1$^{\rm s}$	-44°13′34.1″	263.35	-1.48	5.2	1	2.65	1.00	0.00
387	08403376-4338361	08$^{\rm h}$ 40$^{\rm m}$ 33.8$^{\rm s}$	-43°38′36.2″	262.90	-1.12	8.3	1	3.62	1.00	0.00
388	08403487-4403374	08$^{\rm h}$ 40$^{\rm m}$ 34.9$^{\rm s}$	-44°03′37.4″	263.23	-1.37	4.7	1	2.65	1.00	0.00
389	08403998-4314285	08$^{\rm h}$ 40$^{\rm m}$ 40.0$^{\rm s}$	-43°14′28.5″	262.59	-0.86	6.2	1	2.81	1.00	0.00
390	08404016-4347597	08$^{\rm h}$ 40$^{\rm m}$ 40.2$^{\rm s}$	-43°47′59.7″	263.03	-1.20	5.6	2	2.95	1.00	0.00
391	08404063-4259035	08$^{\rm h}$ 40$^{\rm m}$ 40.6$^{\rm s}$	-42°59′03.6″	262.39	-0.70	6.2	1	4.04	0.80	30.00
392	08404238-4303127	08$^{\rm h}$ 40$^{\rm m}$ 42.4$^{\rm s}$	-43°03′12.8″	262.44	-0.74	6.2	1	8.94	0.30	-75.00
393	08404645-4253520	08$^{\rm h}$ 40$^{\rm m}$ 46.5$^{\rm s}$	-42°53′52.0″	262.33	-0.63	7.3	1	3.40	1.00	0.00
394	08404764-4347365	08$^{\rm h}$ 40$^{\rm m}$ 47.6$^{\rm s}$	-43°47′36.6″	263.04	-1.18	5.6	2	4.94	0.50	-55.00
395	08404831-4335095	08$^{\rm h}$ 40$^{\rm m}$ 48.3$^{\rm s}$	-43°35′09.6″	262.88	-1.05	8.3	1	2.80	1.00	0.00
396	08404852-4347323	08$^{\rm h}$ 40$^{\rm m}$ 48.5$^{\rm s}$	-43°47′32.4″	263.04	-1.17	5.6	2	6.82	0.60	20.00
397	08405025-4353509	08$^{\rm h}$ 40$^{\rm m}$ 50.3$^{\rm s}$	-43°53′50.9″	263.13	-1.23	4.7	1	5.60	0.50	0.00
398	08405090-4347364	08$^{\rm h}$ 40$^{\rm m}$ 50.9$^{\rm s}$	-43°47′36.5″	263.05	-1.17	5.6	2	2.87	1.00	0.00
399	08405573-4410454	08$^{\rm h}$ 40$^{\rm m}$ 55.7$^{\rm s}$	-44°10′45.4″	263.36	-1.39	5.2	1	2.51	1.00	0.00
400	08405802-4253391	08$^{\rm h}$ 40$^{\rm m}$ 58.0$^{\rm s}$	-42°53′39.2″	262.35	-0.6	8.6	1	2.98	1.00	0.00
401	08405943-4257596	08$^{\rm h}$ 40$^{\rm m}$ 59.4$^{\rm s}$	-42°57′59.7″	262.41	-0.64	6.2	1	2.65	1.00	0.00
402	08410086-4354513	08$^{\rm h}$ 41$^{\rm m}$ 00.9$^{\rm s}$	-43°54′51.3″	263.16	-1.22	4.7	1	2.36	1.00	0.00
403	08410154-4351069	08$^{\rm h}$ 41$^{\rm m}$ 01.5$^{\rm s}$	-43°51′06.9″	263.11	-1.18	5.6	1	2.95	1.00	0.00
404	08410188-4251283	08$^{\rm h}$ 41$^{\rm m}$ 01.9$^{\rm s}$	-42°51′28.3″	262.33	-0.57	8.6	1	3.24	1.00	0.00

B.2.2 NIR Photometry

Table B.6 gives the NIR measurements and corrected fluxes and magnitudes for sources in the IRSF survey only as follows:
Column 1: Reference ID
Column 2: Source IRSF ID
Column 3, **Column 6**, **Column 9**: Flux density (mJy) for the J, H, K_s – raw measurements
Column 4, **Column 7**, **Column 10**: Integrated Magnitude (mag) no reddening correction applied; 5% calibration error included
Column 5, **Column 8**, **Column 11**: Integrated Magnitude (mag) – reddening-corrected; 5% calibration error included. The extinction-corrected magnitudes have an error of ∼10% which is not accounted for.
Column 12: Photometric redshift

Table B.6: IRSF Catalogue Measurements.

		J			H			K_s			
ID	Source ID.	f_ν (mJy)	Mag. (mag)	Mag. (mag)	f_ν (mJy)	Mag. (mag)	Mag. (mag)	f_ν (mJy)	Mag. (mag)	Mag. (mag)	Photo-z
57	08323738-4347314	0.103 ±0.106	17.98 ±1.12	16.33 ±1.12	0.239 ±0.047	16.58 ±0.22	15.51 ±0.22	0.408 ±0.050	15.53 ±0.14	14.84 ±0.14	0.2109
58	08323780-4343251	0.322 ±0.029	16.73 ±0.11	14.87 ±0.11	0.783 ±0.014	15.29 ±0.05	14.08 ±0.05	1.026 ±0.020	14.53 ±0.05	13.75 ±0.05	0.1115
59	08323841-4344374	0.476 ±0.026	16.31 ±0.08	14.45 ±0.08	1.039 ±0.012	14.98 ±0.05	13.77 ±0.05	1.346 ±0.019	14.24 ±0.05	13.46 ±0.05	0.1040
60	08323888-4326120	0.484 ±0.031	16.29 ±0.09	14.47 ±0.09	1.116 ±0.016	14.91 ±0.05	13.72 ±0.05	1.686 ±0.019	13.99 ±0.05	13.23 ±0.05	0.1289
61	08324065-4311114	0.133 ±0.074	17.70 ±0.61	15.03 ±0.61	0.543 ±0.024	15.69 ±0.07	13.95 ±0.07	0.974 ±0.024	14.59 ±0.06	13.47 ±0.06	0.1956
62	08324104-4304193	0.166 ±0.044	17.45 ±0.29	15.69 ±0.29	0.299 ±0.029	16.34 ±0.12	15.19 ±0.12	0.401 ±0.048	15.55 ±0.14	14.81 ±0.14	0.1141
63	08324201-4341439	0.085 ±0.062	18.18 ±0.79	16.32 ±0.79	0.235 ±0.027	16.60 ±0.13	15.38 ±0.13	0.415 ±0.031	15.52 ±0.10	14.73 ±0.10	0.2218
64	08324241-4406375	0.063 ±0.114	18.50 ±1.97	17.03 ±1.97	0.167 ±0.046	16.97 ±0.30	16.01 ±0.30	0.291 ±0.051	15.90 ±0.20	15.28 ±0.20	0.2581
65	08324251-4305471	0.164 ±0.017	17.47 ±0.12	15.71 ±0.12	0.355 ±0.126	16.15 ±0.39	15.00 ±0.39	0.581 ±0.103	15.15 ±0.20	14.41 ±0.20	0.1715
66	08324325-4350295	0.092 ±0.111	18.09 ±1.31	16.44 ±1.31	0.165 ±0.064	16.98 ±0.42	15.91 ±0.42	0.296 ±0.063	15.88 ±0.24	15.19 ±0.24	0.2017
67	08324375-4403122	0.081 ±0.112	18.23 ±1.50	16.53 ±1.50	0.198 ±0.041	16.78 ±0.23	15.67 ±0.23	0.312 ±0.046	15.83 ±0.17	15.11 ±0.17	0.2017
68	08324450-4337397	0.141 ±0.054	17.63 ±0.42	15.77 ±0.42	0.312 ±0.024	16.29 ±0.10	15.07 ±0.10	0.434 ±0.039	15.47 ±0.11	14.69 ±0.11	0.1374
69	08324590-4321417	0.076 ±0.105	18.30 ±1.50	15.63 ±1.50	0.323 ±0.030	16.25 ±0.11	14.52 ±0.11	0.563 ±0.031	15.18 ±0.08	14.06 ±0.08	0.1948
70	08324765-4416192	0.531 ±0.029	16.19 ±0.08	14.72 ±0.08	1.157 ±0.039	14.87 ±0.06	13.91 ±0.06	1.476 ±0.022	14.14 ±0.05	13.52 ±0.05	0.1237
71	08324820-4423085	0.082 ±0.092	18.21 ±1.22	16.91 ±1.22	0.156 ±0.039	17.05 ±0.28	16.20 ±0.28	0.251 ±0.055	16.06 ±0.24	15.52 ±0.24	0.2158
72	08324889-4406068	0.079 ±0.084	18.27 ±1.16	16.79 ±1.16	0.163 ±0.044	17.00 ±0.30	16.04 ±0.30	0.230 ±0.053	16.16 ±0.26	15.54 ±0.26	0.1820
73	08324912-4316026	0.075 ±0.067	18.32 ±0.97	15.64 ±0.97	0.217 ±0.040	16.69 ±0.21	14.95 ±0.21	0.320 ±0.047	15.80 ±0.17	14.68 ±0.17	0.1317
74	08324937-4322396	0.065 ±0.083	18.47 ±1.39	15.80 ±1.39	0.248 ±0.031	16.54 ±0.14	14.80 ±0.14	0.507 ±0.028	15.30 ±0.08	14.18 ±0.08	0.2227
75	08324974-4311110	0.034 ±0.032	19.19 ±1.02	16.52 ±1.02	0.112 ±0.022	17.41 ±0.22	15.67 ±0.22	0.224 ±0.035	16.18 ±0.18	15.06 ±0.18	0.2354
76	08325061-4411304	0.182 ±0.070	17.36 ±0.42	15.88 ±0.42	0.469 ±0.026	15.85 ±0.08	14.89 ±0.08	0.714 ±0.033	14.93 ±0.07	14.31 ±0.07	0.1887
77	08325151-4412305	0.258 ±0.035	16.98 ±0.16	15.50 ±0.16	0.529 ±0.017	15.72 ±0.06	14.76 ±0.06	0.752 ±0.023	14.87 ±0.06	14.25 ±0.06	0.1466
78	08325331-4251430	1.075 ±0.028	15.43 ±0.06	13.64 ±0.06	2.818 ±0.013	13.90 ±0.05	12.74 ±0.05	3.611 ±0.017	13.17 ±0.05	12.42 ±0.05	0.0901
79	08325337-4255412	0.078 ±0.053	18.28 ±0.74	16.49 ±0.74	0.177 ±0.031	16.91 ±0.20	15.74 ±0.20	0.300 ±0.036	15.87 ±0.14	15.12 ±0.14	0.2061
80	08325381-4418517	0.076 ±0.116	18.30 ±1.66	16.83 ±1.66	0.202 ±0.057	16.76 ±0.31	15.80 ±0.31	0.227 ±0.094	16.17 ±0.45	15.55 ±0.45	0.1551
81	08325454-4328259	0.074 ±0.102	18.34 ±1.50	16.09 ±1.50	0.167 ±0.072	16.97 ±0.47	15.50 ±0.47	0.322 ±0.063	15.79 ±0.22	14.85 ±0.22	0.1979
82	08325459-4344074	0.086 ±0.061	18.17 ±0.77	16.52 ±0.77	0.199 ±0.033	16.78 ±0.19	15.71 ±0.19	0.274 ±0.039	15.97 ±0.16	15.28 ±0.16	0.1707
83	08325543-4335501	0.351 ±0.018	16.64 ±0.07	14.78 ±0.07	0.906 ±0.007	15.13 ±0.05	13.92 ±0.05	1.440 ±0.009	14.16 ±0.05	13.38 ±0.05	0.1590
84	08330064-4301238	0.128 ±0.056	17.74 ±0.48	15.95 ±0.48	0.432 ±0.018	15.94 ±0.07	14.77 ±0.07	0.572 ±0.032	15.17 ±0.08	14.42 ±0.08	0.1723
85	08330409-4404493	0.081 ±0.131	18.23 ±1.76	16.76 ±1.76	0.205 ±0.047	16.75 ±0.25	15.79 ±0.25	0.340 ±0.056	15.73 ±0.19	15.11 ±0.19	0.2341
86	08330697-4328526	0.048 ±0.124	18.80 ±2.81	16.55 ±2.81	0.155 ±0.059	17.05 ±0.42	15.58 ±0.42	0.351 ±0.044	15.70 ±0.14	14.75 ±0.14	0.2661

Table B.6 continued...

		J			H			K_s			
ID	Source ID.	f_ν (mJy)	Mag. (mag)	Mag. (mag)	f_ν (mJy)	Mag. (mag)	Mag. (mag)	f_ν (mJy)	Mag. (mag)	Mag. (mag)	Photo-z
87	08330839-4332159	0.120 ±0.052	17.80 ±0.47	15.94 ±0.47	0.380 ±0.023	16.08 ±0.08	14.86 ±0.08	0.463 ±0.037	15.40 ±0.10	14.61 ±0.10	0.1467
88	08330882-4352564	0.150 ±0.052	17.56 ±0.38	15.91 ±0.38	0.310 ±0.030	16.30 ±0.12	15.22 ±0.12	0.404 ±0.044	15.54 ±0.13	14.85 ±0.13	0.1318
89	08330932-4422108	0.117 ±0.090	17.83 ±0.84	16.50 ±0.84	0.203 ±0.046	16.76 ±0.25	15.89 ±0.25	0.284 ±0.071	15.93 ±0.28	15.37 ±0.28	0.1621
90	08331000-4258011	0.118 ±0.040	17.83 ±0.37	16.04 ±0.37	0.179 ±0.041	16.89 ±0.25	15.73 ±0.25	0.264 ±0.052	16.00 ±0.22	15.26 ±0.22	0.1257
91	08331030-4420535	0.170 ±0.061	17.43 ±0.39	16.09 ±0.39	0.224 ±0.043	16.65 ±0.21	15.78 ±0.21	0.303 ±0.065	15.86 ±0.24	15.30 ±0.24	0.1169
92	08331163-4257458	0.147 ±0.036	17.58 ±0.27	15.79 ±0.27	0.325 ±0.023	16.25 ±0.09	15.08 ±0.09	0.469 ±0.031	15.38 ±0.09	14.63 ±0.09	0.1494
93	08331221-4254102	0.682 ±0.027	15.92 ±0.07	14.13 ±0.07	1.463 ±0.017	14.61 ±0.05	13.45 ±0.05	1.907 ±0.022	13.86 ±0.05	13.11 ±0.05	0.0881
94	08331241-4422065	0.157 ±0.048	17.51 ±0.34	16.18 ±0.34	0.235 ±0.046	16.60 ±0.22	15.73 ±0.22	0.229 ±0.072	16.16 ±0.34	15.60 ±0.34	0.0553
95	08331295-4422124	0.210 ±0.051	17.20 ±0.27	15.87 ±0.27	0.317 ±0.033	16.27 ±0.12	15.41 ±0.12	0.458 ±0.048	15.41 ±0.12	14.85 ±0.12	0.1397
96	08331391-4300547	0.061 ±0.061	18.54 ±1.09	16.75 ±1.09	0.162 ±0.035	17.00 ±0.24	15.84 ±0.24	0.249 ±0.050	16.07 ±0.22	15.32 ±0.22	0.2078
97	08331652-4423113	0.104 ±0.110	17.96 ±1.15	16.63 ±1.15	0.211 ±0.039	16.71 ±0.21	15.85 ±0.21	0.239 ±0.069	16.11 ±0.32	15.55 ±0.32	0.1333
98	08331675-4259594	0.174 ±0.087	17.40 ±0.55	15.62 ±0.55	0.432 ±0.063	15.94 ±0.17	14.78 ±0.17	0.578 ±0.107	15.15 ±0.21	14.41 ±0.21	0.1397
99	08331759-4423585	0.452 ±0.040	16.37 ±0.11	15.04 ±0.11	0.734 ±0.018	15.36 ±0.06	14.49 ±0.06	0.829 ±0.034	14.76 ±0.07	14.21 ±0.07	0.0776
100	08331840-4301009	0.098 ±0.060	18.03 ±0.67	16.24 ±0.67	0.491 ±0.017	15.80 ±0.06	14.63 ±0.06	1.447 ±0.010	14.16 ±0.05	13.41 ±0.05	0.2230
101	08332108-4300552	0.237 ±0.177	17.07 ±0.81	15.28 ±0.81	0.702 ±0.066	15.41 ±0.11	14.25 ±0.11	1.339 ±0.043	14.24 ±0.06	13.49 ±0.06	0.2234
102	08332207-4402372	0.103 ±0.041	17.98 ±0.43	16.50 ±0.43	0.378 ±0.016	16.08 ±0.07	15.12 ±0.07	0.948 ±0.016	14.62 ±0.05	14.00 ±0.05	0.2319
103	08332560-4403545	0.253 ±0.021	17.00 ±0.10	15.52 ±0.10	0.542 ±0.013	15.69 ±0.06	14.73 ±0.06	0.717 ±0.026	14.92 ±0.06	14.30 ±0.06	0.1366
104	08332934-4311535	0.148 ±0.038	17.58 ±0.28	15.74 ±0.28	0.307 ±0.021	16.31 ±0.09	15.11 ±0.09	0.463 ±0.028	15.40 ±0.08	14.63 ±0.08	0.1490
105	08332949-4315127	0.060 ±0.060	18.56 ±1.09	15.88 ±1.09	0.269 ±0.015	16.45 ±0.08	14.71 ±0.08	0.493 ±0.022	15.33 ±0.07	14.21 ±0.07	0.2175
106	08332986-4404336	0.067 ±0.056	18.43 ±0.91	16.96 ±0.91	0.177 ±0.022	16.91 ±0.14	15.95 ±0.14	0.344 ±0.037	15.72 ±0.13	15.10 ±0.13	0.2771
107	08333095-4311535	0.052 ±0.066	18.71 ±1.38	16.87 ±1.38	0.127 ±0.033	17.26 ±0.29	16.07 ±0.29	0.234 ±0.056	16.14 ±0.27	15.37 ±0.27	0.2396
108	08333187-4330093	0.065 ±0.095	18.48 ±1.59	16.22 ±1.59	0.171 ±0.043	16.95 ±0.28	15.48 ±0.28	0.275 ±0.061	15.96 ±0.25	15.02 ±0.25	0.1782
109	08334058-4405503	0.065 ±0.049	18.47 ±0.82	17.00 ±0.82	0.141 ±0.029	17.15 ±0.23	16.19 ±0.23	0.254 ±0.038	16.05 ±0.17	15.43 ±0.17	0.2474
110	08334327-4340484	0.089 ±0.101	18.14 ±1.23	16.49 ±1.23	0.265 ±0.162	16.47 ±0.67	15.39 ±0.67	0.452 ±0.052	15.42 ±0.14	14.73 ±0.14	0.2362
111	08334375-4321546	0.075 ±0.065	18.31 ±0.94	16.06 ±0.94	0.171 ±0.027	16.94 ±0.18	15.48 ±0.18	0.310 ±0.030	15.83 ±0.12	14.89 ±0.12	0.1845
112	08334433-4329071	0.035 ±0.088	19.14 ±2.73	16.89 ±2.73	0.130 ±0.041	17.24 ±0.35	15.78 ±0.35	0.265 ±0.044	16.00 ±0.19	15.06 ±0.19	0.2787
113	08334542-4305265	0.063 ±0.079	18.50 ±1.36	16.66 ±1.36	0.179 ±0.047	16.89 ±0.29	15.70 ±0.29	0.303 ±0.052	15.86 ±0.19	15.09 ±0.19	0.2279
114	08335677-4319546	0.071 ±0.093	18.38 ±1.42	16.13 ±1.42	0.172 ±0.045	16.93 ±0.29	15.47 ±0.29	0.359 ±0.069	15.67 ±0.21	14.73 ±0.21	0.2212
115	08340029-4323232	0.145 ±0.069	17.60 ±0.52	15.35 ±0.52	0.373 ±0.027	16.10 ±0.09	14.63 ±0.09	0.536 ±0.044	15.24 ±0.10	14.29 ±0.10	0.1285
116	08340083-4346065	0.037 ±0.070	19.10 ±2.06	17.45 ±2.06	0.090 ±0.044	17.65 ±0.53	16.57 ±0.53	0.198 ±0.044	16.32 ±0.25	15.63 ±0.25	0.2994
117	08340231-4401256	0.059 ±0.064	18.57 ±1.18	17.11 ±1.18	0.154 ±0.024	17.06 ±0.18	16.11 ±0.18	0.192 ±0.059	16.35 ±0.34	15.74 ±0.34	0.1859
118	08340272-4332425	0.081 ±0.064	18.23 ±0.86	15.98 ±0.86	0.185 ±0.026	16.86 ±0.16	15.39 ±0.16	0.274 ±0.062	15.96 ±0.25	15.02 ±0.25	0.1396
119	08340285-4413297	0.163 ±0.030	17.48 ±0.21	16.14 ±0.21	0.348 ±0.016	16.17 ±0.07	15.30 ±0.07	0.510 ±0.034	15.29 ±0.09	14.73 ±0.09	0.1806
120	08340306-4253001	0.342 ±0.022	16.67 ±0.09	14.86 ±0.09	0.816 ±0.012	15.25 ±0.05	14.07 ±0.05	1.088 ±0.019	14.47 ±0.05	13.71 ±0.05	0.1150
121	08340506-4336530	0.353 ±0.017	16.63 ±0.07	14.55 ±0.07	0.790 ±0.009	15.28 ±0.05	13.93 ±0.05	1.208 ±0.017	14.36 ±0.05	13.48 ±0.05	0.1311

Table B.6 continued...

ID	Source ID.	J			H			K_s			Photo-z
		f_ν (mJy)	Mag. (mag)	Mag. (mag)	f_ν (mJy)	Mag. (mag)	Mag. (mag)	f_ν (mJy)	Mag. (mag)	Mag. (mag)	
122	08340525-4252559	0.055 ±0.059	18.65 ±1.17	16.84 ±1.17	0.124 ±0.034	17.29 ±0.30	16.11 ±0.30	0.232 ±0.055	16.15 ±0.26	15.39 ±0.26	0.2361
123	08340546-4256344	0.080 ±0.061	18.25 ±0.83	16.41 ±0.83	0.224 ±0.031	16.65 ±0.16	15.46 ±0.16	0.385 ±0.042	15.60 ±0.13	14.83 ±0.13	0.2219
124	08340718-4333183	0.131 ±0.069	17.71 ±0.57	15.46 ±0.57	0.334 ±0.023	16.22 ±0.09	14.75 ±0.09	0.534 ±0.055	15.24 ±0.12	14.30 ±0.12	0.1521
125	08340728-4257538	0.074 ±0.054	18.34 ±0.79	16.50 ±0.79	0.281 ±0.027	16.40 ±0.12	15.21 ±0.12	0.556 ±0.029	15.20 ±0.08	14.43 ±0.08	0.2510
126	08340887-4416511	0.159 ±0.035	17.50 ±0.24	16.17 ±0.24	0.325 ±0.021	16.25 ±0.09	15.38 ±0.09	0.500 ±0.025	15.31 ±0.07	14.76 ±0.07	0.1873
127	08340945-4413341	0.040 ±0.056	19.00 ±1.52	17.66 ±1.52	0.093 ±0.024	17.61 ±0.28	16.74 ±0.28	0.151 ±0.066	16.61 ±0.48	16.05 ±0.48	0.2614
128	08341000-4300414	0.074 ±0.041	18.33 ±0.60	16.50 ±0.60	0.139 ±0.039	17.17 ±0.31	15.97 ±0.31	0.240 ±0.034	16.11 ±0.16	15.34 ±0.16	0.1905
129	08341220-4330200	0.573 ±0.014	16.11 ±0.06	13.86 ±0.06	1.582 ±0.007	14.53 ±0.05	13.06 ±0.05	2.327 ±0.014	13.64 ±0.05	12.70 ±0.05	0.1033
130	08341298-4251439	0.149 ±0.051	17.57 ±0.38	15.76 ±0.38	0.463 ±0.015	15.86 ±0.06	14.68 ±0.06	0.809 ±0.024	14.79 ±0.06	14.03 ±0.06	0.2096
131	08341630-4330529	0.038 ±0.082	19.07 ±2.34	16.81 ±2.34	0.122 ±0.022	17.31 ±0.20	15.84 ±0.20	0.191 ±0.059	16.36 ±0.34	15.41 ±0.34	0.2089
132	08341822-4318533	0.056 ±0.057	18.63 ±1.11	16.43 ±1.11	0.142 ±0.024	17.14 ±0.19	15.72 ±0.19	0.308 ±0.042	15.84 ±0.16	14.92 ±0.16	0.2458
133	08341914-4332191	0.138 ±0.050	17.66 ±0.40	15.57 ±0.40	0.254 ±0.033	16.51 ±0.15	15.16 ±0.15	0.410 ±0.053	15.53 ±0.15	14.65 ±0.15	0.1369
134	08341986-4359582	0.086 ±0.044	18.17 ±0.56	16.71 ±0.56	0.193 ±0.029	16.81 ±0.17	15.87 ±0.17	0.275 ±0.043	15.96 ±0.18	15.35 ±0.18	0.1909
135	08342055-4315195	0.055 ±0.059	18.66 ±1.17	16.47 ±1.17	0.144 ±0.026	17.13 ±0.20	15.71 ±0.20	0.221 ±0.050	16.20 ±0.25	15.28 ±0.25	0.1775
136	08342060-4323449	0.065 ±0.106	18.47 ±1.77	16.28 ±1.77	0.230 ±0.040	16.62 ±0.20	15.19 ±0.20	0.443 ±0.039	15.44 ±0.11	14.52 ±0.11	0.2421
137	08342193-4421221	0.136 ±0.046	17.67 ±0.37	16.34 ±0.37	0.284 ±0.022	16.39 ±0.10	15.52 ±0.10	0.430 ±0.035	15.48 ±0.10	14.92 ±0.10	0.1914
138	08342398-4421130	0.077 ±0.052	18.29 ±0.73	16.95 ±0.73	0.148 ±0.030	17.10 ±0.23	16.23 ±0.23	0.248 ±0.045	16.08 ±0.20	15.52 ±0.20	0.2253
139	08342607-4316438	0.046 ±0.057	18.84 ±1.35	16.65 ±1.35	0.116 ±0.031	17.37 ±0.29	15.94 ±0.29	0.203 ±0.046	16.29 ±0.25	15.37 ±0.25	0.2076
140	08343190-4358137	0.065 ±0.082	18.48 ±1.37	17.02 ±1.37	0.156 ±0.052	17.04 ±0.36	16.09 ±0.36	0.274 ±0.058	15.96 ±0.23	15.35 ±0.23	0.2528
141	08343306-4324351	12.141 ±0.047	12.79 ±0.05	10.60 ±0.05	45.768 ±0.021	10.87 ±0.05	9.45 ±0.05	120.702 ±0.039	9.36 ±0.05	8.44 ±0.05	0.0162
142	08343599-4403034	0.104 ±0.157	17.96 ±1.64	16.50 ±1.64	0.212 ±0.152	16.71 ±0.78	15.76 ±0.78	0.356 ±0.082	15.68 ±0.26	15.07 ±0.26	0.2099
143	08343806-4359159	0.137 ±0.131	17.66 ±1.04	16.21 ±1.04	0.282 ±0.161	16.40 ±0.62	15.45 ±0.62	0.404 ±0.078	15.54 ±0.21	14.93 ±0.21	0.1691
144	08343918-4400493	0.295 ±0.044	16.83 ±0.17	15.37 ±0.17	0.621 ±0.023	15.54 ±0.06	14.59 ±0.06	0.780 ±0.037	14.83 ±0.07	14.22 ±0.07	0.1219
145	08344140-4343398	0.044 ±0.104	18.89 ±2.57	16.81 ±2.57	0.113 ±0.074	17.39 ±0.71	16.04 ±0.71	0.217 ±0.062	16.22 ±0.31	15.35 ±0.31	0.2402
146	08344150-4339111	0.045 ±0.106	18.86 ±2.56	16.78 ±2.56	0.159 ±0.034	17.02 ±0.24	15.67 ±0.24	0.306 ±0.041	15.85 ±0.15	14.97 ±0.15	0.2659
147	08344240-4417049	0.229 ±0.044	17.11 ±0.21	15.91 ±0.21	0.616 ±0.021	15.55 ±0.06	14.77 ±0.06	1.000 ±0.026	14.56 ±0.06	14.06 ±0.06	0.2141
148	08344286-4358028	0.091 ±0.045	18.11 ±0.54	16.65 ±0.54	0.184 ±0.031	16.86 ±0.19	15.91 ±0.19	0.347 ±0.039	15.71 ±0.13	15.10 ±0.13	0.2392
149	08344552-4306144	0.575 ±0.102	16.11 ±0.20	14.27 ±0.20	1.462 ±0.090	14.61 ±0.08	13.42 ±0.08	1.847 ±0.085	13.89 ±0.07	13.12 ±0.07	0.0995
150	08344596-4343437	0.057 ±0.074	18.61 ±1.41	16.52 ±1.41	0.123 ±0.050	17.30 ±0.44	15.95 ±0.44	0.209 ±0.063	16.26 ±0.33	15.39 ±0.33	0.1877
151	08344595-4352511	0.109 ±0.071	17.91 ±0.71	16.60 ±0.71	0.263 ±0.031	16.48 ±0.14	15.62 ±0.14	0.363 ±0.044	15.66 ±0.14	15.11 ±0.14	0.1940
152	08344751-4401224	0.320 ±0.121	16.74 ±0.41	15.29 ±0.41	0.639 ±0.106	15.51 ±0.19	14.56 ±0.19	0.911 ±0.022	14.66 ±0.06	14.05 ±0.06	0.1396
153	08345401-4306499	0.051 ±0.067	18.74 ±1.43	16.54 ±1.43	0.120 ±0.036	17.32 ±0.33	15.89 ±0.33	0.183 ±0.069	16.41 ±0.41	15.48 ±0.41	0.1664
154	08345655-4252401	0.068 ±0.078	18.42 ±1.25	16.22 ±1.25	0.382 ±0.024	16.07 ±0.09	14.64 ±0.09	1.323 ±0.015	14.26 ±0.05	13.33 ±0.05	0.2230
155	08345744-4341199	0.062 ±0.014	18.52 ±0.25	16.43 ±0.25	0.178 ±0.048	16.90 ±0.30	15.54 ±0.30	0.319 ±0.041	15.80 ±0.15	14.93 ±0.15	0.2225
156	08345927-4305527	0.049 ±0.135	18.79 ±2.99	16.58 ±2.99	0.170 ±0.016	16.95 ±0.11	15.52 ±0.11	0.352 ±0.012	15.69 ±0.06	14.77 ±0.06	0.2667

Table B.6 continued...

		J			H			K_s			
ID	Source ID.	f_ν (mJy)	Mag. (mag)	Mag. (mag)	f_ν (mJy)	Mag. (mag)	Mag. (mag)	f_ν (mJy)	Mag. (mag)	Mag. (mag)	Photo-z
157	08345938-4409244	0.063 ±0.051	18.50 ±0.88	17.30 ±0.88	0.121 ±0.023	17.32 ±0.21	16.54 ±0.21	0.249 ±0.053	16.07 ±0.24	15.57 ±0.24	0.2889
158	08350472-4420156	0.118 ±0.069	17.82 ±0.64	16.62 ±0.64	0.218 ±0.044	16.68 ±0.23	15.90 ±0.23	0.372 ±0.046	15.63 ±0.14	15.13 ±0.14	0.2205
159	08350590-4333378	0.097 ±0.063	18.04 ±0.71	16.45 ±0.71	0.172 ±0.042	16.94 ±0.27	15.90 ±0.27	0.310 ±0.061	15.83 ±0.22	15.17 ±0.22	0.2050
160	08350744-4408534	0.458 ±0.089	16.35 ±0.22	15.15 ±0.22	1.017 ±0.101	15.01 ±0.12	14.23 ±0.12	1.452 ±0.077	14.15 ±0.08	13.65 ±0.08	0.1693
161	08350928-4312245	0.043 ±0.079	18.92 ±2.00	16.73 ±2.00	0.134 ±0.026	17.21 ±0.22	15.78 ±0.22	0.230 ±0.059	16.16 ±0.28	15.24 ±0.28	0.2257
162	08350935-4332412	0.219 ±0.072	17.15 ±0.36	15.56 ±0.36	0.666 ±0.169	15.47 ±0.28	14.43 ±0.28	1.010 ±0.221	14.55 ±0.24	13.88 ±0.24	0.1844
163	08351133-4322293	0.132 ±0.038	17.71 ±0.32	15.51 ±0.32	0.461 ±0.260	15.87 ±0.61	14.44 ±0.61	0.787 ±0.297	14.82 ±0.41	13.90 ±0.41	0.1912
164	08351371-4321122	0.092 ±0.246	18.09 ±2.90	15.90 ±2.90	0.267 ±0.024	16.46 ±0.11	15.03 ±0.11	0.412 ±0.016	15.52 ±0.07	14.60 ±0.07	0.1702
165	08351819-4319491	0.963 ±0.020	15.55 ±0.06	13.35 ±0.06	3.847 ±0.006	13.56 ±0.05	12.13 ±0.05	6.350 ±0.006	12.55 ±0.05	11.63 ±0.05	0.0884
166	08351851-4307381	0.232 ±0.021	17.09 ±0.11	15.21 ±0.11	0.561 ±0.009	15.65 ±0.05	14.43 ±0.05	0.833 ±0.022	14.76 ±0.06	13.97 ±0.06	0.1418
167	08351883-4318094	0.093 ±0.080	18.09 ±0.94	15.89 ±0.94	0.273 ±0.025	16.43 ±0.11	15.01 ±0.11	0.492 ±0.049	15.33 ±0.12	14.41 ±0.12	0.2020
168	08352012-4319580	0.071 ±0.054	18.37 ±0.83	16.18 ±0.83	0.219 ±0.026	16.68 ±0.14	15.25 ±0.14	0.350 ±0.044	15.70 ±0.14	14.78 ±0.14	0.1909
169	08352171-4349417	0.042 ±0.076	18.94 ±1.97	17.62 ±1.97	0.119 ±0.040	17.34 ±0.37	16.49 ±0.37	0.190 ±0.037	16.36 ±0.22	15.81 ±0.22	0.2746
170	08352270-4319378	1.082 ±0.303	15.42 ±0.31	13.22 ±0.31	3.441 ±0.277	13.68 ±0.10	12.26 ±0.10	5.663 ±0.251	12.68 ±0.07	11.76 ±0.07	0.0980
171	08352278-4347181	0.141 ±0.003	17.63 ±0.06	16.32 ±0.06	0.242 ±0.064	16.57 ±0.29	15.71 ±0.29	0.370 ±0.091	15.64 ±0.27	15.09 ±0.27	0.1766
172	08352288-4306371	0.157 ±0.230	17.52 ±1.59	15.63 ±1.59	0.499 ±0.244	15.78 ±0.53	14.55 ±0.53	0.640 ±0.084	15.04 ±0.15	14.26 ±0.15	0.1478
173	08352414-4304121	0.154 ±0.025	17.54 ±0.18	15.34 ±0.18	0.439 ±0.015	15.92 ±0.06	14.49 ±0.06	0.656 ±0.015	15.02 ±0.06	14.10 ±0.06	0.1468
174	08352483-4318232	1.480 ±0.013	15.08 ±0.05	12.88 ±0.05	4.659 ±0.005	13.36 ±0.05	11.93 ±0.05	6.391 ±0.009	12.55 ±0.05	11.63 ±0.05	0.0819
175	08352562-4406211	0.092 ±0.067	18.10 ±0.79	16.90 ±0.79	0.178 ±0.031	16.90 ±0.20	16.12 ±0.20	0.310 ±0.047	15.83 ±0.17	15.33 ±0.17	0.2391
176	08352601-4352450	0.057 ±0.079	18.61 ±1.51	17.30 ±1.51	0.127 ±0.031	17.27 ±0.27	16.41 ±0.27	0.198 ±0.043	16.32 ±0.24	15.77 ±0.24	0.2359
177	08352639-4413073	0.082 ±0.043	18.23 ±0.57	17.03 ±0.57	0.164 ±0.027	16.99 ±0.19	16.21 ±0.19	0.219 ±0.044	16.21 ±0.22	15.71 ±0.22	0.1878
178	08352880-4412551	0.049 ±0.045	18.77 ±1.00	17.57 ±1.00	0.115 ±0.026	17.38 ±0.25	16.60 ±0.25	0.194 ±0.052	16.34 ±0.29	15.84 ±0.29	0.2745
179	08352964-4348385	0.066 ±0.054	18.46 ±0.89	17.14 ±0.89	0.129 ±0.035	17.25 ±0.30	16.39 ±0.30	0.174 ±0.051	16.46 ±0.32	15.91 ±0.32	0.1845
180	08352964-4412335	0.104 ±0.037	17.96 ±0.39	16.77 ±0.39	0.229 ±0.023	16.63 ±0.12	15.85 ±0.12	0.301 ±0.050	15.86 ±0.19	15.36 ±0.19	0.1862
181	08353086-4404125	0.138 ±0.097	17.66 ±0.77	16.65 ±0.77	0.240 ±0.065	16.57 ±0.30	15.92 ±0.30	0.265 ±0.097	16.00 ±0.40	15.58 ±0.40	0.1162
182	08353468-4259528	0.121 ±0.039	17.80 ±0.35	15.60 ±0.35	0.272 ±0.030	16.44 ±0.13	15.01 ±0.13	0.447 ±0.026	15.44 ±0.08	14.51 ±0.08	0.1527
183	08353523-4259598	0.089 ±0.059	18.13 ±0.72	15.93 ±0.72	0.268 ±0.030	16.46 ±0.13	15.02 ±0.13	0.506 ±0.027	15.30 ±0.08	14.38 ±0.08	0.2135
184	08353553-4304142	0.225 ±0.032	17.13 ±0.16	15.24 ±0.16	0.601 ±0.016	15.58 ±0.06	14.35 ±0.06	0.811 ±0.026	14.79 ±0.06	14.00 ±0.06	0.1328
185	08354136-4401486	0.161 ±0.020	17.49 ±0.14	16.48 ±0.14	0.283 ±0.014	16.40 ±0.07	15.74 ±0.07	0.379 ±0.032	15.61 ±0.10	15.19 ±0.10	0.1569
186	08354200-4354258	0.123 ±0.070	17.78 ±0.62	16.46 ±0.62	0.214 ±0.067	16.70 ±0.34	15.84 ±0.34	0.362 ±0.038	15.66 ±0.12	15.11 ±0.12	0.2035
187	08354300-4312228	0.460 ±0.089	16.35 ±0.22	14.46 ±0.22	1.622 ±0.021	14.50 ±0.05	13.27 ±0.05	2.300 ±0.045	13.65 ±0.05	12.87 ±0.05	0.1353
188	08354348-4359584	2.642 ±0.010	14.45 ±0.05	13.44 ±0.05	6.052 ±0.006	13.07 ±0.05	12.41 ±0.05	8.091 ±0.008	12.29 ±0.05	11.87 ±0.05	0.0980
189	08354407-4315260	0.113 ±0.063	17.87 ±0.61	15.99 ±0.61	0.379 ±0.020	16.08 ±0.08	14.85 ±0.08	0.484 ±0.048	15.35 ±0.12	14.56 ±0.12	0.1613
190	08354713-4328169	0.087 ±0.059	18.16 ±0.74	16.57 ±0.74	0.175 ±0.032	16.92 ±0.20	15.88 ±0.20	0.318 ±0.059	15.80 ±0.21	15.14 ±0.21	0.2225
191	08355052-4305281	0.259 ±0.105	16.97 ±0.44	15.09 ±0.44	0.661 ±0.042	15.47 ±0.09	14.25 ±0.09	0.872 ±0.039	14.71 ±0.07	13.92 ±0.07	0.1210

Table B.6 continued...

		J			H			K_s			
ID	Source ID.	f_ν (mJy)	Mag. (mag)	Mag. (mag)	f_ν (mJy)	Mag. (mag)	Mag. (mag)	f_ν (mJy)	Mag. (mag)	Mag. (mag)	Photo-z
192	08355195-4401194	0.073 ±0.070	18.34 ±1.04	17.34 ±1.04	0.154 ±0.030	17.06 ±0.22	16.40 ±0.22	0.212 ±0.056	16.24 ±0.29	15.82 ±0.29	0.2050
193	08355302-4314552	1.780 ±0.147	14.88 ±0.10	13.00 ±0.10	5.121 ±0.136	13.25 ±0.06	12.03 ±0.06	6.225 ±0.072	12.57 ±0.05	11.79 ±0.05	0.0723
194	08355447-4302014	0.123 ±0.049	17.78 ±0.43	15.90 ±0.43	0.269 ±0.034	16.45 ±0.15	15.22 ±0.15	0.329 ±0.056	15.77 ±0.19	14.98 ±0.19	0.1109
195	08355529-4407135	0.105 ±0.170	17.95 ±1.76	16.94 ±1.76	0.224 ±0.090	16.65 ±0.44	16.00 ±0.44	0.318 ±0.052	15.80 ±0.18	15.38 ±0.18	0.2011
196	08355735-4300151	0.175 ±0.048	17.40 ±0.30	15.51 ±0.30	0.319 ±0.027	16.27 ±0.10	15.04 ±0.10	0.390 ±0.050	15.58 ±0.15	14.79 ±0.15	0.0853
197	08360276-4311041	0.097 ±0.069	18.04 ±0.77	16.15 ±0.77	0.281 ±0.035	16.40 ±0.14	15.18 ±0.14	0.405 ±0.061	15.54 ±0.17	14.75 ±0.17	0.1785
198	08360280-4413373	0.138 ±0.035	17.66 ±0.28	16.65 ±0.28	0.247 ±0.026	16.54 ±0.13	15.89 ±0.13	0.235 ±0.082	16.13 ±0.38	15.71 ±0.38	0.0837
199	08360975-4422398	0.171 ±0.050	17.42 ±0.32	16.40 ±0.32	0.364 ±0.025	16.12 ±0.09	15.46 ±0.09	0.508 ±0.044	15.29 ±0.11	14.87 ±0.11	0.1795
200	08361832-4315123	0.204 ±0.030	17.23 ±0.17	15.35 ±0.17	0.497 ±0.014	15.78 ±0.06	14.56 ±0.06	0.641 ±0.031	15.04 ±0.07	14.25 ±0.07	0.1195
201	08361967-4406022	0.057 ±0.091	18.61 ±1.73	17.60 ±1.73	0.137 ±0.041	17.18 ±0.33	16.52 ±0.33	0.228 ±0.077	16.17 ±0.37	15.74 ±0.37	0.2677
202	08362343-4406549	0.122 ±0.051	17.79 ±0.46	16.78 ±0.46	0.300 ±0.022	16.33 ±0.09	15.68 ±0.09	0.462 ±0.042	15.40 ±0.11	14.97 ±0.11	0.2244
203	08362678-4358000	0.258 ±0.038	16.97 ±0.17	15.97 ±0.17	0.492 ±0.021	15.80 ±0.07	15.14 ±0.07	0.588 ±0.044	15.14 ±0.10	14.71 ±0.10	0.1273
204	08362694-4251306	0.102 ±0.112	17.99 ±1.19	15.88 ±1.19	0.211 ±0.073	16.71 ±0.38	15.34 ±0.38	0.447 ±0.083	15.43 ±0.21	14.55 ±0.21	0.2092
205	08362695-4300014	0.073 ±0.080	18.35 ±1.19	16.51 ±1.19	0.158 ±0.067	17.03 ±0.46	15.83 ±0.46	0.279 ±0.066	15.95 ±0.26	15.18 ±0.26	0.2091
206	08362761-4404515	0.055 ±0.082	18.65 ±1.62	17.64 ±1.62	0.129 ±0.036	17.25 ±0.31	16.59 ±0.31	0.199 ±0.069	16.32 ±0.38	15.89 ±0.38	0.2511
207	08362815-4257360	0.071 ±0.094	18.37 ±1.44	16.53 ±1.44	0.212 ±0.037	16.71 ±0.20	15.51 ±0.20	0.342 ±0.065	15.72 ±0.21	14.95 ±0.21	0.2184
208	08363189-4306118	6.763 ±0.030	13.43 ±0.05	11.59 ±0.05	14.448 ±0.025	12.13 ±0.05	10.93 ±0.05	16.776 ±0.016	11.50 ±0.05	10.73 ±0.05	0.0294
209	08363338-4420579	0.137 ±0.054	17.67 ±0.43	16.70 ±0.43	0.185 ±0.060	16.86 ±0.36	16.23 ±0.36	0.335 ±0.059	15.75 ±0.20	15.34 ±0.20	0.2079
210	08363380-4304547	0.061 ±0.060	18.54 ±1.07	16.70 ±1.07	0.144 ±0.032	17.13 ±0.25	15.93 ±0.25	0.229 ±0.043	16.16 ±0.21	15.39 ±0.21	0.1989
211	08363551-4258013	0.163 ±0.061	17.47 ±0.41	15.63 ±0.41	0.542 ±0.026	15.69 ±0.07	14.49 ±0.07	0.655 ±0.051	15.02 ±0.10	14.25 ±0.10	0.1420
212	08363719-4412107	0.082 ±0.067	18.22 ±0.89	17.26 ±0.89	0.160 ±0.031	17.02 ±0.22	16.39 ±0.22	0.298 ±0.056	15.88 ±0.21	15.47 ±0.21	0.2650
213	08363727-4414067	0.211 ±0.040	17.20 ±0.21	16.23 ±0.21	0.426 ±0.018	15.95 ±0.07	15.32 ±0.07	0.527 ±0.044	15.26 ±0.10	14.85 ±0.10	0.1492
214	08363885-4311269	0.044 ±0.098	18.89 ±2.42	17.01 ±2.42	0.148 ±0.043	17.10 ±0.32	15.87 ±0.32	0.294 ±0.072	15.89 ±0.27	15.10 ±0.27	0.2788
215	08363984-4304047	0.158 ±0.037	17.51 ±0.26	15.66 ±0.26	0.353 ±0.021	16.16 ±0.08	14.96 ±0.08	0.420 ±0.034	15.50 ±0.10	14.73 ±0.10	0.1046
216	08364027-4302524	0.093 ±0.043	18.09 ±0.50	16.25 ±0.50	0.199 ±0.038	16.78 ±0.21	15.58 ±0.21	0.219 ±0.054	16.21 ±0.27	15.44 ±0.27	0.0947
217	08364075-4305437	0.085 ±0.058	18.18 ±0.74	16.34 ±0.74	0.157 ±0.037	17.04 ±0.26	15.84 ±0.26	0.227 ±0.094	16.17 ±0.45	15.40 ±0.45	0.1440
218	08364298-4257578	0.101 ±0.089	17.99 ±0.96	16.15 ±0.96	0.240 ±0.050	16.57 ±0.23	15.38 ±0.23	0.368 ±0.078	15.65 ±0.23	14.87 ±0.23	0.1758
219	08364308-4302186	0.208 ±0.033	17.21 ±0.18	15.37 ±0.18	0.373 ±0.025	16.10 ±0.09	14.90 ±0.09	0.493 ±0.031	15.33 ±0.09	14.56 ±0.09	0.1000
220	08364471-4310595	0.046 ±0.081	18.84 ±1.91	16.96 ±1.91	0.156 ±0.029	17.05 ±0.21	15.82 ±0.21	0.267 ±0.065	15.99 ±0.27	15.21 ±0.27	0.2543
221	08364645-4319369	0.170 ±0.048	17.43 ±0.31	15.66 ±0.31	0.481 ±0.019	15.82 ±0.07	14.67 ±0.07	0.675 ±0.034	14.99 ±0.07	14.25 ±0.07	0.1613
222	08364700-4317079	0.124 ±0.044	17.77 ±0.39	16.01 ±0.39	0.369 ±0.016	16.11 ±0.07	14.96 ±0.07	0.492 ±0.036	15.33 ±0.09	14.59 ±0.09	0.1664
223	08364769-4304357	0.151 ±0.043	17.56 ±0.31	15.72 ±0.31	0.374 ±0.023	16.09 ±0.08	14.90 ±0.08	0.510 ±0.033	15.29 ±0.09	14.52 ±0.09	0.1438
224	08364864-4354333	0.043 ±0.115	18.93 ±2.90	17.72 ±2.90	0.105 ±0.057	17.48 ±0.59	16.69 ±0.59	0.202 ±0.058	16.29 ±0.32	15.79 ±0.32	0.3042
225	08364908-4403170	0.469 ±0.016	16.33 ±0.06	15.32 ±0.06	0.885 ±0.010	15.16 ±0.05	14.50 ±0.05	1.038 ±0.022	14.52 ±0.06	14.10 ±0.06	0.1073
226	08365359-4316249	0.041 ±0.068	18.98 ±1.80	17.21 ±1.80	0.111 ±0.030	17.41 ±0.30	16.26 ±0.30	0.175 ±0.062	16.45 ±0.39	15.71 ±0.39	0.2308

Table B.6 continued...

		J			H			K_s			
ID	Source ID.	f_ν (mJy)	Mag. (mag)	Mag. (mag)	f_ν (mJy)	Mag. (mag)	Mag. (mag)	f_ν (mJy)	Mag. (mag)	Mag. (mag)	Photo-z
227	08365711-4255502	0.138 ±0.046	17.65 ±0.36	15.81 ±0.36	0.348 ±0.022	16.17 ±0.09	14.97 ±0.09	0.588 ±0.035	15.14 ±0.08	14.36 ±0.08	0.1894
228	08365802-4303255	0.122 ±0.070	17.79 ±0.63	15.95 ±0.63	0.302 ±0.042	16.32 ±0.16	15.13 ±0.16	0.479 ±0.035	15.36 ±0.09	14.59 ±0.09	0.1802
229	08365881-4304055	0.064 ±0.047	18.49 ±0.80	16.65 ±0.80	0.161 ±0.021	17.01 ±0.15	15.81 ±0.15	0.248 ±0.038	16.07 ±0.17	15.30 ±0.17	0.1972
230	08365946-4304027	0.104 ±0.041	17.96 ±0.43	16.12 ±0.43	0.191 ±0.031	16.82 ±0.18	15.63 ±0.18	0.328 ±0.035	15.77 ±0.13	15.00 ±0.13	0.1763
231	08365969-4303347	0.136 ±0.041	17.67 ±0.33	15.83 ±0.33	0.302 ±0.023	16.33 ±0.10	15.13 ±0.10	0.539 ±0.027	15.23 ±0.07	14.46 ±0.07	0.1907
232	08370122-4302534	0.149 ±0.027	17.57 ±0.20	15.73 ±0.20	0.267 ±0.026	16.46 ±0.12	15.26 ±0.12	0.374 ±0.029	15.63 ±0.10	14.86 ±0.10	0.1202
233	08370360-4407476	0.421 ±0.042	16.44 ±0.12	15.48 ±0.12	0.636 ±0.043	15.52 ±0.09	14.89 ±0.09	0.676 ±0.043	14.98 ±0.09	14.58 ±0.09	0.0741
234	08370535-4414245	0.271 ±0.030	16.92 ±0.13	15.96 ±0.13	0.535 ±0.018	15.71 ±0.06	15.08 ±0.06	0.741 ±0.040	14.88 ±0.08	14.48 ±0.08	0.1617
235	08370629-4408034	0.085 ±0.091	18.18 ±1.16	17.21 ±1.16	0.233 ±0.035	16.61 ±0.17	15.98 ±0.17	0.392 ±0.047	15.58 ±0.14	15.17 ±0.14	0.2697
236	08370827-4407091	0.158 ±0.051	17.51 ±0.35	16.55 ±0.35	0.335 ±0.033	16.21 ±0.12	15.59 ±0.12	0.407 ±0.054	15.54 ±0.15	15.13 ±0.15	0.1579
237	08370889-4317373	0.103 ±0.224	17.97 ±2.36	16.20 ±2.36	0.282 ±0.020	16.40 ±0.09	15.25 ±0.09	0.499 ±0.051	15.32 ±0.12	14.57 ±0.12	0.2207
238	08370893-4412105	0.073 ±0.049	18.35 ±0.73	17.39 ±0.73	0.150 ±0.032	17.09 ±0.24	16.46 ±0.24	0.261 ±0.051	16.02 ±0.22	15.61 ±0.22	0.2600
239	08370946-4319383	0.193 ±0.059	17.29 ±0.34	15.52 ±0.34	0.380 ±0.034	16.08 ±0.11	14.93 ±0.11	0.483 ±0.049	15.35 ±0.12	14.61 ±0.12	0.1073
240	08371218-4356104	0.468 ±0.048	16.33 ±0.12	15.13 ±0.12	0.968 ±0.001	15.06 ±0.05	14.28 ±0.05	1.020 ±0.108	14.54 ±0.13	14.03 ±0.13	0.0925
241	08371400-4306231	0.191 ±0.118	17.30 ±0.67	15.46 ±0.67	0.388 ±0.080	16.05 ±0.23	14.86 ±0.23	0.610 ±0.005	15.10 ±0.05	14.32 ±0.05	0.1482
242	08371794-4418112	0.083 ±0.076	18.21 ±0.99	17.24 ±0.99	0.228 ±0.042	16.63 ±0.21	16.00 ±0.21	0.280 ±0.070	15.94 ±0.28	15.54 ±0.28	0.2040
243	08371958-4308521	0.117 ±0.044	17.84 ±0.41	16.02 ±0.41	0.266 ±0.021	16.46 ±0.10	15.28 ±0.10	0.452 ±0.044	15.42 ±0.12	14.66 ±0.12	0.1901
244	08371998-4421461	0.078 ±0.109	18.27 ±1.52	17.30 ±1.52	0.179 ±0.072	16.90 ±0.44	16.27 ±0.44	0.367 ±0.068	15.65 ±0.21	15.24 ±0.21	0.2787
245	08372126-4407275	0.550 ±0.016	16.15 ±0.06	15.02 ±0.06	0.965 ±0.009	15.06 ±0.05	14.33 ±0.05	1.229 ±0.022	14.34 ±0.05	13.86 ±0.05	0.1153
246	08372217-4300317	0.058 ±0.070	18.60 ±1.31	16.76 ±1.31	0.133 ±0.032	17.22 ±0.27	16.02 ±0.27	0.206 ±0.051	16.27 ±0.27	15.50 ±0.27	0.1939
247	08372295-4358225	0.072 ±0.074	18.36 ±1.12	17.15 ±1.12	0.176 ±0.031	16.91 ±0.20	16.13 ±0.20	0.243 ±0.048	16.10 ±0.22	15.59 ±0.22	0.2177
248	08372299-4301216	0.098 ±0.060	18.02 ±0.67	16.18 ±0.67	0.195 ±0.036	16.80 ±0.21	15.60 ±0.21	0.269 ±0.057	15.99 ±0.23	15.21 ±0.23	0.1369
249	08372306-4356371	0.139 ±0.084	17.65 ±0.66	16.44 ±0.66	0.330 ±0.037	16.23 ±0.13	15.44 ±0.13	0.537 ±0.051	15.23 ±0.12	14.73 ±0.12	0.2254
250	08372490-4353237	3.604 ±0.006	14.11 ±0.05	12.91 ±0.05	6.679 ±0.003	12.96 ±0.05	12.18 ±0.05	7.325 ±0.006	12.40 ±0.05	11.89 ±0.05	0.0522
251	08372764-4303101	0.076 ±0.061	18.30 ±0.87	16.46 ±0.87	0.152 ±0.035	17.07 ±0.26	15.87 ±0.26	0.241 ±0.052	16.10 ±0.24	15.33 ±0.24	0.1767
252	08372818-4419504	0.292 ±0.036	16.84 ±0.14	15.88 ±0.14	0.519 ±0.020	15.74 ±0.07	15.11 ±0.07	0.836 ±0.032	14.75 ±0.07	14.35 ±0.07	0.1794
253	08372953-4407128	0.333 ±0.022	16.70 ±0.09	15.57 ±0.09	0.557 ±0.016	15.66 ±0.06	14.93 ±0.06	0.702 ±0.035	14.94 ±0.07	14.47 ±0.07	0.1233
254	08373052-4306496	0.359 ±0.026	16.62 ±0.09	14.80 ±0.09	0.868 ±0.014	15.18 ±0.05	14.00 ±0.05	1.192 ±0.029	14.37 ±0.06	13.61 ±0.06	0.1326
255	08373205-4347180	0.269 ±0.376	16.93 ±1.52	15.72 ±1.52	0.404 ±0.281	16.01 ±0.76	15.23 ±0.76	0.480 ±0.067	15.36 ±0.16	14.85 ±0.16	0.1008
256	08373564-4409162	0.146 ±0.003	17.59 ±0.06	16.46 ±0.06	0.285 ±0.024	16.39 ±0.10	15.65 ±0.10	0.433 ±0.101	15.47 ±0.26	15.00 ±0.26	0.1995
257	08373576-4410365	0.138 ±0.059	17.65 ±0.47	16.52 ±0.47	0.247 ±0.027	16.55 ±0.13	15.81 ±0.13	0.319 ±0.086	15.80 ±0.30	15.33 ±0.30	0.1582
258	08373629-4358532	3.335 ±0.009	14.20 ±0.05	12.99 ±0.05	6.527 ±0.006	12.99 ±0.05	12.21 ±0.05	7.151 ±0.008	12.42 ±0.05	11.92 ±0.05	0.0562
259	08373824-4307588	0.050 ±0.056	18.75 ±1.22	16.94 ±1.22	0.143 ±0.038	17.13 ±0.29	15.95 ±0.29	0.316 ±0.049	15.81 ±0.18	15.05 ±0.18	0.2765
260	08373853-4258258	0.529 ±0.182	16.20 ±0.38	14.36 ±0.38	0.936 ±0.169	15.10 ±0.20	13.90 ±0.20	1.426 ±0.052	14.18 ±0.06	13.40 ±0.06	0.1136
261	08373905-4418235	0.149 ±0.046	17.57 ±0.34	16.61 ±0.34	0.261 ±0.039	16.49 ±0.17	15.86 ±0.17	0.430 ±0.046	15.48 ±0.13	15.07 ±0.13	0.2070

Table B.6 continued...

		J			H			K_s			
ID	Source ID.	f_ν (mJy)	Mag. (mag)	Mag. (mag)	f_ν (mJy)	Mag. (mag)	Mag. (mag)	f_ν (mJy)	Mag. (mag)	Mag. (mag)	Photo-z
262	08373922-4418322	0.329 ±0.031	16.71 ±0.11	15.75 ±0.11	0.663 ±0.024	15.47 ±0.06	14.84 ±0.06	0.959 ±0.032	14.61 ±0.06	14.20 ±0.06	0.1652
263	08373963-4320219	0.051 ±0.127	18.73 ±2.70	16.91 ±2.70	0.165 ±0.043	16.98 ±0.29	15.80 ±0.29	0.269 ±0.084	15.99 ±0.34	15.23 ±0.34	0.2413
264	08374159-4310033	0.047 ±0.094	18.83 ±2.17	17.01 ±2.17	0.126 ±0.031	17.27 ±0.27	16.09 ±0.27	0.232 ±0.067	16.15 ±0.32	15.39 ±0.32	0.2550
265	08374170-4309379	0.118 ±0.056	17.83 ±0.52	16.01 ±0.52	0.283 ±0.031	16.40 ±0.13	15.22 ±0.13	0.442 ±0.055	15.45 ±0.14	14.69 ±0.14	0.1777
266	08374267-4421396	0.391 ±0.020	16.52 ±0.07	15.53 ±0.07	0.719 ±0.015	15.38 ±0.06	14.74 ±0.06	0.795 ±0.029	14.81 ±0.06	14.39 ±0.06	0.0996
267	08374317-4400126	0.150 ±0.056	17.56 ±0.41	16.36 ±0.41	0.273 ±0.032	16.43 ±0.14	15.65 ±0.14	0.433 ±0.045	15.47 ±0.12	14.96 ±0.12	0.1953
268	08374400-4406271	0.251 ±0.029	17.00 ±0.14	15.88 ±0.14	0.476 ±0.019	15.83 ±0.07	15.10 ±0.07	0.674 ±0.031	14.99 ±0.07	14.52 ±0.07	0.1646
269	08374435-4309529	0.064 ±0.069	18.50 ±1.17	16.68 ±1.17	0.143 ±0.033	17.14 ±0.26	15.96 ±0.26	0.252 ±0.063	16.06 ±0.28	15.29 ±0.28	0.2184
270	08374566-4353314	2.767 ±0.038	14.40 ±0.05	13.20 ±0.05	5.154 ±0.033	13.24 ±0.05	12.46 ±0.05	5.514 ±0.038	12.71 ±0.05	12.20 ±0.05	0.0539
271	08374570-4352214	0.078 ±0.043	18.28 ±0.60	17.07 ±0.60	0.147 ±0.030	17.11 ±0.23	16.32 ±0.23	0.181 ±0.054	16.42 ±0.33	15.91 ±0.33	0.1626
272	08374598-4300410	0.083 ±0.107	18.20 ±1.40	16.36 ±1.40	0.279 ±0.036	16.41 ±0.15	15.21 ±0.15	0.313 ±0.073	15.82 ±0.26	15.05 ±0.26	0.1468
273	08374616-4414176	0.773 ±0.026	15.79 ±0.06	14.82 ±0.06	1.535 ±0.037	14.56 ±0.06	13.93 ±0.06	1.796 ±0.033	13.92 ±0.05	13.52 ±0.05	0.1127
274	08375404-4316176	0.150 ±0.044	17.57 ±0.32	15.75 ±0.32	0.365 ±0.018	16.12 ±0.07	14.94 ±0.07	0.492 ±0.043	15.33 ±0.11	14.57 ±0.11	0.1413
275	08375462-4316522	0.201 ±0.035	17.25 ±0.20	15.43 ±0.20	0.426 ±0.013	15.95 ±0.06	14.77 ±0.06	0.637 ±0.032	15.05 ±0.07	14.29 ±0.07	0.1419
276	08375713-4402597	0.106 ±0.043	17.94 ±0.44	16.81 ±0.44	0.219 ±0.024	16.68 ±0.13	15.94 ±0.13	0.418 ±0.031	15.51 ±0.10	15.03 ±0.10	0.2636
277	08375821-4422211	0.126 ±0.056	17.76 ±0.48	16.77 ±0.48	0.212 ±0.041	16.71 ±0.22	16.06 ±0.22	0.330 ±0.057	15.76 ±0.19	15.35 ±0.19	0.1947
278	08380578-4422423	0.083 ±0.069	18.21 ±0.90	17.22 ±0.90	0.171 ±0.041	16.94 ±0.27	16.30 ±0.27	0.226 ±0.081	16.17 ±0.39	15.76 ±0.39	0.1914
279	08380650-4312537	0.091 ±0.102	18.11 ±1.22	16.29 ±1.22	0.238 ±0.070	16.58 ±0.32	15.40 ±0.32	0.357 ±0.047	15.68 ±0.15	14.92 ±0.15	0.1851
280	08380676-4409258	0.195 ±0.060	17.28 ±0.34	16.15 ±0.34	0.376 ±0.047	16.09 ±0.14	15.35 ±0.14	0.578 ±0.134	15.15 ±0.26	14.68 ±0.26	0.1908
281	08381099-4400442	0.241 ±0.034	17.05 ±0.16	15.92 ±0.16	0.421 ±0.019	15.97 ±0.07	15.23 ±0.07	0.527 ±0.044	15.26 ±0.10	14.78 ±0.10	0.1345
282	08381115-4359107	0.280 ±0.030	16.89 ±0.13	15.76 ±0.13	0.518 ±0.023	15.74 ±0.07	15.01 ±0.07	0.716 ±0.035	14.92 ±0.07	14.45 ±0.07	0.1547
283	08381187-4358518	0.513 ±0.019	16.23 ±0.06	15.10 ±0.06	0.983 ±0.014	15.04 ±0.05	14.31 ±0.05	1.211 ±0.022	14.35 ±0.05	13.88 ±0.05	0.1180
284	08381266-4413546	0.110 ±0.040	17.90 ±0.40	16.77 ±0.40	0.201 ±0.031	16.77 ±0.17	16.04 ±0.17	0.324 ±0.055	15.78 ±0.19	15.31 ±0.19	0.2165
285	08381436-4305290	0.455 ±0.071	16.36 ±0.18	14.46 ±0.18	1.161 ±0.052	14.86 ±0.07	13.63 ±0.07	1.670 ±0.058	14.00 ±0.06	13.21 ±0.06	0.1253
286	08381500-4351542	0.081 ±0.083	18.24 ±1.11	16.90 ±1.11	0.173 ±0.034	16.93 ±0.22	16.06 ±0.22	0.259 ±0.067	16.03 ±0.28	15.47 ±0.28	0.2085
287	08381530-4302517	0.057 ±0.081	18.61 ±1.54	16.72 ±1.54	0.144 ±0.035	17.13 ±0.27	15.90 ±0.27	0.292 ±0.045	15.90 ±0.17	15.10 ±0.17	0.2555
288	08381610-4317416	0.072 ±0.081	18.36 ±1.22	16.55 ±1.22	0.227 ±0.019	16.63 ±0.10	15.45 ±0.10	0.447 ±0.043	15.44 ±0.12	14.67 ±0.12	0.2610
289	08381629-4321046	0.079 ±0.093	18.26 ±1.28	16.63 ±1.28	0.151 ±0.050	17.08 ±0.36	16.02 ±0.36	0.273 ±0.057	15.97 ±0.23	15.29 ±0.23	0.2161
290	08381663-4259494	0.201 ±0.032	17.25 ±0.18	15.35 ±0.18	0.395 ±0.023	16.03 ±0.08	14.80 ±0.08	0.572 ±0.036	15.17 ±0.09	14.37 ±0.09	0.1236
291	08381804-4300361	0.099 ±0.044	18.02 ±0.48	16.12 ±0.48	0.224 ±0.030	16.65 ±0.15	15.41 ±0.15	0.371 ±0.039	15.64 ±0.13	14.84 ±0.13	0.1841
292	08382036-4323061	0.509 ±0.023	16.24 ±0.07	14.61 ±0.07	1.054 ±0.011	14.97 ±0.05	13.91 ±0.05	1.131 ±0.023	14.43 ±0.06	13.74 ±0.06	0.0666
293	08382163-4404292	0.055 ±0.111	18.65 ±2.19	17.52 ±2.19	0.157 ±0.045	17.03 ±0.32	16.30 ±0.32	0.212 ±0.083	16.24 ±0.43	15.77 ±0.43	0.2434
294	08382657-4325142	0.130 ±0.066	17.72 ±0.55	16.09 ±0.55	0.261 ±0.132	16.49 ±0.55	15.42 ±0.55	0.411 ±0.015	15.53 ±0.06	14.84 ±0.06	0.1745
295	08382954-4253118	0.080 ±0.056	18.25 ±0.76	15.85 ±0.76	0.178 ±0.039	16.90 ±0.24	15.34 ±0.24	0.294 ±0.074	15.89 ±0.28	14.88 ±0.28	0.1507
296	08382972-4334467	0.086 ±0.102	18.17 ±1.29	16.57 ±1.29	0.201 ±0.095	16.77 ±0.52	15.73 ±0.52	0.285 ±0.041	15.92 ±0.16	15.25 ±0.16	0.1821

Table B.6 continued...

		J			H			K_s			
ID	Source ID.	f_ν (mJy)	Mag. (mag)	Mag. (mag)	f_ν (mJy)	Mag. (mag)	Mag. (mag)	f_ν (mJy)	Mag. (mag)	Mag. (mag)	Photo-z
297	08383023-4304524	0.174 ±0.024	17.41 ±0.16	15.51 ±0.16	0.404 ±0.068	16.01 ±0.19	14.78 ±0.19	0.567 ±0.170	15.18 ±0.33	14.38 ±0.33	0.1358
298	08383175-4324012	0.068 ±0.073	18.43 ±1.17	16.80 ±1.17	0.214 ±0.028	16.70 ±0.15	15.64 ±0.15	0.399 ±0.040	15.56 ±0.12	14.87 ±0.12	0.2684
299	08383456-4351141	0.114 ±0.045	17.86 ±0.43	16.53 ±0.43	0.236 ±0.020	16.59 ±0.10	15.72 ±0.10	0.342 ±0.049	15.72 ±0.16	15.16 ±0.16	0.1875
300	08383629-4320115	0.141 ±0.051	17.64 ±0.40	16.00 ±0.40	0.320 ±0.025	16.26 ±0.10	15.20 ±0.10	0.493 ±0.052	15.33 ±0.13	14.64 ±0.13	0.1785
301	08383876-4355210	0.063 ±0.126	18.51 ±2.17	17.33 ±2.17	0.180 ±0.043	16.89 ±0.26	16.12 ±0.26	0.258 ±0.072	16.03 ±0.31	15.54 ±0.31	0.2478
302	08383974-4332236	0.200 ±0.040	17.25 ±0.22	15.62 ±0.22	0.442 ±0.019	15.91 ±0.07	14.85 ±0.07	0.659 ±0.043	15.01 ±0.09	14.33 ±0.09	0.1582
303	08384043-4309495	0.685 ±0.010	15.91 ±0.05	14.02 ±0.05	1.704 ±0.005	14.45 ±0.05	13.21 ±0.05	2.452 ±0.012	13.59 ±0.05	12.79 ±0.05	0.1077
304	08384288-4356222	0.115 ±0.042	17.85 ±0.40	16.68 ±0.40	0.157 ±0.042	17.04 ±0.29	16.27 ±0.29	0.148 ±0.101	16.63 ±0.74	16.14 ±0.74	0.0528
305	08384628-4413235	0.155 ±0.045	17.53 ±0.32	16.38 ±0.32	0.322 ±0.029	16.25 ±0.11	15.50 ±0.11	0.431 ±0.056	15.47 ±0.15	14.99 ±0.15	0.1749
306	08384680-4358573	0.113 ±0.073	17.87 ±0.70	16.70 ±0.70	0.202 ±0.042	16.76 ±0.23	15.99 ±0.23	0.307 ±0.072	15.84 ±0.26	15.35 ±0.26	0.1967
307	08384711-4359061	0.221 ±0.034	17.14 ±0.17	15.97 ±0.17	0.358 ±0.027	16.14 ±0.10	15.38 ±0.10	0.481 ±0.038	15.36 ±0.10	14.86 ±0.10	0.1409
308	08384963-4254595	0.119 ±0.056	17.82 ±0.51	15.92 ±0.51	0.288 ±0.031	16.38 ±0.13	15.15 ±0.13	0.399 ±0.059	15.56 ±0.17	14.76 ±0.17	0.1479
309	08385142-4404589	0.507 ±0.020	16.24 ±0.07	15.11 ±0.07	0.876 ±0.015	15.17 ±0.05	14.44 ±0.05	0.852 ±0.032	14.73 ±0.07	14.26 ±0.07	0.0646
310	08385443-4401322	0.197 ±0.041	17.27 ±0.23	16.09 ±0.23	0.421 ±0.022	15.96 ±0.08	15.20 ±0.08	0.440 ±0.048	15.45 ±0.13	14.96 ±0.13	0.1162
311	08385517-4402243	1.969 ±0.005	14.77 ±0.05	13.59 ±0.05	3.411 ±0.022	13.69 ±0.05	12.93 ±0.05	3.714 ±0.005	13.13 ±0.05	12.64 ±0.05	0.0596
312	08385562-4409430	0.057 ±0.057	18.61 ±1.09	17.45 ±1.09	0.121 ±0.042	17.32 ±0.38	16.57 ±0.38	0.219 ±0.064	16.21 ±0.32	15.72 ±0.32	0.2781
313	08385692-4414339	0.174 ±0.040	17.41 ±0.26	16.25 ±0.26	0.447 ±0.016	15.90 ±0.06	15.15 ±0.06	0.651 ±0.037	15.03 ±0.08	14.54 ±0.08	0.2055
314	08385734-4300503	0.057 ±0.061	18.62 ±1.16	16.72 ±1.16	0.147 ±0.028	17.11 ±0.21	15.88 ±0.21	0.262 ±0.042	16.01 ±0.18	15.22 ±0.18	0.2313
315	08385931-4409192	0.060 ±0.082	18.55 ±1.49	17.40 ±1.49	0.143 ±0.036	17.14 ±0.28	16.39 ±0.28	0.294 ±0.069	15.89 ±0.26	15.40 ±0.26	0.2882
316	08390113-4316536	0.091 ±0.058	18.11 ±0.69	16.46 ±0.69	0.202 ±0.024	16.76 ±0.14	15.69 ±0.14	0.271 ±0.069	15.98 ±0.28	15.29 ±0.28	0.1593
317	08390206-4251143	0.159 ±0.084	17.50 ±0.58	15.21 ±0.58	0.588 ±0.031	15.60 ±0.08	14.11 ±0.08	0.984 ±0.037	14.58 ±0.07	13.61 ±0.07	0.1774
318	08390594-4340469	0.086 ±0.061	18.16 ±0.77	16.42 ±0.77	0.225 ±0.028	16.64 ±0.14	15.51 ±0.14	0.341 ±0.051	15.73 ±0.17	15.00 ±0.17	0.1936
319	08390983-4418597	0.078 ±0.031	18.28 ±0.43	17.13 ±0.43	0.153 ±0.038	17.06 ±0.27	16.31 ±0.27	0.283 ±0.160	15.93 ±0.62	15.45 ±0.62	0.2637
320	08391113-4415360	0.136 ±0.163	17.68 ±1.30	16.52 ±1.30	0.304 ±0.155	16.32 ±0.56	15.57 ±0.56	0.472 ±0.033	15.38 ±0.09	14.89 ±0.09	0.2167
321	08391139-4418073	0.070 ±0.080	18.39 ±1.24	17.23 ±1.24	0.179 ±0.029	16.90 ±0.18	16.14 ±0.18	0.253 ±0.063	16.05 ±0.28	15.57 ±0.28	0.2327
322	08391189-4405384	3.705 ±0.006	14.08 ±0.05	12.91 ±0.05	6.314 ±0.005	13.03 ±0.05	12.26 ±0.05	6.601 ±0.008	12.51 ±0.05	12.02 ±0.05	0.0412
323	08391218-4416021	0.110 ±0.126	17.91 ±1.25	16.75 ±1.25	0.204 ±0.074	16.75 ±0.40	16.00 ±0.40	0.298 ±0.027	15.88 ±0.11	15.39 ±0.11	0.1946
324	08391267-4308253	0.119 ±0.034	17.81 ±0.31	15.92 ±0.31	0.253 ±0.019	16.52 ±0.10	15.29 ±0.10	0.339 ±0.048	15.73 ±0.16	14.94 ±0.16	0.1280
325	08391282-4413470	0.081 ±0.069	18.23 ±0.93	17.07 ±0.93	0.203 ±0.031	16.76 ±0.17	16.01 ±0.17	0.345 ±0.055	15.72 ±0.18	15.23 ±0.18	0.2637
326	08391319-4409154	0.134 ±0.019	17.69 ±0.16	16.27 ±0.16	0.278 ±0.019	16.41 ±0.09	15.49 ±0.09	0.448 ±0.034	15.43 ±0.10	14.84 ±0.10	0.1979
327	08391541-4401153	2.175 ±0.013	14.66 ±0.05	13.48 ±0.05	4.050 ±0.007	13.51 ±0.05	12.74 ±0.05	4.690 ±0.017	12.88 ±0.05	12.39 ±0.05	0.0731
328	08391584-4419224	0.201 ±0.056	17.25 ±0.31	16.09 ±0.31	0.410 ±0.036	15.99 ±0.11	15.24 ±0.11	0.606 ±0.041	15.10 ±0.09	14.62 ±0.09	0.1851
329	08391947-4418343	0.084 ±0.079	18.20 ±1.02	17.05 ±1.02	0.155 ±0.056	17.05 ±0.40	16.30 ±0.40	0.310 ±0.060	15.83 ±0.22	15.35 ±0.22	0.2721
330	08392484-4308476	0.644 ±0.015	15.98 ±0.06	14.09 ±0.06	1.388 ±0.007	14.67 ±0.05	13.44 ±0.05	1.706 ±0.022	13.98 ±0.05	13.19 ±0.05	0.0769
331	08392501-4400205	0.413 ±0.024	16.46 ±0.08	15.29 ±0.08	1.044 ±0.011	14.98 ±0.05	14.21 ±0.05	1.725 ±0.018	13.97 ±0.05	13.47 ±0.05	0.2035

Table B.6 continued...

		J			H			K_s			
ID	Source ID.	f_ν (mJy)	Mag. (mag)	Mag. (mag)	f_ν (mJy)	Mag. (mag)	Mag. (mag)	f_ν (mJy)	Mag. (mag)	Mag. (mag)	Photo-z
332	08392536-4400171	0.431 ±0.028	16.42 ±0.09	15.24 ±0.09	0.912 ±0.014	15.13 ±0.05	14.36 ±0.05	1.409 ±0.025	14.19 ±0.05	13.70 ±0.05	0.1666
333	08392817-4405279	0.089 ±0.055	18.13 ±0.67	16.72 ±0.67	0.208 ±0.028	16.73 ±0.15	15.81 ±0.15	0.250 ±0.061	16.06 ±0.27	15.47 ±0.27	0.1590
334	08392934-4347456	0.097 ±0.046	18.04 ±0.52	16.52 ±0.52	0.162 ±0.028	17.00 ±0.19	16.01 ±0.19	0.315 ±0.051	15.81 ±0.18	15.18 ±0.18	0.2214
335	08393245-4421456	0.122 ±0.045	17.79 ±0.40	16.64 ±0.40	0.229 ±0.028	16.63 ±0.14	15.88 ±0.14	0.334 ±0.055	15.75 ±0.19	15.27 ±0.19	0.1922
336	08393256-4317336	0.115 ±0.037	17.85 ±0.35	16.21 ±0.35	0.245 ±0.019	16.55 ±0.10	15.48 ±0.10	0.370 ±0.044	15.64 ±0.14	14.95 ±0.14	0.1741
337	08393257-4339000	0.189 ±0.041	17.31 ±0.24	15.56 ±0.24	0.357 ±0.024	16.14 ±0.09	15.01 ±0.09	0.618 ±0.036	15.08 ±0.08	14.35 ±0.08	0.1672
338	08393355-4405207	0.056 ±0.075	18.64 ±1.46	17.22 ±1.46	0.127 ±0.038	17.27 ±0.33	16.34 ±0.33	0.154 ±0.099	16.59 ±0.70	16.00 ±0.70	0.1700
339	08393394-4412221	0.128 ±0.031	17.73 ±0.27	16.32 ±0.27	0.252 ±0.020	16.52 ±0.10	15.60 ±0.10	0.342 ±0.044	15.73 ±0.15	15.13 ±0.15	0.1580
340	08393480-4255169	0.117 ±0.048	17.83 ±0.45	15.86 ±0.45	0.286 ±0.022	16.39 ±0.10	15.10 ±0.10	0.420 ±0.047	15.50 ±0.13	14.68 ±0.13	0.1543
341	08393718-4357246	0.099 ±0.069	18.02 ±0.76	16.84 ±0.76	0.214 ±0.034	16.70 ±0.18	15.93 ±0.18	0.394 ±0.051	15.57 ±0.15	15.08 ±0.15	0.2586
342	08393937-4414206	0.095 ±0.059	18.07 ±0.68	16.65 ±0.68	0.208 ±0.030	16.73 ±0.16	15.81 ±0.16	0.422 ±0.043	15.50 ±0.12	14.90 ±0.12	0.2624
343	08393950-4349176	0.084 ±0.049	18.19 ±0.64	16.67 ±0.64	0.175 ±0.022	16.92 ±0.14	15.93 ±0.14	0.229 ±0.064	16.16 ±0.31	15.52 ±0.31	0.1597
344	08394178-4415444	0.090 ±0.006	18.12 ±0.09	16.70 ±0.09	0.191 ±0.164	16.82 ±0.93	15.90 ±0.93	0.322 ±0.070	15.79 ±0.24	15.20 ±0.24	0.2234
345	08394788-4258024	0.031 ±0.005	19.29 ±0.18	17.32 ±0.18	0.132 ±0.085	17.23 ±0.70	15.94 ±0.70	0.213 ±0.081	16.24 ±0.42	15.41 ±0.42	0.2728
346	08394951-4311421	0.557 ±0.015	16.14 ±0.06	14.50 ±0.06	1.157 ±0.009	14.87 ±0.05	13.80 ±0.05	1.543 ±0.019	14.09 ±0.05	13.40 ±0.05	0.1141
347	08394958-4338518	0.070 ±0.082	18.39 ±1.27	16.64 ±1.27	0.154 ±0.048	17.06 ±0.34	15.92 ±0.34	0.259 ±0.074	16.03 ±0.31	15.30 ±0.31	0.2076
348	08395046-4306273	0.091 ±0.051	18.11 ±0.61	16.47 ±0.61	0.163 ±0.029	16.99 ±0.20	15.92 ±0.20	0.239 ±0.069	16.11 ±0.32	15.42 ±0.32	0.1587
349	08395122-4308378	0.125 ±0.037	17.76 ±0.33	16.12 ±0.33	0.237 ±0.019	16.59 ±0.10	15.52 ±0.10	0.427 ±0.043	15.48 ±0.12	14.80 ±0.12	0.1978
350	08395126-4352460	0.074 ±0.066	18.34 ±0.97	16.81 ±0.97	0.164 ±0.029	16.99 ±0.20	16.00 ±0.20	0.254 ±0.056	16.05 ±0.24	15.41 ±0.24	0.2074
351	08395145-4256169	0.073 ±0.077	18.35 ±1.15	16.38 ±1.15	0.176 ±0.041	16.91 ±0.26	15.63 ±0.26	0.298 ±0.050	15.88 ±0.19	15.05 ±0.19	0.1991
352	08395210-4255515	0.091 ±0.065	18.11 ±0.78	16.13 ±0.78	0.242 ±0.029	16.57 ±0.14	15.28 ±0.14	0.431 ±0.041	15.47 ±0.12	14.64 ±0.12	0.2093
353	08395253-4326065	0.071 ±0.067	18.38 ±1.03	16.39 ±1.03	0.140 ±0.041	17.16 ±0.32	15.87 ±0.32	0.275 ±0.058	15.96 ±0.23	15.13 ±0.23	0.2124
354	08395597-4404297	0.137 ±0.033	17.66 ±0.27	16.25 ±0.27	0.274 ±0.020	16.43 ±0.09	15.51 ±0.09	0.399 ±0.040	15.56 ±0.12	14.96 ±0.12	0.1733
355	08395832-4313525	0.234 ±0.035	17.08 ±0.17	15.44 ±0.17	0.485 ±0.018	15.81 ±0.06	14.74 ±0.06	0.802 ±0.029	14.80 ±0.06	14.11 ±0.06	0.1665
356	08395854-4347595	0.093 ±0.052	18.09 ±0.61	16.56 ±0.61	0.190 ±0.019	16.83 ±0.12	15.84 ±0.12	0.274 ±0.050	15.97 ±0.20	15.33 ±0.20	0.1763
357	08395921-4257596	0.282 ±0.046	16.88 ±0.18	14.90 ±0.18	0.675 ±0.112	15.45 ±0.19	14.17 ±0.19	0.933 ±0.039	14.63 ±0.07	13.81 ±0.07	0.1162
358	08400040-4317220	0.245 ±0.017	17.03 ±0.09	15.39 ±0.09	0.590 ±0.008	15.60 ±0.05	14.53 ±0.05	0.750 ±0.020	14.87 ±0.06	14.19 ±0.06	0.1276
359	08400101-4402106	0.821 ±0.029	15.72 ±0.06	14.30 ±0.06	1.761 ±0.038	14.41 ±0.06	13.49 ±0.06	2.289 ±0.050	13.66 ±0.06	13.07 ±0.06	0.1057
360	08400351-4413386	0.057 ±0.080	18.61 ±1.52	17.19 ±1.52	0.151 ±0.040	17.08 ±0.29	16.16 ±0.29	0.289 ±0.050	15.91 ±0.19	15.31 ±0.19	0.2856
361	08400387-4405227	0.067 ±0.064	18.45 ±1.04	17.03 ±1.04	0.132 ±0.040	17.23 ±0.33	16.31 ±0.33	0.218 ±0.066	16.21 ±0.33	15.62 ±0.33	0.2238
362	08400585-4418557	0.140 ±0.035	17.64 ±0.28	16.60 ±0.28	0.263 ±0.026	16.48 ±0.12	15.80 ±0.12	0.336 ±0.047	15.74 ±0.16	15.31 ±0.16	0.1539
363	08400785-4355445	0.141 ±0.044	17.64 ±0.34	16.11 ±0.34	0.283 ±0.021	16.40 ±0.10	15.40 ±0.10	0.402 ±0.046	15.55 ±0.13	14.91 ±0.13	0.1591
364	08400940-4415596	0.219 ±0.018	17.15 ±0.10	15.74 ±0.10	0.411 ±0.043	15.99 ±0.12	15.07 ±0.12	0.591 ±0.045	15.13 ±0.10	14.54 ±0.10	0.1501
365	08400984-4418202	0.048 ±0.061	18.80 ±1.38	17.75 ±1.38	0.102 ±0.039	17.50 ±0.42	16.82 ±0.42	0.221 ±0.047	16.20 ±0.24	15.76 ±0.24	0.3001
366	08401071-4259087	0.200 ±0.011	17.25 ±0.08	15.28 ±0.08	0.492 ±0.050	15.80 ±0.12	14.51 ±0.12	0.721 ±0.010	14.91 ±0.05	14.09 ±0.05	0.1392

Table B.6 continued...

		J			H			K_s			
ID	Source ID.	f_ν (mJy)	Mag. (mag)	Mag. (mag)	f_ν (mJy)	Mag. (mag)	Mag. (mag)	f_ν (mJy)	Mag. (mag)	Mag. (mag)	Photo-z
367	08401186-4350234	0.242 ±0.025	17.05 ±0.12	15.52 ±0.12	0.460 ±0.014	15.87 ±0.06	14.88 ±0.06	0.598 ±0.026	15.12 ±0.07	14.48 ±0.07	0.1208
368	08401225-4325590	0.105 ±0.039	17.95 ±0.41	15.96 ±0.41	0.221 ±0.025	16.66 ±0.13	15.37 ±0.13	0.250 ±0.056	16.06 ±0.25	15.23 ±0.25	0.0850
369	08401545-4253182	0.051 ±0.077	18.74 ±1.64	16.76 ±1.64	0.158 ±0.045	17.03 ±0.31	15.75 ±0.31	0.277 ±0.056	15.95 ±0.23	15.13 ±0.23	0.2411
370	08401654-4351436	0.068 ±0.052	18.42 ±0.83	16.89 ±0.83	0.143 ±0.026	17.14 ±0.20	16.15 ±0.20	0.291 ±0.033	15.90 ±0.13	15.26 ±0.13	0.2633
371	08401857-4347314	0.093 ±0.069	18.08 ±0.81	16.55 ±0.81	0.170 ±0.035	16.95 ±0.23	15.96 ±0.23	0.278 ±0.062	15.95 ±0.25	15.31 ±0.25	0.1931
372	08401884-4404078	0.053 ±0.074	18.69 ±1.52	17.28 ±1.52	0.147 ±0.032	17.11 ±0.24	16.19 ±0.24	0.271 ±0.047	15.98 ±0.20	15.38 ±0.20	0.2868
373	08402021-4313400	0.075 ±0.045	18.32 ±0.65	16.68 ±0.65	0.146 ±0.030	17.12 ±0.23	16.05 ±0.23	0.204 ±0.069	16.29 ±0.37	15.60 ±0.37	0.1613
374	08402024-4257373	0.126 ±0.031	17.75 ±0.27	15.78 ±0.27	0.235 ±0.024	16.60 ±0.12	15.31 ±0.12	0.437 ±0.046	15.46 ±0.13	14.63 ±0.13	0.1771
375	08402083-4359102	0.168 ±0.028	17.44 ±0.19	16.17 ±0.19	0.335 ±0.040	16.21 ±0.14	15.38 ±0.14	0.449 ±0.043	15.43 ±0.12	14.89 ±0.12	0.1597
376	08402198-4318217	0.055 ±0.100	18.65 ±1.98	17.01 ±1.98	0.148 ±0.028	17.10 ±0.21	16.03 ±0.21	0.190 ±0.080	16.36 ±0.46	15.68 ±0.46	0.1831
377	08402221-4416380	0.323 ±0.054	16.73 ±0.19	15.69 ±0.19	0.669 ±0.071	15.46 ±0.13	14.78 ±0.13	0.935 ±0.063	14.63 ±0.09	14.20 ±0.09	0.1548
378	08402241-4257408	0.415 ±0.024	16.46 ±0.08	14.49 ±0.08	0.980 ±0.093	15.05 ±0.12	13.76 ±0.12	1.264 ±0.088	14.30 ±0.09	13.48 ±0.09	0.1050
379	08402450-4417281	0.162 ±0.056	17.48 ±0.38	16.44 ±0.38	0.415 ±0.024	15.98 ±0.08	15.30 ±0.08	0.499 ±0.065	15.31 ±0.15	14.88 ±0.15	0.1650
380	08402714-4415167	0.072 ±0.075	18.37 ±1.13	16.95 ±1.13	0.219 ±0.033	16.68 ±0.17	15.76 ±0.17	0.491 ±0.031	15.33 ±0.09	14.74 ±0.09	0.2620
381	08402758-4344585	0.059 ±0.122	18.59 ±2.25	17.06 ±2.25	0.179 ±0.040	16.90 ±0.25	15.90 ±0.25	0.249 ±0.069	16.07 ±0.30	15.43 ±0.30	0.2215
382	08402774-4355026	0.364 ±0.004	16.60 ±0.05	15.08 ±0.05	0.669 ±0.009	15.46 ±0.05	14.47 ±0.05	0.694 ±0.014	14.96 ±0.06	14.32 ±0.06	0.0629
383	08402862-4257172	0.215 ±0.034	17.17 ±0.18	15.20 ±0.18	0.507 ±0.017	15.76 ±0.06	14.48 ±0.06	0.824 ±0.025	14.77 ±0.06	13.94 ±0.06	0.1524
384	08402937-4313583	0.083 ±0.064	18.20 ±0.84	16.56 ±0.84	0.167 ±0.031	16.97 ±0.21	15.90 ±0.21	0.296 ±0.051	15.88 ±0.19	15.20 ±0.19	0.2134
385	08403050-4257055	0.070 ±0.109	18.39 ±1.69	16.41 ±1.69	0.217 ±0.037	16.68 ±0.19	15.40 ±0.19	0.409 ±0.044	15.53 ±0.13	14.70 ±0.13	0.2419
386	08403114-4413340	0.122 ±0.042	17.79 ±0.38	16.37 ±0.38	0.197 ±0.028	16.79 ±0.16	15.87 ±0.16	0.282 ±0.053	15.93 ±0.21	15.34 ±0.21	0.1528
387	08403376-4338361	0.266 ±0.028	16.94 ±0.13	14.68 ±0.13	0.520 ±0.019	15.74 ±0.06	14.26 ±0.06	0.745 ±0.027	14.88 ±0.06	13.93 ±0.06	0.0892
388	08403487-4403374	0.139 ±0.048	17.65 ±0.38	16.38 ±0.38	0.241 ±0.022	16.57 ±0.11	15.74 ±0.11	0.359 ±0.042	15.67 ±0.14	15.14 ±0.14	0.1756
389	08403998-4314285	0.072 ±0.061	18.36 ±0.92	16.67 ±0.92	0.189 ±0.033	16.83 ±0.20	15.73 ±0.20	0.288 ±0.050	15.91 ±0.20	15.20 ±0.20	0.2062
390	08404016-4347597	0.104 ±0.113	17.96 ±1.18	16.44 ±1.18	0.215 ±0.112	16.70 ±0.57	15.70 ±0.57	0.316 ±0.038	15.81 ±0.14	15.17 ±0.14	0.1778
391	08404063-4259035	0.078 ±0.113	18.27 ±1.57	16.58 ±1.57	0.195 ±0.056	16.80 ±0.32	15.70 ±0.32	0.322 ±0.061	15.79 ±0.21	15.08 ±0.21	0.2165
392	08404238-4303127	0.176 ±0.059	17.39 ±0.37	15.70 ±0.37	0.349 ±0.034	16.17 ±0.12	15.07 ±0.12	0.472 ±0.052	15.38 ±0.13	14.67 ±0.13	0.1288
393	08404645-4253520	0.200 ±0.046	17.25 ±0.26	15.28 ±0.26	0.625 ±0.016	15.54 ±0.06	14.25 ±0.06	0.941 ±0.019	14.63 ±0.06	13.80 ±0.06	0.1615
394	08404764-4347365	0.215 ±0.088	17.17 ±0.45	15.65 ±0.45	0.415 ±0.113	15.98 ±0.30	14.99 ±0.30	0.468 ±0.014	15.38 ±0.06	14.75 ±0.06	0.0951
395	08404831-4335095	0.083 ±0.064	18.21 ±0.84	15.95 ±0.84	0.200 ±0.029	16.77 ±0.17	15.30 ±0.17	0.258 ±0.055	16.03 ±0.24	15.08 ±0.24	0.1135
396	08404852-4347323	0.406 ±0.024	16.48 ±0.08	14.96 ±0.08	0.933 ±0.024	15.10 ±0.06	14.11 ±0.06	1.221 ±0.086	14.34 ±0.09	13.71 ±0.09	0.1227
397	08405025-4353509	0.387 ±0.022	16.54 ±0.08	15.26 ±0.08	0.748 ±0.011	15.34 ±0.05	14.51 ±0.05	0.943 ±0.022	14.62 ±0.06	14.09 ±0.06	0.1210
398	08405090-4347364	0.116 ±0.110	17.84 ±1.03	16.32 ±1.03	0.186 ±0.060	16.86 ±0.35	15.86 ±0.35	0.217 ±0.051	16.22 ±0.26	15.58 ±0.26	0.0964
399	08405573-4410454	0.119 ±0.053	17.82 ±0.49	16.40 ±0.49	0.229 ±0.027	16.63 ±0.14	15.71 ±0.14	0.382 ±0.037	15.61 ±0.12	15.01 ±0.12	0.2024
400	08405802-4253391	0.052 ±0.119	18.72 ±2.48	16.37 ±2.48	0.178 ±0.047	16.90 ±0.29	15.37 ±0.29	0.305 ±0.060	15.85 ±0.22	14.86 ±0.22	0.2149
401	08405943-4257596	0.046 ±0.119	18.85 ±2.81	17.16 ±2.81	0.141 ±0.032	17.15 ±0.25	16.05 ±0.25	0.241 ±0.054	16.11 ±0.25	15.40 ±0.25	0.2613

Table B.6 continued...

		J			H			K_s			
ID	Source ID.	f_ν (mJy)	Mag. (mag)	Mag. (mag)	f_ν (mJy)	Mag. (mag)	Mag. (mag)	f_ν (mJy)	Mag. (mag)	Mag. (mag)	Photo-z
402	08410086-4354513	0.052 ±0.130	18.70 ±2.71	17.43 ±2.71	0.123 ±0.055	17.30 ±0.49	16.47 ±0.49	0.272 ±0.052	15.97 ±0.21	15.44 ±0.21	0.2901
403	08410154-4351069	0.106 ±0.061	17.94 ±0.63	16.41 ±0.63	0.184 ±0.042	16.86 ±0.25	15.87 ±0.25	0.321 ±0.054	15.79 ±0.19	15.15 ±0.19	0.1978
404	08410188-4251283	0.139 ±0.081	17.64 ±0.64	15.29 ±0.64	0.424 ±0.028	15.96 ±0.09	14.43 ±0.09	0.648 ±0.035	15.03 ±0.08	14.04 ±0.08	0.1481

B.3 Spitzer + IRSF Rejected Sources

These catalogues represent sources with detections, but unreliable photometry due to large errors. Measurements from the *Spitzer* area are listed in Tables B.7, B.8 and B.9.

B.3.1 Rejected sources in the *Spitzer* Area

Table B.7 lists the photometric parameters for sources in the *Spitzer* footprint as follows:
Column 1: Source IRSF ID
Column 2: Right Ascension
Column 3: Declination
Column 4: Galactic Longitude (deg)
Column 5: Galactic Latitute (deg)
Column 6: A_V (mag)
Column 7: Isophotal Radius, a (arcsec)
Column 8: Axis ratio, b/a
Column 9: Position Angle (deg) – measured east of north

Table B.7: Spitzer + IRSF Rejected Sources - Photometric Parameters

Source ID.	R.A. (J2000)	Dec. (J2000)	l (deg)	b (deg)	A_V (mag)	a (arcsec)	b/a	P.A. (deg)
08355286-4323366	$08^{\rm h}\ 35^{\rm m}\ 52.9^{\rm s}$	-43°23′36.6″	262.18	-1.64	5.8	3.66	1.00	0.0
08371914-4345536	$08^{\rm h}\ 37^{\rm m}\ 19.1^{\rm s}$	-43°45′53.7″	262.64	-1.66	4.4	5.31	1.00	0.0
08372771-4346039	$08^{\rm h}\ 37^{\rm m}\ 27.7^{\rm s}$	-43°46′04.0″	262.65	-1.64	4.4	3.66	1.00	0.0
08373659-4326387	$08^{\rm h}\ 37^{\rm m}\ 36.6^{\rm s}$	-43°26′38.7″	262.41	-1.42	5.9	4.49	1.00	0.0
08374998-4337299	$08^{\rm h}\ 37^{\rm m}\ 50.0^{\rm s}$	-43°37′30.0″	262.58	-1.50	5.9	3.66	1.00	0.0

Rejected Sources: MIR measurements

Table B.8 gives the MIR measurements and corrected fluxes and magnitudes for sources in the *Spitzer* footprint as follows:
Column 1: Source IRSF ID
Column 2, **Column 6**, **Column 10**, **Column 14**: Flux density (mJy) for the four IRAC bands - raw measurements and their errors
Column 3, **Column 7**, **Column 11**, **Column 15**: Flux density (mJy) for the four IRAC bands - aperture-corrected measurements and their errors
Column 4, **Column 8**, **Column 12**, **Column 16**: Integrated Magnitude (mag) – no reddening correction applied; 5% calibration error included
Column 5, **Column 9**, **Column 13**, **Column 17**: Integrated Magnitude (mag) – reddening-corrected; 5% calibration error included
Sources with no measurements (...) are due to differing coverage by the IRAC bands, as discussed in Chapter 2.

Table B.8: Rejected Sources: MIR Photometry

	3.6 μm				4.5 μm				5.8 μm				8.0 μm			
	f_ν	f_ν	Mag.	Mag.	f_ν	f_ν	Mag.	Mag.	f_ν	f_ν	Mag.	Mag.	f_ν	f_ν	Mag.	Mag.
Source ID.	(mJy)	(mJy)	(mag)	(mag)	(mJy)	(mJy)	(mag)	(mag)	(mJy)	(mJy)	(mag)	(mag)	(mJy)	(mJy)	(mag)	(mag)
08355286-4323366	0.116	0.13	15.83	15.52	0.147	0.17	15.08	14.87	0.042	0.05	15.90	15.69	0.047	0.06	15.11	14.90
	±0.023	±0.03	±0.22	±0.22	±0.018	±0.02	±0.15	±0.15	±0.016	±0.02	±0.42	±0.42	±0.014	±0.02	±0.32	±0.32
08371914-4345536	0.345	0.37	14.69	14.46	0.237	0.26	14.61	14.45	0.228	0.26	14.13	13.97	0.165	0.19	13.83	13.67
	±0.014	±0.02	±0.07	±0.07	±0.027	±0.03	±0.13	±0.13	±0.018	±0.02	±0.10	±0.10	±0.038	±0.04	±0.25	±0.25
08372771-4346039	0.185	0.21	15.32	15.09	...	0.0	...	...	0.081	0.1	15.19	15.03	...	0.0	...	...
	±0.010	±0.01	±0.08	±0.08	...	...	...	...	±0.012	±0.01	±0.17	±0.17	...	...	...	...
08373659-4326387	0.249	0.27	15.03	14.72	0.200	0.22	14.77	14.56	0.099	0.11	15.01	14.80	0.233	0.27	13.42	13.21
	±0.012	±0.01	±0.07	±0.07	±0.009	±0.01	±0.07	±0.07	±0.015	±0.02	±0.17	±0.17	±0.025	±0.03	±0.13	±0.13
08374998-4337299	0.087	0.1	16.14	15.83	0.080	0.09	15.74	15.53	0.035	0.04	16.10	15.89	0.012	0.01	16.59	16.38
	±0.009	±0.01	±0.13	±0.13	±0.007	±0.01	±0.10	±0.10	±0.017	±0.02	±0.546	±0.54	±0.019	±0.02	±1.7609	±1.7609

Rejected Sources: NIR measurements

Table B.9 gives the NIR measurements and corrected fluxes and magnitudes for sources in the *Spitzer* footprint as follow:

Column 1: Source IRSF ID

Column 2, **Column 5**, **Column 8**: Flux density (mJy) for the J, H, K_s – raw measurements

Column 3, **Column 6**, **Column 9**: Integrated Magnitude (mag) no reddening correction applied; 5% calibration error included. The extinction corrected magnitudes have an error of ∼10% which is not accounted for.

Column 4, **Column 7**, **Column 10**: Integrated Magnitude (mag) – reddening-corrected; 5% calibration error included

Column 11: Photometric redshift

Table B.9: Rejected Sources: NIR Photometry

	J			H			K_s			
Source ID.	f_ν (mJy)	Mag. (mag)	Mag. (mag)	f_ν (mJy)	Mag. (mag)	Mag. (mag)	f_ν (mJy)	Mag. (mag)	Mag. (mag)	Photo-z
08355286-4323366	0.037 ±0.038	19.09 ±1.13	17.50 ±1.13	0.083 ±0.049	17.73 ±0.64	16.69 ±0.64	0.204 ±0.096	16.29 ±0.52	15.62 ±0.52	0.2989
08371914-4345536	0.062 ±0.043	18.52 ±0.76	17.32 ±0.76	0.182 ±0.057	16.88 ±0.34	16.09 ±0.34	0.195 ±0.123	16.34 ±0.69	15.83 ±0.69	0.1825
08372771-4346039	0.024 ±0.027	19.56 ±1.24	18.35 ±1.24	0.085 ±0.038	17.70 ±0.49	16.92 ±0.49	0.158 ±0.077	16.56 ±0.53	16.06 ±0.53	0.3153
08373659-4326387	0.054 ±0.036	18.68 ±0.73	17.08 ±0.73	0.146 ±0.049	17.11 ±0.36	16.08 ±0.36	0.321 ±0.135	15.79 ±0.46	15.12 ±0.46	0.2786
08374998-4337299	0.028 ±0.024	19.39 ±0.93	17.79 ±0.93	0.085 ±0.029	17.70 ±0.38	16.66 ±0.38	0.139 ±0.072	16.70 ±0.56	16.03 ±0.56	0.2572

B.3.2 Rejected Sources with NIR measurements only

Sources with NIR measurements only have their photometric parameters listed in Table B.10 as follows:
Column 1: Source IRSF ID
Column 2: Right Ascension
Column 3: Declination
Column 4: Galactic Longitude (deg)
Column 5: Galactic Latitute (deg)
Column 6: A_V (mag)
Column 7: Number of duplicates (from overlapping fields)
Column 8: Radius, a (arcsec)
Column 9: Axis ratio (b/a)
Column 10: Position Angle (deg) – measured east of north
Duplicate photometry was combined using an inverse-variance weighted mean.

Table B.10: Rejected Sources - IRSF Photometric Parameters.

Source ID.	R.A. (J2000)	Dec. (J2000)	l (deg)	b (deg)	A_V (mag)	Rep.	a (arcsec)	b/a	P.A. (deg)
08324175-4305544	$08^h\ 32^m\ 41.8^s$	-43°05′54.4″	261.06°	-1.93°	6.5	1	5.89″	0.40	-50.00
08324378-4403454	$08^h\ 32^m\ 43.8^s$	-44°03′45.5″	262.38°	-2.50°	5.4	1	3.10″	1.00	0.00
08325424-4338324	$08^h\ 32^m\ 54.2^s$	-43°38′32.4″	262.60°	-2.22°	6.9	1	3.27″	1.00	0.00
08325794-4322119	$08^h\ 32^m\ 58.0^s$	-43°22′12.0″	261.85°	-2.05°	9.8	2	2.95″	1.00	0.00
08325910-4355398	$08^h\ 32^m\ 59.1^s$	-43°55′39.8″	262.30°	-2.38°	6.3	1	2.65″	1.00	0.00
08330000-4408418	$08^h\ 32^m\ 60.0^s$	-44°08′41.9″	262.47°	-2.51°	5.4	1	2.21″	1.00	0.00
08331118-4314238	$08^h\ 33^m\ 11.2^s$	-43°14′23.9″	261.77°	-1.94°	9.8	1	2.80″	1.00	0.00
08332314-4330514	$08^h\ 33^m\ 23.1^s$	-43°30′51.4″	262.01°	-2.08°	8.3	1	1.72″	1.00	0.00
08332567-4423297	$08^h\ 33^m\ 25.7^s$	-44°23′29.8″	262.72°	-2.59°	4.9	1	2.86″	0.75	78.00
08332713-4422297	$08^h\ 33^m\ 27.1^s$	-44°22′29.8″	262.71°	-2.58°	4.9	1	2.16″	0.40	18.00
08332985-4407595	$08^h\ 33^m\ 29.9^s$	-44°07′59.5″	262.52°	-2.43°	5.4	2	1.85″	1.00	0.00
08333403-4416132	$08^h\ 33^m\ 34.0^s$	-44°16′13.2″	262.64°	-2.50°	4.9	1	1.41″	1.00	0.00
08333669-4318390	$08^h\ 33^m\ 36.7^s$	-43°18′39.0″	261.87°	-1.92°	9.8	2	1.70″	0.90	0.00
08333652-4346000	$08^h\ 33^m\ 36.5^s$	-43°45′60.0″	262.23°	-2.19°	6.1	1	1.16″	1.00	0.00
08334275-4305557	$08^h\ 33^m\ 42.8^s$	-43°05′55.8″	261.71°	-1.78°	6.8	1	1.72″	0.80	40.00
08334640-4313220	$08^h\ 33^m\ 46.4^s$	-43°13′22.0″	261.82°	-1.85°	6.8	1	1.93″	0.85	83.00
08334722-4354599	$08^h\ 33^m\ 47.2^s$	-43°54′59.9″	262.37°	-2.26°	6.1	1	2.21″	0.85	-15.00
08335329-4419204	$08^h\ 33^m\ 53.3^s$	-44°19′20.5″	262.71°	-2.48°	4.9	1	1.77″	1.00	0.00
08335357-4355107	$08^h\ 33^m\ 53.6^s$	-43°55′10.8″	262.39°	-2.24°	5.4	2	2.36″	1.00	0.00
08335367-4411069	$08^h\ 33^m\ 53.7^s$	-44°11′07.0″	262.60°	-2.40°	5.4	1	1.71″	1.00	0.00
08335734-4416570	$08^h\ 33^m\ 57.3^s$	-44°16′57.1″	262.69°	-2.45°	4.9	2	1.70″	1.00	0.00
08340037-4422520	$08^h\ 34^m\ 00.4^s$	-44°22′52.1″	262.77°	-2.50°	4.9	1	1.78″	1.00	0.00
08340207-4308527	$08^h\ 34^m\ 02.1^s$	-43°08′52.8″	261.78°	-1.76°	6.8	1	2.33″	0.80	-35.00
08340815-4306315	$08^h\ 34^m\ 08.2^s$	-43°06′31.6″	261.76°	-1.73°	6.8	2	2.08″	0.95	-2.00
08341028-4308385	$08^h\ 34^m\ 10.3^s$	-43°08′38.5″	261.80°	-1.74°	6.8	1	1.19″	1.00	0.00
08342246-4412258	$08^h\ 34^m\ 22.5^s$	-44°12′25.8″	262.67°	-2.35°	4.4	1	3.49″	0.30	18.40

Source ID.	R.A. (J2000)	Dec. (J2000)	l (deg)	b (deg)	A_V (mag)	Dup.	a (arcsec)	b/a	P.A. (deg)
08343025-4319234	$08^{h}\ 34^{m}\ 30.3^{s}$	-43°19′23.4″	261.98°	-1.80°	8.1	1	1.41″	1.00	0.00
08343336-4400595	$08^{h}\ 34^{m}\ 33.4^{s}$	-44°00′59.6″	262.54°	-2.21°	5.4	3	2.79″	1.00	0.00
08343352-4315134	$08^{h}\ 34^{m}\ 33.5^{s}$	-43°15′13.4″	261.93°	-1.75°	8.1	2	1.99″	1.00	0.00
08343448-4401413	$08^{h}\ 34^{m}\ 34.5^{s}$	-44°01′41.4″	262.55°	-2.21°	5.4	3	2.88″	0.93	0.00
08343553-4315062	$08^{h}\ 34^{m}\ 35.5^{s}$	-43°15′06.3″	261.93°	-1.74°	8.1	2	3.84″	0.73	-33.00
08343720-4312313	$08^{h}\ 34^{m}\ 37.2^{s}$	-43°12′31.3″	261.90°	-1.71°	8.1	1	3.02″	0.80	0.00
08344240-4344219	$08^{h}\ 34^{m}\ 42.4^{s}$	-43°44′21.9″	262.33°	-2.02°	7.7	1	2.37″	1.00	0.00
08344597-4343286	$08^{h}\ 34^{m}\ 46.0^{s}$	-43°43′28.7″	262.33°	-2.00°	7.7	2	1.79″	1.00	0.00
08344901-4336088	$08^{h}\ 34^{m}\ 49.0^{s}$	-43°36′08.9″	262.23°	-1.92°	7.7	1	1.74″	1.00	0.00
08345663-4342598	$08^{h}\ 34^{m}\ 56.6^{s}$	-43°42′59.9″	262.34°	-1.97°	7.7	2	4.98″	0.50	-64.00
08345818-4417405	$08^{h}\ 34^{m}\ 58.2^{s}$	-44°17′40.6″	262.80°	-2.31°	4.4	1	2.15″	1.00	0.00
08345950-4412324	$08^{h}\ 34^{m}\ 59.5^{s}$	-44°12′32.5″	262.74°	-2.26°	4.4	1	1.88″	1.00	0.00
08350621-4408427	$08^{h}\ 35^{m}\ 06.2^{s}$	-44°08′42.8″	262.70°	-2.20°	4.4	2	1.84″	1.00	0.00
08351161-4349115	$08^{h}\ 35^{m}\ 11.6^{s}$	-43°49′11.6″	262.45°	-2.00°	4.8	2	1.87″	0.95	0.00
08351239-4352315	$08^{h}\ 35^{m}\ 12.4^{s}$	-43°52′31.5″	262.49°	-2.03°	4.8	1	1.86″	1.00	0.00
08351987-4319395	$08^{h}\ 35^{m}\ 19.9^{s}$	-43°19′39.5″	262.07°	-1.68°	8.1	1	2.70″	1.00	0.00
08352055-4323524	$08^{h}\ 35^{m}\ 20.6^{s}$	-43°23′52.5″	262.13°	-1.72°	5.8	2	6.21″	0.70	85.00
08352353-4353005	$08^{h}\ 35^{m}\ 23.5^{s}$	-43°53′00.6″	262.52°	-2.01°	4.8	1	1.68″	1.00	0.00
08352471-4413522	$08^{h}\ 35^{m}\ 24.7^{s}$	-44°13′52.2″	262.80°	-2.21°	4.4	1	1.82″	1.00	0.00
08352526-4405133	$08^{h}\ 35^{m}\ 25.3^{s}$	-44°05′13.3″	262.69°	-2.12°	3.7	1	1.71″	1.00	0.00
08352557-4414586	$08^{h}\ 35^{m}\ 25.6^{s}$	-44°14′58.7″	262.82°	-2.22°	4.4	1	2.60″	0.50	8.00
08353854-4354504	$08^{h}\ 35^{m}\ 38.5^{s}$	-43°54′50.4″	262.57°	-1.99°	4.8	1	1.89″	1.00	0.00
08354278-4315390	$08^{h}\ 35^{m}\ 42.8^{s}$	-43°15′39.1″	262.06°	-1.59°	6.9	1	2.28″	1.00	0.00
08354649-4314252	$08^{h}\ 35^{m}\ 46.5^{s}$	-43°14′25.3″	262.05°	-1.56°	6.9	1	2.31″	1.00	0.00
08361668-4316273	$08^{h}\ 36^{m}\ 16.7^{s}$	-43°16′27.3″	262.13°	-1.51°	6.5	1	2.72″	1.00	0.00
08363176-4414557	$08^{h}\ 36^{m}\ 31.8^{s}$	-44°14′55.8″	262.94°	-2.06°	3.5	2	2.91″	1.00	0.00
08363197-4354598	$08^{h}\ 36^{m}\ 32.0^{s}$	-43°54′59.9″	262.67°	-1.86°	4.4	2	2.14″	0.95	75.00
08363692-4409267	$08^{h}\ 36^{m}\ 36.9^{s}$	-44°09′26.8″	262.87°	-1.99°	3.7	1	1.62″	1.00	0.00
08363724-4252009	$08^{h}\ 36^{m}\ 37.2^{s}$	-42°52′00.9″	261.84°	-1.22°	7.7	1	3.25″	1.00	0.00
08364352-4415037	$08^{h}\ 36^{m}\ 43.5^{s}$	-44°15′03.7″	262.96°	-2.04°	3.5	1	1.82″	1.00	0.00
08364505-4254413	$08^{h}\ 36^{m}\ 45.1^{s}$	-42°54′41.3″	261.89°	-1.22°	6.8	1	3.11″	1.00	0.00
08364578-4356324	$08^{h}\ 36^{m}\ 45.8^{s}$	-43°56′32.4″	262.72°	-1.84°	4.4	1	4.42″	1.00	0.00
08365320-4317070	$08^{h}\ 36^{m}\ 53.2^{s}$	-43°17′07.0″	262.21°	-1.43°	6.5	1	1.71″	1.00	0.00
08370074-4313449	$08^{h}\ 37^{m}\ 00.7^{s}$	-43°13′44.9″	262.17°	-1.38°	6.5	1	1.46″	1.00	0.00
08370155-4258441	$08^{h}\ 37^{m}\ 01.6^{s}$	-42°58′44.2″	261.98°	-1.22°	6.8	2	3.53″	0.80	-35.00
08370274-4314537	$08^{h}\ 37^{m}\ 02.7^{s}$	-43°14′53.7″	262.19°	-1.38°	6.5	1	2.57″	1.00	0.00
08370477-4314538	$08^{h}\ 37^{m}\ 04.8^{s}$	-43°14′53.8″	262.20°	-1.38°	6.5	1	1.40″	1.00	0.00
08372077-4312393	$08^{h}\ 37^{m}\ 20.8^{s}$	-43°12′39.3″	262.20°	-1.32°	6.7	1	2.80″	1.00	0.00
08372551-4357193	$08^{h}\ 37^{m}\ 25.5^{s}$	-43°57′19.4″	262.80°	-1.76°	4.4	1	3.15″	1.00	0.00
08372709-4343023	$08^{h}\ 37^{m}\ 27.1^{s}$	-43°43′02.4″	262.61°	-1.61°	5.9	1	4.02″	0.50	50.00
08373322-4357320	$08^{h}\ 37^{m}\ 33.2^{s}$	-43°57′32.0″	262.82°	-1.74°	4.4	1	2.06″	1.00	0.00
08380270-4356264	$08^{h}\ 38^{m}\ 02.7^{s}$	-43°56′26.4″	262.85°	-1.66°	4.4	1	2.50″	1.00	0.00
08381633-4300271	$08^{h}\ 38^{m}\ 16.3^{s}$	-43°00′27.1″	262.14°	-1.06°	7.0	1	2.51″	1.00	0.00
08381974-4410169	$08^{h}\ 38^{m}\ 19.7^{s}$	-44°10′17.0″	263.07°	-1.76°	4.2	1	2.71″	0.80	20.00
08382390-4305481	$08^{h}\ 38^{m}\ 23.9^{s}$	-43°05′48.2″	262.22°	-1.10°	7.0	3	2.80″	1.00	0.00
08382696-4410272	$08^{h}\ 38^{m}\ 27.0^{s}$	-44°10′27.3″	263.08°	-1.74°	4.2	2	2.72″	1.00	0.00
08382832-4404487	$08^{h}\ 38^{m}\ 28.3^{s}$	-44°04′48.7″	263.01°	-1.68°	4.2	1	2.81″	1.00	0.00
08384262-4306170	$08^{h}\ 38^{m}\ 42.6^{s}$	-43°06′17.1″	262.26°	-1.06°	7.0	1	2.69″	1.00	0.00
08384466-4313017	$08^{h}\ 38^{m}\ 44.7^{s}$	-43°13′01.8″	262.36°	-1.12°	7.0	1	2.96″	1.00	0.00
08384925-4422559	$08^{h}\ 38^{m}\ 49.3^{s}$	-44°22′56.0″	263.29°	-1.82°	4.2	1	2.86″	1.00	0.00
08385293-4329073	$08^{h}\ 38^{m}\ 52.9^{s}$	-43°29′07.3″	262.58°	-1.26°	6.0	1	3.10″	1.00	0.00

Source ID.	R.A. (J2000)	Dec. (J2000)	l (deg)	b (deg)	A_V (mag)	Dup.	a (arcsec)	b/a	P.A. (deg)
08390289-4402208	$08^{h}\ 39^{m}\ 02.9^{s}$	-44°02′20.8″	263.04°	-1.58°	4.3	2	3.26″	1.00	0.00
08390519-4417312	$08^{h}\ 39^{m}\ 05.2^{s}$	-44°17′31.3″	263.25°	-1.72°	4.2	2	2.88″	1.00	0.00
08390609-4318136	$08^{h}\ 39^{m}\ 06.1^{s}$	-43°18′13.6″	262.46°	-1.12°	6.0	1	2.51″	1.00	0.00
08390854-4414524	$08^{h}\ 39^{m}\ 08.5^{s}$	-44°14′52.4″	263.22°	-1.69°	4.2	2	5.04″	0.35	-45.00
08393042-4421369	$08^{h}\ 39^{m}\ 30.4^{s}$	-44°21′36.9″	263.35°	-1.71°	4.2	1	2.08″	1.00	0.00
08393781-4415575	$08^{h}\ 39^{m}\ 37.8^{s}$	-44°15′57.5″	263.29°	-1.63°	4.2	1	1.62″	1.00	0.00
08394651-4418210	$08^{h}\ 39^{m}\ 46.5^{s}$	-44°18′21.0″	263.33°	-1.63°	4.2	2	2.80″	1.00	0.00
08394797-4254294	$08^{h}\ 39^{m}\ 48.0^{s}$	-42°54′29.5″	262.23°	-0.78°	7.3	1	3.24″	1.00	0.00
08400624-4317209	$08^{h}\ 40^{m}\ 06.2^{s}$	-43°17′21.0″	262.56°	-0.97°	6.0	1	3.36″	0.40	-20.00
08400925-4356150	$08^{h}\ 40^{m}\ 09.2^{s}$	-43°56′15.0″	263.08°	-1.36°	5.6	1	2.21″	1.00	0.00
08401223-4316253	$08^{h}\ 40^{m}\ 12.2^{s}$	-43°16′25.3″	262.56°	-0.94°	6.0	1	2.95″	1.00	0.00
08401755-4304046	$08^{h}\ 40^{m}\ 17.6^{s}$	-43°04′04.7″	262.41°	-0.80°	6.2	1	2.21″	1.00	0.00
08403189-4353272	$08^{h}\ 40^{m}\ 31.9^{s}$	-43°53′27.3″	263.09°	-1.27°	5.6	1	2.98″	0.80	-30.00
08403380-4415328	$08^{h}\ 40^{m}\ 33.8^{s}$	-44°15′32.8″	263.38°	-1.49°	3.8	1	1.77″	1.00	0.00
08403861-4306033	$08^{h}\ 40^{m}\ 38.6^{s}$	-43°06′03.3″	262.48°	-0.77°	6.2	1	2.07″	1.00	0.00
08403928-4306556	$08^{h}\ 40^{m}\ 39.3^{s}$	-43°06′55.7″	262.49°	-0.78°	6.2	1	1.92″	1.00	0.00
08404011-4352482	$08^{h}\ 40^{m}\ 40.1^{s}$	-43°52′48.3″	263.09°	-1.25°	5.6	1	2.65″	1.00	0.00
08404068-4308031	$08^{h}\ 40^{m}\ 40.7^{s}$	-43°08′03.1″	262.51°	-0.79°	6.2	1	2.69″	1.00	0.00
08404071-4348314	$08^{h}\ 40^{m}\ 40.7^{s}$	-43°48′31.4″	263.04°	-1.20°	5.6	1	2.81″	1.00	0.00
08405239-4256385	$08^{h}\ 40^{m}\ 52.4^{s}$	-42°56′38.5″	262.38°	-0.64°	6.2	1	2.67″	1.00	0.00
08405586-4355567	$08^{h}\ 40^{m}\ 55.9^{s}$	-43°55′56.8″	263.16°	-1.24°	4.7	1	3.10″	1.00	0.00
08410139-4419484	$08^{h}\ 41^{m}\ 01.4^{s}$	-44°19′48.5″	263.49°	-1.47°	3.8	1	3.70″	0.30	31.00

The NIR for sources with NIR measurements only can be found in Table B.11 as follows:
Column 1: Source IRSF ID
Column 2, **Column 5**, **Column 8**: Flux density (mJy) for the J, H, K_s - raw measurements
Column 3, **Column 6**, **Column 9**: Integrated Magnitude (mag) no reddening correction applied; 5% calibration error included
Column 4, **Column 7**, **Column 10**: Integrated Magnitude (mag) - reddening-corrected; 5% calibration error included. The extinction corrected magnitudes have an error of ∼10% which is not accounted for.
Column 11: Photometric redshift

Table B.11: Rejected Sources - IRSF Measurements

	J			H			K_s			
Source ID.	f_ν (mJy)	Mag. (mag)	Mag. (mag)	f_ν (mJy)	Mag. (mag)	Mag. (mag)	f_ν (mJy)	Mag. (mag)	Mag. (mag)	Photo-z
08324175-4305544	0.030 ±0.518	19.30 ±18.75	17.54 ±18.75	0.091 ±0.119	17.63 ±1.42	16.48 ±1.42	0.194 ±0.102	16.34 ±0.57	15.60 ±0.57	0.2989
08324378-4403454	0.040 ±0.238	19.01 ±6.46	17.54 ±6.46	0.163 ±0.044	17.00 ±0.30	16.04 ±0.30	0.237 ±0.069	16.12 ±0.32	15.50 ±0.32	0.2781
08325424-4338324	0.039 ±0.207	19.02 ±5.76	17.15 ±5.76	0.135 ±0.064	17.20 ±0.52	15.98 ±0.52	0.173 ±0.100	16.46 ±0.63	15.68 ±0.63	0.1995
08325794-4322119	0.106 ±0.745	17.94 ±7.63	15.27 ±7.63	0.272 ±0.828	16.44 ±3.31	14.70 ±3.31	0.468 ±0.857	15.38 ±1.99	14.26 ±1.99	0.1425
08325910-4355398	0.045 ±0.150	18.87 ±3.62	17.16 ±3.62	0.139 ±0.052	17.17 ±0.41	16.06 ±0.41	0.192 ±0.070	16.35 ±0.40	15.64 ±0.40	0.2149
08330000-4408418	0.047 ±0.133	18.82 ±3.07	17.35 ±3.07	0.119 ±0.048	17.34 ±0.44	16.38 ±0.44	0.197 ±0.062	16.32 ±0.34	15.71 ±0.34	0.2557
08331118-4314238	0.030 ±0.206	19.30 ±7.46	16.63 ±7.46	0.125 ±0.049	17.28 ±0.43	15.55 ±0.43	0.297 ±0.052	15.88 ±0.20	14.76 ±0.20	0.2682
08332314-4330514	0.033 ±0.094	19.22 ±3.09	16.97 ±3.09	0.112 ±0.035	17.40 ±0.34	15.94 ±0.34	0.150 ±0.099	16.62 ±0.72	15.68 ±0.72	0.1826
08332567-4423297	0.094 ±0.115	18.08 ±1.33	16.75 ±1.33	0.179 ±0.060	16.90 ±0.37	16.03 ±0.37	0.271 ±0.086	15.98 ±0.35	15.42 ±0.35	0.1968
08332713-4422297	0.065 ±0.062	18.46 ±1.04	17.13 ±1.04	0.114 ±0.043	17.38 ±0.41	16.52 ±0.41	0.148 ±0.072	16.63 ±0.53	16.08 ±0.53	0.1609
08332985-4407595	0.059 ±0.066	18.59 ±1.22	17.11 ±1.22	0.126 ±0.273	17.27 ±2.35	16.32 ±2.35	0.201 ±0.186	16.30 ±1.01	15.68 ±1.01	0.2234
08333403-4416132	0.049 ±0.089	18.78 ±1.97	17.45 ±1.97	0.086 ±0.055	17.69 ±0.70	16.82 ±0.70	0.104 ±0.101	17.01 ±1.06	16.46 ±1.06	0.1519
08333669-4318390	0.023 ±0.474	19.60 ±22.38	16.93 ±22.38	0.093 ±0.090	17.60 ±1.05	15.87 ±1.05	0.314 ±0.269	15.82 ±0.93	14.70 ±0.93	0.2657
08333652-4346000	0.010 ±0.234	20.54 ±25.41	18.90 ±25.41	0.071 ±0.048	17.89 ±0.74	16.82 ±0.74	0.161 ±0.052	16.54 ±0.35	15.85 ±0.35	0.3087
08334275-4305557	0.023 ±0.151	19.61 ±7.13	17.77 ±7.13	0.083 ±0.053	17.73 ±0.69	16.53 ±0.69	0.135 ±0.079	16.73 ±0.64	15.96 ±0.64	0.2839
08334640-4313220	0.040 ±0.101	18.99 ±2.74	17.16 ±2.74	0.107 ±0.051	17.45 ±0.52	16.25 ±0.52	0.224 ±0.068	16.19 ±0.33	15.42 ±0.33	0.2858
08334722-4354599	0.026 ±0.119	19.46 ±4.97	17.81 ±4.97	0.089 ±0.048	17.65 ±0.59	16.58 ±0.59	0.150 ±0.093	16.62 ±0.68	15.93 ±0.68	0.2957
08335329-4419204	0.038 ±0.125	19.07 ±3.57	17.74 ±3.57	0.092 ±0.061	17.61 ±0.72	16.75 ±0.72	0.172 ±0.064	16.47 ±0.41	15.92 ±0.41	0.3002
08335357-4355107	0.083 ±0.222	18.20 ±2.90	16.75 ±2.90	0.200 ±0.087	16.77 ±0.47	15.82 ±0.47	0.371 ±0.201	15.64 ±0.59	15.03 ±0.59	0.2531
08335367-4411069	0.038 ±0.077	19.04 ±2.20	17.57 ±2.20	0.086 ±0.046	17.68 ±0.58	16.73 ±0.58	0.147 ±0.077	16.64 ±0.57	16.02 ±0.57	0.2583
08335734-4416570	0.034 ±0.536	19.16 ±17.12	17.83 ±17.12	0.148 ±0.176	17.10 ±1.29	16.23 ±1.29	0.293 ±0.110	15.89 ±0.41	15.34 ±0.41	0.2861
08340037-4422520	0.031 ±0.191	19.27 ±6.69	17.94 ±6.69	0.101 ±0.069	17.51 ±0.74	16.65 ±0.74	0.157 ±0.084	16.57 ±0.58	16.01 ±0.58	0.2930
08340207-4308527	0.028 ±0.140	19.38 ±5.43	17.55 ±5.43	0.082 ±0.056	17.74 ±0.74	16.55 ±0.74	0.156 ±0.106	16.58 ±0.74	15.81 ±0.74	0.2890
08340815-4306315	0.109 ±0.343	17.91 ±3.42	16.08 ±3.42	0.311 ±0.145	16.29 ±0.51	15.10 ±0.51	0.491 ±0.125	15.33 ±0.28	14.56 ±0.28	0.1953
08341028-4308385	0.023 ±0.077	19.58 ±3.63	17.74 ±3.63	0.063 ±0.039	18.04 ±0.67	16.84 ±0.67	0.122 ±0.064	16.84 ±0.57	16.07 ±0.57	0.2943
08342246-4412258	0.025 ±0.128	19.50 ±5.56	18.31 ±5.56	0.049 ±0.075	18.30 ±1.66	17.52 ±1.66	0.080 ±0.153	17.31 ±2.08	16.81 ±2.08	0.2721
08343025-4319234	0.025 ±0.082	19.51 ±3.56	17.31 ±3.56	0.064 ±0.037	18.00 ±0.63	16.58 ±0.63	0.172 ±0.040	16.47 ±0.26	15.55 ±0.26	0.2986
08343336-4400595	0.108 ±0.507	17.92 ±5.10	16.46 ±5.10	0.230 ±0.361	16.62 ±1.71	15.67 ±1.71	0.362 ±0.351	15.66 ±1.05	15.05 ±1.05	0.1991
08343352-4315134	0.069 ±0.042	18.41 ±0.66	16.21 ±0.66	0.177 ±0.220	16.91 ±1.35	15.48 ±1.35	0.221 ±0.334	16.20 ±1.64	15.28 ±1.64	0.1214
08343448-4401413	0.074 ±0.032	18.34 ±0.47	16.88 ±0.47	0.137 ±0.175	17.18 ±1.39	16.24 ±1.39	0.210 ±0.227	16.25 ±1.18	15.64 ±1.18	0.1935

Table B.11 continued...

	J			H			K_s			
Source ID.	f_ν (mJy)	Mag. (mag)	Mag. (mag)	f_ν (mJy)	Mag. (mag)	Mag. (mag)	f_ν (mJy)	Mag. (mag)	Mag. (mag)	Photo-z
08343553-4315062	0.087 ±0.203	18.16 ±2.53	15.96 ±2.53	0.213 ±0.219	16.70 ±1.12	15.28 ±1.12	0.269 ±0.401	15.98 ±1.62	15.06 ±1.62	0.1146
08343720-4312313	0.048 ±0.083	18.80 ±1.88	16.61 ±1.88	0.110 ±0.053	17.43 ±0.53	16.00 ±0.53	0.168 ±0.111	16.50 ±0.72	15.58 ±0.72	0.1666
08344240-4344219	0.036 ±0.119	19.12 ±3.59	17.04 ±3.59	0.172 ±0.050	16.94 ±0.32	15.58 ±0.32	0.283 ±0.055	15.93 ±0.22	15.06 ±0.22	0.2695
08344597-4343286	0.026 ±0.650	19.46 ±27.14	17.38 ±27.14	0.107 ±0.309	17.45 ±3.14	16.09 ±3.14	0.205 ±0.277	16.28 ±1.47	15.41 ±1.47	0.2923
08344901-4336088	0.024 ±0.148	19.56 ±6.70	17.47 ±6.70	0.081 ±0.043	17.75 ±0.58	16.40 ±0.58	0.192 ±0.057	16.35 ±0.33	15.48 ±0.33	0.2952
08345663-4342598	0.034 ±0.309	19.17 ±9.87	17.09 ±9.87	0.106 ±0.141	17.46 ±1.45	16.10 ±1.45	0.248 ±0.062	16.08 ±0.28	15.20 ±0.28	0.2839
08345818-4417405	0.066 ±0.080	18.45 ±1.32	17.25 ±1.32	0.157 ±0.048	17.04 ±0.34	16.26 ±0.34	0.217 ±0.071	16.22 ±0.36	15.72 ±0.36	0.2193
08345950-4412324	0.044 ±0.072	18.89 ±1.78	17.69 ±1.78	0.102 ±0.039	17.51 ±0.42	16.73 ±0.42	0.191 ±0.067	16.36 ±0.38	15.86 ±0.38	0.3004
08350621-4408427	0.039 ±0.219	19.02 ±6.10	17.82 ±6.10	0.095 ±0.313	17.58 ±3.58	16.80 ±3.58	0.151 ±0.152	16.61 ±1.09	16.11 ±1.09	0.2727
08351161-4349115	0.039 ±0.237	19.03 ±6.60	17.71 ±6.60	0.093 ±0.133	17.60 ±1.55	16.75 ±1.55	0.176 ±0.065	16.45 ±0.40	15.89 ±0.40	0.3012
08351239-4352315	0.058 ±0.116	18.59 ±2.17	17.28 ±2.17	0.122 ±0.052	17.31 ±0.47	16.45 ±0.47	0.164 ±0.084	16.52 ±0.56	15.97 ±0.56	0.1941
08351987-4319395	0.019 ±0.213	19.78 ±12.17	17.59 ±12.17	0.160 ±0.030	17.02 ±0.21	15.59 ±0.21	0.360 ±0.041	15.67 ±0.13	14.75 ±0.13	0.2657
08352055-4323524	0.248 ±0.485	17.02 ±2.12	15.43 ±2.12	0.609 ±0.395	15.56 ±0.71	14.53 ±0.71	0.890 ±0.396	14.69 ±0.49	14.02 ±0.49	0.1585
08352353-4353005	0.026 ±0.172	19.47 ±7.18	18.15 ±7.18	0.081 ±0.080	17.75 ±1.07	16.90 ±1.07	0.154 ±0.066	16.59 ±0.47	16.04 ±0.47	0.3151
08352471-4413522	0.042 ±0.083	18.94 ±2.15	17.75 ±2.15	0.107 ±0.035	17.45 ±0.36	16.68 ±0.36	0.145 ±0.086	16.66 ±0.65	16.16 ±0.65	0.2371
08352526-4405133	0.055 ±0.064	18.65 ±1.26	17.64 ±1.26	0.099 ±0.044	17.53 ±0.48	16.88 ±0.48	0.121 ±0.079	16.86 ±0.71	16.43 ±0.71	0.1661
08352557-4414586	0.023 ±0.140	19.61 ±6.61	18.41 ±6.61	0.077 ±0.053	17.81 ±0.75	17.03 ±0.75	0.107 ±0.106	16.98 ±1.08	16.48 ±1.08	0.2960
08353854-4354504	0.035 ±0.127	19.14 ±3.94	17.82 ±3.94	0.103 ±0.051	17.50 ±0.54	16.64 ±0.54	0.160 ±0.070	16.55 ±0.48	16.00 ±0.48	0.2796
08354278-4315390	0.031 ±0.095	19.27 ±3.33	17.39 ±3.33	0.102 ±0.051	17.51 ±0.55	16.28 ±0.55	0.218 ±0.055	16.21 ±0.28	15.42 ±0.28	0.2921
08354649-4314252	0.043 ±0.075	18.91 ±1.89	17.03 ±1.89	0.123 ±0.028	17.30 ±0.25	16.07 ±0.25	0.192 ±0.058	16.35 ±0.33	15.56 ±0.33	0.2203
08361668-4316273	0.036 ±0.114	19.10 ±3.44	17.33 ±3.44	0.106 ±0.049	17.46 ±0.50	16.31 ±0.50	0.283 ±0.053	15.93 ±0.21	15.19 ±0.21	0.2820
08363176-4414557	0.136 ±0.497	17.67 ±3.97	16.70 ±3.97	0.267 ±0.241	16.46 ±0.98	15.83 ±0.98	0.327 ±0.350	15.77 ±1.16	15.37 ±1.16	0.1567
08363197-4354598	0.048 ±0.191	18.80 ±4.32	17.60 ±4.32	0.125 ±0.212	17.29 ±1.84	16.50 ±1.84	0.174 ±0.128	16.46 ±0.80	15.95 ±0.80	0.2415
08363692-4409267	0.045 ±0.079	18.88 ±1.91	17.87 ±1.91	0.091 ±0.043	17.63 ±0.52	16.97 ±0.52	0.107 ±0.097	16.99 ±0.99	16.57 ±0.99	0.1763
08363724-4252009	0.037 ±0.236	19.10 ±6.92	16.99 ±6.92	0.129 ±0.064	17.25 ±0.54	15.88 ±0.54	0.213 ±0.106	16.24 ±0.54	15.36 ±0.54	0.2414
08364352-4415037	0.048 ±0.060	18.80 ±1.36	17.83 ±1.36	0.100 ±0.031	17.52 ±0.34	16.89 ±0.34	0.153 ±0.081	16.59 ±0.58	16.19 ±0.58	0.2471
08364505-4254413	0.061 ±0.089	18.54 ±1.58	16.70 ±1.58	0.149 ±0.053	17.09 ±0.39	15.90 ±0.39	0.210 ±0.091	16.26 ±0.47	15.48 ±0.47	0.1755
08364578-4356324	0.104 ±0.113	17.96 ±1.18	16.75 ±1.18	0.158 ±0.092	17.03 ±0.63	16.25 ±0.63	0.213 ±0.127	16.24 ±0.65	15.73 ±0.65	0.1528
08365320-4317070	0.038 ±0.064	19.04 ±1.83	17.27 ±1.83	0.093 ±0.034	17.61 ±0.40	16.46 ±0.40	0.147 ±0.066	16.64 ±0.49	15.90 ±0.49	0.2232
08370074-4313449	0.021 ±0.102	19.70 ±5.27	17.93 ±5.27	0.054 ±0.052	18.20 ±1.05	17.05 ±1.05	0.082 ±0.109	17.27 ±1.44	16.53 ±1.44	0.2400
08370155-4258441	0.105 ±0.379	17.95 ±3.92	16.11 ±3.92	0.246 ±0.038	16.55 ±0.17	15.35 ±0.17	0.436 ±0.065	15.46 ±0.17	14.69 ±0.17	0.2032
08370274-4314537	0.023 ±0.198	19.59 ±9.35	17.82 ±9.35	0.063 ±0.067	18.02 ±1.16	16.87 ±1.16	0.135 ±0.095	16.73 ±0.77	15.99 ±0.77	0.3149
08370477-4314538	0.024 ±0.077	19.56 ±3.48	17.79 ±3.48	0.072 ±0.027	17.88 ±0.41	16.73 ±0.41	0.132 ±0.051	16.76 ±0.42	16.02 ±0.42	0.2959
08372077-4312393	0.046 ±0.124	18.85 ±2.93	17.03 ±2.93	0.121 ±0.049	17.32 ±0.44	16.13 ±0.44	0.233 ±0.093	16.14 ±0.44	15.38 ±0.44	0.2632
08372551-4357193	0.035 ±0.255	19.16 ±7.91	17.95 ±7.91	0.143 ±0.061	17.13 ±0.47	16.35 ±0.47	0.196 ±0.102	16.33 ±0.57	15.83 ±0.57	0.2923

Table B.11 continued...

	J			*H*			K_s			
Source ID.	f_ν (mJy)	Mag. (mag)	Mag. (mag)	f_ν (mJy)	Mag. (mag)	Mag. (mag)	f_ν (mJy)	Mag. (mag)	Mag. (mag)	Photo-z
08372709-4343023	0.056 ±0.094	18.64 ±1.82	17.05 ±1.82	0.150 ±0.054	17.08 ±0.39	16.04 ±0.39	0.161 ±0.098	16.54 ±0.66	15.87 ±0.66	0.1446
08373322-4357320	0.040 ±0.126	19.00 ±3.42	17.79 ±3.42	0.102 ±0.049	17.50 ±0.52	16.71 ±0.52	0.189 ±0.073	16.37 ±0.42	15.86 ±0.42	0.3072
08380270-4356264	0.054 ±0.090	18.68 ±1.81	17.48 ±1.81	0.126 ±0.045	17.27 ±0.39	16.49 ±0.39	0.203 ±0.070	16.29 ±0.38	15.78 ±0.38	0.2603
08381633-4300271	0.030 ±0.153	19.30 ±5.54	17.41 ±5.54	0.098 ±0.063	17.55 ±0.70	16.32 ±0.70	0.196 ±0.060	16.33 ±0.34	15.54 ±0.34	0.2969
08381974-4410169	0.052 ±0.083	18.71 ±1.73	17.58 ±1.73	0.124 ±0.047	17.29 ±0.41	16.56 ±0.41	0.145 ±0.109	16.66 ±0.82	16.18 ±0.82	0.1924
08382390-4305481	0.047 ±0.343	18.83 ±7.92	16.93 ±7.92	0.140 ±0.101	17.16 ±0.79	15.93 ±0.79	0.266 ±0.028	16.00 ±0.13	15.20 ±0.13	0.2650
08382696-4410272	0.049 ±0.564	18.78 ±12.50	17.65 ±12.50	0.141 ±0.091	17.15 ±0.70	16.42 ±0.70	0.293 ±0.008	15.89 ±0.06	15.42 ±0.06	0.2887
08382832-4404487	0.012 ±0.447	20.28 ±40.44	19.15 ±40.44	0.058 ±0.100	18.11 ±1.87	17.37 ±1.87	0.200 ±0.082	16.31 ±0.45	15.84 ±0.45	0.3058
08384262-4306170	0.048 ±0.091	18.80 ±2.06	16.90 ±2.06	0.119 ±0.047	17.34 ±0.43	16.10 ±0.43	0.232 ±0.072	16.15 ±0.34	15.35 ±0.34	0.2522
08384466-4313017	0.041 ±0.114	18.97 ±3.02	17.07 ±3.02	0.098 ±0.048	17.55 ±0.53	16.32 ±0.53	0.210 ±0.077	16.26 ±0.40	15.46 ±0.40	0.2755
08384925-4422559	0.076 ±0.090	18.30 ±1.29	17.15 ±1.29	0.139 ±0.056	17.17 ±0.44	16.42 ±0.44	0.196 ±0.119	16.33 ±0.66	15.85 ±0.66	0.1965
08385293-4329073	0.084 ±0.066	18.20 ±0.85	16.57 ±0.85	0.158 ±0.054	17.03 ±0.37	15.96 ±0.37	0.239 ±0.089	16.11 ±0.41	15.43 ±0.41	0.1738
08390289-4402208	0.087 ±0.310	18.16 ±3.87	16.98 ±3.87	0.198 ±0.009	16.79 ±0.07	16.02 ±0.07	0.314 ±0.061	15.82 ±0.22	15.33 ±0.22	0.2369
08390519-4417312	0.070 ±0.209	18.40 ±3.24	17.24 ±3.24	0.150 ±0.081	17.09 ±0.59	16.33 ±0.59	0.283 ±0.016	15.93 ±0.08	15.45 ±0.08	0.2806
08390609-4318136	0.035 ±0.144	19.15 ±4.47	17.51 ±4.47	0.100 ±0.050	17.53 ±0.55	16.46 ±0.55	0.189 ±0.087	16.37 ±0.50	15.68 ±0.50	0.2949
08390854-4414524	0.086 ±0.411	18.16 ±5.19	17.01 ±5.19	0.190 ±0.265	16.83 ±1.51	16.08 ±1.51	0.285 ±0.104	15.92 ±0.40	15.44 ±0.40	0.2241
08393042-4421369	0.061 ±0.059	18.55 ±1.05	17.39 ±1.05	0.129 ±0.044	17.25 ±0.37	16.50 ±0.37	0.188 ±0.071	16.37 ±0.41	15.89 ±0.41	0.2279
08393781-4415575	0.047 ±0.070	18.83 ±1.62	17.68 ±1.62	0.085 ±0.046	17.70 ±0.59	16.95 ±0.59	0.142 ±0.082	16.68 ±0.63	16.19 ±0.63	0.2540
08394651-4418210	0.075 ±0.233	18.32 ±3.37	17.17 ±3.37	0.186 ±0.031	16.85 ±0.19	16.10 ±0.19	0.326 ±0.003	15.78 ±0.05	15.29 ±0.05	0.2745
08394797-4254294	0.044 ±0.186	18.89 ±4.59	16.91 ±4.59	0.163 ±0.069	17.00 ±0.46	15.71 ±0.46	0.276 ±0.109	15.96 ±0.43	15.13 ±0.43	0.2538
08400624-4317209	0.039 ±0.071	19.04 ±1.98	17.39 ±1.98	0.090 ±0.029	17.64 ±0.35	16.57 ±0.35	0.158 ±0.067	16.56 ±0.46	15.87 ±0.46	0.2543
08400925-4356150	0.044 ±0.094	18.89 ±2.32	17.37 ±2.32	0.105 ±0.048	17.47 ±0.50	16.48 ±0.50	0.179 ±0.072	16.43 ±0.44	15.79 ±0.44	0.2544
08401223-4316253	0.046 ±0.100	18.85 ±2.36	17.21 ±2.36	0.114 ±0.038	17.38 ±0.36	16.31 ±0.36	0.229 ±0.071	16.16 ±0.34	15.47 ±0.34	0.2822
08401755-4304046	0.018 ±0.191	19.88 ±11.52	18.19 ±11.52	0.068 ±0.058	17.94 ±0.93	16.84 ±0.93	0.121 ±0.094	16.85 ±0.84	16.15 ±0.84	0.3210
08403189-4353272	0.039 ±0.134	19.02 ±3.73	17.49 ±3.73	0.105 ±0.070	17.47 ±0.73	16.48 ±0.73	0.180 ±0.084	16.42 ±0.51	15.79 ±0.51	0.2698
08403380-4415328	0.038 ±0.115	19.04 ±3.29	18.00 ±3.29	0.092 ±0.052	17.61 ±0.62	16.93 ±0.62	0.179 ±0.058	16.43 ±0.35	15.99 ±0.35	0.3096
08403861-4306033	0.039 ±0.081	19.03 ±2.25	17.34 ±2.25	0.095 ±0.054	17.58 ±0.62	16.48 ±0.62	0.145 ±0.086	16.66 ±0.65	15.95 ±0.65	0.2211
08403928-4306556	0.027 ±0.106	19.43 ±4.26	17.74 ±4.26	0.063 ±0.058	18.03 ±1.00	16.93 ±1.00	0.133 ±0.074	16.75 ±0.61	16.04 ±0.61	0.3089
08404011-4352482	0.041 ±0.137	18.98 ±3.63	17.46 ±3.63	0.123 ±0.065	17.30 ±0.58	16.31 ±0.58	0.181 ±0.072	16.42 ±0.43	15.78 ±0.43	0.2465
08404068-4308031	0.037 ±0.121	19.10 ±3.55	17.41 ±3.55	0.077 ±0.073	17.81 ±1.03	16.71 ±1.03	0.118 ±0.126	16.88 ±1.16	16.17 ±1.16	0.2082
08404071-4348314	0.050 ±0.136	18.75 ±2.95	17.23 ±2.95	0.134 ±0.056	17.21 ±0.46	16.22 ±0.46	0.193 ±0.076	16.35 ±0.43	15.71 ±0.43	0.2217
08405239-4256385	0.034 ±0.144	19.19 ±4.60	17.50 ±4.60	0.126 ±0.034	17.27 ±0.30	16.17 ±0.30	0.255 ±0.049	16.04 ±0.21	15.34 ±0.21	0.2877
08405586-4355567	0.059 ±0.130	18.58 ±2.39	17.31 ±2.39	0.136 ±0.063	17.19 ±0.51	16.36 ±0.51	0.194 ±0.085	16.34 ±0.48	15.80 ±0.48	0.2218
08410139-4419484	0.037 ±0.198	19.08 ±5.81	18.04 ±5.81	0.087 ±0.081	17.68 ±1.01	17.00 ±1.01	0.256 ±0.051	16.04 ±0.22	15.60 ±0.22	0.2936

Appendix C

NIR Catalogue Postage Stamps

This Appendix contains NIR postage stamps of the sources in the NIR catalogue discussed in Chapter 6 . Source 141 is believed to be a H II region as is not shown. Stamps are arranged in decreasing K_s^0 magnitude. All images are $45'' \times 45''$ except where the galaxy is located near the edge of an image. These images are shown in Fig. C. The individual captions give the Source ID, l and b, the main caption gives the range in K_s^0 magnitude. Sources are at the centre of the image.

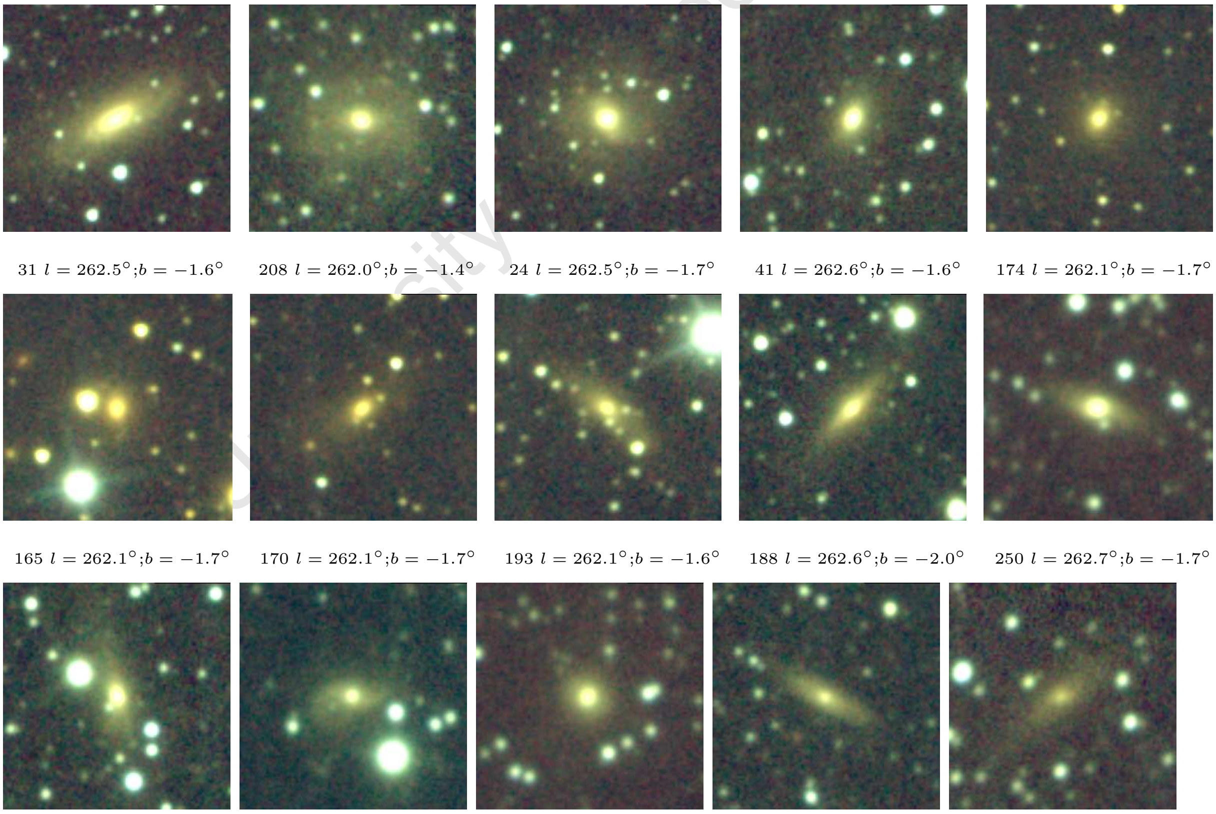

31 $l = 262.5^\circ; b = -1.6^\circ$ 208 $l = 262.0^\circ; b = -1.4^\circ$ 24 $l = 262.5^\circ; b = -1.7^\circ$ 41 $l = 262.6^\circ; b = -1.6^\circ$ 174 $l = 262.1^\circ; b = -1.7^\circ$

165 $l = 262.1^\circ; b = -1.7^\circ$ 170 $l = 262.1^\circ; b = -1.7^\circ$ 193 $l = 262.1^\circ; b = -1.6^\circ$ 188 $l = 262.6^\circ; b = -2.0^\circ$ 250 $l = 262.7^\circ; b = -1.7^\circ$

258 $l = 262.8^\circ; b = -1.7^\circ$ 322 $l = 263.1^\circ; b = -1.6^\circ$ 270 $l = 262.8^\circ; b = -1.7^\circ$ 327 $l = 263.1^\circ; b = -1.5^\circ$ 78 $l = 261.4^\circ; b = -1.8^\circ$

Figure C.1: K_s^0 magnitude from 10.27 –12.42 mag.

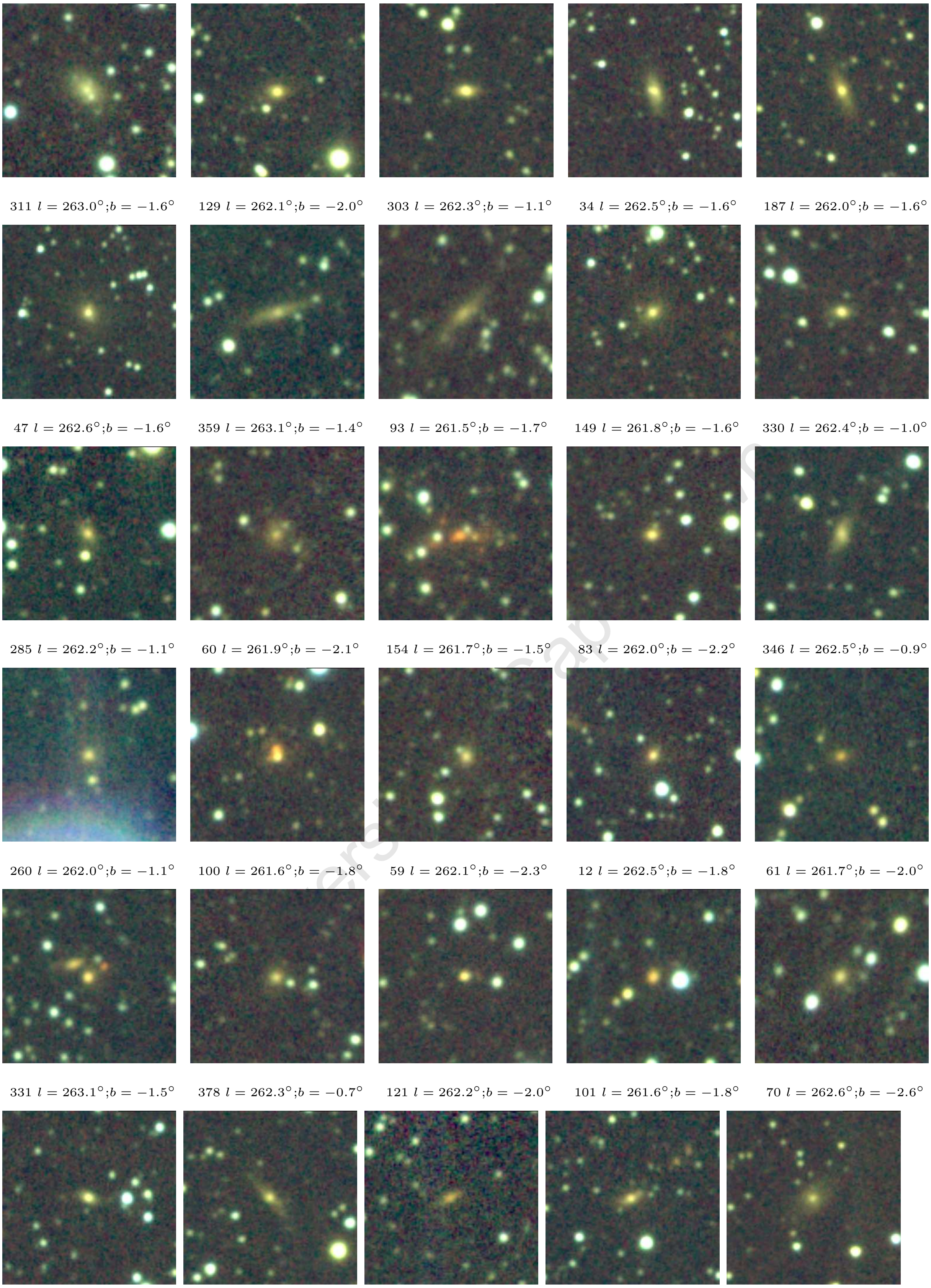

311 $l = 263.0^\circ; b = -1.6^\circ$ 129 $l = 262.1^\circ; b = -2.0^\circ$ 303 $l = 262.3^\circ; b = -1.1^\circ$ 34 $l = 262.5^\circ; b = -1.6^\circ$ 187 $l = 262.0^\circ; b = -1.6^\circ$

47 $l = 262.6^\circ; b = -1.6^\circ$ 359 $l = 263.1^\circ; b = -1.4^\circ$ 93 $l = 261.5^\circ; b = -1.7^\circ$ 149 $l = 261.8^\circ; b = -1.6^\circ$ 330 $l = 262.4^\circ; b = -1.0^\circ$

285 $l = 262.2^\circ; b = -1.1^\circ$ 60 $l = 261.9^\circ; b = -2.1^\circ$ 154 $l = 261.7^\circ; b = -1.5^\circ$ 83 $l = 262.0^\circ; b = -2.2^\circ$ 346 $l = 262.5^\circ; b = -0.9^\circ$

260 $l = 262.0^\circ; b = -1.1^\circ$ 100 $l = 261.6^\circ; b = -1.8^\circ$ 59 $l = 262.1^\circ; b = -2.3^\circ$ 12 $l = 262.5^\circ; b = -1.8^\circ$ 61 $l = 261.7^\circ; b = -2.0^\circ$

331 $l = 263.1^\circ; b = -1.5^\circ$ 378 $l = 262.3^\circ; b = -0.7^\circ$ 121 $l = 262.2^\circ; b = -2.0^\circ$ 101 $l = 261.6^\circ; b = -1.8^\circ$ 70 $l = 262.6^\circ; b = -2.6^\circ$

273 $l = 263.1^\circ; b = -1.9^\circ$ 254 $l = 262.1^\circ; b = -1.2^\circ$ 317 $l = 262.1^\circ; b = -0.9^\circ$ 160 $l = 262.7^\circ; b = -2.2^\circ$ 4 $l = 262.1^\circ; b = -1.6^\circ$

Figure C.2: K_s^0 magnitude from 12.64 – 13.68 mag.

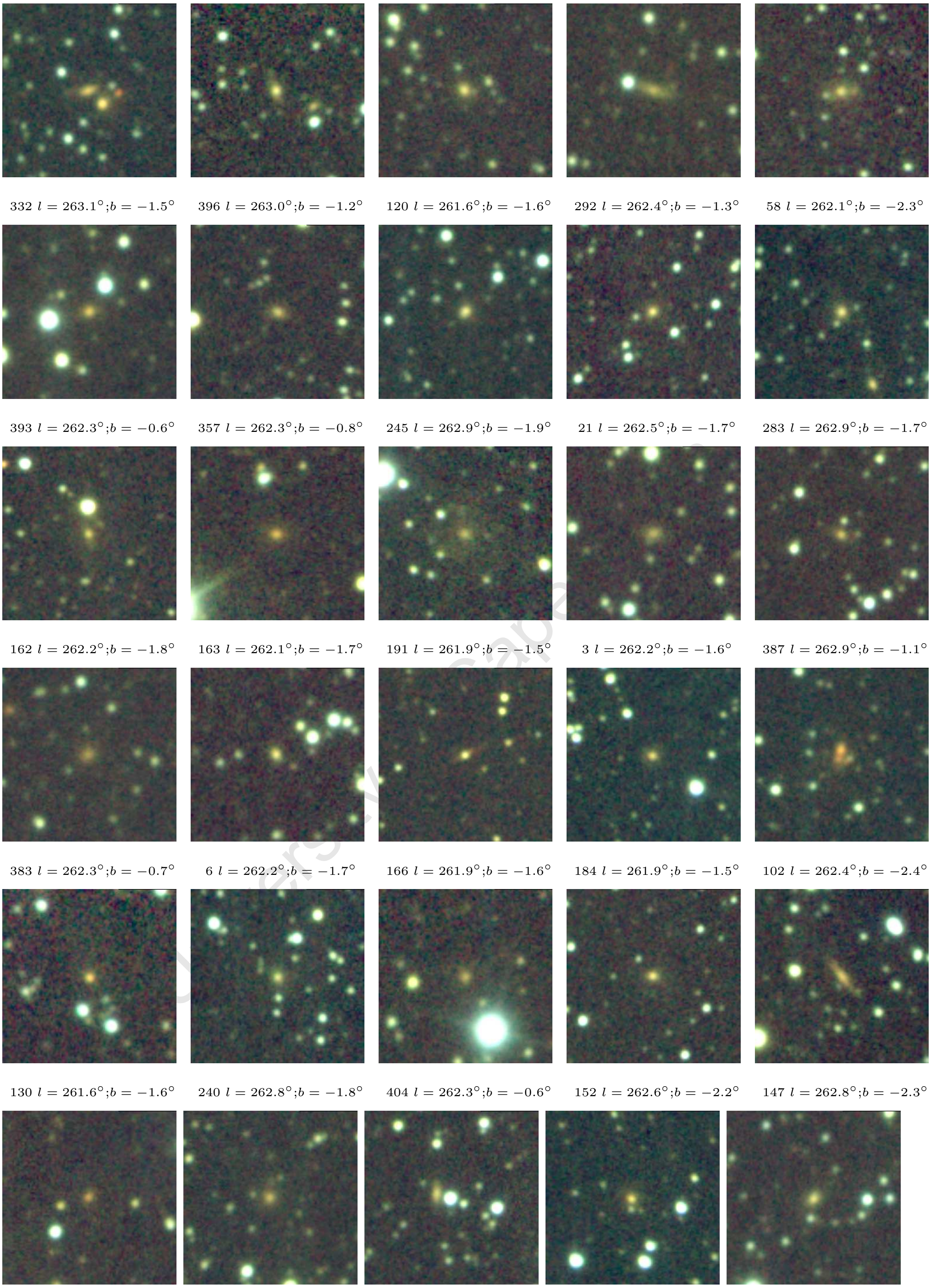

332 $l = 263.1^\circ; b = -1.5^\circ$ 396 $l = 263.0^\circ; b = -1.2^\circ$ 120 $l = 261.6^\circ; b = -1.6^\circ$ 292 $l = 262.4^\circ; b = -1.3^\circ$ 58 $l = 262.1^\circ; b = -2.3^\circ$

393 $l = 262.3^\circ; b = -0.6^\circ$ 357 $l = 262.3^\circ; b = -0.8^\circ$ 245 $l = 262.9^\circ; b = -1.9^\circ$ 21 $l = 262.5^\circ; b = -1.7^\circ$ 283 $l = 262.9^\circ; b = -1.7^\circ$

162 $l = 262.2^\circ; b = -1.8^\circ$ 163 $l = 262.1^\circ; b = -1.7^\circ$ 191 $l = 261.9^\circ; b = -1.5^\circ$ 3 $l = 262.2^\circ; b = -1.6^\circ$ 387 $l = 262.9^\circ; b = -1.1^\circ$

383 $l = 262.3^\circ; b = -0.7^\circ$ 6 $l = 262.2^\circ; b = -1.7^\circ$ 166 $l = 261.9^\circ; b = -1.6^\circ$ 184 $l = 261.9^\circ; b = -1.5^\circ$ 102 $l = 262.4^\circ; b = -2.4^\circ$

130 $l = 261.6^\circ; b = -1.6^\circ$ 240 $l = 262.8^\circ; b = -1.8^\circ$ 404 $l = 262.3^\circ; b = -0.6^\circ$ 152 $l = 262.6^\circ; b = -2.2^\circ$ 147 $l = 262.8^\circ; b = -2.3^\circ$

69 $l = 261.8^\circ; b = -2.1^\circ$ 366 $l = 262.3^\circ; b = -0.8^\circ$ 397 $l = 263.1^\circ; b = -1.2^\circ$ 173 $l = 261.9^\circ; b = -1.5^\circ$ 225 $l = 262.8^\circ; b = -1.9^\circ$

Figure C.3: K_s^0 magnitude from 13.70 – 14.10 mag.

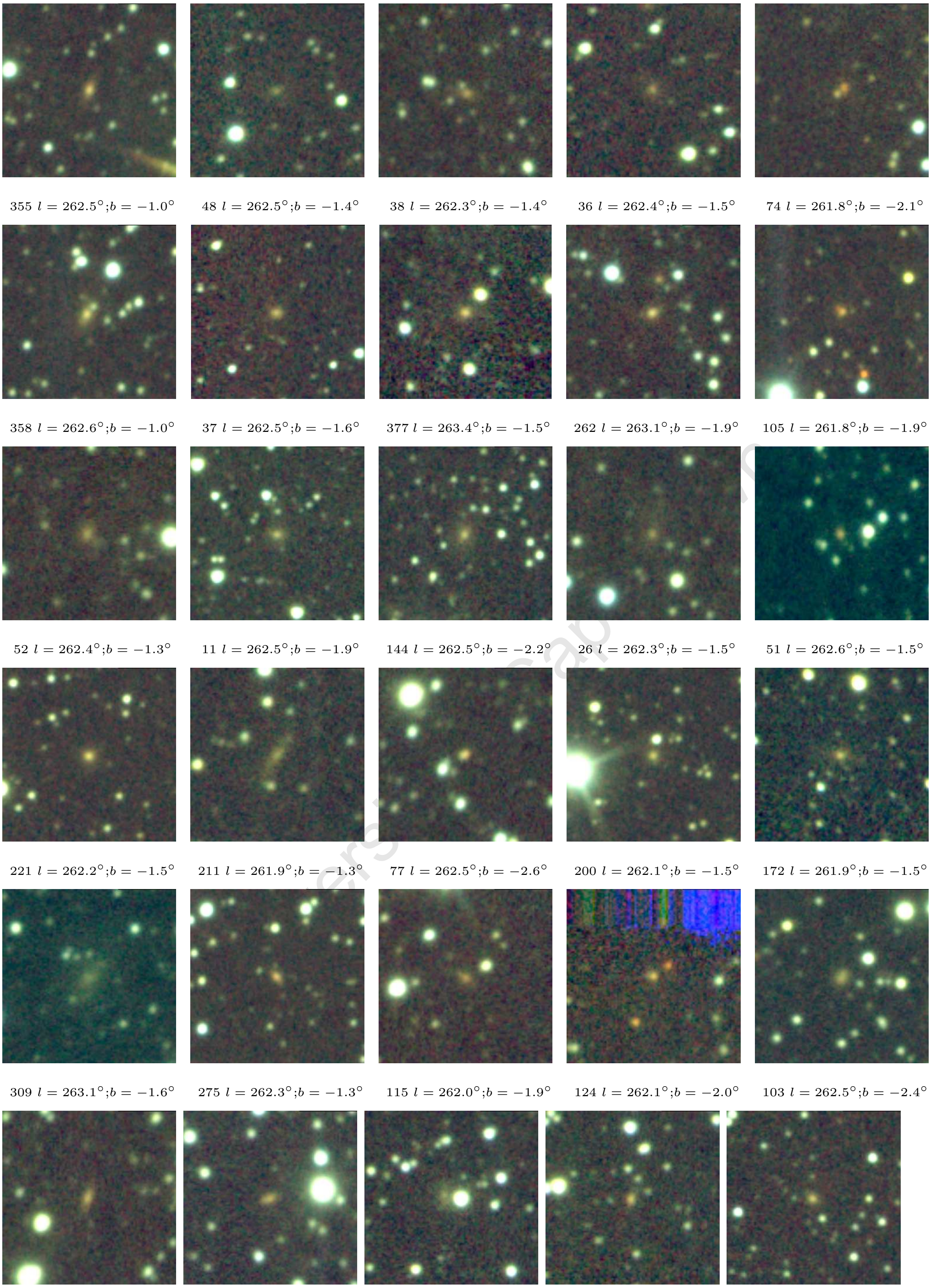

355 $l = 262.5^\circ$;$b = -1.0^\circ$ 48 $l = 262.5^\circ$;$b = -1.4^\circ$ 38 $l = 262.3^\circ$;$b = -1.4^\circ$ 36 $l = 262.4^\circ$;$b = -1.5^\circ$ 74 $l = 261.8^\circ$;$b = -2.1^\circ$

358 $l = 262.6^\circ$;$b = -1.0^\circ$ 37 $l = 262.5^\circ$;$b = -1.6^\circ$ 377 $l = 263.4^\circ$;$b = -1.5^\circ$ 262 $l = 263.1^\circ$;$b = -1.9^\circ$ 105 $l = 261.8^\circ$;$b = -1.9^\circ$

52 $l = 262.4^\circ$;$b = -1.3^\circ$ 11 $l = 262.5^\circ$;$b = -1.9^\circ$ 144 $l = 262.5^\circ$;$b = -2.2^\circ$ 26 $l = 262.3^\circ$;$b = -1.5^\circ$ 51 $l = 262.6^\circ$;$b = -1.5^\circ$

221 $l = 262.2^\circ$;$b = -1.5^\circ$ 211 $l = 261.9^\circ$;$b = -1.3^\circ$ 77 $l = 262.5^\circ$;$b = -2.6^\circ$ 200 $l = 262.1^\circ$;$b = -1.5^\circ$ 172 $l = 261.9^\circ$;$b = -1.5^\circ$

309 $l = 263.1^\circ$;$b = -1.6^\circ$ 275 $l = 262.3^\circ$;$b = -1.3^\circ$ 115 $l = 262.0^\circ$;$b = -1.9^\circ$ 124 $l = 262.1^\circ$;$b = -2.0^\circ$ 103 $l = 262.5^\circ$;$b = -2.4^\circ$

76 $l = 262.5^\circ$;$b = -2.6^\circ$ 10 $l = 262.2^\circ$;$b = -1.7^\circ$ 382 $l = 263.1^\circ$;$b = -1.3^\circ$ 241 $l = 262.1^\circ$;$b = -1.3^\circ$ 302 $l = 262.6^\circ$;$b = -1.3^\circ$

Figure C.4: K_s^0 magnitude from 14.11 – 14.33 mag.

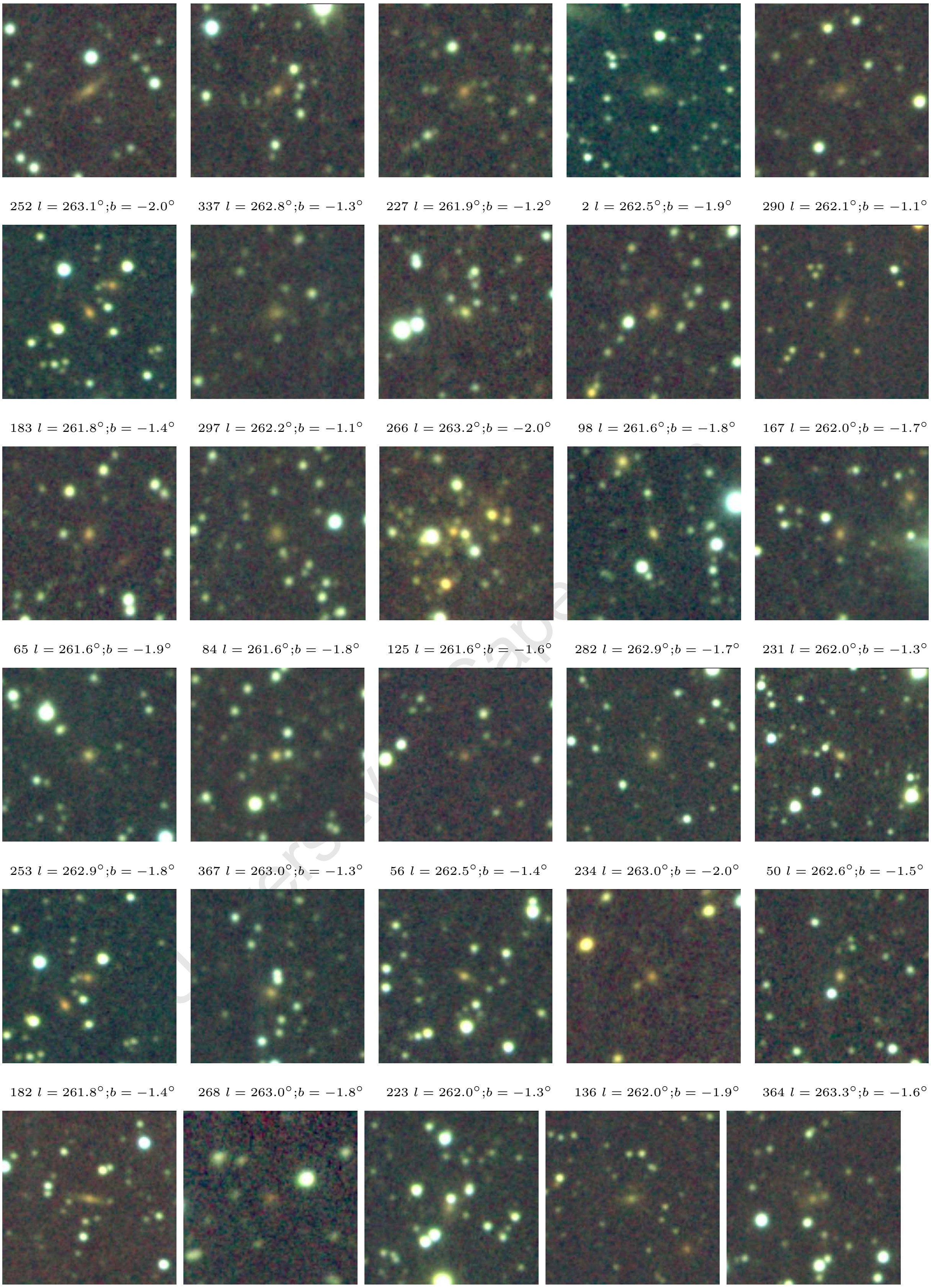

252 $l = 263.1^\circ; b = -2.0^\circ$ 337 $l = 262.8^\circ; b = -1.3^\circ$ 227 $l = 261.9^\circ; b = -1.2^\circ$ 2 $l = 262.5^\circ; b = -1.9^\circ$ 290 $l = 262.1^\circ; b = -1.1^\circ$

183 $l = 261.8^\circ; b = -1.4^\circ$ 297 $l = 262.2^\circ; b = -1.1^\circ$ 266 $l = 263.2^\circ; b = -2.0^\circ$ 98 $l = 261.6^\circ; b = -1.8^\circ$ 167 $l = 262.0^\circ; b = -1.7^\circ$

65 $l = 261.6^\circ; b = -1.9^\circ$ 84 $l = 261.6^\circ; b = -1.8^\circ$ 125 $l = 261.6^\circ; b = -1.6^\circ$ 282 $l = 262.9^\circ; b = -1.7^\circ$ 231 $l = 262.0^\circ; b = -1.3^\circ$

253 $l = 262.9^\circ; b = -1.8^\circ$ 367 $l = 263.0^\circ; b = -1.3^\circ$ 56 $l = 262.5^\circ; b = -1.4^\circ$ 234 $l = 263.0^\circ; b = -2.0^\circ$ 50 $l = 262.6^\circ; b = -1.5^\circ$

182 $l = 261.8^\circ; b = -1.4^\circ$ 268 $l = 263.0^\circ; b = -1.8^\circ$ 223 $l = 262.0^\circ; b = -1.3^\circ$ 136 $l = 262.0^\circ; b = -1.9^\circ$ 364 $l = 263.3^\circ; b = -1.6^\circ$

313 $l = 263.2^\circ; b = -1.7^\circ$ 204 $l = 261.8^\circ; b = -1.2^\circ$ 219 $l = 262.0^\circ; b = -1.3^\circ$ 189 $l = 262.1^\circ; b = -1.6^\circ$ 274 $l = 262.3^\circ; b = -1.3^\circ$

Figure C.5: K_s^0 magnitude from 14.35 – 14.57 mag.

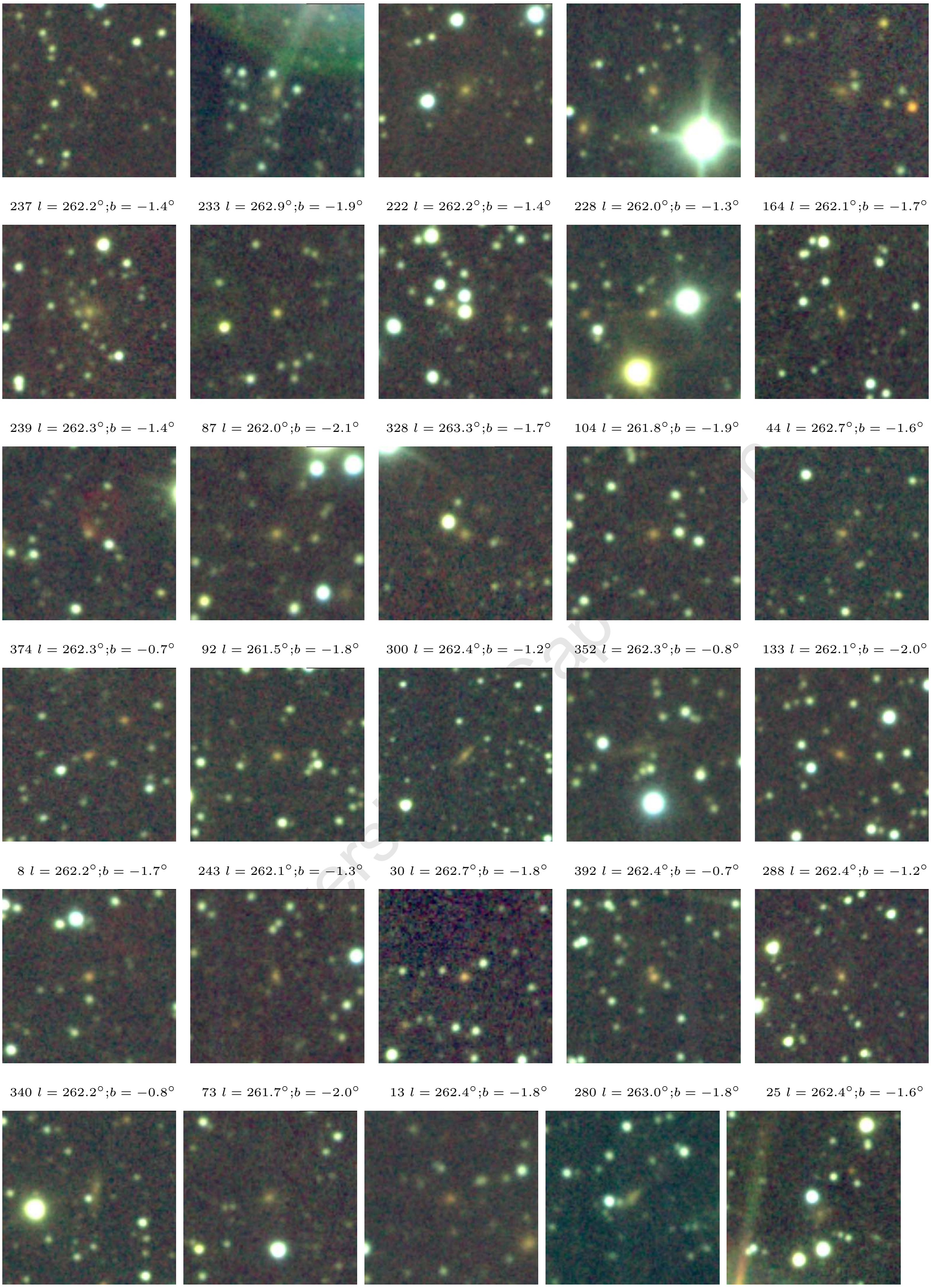

237 $l = 262.2^\circ; b = -1.4^\circ$ 233 $l = 262.9^\circ; b = -1.9^\circ$ 222 $l = 262.2^\circ; b = -1.4^\circ$ 228 $l = 262.0^\circ; b = -1.3^\circ$ 164 $l = 262.1^\circ; b = -1.7^\circ$

239 $l = 262.3^\circ; b = -1.4^\circ$ 87 $l = 262.0^\circ; b = -2.1^\circ$ 328 $l = 263.3^\circ; b = -1.7^\circ$ 104 $l = 261.8^\circ; b = -1.9^\circ$ 44 $l = 262.7^\circ; b = -1.6^\circ$

374 $l = 262.3^\circ; b = -0.7^\circ$ 92 $l = 261.5^\circ; b = -1.8^\circ$ 300 $l = 262.4^\circ; b = -1.2^\circ$ 352 $l = 262.3^\circ; b = -0.8^\circ$ 133 $l = 262.1^\circ; b = -2.0^\circ$

8 $l = 262.2^\circ; b = -1.7^\circ$ 243 $l = 262.1^\circ; b = -1.3^\circ$ 30 $l = 262.7^\circ; b = -1.8^\circ$ 392 $l = 262.4^\circ; b = -0.7^\circ$ 288 $l = 262.4^\circ; b = -1.2^\circ$

340 $l = 262.2^\circ; b = -0.8^\circ$ 73 $l = 261.7^\circ; b = -2.0^\circ$ 13 $l = 262.4^\circ; b = -1.8^\circ$ 280 $l = 263.0^\circ; b = -1.8^\circ$ 25 $l = 262.4^\circ; b = -1.6^\circ$

265 $l = 262.2^\circ; b = -1.2^\circ$ 68 $l = 262.0^\circ; b = -2.2^\circ$ 385 $l = 262.3^\circ; b = -0.7^\circ$ 203 $l = 262.7^\circ; b = -1.9^\circ$ 46 $l = 262.7^\circ; b = -1.6^\circ$

Figure C.6: K_s^0 magnitude from 14.58 – 14.72 mag.

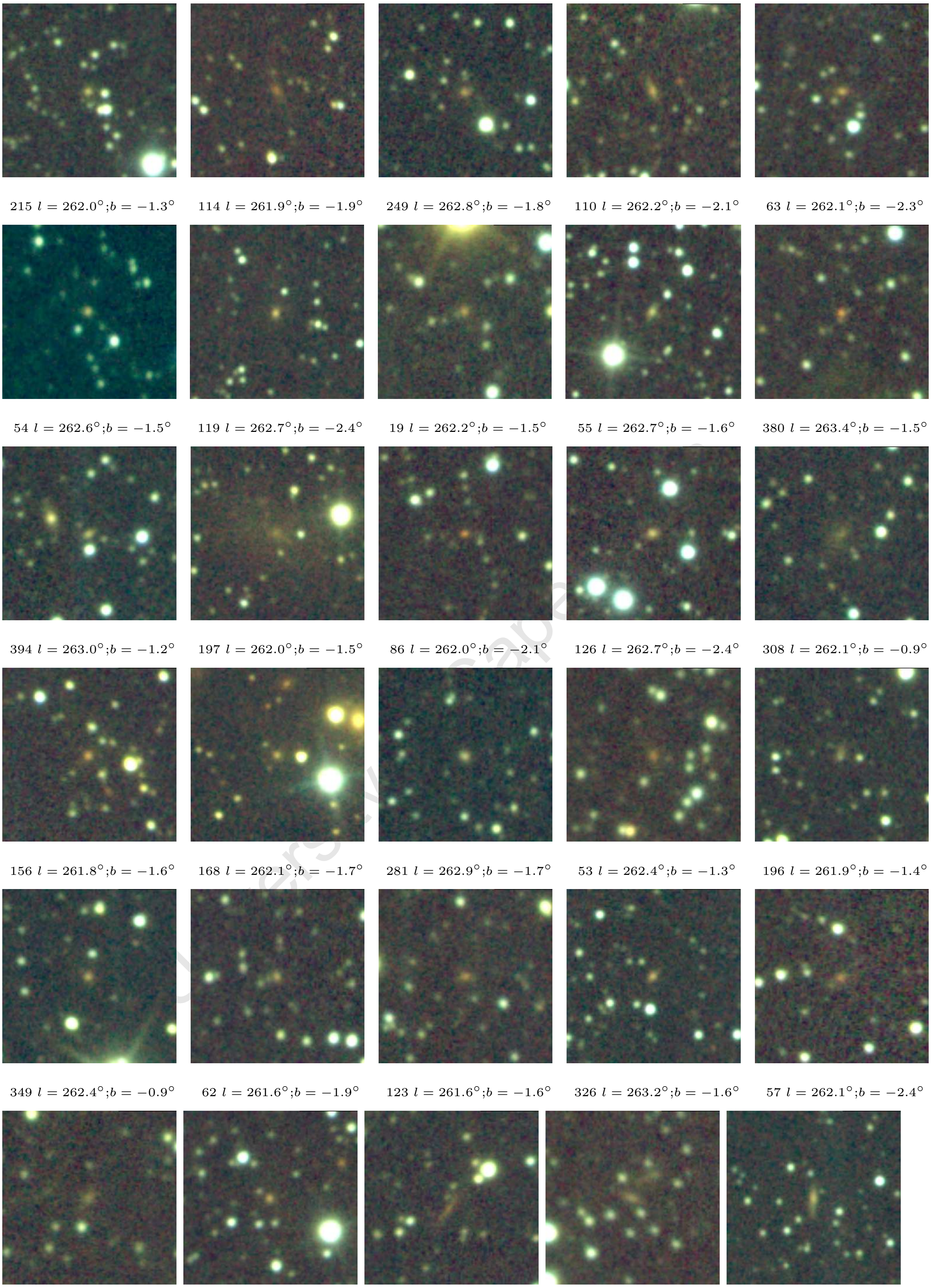

215 $l = 262.0^\circ; b = -1.3^\circ$
114 $l = 261.9^\circ; b = -1.9^\circ$
249 $l = 262.8^\circ; b = -1.8^\circ$
110 $l = 262.2^\circ; b = -2.1^\circ$
63 $l = 262.1^\circ; b = -2.3^\circ$

54 $l = 262.6^\circ; b = -1.5^\circ$
119 $l = 262.7^\circ; b = -2.4^\circ$
19 $l = 262.2^\circ; b = -1.5^\circ$
55 $l = 262.7^\circ; b = -1.6^\circ$
380 $l = 263.4^\circ; b = -1.5^\circ$

394 $l = 263.0^\circ; b = -1.2^\circ$
197 $l = 262.0^\circ; b = -1.5^\circ$
86 $l = 262.0^\circ; b = -2.1^\circ$
126 $l = 262.7^\circ; b = -2.4^\circ$
308 $l = 262.1^\circ; b = -0.9^\circ$

156 $l = 261.8^\circ; b = -1.6^\circ$
168 $l = 262.1^\circ; b = -1.7^\circ$
281 $l = 262.9^\circ; b = -1.7^\circ$
53 $l = 262.4^\circ; b = -1.3^\circ$
196 $l = 261.9^\circ; b = -1.4^\circ$

349 $l = 262.4^\circ; b = -0.9^\circ$
62 $l = 261.6^\circ; b = -1.9^\circ$
123 $l = 261.6^\circ; b = -1.6^\circ$
326 $l = 263.2^\circ; b = -1.6^\circ$
57 $l = 262.1^\circ; b = -2.4^\circ$

294 $l = 262.5^\circ; b = -1.3^\circ$
291 $l = 262.1^\circ; b = -1.1^\circ$
81 $l = 261.9^\circ; b = -2.1^\circ$
95 $l = 262.7^\circ; b = -2.6^\circ$
213 $l = 262.9^\circ; b = -2.0^\circ$

Figure C.7: K_s^0 magnitude from 14.73 – 14.85 mag.

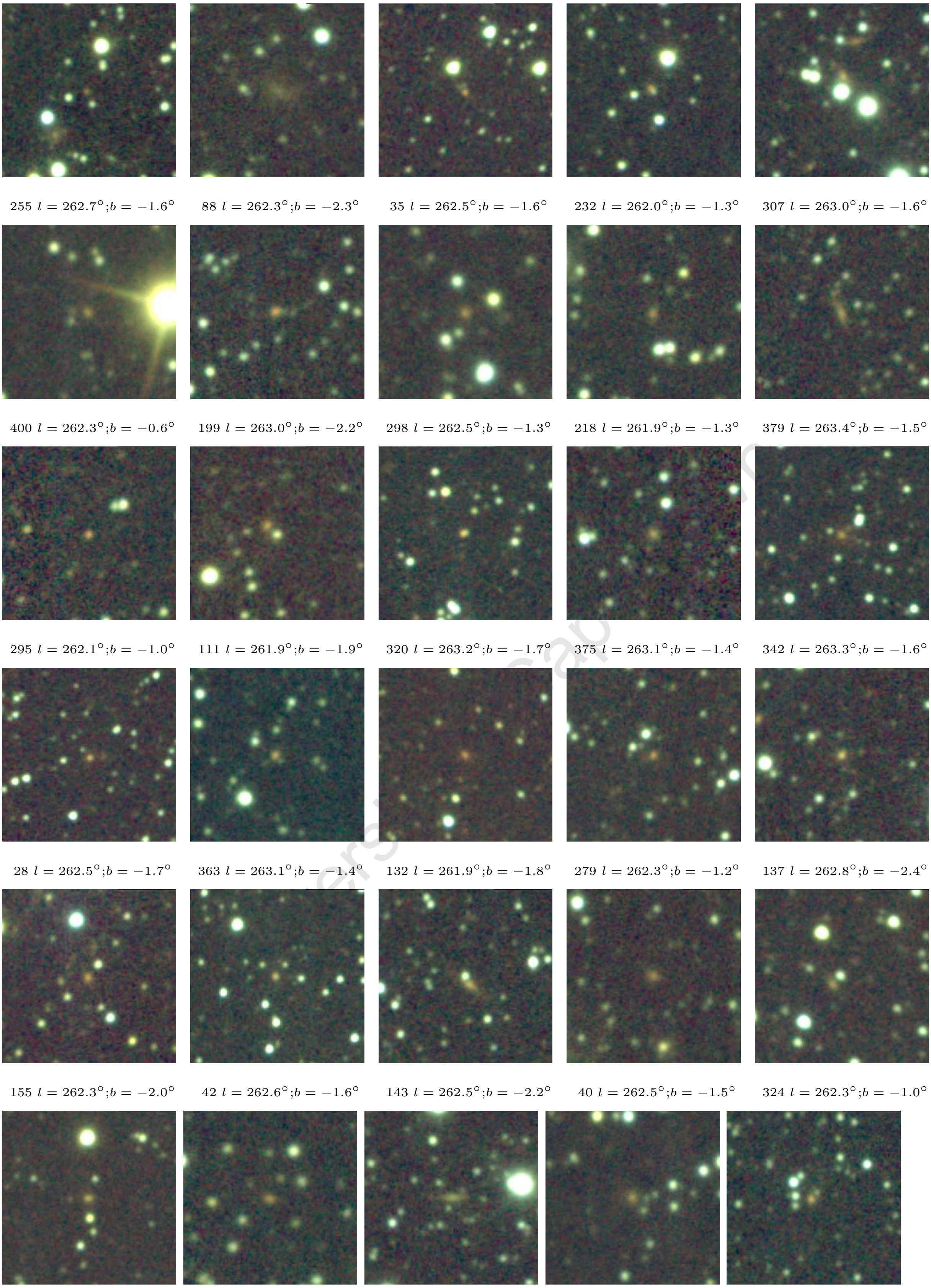

255 $l = 262.7^\circ$;$b = -1.6^\circ$ 88 $l = 262.3^\circ$;$b = -2.3^\circ$ 35 $l = 262.5^\circ$;$b = -1.6^\circ$ 232 $l = 262.0^\circ$;$b = -1.3^\circ$ 307 $l = 263.0^\circ$;$b = -1.6^\circ$

400 $l = 262.3^\circ$;$b = -0.6^\circ$ 199 $l = 263.0^\circ$;$b = -2.2^\circ$ 298 $l = 262.5^\circ$;$b = -1.3^\circ$ 218 $l = 261.9^\circ$;$b = -1.3^\circ$ 379 $l = 263.4^\circ$;$b = -1.5^\circ$

295 $l = 262.1^\circ$;$b = -1.0^\circ$ 111 $l = 261.9^\circ$;$b = -1.9^\circ$ 320 $l = 263.2^\circ$;$b = -1.7^\circ$ 375 $l = 263.1^\circ$;$b = -1.4^\circ$ 342 $l = 263.3^\circ$;$b = -1.6^\circ$

28 $l = 262.5^\circ$;$b = -1.7^\circ$ 363 $l = 263.1^\circ$;$b = -1.4^\circ$ 132 $l = 261.9^\circ$;$b = -1.8^\circ$ 279 $l = 262.3^\circ$;$b = -1.2^\circ$ 137 $l = 262.8^\circ$;$b = -2.4^\circ$

155 $l = 262.3^\circ$;$b = -2.0^\circ$ 42 $l = 262.6^\circ$;$b = -1.6^\circ$ 143 $l = 262.5^\circ$;$b = -2.2^\circ$ 40 $l = 262.5^\circ$;$b = -1.5^\circ$ 324 $l = 262.3^\circ$;$b = -1.0^\circ$

336 $l = 262.5^\circ$;$b = -1.1^\circ$ 207 $l = 261.9^\circ$;$b = -1.3^\circ$ 310 $l = 263.0^\circ$;$b = -1.6^\circ$ 354 $l = 263.2^\circ$;$b = -1.5^\circ$ 267 $l = 262.9^\circ$;$b = -1.7^\circ$

Figure C.8: K_s^0 magnitude from 14.85 – 14.97 mag.

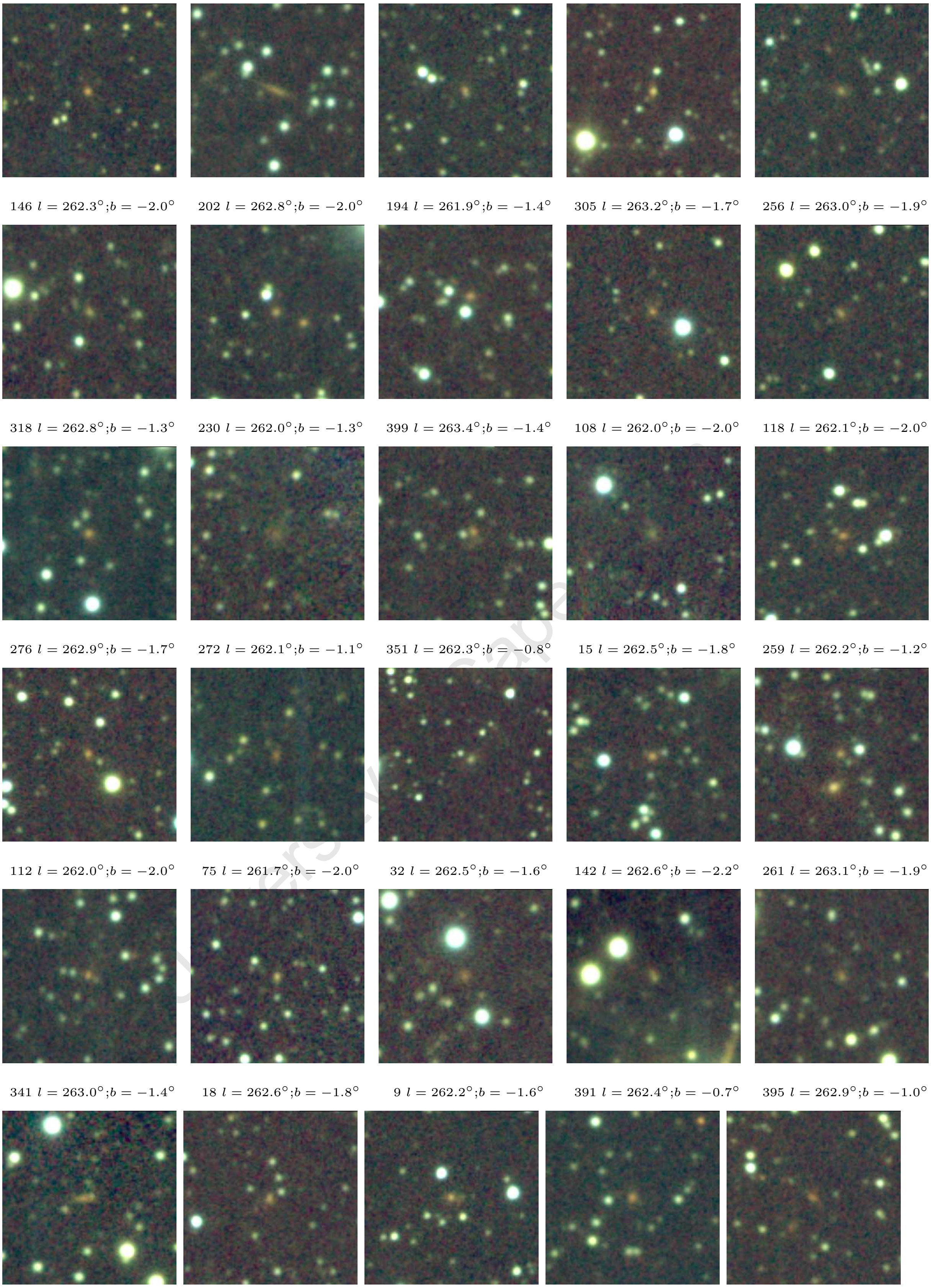

146 $l = 262.3^\circ; b = -2.0^\circ$ 202 $l = 262.8^\circ; b = -2.0^\circ$ 194 $l = 261.9^\circ; b = -1.4^\circ$ 305 $l = 263.2^\circ; b = -1.7^\circ$ 256 $l = 263.0^\circ; b = -1.9^\circ$

318 $l = 262.8^\circ; b = -1.3^\circ$ 230 $l = 262.0^\circ; b = -1.3^\circ$ 399 $l = 263.4^\circ; b = -1.4^\circ$ 108 $l = 262.0^\circ; b = -2.0^\circ$ 118 $l = 262.1^\circ; b = -2.0^\circ$

276 $l = 262.9^\circ; b = -1.7^\circ$ 272 $l = 262.1^\circ; b = -1.1^\circ$ 351 $l = 262.3^\circ; b = -0.8^\circ$ 15 $l = 262.5^\circ; b = -1.8^\circ$ 259 $l = 262.2^\circ; b = -1.2^\circ$

112 $l = 262.0^\circ; b = -2.0^\circ$ 75 $l = 261.7^\circ; b = -2.0^\circ$ 32 $l = 262.5^\circ; b = -1.6^\circ$ 142 $l = 262.6^\circ; b = -2.2^\circ$ 261 $l = 263.1^\circ; b = -1.9^\circ$

341 $l = 263.0^\circ; b = -1.4^\circ$ 18 $l = 262.6^\circ; b = -1.8^\circ$ 9 $l = 262.2^\circ; b = -1.6^\circ$ 391 $l = 262.4^\circ; b = -0.7^\circ$ 395 $l = 262.9^\circ; b = -1.0^\circ$

113 $l = 261.7^\circ; b = -1.8^\circ$ 171 $l = 262.4^\circ; b = -2.0^\circ$ 148 $l = 262.5^\circ; b = -2.2^\circ$ 106 $l = 262.5^\circ; b = -2.4^\circ$ 214 $l = 262.1^\circ; b = -1.4^\circ$

Figure C.9: K_s^0 magnitude from 14.97 – 15.10 mag.

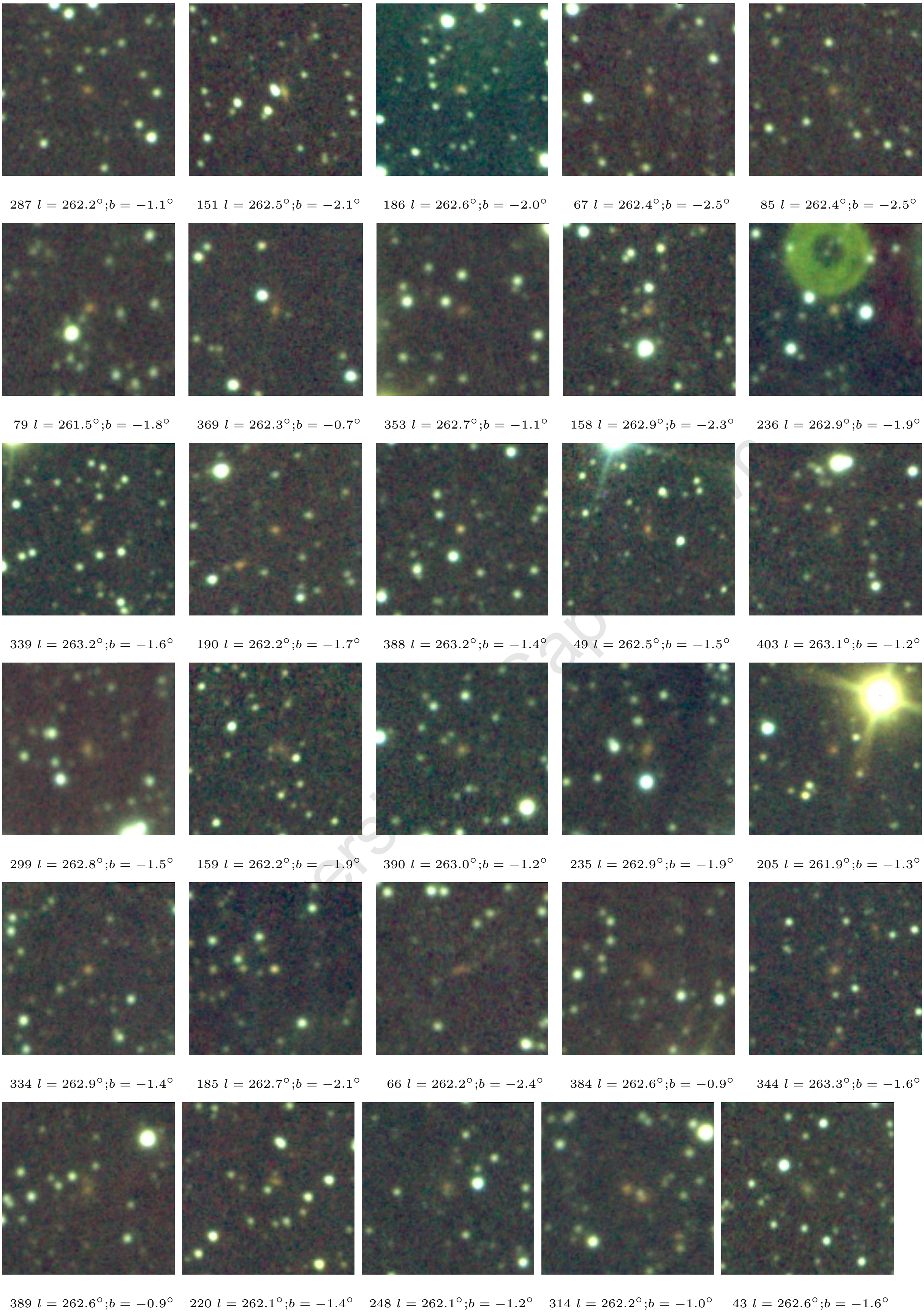

287 $l = 262.2^\circ; b = -1.1^\circ$ 151 $l = 262.5^\circ; b = -2.1^\circ$ 186 $l = 262.6^\circ; b = -2.0^\circ$ 67 $l = 262.4^\circ; b = -2.5^\circ$ 85 $l = 262.4^\circ; b = -2.5^\circ$

79 $l = 261.5^\circ; b = -1.8^\circ$ 369 $l = 262.3^\circ; b = -0.7^\circ$ 353 $l = 262.7^\circ; b = -1.1^\circ$ 158 $l = 262.9^\circ; b = -2.3^\circ$ 236 $l = 262.9^\circ; b = -1.9^\circ$

339 $l = 263.2^\circ; b = -1.6^\circ$ 190 $l = 262.2^\circ; b = -1.7^\circ$ 388 $l = 263.2^\circ; b = -1.4^\circ$ 49 $l = 262.5^\circ; b = -1.5^\circ$ 403 $l = 263.1^\circ; b = -1.2^\circ$

299 $l = 262.8^\circ; b = -1.5^\circ$ 159 $l = 262.2^\circ; b = -1.9^\circ$ 390 $l = 263.0^\circ; b = -1.2^\circ$ 235 $l = 262.9^\circ; b = -1.9^\circ$ 205 $l = 261.9^\circ; b = -1.3^\circ$

334 $l = 262.9^\circ; b = -1.4^\circ$ 185 $l = 262.7^\circ; b = -2.1^\circ$ 66 $l = 262.2^\circ; b = -2.4^\circ$ 384 $l = 262.6^\circ; b = -0.9^\circ$ 344 $l = 263.3^\circ; b = -1.6^\circ$

389 $l = 262.6^\circ; b = -0.9^\circ$ 220 $l = 262.1^\circ; b = -1.4^\circ$ 248 $l = 262.1^\circ; b = -1.2^\circ$ 314 $l = 262.2^\circ; b = -1.0^\circ$ 43 $l = 262.6^\circ; b = -1.6^\circ$

Figure C.10: K_s^0 magnitude from 15.10 – 15.22 mag.

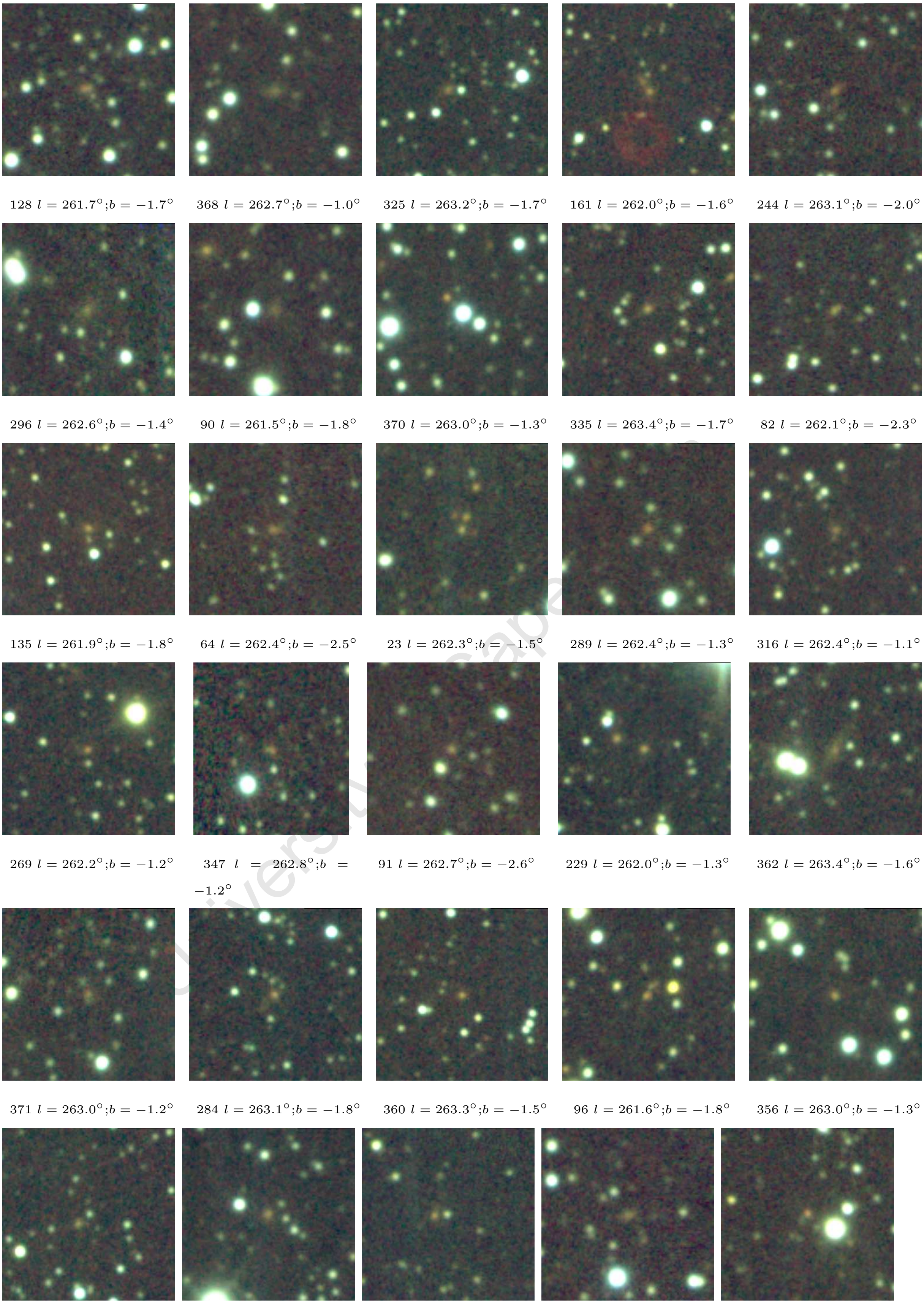

128 $l = 261.7^\circ; b = -1.7^\circ$ 368 $l = 262.7^\circ; b = -1.0^\circ$ 325 $l = 263.2^\circ; b = -1.7^\circ$ 161 $l = 262.0^\circ; b = -1.6^\circ$ 244 $l = 263.1^\circ; b = -2.0^\circ$

296 $l = 262.6^\circ; b = -1.4^\circ$ 90 $l = 261.5^\circ; b = -1.8^\circ$ 370 $l = 263.0^\circ; b = -1.3^\circ$ 335 $l = 263.4^\circ; b = -1.7^\circ$ 82 $l = 262.1^\circ; b = -2.3^\circ$

135 $l = 261.9^\circ; b = -1.8^\circ$ 64 $l = 262.4^\circ; b = -2.5^\circ$ 23 $l = 262.3^\circ; b = -1.5^\circ$ 289 $l = 262.4^\circ; b = -1.3^\circ$ 316 $l = 262.4^\circ; b = -1.1^\circ$

269 $l = 262.2^\circ; b = -1.2^\circ$ 347 $l = 262.8^\circ; b = -1.2^\circ$ 91 $l = 262.7^\circ; b = -2.6^\circ$ 229 $l = 262.0^\circ; b = -1.3^\circ$ 362 $l = 263.4^\circ; b = -1.6^\circ$

371 $l = 263.0^\circ; b = -1.2^\circ$ 284 $l = 263.1^\circ; b = -1.8^\circ$ 360 $l = 263.3^\circ; b = -1.5^\circ$ 96 $l = 261.6^\circ; b = -1.8^\circ$ 356 $l = 263.0^\circ; b = -1.3^\circ$

257 $l = 263.0^\circ; b = -1.9^\circ$ 175 $l = 262.7^\circ; b = -2.1^\circ$ 251 $l = 262.1^\circ; b = -1.2^\circ$ 5 $l = 262.2^\circ; b = -1.7^\circ$ 386 $l = 263.4^\circ; b = -1.5^\circ$

Figure C.11: K_s^0 magnitude from 15.23 – 15.34 mag.

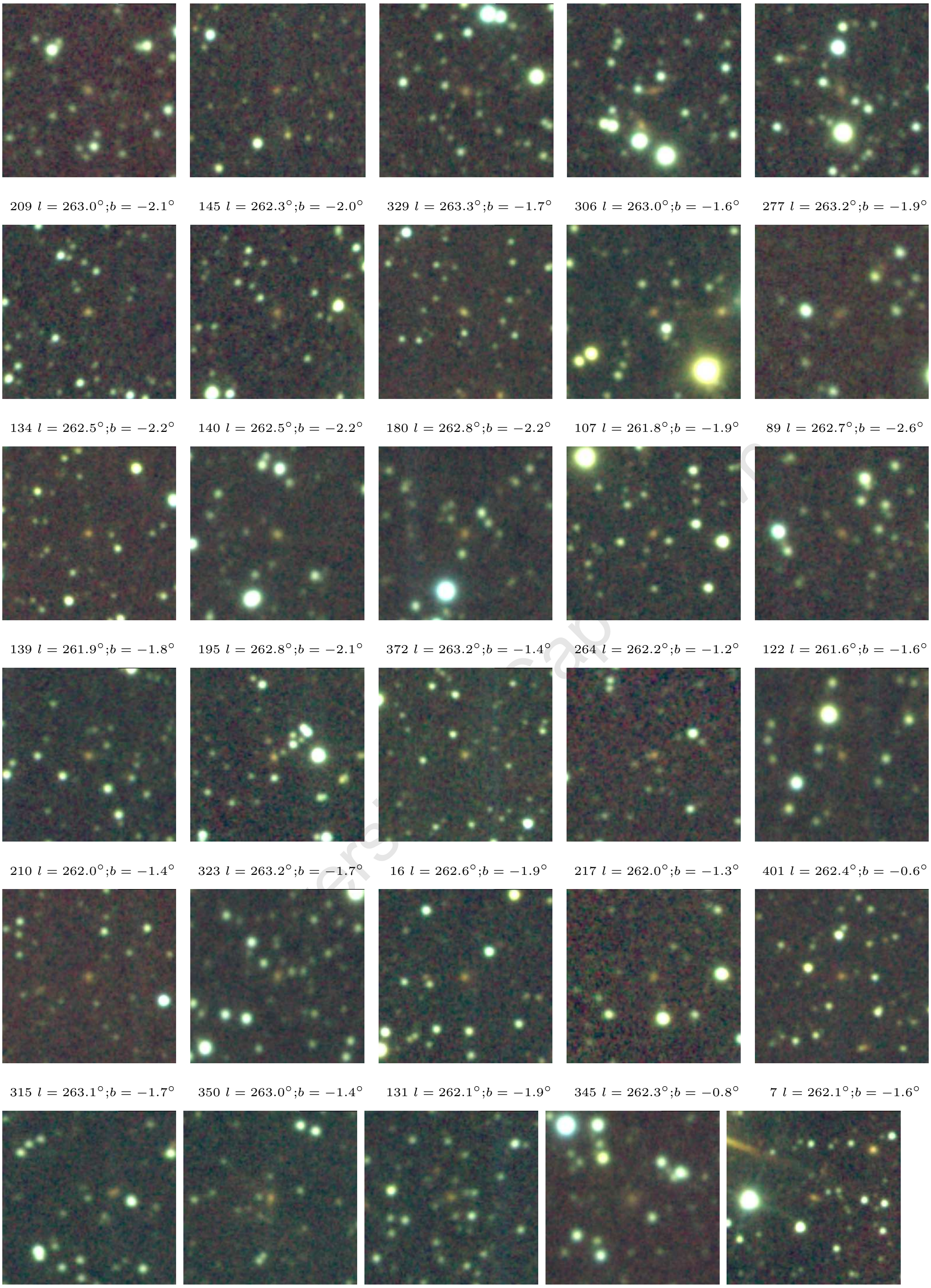

209 $l = 263.0^\circ; b = -2.1^\circ$
145 $l = 262.3^\circ; b = -2.0^\circ$
329 $l = 263.3^\circ; b = -1.7^\circ$
306 $l = 263.0^\circ; b = -1.6^\circ$
277 $l = 263.2^\circ; b = -1.9^\circ$

134 $l = 262.5^\circ; b = -2.2^\circ$
140 $l = 262.5^\circ; b = -2.2^\circ$
180 $l = 262.8^\circ; b = -2.2^\circ$
107 $l = 261.8^\circ; b = -1.9^\circ$
89 $l = 262.7^\circ; b = -2.6^\circ$

139 $l = 261.9^\circ; b = -1.8^\circ$
195 $l = 262.8^\circ; b = -2.1^\circ$
372 $l = 263.2^\circ; b = -1.4^\circ$
264 $l = 262.2^\circ; b = -1.2^\circ$
122 $l = 261.6^\circ; b = -1.6^\circ$

210 $l = 262.0^\circ; b = -1.4^\circ$
323 $l = 263.2^\circ; b = -1.7^\circ$
16 $l = 262.6^\circ; b = -1.9^\circ$
217 $l = 262.0^\circ; b = -1.3^\circ$
401 $l = 262.4^\circ; b = -0.6^\circ$

315 $l = 263.1^\circ; b = -1.7^\circ$
350 $l = 263.0^\circ; b = -1.4^\circ$
131 $l = 262.1^\circ; b = -1.9^\circ$
345 $l = 262.3^\circ; b = -0.8^\circ$
7 $l = 262.1^\circ; b = -1.6^\circ$

348 $l = 262.4^\circ; b = -0.9^\circ$
109 $l = 262.5^\circ; b = -2.4^\circ$
381 $l = 263.0^\circ; b = -1.2^\circ$
45 $l = 262.7^\circ; b = -1.7^\circ$
14 $l = 262.4^\circ; b = -1.8^\circ$

Figure C.12: K_s^0 magnitude from 15.34 – 15.43 mag.

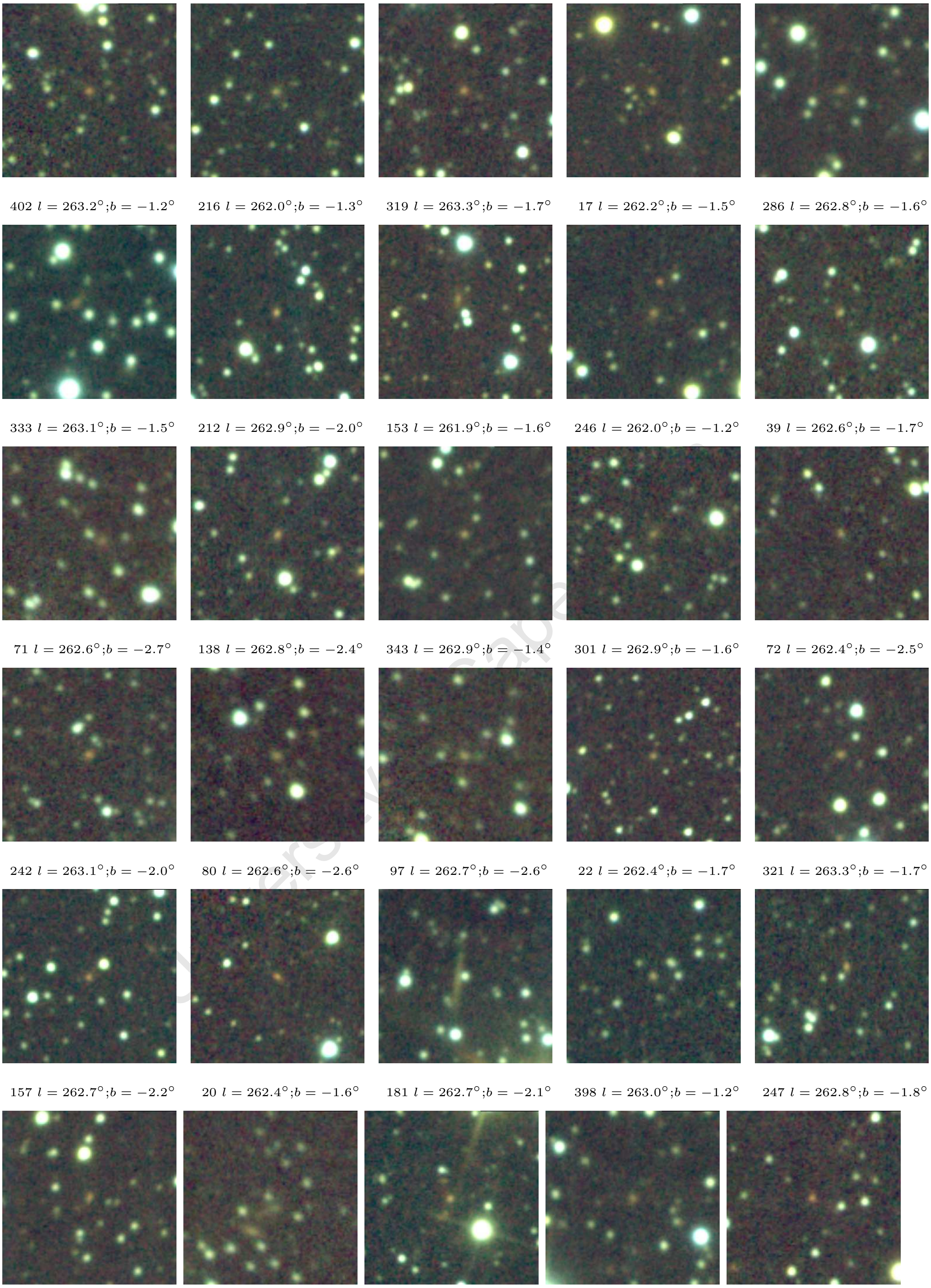

402 $l = 263.2^\circ; b = -1.2^\circ$ 216 $l = 262.0^\circ; b = -1.3^\circ$ 319 $l = 263.3^\circ; b = -1.7^\circ$ 17 $l = 262.2^\circ; b = -1.5^\circ$ 286 $l = 262.8^\circ; b = -1.6^\circ$

333 $l = 263.1^\circ; b = -1.5^\circ$ 212 $l = 262.9^\circ; b = -2.0^\circ$ 153 $l = 261.9^\circ; b = -1.6^\circ$ 246 $l = 262.0^\circ; b = -1.2^\circ$ 39 $l = 262.6^\circ; b = -1.7^\circ$

71 $l = 262.6^\circ; b = -2.7^\circ$ 138 $l = 262.8^\circ; b = -2.4^\circ$ 343 $l = 262.9^\circ; b = -1.4^\circ$ 301 $l = 262.9^\circ; b = -1.6^\circ$ 72 $l = 262.4^\circ; b = -2.5^\circ$

242 $l = 263.1^\circ; b = -2.0^\circ$ 80 $l = 262.6^\circ; b = -2.6^\circ$ 97 $l = 262.7^\circ; b = -2.6^\circ$ 22 $l = 262.4^\circ; b = -1.7^\circ$ 321 $l = 263.3^\circ; b = -1.7^\circ$

157 $l = 262.7^\circ; b = -2.2^\circ$ 20 $l = 262.4^\circ; b = -1.6^\circ$ 181 $l = 262.7^\circ; b = -2.1^\circ$ 398 $l = 263.0^\circ; b = -1.2^\circ$ 247 $l = 262.8^\circ; b = -1.8^\circ$

373 $l = 262.5^\circ; b = -0.9^\circ$ 94 $l = 262.7^\circ; b = -2.6^\circ$ 238 $l = 263.0^\circ; b = -1.9^\circ$ 361 $l = 263.2^\circ; b = -1.5^\circ$ 116 $l = 262.3^\circ; b = -2.1^\circ$

Figure C.13: K_s^0 magnitude from 15.43 – 15.62 mag.

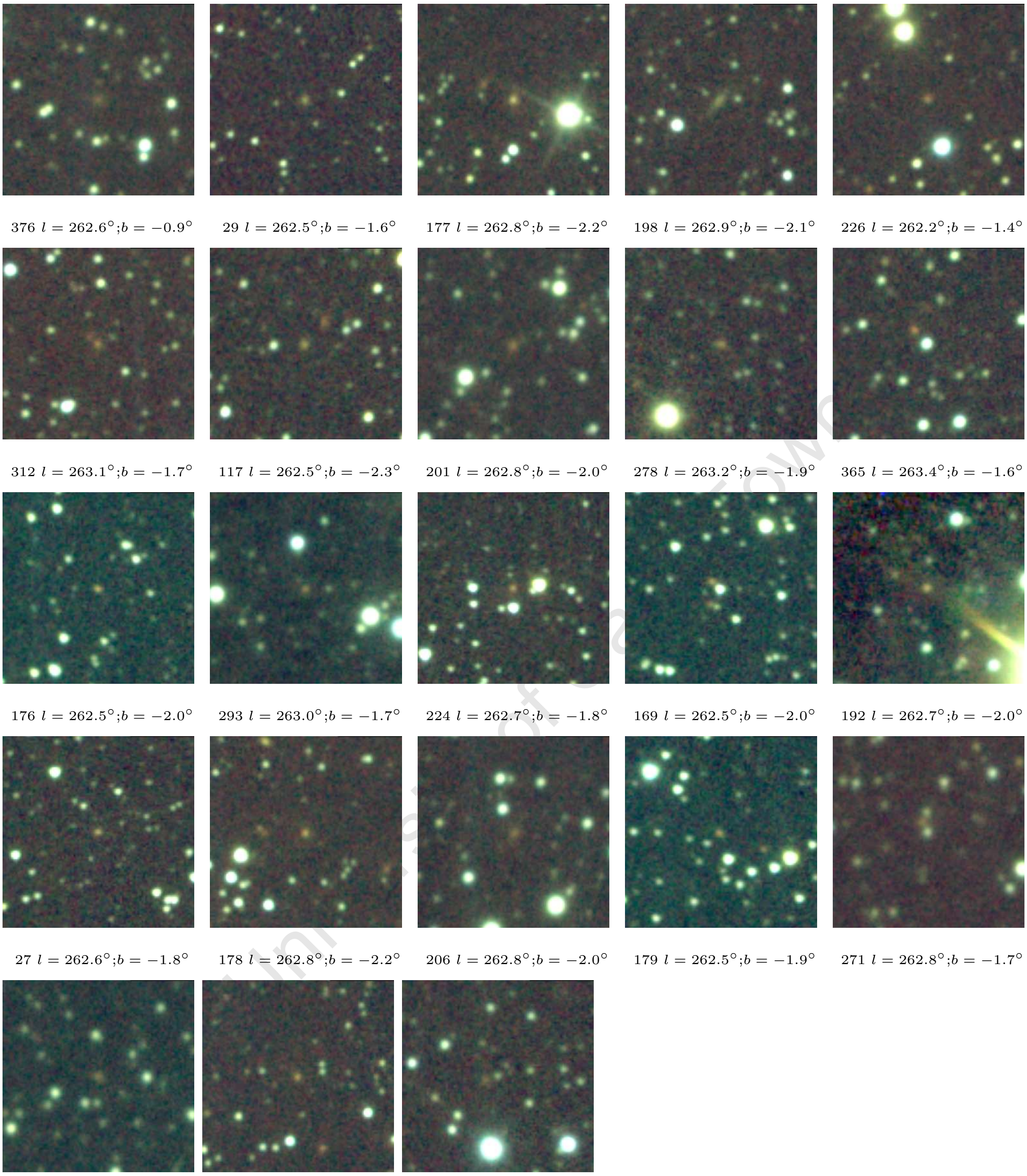
376 $l = 262.6^\circ; b = -0.9^\circ$ 29 $l = 262.5^\circ; b = -1.6^\circ$ 177 $l = 262.8^\circ; b = -2.2^\circ$ 198 $l = 262.9^\circ; b = -2.1^\circ$ 226 $l = 262.2^\circ; b = -1.4^\circ$

312 $l = 263.1^\circ; b = -1.7^\circ$ 117 $l = 262.5^\circ; b = -2.3^\circ$ 201 $l = 262.8^\circ; b = -2.0^\circ$ 278 $l = 263.2^\circ; b = -1.9^\circ$ 365 $l = 263.4^\circ; b = -1.6^\circ$

176 $l = 262.5^\circ; b = -2.0^\circ$ 293 $l = 263.0^\circ; b = -1.7^\circ$ 224 $l = 262.7^\circ; b = -1.8^\circ$ 169 $l = 262.5^\circ; b = -2.0^\circ$ 192 $l = 262.7^\circ; b = -2.0^\circ$

27 $l = 262.6^\circ; b = -1.8^\circ$ 178 $l = 262.8^\circ; b = -2.2^\circ$ 206 $l = 262.8^\circ; b = -2.0^\circ$ 179 $l = 262.5^\circ; b = -1.9^\circ$ 271 $l = 262.8^\circ; b = -1.7^\circ$

338 $l = 263.1^\circ; b = -1.5^\circ$ 127 $l = 262.7^\circ; b = -2.4^\circ$ 304 $l = 262.9^\circ; b = -1.6^\circ$

Figure C.14: K_s^0 magnitude from 15.63 - 16.14 mag

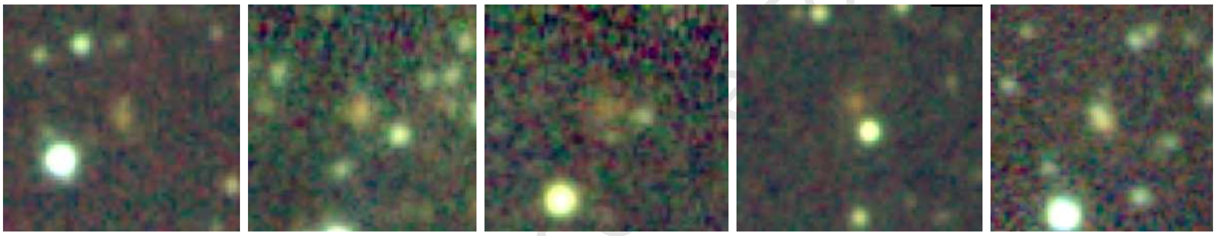

263 $l = 262.3^\circ; b = -1.4^\circ$ 33 $l = 262.2^\circ; b = -1.4^\circ$ 1 $l = 262.1^\circ; b = -1.6^\circ$ 150 $l = 262.3^\circ; b = -2.0^\circ$ 99 $l = 262.7^\circ; b = -2.6^\circ$

Figure C.15: These images are $20'' \times 20''$ due to being close to an edge.

Appendix D

2MASS XSC sources

D.1 Rejected 2MASS XSC Sources

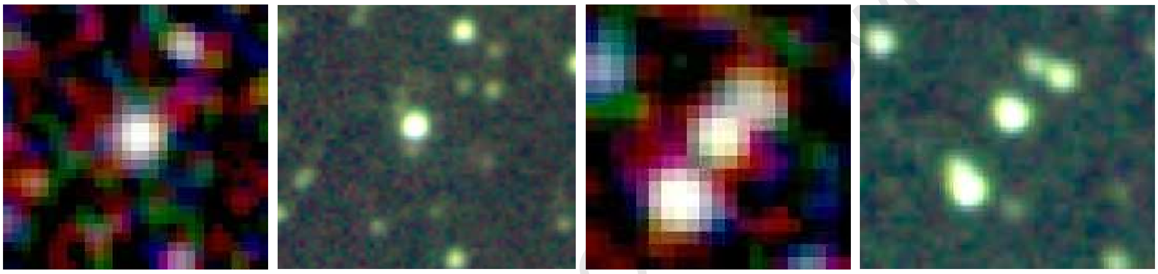

08331721-4310308 IRSF 08351544-4352497 IRSF

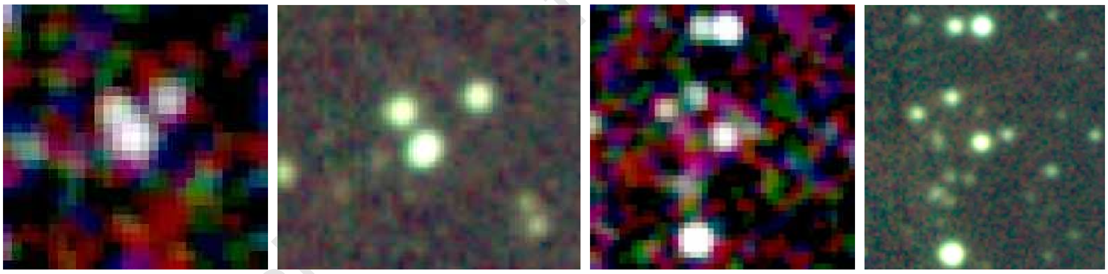

08335545-4418394 08335942-4408005

Figure D.1

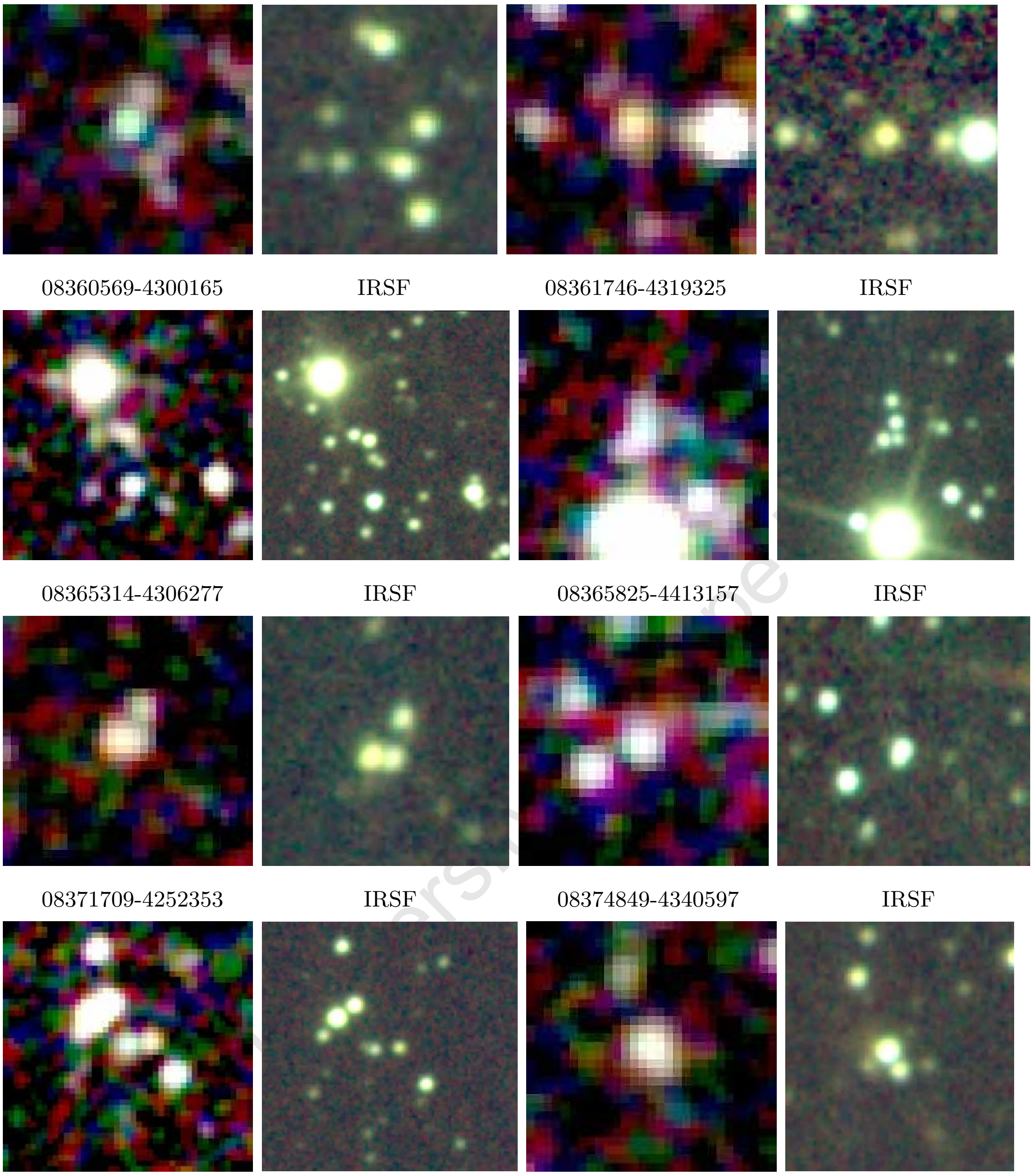

08360569-4300165 IRSF 08361746-4319325 IRSF

08365314-4306277 IRSF 08365825-4413157 IRSF

08371709-4252353 IRSF 08374849-4340597 IRSF

08381485-4329199 IRSF 08382215-4303379 IRSF

Figure D.2

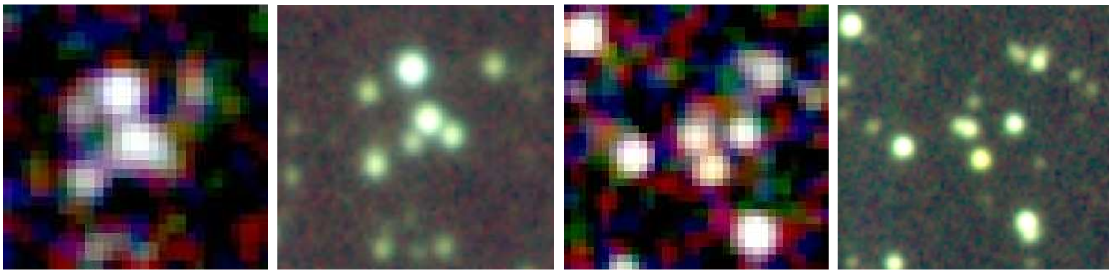

08383624-4350284 IRSF 08384025-4254085 IRSF

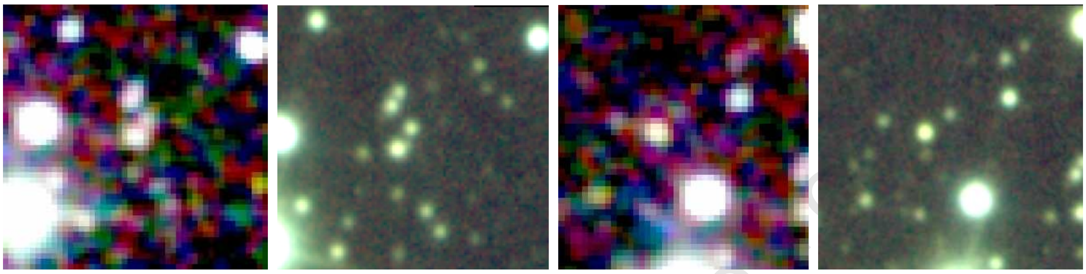

08403554-4255307 IRSF 08403790-4255167 IRSF

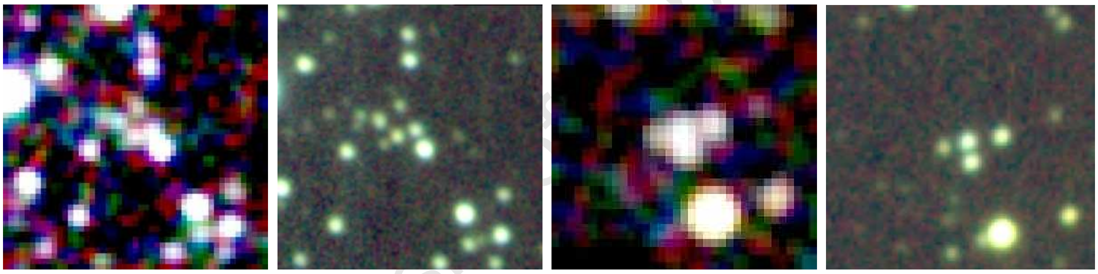

08404082-4423007 IRSF 08392572-4329064 IRSF

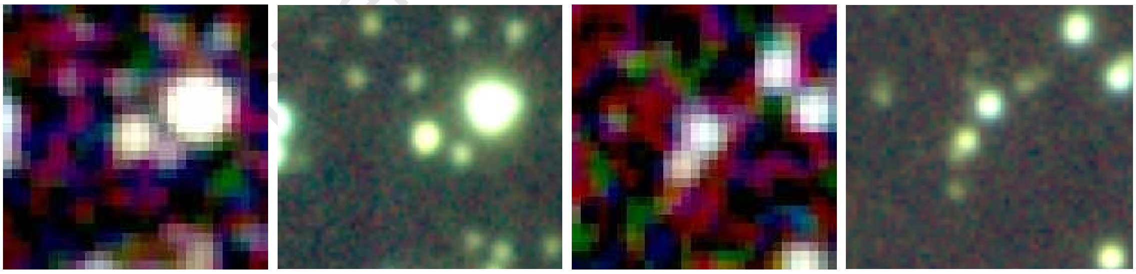

08395600-4338243 IRSF 08404944-4325307 IRSF

Figure D.3

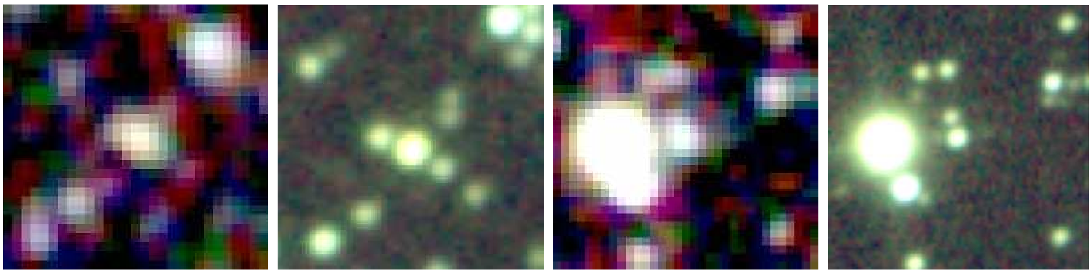

08405617-4348127 IRSF 08410227-4349127 IRSF

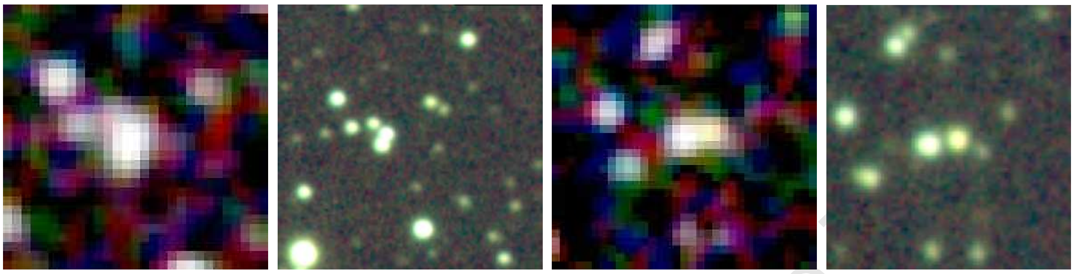

08400575-4253224 IRSF 08344072-4252348 IRSF

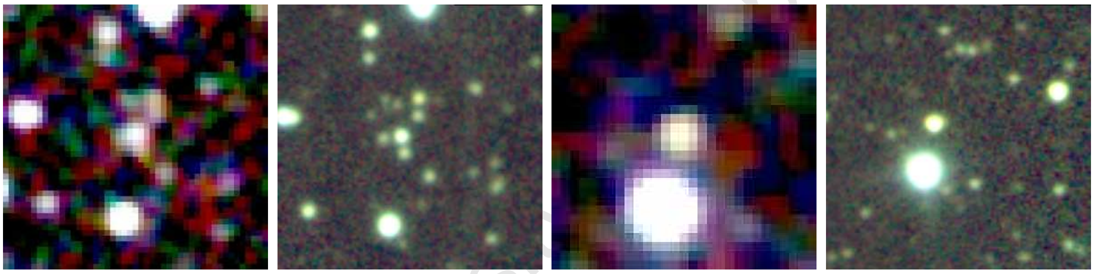

08354369-4327068 IRSF 08323802-4339358 IRSF

08331690-4332178 IRSF

Figure D.4

Bibliography

Alexander, T., Sturm, E., Lutz, D., Sternberg, A., Netzer, H., Genzel, R., 1999, *ApJ*, **512**, 204

Allamandola, L.J., Tielens, A.G.G.M., Barker, J.R., 1985, *ApJL*, **290**, L25

Allende Prieto, C.A., Lambert, D.L., Asplund, M., 2001, *ApJ*, **556**, L63

Alonso-Herrero, A., Rieke, G.H., Rieke, G.H., Colina, L., Pérez-González, P.G., Ryder, S.D., 2006, *ApJ*, **650**, 835.

Appleton, P.N. et al., 2004, *ApJS*, **154**, 147

Armus, L. et al., 2006, *ApJ*, **640**, 204

Armus, L. et al., 2007, *ApJ*, **656**, 148

Baan, W.A., Klöckner, H.-R., 2006, *A&A*, **449**, 559

Barden, M. et al., 2005, *ApJ*, **635**, 959

Barth, A., 2007, *AJ*, **133**, 1085

Bell, E.F., 2003, *ApJ*, **586**, 794

Bell, E.F., 2008, preprint(astro-ph/0801.0599)

Bell, E.F., McIntosh, D.H., Katz, N., Weinberg, M., 2003, *ApJS*, **149**, 289

Bell, E.F., et al., 2005, *ApJ*, **625**, 23

Bertschinger, E., 1998, *ARA&A*, **36**, 599

Blanton, M.R., et al., 2003, *ApJ*, **592**, 794

Boselli, A., Lequeux, J., Gavazzi, G., 2002, *A&A*, **384**, 33

Bothun, G.D., Impey, C.D., Malin, D.F., Mould, J.R., 1987, *AJ*, **94**, 23

Bothun, G., Impey, C., McGaugh, S., 1997, *PASP*, **109**, 745

Bothun, G.D., Schombert, J.M., Impey, C.D., Sprayberry, D., McGaugh, S.S., 1993, *AJ*, **106**, 530

Boulanger, F., Boissel, P., Cesarsky, D., Ryter, C., 1998, *A&A*, **339**, 194

Brandl, B.R. et al., *ApJ*, **653**, 1129

Braun, R., Thilker, D., Walterbos, R.A.M., 2003, *A&A*, **406**, 829

Bregman, J.D., Bregman, J.N., Temi, P., 2006, preprint(astro-ph/0604.4369)

Bressan, A., Silva, L., Granato, G.L., 2002, *A&A*, **392**, 377

Bruzual A.G., Charlot, S., 1993, *ApJ*, **405**, 538

Calzetti, D. et al., 2005, *ApJ*, **633**, 871.

Calzetti, D. et al., 2007, *ApJ*, **666**, 870.

Cardelli, J.A., Clayton, G.C., Mathis, J.M., 1989, *ApJ*, **345**, 245

Chiar, J.E., Tielens, A.G.G.M., 2006, *ApJ*, **637**, 774

Cluver, M.E., Jarrett, T.H., Appleton, P.N., Kraan-Korteweg, R., Woudt, P.A., Koribalski, B.S., Donley, J.L., Wakamatsu, K., Nagayama, T., 2008, *ApJL*, **686**, 17

Cole, S., Lacey, C.G., Baugh, C.M., Frenk, C.M., 2000, *MNRAS*, **319**, 168

Cole, S., et al., 2001, *MNRAS*, **326**, 255

Condon, J.J., 1992, *AR&A*, **30**, 575

Conselice, C.J. et al., 2007, *MNRAS*, **381**, 962

Cowie, L.L., Gardner, J.P., Lilly, S.J., McLean, I.S., 1990, *ApJ*, **360**, L1

Cram, L., Hopkins, A., Mobasher, B., Rowan-Robinson, M., 1998, *ApJ*, **507**, 155

Cutri, R.M., et al., 2000, The 2MASS Explanatory Supplement

Daddi, E., Dannerbauer, H., Elbaz, D., Dickinson, M., Morrison, G., Stern, D., Ravindranath, S., 2008, *ApJ*, **673**, L21

Dale, D.A., Giovanelli, R., Haynes, M.P., Scodeggio, M., Hardy, E., Campusano, L.E., 1997, *AJ*, **114**, 455

Dale, D.A., Helou, G., 2002, *ApJ*, **576**, 159

Dale, D.A. et al., 2000, *AJ*, **120**, 583

Dale, D.A., et al., 2005, *ApJ*, **633**, 857

Dale, D.A. et al., 2006, *ApJ*, **646**, 161

Dale, D.A., et al., 2007, *ApJ*, **655**, 863

Dale, D.A., et al., 2008, in prep.

Das, M., O'Neil, K., Vogel, S.N., McGaugh, S.S., 2006, *ApJ*, **651**, 853

Desai, V., et al., 2007, *ApJ*, **669**, 810

de Naray, R.K., McGaugh, S.S., de Blok, W.J.G., 2004, *MNRAS*, **355**, 887

Donley, J.L., Koribalski, B.S., Staveley-Smith, L., Kraan-Korteweg, R.C., Schroder, A., Henning, P.A., 2006, *MNRAS*, **369**, 1741.

Donley, J.L., et al., 2005, *AJ*, **129**, 220

Draine, B.T., Li, A., 2007, *ApJ*, **657**, 810

Draine, B.T. et al., 2007, *ApJ*, **663**, 866

Dutra, C.M., Santiago, B.X., Bica, E., 2002, *A&A*, **381**, 219

Erdoğdu, P., et al., 2006a, *MNRAS*, **368**, 1515

Erdoğdu, P., et al., 2006b, *MNRAS*, **373**, 45

Fairall, A., 1998, *Large-Scale Structures in the Universe*, John Wiley & Sons Ltd in association with Praxis Publishing Ltd, West Sussex, England.

Farrah, D., et al., 2001, *MNRAS*, **326**, 1333

Fazio, G. et al., 2004, *ApJS*, **154**, 10

Flaherty, K.M., Pipher, J.L., Megeath, S.T., Winston, E.M., Gutermuth, R.A., Muzerolle, J., Allen, L.E., Fazio, G.G., 2007, *ApJ*, **663**, 1069

Fuente, A., Martín-Pintado, J., Rodríguez-Fernández, N.J., Cernicharo, J., Gerin, M., 2000, *A&A*, **354**, 1053

Gao, Y., Solomon P.M., 2004, *ApJ*, **606**, 271

Genzel, R. et al., 1998, *ApJ*, **498**, 579

Gillett, F.C., Forrest, W.J., & Merrill, K.M., 1973, *ApJ*, **183**, 87

Glazebrook, K., Peacock, J.A., Collins, C.A., Miller, L., 1994, *MNRAS*, **266**, 65

Grogin, N.A., Geller, M.J., 2000, *AJ*, **119**, 32

Helou, G., Soifer, B.T., Rowan-Robinson, M., 1985, *ApJ*, **298**, L7

Helou, G., et al., 2004, *ApJS*, **154**, 253

Henning, P.A., Kraan-Korteweg, R.C., Staveley-Smith, L., 2005, in Fairall A.P., Woudt, P.A., eds, ASP Conf. Ser., Vol 329, Nearby Large-Scale Structures and the Zone of Avoidance, Astron. Soc. Pac., San Francisco, p. 199

Hess, R., 1924, *Astronomische Nachrichten*, **220**, 65

Higdon, S.J.U., Armus, L., Higdon, J.L., Soifer, B. T., Spoon, H.W.W., 2006, *ApJ*, **648**, 323

Hinz, J.L., Rieke, G.H., 2006, *ApJ*, **646**, 872

Ho, L.C., Keto, E., 2007, *ApJ*, **658**, 314

Hoffman, Y., Silk, J., Wyse, R.F.G, 1992, *ApJ*, **388**, L13

Hollenbach, D.J., Tielens, A.G.G.M., 1997, *ARA&A*, **35**, 179

Hollenbach, D.J., Tielens, A.G.G.M., 1999, *Rev. Mod. Phys.*, **71**, 173

Houck, J.R. et al., 2004, *ApJS*, **154**, 18

Huang, J.-S., Cowie, L.L., Gardner, J.P., Hu, E.M., Songaila, A., Wainscoat, R.J., 1997, *ApJ*, **476**, 12

Huchra, J., Davis, M., Latham, D., Tonry, J., 1983, *ApJS*, **52**, 89

Huchra, J., Jarrett, T.H., Skrutskie, M., Cutri, R., Schneider, S., Macri, L., Steining, R., Mader, J., Martimbeau, N., George, T., 2005, in Fairall A.P., Woudt, P.A., eds, ASP Conf. Ser., Vol 329, Nearby Large-Scale Structures and the Zone of Avoidance, Astron. Soc. Pac., San Francisco, p. 135

Hudson, M.J., Smith, R.J., Lucey, J.R., Branchini, E., 2004, *MNRAS*, **352**, 61

Impey, C., Bothun, G., 1989, *ApJ*, **341**, 89

Ishida, C.M., 2004, PhD Thesis, University of Hawaii

Indebetouw, R. et al., 2005, *ApJ*, **619**, 931

Jarrett, T.H., 2000, *PASP*, **112**, 1008

Jarrett, T.H., 2004, *PASA*, **31**, 396

Jarrett, T.H., Chester, T., Cutri, R., Schneider, S.E., Huchra, J.P., 2003, *AJ*, **125**, 525

Jarrett, T.H., et al., 2000, *AJ*, **120**, 298

Jones, H. et al., 2004, *MNRAS*, **355**, 747

Kandori, R., et al., 2005, *AJ*, **130**, 2166

Kaneda, H., Onaka, T., Sakon, I., 2005, *ApJ*, **632**, L83

Kato, D., et al., 2007, *ApJ*, **59**, 615

Kauffmann, G., White, S.D.M., Guiderdoni, B., 1993, *MNRAS*, **264**, 201

Kauffmann, G, 1996, *MNRAS*, **281**, 487.

Kauffmann, G., et al., 2003, *MNRAS*, **341**, 33

Kennicutt Jr., R.C., 1992, *ApJ*, **388**, 310

Kennicutt Jr., R.C., 1998a, *ApJ*, **498**, 541

Kennicutt Jr., R.C., 1998b, *ARA&A*, **36**, 189

Kennicutt Jr., R.C., et al., 2003, *PASP*, **115**, 928

Knezek, P.M., 1993, Ph.D. Thesis, University of Massachusetts

Kobulnicky, H.A., Kewley, L.J., 2004, *ApJ*, **617**, 240

Kocevski, D.D., Ebeling, H., 2006, *ApJ*, **645**, 1043

Kochanek, C.S., White, M., Huchra, J., Macri, L., Jarrett, T.H., Schneider, S.E., Mader, J., 2003, *ApJ*, **585**, 161

Kochanek, C.S., et al., 2001, *ApJ*, **560**, 566

Kolatt, T., Dekel, A., Lahav, O., 1995, *MNRAS*, **275**, 797

Kotze, J.P., 2007, MSc Thesis, University of Cape Town

Kraan-Korteweg, R.C., 2005, *Rev. Mod. Astron.*, **18**, 48

Kraan-Korteweg, R.C., Jarrett, T.H., 2005, in Fairall A.P., Woudt, P.A., eds, ASP Conf. Ser., Vol 329, Nearby Large-Scale Structures and the Zone of Avoidance, Astron. Soc. Pac., San Francisco, p. 119

Kraan-Korteweg, R.C., Lahav, O., 2000, *A&ARv*, **10**, 211

Kraan-Korteweg, R.C., Staveley-Smith, L., Donley, J., Koribalski, B. & Henning, P.A., 2005, in Colless, M., Staveley-Smith, L., Stathakis, R., eds, IAU Symp. 216, Maps of the Cosmos, Astron. Soc. Pac., San Francisco, p. 203

Kraan-Korteweg, R.C., Woudt, P.A., Cayatte, V., Fairall, A.P., Balkowski, C., Henning, P.A., 1996, *Nature*, **379**, 519

Laurent, O., Mirabel, I.F., Charmandaris, V., Gallais, P., Madden, S.C., Sauvage, M., Vigroux, L., Cesarsky, C., 2000, *A&A*, **359**, 887

Le Floc'h, E., et al., 2005, *ApJ*, **632**, 169

Léger, A., Puget, J.L., 1984, *A&A*, **137**, L5

Leitherer, C., Heckman, T.M., 1995, *ApJS*, **96**, 9

Lutz, D., Kunze, D., Spoon, H.W.W., Thornley, M.D., 1998, *A&A*, **333**, L75

Lynden-Bell, D., 1967, *MNRAS*, **136**, L101

Lynden-Bell, D., Faber, S.M., Burstein, D., Davies, R.L., Dressler, A., Terlevich, R.J., Wegner, G., 1988, *ApJ*, **326**, 19

Mao, S., Mo, H.J., White, S.D.M., 1998, *MNRAS*, **297**, L71

Marcillac, D., Elbaz, D., Chary, R.R., Dickinson, M., Galliano, F., Morrison, G., 2006, *A&A*, **451**, 57

Masters, K.L., Giovanelli, R., Haynes, M.P., 2003, *ApJ*, **126**, 158

Matthews, L.D., van Driel, W., Monnier-Ragaigne, D., 2001, *A&A*, **365**, 1

McGaugh, S.S., 1994, *ApJ*, **426**, 135

McLeod, B.A., & Rieke, M.J., 1995, *ApJ*, **454**, 611

Melbourne, J., Koo, D.C., Le Floc'h, E., 2005, *ApJ*, **632**, L65

Melbourne, J., et al., 2008, *ApJ*, **135**, 1207

Meyer, M.J. et al., 2004, *MNRAS*, **350**, 1195

Mo, H.J., Mao, S., White, S.D.M., 1998, *MNRAS*, **295**, 319

Murphy, E.J. et al., 2006, *ApJ*, **638**, 157

Nagayama, T., Nagashima, C., Nakajima, Y., Nagata, T., Sato, S., Nakaya, H., Yamamuro, T., Sugitani, K., Tamura, M., 2003, Iye, M., Moorwood, A.F.M., eds, Proc. of SPIE, 4841, 459.

Nagayama, T. et al., 2004, *MNRAS*, **354**, 980

Nagayama, T., et al., 2006, *MNRAS*, **368**, 534

Nagashima, C., Nagayama, T., Tamura, M., Sugitani, K., Nagata, T., Hirao, T., Nakaya, H., Yanagisawa, K., Sato, S., 1999, Nakamoto, T., eds, Proc. of Star Formation 1999, p.397.

Oosterloo, T.A., Morganti, R., Sadler, E.M., van der Hulst, T., Serra, P., 2007, *A& A*, **465**, 787

O'Neil, K., Schinnerer, E., 2004, *ApJ*, **615**, L109

O'Neil, K., Bothun, G.D., van Driel, W., Monnier Ragaigne, D., 2004, *A&A*, **428**, 823

Peebles, P.J.E., 2001, *ApJ*, **557**, 495

Peeters, E., Hony, S., Van Kerckhoven, C., Tielens, A.G.G.M., Allamandola, L.J., Hudgins, D.M., Bauschlicher, C.W., 2002, *A&A*, **390**, 1089

Peeters, E., Spoon, H.W.W., Tielens, A.G.G.M., 2004, *ApJ*, **613**, 986

Pérez-González, P.G. et al., 2005, *ApJ*, **630**, 82.

Pickering, T.E., Impey, C.D., van Gorkom, J.H., Bothun, G.D., 1997, *AJ*, **114**, 1858

Press, W.H., Schechter, P., 1974, *ApJ*, **187**, 425

Puget, J.L., Léger, A., 1989, *ARA&A*, **27**, 161

Rahman, N., Howell, J.H., Helou, G., Mazzarella, J.M., Buckalew, B., 2007, *ApJ*, **663**, 908.

Rapacioli, M., Calvo, F., Joblin, C., Parneix, P., Toublanc, D.., Spiegelman, F., 2006, *A&A*, **460**, 519

Renzini, A., 2007, in ASP Conf. Ser. 380, At the Edge of the Universe: Latest Results from the Deepest Astronomical Surveys, ed. J. Afonso, H.C. Ferguson, B. Mobasher & R. Norris (San Francisco:ASP), 309

Rieke, G. et al., 2004, *ApJS*, **154**, 204

Rigopoulou, D., Kunze, D., Lutz, D., Genzel, R., & Moorwood, A.F.M., 2002, *A& A*, **389**, 374

Roberts, M.S., Haynes, M.P., 1994, *ARA&A*, **32**, 115

Rojas, R.R., Vogeley, M.S., Hoyle, F., Brinkmann, J., 2005, *ApJ*, **624**, 571

Roussel, H., et al., 2007, *ApJ*, **669**, 959

Sancisi, R., Fraternali, F., preprint(astro-ph/0707.2377)

Sanders, D.B., Mirabel, I.F., 1996, *ARA&A*, **34**, 749

Schinnerer, E., Eckhart, A., Quirrenbach, A., Böker, T., Tacconi-Garman, L.E., Krabbe, A., 1997, *ApJ*, **488**, 174

Schlegel, D.J., Finkbeiner, D.P., Davis, M., 1998, *ApJ*, **500**, 525

Schmitt, H.R., Calzetti, D., Armus, L., Giavalisco, M., Heckman, T.M., Kennicutt Jr., R.C., Leitherer, C., Meurer, G.R., 2006, *ApJ*, **643**, 173

Schombert, J., 1998, *AJ*, **116**, 1650

Schombert, J., G.D., Schneider, S.E., McGaugh, S.S., 1992, *AJ*, **103**, 1107

Schröder, A.C., Drinkwater, M.J., Richter, O.-G., 2001, *A&A*, **376**, 98

Schröder, A.C., Mamon, G.A., Kraan-Korteweg, R.C., Woudt, P.A., 2007, *A&A*, **466**, 481

Schröder, A.C., Kraan-Korteweg, R.C., Mamon, G.A., Woudt, P.A., 2005, in Fairall A.P., Woudt, P.A., eds, ASP Conf. Ser., Vol 329, Nearby Large-Scale Structures and the Zone of Avoidance, Astron. Soc. Pac., San Francisco, p. 167

Sérsic, J. L., 1968, Boletin de la Asociacion Argentina de Astronomia La Plata Argentina, 12, 15

Silva, L., Granato, G., Bressan, A., Danese, L., 1998, *ApJ*, **509**, 103

Skelton, R.E., 2007, MSc Thesis, University of Cape Town

Skrutskie, M.F., et al., 2006, *AJ*, **131**, 1163

Smith, J.D.T. et al., 2004, *ApJSS*, **154**, 199

Smith, J.D.T. et al., 2007, *PASP*, **119**, 1133

Solomon, P.M., Van den Bout, P.A., 2005, *ARA&A*, **43**, 677

Solomon, P.M., Barrett, J.W., 1991, in Combes, F., Casoli, F., eds, IAU Symp. 146, Dynamics of Galaxies and Their Molecular Cloud Distributions, Kluwer, Dordrecht, p. 235

Sprayberry, D., Impey, C.D., Bothun, G.D., Irwin, M.J., 1995, *AJ*, **109**, 558

Springel, V. et al., 2005, *Nature*, **435**, 629

Spoon, H.W.W., Marshall, J.A., Houck, J.R., Elitzur, M., Hao, L., Armus, L., Brandl, B.R., Charmandaris, V., 2007, *ApJ*, **654**, L49

Staveley-Smith, L., et al., 1996, *PASA*, **13**, 243

Strauss, M., et al., 2002, *AJ*, **124**, 1810

Stringer, M.J., Benson, A.J., 2007, *MNRAS*, **382**, 641

Sturm, E., Lutz, D., Tran, D., Feuchtgruber, H., Genzel, R., Kunze, D., Moorwood, A.F.M., Thornley, M.D., 2000, *A&A*, **358**, 481

Sturm, E., Lutz, D., Verma, A., Netzer, H., Stermberg, A., Moorwood, A.F.M., Olivia, E., Genzel, R., 2002, *A&A*, **393**, 821

Szomoru, A., Gorkom, J.H., Gregg, M.D., Strauss, M.A., 1996, *AJ*, **111**, 2150

Tagg, J, 2008, MSc Thesis, University of Cape Town

Thilker, D.A., et al., 2007, *ApJSS*, **173**, 572.

Tielens, A.G.G.M., Hollenbach, D., 1985, *ApJ*, **291**, 722

Trujillo, I. et al., 2006, *MNRAS*, **373**, L36

Vallenari, A., Schmidtobreick, L., Bomans, D.J., 2005, *A&A*, **435**, 821

van den Hoek, L.B., de Blok, W.J.G., van der Hulst, J.M., de Jong, T., 2000, *A&A*, **357**, 397

Vazquez, G.A., Leitherer, C., 2005, *ApJ*, **621**, 695

Verma, A., Lutz, D., Sturm, E., Sternberg, A., Genzel, R., Vacca, W., 2003, *A&A*, **403**, 829

Villegas, D., Kissler-Patig, M., Jordán, A., Goudfrooij, P., Zwaan, M., 2008, *AJ*, **135**, 467

Wang, J.L., Xia, X.Y., Mao, S., Cao, C., Wu, Ho., Deng, Z.G., 2006, *ApJ*, **649**, 722

White, S.D.M., Rees, M.J., 1978, *MNRAS*, **183**, 341

Wong, O.I. et al., 2006, *MNRAS*, **371**, 1855

Woudt, P.A., 1998, Ph.D. thesis, University of Cape Town

Wu, H., Cao, C., Hao, C., Liu, F., Wang, J., Xia, X., Deng, Z., Young, C.K., 2005, *ApJ*, **632**, L79

Wyrowski, F., Walmsley, C.M., Goss, W.M., Tielens, A.G.G.M., 2000, *ApJ*, **543**, 245

Yao, L., Seaquist, E.R., Kuno, N., Dunne, L., 2003, *ApJ*, **588**, 771

Young, J.S., Devereux, N.A., 1991, *ApJ*, **373**, 414

Young, J.S., Scoville, N., 1982, *ApJ*, **260**, L41